Physics of the Solid State, Vol. 43, No. 9, 2001, pp. 1599–1602. Translated from Fizika Tverdogo Tela, Vol. 43, No. 9, 2001, pp. 1537–1540.
Original Russian Text Copyright © 2001 by Sevastyanova, Yalovega, Marcelli, Mansour, Soldatov.

METALS AND SUPERCONDUCTORS

Nearest Surroundings of Aluminum Atoms and Features of the Electron Structure of $Al_{90}Fe_xCe_{10-x}$ Alloys (x = 3, 5, 7)

T. I. Sevastyanova*, G. É. Yalovega, A. Marcelli**, A. Mansour***, and A. V. Soldatov***
**Rostov State University, Rostov-on-Don, 344090 Russia*
e-mail: Soldatov@phys.rsu.ru
***INFN Laboratori Nazionali di Frascati, 00044 Frascati, Italy*
****Naval Surface Warfare Center, Caderock Division, 20903-5640 Silver Spring, Maryland, USA*

Received February 2, 2001

Abstract—The spectra of x-ray absorption near-edge structure (XANES) were measured at the *K*-edge of aluminum in $Al_{90}Fe_xCe_{10-x}$ alloys (x = 3, 5, 7). A theoretical XANES analysis at the Al *K*-edge was performed for $Al_{90}Fe_5Ce_5$ by using the multiple scattering algorithm. A comparison of the experimental and theoretical results allowed establishment of the most probable model of local surroundings of aluminum atoms in the alloy system studied. The density of free Al and Fe electron states in the conduction band was determined. It was found that the interaction between Al *p* states and Fe *d* states leads to pushing of the former states by the latter ones. *© 2001 MAIK "Nauka/Interperiodica".*

The physicochemical properties of alloys depend on the particularities of their electron structure, which determined, in turn, by features of the geometric structure of the alloys [1]. Previously, the structure of $Al_{90}Fe_xCe_{10-x}$ alloys was studied using methods of neutron and x-ray scattering [2], while $Al_{100-2x}Co_xCe_x$ (x = 8–10) and $Al_{80}Fe_{10}Ce_{10}$ alloys were studied by measuring the extended x-ray absorption fine structure (EXAFS) [3]. Nevertheless, fine details in the geometric structure of alloys of the Al–Fe(Co)–Ce system still remain insufficiently clear.

The geometric structure of $Al_{90}Fe_xCe_{10-x}$ alloys in the vicinity of iron atom positions was refined by analysis of the x-ray absorption near-edge structure (XANES) at the Fe *K*-edge [4]. However, the features of the geometric structure of these alloys in the environment of aluminum atoms remained undetermined.

Also insufficiently studied are the features of interaction between the electron states of aluminum and those of other atoms. It was demonstrated for the $Al_{63}Cu_{25}Fe_{12}$ alloy that the electron states of aluminum are highly sensitive to the character of the environment: the *p*–*d* states of aluminum in such quasi-crystalline alloys interact with the *d* states of transition element atoms near the Fermi level [5]. It was also established that the *p* states of aluminum overlap with the *s* and *d* states of nickel and cobalt in the conduction band, which results in the formation of a significant pseudogap in the 3*p* and 3*s*–*d* states of aluminum in $Al_{65}Cu_{15}Co_{20}$ and $Al_{70}Co_{15}Ni_{15}$ quasi-crystals [6].

XANES measurements offer a unique method for investigation of the unoccupied electron states of aluminum [7]. The aforementioned structural sensitivity of the unoccupied *p* states of aluminum is manifested in the XANES spectra at the Al *K*-edge being significantly different for aluminum atoms in various compounds [8]. However, useful information can be extracted from the experimental spectra only by means of theoretical analysis. Investigations of the geometric and electron structures of silicate and oxide minerals showed that a promising approach to such a theoretical analysis of XANES is offered by the multiple scattering method [9].

We have measured the Al *K*-edge XANES spectra of $Al_{90}Fe_3Ce_7$, $Al_{90}Fe_5Ce_5$, and $Al_{90}Fe_7Ce_3$ alloys and have theoretically analyzed the XANES spectrum of the $Al_{90}Fe_5Ce_5$ alloy using the algorithm of multiple scattering in the real space.

1. EXPERIMENTAL AND CALCULATION METHODS

The x-ray absorption spectra of aluminum in the alloys studied were measured using a JUMBO facility at the Stanford Synchrotron Radiation Laboratory (SSRL). The measurements were performed by the total electron yield method using an YB_{66} crystal as a monochromator. The experimental energy resolution in the spectral range studied was 0.6 eV. The energy scale was calibrated with respect to an Al foil. The spectra were corrected for the storage ring current function.

The algorithm of the multiple scattering method used in this study was described elsewhere [10]. The phase shifts were calculated in the crystal muffin-tin (MT) potential with touching MT spheres. The MT radii and constants were determined using the procedure of MT potential construction described in [10]. The crystal field potential was constructed using the

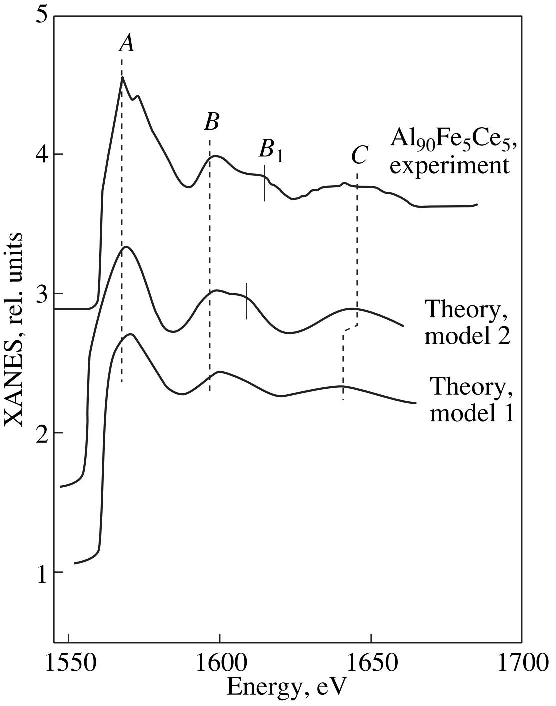

Fig. 1. A comparison of the experimental XANES spectrum at the Al *K*-edge of the $Al_{90}Fe_5Ce_5$ alloy and theoretical spectra calculated for two models 1 and 2, corresponding to the $FeAl_3$ alloy [13] and the $FeAl_6$ alloy [14] with a 3.4% shorter interatomic distance.

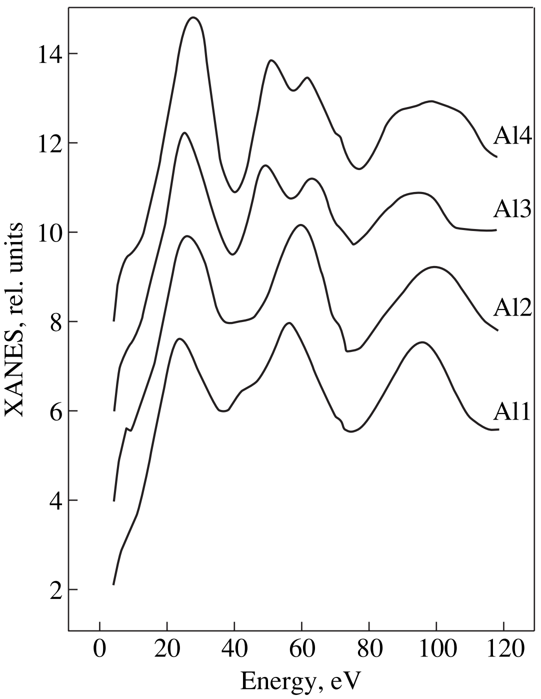

Fig. 2. Theoretical x-ray absorption spectra calculated for four inequivalent Al positions in model 2. The energy scale zero corresponds to that of the muffin-tin potential used in the calculation.

Mattheiss scheme with an exchange parameter of 1.0. The charge densities of atoms were determined by a self-consistent Dirac–Slater calculation involving phase shifts for an orbital momentum of up to 2.

A comparison of the experimental and theoretical XANES spectra was performed taking into account the experimental spectrum broadening due to a finite lifetime of the x-ray core hole, a finite mean free path of photoelectrons, and the experimental resolution. The imaginary part of the complex potential took into account the internal Al *K*-level width (0.42 eV) [11], the photoelectron mean free path as a function of the energy [12], and the experimental energy resolution (0.6 eV).

2. RESULTS AND DISCUSSION

An analysis of the crystallographic data available for the ternary alloy system studied suggests that the most probable models for a local structure description are offered by the binary alloys $FeAl_6$ and $FeAl_3$ [13, 14]. Previously [4], we demonstrated that a local structure in the vicinity of iron atoms in $Al_{90}Fe_3Ce_7$ is better described by the $FeAl_6$ alloy model with a 3.4% shorter interatomic distance, which corresponds to the experimental data obtained from an analysis of the EXAFS spectra of structurally close alloy systems [15]. For this reason, the most probable structure of the environment for aluminum atoms in the $Al_{90}Fe_5Ce_5$ alloy was also determined taking into account the following model compounds: model 1, $FeAl_3$ alloy [13]; and model 2, $FeAl_6$ alloy [14] with a 3.4% shorter interatomic distance.

Figure 1 presents a comparison of the experimental XANES spectrum at the Al *K*-edge in the $Al_{90}Fe_5Ce_5$ alloy and theoretical spectra calculated for the aforementioned model alloys. As is seen, the structure of theoretical XANES spectra for both models reflects the main features observed in the experimental curve. However, splitting of the second peak into two components (*B* and B_1) is reflected only by the $FeAl_6$ model. The x-ray spectrum of this model also provides better agreement with the experiment in the energy position of peak *C*. Thus, we may conclude that a local structure of the environment of aluminum atoms in the $Al_{90}Fe_5Ce_5$ alloy is close to that in the $FeAl_6$ model alloy with a 3.4% shorter interatomic distance. A structure of the cluster of nearest neighbors surrounding an Al atom in the $FeAl_6$ model is presented in the table.

The $FeAl_6$ model structure exhibits four inequivalent positions of Al atoms [14]. Since the local environments of Al atoms in these positions are different, the shape of theoretical XANES spectra must also change on passage from one to another position. Figure 2 shows the Al *K*-edge XANES spectra calculated for the four inequivalent positions of model 2. In order to obtain a resultant spectrum that is comparable to the experiment (Fig. 1), the four partial spectra were added with the relative weights 1 : 2 : 2 : 1.

In the dipole approximation, the x-ray absorption coefficient $\alpha(E)$ at the Al *K*-edge is proportional to the density of unoccupied Al *p* states and to the matrix element of the dipole transition probability [16]. In the case of a smoothly varied matrix element, the x-ray absorption spectra can be used for obtaining information concerning the distribution of the corresponding partial densities of states in the conduction band [16].

Figure 3 shows the partial densities of Al *p* and Fe *d* states. As is seen from these curves, the matrix element of the transition probability varies by a factor of several tens in the energy range studied. Therefore, the spectra of x-ray absorption at the Al *K*-edge cannot be used for analysis of the distribution of the partial density of free Al *p* states in the conduction band of the $Al_{90}Fe_5Ce_5$ alloy. For this reason, we have theoretically calculated the density of Al *p* states for a crystal potential. We managed to obtain a good coincidence of the theoretical and experimental x-ray absorption spectra. For an analysis of the mutual influence of the Al *p* and Fe *d* states, we calculated the density of the latter states as well.

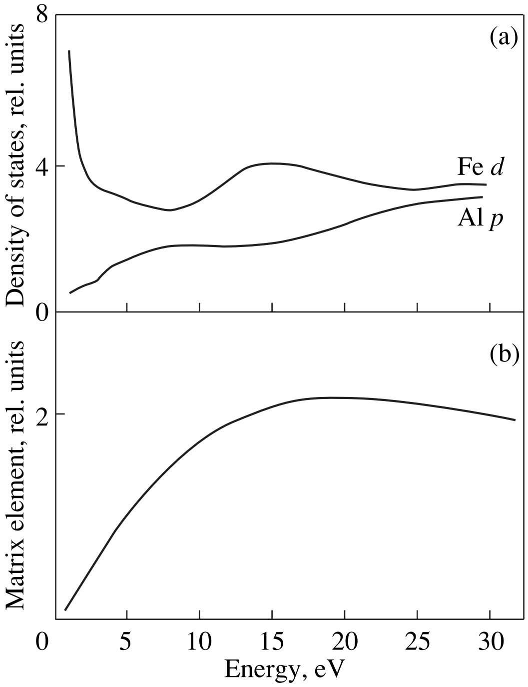

Fig. 3. Model alloy 2: (a) density of unoccupied electron states in the conduction band; and (b) matrix elements of the transition probability at the Al *K*-edge. Dashed line indicates the position of the Fermi energy.

In the pure aluminum, electrons in the conduction band are adequately described by a model of nearly free electrons, in which the density of states is proportional to the square root of the energy. However, the states of aluminum in the alloy under consideration (containing 5 at. % Fe) exhibit a specific interaction with Fe *d* states, which significantly changes the shape of the Al *p* density of states. In the energy intervals containing peaks in the Fe *d* density of states (1–3 and 11–20 eV), the Al *p* density of states exhibits troughs indicating that Fe *d* states push the free Al *p* states out of these intervals. Previously, an analogous interaction in the region of unoccupied states was observed for the *p* states of oxygen and the *d* states of iron in some oxides, as manifested in the characteristic features in their x-ray absorption spectra [17].

Thus, a theoretical analysis of the experimental XANES spectra at the Al *K*-edge allowed us to conclude that the most probable local structure in the environment of aluminum atoms in the $Al_{90}Fe_5Ce_5$ alloy is offered by that of the model binary alloy $FeAl_6$ with a 3.4% shorter interatomic distance. A specific interaction between free Al *p* states and Fe *d* states was observed in the alloys studied, which leads to a mutual repulsion of these states.

The structure of the atomic cluster surrounding the central absorbing Al atom in the $FeAl_6$ alloy model with a 3.42% shorter interatomic distance. The data refer to four inequivalent positions of Al atoms (Al1, Al2, Al3, and Al4)

Coordination sphere	Number of atoms in the sphere	Average radius of the sphere, Å	Coordination sphere	Number of atoms in the sphere	Average radius of the sphere, Å
	Al1			Al3	
1	1Fe + 2Al	2.4339	1	2Fe + 6Al	2.5901
2	8Al	2.7318	2	3Al	2.8217
3	2Al	2.2780	3	2Al	3.2986
	Al2			Al4	
1	2Al + 2Fe	2.5546	1	1Al + 4Fe	2.4862
2	7Al	2.7961	2	6Al	2.8239
3	4Al	3.2765	3	2Al	3.2789

REFERENCES

1. K. Lawniczak-Jablonska, R. Wojnecki, and J. Kachniarz, J. Phys.: Condens. Matter **12** (10), 2333 (2000).
2. H. Y. Hsieh, B. H. Toby, T. Egami, *et al.*, J. Mater. Res. **5** (12), 2807 (1990).
3. A. N. Mansour, C.-P. Wong, and R. A. Brizzolara, Phys. Rev. B **50** (17), 12401 (1994).
4. T. I. Sevastyanova, G. É. Yalovega, A. Mansour, *et al.*, Fiz. Tverd. Tela (St. Petersburg) **43** (6), 961 (2001) [Phys. Solid State **43**, 993 (2001)].
5. G. T. Laissardiere, Z. Dankhazi, E. Belin, *et al.*, Phys. Rev. B **51** (20), 14035 (1995).
6. E. Belin-Ferre, Z. Dankhazi, V. Fournee, *et al.*, J. Phys.: Condens. Matter **8** (34), 6213 (1996).
7. J. Wong, G. N. George, I. J. Pickering, *et al.*, Solid State Commun. **92** (7), 559 (1994).
8. Z. H. Levine and B. Ravel, J. Appl. Phys. **85** (1), 558 (1999).
9. D. Cabaret, P. Sainctavit, P. Ildefonse, and A.-M. Flank, J. Phys.: Condens. Matter **8** (20), 3691 (1996).
10. S. Della Longa, A. V. Soldatov, M. Pompa, and A. Bianconi, Comput. Mater. Sci. **4** (3), 199 (1995).
11. J. C. Fuggle and J. H. Inglesfield, *Unoccupied Electronic States* (Springer-Verlag, Berlin, 1992).
12. J. E. Muller, O. Jepsen, and J. W. Wilkins, Solid State Commun. **42** (5), 365 (1982).
13. P. J. Black, Acta Crystallogr. **8** (1), 43 (1955).
14. P. Villars and L. D. Calvert, in *Pearson's Handbook of Crystallographic Data for Intermetallic Phases* (American Society for Metals, Metals Park, 1985), Vol. 2, p. 920.
15. A. N. Mansour, G. Gibin, A. Marcelli, *et al.*, J. Synchrotron Radiat. **8** (3), 809 (2001).
16. A. Bianconi, in *X-ray Absorption: Principles, Applications and Techniques of EXAFS, SEXAFS, and XAFS*, Ed. by D. C. Koningsberger and R. Prins (Wiley, New York, 1989).
17. N. A. Povahzynaja, G. E. Yalovega, and A. V. Soldatov, Phys. Status Solidi B **195** (1), K1 (1996).

Translated by P. Pozdeev

Physics of the Solid State, Vol. 43, No. 9, 2001, pp. 1603–1610. Translated from Fizika Tverdogo Tela, Vol. 43, No. 9, 2001, pp. 1541–1547.
Original Russian Text Copyright © 2001 by Khokhlov, Krzhizhanovskiĭ, Prokhorov, Drobot'ko, Klimov, Levchenko.

METALS AND SUPERCONDUCTORS

An YBCO Film as a Josephson Medium Near T_c: Frequency and Field Dependences and Scaling Relationships

V. A. Khokhlov*, V. V. Krzhizhanovskiĭ*, A. Yu. Prokhorov*, V. F. Drobot'ko*, A. V. Klimov, and G. G. Levchenko***

**Donetsk Physicotechnical Institute, National Academy of Sciences of Ukraine, 83114 Donetsk, Ukraine*
e-mail: suhar@host.dipt.donetsk.ua
***Institute of Physics, Polish Academy of Sciences, 02-668 Warsaw, Poland*

Received August 18, 2000; in final form received January 26, 2001

Abstract—The diamagnetic response of a laser-deposited YBCO film was studied in weak exciting magnetic fields $H_{ac} = H_0 \sin\omega t$ (H_0 = 2–500 mOe, $\omega/2\pi$ = 1–30 kHz). An analysis of the experimentally measured diamagnetic response showed evidence of a ring character of the electric field flowing in the sample at small H_0 values. The plots of T_m (the temperature of maximum dissipative losses χ_1'') versus H_0 measured at various frequencies showed the existence of a certain critical field strength $H^*(\omega)$ at which the $(1 - T_m/T_c)$ versus $H_0^{2/3}$ plots exhibit a break. A logarithmic dependence of T_m on the frequency ω of the exciting field H_{ac} is reliably valid only in the region of $(\omega/2\pi) > 5$ kHz. Verification of the scaling relationship showed that this relationship is valid (to within the experimental accuracy) for the frequencies ω above 5 kHz and the field amplitudes $H_0 > H^*(\omega)$. However, the exponent n in the scaling relationship under consideration is not correlated with the exponent n in the power relationship describing the current–voltage characteristic. *© 2001 MAIK "Nauka/Interperiodica".*

1. INTRODUCTION

Experiments on the diamagnetic response of superconductors usually involve measurements of the temperature dependence of the real part $\chi_1'(T)$ (in-phase or linear signal) and the imaginary part $\chi_1''(T)$ (quadratic signal) of the sample susceptibility at various amplitudes of the exciting (ac) magnetic field H_{ac} and constant (dc) magnetic field H_{dc}. The linear signal $\chi_1'(T)$, related to the sample screening currents, is proportional to the external magnetic flux density pushed out by the superconducting sample. The quadratic signal $\chi_1''(T)$ is proportional to dissipative losses in the sample including both the remagnetization losses and the resistive losses (related to finite (albeit small) sample resistance in the vicinity of T_c). Similar to the $\chi_1''(T)$ component, the third harmonic $\chi_3''(T)$ of the quadratic signal is measured due to its higher sensitivity with respect to features in the hysteresis behavior during remagnetization of the sample.

The high-T_c superconductor films, in contrast to the traditional low-temperature metal superconductors, usually represent a medium in which grains (crystallites with their axes *c* oriented perpendicular to the film plane) are linked by weak bonds. The grain size is typically on the order of several microns. In the range of constant magnetic fields H_{dc} below the first critical value H_{c1} for crystallites ($0 \le H_{dc} \le H_{c1}$) and in a narrow interval of temperatures ($\Delta T/T_c \cong 10^{-3}$–$10^{-2}$) in the immediate vicinity of T_c (a point where the diamagnetic response appears), all the electrical and magnetic characteristics of the films are determined by currents passing through the system of weak bonds. In this range, we may ignore the influence of crystallites (where only the Meissner currents are circulating) upon the Josephson current through weak bonds.

Under these conditions, the physical properties of high-T_c films as the Josephson media must be most clearly manifested, with the diamagnetic response being strongly affected by the magnetic flux creep and diffusion. Since the high-T_c samples still possess a small resistance (~10^{-3}–10^{-1} Ω) near T_c, the magnetic susceptibility is naturally described within the framework of the diffusion model rather than using the critical state model. Gioacchino *et al.* [1] theoretically calculated shapes of the $\chi_1''(T)$ and $\chi_3''(T)$ curves with the magnetic flux diffusion described within the framework of the parallel resistance model [2]. However, none of the three vortex pinning models considered in [1] satisfactorily described the experimental $\chi_1''(T)$ and $\chi_3''(T)$

1063-7834/01/4309-1603$21.00 © 2001 MAIK "Nauka/Interperiodica"

curves reported by us [3] and by other researchers [1, 4].

In the narrow temperature interval under consideration, the shapes of the linear $\chi_1'(T)$ and quadratic $\chi_1''(T)$ diamagnetic response signals are much like those observed at low temperatures, where the magnetic flux creep is insignificant and the sample susceptibility is adequately described within the framework of the Bean critical state model [5, 6]. The main conclusions of that theory are as follows: (i) the temperature T_m of maximum dissipative losses $\chi_1''(T)$ depends only on the amplitude H_0 of the exciting field H_{ac} and is independent of the excitation frequency and (ii) the magnitude of the $\chi_1''(T)$ peak is independent of the H_0 value. However, experiments in the vicinity of T_c show that both χ_1' and χ_1'' vary with the frequency and that the $\chi_1''(T)$ peak magnitude ($\chi''_{1\max}$) grows as H_0 increases up to a certain critical value $H_1^*(\omega)$ [4, 5]. Brandt [7] has numerically calculated the susceptibility of high-T_c films within the framework of the critical state model with allowance for the magnetic flux creep, but these data are difficult to compare with the results of our measurements. To our knowledge, no general theory is available at present describing the magnetic bahavior of high-T_c materials exposed to low excitation fields at temperatures in the narrow ($\Delta T/T_c \sim 10^{-3}$–$10^{-2}$) vicinity of T_c. This is partly explained by the lack of experimental data in this range.

The purpose of our investigation was to experimentally study the character of currents flowing in an YBCO film possessing a high current-carrying capacity in the range of weak exciting magnetic fields ($H_{ac} < H_{c1}$) in the immediate vicinity of T_c. Another task was to study the frequency and field dependence of the susceptibility components χ_1' and χ_1'' of the film and to verify the scaling relationships [7].

2. EXPERIMENTAL RESULTS AND DISCUSSION

The diamagnetic response of a film sample was studied in an induction setup [8] in the range of frequencies ($\omega/2\pi = 1$–30 Hz) and exciting magnetic fields $H_{ac} = H_0 \sin\omega t$ ($H_0 = 2$–500 mOe). The experiments were performed with a 2000-Å-thick laser-deposited YBCO film on an Nd-doped $LaCaO_3$ substrate. The crystal grains in the film had an average size of ~1×1 μm and were oriented with their *c* axis perpendicular to the film plane.

2.1. The Character of the Current Flowing in the YBCO Film in the Vicinity of T_c

It is commonly accepted that a superconducting state in granulated bulk high-T_c materials and in films composed of oriented grains linked by weak bonds is established upon the formation of an infinite percolation cluster [9]. This cluster, carrying all the microscopic current I_c passing through the sample, represents a system of grains combined by a network of Josephson's contacts into a cellular structure with a cell size L (corresponding to a correlation radius in the thermodynamic problem of spheres [10]). Since the lower critical field for Josephson's contacts is $H_{c1j} \cong \Phi_0/\pi L^2$, we obtain $L = \sqrt{\Phi_0/\pi H_{c1j}}$ (where $\Phi_0 \cong 2 \times 10^{-7}$ G cm^2 is the flux quantum). Thus, assuming that (i) the transport current at a temperature close to T_c flows in the sample via an infinite cluster comprising L-sized cells linked by a network of Josephson's contacts and (ii) the applied magnetic field induces a circular current in the sample, we may conclude that the percolation cluster would acquire a ring shape. Since the weak bonds cannot simultaneously transform into a superconducting state, the radius L (we assume that the current ring width is equivalent to the cell size L) is large for $T \longrightarrow T_c$ and decreases with the temperature. As a result, decreasing the temperature is accompanied by the formation of new rings with gradually decreasing radii which are embedded one into another, so that the total width W of the current ring increases. This process may continue until L reaches the grain size and the current flows over the entire sample film area.

Let us try to justify the above assumptions. Recently, Herzog *et al.* [4] studied the diamagnetic response of disks and narrow rings made of an YBCO film by measuring the temperature dependence of χ_1', χ_1'', and χ_3''. In contrast to the disks and wide rings, the $\chi_3''(T)$ curves, which display two small positive peaks (that may be absent) and a large negative minimum [4, 10], the narrow rings with $a/b \geq 2$ (a and b being the outer diameter and width of the ring, respectively) exhibit a significantly increased low-temperature positive maximum. In addition, the plots of χ_1'' versus χ_1' for a narrow ring are symmetric, whereas those for the disks and wide rings are not.

We have measured the $\chi_3''(T)$ curves in both weak ($H_0 = 10$ mOe) and relatively large ($H_0 = 200$ mOe) fields at a frequency of 15 kHz (Figs. 1, 2). As is seen from these data, the high-temperature positive maximum at $H_0 = 10$ mOe is very small and the χ_1'' versus χ_1' plot is symmetric with a peak at $\chi_1' = 0.5$ (Fig. 3). For $H_0 = 200$ mOe, the positive peaks are close in magnitude (especially in the presence of a dc field) and the χ_1'' versus χ_1' curve is asymmetric with a peak at $\chi_1' \cong 0.4$. The L value estimated for $H_0 = 10$ mOe is approximately 178 μm, while that for $H_0 = 200$ mOe is $L \sim 56$ μm. The H_{c1j} values estimated in both cases accord-

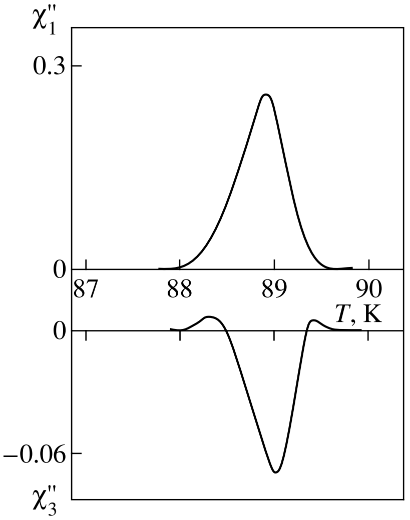

Fig. 1. The plots of χ''_1 and χ''_3 versus temperature measured at H_0 = 200 mOe and f = 15 kHz.

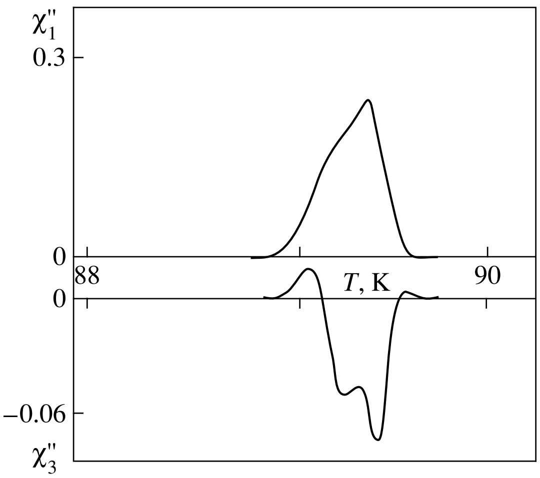

Fig. 2. The plots of χ''_1 and χ''_3 versus temperature measured at H_0 = 10 mOe and f = 15 kHz.

ing to [11, 12] were approximately equal: 2×10^{-4} and 2×10^{-3} Oe for H_0 = 10 and 200 mOe, respectively.

Thus, the results of our measurements, as well as the data on the diamagnetic response of YBCO film rings [4], confirm the assumption concerning the ring character of the induced current flowing in the YBCO films at temperatures near T_c. A decrease in the temperature as small as 0.4 K (corresponding to the temperature difference between the χ''_1 peaks at H_0 = 10 and 200 mOe) accounts for the difference in the shapes of curves in Figs. 1 and 2. At still lower temperatures and higher fields, the current passes across the entire film or a wide ring with $a/b < 2$, although the correlation radius decreased only by a factor of about 3, remaining far from the grain size. Note that the χ'_1 value (determining the degree of the external field screening in the sample) at $H_0 \le 10$ mOe is only a few per cent lower than that for $H_0 \ge 10$ mOe, which indicates that the current ring provides for virtually complete screening of the sample.

2.2. Frequency and Field Dependence of Susceptibility

Figure 4 shows plots of the temperature T_m of maximum dissipative losses $\chi''_1(T)$ versus $H_0^{2/3}$ measured at various frequencies of the exciting field. As is seen, the T_m value in small fields $H_0 \le 10$ mOe (especially at high frequencies) is virtually independent of H_0 (to within the experimental accuracy). As the H_0 value increases (passing some region of intermediate exciting fields and strong fluctuations), the T_m value begins to shift toward lower temperatures as described by the law

$$\left(1-\frac{T_m}{T_{c1}}\right) \propto H_0^{2/3}. \tag{1}$$

Upon reaching a certain field strength $H_1^*(\omega)$, the slope of the linear plot exhibits a change and T_m varies by the law $\left(1-\frac{T_m}{T_{c2}}\right) \propto H_0^{2/3}$. As the field strengths increases

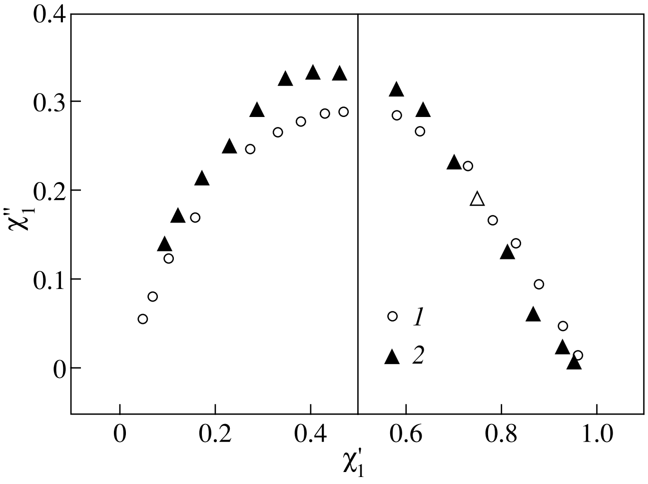

Fig. 3. The plots of χ''_1 versus χ'_1 measured at the external *ac* field amplitude H_0 = (*1*) 10 and (*2*) 200 mOe. The peak of χ''_1 at χ'_1 = 0.5 corresponds to a symmetric shape of the $\chi''_1(\chi'_1)$ curve.

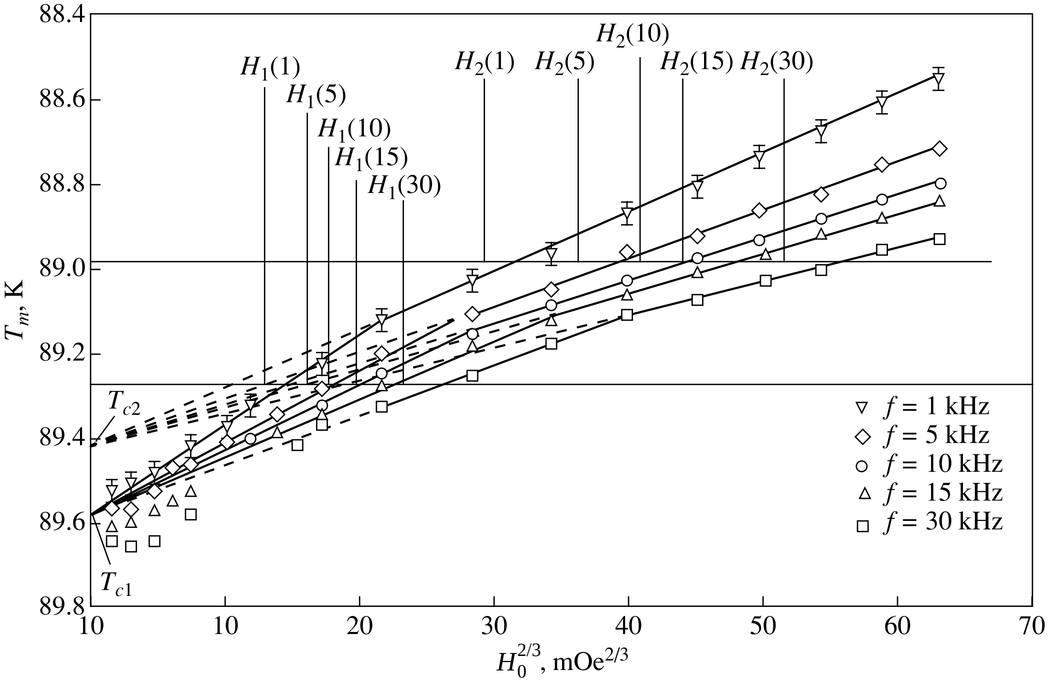

Fig. 4. Plots of the temperature T_m (corresponding to the maximum of χ_1'') versus $H_0^{2/3}$ measured at various excitation frequencies. The H_0 values H_1(1 kHz)–H_1(30 kHz) for $H_0 < H_1^*$ ($T_m \cong 89$ K) and H_2(1 kHz)–H_2(30 kHz) for $H_0 > H_1^*$ ($T_m \cong 89.3$ K) are listed in Table 2.

in the range of $H_0 < H_1^*(\omega)$, the magnitude of the $\chi_1''(T)$ maximum increases from $0.22\chi_1'$ to $\approx 0.3\chi_1'$. At $H_0 > H_1^*(\omega)$, the $\chi_{1\max}''$ remains virtually unchanged. Discussion of the factors responsible for the appearance of break points in the T_m versus $H_0^{2/3}$ plots is beyond the scope of this paper.

As the excitation frequency grows, the $\chi_1''(T)$ maximum shifts toward higher temperatures. As is seen from Fig. 5, the T_m value for $(\omega/2\pi) \geq 5$ kHz is a logarithmic function of the frequency:

$$1 - \frac{T_m}{T_{ci}} \propto -\ln\omega. \tag{2}$$

At a frequency of 1 kHz, the T_m values deviate from the logarithmic law (2). Above and below the critical field strengths $H_1^*(\omega)$, the $T_m(\omega)$ values plotted in the logarithmic scale are straight lines, the slope of which increases with H_0. The family of experimental plots corresponding to various exciting field amplitudes H_0 originate from the same point corresponding to the critical temperature T_c and a certain frequency ω^*. To within the experimental accuracy, these critical values are $\omega_1^*/2\pi = 1.64$ MHz, $T_{c1} = 89.58$ K below $H_1^*(\omega)$ and $\omega_2^*/2\pi = 1.48$ MHz, $T_{c2} = 89.43$ K above $H_1^*(\omega)$.

Upon combining (as described in [13]) the field and frequency dependences, we obtain an empirical relationship,

$$T_m(H_0, \omega) = T_{c1,2}\left[1 - \left(\frac{H_0}{H_{1,2}^*}\right)^{2/3} \ln\frac{\omega_{1,2}^*}{\omega}\right], \tag{3}$$

where subscript 1 refers to the case of $H_0 < H_1^*(\omega)$ and subscript 2, to the case of $H_0 > H_1^*(\omega)$. In [13], the experimentally observed behavior of $T_m(\omega)$ was interpreted within the framework of the Anderson model of the magnetic flux creep [14, 15], which extends the Bean critical state concept [5] by taking into account the thermally activated flux flow. It should be recalled that our study refers to the interval of temperatures differing from T_c by no more than 1.5%. In the region of temperatures and fields studied, the system features a single-vortex pinning (the vortex density $\propto H_0/\Phi_0$ is small) and exhibits a strong magnetic flux creep. The obtained shapes of the χ' versus χ'' curves and their temperature variation are best described in terms of the critical state model. According to this, the diamagnetic response is a function of only one parameter [6],

$$h = \frac{cH_0}{4\pi d j_c(T)}, \tag{4}$$

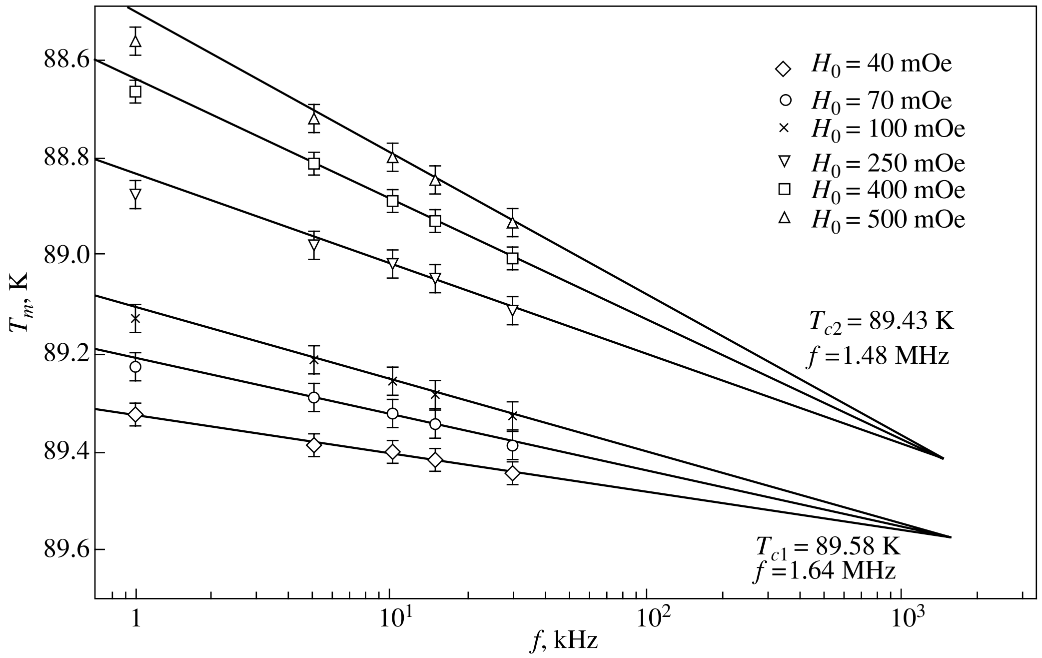

Fig. 5. The plots of T_m versus $\omega/2\pi$ measured at various amplitudes of the applied exciting field.

where d is the film thickness in a parallel filed. The diamagnetic response of high-T_c films is usually studied using fields that are perpendicular to the film plane, in which case the signal is proportional to R^3 (R is the sample radius) [16]. For this geometry, Brandt [7] derived the following relationship:

$$2.474 = \frac{8H_0}{\pi d j_c(T)}. \qquad (5)$$

The $j_c(T)$ values determined from (5) differ rather insignificantly (by ~1%) from those given by formula (4). Relationships (4) and (5) are derived within the framework of the simple Bean model ignoring the flux creep. We failed to find in the literature any analytical expression relating $j_c(T)$ to the measurable quantities with an allowance for the flux creep. For this reason, the experimental data were processed in terms of formula (5).

The experimental field dependence (1) can be realized if the temperature dependence of the critical current density $j_c(T)$ is selected in the form of an inverse power law,

$$j_c(T) = j_c(0)\left(1 - \frac{T}{T_c}\right)^{3/2}, \qquad (6)$$

where T_c is the temperature at which a macroscopically coherent state is established. As a result, the condition of loss maximum can be presented in the following form [13]:

$$\frac{T_m}{T_c} = 1 - \left(\frac{8H_0}{2.474\pi d j_c(0)}\right)^{2/3}\left[1 - \frac{2}{3}\frac{kT_c}{U}\ln\frac{\nu_0 x}{\omega d}\right], \qquad 1 - \frac{T_m}{T_c} \ll 1. \qquad (7)$$

This equation corresponds to the empirical relationship (3) with

$$H^* = \frac{2.474\pi d j_c(0)}{8}\left[\frac{3}{2}\frac{U}{2kT_c}\right]^{3/2}, \qquad \omega^* = \nu_0\frac{x}{d}\exp\left(\frac{3}{2}\frac{U}{kT_c}\right), \qquad (8)$$

where U is the pinning potential, ν_0 is the vortex oscillation frequency in the potential well, and x is the distance between the pinning centers.

Using formulas (5) and (6), we may determine $j_c(0)$ from (8). Then, taking x to be equal to the grain size, we may use the same formula for determining U and ν_0. Table 1 gives the values of $j_c(0)$, U, ν_0, and U/kT_c for the fields above and below $H_1^*(\omega)$. The $j_c(0)$ values were determined using the $T_m(H_0^{2/3})$ curves measured at the maximum frequency (30 kHz), where the flux creep effect is minimum and the estimates $j_c(0)$ are closest to real values.

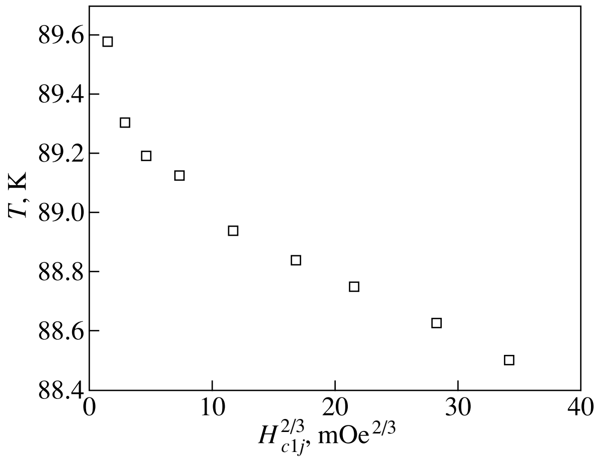

Fig. 6. Temperature dependence of the first critical field H_{c1j} .

In the case of a single-vortex pinning, the potential has the form $U(j) = U_0\ln(j_c/j)$ [18], according to which U is a logarithmic function of the ratio of true and measured critical currents. However, the $T_m(H_0^{2/3})$ curves measured at various frequencies are straight lines, which implies that the activation energies in weak exciting fields at temperatures close to T_c probably depend neither on H_{ac} nor on T.

As indicated above, a sample in this temperature interval represents a Josephson medium containing a network of grains coherently linked by weak bonds. At a low temperature and a small field strength, the network cell size is approximately equal to the grain size. For $T \longrightarrow T_c$, the cell size rapidly grows in proportion to the correlation radius L, while the critical current drops. The Josephson vortex transforms into a hypervortex (e.g., of the size L) that shifts under the action of the Lorentz force by breaking the weakest bond and switching to a nearest stronger bond. Then, the U value can be estimated as the work performed by the Lorentz force $\sim c^{-1}j_c(T)\Phi_0$ on moving the L-sized vortex by a distance x equal to the pinning center spacing. From this we obtain

$$U \sim c^{-1}j_c(T)\Phi_0 Lx. \tag{9}$$

The absence of the temperature dependence of U near T_c can be explained assuming that the increase in L with $T \longrightarrow T_c$ is accompanied by a simultaneous proportional decrease in $j_c(T)$. Let us estimate and compare the rates of decrease in $j_c(T)$ and increase in L. First, let us take $j_c(T) \cong 14.8 \times 10^4$ and 22.5×10^4 A/cm^2 calculated by formula (6) for 15 kHz and $T = 89.125$ and 88.85 K ($H_0 = 200$ and 500 mOe, respectively, Fig. 4). The ratio is approximately 1.5. The correlation radii $L = \sqrt{\dfrac{\Phi_0}{\pi H_{c1j}}}$ at the same temperatures are 178 and 85 μm (the first critical Josephson vortex field $H_{c1j} \cong 20$ and 85 mOe, respectively, Fig. 6; $\Phi_0 \gg 2 \times 10^{-7}$ G cm^2), which yields a ratio of ~2.13. These rough estimates of $j_c(T)$ and the percolation cell size confirm the possibility of joint variation in $j_c(T)$ and L such that the U values according to (9) remain virtually constant in a certain temperature interval.

2.3. Scaling Relationships

The scaling laws are very important for understanding the mechanisms and relationships between fundamental parameters of high-T_c superconductors. Scaling considerations usually imply determination of the static (ν) and dynamic (z) indices necessary for calculating the temperature of glass transition in the vortex lattice, which is a thermodynamic phase transition to a true superconducting phase [17]. Recently, Brandt [7] suggested a scaling relationship for a nonlinear response of the ac susceptibility of type II superconductors. This scaling law is a consequence of the Maxwell equations and a fundamental relationship between current density and electric field strength. It was demonstrated that the law applies to nonlinear superconductors with any exponent in the current–voltage power law $E(j) = E_c\left(\dfrac{j}{j_c}\right)^n$, where $n = \dfrac{U_0}{kT}$. According to the proposed scaling law, the *ac* susceptibility response for any creep exponent $\bar{n} = \dfrac{\partial E}{\partial j}$ is invariant relative to the simultaneous variation of the *ac* field amplitude H_0 and frequency ω, provided that this variation is such that

$$\frac{\omega}{H_0^{n-1}} = \text{const.} \tag{10}$$

Table 1. The values of parameters in formula (8) for the excitation amplitudes above and below $H_1^*(\omega)$

	d, μm	$T_{c1,2}$, K	$j_c(0)$, A/cm^2	H_1^*, kOe	ω*/2π, MHz	ν_0, kHz	U, meV	U/kT_c
$H_0 > H_1^*(\omega)$	0.2	89.43	5×10^7	9.5	1.48	43	20.15	2.9
$H_0 < H_1^*(\omega)$	0.2	89.58	2.78×10^7	4.75	1.64	54	18.8	2.7

Table 2. The values of excitation amplitudes H_0 (mOe) for various frequencies f at T = 89 K ($H_0 < H_1^*$) and 89.3 K ($H_0 > H_1^*$)

T, K	f, kHz				
	1	5	10	15	30
89	167	234	281	319	397
89.3		64	81	92.5	115

Table 3. The values of n in relationship (10) for various frequency ratios (the values in the numerator and denominator refer to 89 and 89.3 K, respectively)

f, kHz	1	5	10	15
5	≅5.7			
10	5.4	$\frac{4.8}{3.9}$		
15	5.2	$\frac{4.5}{4.0}$	$\frac{4.2}{4.0}$	
30	4.9	$\frac{4.4}{4.0}$	$\frac{4.2}{4.1}$	$\frac{4.2}{4.2}$

In fact, formula (10) implies the following. If T_m is the temperature of the χ'' maximum corresponding to the amplitude H_0 and frequency ω, a peak in χ'' for a higher frequency will be observed at the same temperature if the field strength is increased as stipulated by (10). Table 2 gives the exciting field amplitudes $H_0 = H_{1,2}(f)$ (Fig. 4) for various frequencies. Table 3 lists the n values for various frequency ratios corresponding to formula (10). As is seen from these data, the value $n \cong 4.2$ at T_m = 89 K is retained (to within the experimental accuracy) only in the frequency range from 10 to 30 kHz, while $n \cong 4$ at T_m = 89.3 K remains constant in the 5–30 kHz range.

Jonsson-Akerman *et al.* [18] verified the scaling law for an $HgBa_2Cu_2O_{6+\delta}$ film with T_c = 120 K by measuring the χ_1' values at T = 100 K, H_0 = 2 Oe, and various values of the dc magnetic field strengths (20–100 Oe) in the frequency range from 89.1 to 891 Hz. The experimental data were used to determine the ratio

$$\bar{n} = \frac{\partial \ln E}{\partial \ln j} = \frac{U_0}{kT}\left(\frac{j_c}{j}\right)^{\alpha} \geq \frac{U_0}{kT} = n,$$

where α is a positive constant [19]. The results confirmed the validity of the scaling relationship (10) but only within a narrow range of dc field strengths.

In our experiments, the scaling law is also valid within a certain frequency range, but the obtained n values are too large for the temperature interval in which the measurements were carried out. The n values determined from estimates of the pinning potential are $n = U/kT_c$ = 2.9 for $H_0 > H_1^*(\omega)$ and 2.7 for $H_0 < H_1^*(\omega)$ and are much closer to $n \cong 1.5$ as reported in [20] for an YBCO film, but they are also too large. Note that, owing to the linear character of the $T_m(H_0^{2/3})$ relationships measured at various excitation frequencies (Fig. 4), the H_0 values indicated in Table 2 will vary at other temperatures (with a certain coefficient). Following relationship (10), we may consider n as a temperature-independent quantity, which obviously contradicts the current–voltage characteristic described by the power law.

3. CONCLUSIONS

The results of our experiments led to the following conclusions:

(1) In a narrow temperature interval near T_c, the current induced in an YBCO film sample by an exciting field H_{ac} is concentrated within a ring with a width L. As the temperature slightly decreases, the number of rings embedded one into another increases. When the total ring width becomes on the order of the grain size, a current in the superconducting sample flows across the entire film surface or in a wide ring with $a/b > 2$.

(2) In the range of temperatures, field strengths H_{ac}, and frequencies, the variation of the χ_1'' maximum temperature T_m described by Eq. (7) is valid both for films with a low current-carrying capacity and low T_c [13] and for the film (studied in our experiments) with a high current-carrying capacity and high T_c. Factors accounting for the deviation from Eq. (7) observed at the frequencies below 5 kHz are unclear. A possible reason for this is the magnetic flux relaxation being more pronounced in this frequency interval [21].

(3) The scaling relationship proposed in [7] is valid in the range of frequencies above 10 kHz for $H_0 > H_1^*(\omega)$, but the n value is too large for the temperature interval studied and, apparently, has nothing in common with the creep exponent in the power relationship describing the current–voltage characteristics. Probably, the obtained experimental data can be better rationalized using an approach developed in [22] based on analysis of the uncorrelated interaction of isolated vortices with a modified pinning potential. However, solving this task would require conducting simultaneous measurements of the diamagnetic response and current–voltage characteristics in the same temperature interval and developing a theoretical description of the diamagnetic response of high-T_c films at temperatures near T_c.

REFERENCES

1. D. Di Gioacchino, F. Gelani, P. Tripodi, *et al.*, Phys. Rev. B **59**, 11539 (1999).
2. R. Griessen, Phys. Rev. Lett. **64**, 1674 (1990).

3. V. A. Khokhlov and V. F. Drobot'ko, Fiz. Nizk. Temp. **21**, 200 (1995) [Low Temp. Phys. **21**, 152 (1995)].
4. Th. Herzog, H. A. Radovan, P. Ziemann, and E. H. Brandt, Phys. Rev. B **56**, 2871 (1997).
5. C. P. Bean, Phys. Rev. Lett. **8**, 250 (1962); Rev. Mod. Phys. **36**, 31 (1964).
6. A. N. Artemov, A. M. Grishin, V. N. Korenivskii, *et al.*, Int. J. Mod. Phys. B **4** (4), 591 (1990).
7. E. H. Brandt, Phys. Rev. B **55**, 14513 (1997).
8. A. M. Grishin, V. F. Drobot'ko, V. D. Stasovskiĭ, and V. A. Khokhlov, Zh. Tekh. Fiz. **63** (8), 190 (1993) [Tech. Phys. **38**, 730 (1993)].
9. N. F. Vedernikov, K. M. Mukimov, G. P. Sigal, and B. Yu. Sokolov, Sverkhprovodimost: Fiz., Khim., Tekh. **7** (2), 316 (1994).
10. B. I. Shklovskiĭ and A. L. Efros, *Electronic Properties of Doped Semiconductors* (Nauka, Moscow, 1979; Springer-Verlag, New York, 1984).
11. T. Ishida and H. Mazaki, J. Appl. Phys. **52**, 6798 (1981).
12. A. P. Malozemoff, in *Physical Properties of High Temperature Superconductors*, Ed. by D. M. Ginsberg (World Scientific, Singapore, 1989; Mir, Moscow, 1990).
13. A. N. Artemov, V. F Drobot'ko, D. G. Emel'yanenkov, *et al.*, Phys. Lett. A **157** (1), 85 (1991).
14. P. W. Anderson, Phys. Rev. Lett. **9**, 309 (1962).
15. C. W. Hagen, R. P. Griessen, and E. Solomons, Physica C (Amsterdam) **157**, 199 (1989).
16. V. A. Atsarkin, G. V. Vasneva, and N. E. Noginova, Sverkhprovodimost: Fiz., Khim., Tekh. **5** (3), 423 (1992).
17. J. Kotzler, G. Nakielsky, M. Baumann, *et al.*, Phys. Rev. B **50** (5), 3384 (1994).
18. B. J. Jonsson-Akerman, V. V. Rao, and E. H. Brandt, Phys. Rev. B **60** (21), 14913 (1999).
19. E. H. Brandt, Phys. Rev. B **58**, 6506 (1998); **58**, 6523 (1998).
20. P. N. Mikheenko, I. S. Abalesheva, and S. I. Levandovskiĭ, Fiz. Nizk. Temp. **22** (4), 364 (1996) [Low Temp. Phys. **22**, 281 (1996)].
21. R. Prozorov, A. Shaulov, Y. Wolfus, and Y. Yeshurun, Phys. Rev. B **52** (17), 12541 (1995).
22. A. N. Lykov, Supercond. Sci. Technol. **12** (4), 219 (1999).

Translated by P. Pozdeev

Physics of the Solid State, Vol. 43, No. 9, 2001, pp. 1611–1620. Translated from Fizika Tverdogo Tela, Vol. 43, No. 9, 2001, pp. 1548–1557.
Original Russian Text Copyright © 2001 by Bdikin, Mozhaev, Ovsyannikov, Komissinskiĭ, Kotelyanskiĭ, Raksha.

METALS AND SUPERCONDUCTORS

The Growth and Domain Structure of $YBa_2Cu_3O_x$ Films on Neodymium Gallate Substrates with a Deviation of the Normal to the Surface from the [110] Direction in $NdGaO_3$

I. K. Bdikin*, P. B. Mozhaev, G. A. Ovsyannikov**, F. V. Komissinskiĭ**,**
I. M. Kotelyanskiĭ, and E. I. Raksha****

** Institute of Solid-State Physics, Russian Academy of Sciences, Chernogolovka, Moscow oblast, 142432 Russia*
***Institute of Radio Engineering and Electronics, Russian Academy of Sciences, ul. Mokhovaya 18, Moscow, 103907 Russia*

Received December 28, 2000; in final form; February 25, 2001

Abstract—The growth, crystal structure, and electrophysical properties of $YBa_2Cu_3O_x$ (YBCO) epitaxial films grown with and without a CeO_2 epitaxial sublayer on $NdGaO_3$ (NGO) substrates with the normal to the surface deviating from the [110] axis by 5° to 26.6° around the [001] axis are investigated. It is shown that the orientation of YBCO epitaxial films grown on such substrates is determined by the existence of symmetry-equivalent directions in the substrate and in the CeO_2 layer, as well as by the rate of film deposition. For a high deposition rate, YBCO films grow on the CeO_2 sublayer in the [001] orientation irrespective of the orientation of the substrate and the sublayer. It was found that when the angle of deviation of the substrate plane is from the (110) NGO plane, twinning of one or both twinning complexes in YBCO may be suppressed. © *2001 MAIK “Nauka/Interperiodica”.*

1. INTRODUCTION

High-temperature metal-oxide superconductors (HTSC) such as $YBa_2Cu_3O_x$ (YBCO) display a clearly manifested crystalline anisotropy [1]. In view of the preferred electron transport in the basal plane (001) of YBCO, films with (001) orientation (*c*-oriented films) are used most frequently [2, 3]. Obtaining *c*-oriented films with a high degree of perfection of the crystalline structure necessitates the use of substrates with translation distances on the surface close to the lattice constants *a* and *b* of the YBCO lattice. Among such substrates are (001) $SrTiO_3$, (001) $LaAlO_3$, and (110) $NdGaO_3$ substrates with perovskite-type crystal lattices whose structures are close to the YBCO lattice, which are used most frequently.

Recently, YBCO films in which the [001] direction forms a certain angle with the normal to the substrate surface (films with tilted axes) have become intensely studied. An analysis of the growth of these films is important for preparing high-quality HTSC films on surfaces with intricate shapes [4] (including those obtained as a result of thin film processing [2, 5]) and for studying the mechanisms of current conduction through grain boundaries [5–7]. In addition, it is often important to organize the electron transport in HTSC films perpendicular to the substrate, which is a complicated problem for *c*-oriented YBCO films [2]. In this connection, the (100) (*a*-oriented) YBCO films, which can also be grown on the substrates listed above owing to the closeness of the values of *b* and *c*/3 for a YBCO film, have been studied intensely [3]. However, considerable anisotropy of the electron transport and of the thermal expansion coefficient in the substrate plane complicates the use of such films. The YBCO films with tilted axes are free of this drawback of *a*-oriented YBCO films and make it possible to realize electron transport perpendicular to the substrate plane.

Considerable attention has been paid to YBCO films grown on (110) $SrTiO_3$ substrates [6, 8–11]. These films contain crystallites of the (103) and (013) orientations with the [001] axis of YBCO forming an angle of 45° to the normal of the substrate and have features similar to electron transport in the plane of the substrate and at right angles to it. The application of such films has made it possible to obtain multilayered Josephson junctions [10, 11]; however, the presence of slightly disoriented domain systems in these films complicates their practical application.

Another frequently used version involves the use of substrates with an insignificant (1°–5°) deviation of the surface from low-index planes, viz., vicinal substrates [4, 12]. The emergence of periodic inhomogeneities (steps) on the surface of such substrates ensures favorable conditions for the nucleation and growth of YBCO films. The films grown on vicinal substrates exhibit, as a rule, a higher perfection of the crystalline structure and high superconducting properties. The intermediate range of angles of substrates from vicinal angles to 45° was analyzed in [7, 13, 14]. It was found that in a certain angular interval, perpendicularly disoriented domains are formed in the film. For all the angles under investigation, the axes of the YBCO film were parallel to the axes of the substrate due to the closeness of the crystal structures of the film and the substrate.

The growth of YBCO films on nonperovskite substrates (MgO and Y-stabilized ZrO_3) with tilted axes has a number of distinctions. In [15, 16], the growth of YBCO with the orientation of the [001] axis of the film parallel to the normal of the substrate was observed. A combination of the perovskite-type $SrTiO_3$ substrate with a MgO buffer layer can be employed for obtaining biepitaxial structures in which the contacting regions have different angles of inclination of the film axes [17].

In the present work, we present the results of investigations of the crystal structure and electrophysical properties of thin YBCO films deposited on $NdGaO_3$ (NGO) substrates with a deviation angle of the normal from the [110] axis in the range from 5° to 26°. Special attention was paid to the domain structure of the obtained films, which was studied using x-ray diffractometry methods. The effect of the crystalline structure of the substrate on the growth of YBCO films was studied by introducing an intermediate CeO_2 epitaxial layer between the film and the substrate.

2. EXPERIMENTAL TECHNIQUE

YBCO films were deposited using pulsed laser sputtering and dc cathode sputtering under high oxygen pressure. The details of the film deposition technique are described in [18]. Typical deposition rates were 10–20 Å/min for cathode sputtering and more than 300 Å/min for pulsed laser sputtering. The typical thickness of the YBCO films was 2000 Å. The parameters of both deposition processes were optimized to obtain films with the highest superconducting transition temperature.

For experiments with deposition on substrates with tilted axes (TASs), we chose $NdGaO_3$ (NGO) substrates with a perovskite structure. The deviation of the substrate plane from (110) was usually achieved through rotation around the [001] axis of NGO. It is convenient to characterize a TAS by the angle γ of deviation of the substrate normal from the [110] direction of NGO. The substrates were subjected to chemical etching and mechanical polishing, ensuring the required structural perfection of the surface layer of the substrate.

We also used an NGO TAS coated with a thin epitaxial CeO_2 layer for growing YBCO. For the lattice constant $a = 5.41$ Å, close to the YBCO lattice translation along the $\langle 110 \rangle$ direction, this material has a fluorite-type crystal structure (in contrast to the perovskite structure of NGO and perovskite-type YBCO lattice). The epitaxial CeO_2 layer was deposited on the surface of NGO substrates by rf magnetron sputtering of a metallic cerium target in an argon–oxygen mixture (reactive rf magnetron sputtering) and by electron-beam sputtering of ceramic CeO_2. Typical deposition rates were 70 Å/min for the rf sputtering and 5 Å/min for the electron-beam sputtering, the typical thickness of the CeO_2 layer being 300 Å.

The morphology of the films was studied using an atomic force microscope. The electrophysical properties of YBCO films were studied by both contact and contactless methods. In the latter methods, the superconducting transition temperature T_{cM} and the critical current density j_c were determined at various temperatures from the magnetic susceptibility of the films. In the measurements based on the contact methods, bridges were created in the films by photolithography and ion-beam or chemical etching.

In x-ray diffraction experiments, we used a modified method of recording rocking curves in a wide scanning range [19] along with recording traditional θ–2θ and θ scanning diffraction patterns, as well as 2D spectra in the (θ, 2θ) coordinates. In the modified method, as in the conventional method of rocking curve recording, the sample is scanned at a fixed position of the detector corresponding to the Bragg reflection angle from a chosen plane in the sample in the vicinity of this reflection. However, the scanning interval is much larger than the range of existence of the given peak. In this case, the diffraction pattern also displays diffraction reflection peaks from the crystallographic substrate planes. Such peaks exist in the continuous part of the emission spectrum of the x-ray tube; for this reason, the frequency range of gamma-quanta registered by the detector must be extended in order to observe these peaks. Additional peaks can be used for reference in order to determine the mutual orientation of the film and substrate lattices. The application of this method makes it possible to establish the orientation relationships using only one diffraction pattern. The mutual orientation can also be determined in a similar way from 2D spectra, but the recording time required is much longer. The condition for applicability of the rocking-curve recording technique in a wide scanning range is the coincidence of one of the symmetry axes of the film with that of the substrate (the substrate is rotated about this axis). In our case, this axis was the [001] axis of the NGO substrate. The existence of a common symmetry axis was verified by recording the Laue diffraction pattern of the heterostructure prior to the main experiments.

3. DISCUSSION OF RESULTS

All the YBCO films grown by us were superconducting (with the superconducting transition temperature T_{cM} exceeding 87 K, and the superconducting transition width ΔT_c smaller than 2 K) and had an orthorhombic crystal lattice with the parameters $a = 3.82$–3.83 Å, $b = 3.88$–3.89 Å, and $c = 11.67$–11.68 Å. After deposition of the YBCO film on the (110) $NdGaO_3$ substrates, the following epitaxial relations hold:

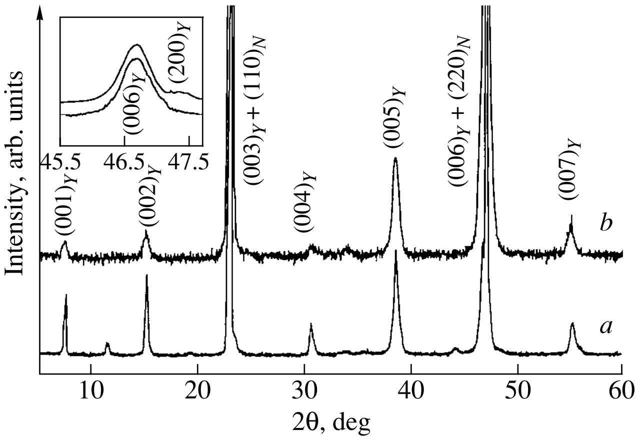

Fig. 1. Typical diffraction patterns of θ/2θ scanning of YBCO films on NGO substrates [(001)YBCO || (110)NGO for all substrates]: (*a*) (110) NGO substrate and (*b*) (130) NGO substrate. The inset shows domains observed in a number of YBCO films with the (100) orientation.

$(001)_Y \parallel (110)_N$, with $[100]_Y \parallel [001]_N$ or $[010]_Y \parallel [001]_N$ (*c*-oriented films). Usually, inclusions are also observed for which the relation $(100)_Y \parallel (110)_N$ holds (*a*-oriented inclusions, Fig. 1). Here and below, subscript *Y* indicates that a given direction or plane corresponds to a YBCO plane and subscript *N* corresponds to directions and planes of the NGO substrate; subscript *C* corresponds to a thin epitaxial CeO_2 layer.

3.1. Growth of YBCO Films on Tilted-Axis $NdGaO_3$ Substrates

Irrespective of the angle γ, the epitaxial relations $(001)_Y \parallel \langle 110\rangle_N$ are preserved for YBCO films deposited on NGO TASs (Fig. 1b). However, the presence of two symmetry equivalent planes $(110)_N$ and $(1\bar{1}0)_N$ in the substrate, which ensure the fulfillment of the epitaxial relations, leads to the formation of two domain systems in the YBCO film. In analogy with the growth of *c*-oriented YBCO films on NGO substrates with (110) orientation, we will refer to domains with the $[001]_Y$ axis close to the normal to the substrate plane as pseudo-*c*-oriented, while domains with the $[001]_Y$ axis close to the substrate plane will be referred to as pseudo-*a*-oriented.

The proportions of pseudo-*c*- and pseudo-*a*-oriented domains varied depending on the deflection angle γ. Figure 2 shows the rocking curves over a wide angular range for the (3 0 10) planes in YBCO for various angles γ. For both pseudo-*a*- and pseudo-*c*-oriented domains, this peak lies in the vicinity of the reflection $(010)_N$, which enables us to estimate the ratio of volumes for domains with corresponding orientations in the films from the ratio of the integrated intensities of the peaks. For small values of γ (less than 10°), the formation of pseudo-*a*-oriented domains is suppressed. An increase in γ leads to a rapid increase in the fraction of pseudo-*a*-oriented domains (a similar behavior was observed by Divin *et al.* [13]), which is probably associated with the nature of nucleation and growth of a YBCO film on a substrate whose surface deviates from low-index planes. Such a surface is a set of “steps” whose terraces and end faces are parallel to low-index planes [4]. The junction between a terrace and an end face is an advantageous site for the nucleation of a YBCO film from the energy point of view. The direction of fastest growth is the most densely packed direction; for this reason, the nuclei in which the $[001]_Y$ axis

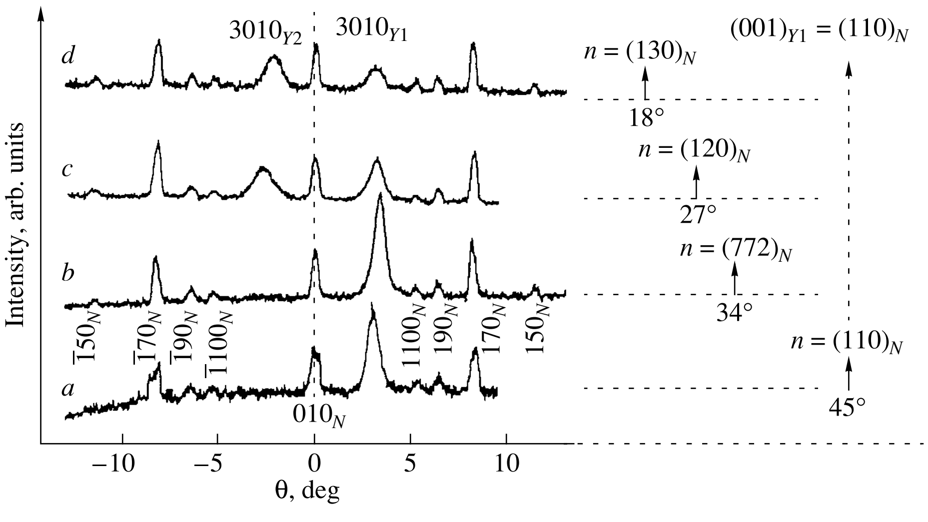

Fig. 2. Rocking curves recorded in a wide range of scanning of (3 0 10) YBCO peaks for various angles of deflection of the substrate normal from the [110] direction of NGO: Y_1 and Y_2 are pseudo-*c*- and pseudo-*a*-oriented domains, respectively. The angles are measured from the direction of the (010) NGO reflection.

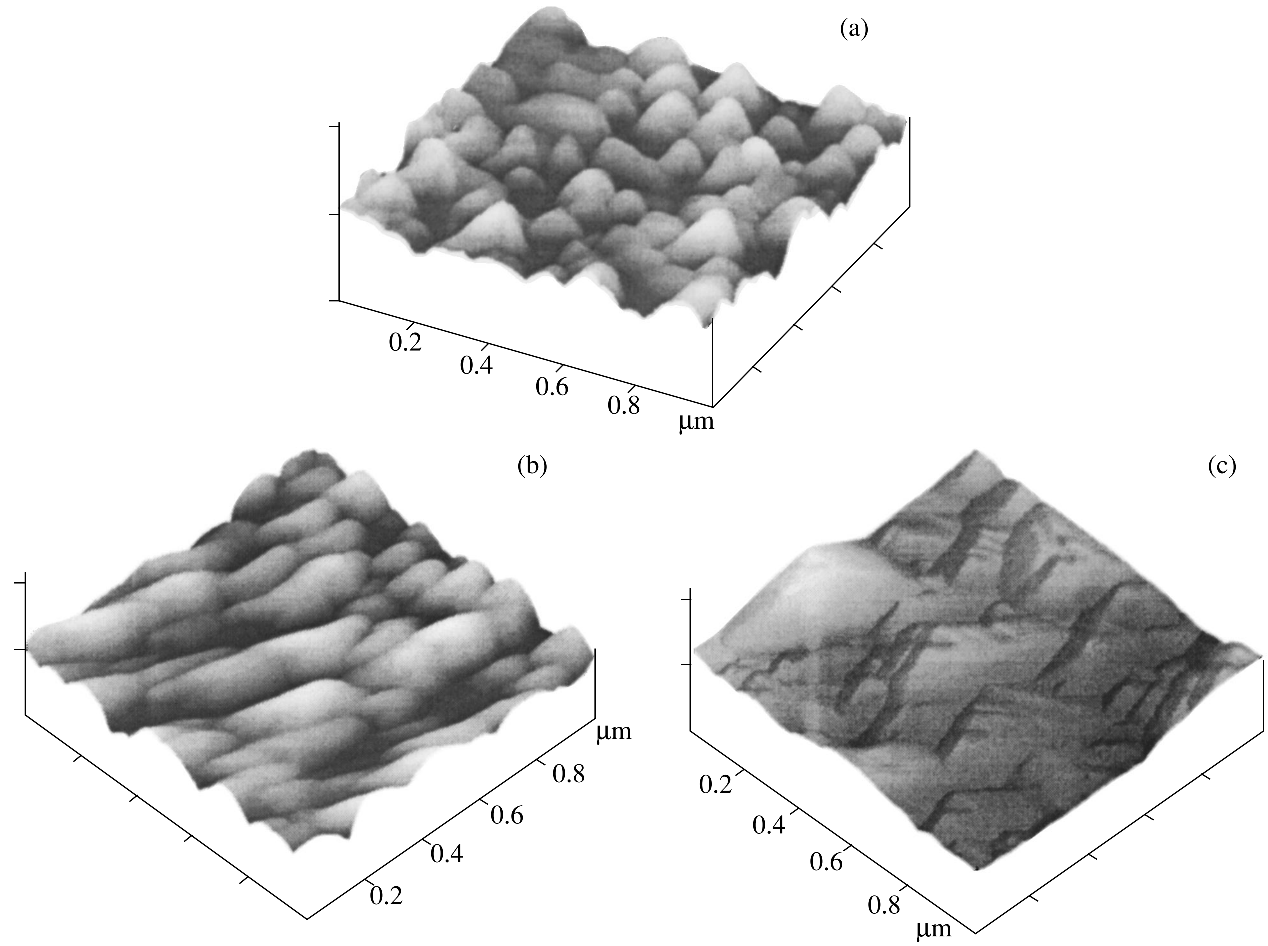

Fig. 3. Surface profilograms for typical YBCO films deposited on NGO substrates, obtained with the help of an atomic-force microscope: (a) (110) NGO substrate, (b) (120) NGO substrate, and (c) (120) NGO substrate coated with a thin CeO_2 epitaxial layer. In all the figures, one division corresponds to 0.2 μm along the horizontal and to (a, b) 760 Å and (c) 0.5 μm along the vertical.

is parallel to the end face of the step (pseudo-*c*-orientation) grow predominantly along terraces, while fragments with their $[001]_Y$ axis oriented along a terrace (pseudo-*a*-orientation) grow predominantly along the end faces of the steps. For small deflection angles, the length of the end face of a step is small (1–2 lattice constants of the substrate) and, hence, the growth of pseudo-*a*-oriented domains is suppressed. An increase in angle γ leads to comparable lengths of the end face and the terrace of a step, and the growth of pseudo-*a*-oriented domains in the film starts competing with the growth of pseudo-*c*-oriented domains. The experimentally determined fractions of pseudo-*a*-oriented domains for various angles γ are presented in Table 1.

Table 1. Fractions of domains with various orientations in YBCO films on tilted-axis NGO substrates

Substrate	Deflection angle γ, deg	$I(3\ 0\ 10)_a/I(3\ 0\ 10)_c$	Fraction of pseudo-*a*-oriented domains, %
(110)	0	0–0.1	0–10
(772)	11	0	0
(120)	18	0.8	45
(130)	26	1.6	60

Note: The third column contains the ratio of quantities $I(3\ 0\ 10)$ for pseudo-*a*- and pseudo-*c*-oriented films.

The observation of the surface of YBCO films with the help of an atomic force microscope shows that the surface of the films consists of coarse steps which are much larger than the steps on the surface of the substrate as regards both the width of the terrace and the height of the end face (Fig. 3). A film deposited on the (110) NGO substrate has no clearly manifested directions on the surface (Fig. 3a), while films deposited on a TAS exhibit extended steps (ridges) on the surface of the film (Fig. 3b). The height of the steps is 200–500 Å and increases with the deflection angle γ. A similar pattern was observed in [20, 21] for a $SrTiO_3$ film growing on a TAS.

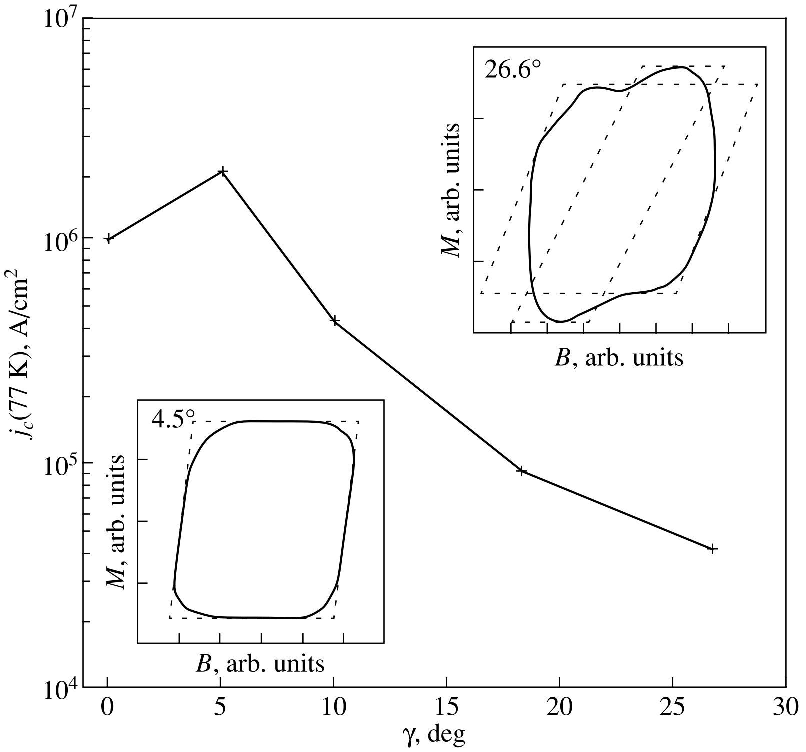

Fig. 4. Dependence of the critical current density j_c (77 K), determined by the contactless method, on the angle γ of deflection of the substrate normal from the [110] direction of NGO. The lower inset shows the magnetization curve for the deflection angle 4.5°; the upper, for the deflection angle 26.6°.

In order to determine the critical current density j_c of the films, we measured the dependence of the film magnetization M on the applied magnetic field B. Such a dependence has the shape of a parallelogram for a homogeneous film. The variation of the properties upon a transition from one domain to another leads to a smoothing of the angles of the parallelogram as a result of averaging the dependences for individual fragments of the film. The $M(B)$ dependences for films deposited on an NGO TAS with $\gamma < 20°$ demonstrate a closeness to a perfect parallelogram (lower inset in Fig. 4). For small deviation angles $\gamma < 5°$, the attainment of structural perfection of the films leads to an increase in the critical current (Fig. 4). In addition, the superconducting transition temperature of such films increases by 1–1.5 K. A decrease in the critical current density upon further increase in the deviation angle γ is associated with the passage of the current at right angles to the basal planes of YBCO. The deviation of the substrate plane by $\gamma = 26.6°$ [the (130) plane of the substrate] leads, apart from a further decrease in the current density, to a sharp change in the shape of the $M(B)$ curve (upper inset to Fig. 4). The two-loop dependences $M(B)$ may be due to the emergence of a considerable number of pseudo-*a*-oriented domains.

The twinning of YBCO films on NGO TASs, as well as on (110) NGO substrates [22], occurs in accordance with the {110}/⟨110⟩ scheme. As a result of twinning, regions with different orientations of the *a* and *b* crystallographic axes appear in the film. In these regions, the axes are interchanged and simultaneously rotated through the twinning angle, which leads to the splitting of reflections in x-ray diffraction experiments. For example, reflections of the (*h*0*l*) type exhibit splitting in 2θ, i.e., in the crystal lattice parameter, due to interchange of the *a* and *b* axes and in θ as a result of disorientation. Since the twinning in YBCO can occur in the two equivalent planes (110) and $(1\bar{1}0)$, this type of reflection is characterized by four components (Fig. 5a). In the 2θ vs. θ coordinates, the disorientation of domains is manifested in the splitting of reflections relative to the 2θ–θ (dashed) line and the split reflections lying on this line are not disoriented. All four components for films deposited on NGO TASs with small γ were observed for reflections $(3\,0\,10)_Y$ (Fig. 5a). However, for large angles of deviation ($\gamma > 15°$), twinning can be suppressed, which follows from the absence of splitting relative to the 2θ–θ line (Fig. 5c). It should be noted that the domains with different orientations of $[100]_Y$ in a YBCO film have approximately the same volume irrespective of the presence or absence of twinning in the film. In order to determine the effect of the orientation of the substrate plane on twinning, we deposited YBCO films on a substrate tilted to the $(110)_N$

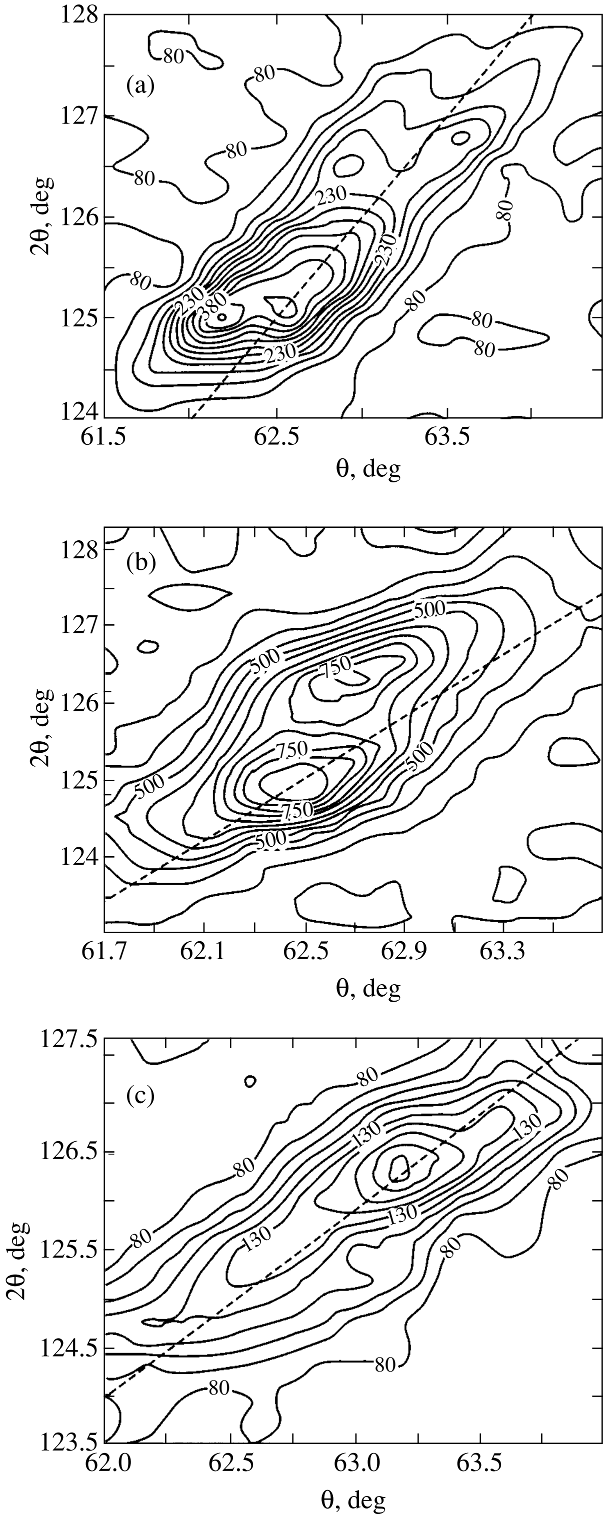

Fig. 5. Two-dimensional x-ray diffraction spectra in the (θ, 2θ) coordinates in the vicinity of the (103) and (013) peaks, exhibiting twinning features in YBCO films on NGO substrates with tilted axes. The film orientation: (a) $\gamma = 5°$, rotation around $[001]_N$; (b) $\gamma = 11°$, rotation around $[111]_N$; and (c) $\gamma = 26.6°$, rotation around $[001]_N$. The dashed line is the θ–2θ straight line.

plane by 11°, with the tilt axis being $[\bar{1}11]_N$ or $[1\bar{1}1]_N$ rather than the $[001]_N$ axis. The surface of the obtained substrate was close to the $(772)_N$ crystallographic plane. For such a deviation of the substrate surface from the $(110)_N$ plane, one of the twinning directions preserves its orientation relative to the substrate plane, while the other changes its orientation. The YBCO films obtained on (772) NGO substrates demonstrated the presence of a single twinning complex, which is confirmed by the splitting of the reflections relative to the 2θ–θ line but not along this line (Fig. 5b). The twinning structure in YBCO films is formed during the phase transition from the tetragonal to the orthorhombic phase and compensates the stresses emerging due to mismatching of the film and substrate lattices. It is well known, however, that for small grain sizes, stresses in the film are released at the grain boundaries and no twinning takes place. As the crystallographic orientation of the film changes, relaxation of stresses can occur on its surface, and hence even small (about 10°) deviations of the orientation of a thin film can considerably change the number of twinning components, which was actually observed in YBCO films deposited on TASs.

3.2. Growth of Thin Epitaxial CeO_2 Layers on Tilted-Axis NGO Substrates

During the formation of thin CeO_2 epitaxial layers on NGO TASs, the deflection angle γ, as well as the deposition rate, considerably influences the epitaxial relations. In the entire range of angles and deposition rates, two types of epitaxy (which can coexist) are observed (Fig. 6, Table 2). Type I epitaxy corresponds to the traditionally observed growth of CeO_2 films on perovskite substrates [23, 24], in particular, on the (110) NGO substrate: $(001)_C \parallel (110)_N$ with $(1\bar{1}0)_C \parallel [001]_N$ (Fig. 6, type Ia). In the case of the deposition of the CeO_2 layer by electron-beam sputtering, type Ia epitaxy was observed in the entire range of reflection angles under investigation (except the case of the (010) NGO substrate).

In the case of magnetron reactive rf sputtering, this type of epitaxy is observed only on (110) NGO substrates. For (130) NGO substrates, the same type of epitaxy was observed, but with a transposition of the $[110]_C$ and $[001]_C$ directions (Fig. 6, type Ib), which is due to the presence of symmetry-equivalent directions $[110]_N$ and $[1\bar{1}0]_N$ of the substrate. With an increasing deflection angle, another type of epitaxy is observed, for which the $[111]_C$ direction is close to the $[010]_N$ direction; as before, $[1\bar{1}0]_C \parallel [001]_N$ in this case (Fig. 6, types IIa, IIb). A thin epitaxial CeO_2 layer on the (010) NGO substrate has (111) orientation. For substrate orientations intermediate between $(110)_N$ and $(010)_N$, the $[111]_C$ direction deviates from $[010]_N$ within 3° (Table 2).

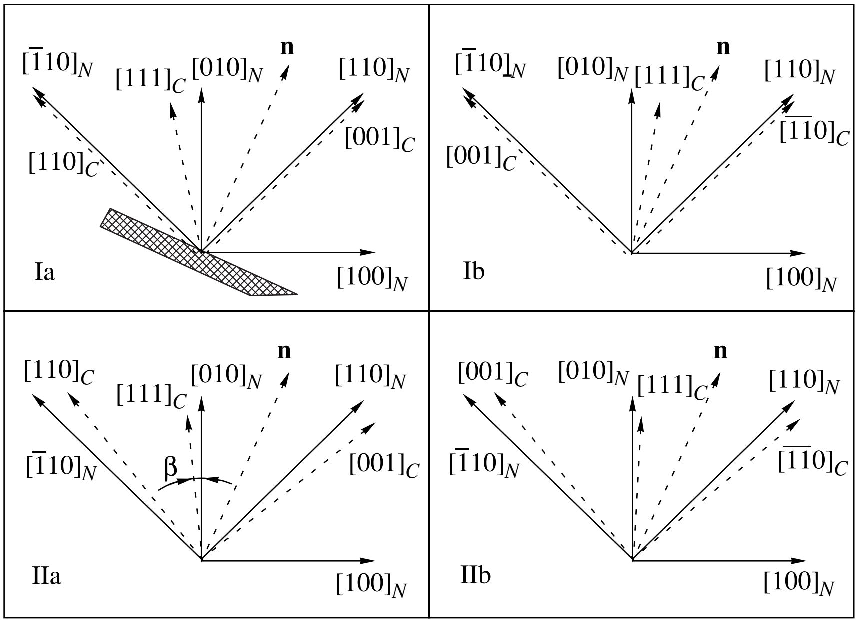

Fig. 6. Schematic diagram of epitaxial growth of CeO_2 on an NGO TAS. The normal **n** to the surface lies between $[010]_N$ and $[110]_N$.

Type II epitaxy, as well as type I epitaxy, can be realized in two versions with mutual transposition of the $[110]_C$ and $[001]_C$ directions. One of the (130) NGO substrates contained domains with both versions of epitaxy, IIa and IIb. In the case of electron-beam sputtering, type II epitaxy was observed only on (010) NGO substrates.

Thus, the rotation of the substrate plane from $(110)_N$ to $(010)_N$ changes the epitaxy type from I to II irrespective of the deposition method, but such a change occurs for $\gamma > 26°$ in the case of electron-beam sputtering and for $\gamma \geq 18°$ for rf sputtering. The reason for this discrepancy may be different deposition rates. For low deposition rates (electron-beam sputtering), the material being deposited is oxidized completely, which ensures epitaxial growth, preserving the structure of the oxygen sublattice of the substrate in the growing film. In this case, type I epitaxy is realized. An increase in the deposition rate leads to incomplete oxidation of the material being deposited. The difference in the perovskite (substrate) and fluorite (film) structures can lead to a change in the epitaxial relations (see, for example, [25, 26]). The effect of the oxygen concentration on the orientation of a deposited CeO_2 layer was observed, for example, in the case of CeO_2 deposition on a sapphire substrate [26–28], when the epitaxy in the oxygen sublattice was replaced by the epitaxy with the rotation of $(111)_C$ planes parallel to the substrate plane upon a decrease in the oxygen concentration in the growing film.

3.3. Growth of YBCO/CeO$_2$ Heterostructures on Tilted-Axis NGO Substrates

The orientation of YBCO films deposited on a thin CeO_2 epitaxial layer on an NGO TAS depends to a considerable extent on the sputtering method. In the case of pulsed laser sputtering, *c*-oriented YBCO films are formed irrespective of the orientation of the CeO_2 layer. Figure 7 (curve *a*) displays Bragg reflection peaks from the $(001)_Y$ planes for $\theta/2\theta$ scanning along the normal to the substrate. In this case, the $[100]_Y$ and $[010]_Y$ axes were oriented along the $[001]_N$ $[1\bar{1}0]_C$ direction, which was confirmed by the x-ray diffraction φ-scanning

Table 2. Epitaxy type of CeO_2 on tilted-axis NGO substrates for various deposition methods. The angles of deflection β of the $[111]_C$ direction of the CeO_2 layer from the $[010]_N$ axis of the NGO substrate are indicated. Notation for epitaxy types is given in Fig. 6

Substrate orientation	Deposition technique	Epitaxy type	β, deg
(110)	Rf sputtering	Ia	10
	Electron-beam sputtering	Ia	10
(120)	Rf sputtering	IIa	3
	Electron-beam sputtering	Ia	10
(130)	Rf sputtering	Ib	–8
		IIb (+IIa)	–3 (and 3)
	Electron-beam sputtering	Ia	10
(010)	Electron-beam sputtering	II	0

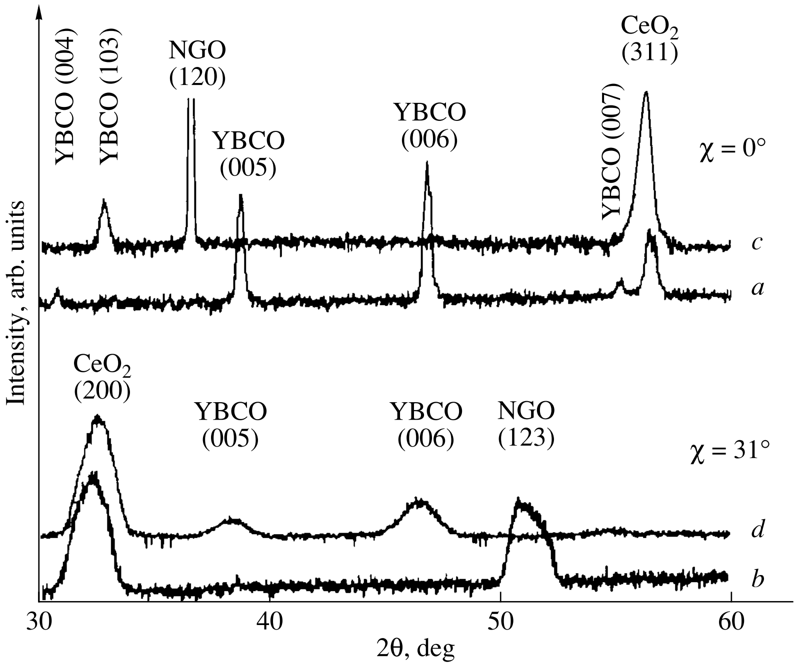

Fig. 7. X-ray diffraction patterns for θ/2θ scanning of YBCO/CeO_2 heterostructures on (120) NGO substrates. YBCO films are deposited by (*a*, *b*) laser sputtering and (*c*, *d*) dc sputtering; (*a*, *c*) scanning along the normal to the substrate and (*b*, *d*) scanning along the $[001]_C$ axis, deflected through 31° from the substrate normal.

method. In the observation of such a film through an atomic-force microscope, the film morphology differed insignificantly from that of the film deposited on the (110) NGO substrate (Fig. 3a). No other orientations of domains were observed in YBCO. For example, curve *b* in Fig. 7 depicts a diffraction pattern obtained as a result of θ/2θ scanning along the $[001]_C$ direction of a thin CeO_2 epitaxial layer tilted by 31° to the normal of the substrate. One might expect the emergence of Bragg reflection peaks from the $(00l)_Y$ planes along this direction if the films obeyed conventional epitaxial relations $(001)_Y \parallel (001)_C$ observed for the growth of two-layered YBCO/CeO_2 heterostructures on substrates in a standard orientation.

The YBCO films deposited by cathode sputtering were oriented so that $[001]_Y \parallel \langle 001\rangle_C$ are also irrespective of the orientation of the CeO_2 layer relative to the substrate. Curve *c* in Fig. 7 recorded for θ/2θ scanning along the normal to the substrate does not display the family of the (00*l*) peaks of YBCO that can be seen in the case of θ/2θ scanning along the $[001]_C$ direction (curve *d* in Fig. 7). In view of the cubic symmetry of CeO_2, the YBCO film can grow in three domain orientations. Preferred growth was observed for domains with the smallest angle between $[001]_Y$ and the normal to the substrate. This effect is similar to the preferential growth of *c*-oriented films compared to the *a*-oriented films on (110) NGO substrates at a high temperature of the YBCO film deposition. As a result of suppression of orientations with the $[001]_Y$ axis close to the substrate plane, different numbers of YBCO domain systems were formed on thin epitaxial CeO_2 layers depending on the type of CeO_2 epitaxy and the angle of deviation γ. The number of domains observed was one for type Ia epitaxy, two for type Ib and IIb types on (130) NGO substrates, and three for type IIa on a (120) NGO substrate. The morphology of such films studied by atomic-force microscope (Fig. 3c) demonstrates a characteristic pyramidal structure similar to that observed by Eom *et al.* [6] with the help of a transmission electron microscope. The reason behind such a morphology is the preferential growth of YBCO along the $[100]_Y$ and $[010]_Y$ directions coinciding with one of the $\langle 110\rangle_C$ directions, which are deflected from the normal.

The two types of epitaxy observed for different sputtering rates in the case of deposition of YBCO films on a thin epitaxial CeO_2 layer with a deviation of $\langle 110\rangle_C$ from the normal are similar to the two types of epitaxy observed for a CeO_2 epitaxial layer deposited on an NGO TAS. In both cases, the structure of the oxygen sublattice for low deposition rates determines the structure of the growing film, thus ensuring that the $[001]_Y$ axis follows the $\langle 001\rangle_C$ direction and $[001]_C$ follows $\langle 110\rangle_N$. An increase in the deposition rate leads to incomplete oxidation of the material being deposited; hence, the structure of the oxygen sublattice is not preserved and the epitaxial growth is determined by the kinetics of deposition. In this case, the condition for the minimization of surface energy becomes the most significant and the film grows so that the planes corresponding to the minimum energy are rotated parallel to the substrate plane. These planes in YBCO are the $(001)_Y$ planes, which leads to the formation of *c*-oriented films. Similar effects were observed earlier for YBCO films deposited on the oblique cuts of substrates and buffer layers in the case when the crystal lattices of the film and the substrate differ significantly [2, 5, 15–17]. However, the authors of these publications attributed such a behavior of the films to noticeable mismatching of the lattices of the film and the substrate (exceeding 5% for Y-stabilized ZrO_2 and 8% for MgO). We used CeO_2 with good lattice matching with that of the growing film (the mismatching of the lattice constant of the CeO_2 lattice and the $[110]_Y$ translation was less than 1%), which means that the difference in the type of the crystal structures of the film and the substrate is responsible for the *c*-oriented growth of YBCO on the CeO_2 sublayer with tilted axes.

Irrespective of the mutual orientation of the YBCO film, the CeO_2 layer, and the substrate plane, the YBCO film had a considerable (more than 60%) untwinned part (Fig. 8). Twinning complexes were oriented in the traditional way. Consequently, the twinning pattern is similar to that observed by us earlier on sapphire substrates with a CeO_2 buffer layer [22].

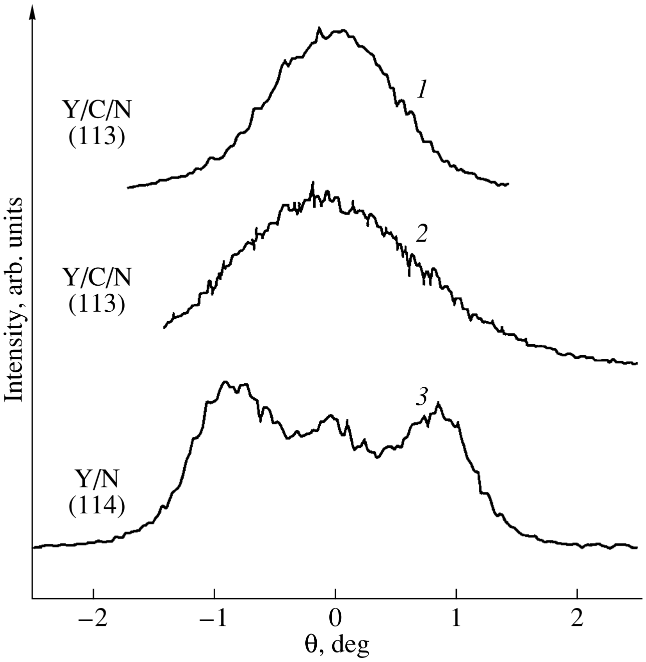

Fig. 8. Rocking curves for diffraction reflection peaks for YBCO films and YBCO/CeO_2 heterostructures on NGO TASs: (*1*) YBCO film oriented along $\langle 100\rangle_C$, (*2*) *c*-oriented YBCO film, and (*3*) twinned YBCO film on a (772) NGO substrate (given for comparison).

4. CONCLUSIONS

We obtained YBCO films and YBCO/CeO_2 heterostructures on NGO substrates with the normal deflected from [110] (the angle of deviation varied from 5° to 26.6°) and studied their growth, structure, and electrophysical properties. It was proved that the existence of symmetrically equivalent directions $[110]_N$ and $[1\bar{1}0]_N$ in the substrate with large deflection angles leads to the formation of a second system of domains in YBCO, which are rotated 90° relative to the initial system. The twinning in YBCO films on NGO TASs occurs in the same way as for ordinary substrates, but it is suppressed upon an increase in the deflection angle. The violation of the symmetric orientation of twins upon rotation of the substrate around the $[111]_N$ direction leads to the suppression of one of the twins.

The orientation of a thin epitaxial CeO_2 layer on an NGO TAS relative to the crystallographic axes of the substrate changes with an increase in the deflection angle. The application of reactive magnetron rf sputtering for depositing CeO_2 leads to an earlier change in the epitaxy type compared to the case of electron-beam sputtering. The presence of a thin epitaxial CeO_2 layer radically changes the orientation of the YBCO film growing on an NGO TAS. For high deposition rates (laser sputtering), the growing superconducting film has the (001) orientation (*c*-oriented film) and its domain and twin structures correspond to those of a film grown on a CeO_2 buffer layer on a $(1\bar{1}02)$ sapphire substrate. For low deposition rates (cathode sputtering), the multidomain YBCO film grows with the $[001]_Y$ axis oriented along the symmetry-equivalent directions $\langle 100\rangle_C$ of the CeO_2 layer. Twinning in YBCO films on a CeO_2 layer is suppressed irrespective of the orientations of the CeO_2 layer and of the YBCO film.

ACKNOWLEDGMENTS

The authors are grateful to K.Sh. Yakobsen for his help in contactless measurements of electrophysical properties of the films and to Yu.A. Boĭkov, I.V. Borisenko, Z.G. Ivanov, T. Claeson, and E.A. Stepantsov for fruitful discussions.

This study was supported in part by the Russian Foundation for Basic Research, INTAS (grant no. 11459), the Russian Federal program "Contemporary Problems in the Physics of Condensed State" (subprogram "Superconductivity"), the International Center of Science and Technology (project no. 1199), and the program "Science for Peace" (grant no. 973559).

REFERENCES

1. L. P. Gor'kov and N. B. Kopnin, Usp. Fiz. Nauk **156** (1), 117 (1988) [Sov. Phys. Usp. **31**, 850 (1988)].

2. F. C. Wellstood, J. J. Kingston, and J. Clarke, J. Appl. Phys. **75** (2), 683 (1994).
3. F. Vassenden, G. Linker, and J. Geerk, Physica C (Amsterdam) **175**, 566 (1991).
4. M. Mukaida, S. Miyazawa, and M. Sasaura, Jpn. J. Appl. Phys. **30** (8), 1474 (1991).
5. J. A. Edwards, J. S. Satchell, N. G. Chew, *et al.*, Appl. Phys. Lett. **60** (19), 2433 (1992).
6. C. B. Eom, A. F. Marshall, Y. Suzuki, *et al.*, Phys. Rev. B **46** (18), 11902 (1992).
7. K. Hermann, G. Kunkel, M. Siegel, *et al.*, J. Appl. Phys. **78** (2), 1131 (1995).
8. J. W. Seo, B. Kabius, C. L. Jia, *et al.*, Physica C (Amsterdam) **225**, 158 (1994).
9. J. P. Zheng, S. Y. Dong, D. Bharattacharya, and H. S. Kwok, J. Appl. Phys. **70** (11), 7167 (1991).
10. H. Sato, H. Akoh, and S. Takada, Appl. Phys. Lett. **64** (10), 1286 (1994).
11. F. Gire, D. Robbes, C. Gonzalez, *et al.*, IEEE Trans. Appl. Supercond. **7** (2), 3200 (1997).
12. T. Haage, H.-U. Habermeier, and J. Zegenhagen, Surf. Sci. Lett. **370**, 158 (1997).
13. Yu. Ya. Divin, U. Poppe, J.-W. Seo, *et al.*, Physica C (Amsterdam) **235**, 675 (1994).
14. Y. Y. Divin, U. Poppe, C. L. Jia, *et al.*, Inst. Phys. Conf. Ser., No. 167, 29 (1999).
15. M. G. Norton, B. Moeckly, C. B. Carter, and R. A. Buhrman, J. Cryst. Growth **114**, 258 (1991).
16. J. H. Kim and D. Youm, Physica C (Amsterdam) **275**, 273 (1997).
17. F. Tafuri, F. Miletto Granocio, F. Carillo, *et al.*, Physica C (Amsterdam) **326–327**, 63 (1999).
18. P. B. Mozhaev, P. V. Komissinski, N. P. Kukhta, *et al.*, J. Supercond. **10** (3), 221 (1997).
19. I. K. Bdikin, I. M. Kotelyanskii, E. K. Raksha, *et al.*, Inst. Phys. Conf. Ser., No. 167, 121 (1999).
20. U. Poppe, Y. Y. Divin, M. I. Faley, *et al.*, IEEE Trans. Appl. Supercond. (2001) (in press).
21. T. Haage, J. Q. Li, B. Leibold, *et al.*, Solid State Commun. **99** (8), 553 (1996).
22. I. K. Bdikin, A. D. Mashtakov, P. B. Mozhaev, and G. A. Ovsyannikov, Fiz. Tverd. Tela (St. Petersburg) **40** (4), 609 (1998) [Phys. Solid State **40**, 558 (1998)].
23. Yu. A. Boikov and Z. G. Ivanov, J. Alloys Compd. **251**, 193 (1997).
24. M. A. A. M. van Wijck, M. A. J. Verhoeven, E. M. C. M. Reuvekamp, *et al.*, Appl. Phys. Lett. **68** (4), 553 (1996).
25. A. L. Vasiliev, G. van Tendeloo, A. Amelinckx, *et al.*, Physica C (Amsterdam) **244**, 373 (1995).
26. Yu. A. Boikov, T. Claeson, D. Erts, *et al.*, Phys. Rev. B **56** (17), 11312 (1997).
27. P. B. Mozhaev, G. A. Ovsyannikov, and I. L. Skov, Zh. Tekh. Fiz. **69** (2), 119 (1999) [Tech. Phys. **44**, 242 (1999)].
28. I. M. Kotelyanskii, V. A. Luzanov, Y. M. Dikaev, *et al.*, Thin Solid Films **280**, 163 (1996).

Translated by N. Wadhwa

Physics of the Solid State, Vol. 43, No. 9, 2001, pp. 1621–1625. Translated from Fizika Tverdogo Tela, Vol. 43, No. 9, 2001, pp. 1558–1561.
Original Russian Text Copyright © 2001 by Belyavsky, Konchakov.

Hyperbolic Excitons in Semiconductors

V. I. Belyavsky and R. A. Konchakov
Voronezh Pedagogical University, ul. Lenina 86, Voronezh, 394043 Russia
e-mail: vib@vspu.ac.ru

Received December 6, 2000

Abstract—The energy and damping of the quasi-stationary state corresponding to a hyperbolic exciton in a semiconductor crystal are calculated. It was assumed that the screened Coulomb potential describes the interaction between the electron and hole. The resonance conditions due to the hyperbolic exciton are determined. *© 2001 MAIK “Nauka/Interperiodica”.*

1. The peculiarities of the optical spectra of semiconductor crystals in the range of fundamental absorption are related to the van Hove singularities in the combined density of states of the electrons and holes. The exciton effects due to Coulomb interaction give rise to a set of states at energies which are smaller than the energy corresponding to the minimum density of states. Saddle points of the dispersion law are situated at the depth of the energy band. In this case, the bound states of electrons and holes definitely get into the continuous spectrum. Therefore, they are quasi-stationary states.

The concept of the hyperbolic exciton (the saddle point) put forward by Phillips [1–4] assumes the presence of a resonance (or several resonances) in the optical spectra at an energy corresponding to a saddle point. The experimental studies of hyperbolic excitons in semiconductor crystals [5–12] indicate that the corresponding exciton resonances manifest themselves in the form of clearly pronounced bands in the absorption and reflection spectra. In the vicinity of a saddle point, the principal values of the inverse effective mass tensor have different signs and, therefore, the isoenergetic surfaces are hyperboloids to a first approximation. The hyperbolic metric of the k space does not permit one to obtain an exact solution for the wave functions and energy spectrum of the hyperbolic exciton. In the case of an exciton associated with a minimum in the density of states [13], the situation is similar. When the effective masses are extremely anisotropic, the fast motion with small mass and slow motion with large mass can be separated in the adiabatic approximation [14]. Thus, an approximate solution corresponding to the exciton resonance and existing during the lifetime of the exciton can be found. The question of the lifetime of the hyperbolic exciton remains open.

2. In a nonconducting crystal, free carriers screen the correlation interaction between electrons and holes,

$$U(r) = -\frac{e^2}{\varepsilon_0 r}\exp(-k_0 r), \tag{1}$$

where $k_0^{-1} \equiv r_0$ is the screening length and ε_0 is the static dielectric permittivity of the crystal. For this reason, a restricted domain of k space, $k \le k_0$, which is essentially smaller than the Brillouin zone, gives the dominant contribution to the linear combination of the products of the electron and hole Bloch functions forming the exciton wave function. In this case, the quasi-stationary state due to the interaction between the electron and hole can be qualitatively investigated using a method [15, 16] applied to consider the correlation between electrons in superconductors.

We considered the simplest two-band model of a semiconductor. Let $\varepsilon_c(k_e)$ and $\varepsilon_v(k_h)$ be the dispersion laws of the electrons in the conduction and valence bands, respectively. Then, the excitation energy of a free electron–hole pair is

$$E_{\mathrm{EHP}}(K, k) = E_g + \varepsilon_c\left(\frac{K}{2} + k\right) - \varepsilon_v\left(\frac{K}{2} - k\right), \tag{2}$$

where $K = k_e + k_h$ is the quasi-momentum of the pair, with k_e and k_h being the quasi-momenta of the electron and hole, respectively; E_g is the (direct) band gap; and $k = (k_e - k_h)/2$ is the quasi-momentum of the relative motion of the electron–hole pair. Since the characteristic range of the electron–hole interaction is $r_0 \gg a$, where a is the interatomic distance, only the values of k satisfying the inequality $k < k_0$ are important in Eq. (2). Thus, Eq. (2) can be represented as

$$\begin{aligned} E_{\mathrm{EHP}}(K, k) &= E_g + \varepsilon^{(-)}(K) \\ &+ \hbar v_\alpha(K) k_\alpha + \frac{\hbar}{2m}\nu_{\alpha\beta}(K) k_\alpha k_\beta, \end{aligned} \tag{3}$$

where $\varepsilon^{\pm}(K) = \varepsilon_c(K/2) \pm \varepsilon_v(K/2)$, m is a parameter with the dimensions of mass,

$$v_\alpha(K) = \frac{1}{\hbar}\frac{\partial\varepsilon^{(+)}(K)}{\partial k_\alpha}, \quad \nu_{\alpha\beta}(K) = \frac{2m}{\hbar^2}\frac{\partial^2\varepsilon^{(-)}(K)}{\partial k_\alpha \partial k_\beta}, \tag{4}$$

and summation over repeated indices is implied.

3. In the Wannier exciton representation, the effective Hamiltonian of the electron–hole pair is

$$\hat{H}_K = -\frac{\hbar^2}{2m}\nu_{\alpha\beta}(K)\frac{\partial^2}{\partial x_\alpha \partial x_\beta} - i\hbar v_\alpha(K)\frac{\partial}{\partial x_\alpha} + U(r). \quad (5)$$

The energy of the relative motion of the pair is reckoned from the value $E_g + \varepsilon^{(-)}(K)$. The envelope function of the electron–hole pair with quasi-momentum K is represented in factorized form as

$$\psi_K(R, r) = \varphi_K(r)\exp(iKR), \quad (6)$$

where R is the radius vector of the pair as a whole, r is the radius vector of the relative motion, and $\varphi_K(r)$ is the eigenfunction of Hamiltonian (5). To eliminate the term linear in the quasi-momentum in the effective Hamiltonian, the eigenfunction is represented in the form

$$\begin{gathered}\varphi_K(r) = \chi_K(r)\exp(i\lambda_\alpha x_\alpha), \\ \lambda_\alpha \equiv \lambda_\alpha(K) = -\frac{m}{\hbar}\nu^{-1}_{\alpha\beta}(K)v_\beta(K).\end{gathered} \quad (7)$$

In this case, the equation for the envelope function $\chi_K(r)$ takes the form

$$-\frac{\hbar^2}{2m}\nu_{\alpha\beta}(K)\frac{\partial^2\chi_K(K)}{\partial x_\alpha \partial x_\beta} + U(r)\chi_K(K) = \varepsilon_K\chi_K(K), \quad (8)$$

where

$$\varepsilon_K = E + \frac{m}{2}v_\alpha(K)\nu^{-1}_{\alpha\beta}(K)v_\beta(K). \quad (9)$$

For any value of K, the matrix $\nu_{\alpha\beta}(K)$ can be reduced to principal axes. Then, it takes the form $\nu_{\alpha\beta}(K) = \nu^{(\alpha)}(K)\delta_{\alpha\beta}$ and Eq. (8) can be rewritten as

$$-\frac{\hbar^2}{2m}\sum_\alpha \nu^{(\alpha)}(K)\frac{\partial^2\chi_K(r)}{\partial^2 x_\alpha^2} + U(r)\chi_K(r) = \varepsilon_K\chi_K(r). \quad (10)$$

4. As should be expected in the case of a continuous spectrum, the relative motion of the electron–hole pair described by Eq. (10) is infinite. It does not exclude the possibility of the appearance of a relatively long-lived quasi-stationary state characterized by the complex energy $\tilde{E}_K^0 = E_K^{(0)} - i\Gamma_K$, which manifests itself as a pole of the scattering amplitude at the energy $E = \tilde{E}_0$. The Fourier transform of the scattered wave $\tilde{\chi}_K(k)$ satisfies the integral equation [16]:

$$\begin{gathered}\frac{\hbar^2}{2m}(q^2 - k^2)\tilde{\chi}_K(k) \\ = \tilde{U}(k-q) + \int \tilde{U}(k-k')\tilde{\chi}_K(k')\frac{d^3k'}{(2\pi)^3}, \\ k^2 \equiv \sum_\alpha \nu^{(\alpha)}(K)k_\alpha^2, \\ \varepsilon_K = (\hbar^2/2m)\sum_\alpha \nu^{(\alpha)}(K)q_\alpha^2 \equiv q^2.\end{gathered} \quad (11)$$

The character of solutions to Eq. (11) can be investigated qualitatively by using the estimate of the integral according to the mean-value theorem. We replace the original potential in Eq. (1) by a singular potential $U(r) \longrightarrow U_0 r_0^3\delta(r)$, where the factor r_0^3 provides the proper dimensions of the parameter U_0 naturally defined as

$$U_0 = -\frac{4\pi e^2}{\varepsilon_0 r_0}. \quad (12)$$

We determine the truncated region of the Fourier transform of the potential in Eq. (1) using the condition $|k| \le k_0$ and denote it by $\{Q\}$. Equation (11) can be solved easily to give

$$\tilde{\chi}_{Kq}(K) = -\frac{w}{1 + wB_K(q^2)}\frac{1}{k^2 - q^2 - i0 \times \mathrm{sgn}\,q^2}. \quad (13)$$

Here, $w = 2mU_0r_0^3/\hbar$, the sign function $\mathrm{sgn}\,q^2$ ensures the necessary asymptotic behavior of the diverging wave, and

$$\begin{aligned}B_K(q^2) &= \int_{\{Q\}} \frac{1}{k^2 - q^2 - i0 \times \mathrm{sgn}\,q^2}\frac{d^3k}{(2\pi)^3} \\ &\equiv B_{K1}(q^2) + iB_{K2}(q^2).\end{aligned} \quad (14)$$

The real and imaginary parts (for the real argument q^2) of the function in Eq. (14) are written in the form

$$\begin{aligned}B_{K1}(q^2) &= \int_{\{Q\}} \frac{1}{k^2 - q^2}\frac{d^3k}{(2\pi)^3}, \\ B_{K2}(q^2) &= \pi\int_{\{Q\}} \delta(k^2 - q^2)\frac{d^3k}{(2\pi)^3}\mathrm{sgn}\,q^2,\end{aligned} \quad (15)$$

where the integral defining $B_{K1}(q^2)$ is understood in terms of its principal value.

5. The denominator of the scattering amplitude, $1 + wB_K(q^2)$, is nonzero at any real value of q^2. The only exception is the case when $B_{K2}(q^2)$ is identically zero. The poles of the scattering amplitude, determined by the equation

$$1 + wB_{K1}(q^2) = 0, \quad (16)$$

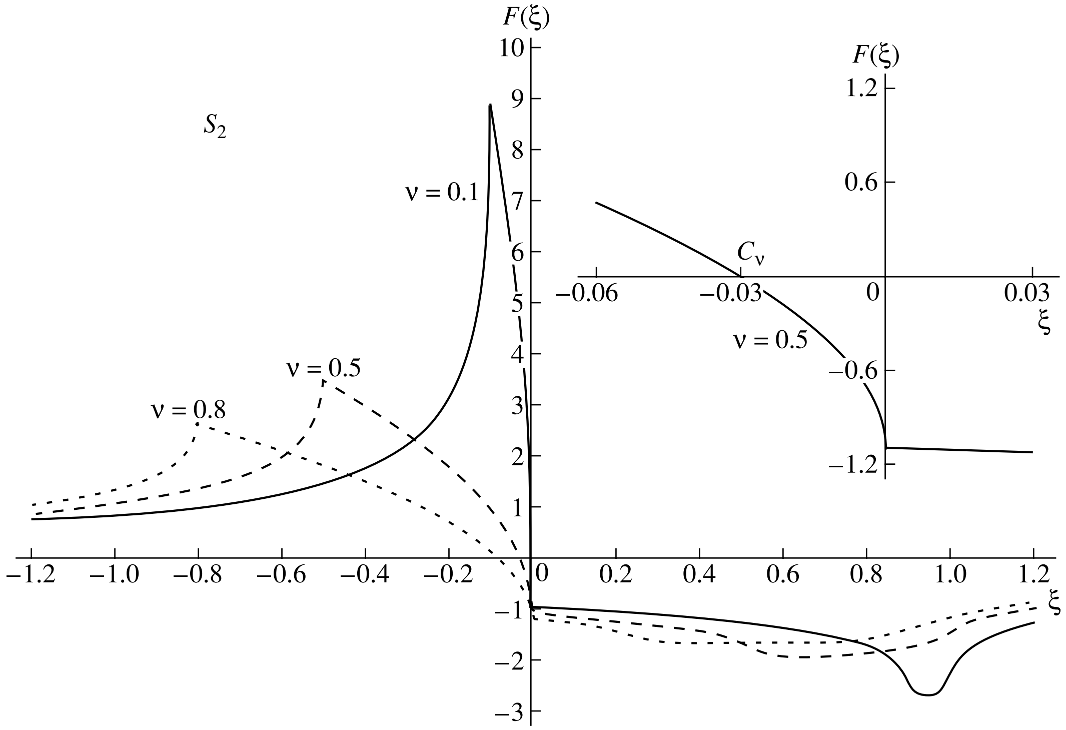

Fig. 1. Graph of the dimensionless function $F(\xi)$ [$B_{K1}(q^2) = k_0F(\xi)$), where $\xi = q^2/k_0^2$ is a dimensionless variable] for the case of saddle point S_2 at $\nu = 0.1$, 0.5, and 0.8. The character of the singularity of $F(\xi)$ at the point $\xi = 0$ is shown at the top right.

correspond to bound states. For the electron–hole pair, this situation appears in the energy range below the minimal energy of the dispersion law $\varepsilon^{(-1)}(k)$. If Eq. (16) admits a solution at some value of the argument $q^2 = q_0^2$ and $B_{K2}(q_0^2) \neq 0$ is nonzero, then, in the vicinity of the point q_0^2, the function $B_{K1}(q^2)$ can be represented as

$$B_{K1}(q^2) \approx B_{K1}(q_0^2) + B'_{K1}(q_0^2)(q^2 - q_0^2), \tag{17}$$

where the prime denotes differentiation with respect to q^2. In this case, the scattering amplitude is written in the form

$$f_K(q^2) = -\frac{w_K}{1 + w_K B_K(q^2)} \approx -\frac{\hbar^2}{2m}\frac{1}{B'_{K1}(q_0^2)}\frac{1}{E - E_K^{(0)} + \frac{i\Gamma_K}{2}}. \tag{18}$$

Here, $E_K^{(0)} = \hbar^2 q_0^2/2m$ is the energy of the quasi-stationary state and $E = \hbar^2q^2/2m$. The damping of the state is

$$\Gamma_K = \frac{\hbar^2}{m}\frac{B_{K2}(q_0^2)}{B'_{K1}(q_0^2)}. \tag{19}$$

6. Further, the dispersion law is assumed to possess axial symmetry in the vicinity of the saddle point. In this case, we define $q^2 = \nu q_t^2 - q_3^2$ in the vicinity of point S_1 and $q^2 = -\nu q_t^2 + q_3^2$ in the vicinity of point S_2. Here, $q_t^2 = q_1^2 + q_2^2$ and ν is a dimensionless parameter characterizing the anisotropy of the dispersion law. For simplicity, the cylinder $k_t \leq k_0$, $|k_3| \leq k_0$ is considered to be the range of integration $\{Q\}$. Like the sphere $k^2 \leq k_0^2$, this region has the only characteristic scale k_0 in momentum space. We note that integrals in Eq. (15) weakly depend on the shape of region $\{Q\}$. Due to the axial symmetry, $B_{K1}(q^2)$ can be expressed in terms of elementary functions. The corresponding expression is complicated, and we present only graphs of the function $B_{K1}(q^2)$ for several values of the parameter ν in the case of the saddle point S_2 (Fig. 1).

The asymptotic behavior of function (15) at $|q^2| \longrightarrow \infty$ is $B_{K1}(q^2) \sim -Q^3/(2\pi)^3q^2$, where Q^3 is the volume of region $\{Q\}$. As is seen from Fig. 1, the function $B_{K1}(q^2)$ is restricted from both above and below. In addition, it possesses a special symmetry, namely, $B_{K1}^{(S_2)}(q^2) = -B_{K1}^{(S_1)}(-q^2)$ in the case of the dispersion law defined above. Here, the upper index indicates the particular saddle point with which the function $B_{K1}(q^2)$ is associ-

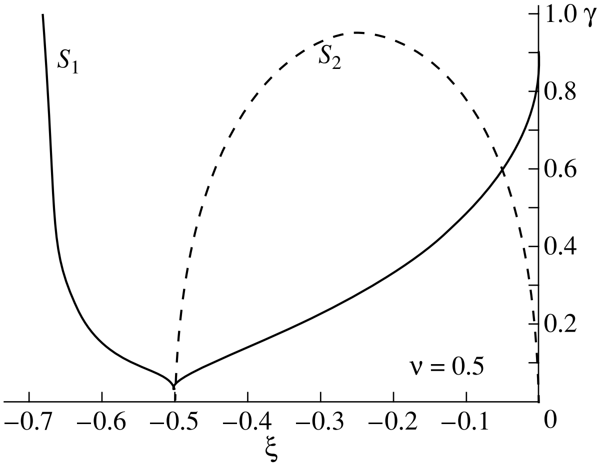

Fig. 2. Graph of the dimensionless quantity $\gamma = \Gamma_K/\Gamma_K^{(0)}$ as a function of the dimensionless variable $\xi = q^2/k_0^2$ for saddle points S_1 and S_2.

ated. Therefore, Fig. 1 makes it possible to analyze the conditions for the appearance of quasi-stationary states at saddle points of both types.

The condition $w < 0$ corresponds to attraction between the electron and hole. For this reason, as seen from Fig. 1, Eq. (16) has a solution not for any value of $|w|$ but only above a certain minimal value $|w_m|$. For point S_2, we have

$$\frac{1}{(w_m)} = B_{K1}(-\nu k_0^2) = \frac{k_0}{4\pi^2\nu}\left\{2\sqrt{\nu}\arctan\frac{1}{\nu} + \ln(1+\nu)\right\}. \tag{20}$$

At $\nu \ll 1$, the states of the electron–hole pair can be considered quasi-one-dimensional (1D) because the limitation on $|w_m|$ is actually removed in this case: $|w_m| \sim \sqrt{\nu}$. The quasi-two-dimensional (2D) case, corresponding, for example, to a layered crystal, can be considered analogously under the assumption that $\nu \gg 1$ at ν/m = const. In this case, the limitation on $|w_m|$ is much weaker in comparison with the three-dimensional (3D) case: $|w_m| \sim 1/\ln\nu$.

It follows from definition (15) that $B_{K2}(q^2) > 0$ at $q^2 > 0$ and $B_{K2}(q^2) < 0$ at $q^2 < 0$. Therefore, Eq. (16) admits a solution corresponding to a quasi-stationary state if $-\nu < q^2 < C_\nu$ in the case of saddle point S_2. Here, C_ν is a root of the equation $B_{K1}(q^2) = 0$. Damping of the quasi-stationary state (19) is positive in the interval $-\nu < q^2 < C_\nu$, since $B'_{K1}(q^2) < 0$. Moreover, the damping is small in a wide interval of the values of parameter ν: $\Gamma_K/E_K(0) = 2B_{K2}(q_0^2)/q_0^2 B'_{K1}(q_0^2) \ll 1$. The quantity $\gamma = \Gamma_K/E_K^{(0)}$ as a function of $\xi = q^2/k_0^2$ is shown in Fig. 2.

The exciton states associated with the singularity of the electron–hole spectrum at saddle point S_1 can be considered analogously. The solutions corresponding to the quasi-stationary state exist in the interval $C'_\nu < q^2 < 0$, where C'_ν is a root of the equation $B'_{K1}(q^2) = 0$. In this case, as seen from Fig. 1, the values of $|w|$ at which the quasi-stationary state is possible are restricted from both above and below, contrary to the case of the S_2 exciton. The dependence of the damping of the S_1 exciton on $\xi = q^2/k_0^2$ differs significantly from the case of the S_2 exciton (Fig. 2).

7. The dependence of the condition for the appearance of the quasi-stationary state on parameter k_0 follows immediately from Eq. (20). Indeed, the function $B_{K1}(q^2)$ can be represented in the form $B_{K1}(q^2) = k_0 F(\xi)$, where $F(\xi)$ is a function of the dimensionless variable $\xi = q^2/k_0^2$. The parameter w can be written as $w = -8\pi/k_0^2 a^*$, where $a^* = \varepsilon_0\hbar^2/me^2$ is the effective Bohr radius. According to Eq. (20), for the quasi-stationary state to appear, the condition $F(-\nu) \geq k_0 a^*/8\pi$ must be fulfilled. In the 1D case ($\nu \ll 1$), this condition is $k_0 a^* \leq 2/\sqrt{\nu}$, while in the 2D case ($\nu \gg 1$ and ν/m = const), we have $k_0 a^* \leq 2\ln\nu$. If there is no clearly pronounced anisotropy (the 3D case, $\nu \approx 1$), this condition can be approximately written as $k_0 a^* \leq 1$. Thus, the anisotropy of the electron dispersion law, corresponding to the effective lowering of the dimensionality of the electron system, can essentially expand the interval of the values of k_0 in which the appearance of the quasi-stationary state can take place.

It follows from Fig. 1 that Eq. (16) admits not only a solution corresponding to the quasi-stationary state but also a solution with negative damping. Similar to electrons and phonons in a crystal with a point defect, such a solution can be interpreted [17] as a state corresponding to resonant scattering in the relative motion of an electron–hole pair. It should be noted that Eq. (16) also admits a resonant solution at $q^2 > 0$ in the case of the S_1 saddle point and a sufficiently large value of $|w|$.

ACKNOWLEDGMENTS

This work was supported by the Russian MNTP "Physics of Solid-State Nanostructures."

REFERENCES

1. J. C. Phillips, Phys. Rev. A **136** (6), 1721 (1964).
2. J. C. Phillips, Phys. Rev. A **139** (4), 1291 (1965).
3. J. C. Phillips, Solid State Phys. **18**, 55 (1966).

4. J. C. Phillips and B. O. Seraphin, Phys. Rev. Lett. **15** (3), 107 (1965).
5. V. K. Subashiev and Le Hak Bin, Pis'ma Zh. Éksp. Teor. Fiz. **12** (3), 139 (1970) [JETP Lett. **12**, 97 (1970)].
6. V. K. Subashiev, Solid State Commun. **9** (6), 369 (1971).
7. A. I. Savchuk, N. L. Govaleshko, G. D. Dalevskiĭ, and Z. D. Kovalyuk, Ukr. Fiz. Zh. **17** (9), 1548 (1972).
8. V. I. Sokolov and V. K. Subashiev, Phys. Status Solidi B **65** (2), K74 (1974).
9. G. I. Abutalypov and M. L. Belle, Fiz. Tekh. Poluprovodn. (Leningrad) **9** (7), 1330 (1975) [Sov. Phys. Semicond. **9**, 878 (1975)].
10. V. T. Agekyan, Yu. F. Solomonov, Yu. A. Stepanov, and V. K. Subashiev, Fiz. Tekh. Poluprovodn. (Leningrad) **10** (9), 1776 (1976) [Sov. Phys. Semicond. **10**, 1058 (1976)].
11. G. F. Glinskiĭ, A. A. Kopylov, and A. A. Pikhtin, Fiz. Tekh. Poluprovodn. (Leningrad) **12** (7), 1237 (1978) [Sov. Phys. Semicond. **12**, 785 (1978)].
12. S. V. Virko, M. P. Lisitsa, and F. V. Motsnyĭ, Fiz. Tverd. Tela (St. Petersburg) **42** (9), 1579 (2000) [Phys. Solid State **42**, 1622 (2000)].
13. R. S. Knox, *Theory of Excitons* (Academic, New York, 1963; Mir, Moscow, 1966).
14. B. Velicky and I. Sak, Phys. Status Solidi **16** (1), 147 (1966).
15. V. I. Belyavsky, V. V. Kapaev, and Yu. V. Kopaev, Zh. Éksp. Teor. Fiz. **118** (4), 941 (2000) [JETP **91**, 817 (2000)].
16. L. D. Landau and E. M. Lifshitz, *Course of Theoretical Physics*, Vol. 3: *Quantum Mechanics: Non-Relativistic Theory* (Nauka, Moscow, 1989, 4th ed.; Pergamon, New York, 1977, 3rd ed.).
17. W. A. Harrison, *Solid State Theory* (McGraw-Hill, New York, 1970; Mir, Moscow, 1972).

Translated by A. Poushnov

Physics of the Solid State, Vol. 43, No. 9, 2001, pp. 1626–1632. Translated from Fizika Tverdogo Tela, Vol. 43, No. 9, 2001, pp. 1562–1568.
Original Russian Text Copyright © 2001 by Agekyan, Vasil'ev, Serov, Filosofov, Yakimovich.

SEMICONDUCTORS AND DIELECTRICS

Relaxation Dynamics of Mn^{2+} Intraion Excitation in $Cd_{0.5}Mn_{0.5}Te$: Dependence on the Optical Pumping Level

V. F. Agekyan*, N. N. Vasil'ev*, A. Yu. Serov*, N. G. Filosofov*, and V. N. Yakimovich**
**Institute of Physics, St. Petersburg State University, Petrodvorets, St. Petersburg, 198904 Russia*
***Institute of Solid State and Semiconductor Physics, Belarussian Academy of Sciences, ul. Brovki 17, Minsk, 220072 Belarus*

Received February 8, 2001

Abstract—A study is reported of the Mn^{2+} intracenter 3*d* luminescence in a dilute $Cd_{0.5}Mn_{0.5}Te$ magnetic semiconductor at pulsed excitations of up to 3.5 MW/cm^2. At high excitation levels and at a temperature of 77 K, the kinetics varies strongly over the emission band profile. The luminescence decay curve can be resolved into a fast and a delayed component, which correspond to the excitation of extended and localized states in the manganese ion system. The fast relaxation of the extended states is largely determined by the up-conversion. As the temperature is lowered, the contribution of the fast component at the center of the emission band and in its low-energy wing decreases because of the weakening role of the extended states lying above the mobility edge. *© 2001 MAIK "Nauka/Interperiodica".*

1. INTRODUCTION

The 3*d* absorption and emission spectra of iron-group ions in various crystalline matrices have already been studied over a long period of time. These studies use, for a model, divalent manganese ions (see, e.g., [1–3]) that exhibit strong intracenter luminescence (IL) in matrices; this luminescence is widely employed in electroluminescent devices [4, 5]. The divalent iron-group ions substitute isoelectronically for cations in the II–VI semiconductor crystals to form solid solutions with a magnetic component, more specifically, with dilute magnetic semiconductors (DMSs), which are sometimes called semimagnetic semiconductors. Studies of the DMSs and of the related quantum systems are pursued primarily in two areas, namely, (i) in electron–ion interaction at high concentrations of localized magnetic-ion moments and the associated magnetooptic effects involving electronic (excitonic) states and (ii) in ion–ion interaction and its effect on the magnetic properties and intracenter 3*d* transitions in magnetic ions.

Attempts at investigating Mn^{2+} IL over a wide concentration range, from strongly dilute systems (single ions) to nearly complete substitution of manganese for a nonmagnetic cation in the same II–VI type matrix, have thus far been unsuccessful. In broad-bandgap crystals, for instance, CdS and ZnS, a high Mn concentration results in a strong lattice deformation, up to the formation of microinclusions of metallic manganese. In CdTe and CdSe crystals, which can be used to obtain $Cd_{1-x}Mn_xTe$ and $Cd_{1-x}Mn_xSe$ solid solutions over a broad range of x, the bandgap $E_g(x)$ is such that the IL is observed only starting from $x = 0.3–0.4$ [for small x, $E_g(x)$ is less than the 3*d* excitation threshold of manganese]. This accounts for certain difficulties encountered when investigating the dependence of the IL spectral structure and kinetics on the optical excitation level for various magnetic-ion concentrations. Combining the data obtained in different matrices meets only with limited success because of the large differences between the *LS* coupling constants for lattices containing different Group VI elements. The spin–lattice processes are governed by the *LS* coupling constant, and the 3*d* luminescence decay time is inversely proportional to it. For this reason, our understanding of the IL of Mn^{2+} and of other magnetic ions in crystalline matrices of the II–VI semiconductors is far from complete. The IL decay times of single manganese ions and of large clusters should differ by orders of magnitude. Excitation migration over clusters, first, facilitates the coupling of 3*d* electrons to acoustic phonons and, second, increases the probability of relaxation due to other excited Mn^{2+} ions and defects.

There is a wealth of experimental evidence supporting the interaction and competition among the intracenter and conventional band states in the course of the relaxation of electronic excitations in DMSs. For instance, in $Cd_{1-x}Mn_xTe$, as x increases above 0.4, the luminescence of the Wannier excitons weakens rapidly as a result of the excitation transfer from the band states to the manganese 3*d* shell. The excitation conditions that favor fast relaxation (with the emission of optical phonons) to the Wannier exciton level resonantly amplify the emission from this level while weakening the IL at the same time. It is also well known that doping iron-group ions into a semiconductor lattice suppresses optical orientation of the conduction electrons because of their spin direction undergoing fast relaxation due to interaction with magnetic ion moments.

The position of the lowest term T_1 of the Mn^{2+} 3*d*-shell excited state in a cubic lattice depends strongly on the magnitude of the local crystal field, whereas that of the $^6A_1$ ground state is affected by the field to a much lesser extent. For this reason, the parameters of the intracenter optical transitions, in particular, the absorption edge and the maximum of the emission band, depend on the local symmetry, elemental lattice composition, and the cation–cation and cation–anion distances. The position of the Mn^{2+} IL band maximum in various II–VI matrices can vary within a few tenths of an electronvolt. It was proposed to determine the temperature-induced variation of the lattice constant in wide-bandgap materials from the shift of the Mn^{2+} IL maximum [6]. Similar information can also be derived in hydrostatic-pressure experiments from the change in the Stokes losses, the shift of the IL band, and the variation of its shape in samples with different relative concentrations of magnetic and nonmagnetic ions. This is particularly important for multicomponent solid solutions containing one magnetic and two nonmagnetic ions ($Cd_{1-x-y}Mn_xMg_yTe$ and others) [7]. The interest in such three-cation solutions stems from the possibility of independently varying the bandgap width $E_g(x, y)$ and the magnetic properties determined by the magnitude of x.

DMSs were used to prepare a series of quasi-two-dimensional semiconductor structures, $CdTe/Cd_{1-x}Mn_xTe$ being the most studied among them. Structures with $x > 0.4$, whose barrier material exhibits IL [3], have been attracting considerable interest in recent years. In this case, the slow excitation relaxation in the 3d shells of barrier magnetic ions may considerably affect the photocarrier dynamics in nonmagnetic quantum wells. DMS nanocrystals, including their self-organized systems, have recently been synthesized [8, 9]. The increase in E_g in nanocrystals due to size quantization makes possible the observation of Mn^{2+} IL in $Cd_{1-x}Mn_xTe$ and $Cd_{1-x}Mn_xSe$ at lower manganese concentrations than is the case with bulk crystals. In addition, one may expect a change in the IL quantum efficiency and kinetics due to the stronger hybridization of the p and s states with the d states induced by quantum confinement. These new systems and areas of research stimulate interest in more comprehensive investigation of the electro- and photoluminescence of manganese ions in various semiconductor matrices.

The IL in $Cd_{1-x}Mn_xTe$ crystals with $x > 0.4$ manifests itself as a band with a half-width of 0.2 eV and a maximum at approximately 2.0 eV. Some authors assumed this band to originate from electron transitions from the 3d shell to valence band levels. In this case, however, this band should have exhibited a noticeable effect of the magnetic field causing a giant Zeeman splitting of the hole levels. This effect has not been noticed, and the band should be interpreted as being due to an intracenter transition. The Mn^{2+} IL kinetics in $Cd_{1-x}Mn_xTe$ was studied in [10–12]. Our poor understanding of the properties of this luminescence was revealed by an unexpected conclusion drawn in [13]. It maintains that the inhomogeneous broadening of the Mn^{2+} band profile in $Cd_{0.54}Mn_{0.46}Te$ and $Cd_{0.3}Mn_{0.7}Te$ decreases with increasing temperature, to vanish altogether for $T > 60$ K. One could hardly agree with this, because during the time an excitation exists, it would become redistributed over the inhomogeneously broadening ensemble of Mn^{2+} ions, even if the excitation was produced selectively and monoenergetically. This is supported, in particular, by the strong variation in the kinetics over the Mn^{2+} IL profile in the experimental conditions chosen in [13]. The maximum shift of the 2-eV band reached in delayed IL detection was used [10] to estimate the homogeneous and inhomogeneous contributions to the band profile. That fairly crude estimate yielded about 0.06 eV for the inhomogeneous broadening.

The contribution of inhomogeneous broadening to the IL spectra of the manganese-containing group II–VI DMSs can be judged from the $ZnS : Mn^{2+}$ spectra [14], which show that the no-phonon emission lines of Mn^{2+} pairs and single ions differ considerably in energy. Coexistence of regions with different local lattice symmetries (structural defects) and impurities produces an additional contribution to the inhomogeneous broadening. Cubic $Cd_{1-x}Mn_xTe$, which usually has a zinc blende structure, reveals the formation of rocksalt structure microdomains at large values of x. In this case, the anion environment of the manganese ion changes from tetrahedral to octahedral, which naturally affects the crystal field markedly.

The IL kinetics of a system of interacting ions with incompletely filled inner shells incorporated in crystal matrices depends on the optical excitation level. Our previous works [15, 16] reported on saturation of the Mn^{2+} 2-eV IL band, which was observed under strong excitation of the $Cd_{1-x}Mn_xTe$ and $Cd_{1-x-y}Mn_xMg_yTe$ DMSs, and on a study of the integrated variation of IL kinetics with increasing optical excitation intensity I_{ex}. The present work deals with the spectral response of the kinetics over the IL band profile in $Cd_{0.5}Mn_{0.5}Te$ measured at different temperatures and I_{ex} levels.

2. SPECTRAL AND KINETIC PROPERTIES OF THE 3d LUMINESCENCE IN $Cd_{0.5}Mn_{0.5}Te$

$Cd_{0.5}Mn_{0.5}Te$ single crystals were grown using the Bridgman method. The spectra (a time resolution of approximately 0.2 μs) and the decay kinetics of the 2-eV IL band were measured from freshly cleaved surfaces at $T = 77$ and 4 K. The crystals were optically pumped by the second harmonic of an Nd : YAG laser with a photon energy of 2.34 eV and a pulse repetition frequency of 2 kHz. The light spot area on the sample surface was estimated at 10^{-5} cm^2, and the I_{ex} level on the sample surface was varied up to 4.5 MW/cm^2.

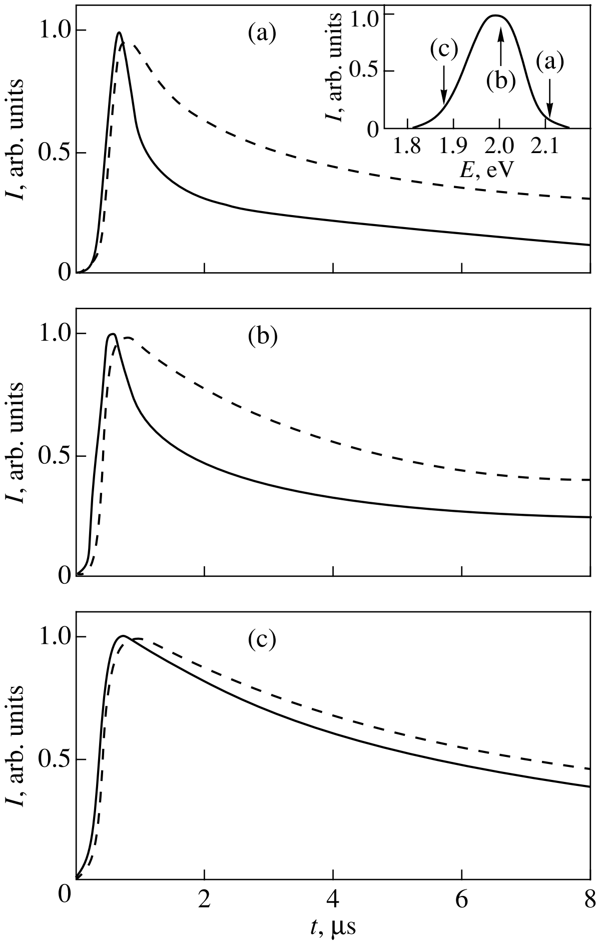

Fig. 1. Mn^{2+} IL decay curves for $Cd_{0.5}Mn_{0.5}Te$ measured at $T = 77$ K at excitation levels of 150 kW/cm^2 (dashed lines) and 3.5 MW/cm^2 (solid lines). The inset shows the points in the IL band profile corresponding to cases (a)–(c). The curves are normalized against the maximum IL intensity.

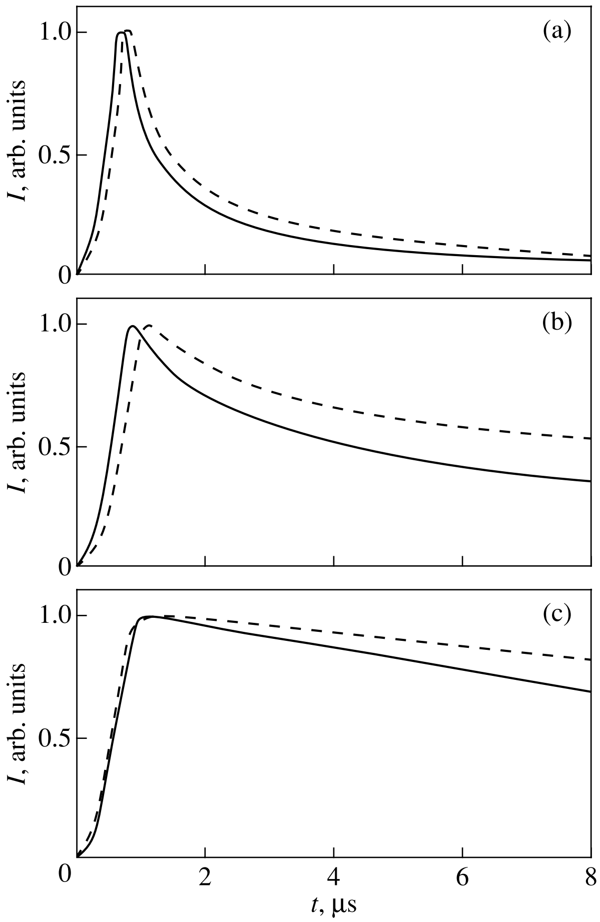

Fig. 2. Mn^{2+} IL decay curves for $Cd_{0.5}Mn_{0.5}Te$ measured at $T = 4$ K at excitation levels of 150 kW/cm^2 (dashed lines) and 3.5 MW/cm^2 (solid lines). Cases (a)–(c) correspond to the three points in the IL band profile identified in Fig. 1. The curves are normalized against the maximum IL intensity.

Because the laser photon energy was less than the Wannier exciton ground state energy in $Cd_{0.5}Mn_{0.5}Te$, the 3*d* shells of Mn^{2+} were excited directly.

The IL kinetics exhibits a strong spectral dependence and varies with increasing excitation level. Figure 1 displays the luminescence decay over the 2-eV band profile at 77 K. While the luminescence kinetics was measured over the profile of this band before [10–12], the pumping density effect was not investigated. The IL decay time is seen to decrease with increasing I_{ex}, this effect being particularly pronounced in the short-wavelength wing of the band. For the I_{ex} levels used in [10], the IL kinetics at $T = 77$ K measured at half-maximum of the band profile on both its sides is the same. We found that the IL decay varies noticeably over the 2-eV band profile even at a relatively high temperature $T = 77$ K already at $I_{ex} = 50$ W/cm^2, the decay becoming faster as one moves toward higher energies. The time delay of the maximum IL intensity relative to the laser pulse maximum decreases with increasing I_{ex}. At $T = 4$ K, the IL decay exhibits similar features (Fig. 2), but the kinetics depends more strongly on the position of the point in the IL band profile and more weakly on the I_{ex} pump level.

Analysis of the IL decay time dependences yields the following results. Two components, a fast and a delayed one, can be discriminated. The short-lived component is fairly strong at the high-energy band edge at strong excitations. At low pumping levels, $I_{ex} \le 70$ kW/cm^2, only the delayed component shows up at the low-energy band edge. In the region of the 2-eV band maximum, both components provide substantial contributions. At $T = 77$ K, the characteristic decay time of the delayed component $t_1 = 5$ μs and it varies little with the excitation level. At $T = 4$ K, the time t_1 depends more strongly on I_{ex}; indeed, it is 16 μs for $I_{ex} = 3.5$ MW/cm^2 and 27 μs for $I_{ex} = 50$ kW/cm^2 (the latter value is close to the one quoted in [10]). As for the decay time of the fast component t_2, it does not exceed the time resolution 0.2 μs of the experimental setup. Figure 3 shows the shift of the IL band of $Cd_{0.5}Mn_{0.5}Te$ obtained for I_{ex} = 3.5 MW/cm^2 at T = 77 K with a time delay. When measuring spectra with zero delay, decreasing the excitation level to I_{ex} = 150 kW/cm^2 also shifts the IL band toward lower energies. At I_{ex} = 3.5 MW/cm, a delay τ = 6 μs not only shifts the band maximum by 0.02 eV toward lower energies but also reduces its half-width. This behavior of the spectrum is associated with the effect of the excitation level on the migration of the excitation and its energy relaxation over inhomogeneously broadened states. In what follows, we primarily discuss the spectral characteristics at high excitation levels.

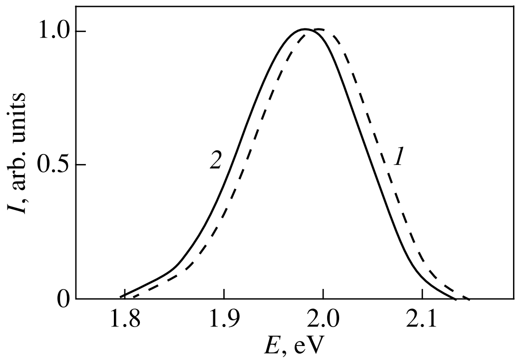

Fig. 3. Normalized Mn^{2+} IL spectra in $Cd_{0.5}Mn_{0.5}Te$ measured (*1*) at the excitation pulse and (*2*) with a time delay of 6 μs. T = 77 K.

3. RELAXATION OF Mn^{2+} 3*d*-SHELL EXCITATION IN $Cd_{0.5}Mn_{0.5}Te$

The fast and delayed components in Mn^{2+} IL kinetics at low temperatures should be related to two types of states of the excited Mn^{2+} system. The excitation migration over the Mn^{2+} ions can be described in terms of the Frenkel exciton model. The electronic states of a concentrated Mn^{2+} system correspond to the energy spectrum of large, including infinite, clusters and include states of both a quasi-band and localized nature. Excitations in a system of interacting Mn^{2+} ions, in particular, their properties associated with inhomogeneous broadening, should have some features in common with those of a system of large excitons in semiconducting solid solutions [17]; one should naturally take into account the strong difference in their temporal and energy parameters. When discussing the excited states of Mn^{2+} ions in $Cd_{0.5}Mn_{0.5}Te$, one can conveniently introduce the concept of the mobility edge, above which the small Frenkel exciton becomes delocalized. At low temperatures, the short- and the long-lived components, which contribute differently to the IL decay kinetics at different excitation intensities (Fig. 2), are related to the delocalized and localized excitations, respectively.

We consider the origin of the localized states. A study [14] of the IL of wide-bandgap ZnS : Mn^{2+} crystals with a low manganese concentration found the no-phonon emission line of single manganese ions to lie substantially higher in energy than that of manganese pairs. Whence it follows that the no-phonon lines of large clusters lie at a still lower energy (substitution of manganese for zinc increases the crystal field). That an increase in the crystal field does indeed shift the IL band of Mn^{2+} in II–VI compounds to lower energies follows from hydrostatic compression experiments [18]. The IL decay time of single ions is longer by an order of magnitude than that of pairs and larger clusters. For this reason, the slower kinetics corresponds to the high-energy edge of the 3*d*-luminescence band of ZnS : Mn^{2+}. Substitution of manganese for cadmium in $Cd_{1-x}Mn_xTe$ reduces the crystal field and shifts the IL band toward higher energies [16]; i.e., in $Cd_{1-x}Mn_xTe$, the lowest energy excited 3*d* states belong to the manganese ions that have the maximum number of cadmium ions in their nearest cation environment. Thus, $Zn_{1-x}Mn_xS$ and $Cd_{1-x}Mn_xTe$ are radically different in this sense. In the former case, the low-energy region of the IL is formed by the emission of Mn^{2+} ions with the maximum number of manganese ions in their environment. In the latter (our) case, the tail of the localized states with longer IL decay time is produced by the manganese ions that are either single, a part of small clusters, or in the periphery of large manganese clusters.

The contribution of the fast component to the IL kinetics increases as the localized-state tail of the Mn^{2+} system saturates with growing I_{ex}. Under these conditions, the change in the dynamics of the Frenkel excitons, which are above the mobility edge, and their contribution to the luminescence become essential, because these excitations no longer pump the localized system (the migration occurs only through extended states). A similar situation was studied, both experimentally and theoretically, for large-radius excitons interacting with fluctuation potentials in $CdS_{1-x}Se_x$ solid solutions [19]. Estimates show that for I_{ex} = 3.5 mW/cm^2, the concentration of excited ions is only one or one and a half orders of magnitude less than their total concentration. In these conditions, the density-of-states tail corresponding to localized states should certainly become saturated. The high-energy shift of the IL band maximum in $Cd_{1-x}Mn_xTe$ observed to occur with increasing I_{ex} supports growth of the contribution due to the delocalized excitations.

When analyzing the structure of the IL band, one should take into account that no-phonon transitions have phonon replicas with different numbers of emitted

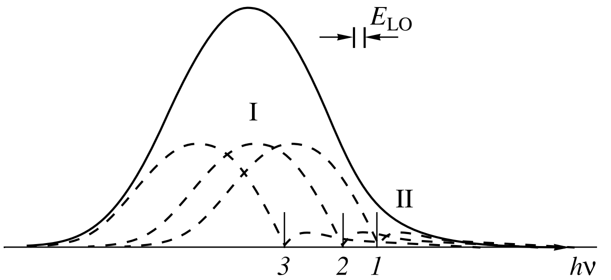

Fig. 4. Simplified diagram of the Mn^{2+} IL band formation in $Cd_{1-x}Mn_xTe$. (*1*)–(*3*): no-phonon emission (absorption) of single ions, small and large clusters, respectively; I and II: replicas involving phonon emission and absorption. E_{LO} is the characteristic optical phonon energy

phonons. These replicas are many times stronger than the no-phonon transitions and extend more in energy. Strong coupling of the 3*d* electrons of a Mn^{2+} ion incorporated in a II–VI compound lattice and phonons is indicated by the large Stokes shift between the absorption and luminescence maxima, which is 0.3 eV in $Cd_{1-x}Mn_xTe$. The same conclusion is reached in an analysis of the emission band structure of a strongly diluted manganese ion system in wide-bandgap ZnS crystals, which exhibits clearly seen weak no-phonon lines and strong replicas of them involving acoustic and optical phonons [14]. The spectra of dilute systems permit one to estimate the energy interval that provides a noticeable contribution to the no-phonon emission. The difference between the positions of the $^4T_1$ level of the manganese ions having, in the nearest cation environment, only ions of Cd (single Mn ions) or only Mn ions (inside a cluster) is approximately 0.1 eV for $Cd_{0.5}Mn_{0.5}Te$. In view of the fact that, at such high concentrations, single manganese ions and their pairs exist only due to statistical fluctuations in the concentration of the cation components, the inhomogeneous broadening interval can be estimated at 0.05 eV. Thus, the extent of the no-phonon states is several times more narrow than the half-width of the 2-eV IL band profile and the shift of the phonon replica maximum corresponds to an energy of approximately ten LO phonons of the CdTe or MnTe type. The IL kinetics in different points of the 2-eV band is dominated by the superposition of phonon replicas of different no-phonon states. Only the extreme parts of the band profile are formed at low temperatures by only the upper or only the lower states of an inhomogeneously broadened Frenkel exciton spectrum; the low-energy edge is determined by the emission of the phonon-wing tail of the lowest energy manganese no-phonon state (localized states); the high-energy edge, by the emission of the highest energy no-phonon state (Mn^{2+} ions inside a large manganese cluster). At high temperatures, where the anti-Stokes contribution becomes noticeable, the pattern is still more complex. A strongly simplified scenario of the formation of the 2-eV band is shown in Fig. 4.

Under strong-pumping conditions, where the localized-state tail saturates, the efficiency of the Frenkel exciton migration increases even at low temperatures. As already mentioned, at the highest I_{ex} levels, the excited-ion concentration reaches a sizable fraction of the total Mn^{2+} concentration. The IL quenching is determined by two processes, namely, the excitation transfer to impurities and intrinsic defects and the up-conversion [20]. The up-conversion efficiency varies linearly with the parameter describing the migration and quadratically with the excited-center concentration. In our case, the Frenkel exciton transfer from an excited Mn^{2+} ion to a previously excited ion is the up-conversion process. As a result of the transition, one ion is excited from the $^4T_1$ level to a still higher level, while the other drops to the ground state $^6A_1$. After this, the strongly excited ion relaxes nonradiatively to $^4T_1$ with a subsequent radiative transition to the $^6A_1$ level. The relaxation can also proceed via conventional band states to the Wannier exciton level, which lies at 2.4 eV in $Cd_{0.5}Mn_{0.5}Te$, after which the excitation migrates back to the 3*d* shell of Mn^{2+}. It is these processes that become manifest in the properties of the IL with increasing I_{ex} as an acceleration of its decay and intensity saturation of the 2-eV band. The superposition of the band states of the $Cd_{1-x}Mn_xTe$ semiconductor on the excited state system of the Mn^{2+} ion precludes direct observation of the up-conversion as luminescence from the high excited 3*d* states.

One can follow the IL saturation of $Cd_{0.5}Mn_{0.5}Te$ with increasing I_{ex} at different points of the 2-eV band by setting different gating times relative to the pump pulse maximum (Fig. 5). We readily see that the IL saturation is clearly pronounced in the low-energy wing and that increasing the IL measurement delay at a constant I_{ex} also enhances the saturation. Because only localized states are seen in the low-energy wing and at long delays, the experiment indicates their saturation. The dependences of the IL intensity on I_{ex} are presented in [15] for different points of the 2-eV band under continuous spectral measurement. These dependences vary little within the 1.9–2.1 eV interval, apparently as a result of the superposition of phonon replicas of different no-phonon states. The IL saturation in a sample heated from 4 to 77 K is reached at a lower I_{ex}. This behavior of the IL can be accounted for by a decrease in the number of localized states and by enhancement of the migration, which results in up-conversion involving extended quasi-band states. Under strong optical excitation, the part played by the up-conversion as an essentially nonlinear effect should increase compared to other mechanisms. The cooperative quenching, which in our case cannot be saturated, provides the largest contribution in the initial stage of the IL decay, where the total number of excited manganese ions is large. The large effect of the excitation level on the IL kinetics at $T = 77$ K is a result of the extended states becoming more significant with increasing I_{ex}. That the contribution of up-conversion to the IL saturation is significant is confirmed by the direct observation of the decrease in the extended-state lifetime with increasing I_{ex}.

As a sample is cooled from 77 to 4 K, the decay time of the delayed IL component increases, which can be attributed to a weakening of the electron–phonon coupling. At 4 K, another difference is seen, namely, a decrease in the delayed-component decay time with increasing excitation level. This is associated most likely with the filling of the states having a low localization energy and a comparatively high density. Due to tunneling, such states make an analog of up-conversion possible.

Notice the small contribution of the delayed component and the weak dependence of the IL decay kinetics on I_{ex} in the high-energy wing of the band at 4 K, whereas at 77 K the pattern is radically different (Figs. 1a, 2a). The excitation migration at 4 K occurs only with a decrease in the energy, and the IL decay kinetics in the high-energy wing of the band is determined by the rate of excitation relaxation to lower states. The kinetics in the high-energy wing of the IL band in a heated sample is slowed down not only by excitation migration involving phonon absorption but also by an increase in intensity of the anti-Stokes phonon replicas of the long-lived no-phonon states.

A quantitative description of the Frenkel exciton dynamics should include two subsystems of the Mn^{2+} $3d$-shell excitations, namely, localized and delocalized ones. The excitation process and its relaxation can be treated in terms of the ${}^6A_1 - {}^4T_1$ two-level model with saturation of the localized excited states, which are populated primarily through the extended states. The up-conversion gives rise to a nonlinearity in the delocalized subsystem. In order to quantitatively consider these processes, one should determine the density of the localized states, the dynamics of their population, and the parameters describing the up-conversion.

Quenching centers can also affect the excitation relaxation dynamics with increasing I_{ex} in a number of ways. If the excitation migration is enhanced in the case where the manganese localized states are saturated, quenching by impurities and defects will contribute to the nonlinearity of the IL dependence on I_{ex}. Saturation of the quenching impurity and defect states should increase the IL quantum yield. The impurity and defect concentrations in our samples are three orders of magnitude lower than the total manganese ion concentration, which makes it difficult to answer the question as to what saturates faster, defects and impurities or the manganese localized states. The majority of impurities responsible for the IL quenching can be iron-group elements other than manganese. To the intrinsic quenching centers one should assign structural defects that change the tetrahedral anion environment of the cation to octahedral. The strong effect of structural defects on the spectral position of the Mn^{2+} IL is confirmed by experiments on the hydrostatic compression of the $Zn_{1-x}Mn_xS$ [21]. The phase transition of $Zn_{1-x}Mn_xS$ lattice from the zinc blende to rocksalt structure induced by strong hydrostatic pressure is accompanied by the quenching of the 2.1-eV IL band and an increase in intensity of the 1.4-eV band.

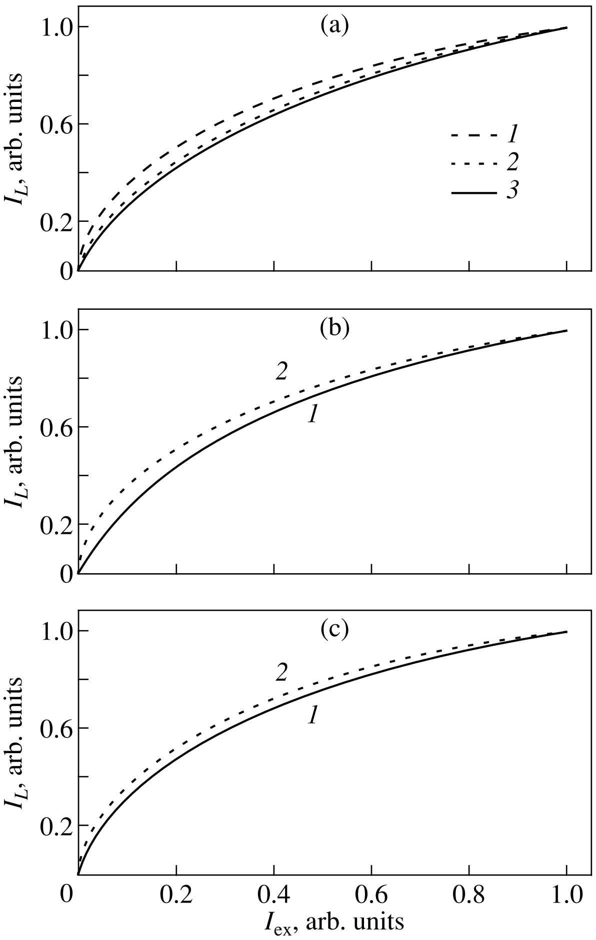

Fig. 5. Dependence of the Mn^{2+} IL intensity I_L on the optical excitation level I_{ex} measured at $T = 77$ K. (a) I_L at the instant of excitation for photons with energies (*1*) 1.92, (*2*) 2.01, and (*3*) 2.08 eV; (b) and (c): the intensity I_L (*1*) at the instant of excitation and (*2*) after a 6 μs delay for energies of 2.01 and 1.92 eV. The values of I_L are normalized at $I_{ex} = 1$, which corresponds to 3.5 MW/cm^2.

An increase in the manganese concentration favors a decrease in the fraction of the manganese ions that have many cadmium ions in their nearest cation environment. This should reduce the inhomogeneous broadening and weaken the localized-state tail and, thus, enhance the significance of the up-conversion. It is possible that the weakening of the 2-eV emission band observed to occur in $Cd_{1-x}Mn_xTe$ with increasing x in the 0.6–0.8 interval originates not only from the enhancement of the up-conversion but also with an increase in the structural defect concentration. The above considerations on the relaxation dynamics of the manganese 3*d*-shell excitation are in full accord with the observation that, as the manganese concentration is increased and the temperature is raised, the IL saturates at lower levels of I_{ex} [15].

The temperature dependence of the 2-eV band intensity exhibits a sharp falloff in samples heated above 80 K. This temperature region corresponds in our model to thermal delocalization of the Frenkel excitons, which is accompanied by a decrease in the IL quantum yield because of the quenching by impurities and up-conversion. Extending the analogy with the Wannier excitons in II–VI semiconducting solid solutions, it can be noted that thermal delocalization of the Wannier excitons weakens the integrated exciton luminescence by one to two orders of magnitude. The Wannier exciton emission spectrum transforms in two ways with increasing temperature. In one case ($CdS_{1-x}Se_x$), the localized-exciton band weakens and, at the same time, the free-exciton band forms and grows stronger [22], while in the other ($Zn_{1-x}Gd_xSe$), the only emission band shifts gradually toward higher energies to the free-exciton absorption band [23]. The behavior of the manganese IL in $Cd_{1-x}Mn_xTe$ with $x > 0.4$ agrees with the second case.

4. CONCLUSION

Thus, this study has permitted us to determine the effect of the optical excitation level on the kinetics of the manganese 3*d* luminescence in $Cd_{0.5}Mn_{0.5}Te$ over the emission band profile at 4 and 77 K. A delayed and a fast component were isolated in the luminescence decay, which correspond, at low temperatures, to the localized and extended excited states, respectively, in the energy spectrum of the 3*d* electrons of the Mn^{2+} ensemble. As the excitation level increases, the localized states saturate and the extended states become involved in an up-conversion process.

REFERENCES

1. O. Goede and W. Heimbrodt, Phys. Status Solidi B **146**, 11 (1988).
2. J. K. Furdyna, J. Appl. Phys. **64**, R29 (1988).
3. J. Nakahara, K. Takamura, and S. Yamamoto, Phys. Status Solidi B **211**, 223 (1999).
4. M. Beale, Philos. Mag. B **68**, 573 (1993).
5. X. Yang and X. Xu, Appl. Phys. Lett. **77**, 797 (2000).
6. H. Schenk, M. Wolf, G. Mackh, *et al.*, J. Appl. Phys. **79**, 8704 (1996).
7. V. F. Aguekian, L. K. Gridneva, and A. Yu. Serov, Solid State Commun. **87**, 635 (1993).
8. R. N. Bhargava and D. Gallagher, Phys. Rev. Lett. **72**, 416 (1994).
9. Y. Terai, S. Kuroda, K. Takita, *et al.*, J. Lumin. **87–89**, 396 (2000).
10. E. Muller, W. Gebhardt, and V. Gerhardt, Phys. Status Solidi B **113**, 209 (1982).
11. V. F. Agekyan, Yu. V. Rud', and R. Schwabe, Fiz. Tverd. Tela (Leningrad) **29**, 1685 (1987) [Sov. Phys. Solid State **29**, 970 (1987)].
12. J. D. Park, S. Yamamoto, J. Watanabe, *et al.*, J. Phys. Soc. Jpn. **66**, 3289 (1997).
13. J. Gregus, J. Watanabe, and J. Nakahara, J. Phys. Soc. Jpn. **66**, 1810 (1997).
14. H. E. Gumlich, J. Lumin. **23**, 73 (1981).
15. V. F. Agekyan, N. N. Vasil'ev, and A. Yu. Serov, Fiz. Tverd. Tela (St. Petersburg) **41**, 49 (1999) [Phys. Solid State **41**, 41 (1999)].
16. V. F. Agekyan, N. N. Vasil'ev, A. Yu. Serov, and N. G. Filosofov, Fiz. Tverd. Tela (St. Petersburg) **42**, 816 (2000) [Phys. Solid State **42**, 836 (2000)].
17. E. Cohen and M. D. Sturge, Phys. Rev. B **25**, 3828 (1982).
18. V. F. Agekyan and Fan Zung, Fiz. Tverd. Tela (Leningrad) **30**, 3150 (1988) [Sov. Phys. Solid State **30**, 1812 (1988)].
19. A. G. Abdukadyrov, S. D. Baranovskiĭ, S. Yu. Verbin, *et al.*, Zh. Éksp. Teor. Fiz. **98**, 2056 (1990) [Sov. Phys. JETP **71**, 1155 (1990)].
20. V. V. Ovsyankin and P. P. Feofilov, Opt. Spektrosk. **37**, 262 (1973).
21. M. Kobayashi, Y. Nakamura, S. Endo, and W. Giriat, Phys. Status Solidi B **211**, 359 (1999).
22. V. F. Agekyan, B. G. Aleksandrov, and Yu. A. Stepanov, Fiz. Tekh. Poluprovodn. (Leningrad) **23**, 1951 (1989) [Sov. Phys. Semicond. **23**, 1208 (1989)].
23. A. S. Nasibov, L. G. Suslina, D. L. Fedorov, *et al.*, Fiz. Tverd. Tela (Leningrad) **31**, 70 (10) (1989) [Sov. Phys. Solid State **31**, 1691 (1989)].

Translated by G. Skrebtsov

Physics of the Solid State, Vol. 43, No. 9, 2001, pp. 1633–1636. Translated from Fizika Tverdogo Tela, Vol. 43, No. 9, 2001, pp. 1569–1572.

SEMICONDUCTORS
AND DIELECTRICS

X-ray and Luminescent Analysis of Finely Dispersed β-$FeSi_2$ Films Formed in Si by Pulsed Ion-Beam Treatment

R. M. Bayazitov*, R. I. Batalov*, E. I. Terukov, and V. Kh. Kudoyarova****

**Zavoĭskiĭ Physicotechnical Institute, Kazan Scientific Center, Russian Academy of Sciences,*
Sibirskiĭ trakt 10/7, Kazan 29, 420029 Tatarstan, Russia
e-mail: bayaz@kfti.knc.ru
***Ioffe Physicotechnical Institute, Russian Academy of Sciences, Politekhnicheskaya ul. 26, St. Petersburg, 194021 Russia*
e-mail: kudoyarova@pop.ioffe.rssi.ru

Received February 8, 2001

Abstract—Finely dispersed β-$FeSi_2$ films were formed by implanting Fe^+ ions with an energy of 40 keV and a dose of 1×10^{16} cm^{-2} in Si single crystals, followed by nanosecond pulsed ion-beam treatment. The results of glancing incidence x-ray diffraction indicate the formation of a highly grain-oriented film consisting of inclusions of the iron disilicide phase (β-$FeSi_2$) with a grain size of approximately 40 nm surrounded by a polycrystalline Si matrix. The photoluminescence spectroscopy data reveal that the photoluminescence signal with a peak around 1.56 μm, which is observed up to 210 K, is associated with direct interband transitions in β-$FeSi_2$ and not with the contribution from the dislocation-induced line *D*1. *© 2001 MAIK "Nauka/Interperiodica".*

1. INTRODUCTION

A new branch in optoelectronics called Si-based optoelectronics has been developed intensively over the last decade. This branch is associated with the creation of silicon-based optoelectronic devices (primarily light diodes, injection lasers, and optical microprocessors) integrated with advanced microelectronic device technology. The silicon structures emitted in the region of wavelength 1.5 μm corresponding to the transparency window in silicon and quartz fibers are constructed mainly through the formation of Si : Er and β-$FeSi_2$ layers. In the former case, solid solutions of Er and Si are formed through ion implantation, magnetron sputtering, and molecular-beam epitaxy [1–3]. The Si : Er layers emit at a wavelength $\lambda = 1.54$ μm, corresponding to the transition ${}^4I_{13/2} \longrightarrow {}^4I_{15/2}$ in the inner 4*f* shell of the Er^{3+} ion in the optically active state.

The second method of fabrications of light-emitting structures (in the region of 1.5 μm) involves the formation of continuous layers and finely dispersed films of semiconducting iron disilicide β-$FeSi_2$. Ion-beam synthesis (IBS) [4–9] and a combination of reactive and molecular-beam epitaxies [10, 11] are the two main methods of the formation of emitting finely dispersed β-$FeSi_2$ films. The IBS technique combines the implantation of Fe^+ ions in Si over a wide range of doses ($\sim 2 \times 10^{15}$–1×10^{17} cm^{-2}) followed by high-temperature and prolonged thermal annealing (TA). This results in the formation of β-$FeSi_2$ precipitates 10–100 nm in size depending on the implantation conditions and the subsequent TA. The second method combines the deposition of Fe on a heated Si substrate followed by TA for aggregating the formed film into spherical β-$FeSi_2$ precipitates approximately 100 nm in size. At the final stage, the β-$FeSi_2$ precipitates are covered by an epitaxial layer of Si.

The above methods of formation of β-$FeSi_2$ precipitates are quite expensive and require prolonged high-temperature treatment. In the creation of integrated microcircuits for microelectronic applications, such thermal treatments are undesirable since they result in the diffusion of iron atoms into the bulk Si matrix owing to the high diffusion coefficient for Fe at high temperatures ($D_{Fe} \sim 5 \times 10^{-6}$ cm^2/s at $T \sim 1000$°C), which leads to degradation of the main parameters of silicon devices [12].

These drawbacks in the formation of β-$FeSi_2$ precipitates can be overcome by pulsed (laser, ionic, or electron) beam treatment, which affects only the surface layers of the material (~1 μm) over a short interval of time (<1 μs), thus ruling out the possibility of undesirable diffusion of impurities into the matrix. Moreover, the high rates of heating, melting, and subsequent solidification (~1 m/s) lead to the formation of defect-free, epitaxial, and heavily-doped layers of Si [13–15]. The distinguishing features of pulsed ion-beam treatment (PIT) in comparison with pulsed-laser processing are (1) a deeper and more uniform distribution of the energy losses by ions in the material, which results in weaker overheating and less surface degradation, and (2) the independence of the results of processing from the optical properties of the material being exposed [16]. In this work, the finely dispersed films of β-$FeSi_2$

in Si were formed using the PIP of implanted Si layers. The synthesized film of β-$FeSi_2$ was studied using the x-ray diffraction technique and photoluminescence spectroscopy.

2. EXPERIMENT

A monocrystalline (100) Si wafer was implanted at room temperature by a 1×10^{16} cm^{-2} dose of $^{56}Fe^+$ ions with an energy of 40 keV and ion beam current density of 5 μA/cm^2. The sample temperature did not exceed 100°C during implantation, which ruled out *in situ* annealing of the radiation defects. After ion implantation, the Si sample was processed in a pulsed ion accelerator (80% C^+, 20% H^+, τ = 50 ns, E = 300 keV, $j \sim$ 50 A/cm^2, $W \sim$ 0.75 J/cm^2) by five pulses at a pulse repetition rate of 0.1 Hz. In order to remove the stresses introduced in the crystal lattice during PIP and to synthesize the film consisting of the β-$FeSi_2$ phase only, the sample was subjected additionally to short-time TA at 800°C for 20 min. It was shown earlier [17] that this combination of ion-pulse and thermal treatment is quite effective.

The structure and phase composition of the formed film were studied using the glancing incidence x-ray diffraction technique (the beam incidence angle φ was ~1°) with FeK_α radiation (λ = 1.9373 Å). The azimuthal dependence of the highest-intensity diffraction peak was recorded by fixing the detector at the position of the given reflection and azimuthal scanning. The photoluminescence (PL) of the synthesized β-$FeSi_2$ film was studied in the near-IR spectral region (λ = 1.0–1.7 μm) in the temperature interval 77–250 K. The PL signal was excited by an argon laser (λ = 514.5 nm, P = 50 mW), and the signal was registered by a germanium detector cooled to 77 K.

3. DISCUSSION OF RESULTS

Figure 1 shows the x-ray diffraction spectrum of implanted Si after PIP by five pulses and additional TA (800°C, 20 min). It can be seen that the spectrum contains the β-$FeSi_2$ phase only (without inclusions of the metallic phase of FeSi), which is characterized by the highest intensity Bragg reflection from the (202)/(220) planes and a weakly manifested reflection in the region of 2θ = 60°–65°. In addition, the spectrum contains a signal from the Si matrix (Si(111) reflection), thus indicating that the surface layers of Si have a polycrystalline structure formed as a result of rapid recrystallization of the implanted amorphous layer after PIP. The ratio of the intensities of diffraction peaks β(202)/(220) and β(422) is equal to 4, while the value of this ratio in randomly oriented β-$FeSi_2$ powders is 1.25. This fact points towards a high degree of grain orientation in the silicide film, which is confirmed by the results of measuring the azimuthal dependence of the diffraction peak β(202)/(220) (inset to Fig. 1). Four sharp peaks associ-

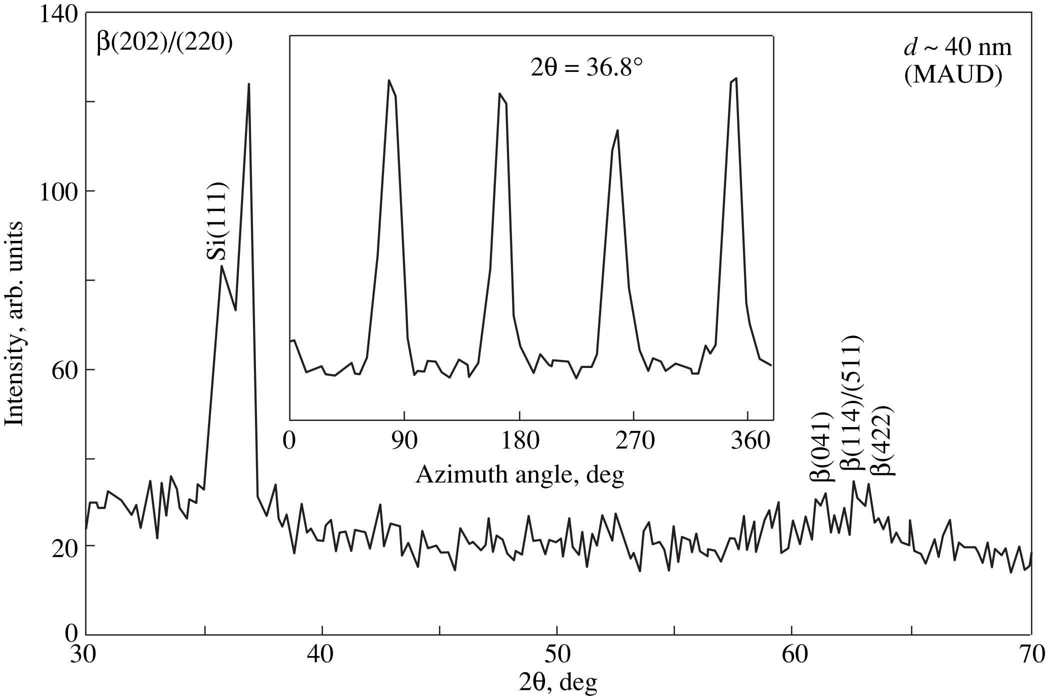

Fig. 1. The spectrum of grazing x-ray diffraction (φ = 1°, λ = 1.9373 Å) of implanted (100) Si (40 keV, 1×10^{16} Fe^+/cm^2) after PIP (50 ns, 50 A/cm^2) and additional TA (800°C, 20 min). The inset shows the azimuthal dependence of the diffraction peak β(202)/(220) for 2θ = 36.8°.

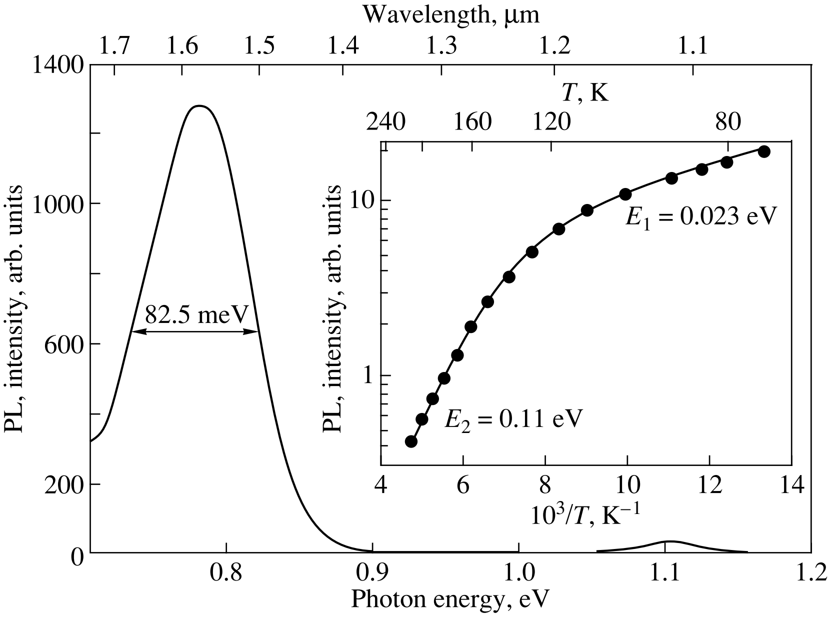

Fig. 2. PL spectrum of implanted (100) Si (40 keV, 1×10^{16} Fe^+/cm^2) recorded at 77 K after PIP (50 ns, 50 A/cm^2) and additional TA (800°C, 20 min). The inset shows the temperature dependence of the integrated intensity of the PL signal. The solid curve is an approximation of the experimental data (points) according to formula (1).

ated with the formation of a silicide film on the Si substrate with orientation (100) are clearly seen. The processing of the x-ray spectrum using the MAUD program [18] gives an average size of approximately 40 nm for the β-$FeSi_2$ precipitates, which is close to the size of the β-$FeSi_2$ precipitates obtained under nearly identical implantation conditions in [9].

Figure 2 shows the PL spectrum recorded at 77 K in the interval 0.7–1.2 eV for a β-$FeSi_2$ film formed after PIP and TA. Two peaks at 0.78 and 1.11 eV can be seen in the PL spectrum. Apparently, the second peak ($E \sim 1.11$ eV) is associated with indirect transitions in the band gap of Si. The highest-intensity line in the spectrum, having a peak at approximately 0.78 eV (1.56 μm), is associated with direct interband transitions within the band gap of β-$FeSi_2$ of width $E_g \sim 0.8$ eV at 300 K [6, 9]. It should be noted that this spectrum does not contain PL signals from the dislocation-induced lines *D*2–*D*4 [19], which were observed in the low-temperature PL spectra of the precipitates of β-$FeSi_2$ obtained through ion-beam synthesis [6, 9]. The origin of the dislocation-induced line *D*1, whose position (0.81 eV) is close to the position of the observed PL peak, will be discussed below. The difference between the actual value of the band gap and the experimentally observed PL peak is probably due to the introduction of defect and impurity levels in the band gap of β-$FeSi_2$ during ion implantation. The presence of these defect and impurity levels leads to strong quenching of the PL signal at temperatures above 100 K and to its disappearance at temperatures above 210 K (inset to Fig. 2). The temperature dependence of the PL signal $I(T)$ can be approximated quite accurately using an expression containing two activation energies (E_1 and E_2):

$$I_{\rm PL}(T) = \frac{I(0)}{1 + A\exp\left(\frac{-E_1}{kT}\right) + B\exp\left(\frac{-E_2}{kT}\right)}, \qquad (1)$$

where *A* and *B* are the paired coefficients and $I(0)$ is the PL intensity at low temperatures. The values of activation energy obtained by fitting the theoretical curve to the experimental data are 23 and 110 meV. A comparison of the obtained values of E_1 and E_2 with the activation energy values for the *D*1 and *D*2 dislocation-induced lines (4–12 meV) shows [4] that they are quite different. Keeping this circumstance and the absence of other dislocation-induced lines *D*2–*D*4 in view, we can disregard the contribution of the *D*1 line to the PL signal in the region of 1.55 μm and assume that it is connected with direct interband transitions in β-$FeSi_2$.

ACKNOWLEDGMENTS

The authors are indebted to V.F. Valeev for his help in ion implantation, R.G. Mustafin for ion-pulse processing of the samples, and V.A. Shustov for x-ray diffraction measurements.

This study was supported by the Research and Educational Center of the Kazan State University under the program “Materials and Technologies of the XXI Century” (BRHE REC-007), by the Russian Foundation for Basic Research (project no. 01-02-16649), and by the

State Program of the Ministry of Science of the Russian Federation (project no. 9V 41.108F).

REFERENCES

1. G. Franzo, F. Priolo, S. Coffa, *et al.*, Appl. Phys. Lett. **64**, 2235 (1994).
2. W. Fuhs, I. Ulber, G. Weiser, *et al.*, Phys. Rev. B **56**, 9545 (1997).
3. A. Reittinger, J. Stimmer, and G. Abstreiter, Appl. Phys. Lett. **70**, 2431 (1997).
4. H. Katsumata, Y. Makita, N. Kobayashi, *et al.*, J. Appl. Phys. **80**, 5955 (1996).
5. K. J. Reeson, M. S. Finney, M. A. Harry, *et al.*, Nucl. Instrum. Methods Phys. Res. B **106**, 364 (1995).
6. M. G. Grimaldi, S. Coffa, C. Spinella, *et al.*, J. Lumin. **80**, 467 (1998).
7. C. Spinella, S. Coffa, C. Bongiorno, *et al.*, Appl. Phys. Lett. **76**, 173 (2000).
8. K. P. Homewood, K. J. Reeson, R. M. Gwilliam, *et al.*, Thin Solid Films **381**, 188 (2001).
9. K. Oyoshi, D. Lenssen, R. Carius, and S. Mantl, Thin Solid Films **381**, 194 (2001); **381**, 202 (2001).
10. T. Suemasu, Y. Iikura, K. Takakura, and F. Hasegawa, J. Lumin. **87–89**, 528 (2000).
11. T. Suemasu, Y. Negishi, K. Takakura, and F. Hasegawa, Jpn. J. Appl. Phys. **39**, L1013 (2000).
12. B. O. Kolbesen and H. Cerva, Phys. Status Solidi B **222**, 303 (2000).
13. R. Hodgson, J. E. E. Baglin, R. Pal, *et al.*, Appl. Phys. Lett. **37**, 187 (1980).
14. L. J. Chen, L. S. Hung, J. W. Mayer, *et al.*, Appl. Phys. Lett. **40**, 595 (1982).
15. R. M. Bayazitov, L. Kh. Zakirzyanova, I. B. Khaibullin, *et al.*, Vacuum **43**, 619 (1992).
16. R. M. Bayazitov, L. Kh. Antonova, I. B. Khaibullin, and G. E. Remnev, Nucl. Instrum. Methods Phys. Res. B **139**, 418 (1998).
17. R. M. Bayazitov and R. I. Batalov, J. Phys.: Condens. Matter **13**, L113 (2001).
18. M. Ferrari and L. Lutterotti, J. Appl. Phys. **76**, 7246 (1994).
19. N. A. Drozdov, A. A. Patrin, and V. D. Tkachev, Pis’ma Zh. Éksp. Teor. Fiz. **23** (11), 651 (1976) [JETP Lett. **23**, 597 (1976)].

Translated by N. Wadhwa

Physics of the Solid State, Vol. 43, No. 9, 2001, pp. 1637–1638. Translated from Fizika Tverdogo Tela, Vol. 43, No. 9, 2001, pp. 1573–1574.
Original Russian Text Copyright © 2001 by Zaitsev, Fedorov, Golikova, Orlov.

Optical Properties of Aluminum Dodecaboride (α-AlB_{12}) in the Region of the Transparency Window

V. K. Zaitsev, M. I. Fedorov, O. A. Golikova, and V. M. Orlov[†]

Ioffe Physicotechnical Institute, Russian Academy of Sciences, ul. Politekhnicheskaya 26, St. Petersburg, 194021 Russia
e-mail: M.Fedorov@pop.ioffe.rssi.ru

Received February 20, 2001

Abstract—The absorption coefficient of α-AlB_{12} was measured on single crystal samples at $T = 300$ K within a broad spectral region (0.6–25 μm). In the region of the transparency window (3–6 μm), the absorption coefficient was measured in the temperature range from 165 to 650 K. An analysis of the experimental data shows that the energy spectrum of local states in the α-AlB_{12} bandgap has certain features. It was established that a broad band of local states lies near the conduction band and that a trap level is located at 0.11 ± 0.02 eV from the top of the valence band. © *2001 MAIK “Nauka/Interperiodica”.*

Aluminum dodecaboride α-AlB_{12} is a crystal-chemical analog of a complex tetragonal modification of boron. As in other modifications of boron and higher borides, the main nanostructural fragment of its crystal structure is the B_{12} icosahedron. As pointed out by us earlier, local states in α-AlB_{12} single crystals play a dominant role in the transport phenomena and the lack of reliable information on the energy spectrum of local states considerably complicates analysis of the specific features that become manifest in both weak and strong electric fields [1, 2].

To study the features in the energy spectrum of bandgap local states, we measured the absorption coefficient α of single-crystal α-AlB_{12} samples at $T = 300$ K over a broad spectral range (0.6–25 μm). Within the transparency window (3–6 μm), the absorption coefficient was measured at temperatures ranging from 165 to 650 K.

Single-crystal α-AlB_{12} samples were prepared by spontaneous crystallization from a boron solution in an aluminum melt in the form of plates measuring $3 \times 5 \times 0.5$ mm [3]. The samples were thinned by mechanical grinding, followed by polishing with a diamond paste.

The spectral response of the reflection coefficient needed to calculate the absorption coefficient in the 2–25 μm region was reported by us earlier [4], and the reflection coefficient in the 0.6–2 μm region was assumed to be wavelength-independent and equal to 0.27.

Figure 1 presents the dependence of the absorption coefficient of α-AlB_{12} on photon energy measured in the 0.05–2 eV interval at $T = 300$ K. For comparison, the absorption spectra of two of the structural analogs of α-AlB_{12}, namely, $MgAlB_{14}$ [5] and $BeAlB_{24}$, are also shown. As seen from Fig. 1, a region of relatively low absorption coefficients, which transforms with increasing photon energy to a broad band adjoining the fundamental absorption edge, lies close to the lattice absorption interval (0.05–0.2 eV). The bandgap width, estimated from the onset of a sharp rise in the absorption coefficient at high frequencies, is 1.9 ± 0.2 eV, which is in good agreement with earlier measurements [6].

The lattice vibration band in α-AlB_{12} attracted our interest earlier in its specific features observed in the crystal structure of higher borides and in the dominant role played by the short-range order in the formation of vibrational spectra in these compounds [6]. We consider the region that exhibits small absorption coefficients. As seen from the isotherms of the absorption

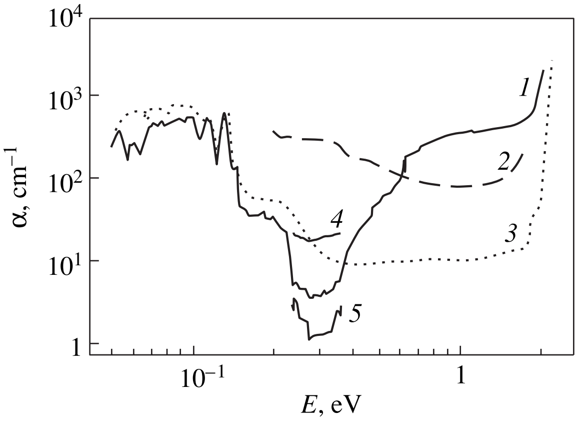

Fig. 1. Dependence of the absorption coefficient α on photon energy E at room temperature for (*1*) α-AlB_{12}, (*2*) $MgAlB_{14}$, and (*3*) $BeAlB_{24}$; (*4*) and (*5*) are the absorption coefficient of α-AlB_{12} in the 0.2–0.4 eV interval measured at 580 and 165 K, respectively.

[†] Deceased.

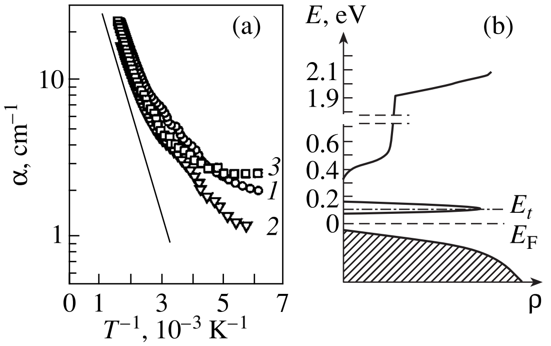

Fig. 2. (a) Dependence of the absorption coefficient α on the inverse temperature for three wavelengths equal to (*1*) 5, (*2*) 4, and (*3*) 3.5 μm; and (b) the assumed dependence of the density of states ρ on energy *E* for α-AlB_{12}.

coefficient, also presented in Fig. 1, the absorption in the region of the transparency window depends noticeably on temperature. A similar effect was observed earlier in studies of the optical properties of β-rhombohedral boron and was assigned to the existence of a trap level in the bandgap [7]. In this case, the interaction of a valence electron with light takes place in two stages. First, the valence-band electron is excited to the trap level, after which a photon ejects it into an upper-lying band. Therefore, the absorption coefficient can be written as $\alpha \sim n_t \sim \exp\left(-\frac{E_t}{kT}\right)$, where n_t and E_t are the concentration of thermally excited carriers and the trap level energy, respectively. Indeed, Fig. 2a, which displays the dependence of the absorption coefficient of α-AlB_{12} on the inverse temperature for several wavelengths, shows that α asymptotically approaches a straight line with increasing temperature. The trap level energy derived from the slope of this asymptote was found to be 0.11 ± 0.02 eV.

The broad absorption band lying between the region of small absorption coefficients and the fundamental absorption edge in the 0.4–1.9 eV interval indicates, most probably, the existence of a broad band of local states in the bandgap of the α-aluminum dodecaboride. It should be pointed out that the energy ~0.4 eV, which corresponds to the activation energy needed to excite carriers from the valence band to a local-state band, was also observed earlier in a study of the temperature dependence of the electrical conductivity in the impurity region [8].

A probable location of the localized states in the bandgap of α-aluminum dodecaboride is shown in the energy diagram of Fig. 2b.

The nature of the broad band of localized states near the conduction band is of particular interest. It would hardly be possible to venture a correct opinion at this time on the nature of such a broad band of local states. It can only be pointed out that this band is not connected in any way with foreign impurities [3] and is most likely due to the statistical character of the aluminum atom distribution over a large number of possible sites [9].

It should also be noted that such an absorption band is observed neither in β-rhombohedral boron [7] nor in $BeAlB_{24}$ (Fig. 1), compounds whose crystal structure is more ordered [9]. The absorption coefficient of $MgAlB_{14}$ is larger in the wavelength region under study, apparently due to a considerable contribution from free-carrier absorption.

ACKNOWLEDGMENTS

This study was supported by the Russian Foundation for Basic Research, project no. 99-02-18035.

REFERENCES

1. V. K. Zaitsev, O. A. Golikova, M. M. Kazanin, *et al.*, Fiz. Tekh. Poluprovodn. (Leningrad) **9** (11), 2101 (1975) [Sov. Phys. Semicond. **9**, 1372 (1975)].
2. O. A. Golikova, Usp. Fiz. Nauk **158** (4), 581 (1989) [Sov. Phys. Usp. **32**, 665 (1989)].
3. O. A. Golikova, V. K. Zaitsev, A. V. Petrov, *et al.*, Fiz. Tekh. Poluprovodn. (Leningrad) **6** (9), 1724 (1972) [Sov. Phys. Semicond. **6**, 1488 (1972)].
4. A. A. Berezin, O. A. Golikova, V. K. Zaitsev, *et al.*, in *Proceedings of the 12th International Conference of the Physics of Semiconductors, Stuttgart, 1974*, p. 291.
5. H. Werheit, G. Krach, U. Kuhlmann, *et al.*, in *Proceedings of the 11th International Symposium on Boron, Borides and Related Compounds, Tsukuba, 1993*, Ed. by R. Uno and I. Higashi, JJAP Ser. **10**, 98; 106 (1994).
6. O. A. Golikova, V. K. Zaitsev, V. M. Orlov, I. A. Drabkin, I. V. Nel'son, and É. N. Tkalenko, in *Boron: Production, Structure and Properties* (Metsniereba, Tbilisi, 1974), p. 44.
7. J. Jaumann and H. Werheit, in *Boron*, Ed. by T. Niemyski (PWN, Warsaw, 1970), Vol. 3, p. 227.
8. O. A. Golikova, A. A. Berezin, V. K. Zaitsev, *et al.*, J. Less-Common Met. **47**, 129 (1976).
9. V. I. Matkovich and J. Economy, in *Boron and Refractory Borides*, Ed. by V. I. Matkovich (Springer-Verlag, Berlin, 1977), pp. 78, 106.

Translated by G. Skrebtsov

Physics of the Solid State, Vol. 43, No. 9, 2001, pp. 1639–1643. Translated from Fizika Tverdogo Tela, Vol. 43, No. 9, 2001, pp. 1575–1579.
Original Russian Text Copyright © 2001 by Bordonskiĭ, Filippova.

A Difference in the Electromagnetic Properties of D_2O and H_2O Ice Revealed by Resonance Measurements

G. S. Bordonskiĭ and T. G. Filippova

Institute of Natural Resources, Siberian Division, Russian Academy of Sciences, Chita, 672090 Russia

Received November 23, 2000

Abstract—The dielectric parameters of H_2O and D_2O ice samples were studied by a resonance technique in the region of 6 GHz. The ratio of the resonance curve halfwidths at half maximum was measured for light and heavy ice in the temperature range from 0 to –130°C. The temperature dependences of the resonance peak asymmetry of the two types of ice are qualitatively different. The ratio of the higher-frequency halfwidths at half maximum to the lower-frequency one plotted versus temperature exhibits a positive slope for light ice and a negative slope for heavy ice. It is suggested that the difference reflects the different quantum statistics of the hydrogen and deuterium nuclei in ice. *© 2001 MAIK “Nauka/Interperiodica”.*

One of the methods of determining the electromagnetic properties of a substance in the microwave range consists in measuring the parameters of resonators filled with a sample of this substance [1]. If the magnetic parameters of a substance are known, measurements of the resonance frequency shift and resonance curve broadening allow us to determine the real (ε') and imaginary (ε") parts of the relative complex permittivity. This method was used, for example, for determining the permittivity of ice prepared from heavy water $D_2^{16}O$ [2, 3].

During the measurement of the dielectric characteristics of resonators filled with D_2O, we noticed asymmetry in the shape of the resonance curves. This fact is usually not surprising in itself, since the asymmetry may be caused by some features in the cavity design or by particularities of the oscillating system studied. However, the character of the asymmetry observed in our case varied with the ice sample temperature, which was indicative of the determining role of the medium properties played in variation of the resonator parameters.

Nigmatullin [4] pointed out that the fractal properties of a medium may lead to asymmetry of the resonance curves, which is significantly different from that observed in a medium comprising a set of classical harmonic oscillators. Therefore, a more detailed study of the characteristics of resonance curves using the resonance techniques may provide additional information on structure of the medium.

This work aimed at determining the asymmetry of a resonance transmission curve measured for a cavity filled with heavy ice ($D_2^{16}O$) and studying the effect of temperature on this system. In parallel, we performed analogous measurements for the same cavity filled with frozen H_2O (light ice). The asymmetry of a resonance curve was determined as the ratio of halfwidths of the transmission curve (determined at a certain level with respect to the maximum).

1. METHOD OF MEASUREMENTS

Figure 1 shows a schematic diagram of the experimental setup used to study substances using a resonance technique. The setup is based on a standard frequency characteristic meter (e.g., of the R2-56 type). A resonator (cavity with a sample) is placed into a break of the waveguide line. The cavity also contains temperature sensors, which represent a thermocouple for measurements in a broad temperature range and a thermoresistor for precise measurements in the vicinity of the phase transition.

The resonator temperature was controlled by a programmed heater and by cooling with liquid nitrogen vapors. Our experiments were performed with a rectangular duralumin cavity of the H_{101} type. The resonator coupling to the waveguide line was provided by copper foil diaphragms with slots arranged in the magnetic field plane. The resonator geometry is schematically depicted in Fig. 2a. The resonance frequency of the lowest mode for the unfilled cavity was 11.58 GHz. The same cavity filled with ice has a lower resonance frequency in the range from 6.1 to 6.4 GHz, depending on the ice temperature and type: the ε' values for D_2O ice were 2–3% lower as compared to those for H_2O ice [3].

The resonance measurements were carried out in the range of temperatures from 0 to –130°C. On cooling the samples with liquid nitrogen vapors, the vapor flow rate was controlled by a heating element. Each cooling–heating cycle in the above temperature range took several hours. The samples of ice were prepared by freezing water immediately in the cavity. For this purpose, the rectangular cavity was closed with a plate on one

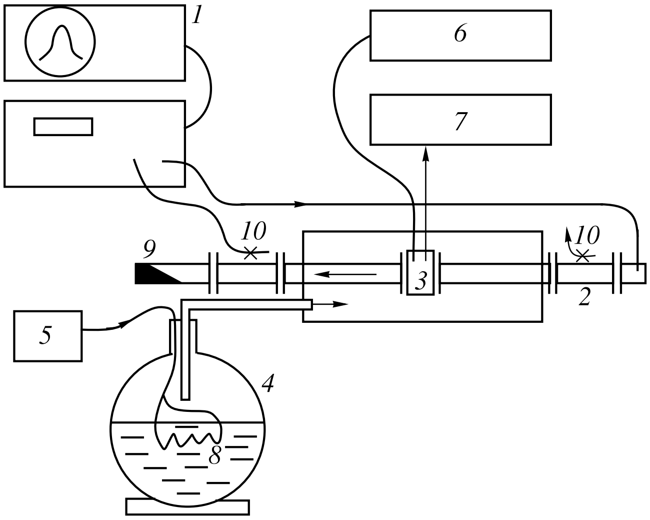

Fig. 1. A schematic diagram of the experimental setup: (*1*) frequency characteristic meter (R2-56); (*2*) waveguide line; (*3*) cavity in a thermostat; (*4*) Dewar vessel with liquid nitrogen; (*5*) evaporator power supply; (*6, 7*) thermoresistor and thermocouple transducers monitoring the cavity housing temperature; (*8*) resistor of the liquid nitrogen evaporator; (*9*) matched load; and (*10*) directional couplers with crystal detectors.

side, filled with water, and allowed to cool for some time at a temperature from –5 to –10°C. After freezing of the sample, the ice protruding on the open side of the cavity was cut to fit the cavity edge flange and the cavity with the sample was mounted in the waveguide line.

We measured the resonance frequency f_r and the resonance curve halfwidths on the high-frequency $(f_h - f_r)$ and low-frequency $(f_r - f_l)$ sides at the 0.5 or 0.25 peak height levels and determined their ratio $r = (f_h - f_p)/(f_p - f_l)$. The error of measurements was ±1 MHz for the frequency, ±0.1°C for the temperature measured with the thermoresistor sensor, and ±2°C for the thermocouple. The resonance parameters are illustrated in Fig. 2b.

The experiments were performed with heavy water $D_2^{16}O$ deuterated to 99.8% (conductivity, 1×10^{-4} $(\Omega\ \mathrm{m})^{-1}$, and distilled water from a natural source 5×10^{-4} $(\Omega\ \mathrm{m})^{-1}$).

2. EXPERIMENTAL RESULTS

Figure 3 shows the results of measurements of the resonance curve halfwidths at the 0.5 peak height level in the temperature intervals from 0 (for D_2O) and –5°C (for H_2O) to –130°C. The resonance curves exhibited a significant asymmetry, with a pronounced temperature dependence of the halfwidth ratio *r*. An important feature revealed by these data is the different character of asymmetry observed for the two types of ice. The phenomenon is manifested by the fact that the slope of the temperature dependence of *r* is positive for H_2O ice and negative for D_2O ice.

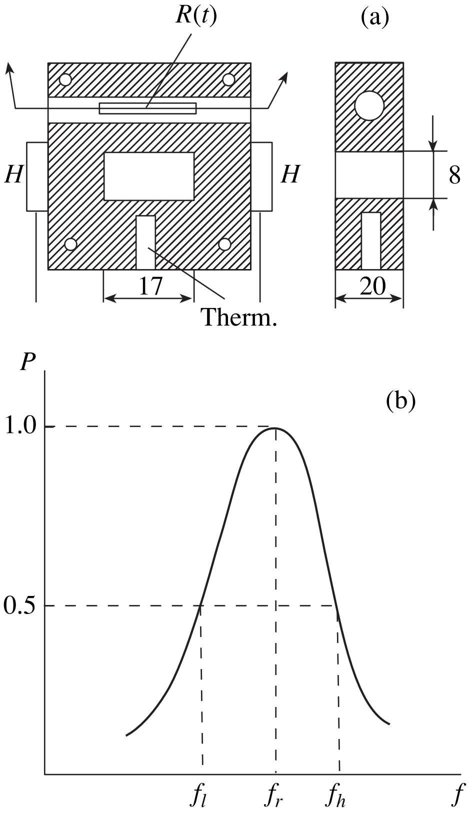

Fig. 2. (a) Schematic diagram of a rectangular cavity of the H_{101} type (diafragms are omitted): $R(t)$, thermoresistor; *H*, heater elements; (Therm.), thermocouple junction. (b) Measured resonance parameters: *P* is the signal power; f_r is the resonance frequency; f_h and f_l are the higher and lower resonance frequencies on the 0.5 peak height level, respectively; and $\Delta f_h = f_h - f_r$ and $\Delta f_l = f_r - f_l$ are the upper- and lower-frequency halfwidths of the resonance curve.

We have studied a total of eight samples, four of each kind of ice. The plots of the halfwidth ration versus temperature were somewhat different for various samples, but the general trends in behavior were the same for all samples of each kind. For example, Fig. 4 presents analogous data for two other light and heavy ice samples. The results of measurements using halfwidths determined at the 0.25 peak height level were close to those using the 0.5 level. Note that the resonance curves are symmetric for both types of ice in the region of temperature from –30 to –50°C.

Another characteristic feature revealed by the experimental results is a significant difference in the magnitude of the halfwidth ratio observed in the temperature interval from 0 to –20°C. This ratio is greater than unity and may reach up to 1.5 for light ice, while being always smaller than unity for heavy ice. These results are manifested by the resonance curve being extended toward higher frequencies for the cavity filled with H_2O ice and toward lower frequencies for D_2O ice.

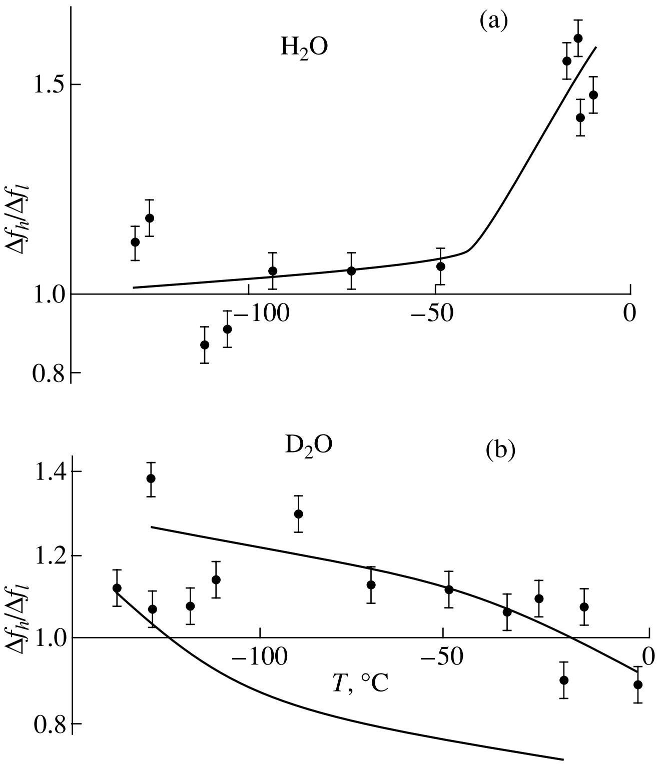

Fig. 3. Temperature dependence of the ratio of the higher frequency halfwidths to the lower frequency one at the 0.5 peak height level for (a) H_2O ice and (b) D_2O ice.

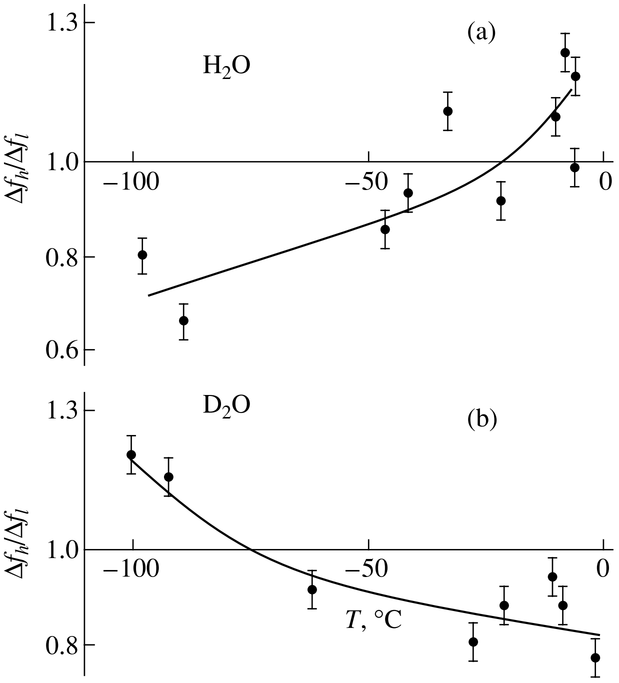

Fig. 4. Temperature dependence of the asymmetry ratio for the samples of (a) H_2O ice and (b) D_2O ice different from those presented in Fig. 3.

Interesting results were also obtained for the other parameters. The plots of the resonance frequency versus temperature are indicative of a decrease in the real part of the dielectric permittivity with decreasing temperature, which follows from a growth in the f_r value on cooling the sample (Fig. 5). The data in Fig. 5 refer to the same couple of samples as that presented in Fig. 3. Note also a feature in the region of –30°C, where the plot appears as the intersection of two straight lines with significantly different slopes. The rate of the resonance frequency variation with the temperature is higher in the interval from 0 to –30°C. This effect is also related to the properties of ice, rather than to the thermal expansion of the resonator (estimated to be low).

Another feature observed during the measurements was manifested by smooth pulsations in the parameters of the resonance curve accompanying variation of the ice temperature. This effect was observed even with small (on the order of a few tenths of degree) changes in the sample temperature. As a result, the points in the plots presented in Figs. 3 and 4 exhibit a considerable scatter exceeding the calculated errors of measurements. This phenomenon is probably related to the development of mechanical stresses, either as a result of inhomogeneous thermal fluxes in the sample or due to a difference in the thermal expansion coefficients of ice and the cavity material. In order to reduce the effect of ice and cavity expansion and contraction on the results of measurements, the process of cooling (or heating) in each experimental cycle was very slow (the cycle duration reaching 3–6 h). Taking into account that polycrystalline ice exhibits significant flowability even at pressures of a few atmospheres, we may assume that, due to the stress relaxation process, the medium occurred during measurements, on the average, in a nonstressed state.

Previously, we employed this effect in a series of experiments performed with H_2O ice in a close frequency range. In one of those experiments, the sample temperature was slowly increased from –31 to –25°C. Figure 6 presents the results of determination of some resonance parameters in that experiment, including variation of the radiation power transmitted through the cavity, the resonance curve width at the 0.5 peak height level, and the resonance frequency. The rate of sample heating in the temperature interval from –31 to –28°C was nearly constant (Fig. 6d). As is seen, all parameters exhibit pulsations with a characteristic time on the order of 1 min at a temperature variation rate of 3 K/h. We also noticed that the pulsations only appeared during variation of the temperature: when the temperature was kept constant, the cavity parameters remained unchanged. The observed phenomena can be qualitatively explained by the development of thermal stresses influencing the dielectric properties, which is followed

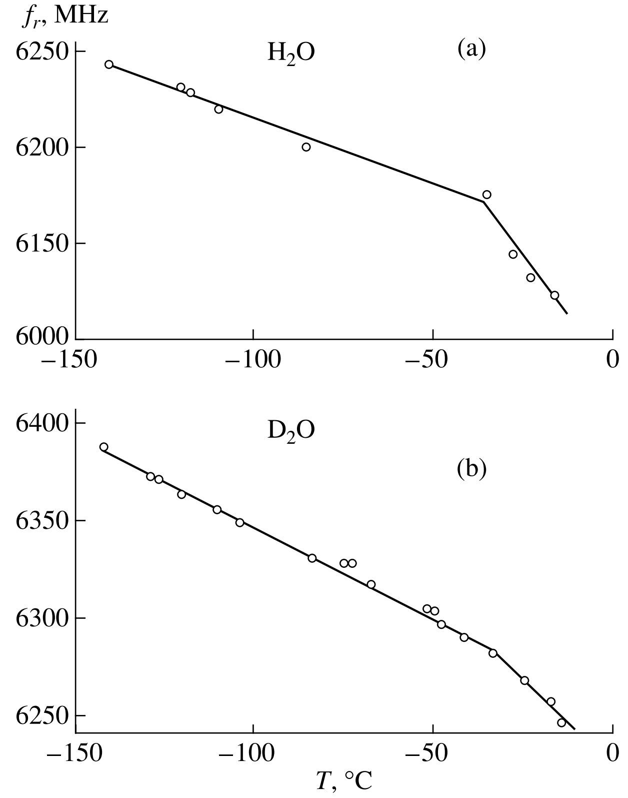

Fig. 5. Plots of the resonance cavity frequency versus temperature for (a) light and (b) heavy ice.

by the relaxation of these stresses related to the ice flow. However, the unusual electromagnetic behavior of H_2O ice is manifested in that increasing losses (e.g., in the jump between points *9* and *10* in Fig. 6) are accompanied by a growth in the resonance frequency. In usual media, an increase in the cavity losses (accompanied by broadening of the resonance curve) is accompanied by decreasing resonance frequency. This effect was also observed in the reverse process of cooling (between points *13* and *16* in Fig. 6).

Thus, the scatter of experimental points in Figs. 3 and 4 is explained by the appearance of sets of experimental values pulsating within certain small limits due to the special properties of ice. In order to exclude the effect of thermal stresses on the results of permittivity measurements, the sample should be equilibrated for several days at a constant temperature as in [5].

3. DISCUSSION OR RESULTS

As is known, the physical properties of H_2O and D_2O in liquid (water) and solid (ice) forms are rather close. For example, the permittivity ε' of D_2O ice in the microwave range is only 3% lower than the value for H_2O ice [3]. For this reason, we might expect that the shapes of resonance curves for the two types of ice will be similar as well. However, the experiment revealed a

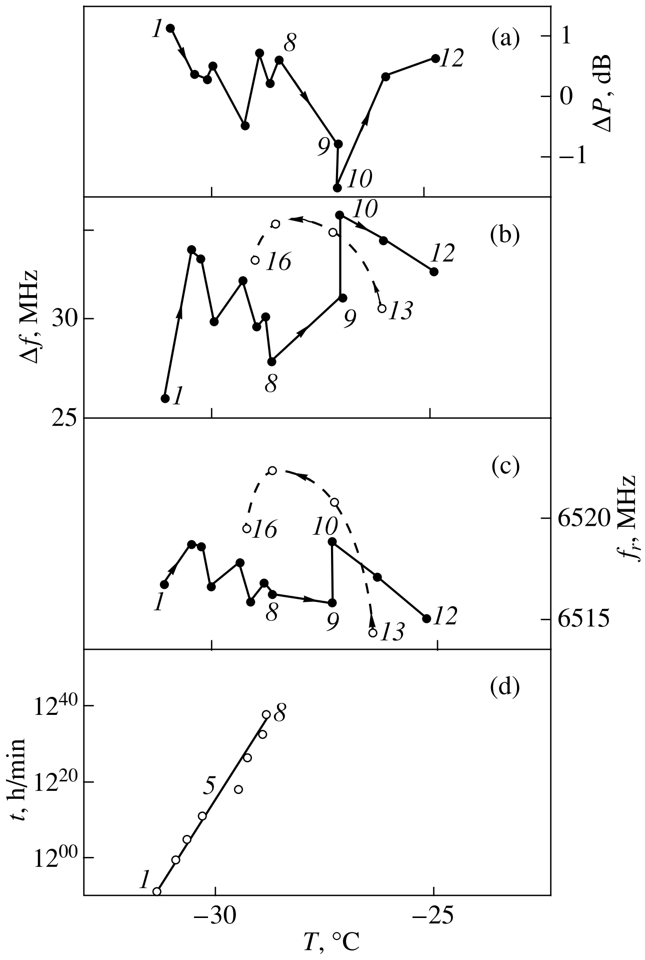

Fig. 6. Pulsating characteristics observed during temperature variation of a cavity with H_2O ice (numbers indicate the sequence of experimental points in time): (a) variation of the radiation power transmitted through the cavity; (b) resonance curve width at the 0.5 peak height level; (c) resonance frequency; and (d) temperature variation schedule showing the rate of ice sample heating in the cavity.

qualitatively different behavior of the temperature dependence of asymmetry of the resonance curves measured in the cavities filled with these media. The observed difference excluded the influence of the cavity design (e.g., of the frequency dependence of the diaphragm transmission, etc.), since such distortions would be manifested in a similar manner for the two types of ice possessing close physical properties.

For the first type, the experimental results show evidence of some structural distinctions related to the isotope composition of ice samples. Probably, this is a manifestation of the different quantum statistics of the hydrogen and deuterium nuclei (possessing half-integer and integer spins). Although the systems composed of such particles are nondegenerate at usual temperatures, we may nevertheless note that the Debye temperature (characterizing the transition from classical to quantum statistics) significantly increases for the water–ice phase transition to reach, for example, about

350 K for H_2O ice. In this context, we may expect some difference in the electric properties of particles and in their influence on the properties of the medium.

For the second type, a difference related to the isotope composition may also be manifested if the particles involved in the polarization process exhibit correlations with the formation of some structures on the scale exceeding interatomic distances. Indeed, the existence of mesostructures in H_2O and D_2O ice was indicated by the results of observation of the low-frequency Raman light scattering in the range from 0.1 to 80 cm^{-1} [6]. The analogous phenomenon observed in glassy materials was related to the scattering of light on vibrational excitations obeying the Bose statistics [7]. It was established that thermal treatment, mechanical, and other factors acting upon the sample produced significant changes in the low-frequency Raman spectrum. It was noted that these low-frequency spectra carry information on microinhomogeneities in the samples studied. In particular, a model of low-molecular fractal structures was proposed. However, the nature of the low-frequency Raman spectrum is still incompletely clear. Assuming that the ice structure includes clusters, we may expect that their parameters, such as the fractal dimensionality, depend on the type of particle statistics.

Clusters are known to form in media of many types. For example, the anomalies of dielectric permittivity of emulsions are explained by the formation of percolation clusters [8]. Deviation of the dielectric relaxation from the Debye law was also considered [9] as a manifestation of the fractal properties of the medium. As for ice, a strong deviation of its dielectric relaxation from the Debye law at frequencies below 10^2 Hz has been known for a long time [5], but is still given no satisfactory explanation. This anomaly is probably related to the existence of clusters with a relaxation time greater by several orders of magnitude than the value for the molecular structures in ice. Such clusters are formed, as was noted above, in emulsions [8].

Observations of the instability of the cavity parameters accompanying changes in the temperature also provide evidence for the existence of structural features and their variation under the action of mechanical stresses. This phenomenon is known in mechanochemistry. At present, investigations of the formation of dissipative structures during the relaxation of mechanical stresses in solids are in progress [10].

REFERENCES

1. A. A. Brandt, *Researches of Dielectrics on Ultrahigh Frequencies* (Moscow, 1963).
2. S. D. Krylov, Available from VINITI No. 2621-B98 (1998).
3. G. S. Bordonskiĭ and S. D. Krylov, Zh. Fiz. Khim. **75** (5), 938 (2001).
4. R. R. Nigmatullin, Author's Abstract of Candidate's Dissertation (Kazansk. Univ., Kazan, 1992).
5. R. P. Auty and R. H. Cole, J. Chem. Phys. **20** (8), 1309 (1952).
6. A. Amoruso, Phys. Rev. B **57** (13), 7415 (1998).
7. V. K. Malinovskiĭ, V. N. Novikov, and A. P. Sokolov, Fiz. Khim. Stekla **15** (3), 331 (1989).
8. Y. Feldman, N. Kozlovich, and Y. Alexandrov, Phys. Rev. E **54** (5), 5420 (1996).
9. R. R. Nigmatullin and Ya. E. Ryabov, Fiz. Tverd. Tela (St. Petersburg) **39** (1), 101 (1997) [Phys. Solid State **39**, 87 (1997)].
10. N. Lyakhov, in *Reactivity of Solids: Past, Present and Future, Chemistry for the 21st Century,* Ed. by V. V. Boldyrev (Blackwell Science, Cambridge, 1997), p. 121.

Translated by P. Pozdeev

Physics of the Solid State, Vol. 43, No. 9, 2001, pp. 1644–1647. Translated from Fizika Tverdogo Tela, Vol. 43, No. 9, 2001, pp. 1580–1583.
Original Russian Text Copyright © 2001 by Kulikov.

SEMICONDUCTORS AND DIELECTRICS

Concentration and Lifetime of Nonequilibrium Charge Carriers in CsI and NaCl Subjected to X-ray Irradiation

V. D. Kulikov
Tomsk Polytechnical University, Tomsk, 634034 Russia
e-mail: kulikov@list2.epd.tpu.edu.ru

Received January 16, 2001

Abstract—The temperature dependence of radiation-induced conductivity was studied in the range of 80–300 K in alkali halide CsI and NaCl crystals subjected to pulsed x-ray irradiation. It is shown that an increase in electrical conductivity with increasing temperature is satisfactorily accounted for by the thermal separation of electrons and holes with common origins. The concentration and lifetime of conducting electrons, as well as the spatial distribution and the probability of thermal separation of nonequilibrium charge carriers in the common-origin electron–hole pairs after thermalization were estimated. The possible effect of the two common-origin holes generated in the Auger process on the enhancement of recombination rate of electrons is discussed. *© 2001 MAIK “Nauka/Interperiodica”.*

1. INTRODUCTION

Information on the concentration and lifetime of nonequilibrium charge carriers is important for gaining insight into the mechanisms of many radiation-stimulated phenomena, such as electrical conductivity, defect formation, and luminescence.

In ionic crystals, the concentration of charge carriers generated by radiation is limited by the recombination of electrons and holes in pairs due to Coulomb interaction and by capture by radiation defects. The recombination rate of charge carriers decreases for more extended pairs with increasing temperature and in the presence of an external electric field [1, 2]. The available results of estimating the yield and lifetime of charge carriers in alkali halide crystals are incomplete. According to the results of numerical simulation of the carrier-generation stages in the NaCl crystal irradiated by photons with energies of 20–250 eV, the mean energy of the generated electrons is ~5 eV and the electron–hole separation is smaller than 5 nm [2, 3]. In particular, it has been noted that the electric field of a hole only slightly affects the motion of a hot electron in the electron–hole pairs during thermalization. The mean thermalization distance is ~100 nm. In the pairs of common origin electrons and holes, electrons with energies of about 1–2 eV recombine, which limits the yield of free charge carriers to ~60–70% of the total number of carriers. Experimental estimations of the free-carrier yield by the excitation of KCl with a high-current electron beam [4] show that this yield is ~6%. In our opinion, the low electrical conductivity may be caused by a high concentration of defects in alkali halide crystals, which results in the capture and scattering of charge carriers.

Direct measurements of the lifetime of free electrons in the conduction band of a dielectric involve serious difficulties because, in the majority of cases, the reliability of estimating the lifetime from the conductivity decay upon the termination of the excitation pulse is limited by the time resolution of the equipment.

In this paper, we report the results of studying the temperature dependence of radiation-induced conductivity at temperatures of 80–300 K in CsI and NaCl crystals subjected to pulsed x-ray irradiation. The choice of these crystals is motivated by the low efficiency of the color center production and buildup under the effect of ionizing radiation; this is especially true for CsI. We may expect that the effect of defects on radiation-induced conductivity is minimal in materials exposed to x-ray radiation. The experimental data are used to suggest a model for radiation-induced conductivity.

2. EXPERIMENTAL

In the experiments, we used high-purity CsI and NaCl single crystals grown from the melt of an extra-pure salt. The radiation-induced electrical conductivity σ and the charge-carrier concentration n were estimated from measurements of the current–voltage (I–V) characteristics:

$$i = \sigma E, \tag{1}$$

where $\sigma = en\mu$, e is the elementary charge, μ is the mobility, and E is the electric-field strength. The method for measuring characteristics I–V has been described recently [5]. X-ray radiation was generated by irradiating an ~300-μm-thick Al target with a high-current pulsed electron beam; the highest electron energy was ~0.3 MeV, the pulse duration was ~20 ns, and the current density was ~400 A/cm^2. Irradiations at low temperatures were performed on samples installed in a vessel filled with liquid nitrogen. Characteristics *I*–*V* were plotted using the amplitude values of the current pulse for the corresponding voltages. The energy of x-ray radiation W_0 absorbed in the sample was estimated using a method reported recently [5]. The values of $\sigma(T)$ were determined at low levels of the electric-field strength $E \sim 10^4$ V/cm in the sample; these values corresponded to the range of linear dependence of the conduction current on *E*. As was shown recently [5], we may disregard the impact ionization of *F* and F^- color centers, the Onsager effect, and the effect of the electric field on the charge-carrier mobility if *E* is no higher than about 1.5×10^4 V/cm. We used data on the Hall mobility in the alkali halide crystals reported previously [6, 7]. At temperatures higher than 30 K, the capture time at shallow-level traps is much shorter than the lifetime of the charge carriers in the conduction band due to thermal activation; thus, we may assume that the Hall and drift mobilities are nearly identical [4].

3. RESULTS

The dependence of the radiation-induced conductivity in CsI on the energy density of the incident x-ray radiation *W* at room temperature is shown in the inset in Fig. 1a. Since the duration of the excitation pulse (~10^{-8} s) is larger than the charge-carrier lifetime, which does not exceed 10^{-11}–10^{-9} s depending on the excitation density [4], we may assume that the generation of carriers and the electrical conductivity are quasi-steady-state. The dependence of the conductivity amplitude on the excitation-energy density may be approximated with the power-law curve $\sigma \sim W^{1/2}$, which corresponds to the quadratic charge-carrier recombination. The latter is observed in CsI, KBr, KCl, and NaCl samples exposed to x-ray radiation both at room and liquid nitrogen temperatures. This experimental data suggest that x-ray-induced conductivity in such materials is related to thermalized conduction-band electrons, the lifetime of which is controlled by recombination with relaxed holes (V_k centers).

Temperature dependences of the radiation-induced conductivity $\sigma(T)$ in the CsI and NaCl crystals are shown in Figs. 1a and 1b. The electrical conductivity in CsI exceeds that in NaCl by more than an order of magnitude. At low temperatures (77–130 K for CsI and 77–160 K for NaCl), an insignificant increase in conductivity with temperature is observed; a sharp increase in σ with temperature sets in at 130 K for CsI and at a somewhat higher temperature (~160 K) for NaCl. Dips in the $\sigma(T)$ curves at higher temperatures ($T \sim 270$–280 K) are possibly related to the capture and scattering of conduction-band electrons by the color centers in these materials.

Temperature dependence $n(T)$ is shown in Fig. 2 as a plot of $\log(n)$ versus $1/T$. For both materials, the values of *n* increase by more than an order of magnitude as temperature increases from 80 to 300 K. Experimental dependences $n(T)$ in the CsI and NaCl crystals are satisfactorily described by a sum of two exponential components: one for low temperatures (straight line *1* in Fig. 2) and the other for higher temperatures (line *2*). Such a law of variation in *n* with temperature corresponds to the thermally activated separation of common-origin electrons and holes. The fact that there are two components in $n(T)$ is apparently related to the existence of two types of electron–hole pairs that differ in the mean energy of the generated electrons.

4. MODEL

Using the above experimental data, we can suggest a model that describes the mechanism of radiation-induced conductivity in alkali halides exposed to x-rays in the temperature range of $T \sim 80$–300 K. In the absence of an electric field, the probability of the separation of charge carriers in electron–hole pairs $f(T)$ or the yield of free charge carriers can be written as

$$f(T) = \exp(-\Delta W/kT), \tag{2}$$

where ΔW is the activation energy for the thermal separation of charge carriers and *k* is Boltzmann's constant [4]. A variation in the charge-carrier concentration is accounted for by introducing an effective carrier-generation rate G_e. Under the conditions of quasi-steady-state generation, we have

$$G_e = np\gamma v, \tag{3}$$

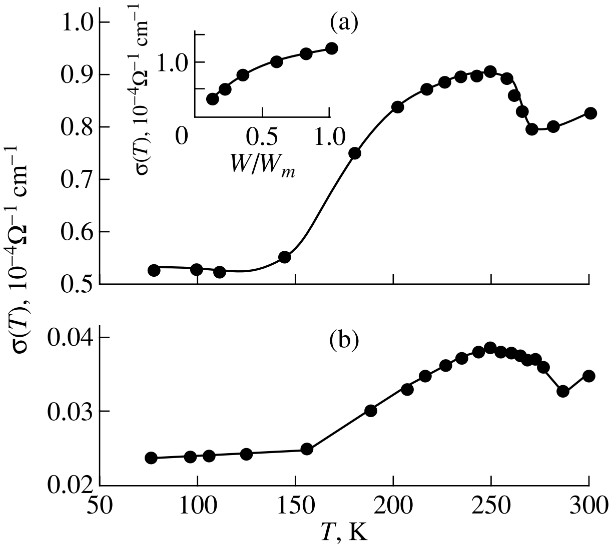

Fig. 1. Temperature dependences of electrical conductivity σ in the (a) CsI and (b) NaCl crystals subjected to x-ray radiation with an incident energy density of *W*. The dependence $\sigma(W)$ for CsI is shown in the inset; W_m is the maximum energy density of x-ray radiation.

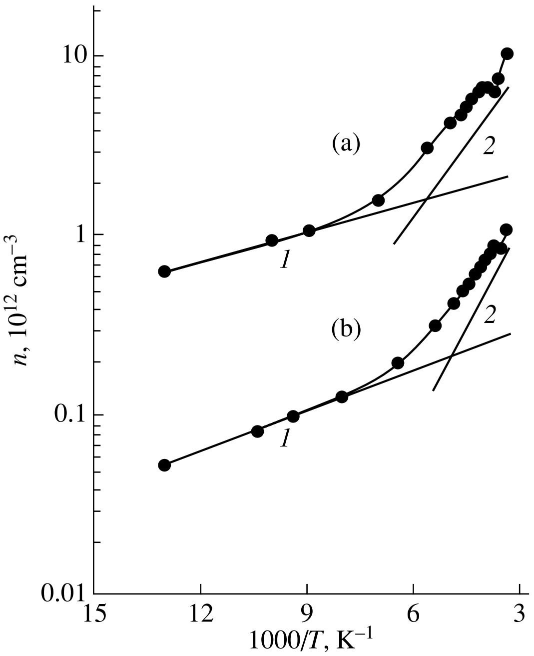

Fig. 2. Temperature dependence of electron concentration in the (a) CsI and (b) NaCl crystals. Decomposition of the curves into the (*1*) low-temperature and (*2*) high-temperature exponential components is shown.

where $G_e = G_0 f(T)$, $G_0 = W_0/A$ is the generation rate of electron–hole pairs per unit volume (W_0 is the radiation energy absorbed in one unit volume of the sample per unit time and A is the mean energy spent on formation of a single electron–hole pair in the material), p is the hole concentration, γ is the cross section of capture by the recombination center, and v is the thermal velocity.

If the recombination of charge carriers is quadratic ($n \approx p$), expression (3) can be rewritten as $G_e = n^2\gamma v$. The exponential dependences—the low-temperature component (line *1* in Fig. 2) and the high-temperature component (line *2*) for CsI and NaCl—may correspond to two types of nonequilibrium electrons differing in their generation rates and in the thermal-separation probability. For these components, the temperature dependence of the charge-carrier concentrations n_1 and n_2 is given by

$$n_1 = \sqrt{G_{01}}(\exp(-\Delta W_1/2kT))/\sqrt{\gamma v}, \qquad (4)$$

$$n_2 = \sqrt{G_{02}}(\exp(-\Delta W_2/2kT))/\sqrt{\gamma v}, \qquad (5)$$

where $G_0 = G_{01} + G_{02}$.

Comparing (4) and (5) with the data in Fig. 2 (straight lines *1* and *2*) for CsI, we obtain $\Delta W_1 = 0.025 \pm 0.003$ eV, $\Delta W_2 = 0.1 \pm 0.01$ eV, and $G_{02}/G_{01} \approx 85$, and the yields of free charge carriers at $T = 300$ K are $f_1 \approx 0.37$ and $f_2 \approx 0.02$. The effective yield of charge carriers f_e is determined from the equality $\sqrt{G_{01} f_1} + \sqrt{G_{02} f_2} = \sqrt{G_0 f_e}$; thus, we have $f_e \approx 0.04$. The spatial distribution of charge carriers can be obtained if dependence (2) is represented as $f = \exp(-r_c/r_0)$, where $r_c = e^2/4\pi\varepsilon\varepsilon_0 kT$ is the Onsager radius and r_0 is the distance over which the common-origin electron and hole become thermalized. In the case of x-ray excitation of CsI, we have two spatial peaks of low-energy electrons: a low-intensity peak with $r_{01} \approx 10$ nm and a high-temperature peak with $r_{02} \approx 2.5$ nm. The obtained value of $r_{02} \sim 2.5$ nm for CsI is consistent with the data for a 3-MR glass exposed to gamma-ray radiation, in which case the peak of the charge-carrier distribution in pairs is located at 4–5 nm [8].

For NaCl, we obtain $\Delta W_1 = 0.03 \pm 0.004$ eV, which is comparable to the data for CsI; however, ΔW_2 is appreciably larger and is equal to $\sim 0.14 \pm 0.015$ eV. In addition, we have $G_{02}/G_{01} \approx 200$, $f_1 \approx 0.3$, $f_2 \approx 0.004$, and $f_e \approx 0.01$ for NaCl at $T = 300$ K.

The obtained values for the free-carrier yield at room temperature in CsI are equal to ~4%, which does not exceed similar estimates for KCl [4]; however, for NaCl, this yield is much lower (~1%).

Under x-ray excitation, the energy spectrum of conduction electrons is formed owing both to the ionization of the valence shells of atoms in the crystal and to the generation of Auger electrons. In an NaCl crystal [2, 3], single-atom Auger transitions with the generation of two holes in the Cl^- 2*p* and 3*s* shells and of an electron with an energy of ~1 eV are possible. If the 2*p* shell of Na^+ is ionized, the interatomic Auger transitions form the 3*s* and 3*p* levels of Cl^-. These transitions result in the occupation of the states at 3–4 and 12.5 eV above the conduction band bottom [3].

The cause of a low yield of charge carriers can be related to specific features of Auger generation. Two holes and an electron can be generated as a result of the Auger process. Although the atomic localization time of a hole is fairly short ($\sim 10^{-13}$ s), it may be expected that the delocalization range of holes will not exceed one or two lattice parameters in the electron-thermalization time ($\sim 10^{-12}$ s) [2]. For light elements ($Z < 30$), the probability of Auger transitions is higher than that of x-ray transitions if the hole is localized in the inner atomic shells [2, 9]. Therefore, we may expect that the Auger effect is more pronounced in NaCl than in CsI; correspondingly, the charge-carrier recombination rate should be higher in NaCl than in CsI.

The dependence of the formation efficiency for self-trapped excitons η on the atomic number of elements in the alkali halide compounds corroborates the estimates obtained. Excitons are formed as a result of the recombination of the conduction-band electron with a relaxed hole. The efficiency η at room temperature is equal to ~18, 15, and 12% in the CsBr, KI, and KCl crystals, respectively [10]. The total number of electron–hole pairs was estimated from the absorption of the electron-beam energy in the crystal, and the exciton concentration was determined using the Smakula formula on the basis of absorption by the V_k centers.

The lifetime of charge carriers in the conduction band of a dielectric τ can be found (see [5]) from the equality $n = G_e\tau$, where $\tau = 1/p\gamma v$. For CsI at $T = 300$ K, we have $\mu = 46$ cm^2/(V s) [6]. Thus, for $E = 10^4$ V/cm, we use the I–V characteristic to find that $n = 1.1 \times 10^{13}$ cm^{-3}. Also, for CsI with $W_0 = 4.2 \times 10^{-3}$ J/cm^3, we have $G_0 = 2.9 \times 10^{23}$ cm^{-3} s^{-1}, $f_e \approx 0.04$, $G_e \approx 1.16 \times 10^{22}$ cm^{-3} s^{-1}, and $\tau \approx 1.1 \times 10^{-9}$ s. The value obtained for τ agrees with the experimental estimate of the lifetime in CsI [11], according to which the lifetime is approximately equal to 1 ns at room temperature. For NaCl at $T = 300$ K, $\mu = 20$ cm^2/(V s) [6]; thus, we have $n = 1.15 \times 10^{12}$ cm^{-3}, $G_0 \approx 2.9 \times 10^{23}$ cm^{-3} s^{-1}, $f_e \approx 0.01$, $G_e \approx 2.9 \times 10^{21}$ cm^{-3} s^{-1}, and $\tau \approx 4 \times 10^{-10}$ s.

The observed increase in the radiation-induced electrical conductivity with increasing temperature (in the range of 80–300 K) in CsI and NaCl crystals subjected to x-ray excitation can be satisfactorily described by the mechanism of thermal separation of common-origin electrons and holes. The lifetimes of electrons in CsI and NaCl are quite close to each other (~1.1×10^{-9} and 4×10^{-10} s). However, the charge-carrier concentrations differ by an order of magnitude: ~1.1×10^{13} cm^{-3} (CsI) and 1.15×10^{12} cm^{-3} (NaCl). Apparently, this is related to the Auger generation of low-energy electrons in NaCl, in which case two holes in the same electron–hole pair enhance the recombination rate of the charge carriers.

ACKNOWLEDGMENTS

I thank V.Yu. Yakovlev for his fruitful participation in discussion of the results.

REFERENCES

1. É. D. Aluker, D. Yu. Lusis, and S. A. Chernov, *Electron Excitations and Radiation-Induced Luminescence in Alkali Halide Crystals* (Zinatne, Riga, 1979).
2. M. A. Elango, *Elementary Inelastic Radiation-Induced Processes* (Nauka, Moscow, 1988; American Inst. of Physics, New York, 1991).
3. A. Ausmess, M. Elango, A. Kikas, and J. Pruulman, Phys. Status Solidi B **137** (2), 495 (1986).
4. B. P. Aduev, V. M. Fomchenko, and V. N. Shvaĭko, Fiz. Tverd. Tela (St. Petersburg) **41** (3), 429 (1999) [Phys. Solid State **41**, 384 (1999)].
5. V. D. Kulikov and Yu. V. Lisyuk, Zh. Tekh. Fiz. **70** (9), 51 (2000) [Tech. Phys. **45**, 1141 (2000)].
6. C. H. Seager and D. Emin, Phys. Rev. B **2** (8), 3421 (1970).
7. F. C. Brown, in *Point Defects in Solids* (Plenum, New York, 1972), p. 491.
8. D. L. Ivanov and B. S. Yakovlev, Khim. Vys. Énerg. **29** (6), 410 (1995).
9. W. Bambynek, B. Crasemann, R. W. Fink, *et al.*, Rev. Mod. Phys. **44** (4), 716 (1972).
10. V. Yu. Yakovlev, Author's Abstract of Doctoral Dissertation (Yekaterinburg, 1996).
11. B. P. Aduev, G. M. Belokurov, and V. N. Shvaĭko, Fiz. Tverd. Tela (St. Petersburg) **37** (8), 2537 (1995) [Phys. Solid State **37**, 1392 (1995)].

Translated by A. Spitsyn

Physics of the Solid State, Vol. 43, No. 9, 2001, pp. 1648–1654. Translated from Fizika Tverdogo Tela, Vol. 43, No. 9, 2001, pp. 1584–1589.

SEMICONDUCTORS AND DIELECTRICS

Vibrational Spectrum of $Li_2B_4O_7$ Crystals

A. V. Vdovin, V. N. Moiseenko, V. S. Gorelik, and Ya. V. Burak

Lebedev Physical Institute, Russian Academy of Sciences, Leninskiĭ pr. 53, Moscow, 117924 Russia

Received February 8, 2001

Abstract—The polarized infrared reflection spectra of $Li_2B_4O_7$ were studied in the spectral range 80–1600 cm^{-1} and compared with Raman spectra. From the spectrum dispersion analysis, the frequencies, damping, and dielectric oscillator strengths were determined for all vibrational modes observed. A calculation of the effective charges and an analysis of the chemical-bond types of the $Li_2B_4O_7$ crystal structural units were carried out on the basis of the obtained data. © *2001 MAIK "Nauka/Interperiodica".*

Crystalline lithium tetraborate (LTB) $Li_2B_4O_7$ is a perspective material for nonlinear optics because of its high radiation resistance, its transparence in a wide spectral range, including the ultraviolet region, its high nonlinear optical coefficients characterizing frequency transformation of laser radiation, and its intense Raman scattering (RS).

The vibrational spectrum of this material has been studied extensively using RS spectroscopy methods [1–3]. However, the infrared spectra of LTB have been studied only in a few papers [4, 5]. In particular, the frequencies of longitudinal and transverse phonons were determined in [4] using extremum values of the calculated optical functions $\varepsilon''(\omega) = \mathrm{Im}[\tilde{\varepsilon}(\omega)]$ and $\eta''(\omega) = \mathrm{Im}[-1/\tilde{\varepsilon}(\omega)]$ for two polarizations of light. However, the obtained values of the vibration frequencies for the polarization $\mathbf{E} \parallel \mathbf{c}$ (vector $\mathbf{c}$ is directed along the optical axis of the crystal) differed considerably from the frequencies of A_1 vibrational modes observed in the RS spectra [1–3]. In addition, the total number of spectral lines in the range 215–1010 cm^{-1} exceeded its value predicted by group theory [1].

The present work is dedicated to an investigation of the infrared (IR) reflection spectra of $Li_2B_4O_7$ crystals and to their comparison with RS spectra with the aim of obtaining more reliable information on the vibrational spectrum of these crystals.

In LTB crystals (space group C_{4V}^{12}), polar vibrations are characterized by A_1 and E symmetries and are revealed when the polarization of exiting radiation is $\mathbf{E} \parallel \mathbf{c}$ and $\mathbf{E} \perp \mathbf{c}$, correspondingly. The reflection spectra in the range 200–4000 cm^{-1} were obtained using a Specord-M80 spectrophotometer with a resolution better than 0.8 cm^{-1}. In the range 80–400 cm^{-1}, measurements were carried out using a laboratory LAFS-1000 automated Fourier spectrometer with a spectral resolution of 0.1 cm^{-1} for unpolarized light. This allowed us to obtain the reflection spectra from the *xy* plane, in which the *E*-symmetry vibrations were manifested, as well as the reflection spectra from the *zy* plane, in which both the A_1- and *E*-symmetry vibrations were revealed.

A preliminary determination of the frequencies and damping of longitudinal (LO) and transverse (TO) vibrations was carried out using the dispersion analysis (DA) method [6]. The optimized $R(\omega)_{calc}$ spectra and $R(\omega)_{exp}$ are shown in Figs. 1 and 2a. As is clear from these figures, the vibration spectrum of LTB crystals possess a complicated structure in the frequency ranges 100–200 and 850–1000 cm^{-1}, where the separation between spectral lines becomes comparable with their widths. The model of weakly interacting oscillators becomes inadequate in this case, and the values of parameters obtained using the DA method can be considerably different from their true values. For this reason, in addition to the DA method, the Kramers–Kronig dispersion relations [6] were used. The obtained spectra of the $\varepsilon''(\omega)$ and $\eta''(\omega)$ functions are presented in Figs. 1 and 2b, and the RS spectra involving phonons of the corresponding symmetry [2, 3] are shown in Figs. 1 and 2c. The frequencies (ω), damping (γ), and dielectric oscillator strengths ($\Delta\varepsilon$) obtained using the DA method and from the $\varepsilon''(\omega)$ and $\eta''(\omega)$ spectra are shown in Table 1. The data needed for a comparative analysis of the dipole oscillation frequencies observed in the RS and IR spectra are presented in Table 2.

It is shown that the upper limit of the vibrational spectrum of LTB crystals is 1500 cm^{-1}. The reflection bands are not observed for higher frequencies. A total of 16 oscillators of A_1 symmetry having frequencies above 220 cm^{-1} and 22 oscillators of E symmetry with frequencies above 100 cm^{-1} are identified using the DA method.

The obtained IR spectra of A_1 phonons differ considerably from those reported in previous publications [4, 5], while the values of the phonon frequencies are

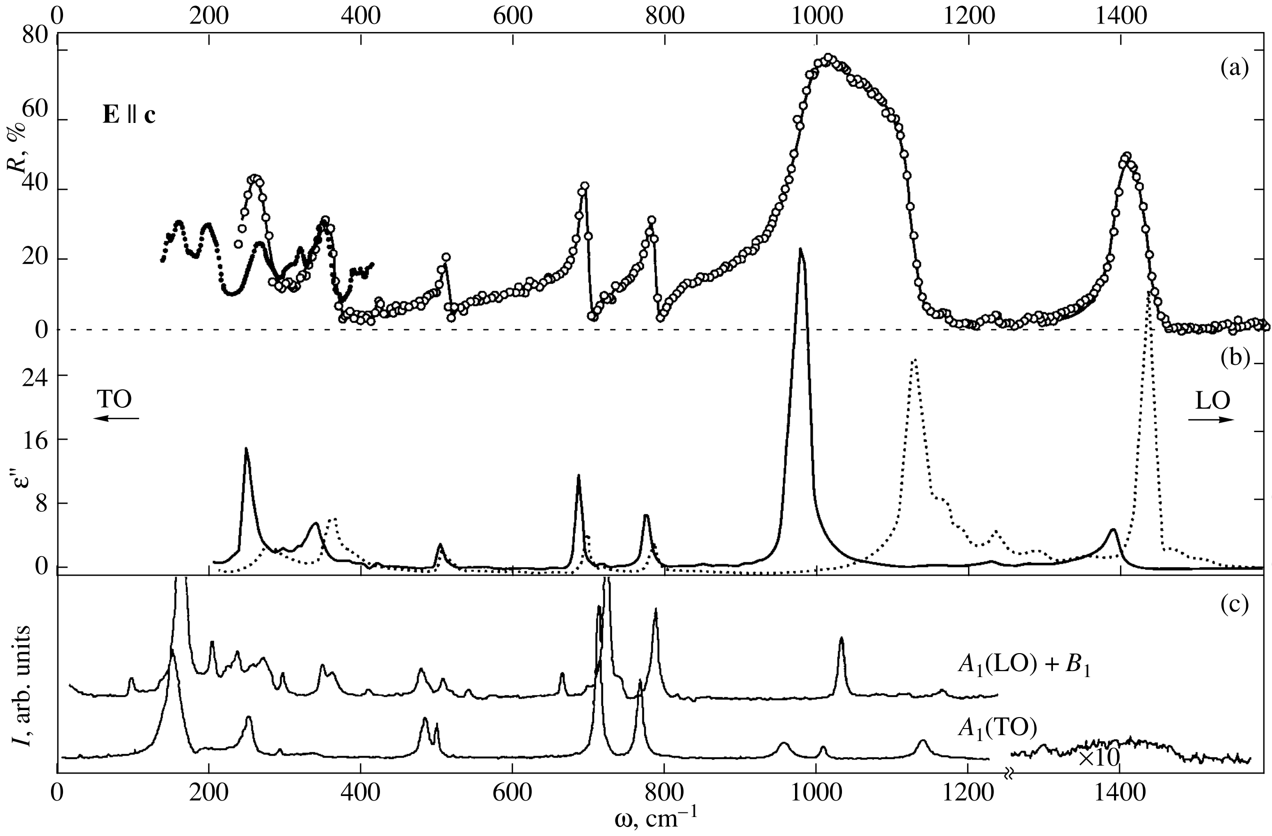

Fig. 1. IR and RS spectra of the A_1-symmetry polar vibrations for $Li_2B_4O_7$ crystals and the results of DA and Kramers–Kronig relation analysis: (a) IR reflection spectra (points are the experiment, the curve is the results of DA), (b) spectra of the ε''(ω) (solid line) and of the η''(ω) (dashed line) functions, and (c) Raman spectra.

in good agreement with the RS spectroscopic data (Table 2). To improve the agreement between the $R(\omega)_{calc}$ and $R(\omega)_{exp}$ spectra, additional oscillators, having frequencies 382, 689, and 1222 cm^{-1} (not observed in the RS spectrum), were introduced into the theoretical IR spectrum of A_1 phonons. The absence of the above-mentioned lines in the RS spectra can be due to small scattering cross sections for corresponding vibrations. The line with a frequency of 689 cm^{-1} is possibly veiled by a stronger line with a frequency of 719 cm^{-1} in the TO-phonon spectrum. The increase in frequency of this latter vibration leads to the appearance of a 694 cm^{-1} line in the LO spectrum, which was mistakenly attributed in [1] to the B_1 symmetry vibration.

The intense reflection band in the frequency range 900–1150 cm^{-1} in the A_1 spectrum with a shallow minimum near the 1038 cm^{-1} frequency was calculated using two oscillators: a strong one, having a frequency ω_{t1} = 977 cm^{-1}, and a weak one, having a frequency ω_{t2} = 1038 cm^{-1}. In the case at hand, the LO-phonon frequencies are determined by the dielectric oscillator strengths $\Delta\varepsilon_i$. The frequency of the strong LO oscillator is calculated using the formula [7]

$$\left(\frac{\omega_{LOj}}{\omega_{TOj}}\right)^2 = \frac{\varepsilon_\infty + \sum_{i=1}^{j}\Delta\varepsilon_i}{\varepsilon_\infty + \sum_{i=1}^{j-1}\Delta\varepsilon_i}. \qquad (1)$$

This frequency is close to the value ω_{l1} = 1128 cm^{-1} obtained using the DA method and from the Kramers–Kronig relations. Therefore, the weak band in the vicinity of 1130 cm^{-1} in the RS spectrum can also be identified with ω_{l1}. Cases of the overlapping of longitudinal–transverse splittings of vibrations having identical symmetry were reported in the literature and have been previously observed, e.g., in SiO_2, Al_2O_3, $LiAlSi_2O_6$, $Gd_2(MoO_4)_3$, $Cd_{1-x}Zn_xS$, and $In_{1-x}Ga_xP$ crystals [7, 8]. Similar phenomena can be observed in the case of direct interaction of oscillations having identical symmetry and close frequencies and wave vectors but considerably different values of oscillator strengths [8].

A broad diffuse band in the RS spectra corresponds to the band near 1400 cm^{-1} in the A_1 reflection spec-

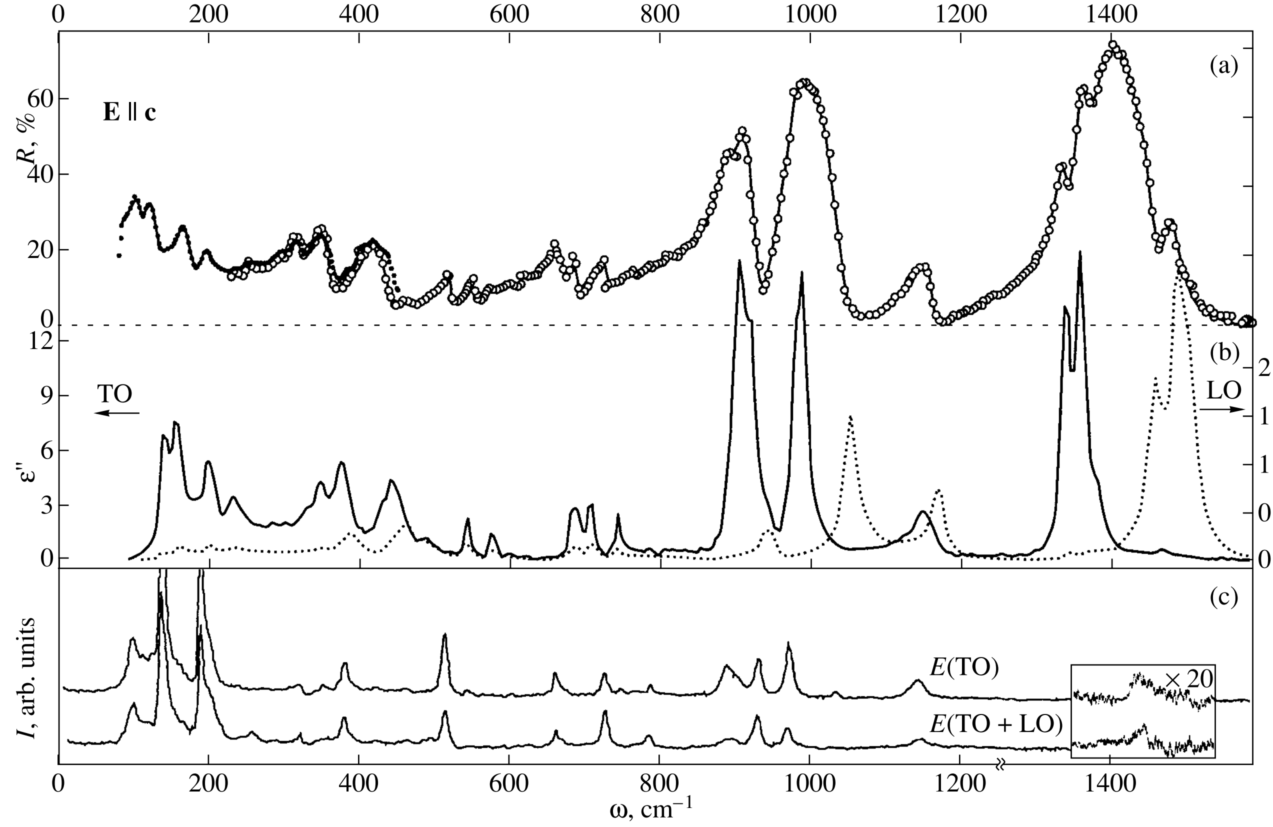

Fig. 2. IR and RS spectra of the *E*-symmetry polar vibrations for $Li_2B_4O_7$ crystals and the results of DA and Kramers–Kronig relation analysis: (a) IR reflection spectra (points are the experiment, the curve is the results of DA), (b) spectra of the ε''(ω) (solid line) and of the η''(ω) (dashed line) functions, and (c) Raman spectra.

trum. The lines in the ε''(ω) and η''(ω) spectra in this range are strongly asymmetrical. This is evidence that the model of weakly interacting oscillators with frequency-independent damping is not adequate and that anharmonic effects are significant. For this reason, it seems reasonable to attribute the above-mentioned band to biphonon processes (combinations of phonons with frequencies of 689 and 719 cm^{-1} are the most probable).

Correct analysis of the observed *E*-phonon spectra is complicated by the presence of a great number of oscillators having close values of frequencies. This can lead to interaction of vibrations. Moreover, for the *E*-symmetry RS spectra, one should take into account distortions of the scattering polarization geometry, because the scattering cross sections are low [1]. The above-mentioned phenomena can be the reason for the relative deviation of the LO–TO vibration frequencies observed in the IR and RS spectra, in particular, in the frequency range 100–200 cm^{-1}.

The intensive structured reflection band in the range 1250–1500 cm^{-1} of the *E* spectrum is calculated using four oscillators. The RS spectra contain only one weak line with a frequency of 1430 cm^{-1} in this range. The complicated spectrum structure in this range is possibly due to shifts of the vibration frequencies of isotopically substituted boron–oxygen rings (substitution of the ^{10}B isotope for ^{11}B atoms in different positions), as well as to biphonon processes.

The obtained data on the phonon frequencies and oscillator strengths allow one to calculate the static dielectric permittivity of the crystal, using the Lyddane–Sachs–Teller relation

$$\varepsilon_0 = \varepsilon_\infty \prod_j \left(\frac{\omega_{\mathrm{LO}j}}{\omega_{\mathrm{TO}j}}\right)^2. \qquad (2)$$

The values thus calculated are $\varepsilon_0^{11} = 8.3$ and $\varepsilon_0^{33} = 6.6$ (the experimental values are $\varepsilon_0^{11} = 8.9$ and $\varepsilon_0^{33} = 8.07$ [9]). The good agreement between the theoretical value of ε_0^{11} and the experimental value indicates that the description of the permittivity dispersion in terms of the ensemble of oscillators observed in the *E* spectrum is adequate. The difference between the experimental and theoretical values of ε_0^{33} can be due to the absence of reliable spectral data for frequencies below 220 cm^{-1} in the IR spectrum and to the discrepancy between

Table 1. Frequencies, damping, and dielectric oscillator strengths of polar forces for vibrations in $Li_2B_4O_7$ crystals

A_1^*

DA method					Kramers–Kronig method				
ω_{TO}, cm^{-1}	γ_{TO}, cm^{-1}	ω_{LO}, cm^{-1}	γ_{LO}, cm^{-1}	$\Delta\varepsilon$	ω_{TO}, cm^{-1}	γ_{TO}, cm^{-1}	ω_{LO}, cm^{-1}	γ_{LO}, cm^{-1}	$\Delta\varepsilon$
157		164		0.747	157		165		0.792
194		205		0.679	194		206		0.690
255	19	278	28	0.819	256	17	280	21	0.844
303	12	304	12	0.021	303	24	304	23	0.042
347	29	367	13	0.412	342	26	367	31	0.375
382	23	388.5	28	0.052	393	25	395	22	0.023
426	6	427	6	0.011	427	9	429	14	0.008
489.5	10	489.5	9	0					
509.5	7	513.5	7	0.053	509	8	513	9	0.049
689	8	698.5	7	0.128	688	8	699	9	0.145
719	10	719.5	10	0.005	719	8	719	8	0.004
779.5	11	788.5	9	0.103	778	11	788	10	0.106
980.5	20	1128	23	0.907	979	21	1127	24	0.895
1038.5	21	1038	19	0.005	1039	54			0.028
1154.5	40	1170.5	48	0.015	1160	42	1165	34	0.010
1222.5	38	1234.5	47	0.020	1227	27	1235	25	0.013
1276	37	1280	54	0.008	1287	45	1288	57	0.016
1390.5	20	1436	21	0.088	1389	18	1436	19	0.064

E

DA method					Kramers–Kronig method				
ω_{TO}, cm^{-1}	γ_{TO}, cm^{-1}	ω_{LO}, cm^{-1}	γ_{LO}, cm^{-1}	$\Delta\varepsilon$	ω_{TO}, cm^{-1}	γ_{TO}, cm^{-1}	ω_{LO}, cm^{-1}	γ_{LO}, cm^{-1}	$\Delta\varepsilon$
107	13	109.5	11	0.695	106	4	108	18	0.241
120	21	133.5	28	1.493	124	23	134	33	1.305
166	27	181	22	0.847	167	25	176	20	0.665
191.5	24	196.5	57	0.131	207	27	210	46	0.282
255	21	255.5	24	0.018	258	39	266	38	0.04
314.5	22	319	24	0.162	314	33	321	26	0.357
348	21	358.5	20	0.252	345	21	360	27	0.261
418.5	30	434	25	0.271	413	35	434	34	0.358
461	25	464	23	0.032	465	16	467	23	0.027
519.5	5	521	3	0.021	517	8	519	9	0.030
553	11	555	9	0.026	533	11	553	11	0.016
660.5	11	663.5	12	0.048	663	12	666	18	0.064
685.5	13	689.5	10	0.051	682	4	687	9	0.019
729.5	15	724.5	17	0.046	721	19	725	28	0.032
883.5	24	924.5	17	0.360	883	15	925	19	0.336
898	19	892.5	18	0.157	898	21	893	14	0.147
964.5	20	1034.5	29	0.289	967	21	1036	28	0.356
1134	49	1152	8	0.065	1131	42	1152	28	0.096
1325.5	14	1334	21	0.128	1325	11	1333	10	0.101
1347	11	1483.5	33	0.139	1344	16	1484	35	0.185
1370	26	1363.5	30	0.066	1368	25	1365	10	0.044
1461.5	22	1450.5	26	0.006	1461	42	1448	22	0.013

Note: Data on frequencies of the A_1-symmetry longitudinal and transverse vibrations in the range 0–255 cm^{-1} are obtained from the RS spectra.

Table 2. Comparison of frequencies of polar vibrations observed in the IR and RS spectra of $Li_2B_4O_7$ crystals

A_1(TO)		A_1(LO)		E(TO)		E(LO)	
RS	IR	RS	IR	RS	IR	RS	IR
				101	107	100	109.5
				114	120	114	
				139		139	133.5
157		164		158	166	152	181
194		205		191	191.5	191	
				200		202	196.5
255	255	271	278		255	256	255.5
295	303	296	304		255	289	
				317	314.5	318	319
338	347	362	367	350	348	351	358.5
	382		388.5	379		379	
	426		427	419	418.5	419	434
491	489.5	479	489.5	459	461	462	464
507	509.5	508	513.5	512	519.5	512	521
				541	553		555
				658	660.5	658	
				667		665	663.5
688	689	694	698.5		685.5		689.5
722	719	723	719.5	723	720.5	723	724.5
778	779.5	788	788.5	782		781	
				884	883.5	887	892.5
				899	898	919	924.5
				926		926	
974	980.5		1128	976	964.5	965	
1027	1038.5	1031	1038	1029			1034.5
1159	1154.5	1164	1170.5	1136	1134	1139	1152
	1222.5		1234.5		1325.5		1334
1296	1276		1280		1347		1483.5
					1370		1363.5
1400	1390		1436	1428	1461.5	1430	1450.5

$R(\omega)_{calc}$ and $R(\omega)_{exp}$ in the vicinity of 1400 cm^{-1}. Another reason for the above-mentioned difference can be the fact that not only phonons contribute to ε_0^{33}. This assumption is supported by the observations of low-frequency dielectric relaxation in the LTB crystals. According to [10], this relaxation is due to heat-activated jumps of lithium ions.

The LO–TO splittings in $Li_2B_4O_7$ crystals have an average value lying between 2 and 23 cm^{-1}. Larger splittings are observed in the frequency range 900–1000 cm^{-1}, where the $\nu_3[BO_4]$ and $\nu_1[BO_3]$ valence oscillations are detected, and at frequencies higher than 1300 cm^{-1}, corresponding to $\nu_3[BO_3]$ valence oscillations [1]. High values of the LO–TO splitting in the frequency range indicated above were also observed in LiB_3O_5 crystals [11], whose structure also contains boron atoms having tetragonal and trigonal oxygen atom surroundings. Thus, the considerable oscillator strengths observed in this frequency range are characteristic of structures containing boron–oxygen complexes with mixed boron atom coordination.

Data on the LO–TO splittings for polar vibrations are presented in Fig. 3. The low-frequency vibrations possess the highest dipole moment. This indicates a mixed character of chemical bonds between the crystal structural units. Therefore, the spectrum of LTB crystals has regions corresponding to crystal vibrations which involve only individual structural units.

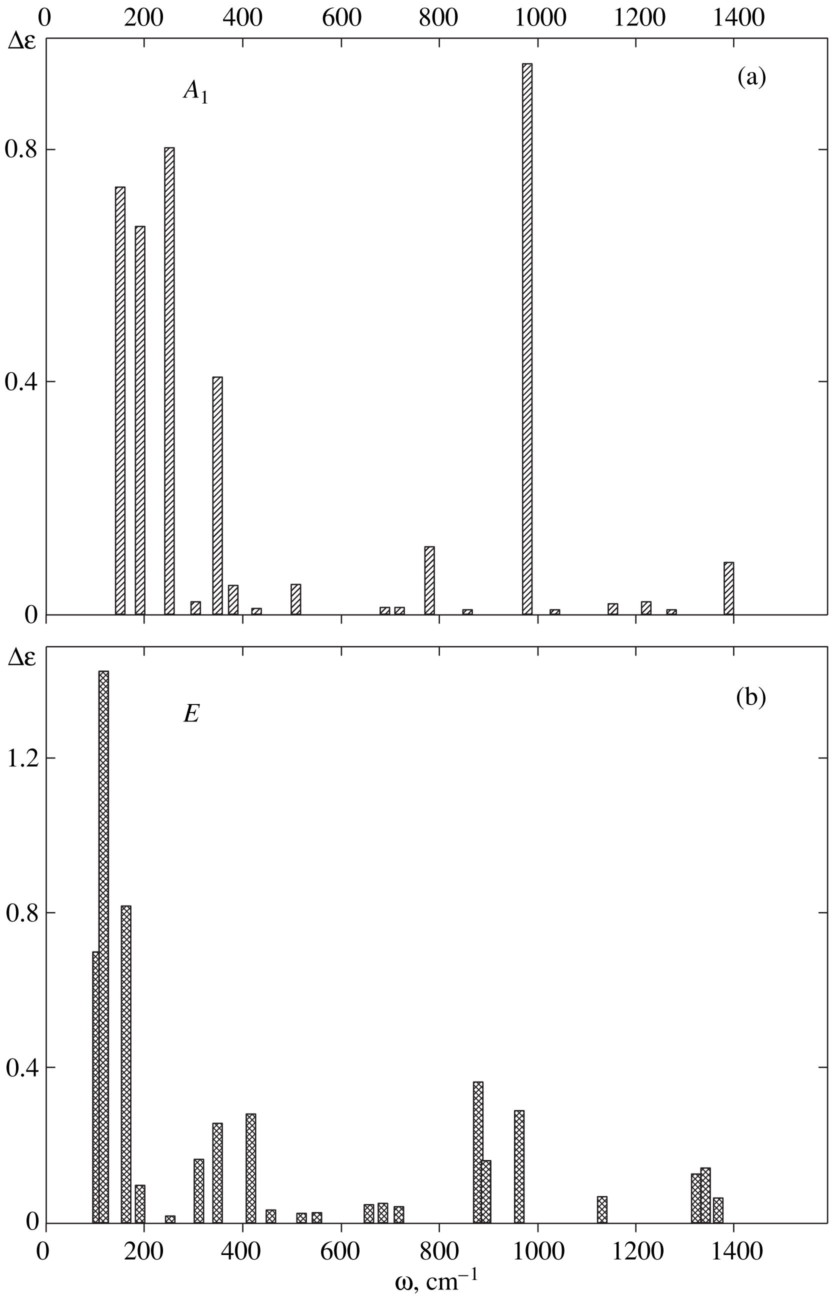

Fig. 3. Calculated values of the dielectric oscillator strengths for (a) A_1 and (b) E vibrations.

The obtained data on the longitudinal–transverse splittings also make it possible to calculate the mean values of the effective charges of the crystal structural groups [12]. The effective charges for boron and oxygen can be calculated with a high precision, taking into account the ionic character of the Li–O bonds. The results of calculations of the effective charges Ze (e is the electron charge) are shown in Table 3.

Given the effective charges, one can approximately estimate the B–O bond ionicity. Using the data from [12], we obtained the value f_i(B–O) = 0.62. A comparison of f_i(B–O) with the Al–O bond ionicity in the ionic–covalent corundum crystal, Al_2O_3 ($f_i = 0.80$), and with $f_i = 0.65$ [13] for the Ga–O covalent bonds in $LiGaO_2$ crystals indicates a strong covalent character of the B–O bonds in $Li_2B_4O_7$ crystals.

Thus, the polarized IR reflection spectra for $Li_2B_4O_7$ crystals in the range 80–1600 cm^{-1} were obtained in the present work and the parameters of all vibrations observed were determined. The obtained data are in satisfactory agreement with results of RS spectroscopy studies. The analysis of the characteristics of the

Table 3. Effective charges in an $Li_2B_4O_7$ crystal

Ion	Effective charge, $\|Z\|e$
Li	$(0.8 \pm 0.1)e$
B	$(1.23 \pm 0.05)e$
O	$(0.93 \pm 0.01)e$

observed vibrations allowed us to estimate the effective charges of the structural groups of the crystal and to determine the boron–oxygen bond type.

In contrast with ferroelectric crystals of lithium niobate and lithium tantalate, lithium tetraborate crystals do not exhibit the ferroelectric phase transition and remain pyroelectric in the whole interval of temperatures studied. This is due to the relatively high frequencies of the A_1(TO) (157 cm^{-1}) and E(TO) (107 cm^{-1}) polar lattice vibrations and to their high quality factor (Table 1). It is well known that in ferroelectric crystals, such vibrations are responsible for the crystalline lattice instability and for the dielectric anomalies in the vicinity of the Curie point.

Due to the stability of lithium tetraborate crystals in the polar phase in a wide temperature interval and their high nonlinear optical characteristics, these crystals are employed as frequency converters on the basis of harmonic generation and induced RS.

ACKNOWLEDGMENTS

This work was supported by the Russian Foundation for Basic Research, grant no. 99-02-17264.

REFERENCES

1. G. L. Paul and W. Taylor, J. Phys. C **15**, 1753 (1982).
2. V. N. Moiseenko, A. V. Vdovin, and Ya. V. Burak, Opt. Spektrosk. **81** (4), 620 (1996) [Opt. Spectrosc. **81**, 565 (1996)].
3. V. N. Moiseenko, A. V. Vdovin, V. S. Gorelik, and Ya. V. Burak, Kratk. Soobshch. Fiz., No. 2, 3 (2000).
4. Ya. V. Burak, Ya. O. Dovgiĭ, and I. V. Kityk, Zh. Prikl. Spektrosk. **52** (1), 126 (1990).
5. V. T. Adamiv, T. Ĭ. Berko, I. V. Kitik, *et al.*, Ukr. Fiz. Zh. **37** (3), 368 (1992).
6. G. N. Zhizhin, B. N. Mavrin, and V. F. Shabanov, *Optical Vibration Crystal Spectra* (Nauka, Moscow, 1984).
7. E. A. Vinogradov, G. N. Zhizhin, I. I. Khammadov, *et al.*, Fiz. Tverd. Tela (Leningrad) **24** (1), 103 (1982) [Sov. Phys. Solid State **24**, 58 (1982)].
8. F. Gervais, Opt. Commun. **22** (1), 116 (1977).
9. T. Shiosaki, M. Adachi, and A. Kawabata, in *Proceedings of the 6th IEEE International Symposium on Application of Ferroelectrics, ISAF86, 1986*, p. 455.
10. A. É. Aliev, Ya. V. Burak, and I. T. Lyseĭko, Izv. Akad. Nauk SSSR, Neorg. Mater. **26**, 1991 (1990).
11. Y. Wang, Y. J. Jiang, and L. Z. Zeng, in *Proceedings of the XIV International Conference on Raman Spectroscopy, Hong Kong, 1994*, p. 265.
12. F. Gervais, Solid State Commun. **18** (2), 191 (1976).
13. B. F. Levine, J. Chem. Phys. **59** (3), 1463 (1973).

Translated by A. Sonin

Physics of the Solid State, Vol. 43, No. 9, 2001, pp. 1655–1658. Translated from Fizika Tverdogo Tela, Vol. 43, No. 9, 2001, pp. 1590–1593.
Original Russian Text Copyright © 2001 by Egorysheva, Burkov, Gorelik, Kargin, Koltashev, Plotnichenko.

SEMICONDUCTORS AND DIELECTRICS

Raman Scattering in Monocrystal $Bi_3B_5O_{12}$

**A. V. Egorysheva, V. I. Burkov, V. S. Gorelik, Yu. F. Kargin,
V. V. Koltashev, and V. G. Plotnichenko**

Lebedev Physical Institute, Russian Academy of Sciences, Leninskiĭ pr. 53, Moscow, 117924 Russia

Received February 8, 2001

Abstract—Raman spectra of a $Bi_3B_5O_{12}$ monocrystal are investigated for the first time and compared with the Raman spectra of crystals α-Bi_2O_3 and $Bi_{12}SiO_{20}$. The most intensive lines observed in the Raman spectrum of $Bi_3B_5O_{12}$ are identified. Promising prospects of use of $Bi_3B_5O_{12}$ crystals as SRS converters of radiation are shown. *© 2001 MAIK “Nauka/Interperiodica”.*

The first $Bi_3B_5O_{12}$ monocrystals were obtained in 1983 [1] as potential luminophors with high radiation strength. Until recently, the properties of these materials were almost entirely neglected. It is well known [2] that the absorption edge of $Bi_3B_5O_{12}$ corresponds to 290 nm. At temperatures below 150 K, blue luminescence characteristic of many Bi-bearing crystals [3] is observed in these crystals. The maximum of luminescence excitation is in the range of approximately 265 nm. The unstructured band of radiation has a maximum at 460 nm, which specifies a large magnitude of the Stokes shift, approximately 17000 cm^{-1} [2]. Up to 28 overlapping broad bands can be found in the IR spectrum of $Bi_3B_5O_{12}$ in the range 300–1500 cm^{-1} at $T = 300$ K [4]. However, there has been no detailed study of the IR spectrum of this crystal. Information on the Raman scattering (RS) spectra of $Bi_3B_5O_{12}$ is also absent.

In the present work, our objective was to obtain an RS spectrum of monocrystal $Bi_3B_5O_{12}$ and to carry out group-theoretical analysis of the vibrational excitations of this crystal.

Monocrystals of $Bi_3B_5O_{12}$ were grown by the method of Czochralski. The RS spectra were studied with the help of a spectrograph *T*64000 (Raman scattering microscope), at the output of which there was a multielement receiver cooled by liquid nitrogen. The RS spectra were recorded in the range 20–1000 cm^{-1}. The spectral resolution of recorded spectra corresponded to 1 cm^{-1}. The RS spectrum was excited by an argon laser (λ = 488.0 nm, power 100 mW). A back scattering geometry with an aperture of 1 : 2 was used. The recording time of one spectrum was ~1 min. Since the wavelength of the exciting radiation was in the transmission band of the investigated crystals, there was no considerable heating of the samples. The investigation was carried out with samples split in the cleavage plane corresponding to the (001) crystallographic plane.

In Fig. 1, the RS spectrum of $Bi_3B_5O_{12}$ is represented in the range 20–1000 cm^{-1}. The spectrum contains a large number of overlapping bands. The exceptions to this are the two narrow (half-width ~1.5–2.0 cm^{-1}) lines at 66 and 147 cm^{-1}, the intensities of which are one order of magnitude greater than the intensities of most of the lines in the spectrum. The third, by intensity, line in the spectrum is observed at 683 cm^{-1} in the range corresponding to weak lines. Thirty-eight bands can be distinguished in the RS spectrum of $Bi_3B_5O_{12}$ at room temperature (Table 1). How-

Table 1. Frequency (cm^{-1}) and intensity (photons/s) of bands in the RS spectra of $Bi_3B_5O_{12}$ crystals

No.	Frequency	Intensity	No.	Frequency	Intensity
1	50.0	10	20	393.6	18
2	66.5	140	21	412.7	5
3	79.5	32	22	439.0	17
4	86.4	11	23	452.1	6
5	91.6	4	24	469.3	4
6	100.7	5	25	495.5	10
7	110.6	3	26	553.1	4
8	118.9	8	27	584.3	10
9	138.3	19	28	615.7	4
10	146.4	216	29	628.8	9
11	159.9	11	30	637.9	4
12	166.9	13	31	683.3	35
13	193.3	14	32	699.4	14
14	198.5	28	33	733.7	5
15	213.2	21	34	766.0	8
16	237.4	8	35	822.6	8
17	289.3	25	36	837.8	6
18	339.1	9	37	849.9	5
19	355.2	13	38	892.3	7

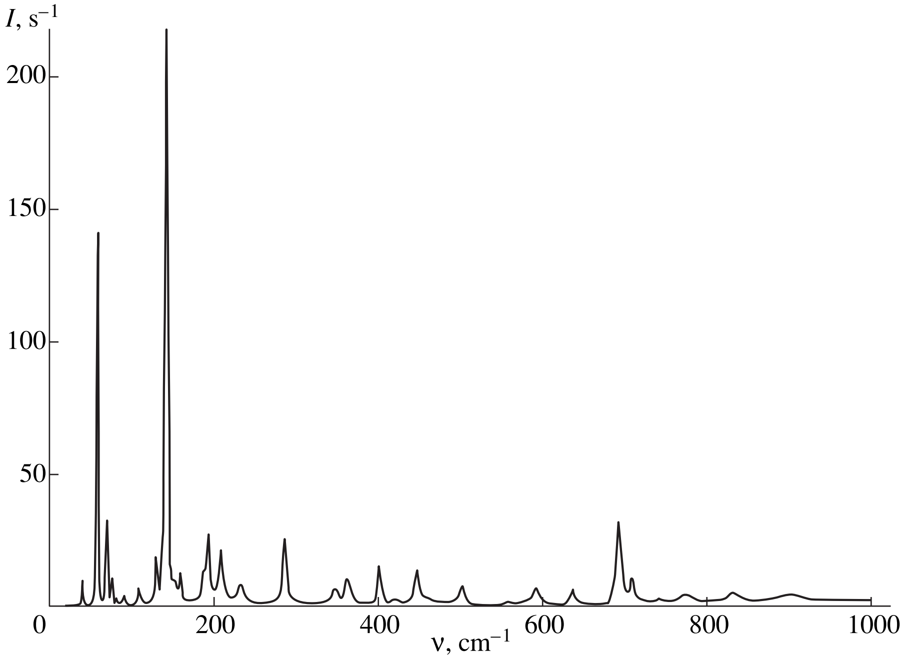

Fig. 1. Raman spectrum of monocrystal $Bi_3B_5O_{12}$.

ever, the asymmetric form of the bands testifies the presence of a much greater number of modes in the vibrational spectrum. It is necessary to note that the positions of lines in the RS (Fig. 1) and IR spectra [4] of $Bi_3B_4O_{12}$ do not coincide.

The orthorhombic unit cell of the $Bi_3B_5O_{12}$ crystal contains four formula units and belongs to the space group D_{2h}^{16}–*Pnma* [5]. Two groups of atoms can be marked out in the structure of this compound: $[OBi_3]^{7+}$ and $[B_5O_{11}]^{7-}$. The symmetry of the triangle $[OBi_3]^{7+}$ (D_{3h}) in the $Bi_3B_5O_{12}$ lattice is reduced to C_s. The complex anion $[B_5O_{11}]^{7-}$ consists of two asymmetrical rings lying in perpendicular planes and is formed by two $[B(1)O_4]$ and $[B(2)O_4]$ tetrahedra (positional symmetry C_s) and three $[BO_3]$ groups. The positional symmetry of the B(3) atom in one of the triangles is C_s; in the two other triangles, the B(4) atoms take general positions.

Table 2. Correlation between vibrations of isolated complexes and crystal vibrations

Effect of isolated-complex symmetry	Effect of positional symmetry	Effect of point symmetry of the crystal
	$[OBi_3]^{7+}$, $[B(3)O_3]^{3-}$	
D_{3h}	C_s	D_{2h}
A_1', A_2'', E', E''	A'	A_g, B_{3g}, B_{1u}, B_{2u}
A_2', E', E''	A''	B_{1g}, B_{2g}, A_u, B_{3u}
	$[B(1)O_4]^{5-}$, $[B(2)O_4]^{5-}$	
T_d	C_s	D_{2h}
A_1, E, F_1, $2F_2$	A'	A_g, B_{3g}, B_{1u}, B_{2u}
A_2, E, $2F_1$, F_2	A''	B_{1g}, B_{2g}, A_u, B_{3u}

With the help of group-theoretical analysis of the symmetry of normal vibrations with wave vector $k = 0$, one can determine the correlation between vibrations of the isolated groups that form the structure of $Bi_3B_5O_{12}$ and vibrations of the crystal (Table 2). For the triangles $[B(4)O_3]$ corresponding to general positions in the lattice of $Bi_3B_5O_{12}$, each vibration of the isolated complex $[BO_3]$ generates all eight vibrations belonging to group D_{2h}. Using irreducible representations of groups D_{3h} and T_d, it is possible to determine the distribution of vibrations over internal and external classes for the complexes $[OBi_3]^{7+}$, $[B(3)O_3]^{3-}$ and $[B(1)O_4]^{5-}$, $[B(2)O_4]^{5-}$, respectively (Table 3).

It is easy to verify that the distribution over irreducible representations of the 237 optical vibrations of the crystalline lattice of $Bi_3B_5O_{12}$ has the form

$$\Gamma_{\text{vibr}}^{\text{opt}} = (34A_g + 26B_{1g} + 26B_{2g} + 34B_{3g}) + (26A_u + 33B_{1u} + 33B_{2u} + 25B_{3u}).$$

One hundred twenty-eight of them are internal normal vibrations: 56 vibrations are libratory and 53 vibrations are translational (Table 4).

Taking into account the central symmetry of the crystal, one might expect vibrations of symmetries A_g, B_{1g}, B_{2g}, and B_{3g} (120 modes) in the RS spectrum. The vibrations A_u, B_{1u}, B_{2u}, and B_{3u} are active in the IR spec-

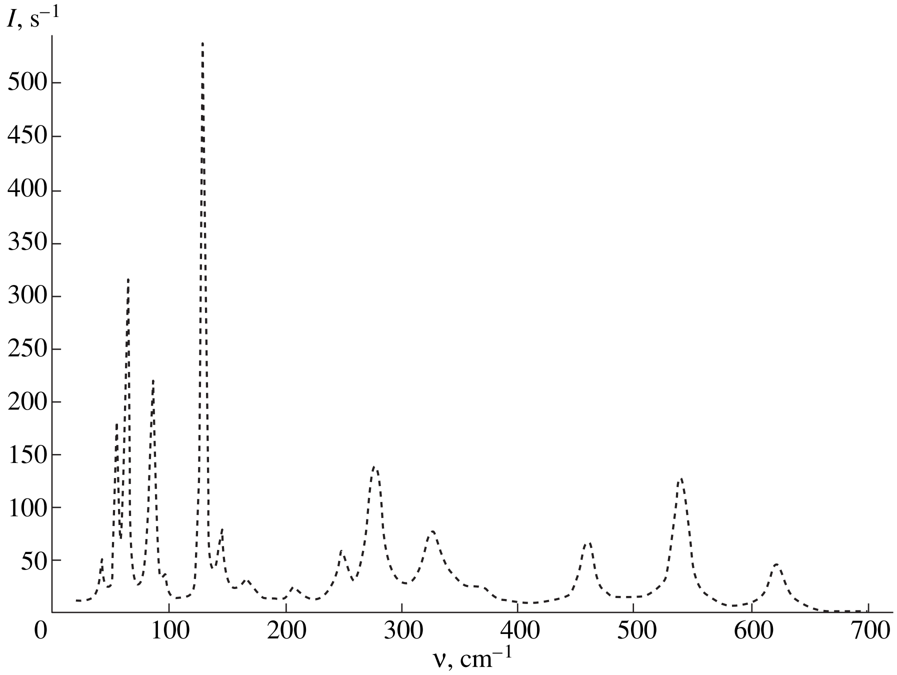

Fig. 2. Raman spectrum of monocrystal $Bi_{12}SiO_{20}$; edges of the sample correspond to crystallographic planes {100}.

trum. This explains the differences in position and intensity of lines observed in the RS (Fig. 1) and IR spectra [4]. The low symmetry of the crystalline lattice of $Bi_3B_5O_{12}$, dictating the number of optical vibrations, also determines the form of the RS spectrum, consisting of low-intensity broad bands. At room temperature, it is obviously impossible to resolve all 120 vibrational modes active in the RS spectrum.

A comparison of the RS spectrum of $Bi_3B_5O_{12}$ with the spectra of a monoclinic crystal of α-Bi_2O_3 (C_{2h}^5–$P2_1/c$) [6–8] and a cubic crystal of $Bi_{12}SiO_{20}$ (T^3–123) (Fig. 2) reveals some similarity of these spectra in the range $\nu < 150$ cm^{-1}. Among the numerous intensive lines in the spectra of α-Bi_2O_3 and $Bi_{12}SiO_{20}$, there are narrow lines, the positions of which, within several cm^{-1}, coincide with those of the lines at 66 and 147 cm^{-1} observed in the RS spectrum of $Bi_3B_5O_{12}$. As shown in [6, 7], the vibrations in the range 0–150 cm^{-1} in the RS spectrum of α-Bi_2O_3 are external vibrations for the Bi atoms. Libratory and translational vibrations of oxygen are found in the range $\nu > 150$ cm^{-1}. Internal modes of α-Bi_2O_3 are found in the range 200–600 cm^{-1} [8]. Thus, the lines at 66 and 147 cm^{-1} in the RS spectrum of $Bi_3B_5O_{12}$ can be referred to the libratory or translational vibrations of the Bi atoms, which corresponds to the interpretation of similar lines in the RS spectrum of α-Bi_2O_3 [7].

A method for interpreting RS spectra of complex bismuth–oxygen compounds based on the empirically obtained correlation between the length of the Bi–O bond, the strength of the bond, and the vibration frequency was offered in [8]. This method gives the most correct results for Bi–O bond lengths less than 2.6 Å, which corresponds to the range 200–600 cm^{-1}, i.e., in the range of frequencies of internal vibrations. This calculational method gives magnitudes of the characteristic frequencies that coincide, in a number of cases, with experimentally measured frequencies. However, there is no detailed substantiation of the given method. Making use of the structural data [5] and the empirically obtained dependence [8], we evaluated the position of lines in the RS spectrum of $Bi_3B_5O_{12}$ corresponding to

Table 3. Classification of vibrations of complexes $[OBi_3]^{7+}$, $[BO_3]^{3-}$ (D_{3h}), and $[BO_4]^{5-}$ (T_d) as internal or external

Symmetry group	Vibration		
	internal	libratory	translational
D_{3h}	$A_1' + 2E' + A_2''$	$A_2' + E''$	$E' + A_2''$
T_d	$A_1 + E + 2F_2$	F_1	F_2

Table 4. Distribution of optical vibrations of $Bi_3B_5O_{12}$ over irreducible representations

Vibrations	A_g	B_{1g}	B_{2g}	B_{3g}	A_u	B_{1u}	B_{2u}	B_{3u}
Internal	20	12	12	20	12	20	20	12
Libratory	6	8	8	6	8	6	6	8
Translational	8	6	6	8	6	7	7	5

Table 5. Results of calculations* of vibrational frequencies from the Bi–O bond lengths

Atoms	Distance, Å	Frequency, cm^{-1}	Atoms	Distance, Å	Frequency, cm^{-1}
Bi(1)–O(5)	2.12	452	Bi(1)–O(3)$_{iii}$	2.11	464
O(9)$_i$	2.23	343	O(5)$_{iii}$	2.22	352
O(9)$_{xx}$	2.23	343	O(7)$_i$	2.27	310

* Calculations on the basis of method [8].

the vibrations of short (down to 2.6 Å) Bi–O bonds (Table 5). A comparison of the calculated (Table 5) and experimental data (Table 1) shows that a good correlation is observed.

A significant contribution to the RS spectrum of $Bi_3B_5O_{12}$ comes from the vibrations of a low-symmetric polyborate anion $[B_5O_{11}]^{7-}$ consisting of two tetrahedral $[BO_4]$ and three trigonal $[BO_3]$ groups. It is well known [4] that the four normal vibrations with frequencies ν_1 ~ 800–955 cm^{-1}, ν_2 ~ 400–600 cm^{-1}, ν_3 ~ 1000 cm^{-1}, and ν_4 ~ 600 cm^{-1} correspond to the tetrahedron $[BO_4]$. The frequencies of normal vibrations of the $[BO_3]$ groups are in the ranges ν_1 ~ 950 cm^{-1}, ν_2 ~ 650–800 cm^{-1}, ν_3 ~ 1100–1300 cm^{-1}, and ν_4 ~ 500–600 cm^{-1} [4]. It was shown (Table 2) that low positional symmetry of the $[BO_4]$ and $[BO_3]$ groups in the crystalline lattice of $Bi_3B_5O_{12}$ results in splitting of these vibrations. Therefore, the vibrations of these groups in the RS spectrum (Fig. 1) in the range 450–1000 cm^{-1} are exhibited as a number of low-intensity broad bands being a superposition of various vibrations of the B–O sublattice, which are not resolved at room temperature. The most intensive bands in this spectral range at 680 and 700 cm^{-1} correspond to the symmetrical deformation vibration of the group $[BO_3]$, which is not active in the RS spectra in the case of the D_{3h} symmetry but is allowed in the case of $Bi_3B_5O_{12}$ (Table 2). The position, intensity, and form of this doublet are characteristic of the IR spectra of Bi-bearing crystals in which the B atoms are solely in trigonal surroundings: $Bi_{24}B_2O_{39}$ and $Bi_4B_2O_9$ [4, 9].

An interesting feature of the RS spectra of the $Bi_3B_5O_{12}$ crystal is the presence of two lines at 66 and 147 cm^{-1}, the intensities of which are one order of magnitude greater than the intensities of the other bands. The intensity of the line with a frequency of 147 cm^{-1} is approximately 2 times lower than the intensity of the corresponding line in the RS spectrum of a $Bi_{12}SiO_{20}$ crystal (Figs. 1, 2), which allows us to evaluate the order of magnitude of the RS efficiency of this line: $k \sim 10^7$ cm^{-1} sr^{-1} [10]. Taking into account the high transparency of the crystal in a wide spectrum range (the fundamental absorption edge ~290 nm) and the fact that the crystal belongs to the class of borates, which are of high radiation strength (>1 GW/cm^2), this crystal can be considered a rather promising material for use as a frequency converter of laser radiation on the basis of stimulated RS.

Thus, the RS spectrum of monocrystal $Bi_3B_5O_{12}$ is obtained for the first time in this work. On the basis of group-theoretical analysis, an explanation for the splitting of vibrations in the crystalline field is given. A comparison of the RS spectra of $Bi_3B_5O_{12}$ with the spectra of earlier investigated α-Bi_2O_3 and $Bi_{12}SiO_{20}$ allowed assignment of the most intensive lines in the RS spectrum of $Bi_3B_5O_{12}$. The detection of two narrow (half-width ~1.5–2.0 cm^{-1}) intensive lines (RS coefficient ~10^7 cm^{-1} sr^{-1}) in the RS spectrum of $Bi_3B_5O_{12}$ opens prospects for the realization of new SRS converters on the basis of $Bi_3B_5O_{12}$.

REFERENCES

1. J. Liebertz, Prog. Cryst. Growth Charact. **6**, 361 (1983).
2. G. Blasse, E. W. Oomen, and J. Liebertz, Phys. Status Solidi B **137**, K77 (1986).
3. C. W. M. Timmermans and G. Blasse, J. Solid State Chem. **52**, 222 (1984).
4. C. E. Weir and R. A. Schroeder, J. Res. Natl. Bur. Stand., Sect. A **68** (5), 465 (1964).
5. A. Vegas, F. H. Cano, and S. Garcia-Blanco, J. Solid State Chem. **17**, 151 (1976).
6. V. N. Denisov, A. N. Ivlev, A. S. Lipin, *et al.*, J. Phys.: Condens. Matter **9**, 4967 (1997).
7. S. N. Narang, N. D. Patel, and V. B. Kartha, J. Mol. Struct. **327**, 221 (1994).
8. F. D. Hardcastle and I. E. Wachs, J. Solid State Chem. **97**, 319 (1992).
9. Yu. F. Kargin and A. V. Egorysheva, Neorg. Mater. **34** (7), 859 (1998).
10. B. Kh. Baĭramov, B. P. Zakharchenya, R. V. Pisarev, and Z. M. Khashkhozhev, Fiz. Tverd. Tela (Leningrad) **13** (11), 3366 (1971) [Sov. Phys. Solid State **13**, 2827 (1971)].

Translated by O. Ivanov

Physics of the Solid State, Vol. 43, No. 9, 2001, pp. 1659–1664. Translated from Fizika Tverdogo Tela, Vol. 43, No. 9, 2001, pp. 1594–1599.
Original Russian Text Copyright © 2001 by Randoshkin, Vasil'eva, Vasil'ev, Plotnichenko, Lavrishchev, Saletskiĭ, Stashun, Sysoev, Churkin.

SEMICONDUCTORS AND DIELECTRICS

Liquid-Phase Epitaxy and Optical Absorption of Gadolinium–Gallium Garnet Films Grown from a PbO–B_2O_3 Solution Melt on $Gd_3Ga_5O_{12}$ Substrates

V. V. Randoshkin*, N. V. Vasil'eva, A. V. Vasil'ev***, V. G. Plotnichenko****, S. V. Lavrishchev*****, A. M. Saletskiĭ*, K. V. Stashun*, N. N. Sysoev*, and A. N. Churkin***

**Moscow State University, Moscow, 119899 Russia*
e-mail: antonv@aha.ru
***Institute of General Physics, Russian Academy of Sciences, Moscow, 119991 Russia*
****LAL Research and Production Corporation, Moscow, 125502 Russia*
*****Scientific Center for Fiber Optics, Institute of General Physics, Russian Academy of Sciences, Moscow, 119991 Russia*
******Scientific Center for Laser Materials and Technologies, Institute of General Physics, Russian Academy of Sciences, Moscow, 119991 Russia*

Received February 8, 2001

Abstract—The optical absorption due to impurity ions was studied in gadolinium–gallium garnet single crystal films with a stoichiometric composition $Gd_3Ga_5O_{12}$ grown by liquid-phase epitaxy from a supercooled PbO–B_2O_3 solution melt on (111)-oriented $Gd_3Ga_5O_{12}$ substrates. *© 2001 MAIK "Nauka/Interperiodica".*

Single crystal garnet films grown by liquid-phase epitaxy (LPE) from a supercooled solution melt are employed in high-efficiency and waveguide lasers [1]. In the former case, the mirrors are evaporated onto the film and substrate surfaces; the system is pumped from one side and the output radiation is taken from the other side. In the latter case, the mirrors are deposited onto the edge faces and a waveguide structure is created by depositing an additional epitaxial layer onto the surface of the optically active film-substrate.

Epitaxial single crystal films possess a markedly greater isomorphous capacitance as compared to the bulk single crystals with the same structure grown, for example, by the Czochralski method. In order to obtain high-quality single crystals of large diameter, it is necessary to ensure that the distribution coefficients of the garnet-forming elements are close to unity. This condition restricts the possibility of introducing some elements at a necessary concentration into growing crystals. During the synthesis of epitaxial films, the difference in the distribution coefficients of the garnet-forming elements can always be compensated by varying the charge composition. Thus, it is possible to obtain materials that can never be synthesized in the form of bulk crystals. The necessary condition of matching between the crystal lattice parameters of the film and substrate is usually readily provided for by introducing nonactive ions of appropriate size into the film composition.

Optically active single-crystal garnet films are usually grown by LPE from a supercooled PbO–B_2O_3 solution melt [1–5]. A disadvantage of this process is the appearance of solvent components (Pb^{2+} and Pb^{4+} ions) in the composition of epitaxial films. Since the epitaxial films are usually grown in platinum crucibles, Pt^{4+} may enter into the film composition as well. These impurities account for an additional optical absorption in the visible spectral range [6], which hinders creation of the film lasers. Moreover, it was found that the optical absorption spectra of the films sequentially grown under identical conditions from the same Pb-containing solution melt may significantly differ from one another [7]. The difference is manifested, in particular, by the epitaxial films having different colors [8].

In order to elucidate the possible reasons of the latter effect, we have studied the optical absorption of epitaxial single crystal $Gd_3Ga_5O_{12}$ gallium–gadolinium garnet (GGG) films grown by liquid-phase epitaxy from a supercooled PbO–B_2O_3 solution melt on (111)-oriented GGG substrates.

1. LPE FILM GROWTH

A charge used for the epitaxial film growth was characterized by the following molar ratios of components: $R_1 = Ga_2O_3/Gd_2O_3 \approx 14.4$; $R_2 = PbO/B_2O_3 \approx 16.0$; $R_3 = (Gd_2O_3 + Ga_2O_3)/(Gd_2O_3 + Ga_2O_3 + PbO + B_2O_3) \approx 0.08$. The saturation temperature of this solution was T_s = 1048°C. Prior to the LPE process, the solution melt composition was homogenized by heating in a platinum crucible for 4 h. Then, the temperature of the melt was decreased in a stepwise manner until the solution crystallization point was reached. In each

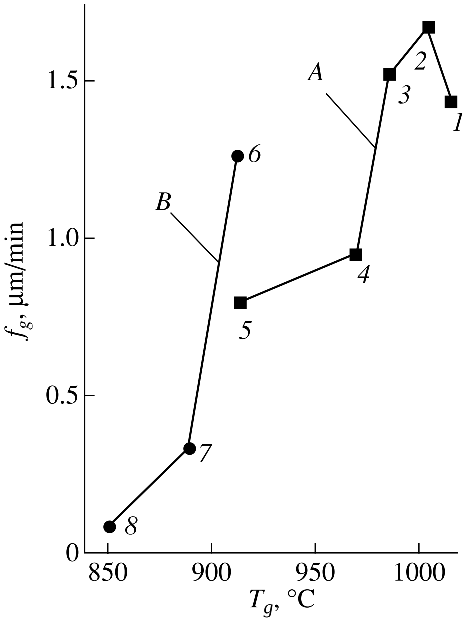

Fig. 1. Plots of the film growth rate f_g versus growth temperature T_g for colorless (curve *A*) and violet (curve *B*) epitaxial garnet films.

step, a sample film was grown by epitaxy for 10 min. We observed the epitaxial film growth in two temperature intervals. In the first (high-temperature) region at $914 \leq T < 1048$°C, which corresponds to a solution supercooling of $\Delta T \leq 134$°C, the LPE films are transparent and colorless. LPE in the second region, where $851 \leq T \leq 914$°C ($134 \leq \Delta T \leq 197$°C), yields transparent violet films (Fig. 1).

Figure 1 shows plots of the film growth rate f_g versus growth temperature T_g for colorless (curve *A*) and violet (curve *B*) films. The experimental data were obtained in the course of stepwise decrease in the growth temperature T_g (no homogenization of the solution melt was performed upon going to each next step, and only one sample film was grown at each T_g value).

It was found that, simultaneously with a decrease in the film growth rate (Fig. 1), a spontaneous crystallization takes place in the bulk of the solution melt. This leads to the appearance of GGG single crystals, having the shape of a tetragon trioctahedron with {211} faces (Fig. 2), on the melt surface and on the platinum crucible parts. It must be noted that the formation of GGG single crystals begins only upon introducing a substrate into the solution melt. The maximum linear size of single crystals reached within 3 h after the growth onset was ~100 µm.

In order to elucidate the nature of violet coloration of the epitaxial films and the laws of spontaneous crystallization, we have synthesized seven series of samples (each series containing three films) at the same solution melt temperature of $t_g = 935$°C (table). In series I and II, the film growth time was $t_g = 2$ and 30 min, respectively, with a time interval of $\Delta t_g = 10$ min between extracting the sample with grown films and immersing a new substrate. In series III–VI, the growth times were $t_g = 2$, 5, 10, and 20 min at $\Delta t_g = 60$ min. Finally, in series VII ($T_g = 10$ min; $\Delta t_g = 20$ min), the films were grown after additional treatment of the solution melt for 2 h at $T_g = 935$°C. Prior to growing each subsequent series of samples, the solution melt was homogenized.

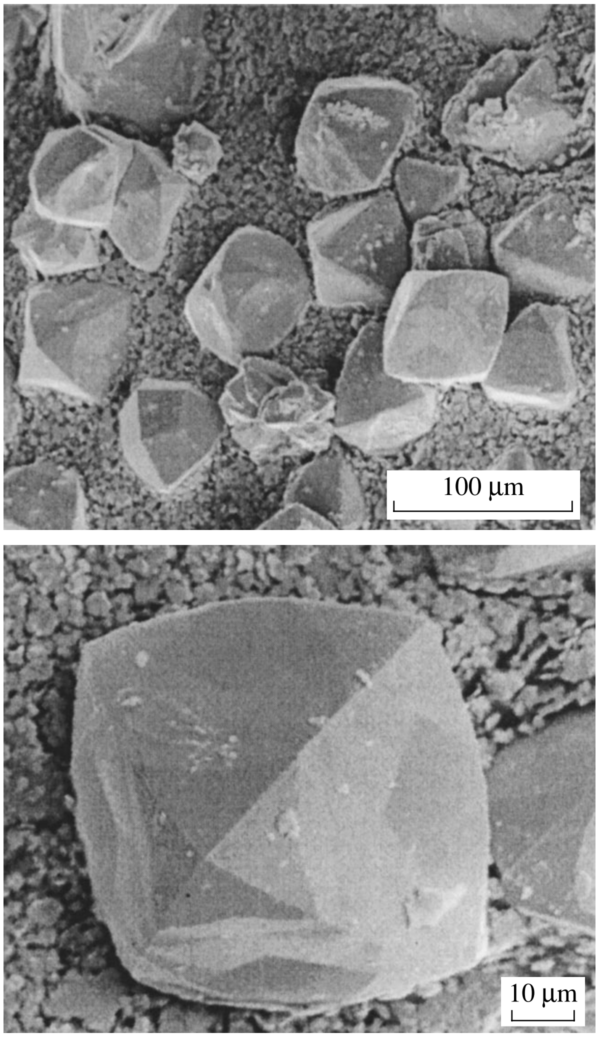

Fig. 2. Micrographs of spontaneously grown violet garnet crystals.

It was found that the first film in each series had a violet color, while the third sample was always colorless. The first spontaneously formed GGG single crystals were violet colored as well.

2. EXPERIMENTAL

The total thickness (2*h*) of epitaxial films grown on two sides of each substrate was determined from the

Parameters of epitaxial garnet films with the stoichiometric composition $Gd_3Ga_5O_{12}$

Sample no.	t_g, min	$2h$, µm	f_g, µm/min	Sample no.	t_g, min	$2h$, µm	f_g, µm/min
I-1	2	4.4	1.12	IV-2	5	4.6	0.46
I-2	2	3.1	0.78	IV-3	5	2.0	0.20
I-3	2	0.9	0.24	V-1	10	35.9	1.80
II-1	30	75.2	1.25	V-2	10	8.0	0.40
II-2	30	47.5	0.79	V-3	10	3.1	0.15
II-3	30	16.9	0.28	VI-1	20	64.9	1.62
II-4	30	11.5	0.19	VI-2	20	29.8	0.74
III-1	2	5.6	1.39	VI-3	20	9.4	0.24
III-2	2	1.5	0.37	VII-1	10	23.8	1.19
III-3	2	1.1	0.27	VII-2	10	12.1	0.61
IV-1	5	9.5	0.95	VII-3	10	3.0	0.15

difference in weights of the initial substrate and the grown epitaxial structure (film–substrate–film) [8]. The optical transmission spectra were measured on a Perkin–Elmer Lambda 900 spectrophotometer.

The absorption spectra were calculated from the results of transmission measurements using the following procedure. First, the transmission spectrum of a substrate with grown epitaxial films was divided by the transmission spectrum of the initial substrate. Second, the natural logarithm of this ratio was divided by the total thickness of the epitaxial layers grown on both sides of the substrate. The micrographs of single crystals were obtained on a CAMEBAX SX-50 microanalyzer.

3. RESULTS AND DISCUSSION

Figure 3a shows plots of the epitaxial growth rate f_g versus growth time t_g for the first, second, and third films (curves *1–3*, respectively) in series I, II, and VII. Analogous plots for series III–VI are presented in Fig. 3b. As is seen, the growth rate generally decreases (despite nonmonotonic time variation) with the film number. This is explained by a decrease in supercooling of the solution melt as a result of spontaneous crystallization, since the saturation temperature of the solution melt drops with decreasing Gd_2O_3 concentration in the growth medium.

Figure 4 shows the most characteristic transmission and absorption spectra of the initial substrate (*0*) and films (*1–3*, *5–8*) grown in the two temperature regions (the film numbering corresponds to the numbers of points in Fig. 1). As is seen, the spectra of epitaxial films *1–3* are much like that of the substrate, except for an additional absorption maximum at $\lambda = 280$ nm (35600 cm^{-1}) and a different general level of absorption. The absorption maximum at 280 nm is related to the electron transition $(6s^2) \longrightarrow {}^1S_0 \longrightarrow {}^3P_1$ in Pb^{2+} ions [9]. The absorption spectra of films *5–8* contain a broad absorption peak with a maximum at $\lambda = 550$ nm (18000 cm^{-1}) attributed to intervalence pairwise transitions in Pb^{2+} and Pb^{4+} ions ($Pb^{2+} + Pb^{4+} + h\nu \longrightarrow Pb^{3+} + Pb^{3+}$) [9]. The spectra of violet films exhibit an additional maximum at $\lambda \approx 325$ nm ($\approx$31000 cm^{-1}) assigned to the charge-transfer transition $O^{2-} + Pb^{4+} + h\nu \longrightarrow Pb^{3+} + V_0^{2-}$ (Fig. 5).

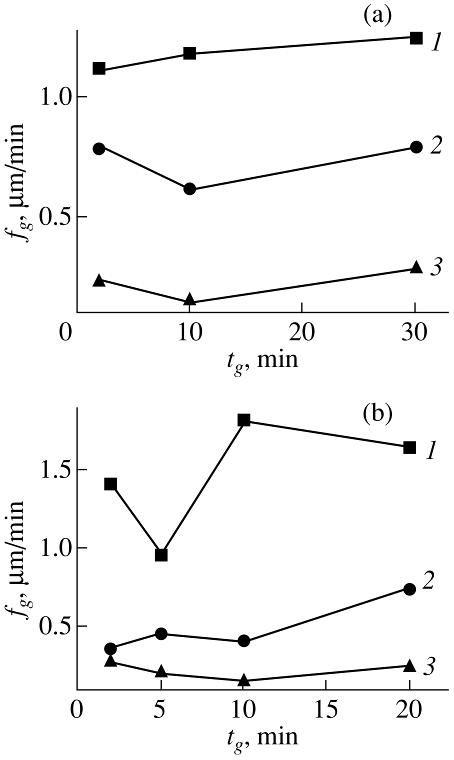

Fig. 3. Plots of the epitaxial growth rate f_g versus growth time t_g for the (*1*) first, (*2*) second, and (*3*) third films in series (a) I, II, and VII and (b) III–VI.

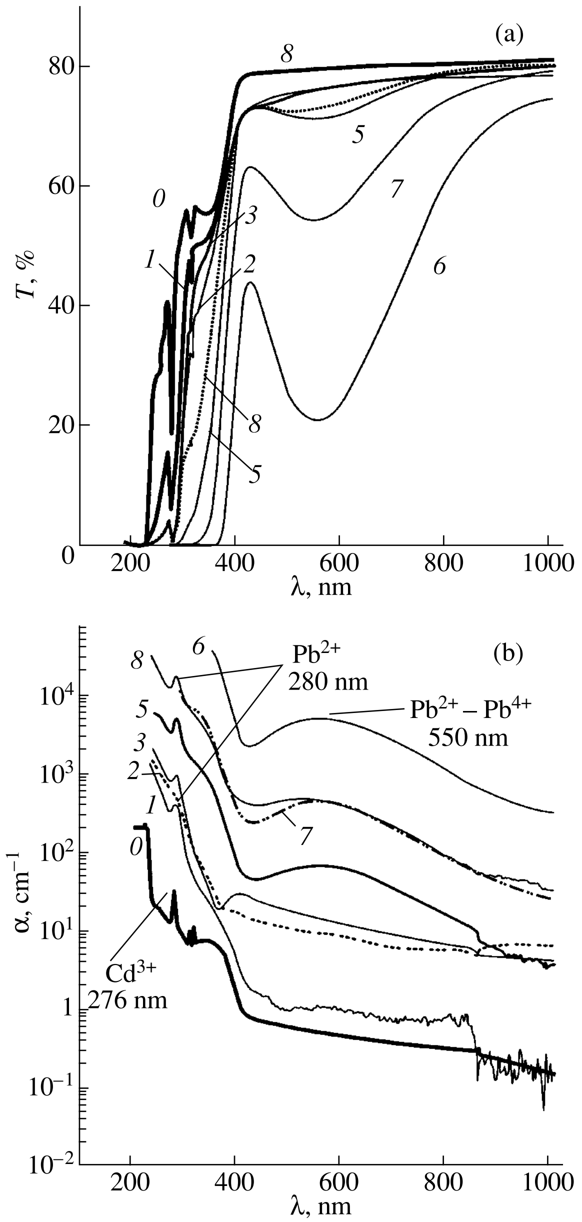

Fig. 4. Characteristic (a) transmission and (b) absorption spectra of the initial substrate (*0*) and films (*1–3*, *5–8*) (the film numbering corresponds to the numbers of points in Fig. 1).

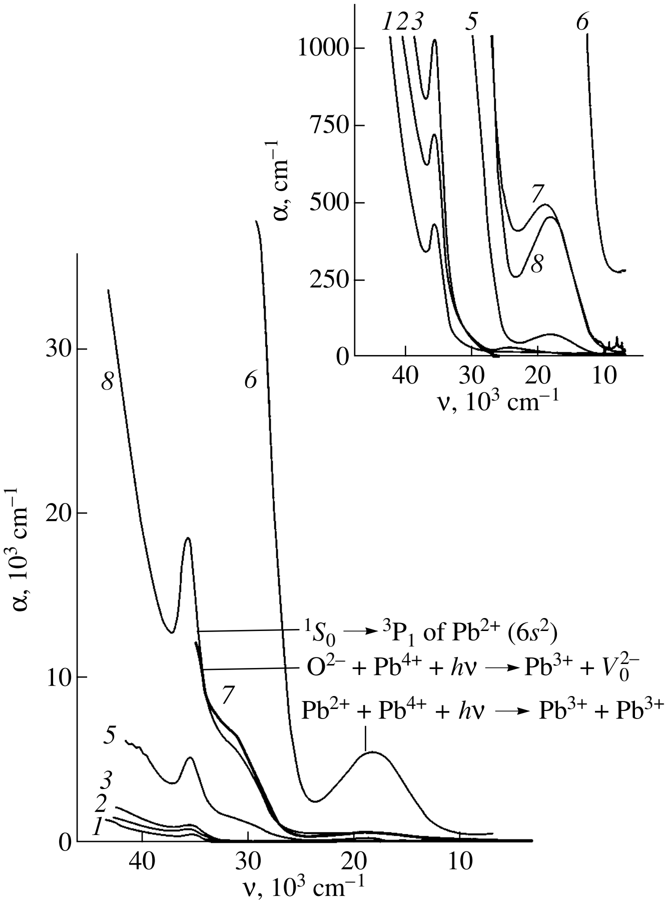

Fig. 5. The plots of absorption α versus ν for the epitaxial garnet films (*1–3*, *5–8*) grown in the two temperature regions (the film numbering corresponds to the numbers of points in Fig. 1).

Figures 6a and 6b show the optical transmission spectra of the epitaxial films grown (for t_g = 2 min) in series I and III, respectively. As expected, the first films of these series possess virtually coinciding spectra (curves *2*) with a local transmission minimum near λ = 550 nm. The spectra of the third films (curves *4*) in both series are also close to each other and to the substrate spectrum (curves *1*). The second film in series I (which is characterized by a less intense violet coloration) has a spectrum (curve *3* in Fig. 6a) occupying an intermediate position between curves *2* and *3* with a less pronounced local transmission minimum at λ = 550 nm. The transmission band edge of this sample is shifted (as compared to the first film) toward shorter wavelengths, and the spectrum displays absorption bands characteristic of the substrate. The second (colorless) film in series III has a spectrum (curve *3* in Fig. 6b) analogous to that of the third film (curve *4*).

Figure 7 shows the absorption spectra of the same samples as in Fig. 6. As is seen, the spectra of violet films (curves *2* and *3* in Fig. 7a, curve *2* in Fig. 7b) exhibit absorption peaks centered at λ = 280 nm (35600 cm^{-1}) and a broad absorption band in the wavelength range λ = 430–720 nm (22790–14000 cm^{-1}). The absorption spectra of colorless films (curve *4* in Fig. 7a, curves *3* and *4* in Fig. 7b) are similar to (albeit lying well above) the absorption spectrum of the substrate (curves *1*). These results indicate that, within a time period of about 60 min after the growth onset (i.e., at a film thickness of $2h \le 2$ μm), the solution melt features certain changes, making the incorporation of Pb^{4+} ions into the epitaxial film unfavorable.

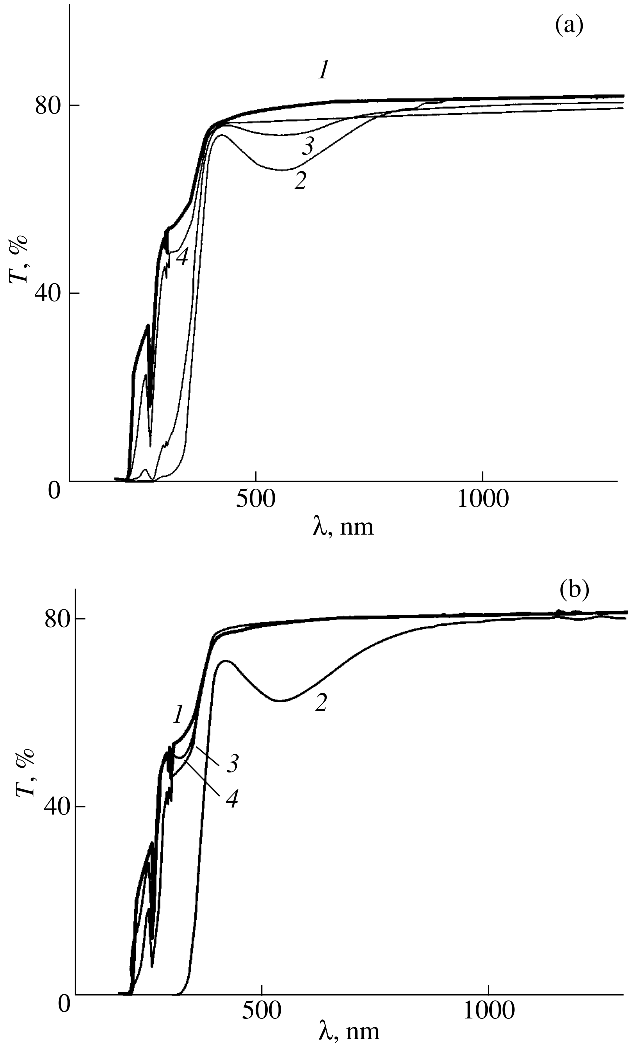

Fig. 6. The optical transmission spectra of the epitaxial garnet films grown (for t_g = 2 min) in series (a) I and (b) III.

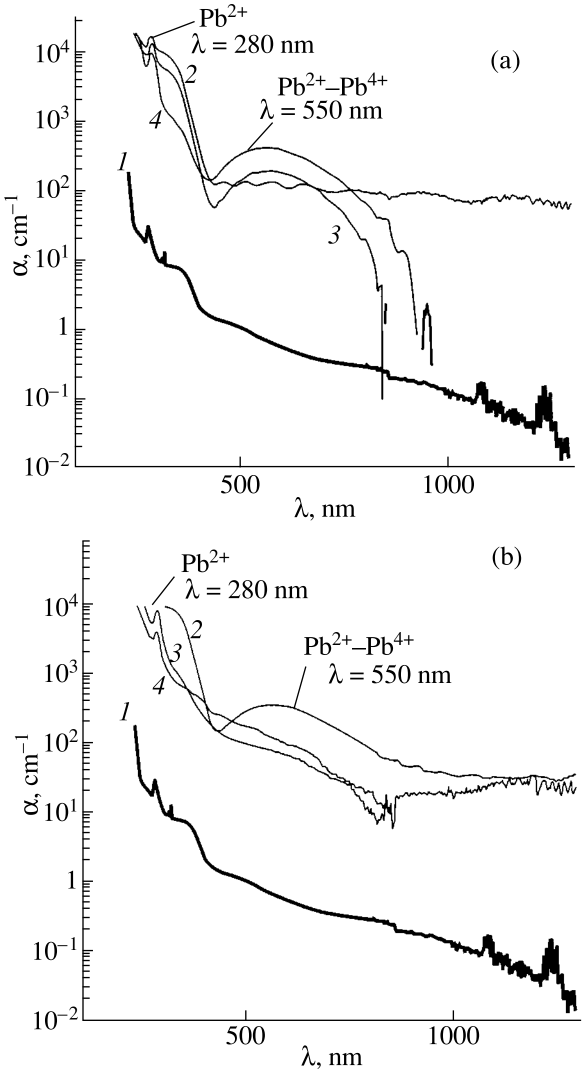

Fig. 7. The optical absorption spectra of the epitaxial garnet films grown (for t_g = 2 min) in series (a) I and (b) III.

As the solution melt occurs in a supercooled state, the system features the aforementioned strong decrease in the film growth rate f_g. As a result, the thickness h of the films sequentially grown under identical conditions differ from one series to another (table). Following [8], we explain the observed decrease in f_g by degradation of a supersaturated state of the solution melt (this phenomenon is well known for single crystal garnet ferrite films [6]).

Note that the observed decrease in f_g cannot be explained by evaporation of the solution melt, since such evaporation also takes place during the sequential growth of films in a series with small t_g = 2 min (where f_g changes from 2.23 μm/min for the first sample to 0.47 μm/min for the fourth sample). Note also that an additional absorption in films as compared to substrates is especially pronounced for thick films. The presence of additional optical absorption must be born in mind during the development of new film laser materials obtained by LPE from supercooled solution melts.

CONCLUSIONS

Thus, we demonstrated that (i) epitaxial garnet films of the stoichiometric composition $Gd_3Ga_5O_{12}$ exhibit additional optical absorption as compared to that of the GGG substrate; (ii) in films grown at a relative small supercooling ($\Delta T \le 134$°C), the additional optical absorption is due to the electron transition $^1S_0 \longrightarrow {}^3P_1$ in Pb^{2+} ($6s^2$) ions at 280 nm; (iii) in films grown at a large supercooling $134 \le \Delta T \le 197$°C, the contribution to the additional absorption is due to intervalence pairwise transitions in Pb^{2+} and Pb^{4+} ions (Pb^{2+} + Pb^{4+} +

$h\nu \longrightarrow \mathrm{Pb}^{3+} + \mathrm{Pb}^{3+}$) and charge-transfer transitions $\mathrm{O}^{2-} + \mathrm{Pb}^{4+} + h\nu \longrightarrow \mathrm{Pb}^{3+} + V_0^{2-}$ (550 and 325 nm, respectively).

ACKNOWLEDGMENTS

This study was partly supported by the Russian Foundation for Basic Research, project no. 99-02-18427.

REFERENCES

1. B. Ferrand, B. Chambaz, and M. Couchaud, Opt. Mater. **11**, 101 (1999).
2. M. V. Dmitruk, M. I. Timoshechkin, and E. O. Kirpichenkova, Izv. Akad. Nauk SSSR, Neorg. Mater. **15**, 1978 (1979).
3. P. A. Arsen’ev, Kh. S. Bagdasarov, and V. V. Fenin, *Single-Crystal Film Growth for Quantum Electronics* (Mosk. Énerg. Inst., Moscow, 1981).
4. W. Tolksdorf and C.-P. Klages, Thin Solid Films **114**, 33 (1984).
5. J. M. Robertson and M. W. van Tool, Thin Solid Films **114**, 221 (1984).
6. V. V. Randoshkin and A. Ya. Chervonenkis, *Applied Magnetooptics* (Énergoatomizdat, Moscow, 1990).
7. V. V. Randoshkin, N. V. Vasil’eva, A. M. Saletskiĭ, and N. N. Sysoev, Pis’ma Zh. Tekh. Fiz. **25** (17), 18 (1999) [Tech. Phys. Lett. **25**, 683 (1999)].
8. V. V. Randoshkin, A. M. Belovolov, M. I. Belovolov, *et al.*, Kvantovaya Élektron. (Moscow) **25** (3), 233 (1998).
9. G. B. Scott and J. L. Page, J. Appl. Phys. **48** (3), 1342 (1977).

Translated by P. Pozdeev

Physics of the Solid State, Vol. 43, No. 9, 2001, pp. 1665–1674. Translated from Fizika Tverdogo Tela, Vol. 43, No. 9, 2001, pp. 1600–1608.
Original Russian Text Copyright © 2001 by Kovalev, Usatenko, Gorbach.

SEMICONDUCTORS AND DIELECTRICS

Traveling Solitons in Modulated Elastic Media

A. S. Kovalev*, O. V. Usatenko, and A. V. Gorbach****

**Verkin Institute of Low-Temperature Physics and Engineering, National Academy of Sciences of Ukraine, Kharkov, 61164 Ukraine*

***Kharkov State University, Kharkov, 61077 Ukraine*

e-mail: univ@kharkov.ua

Received November 9, 2000; in final form, February 22, 2001

Abstract—A diatomic elastic chain with nonlinear interparticle interaction placed in a nonlinear external potential is considered. A detailed classification of possible two-parametric traveling gap- and near-gap-soliton solutions for this system is given for different relative strengths of the nonlinearities. Analytical expressions are derived for traveling near-gap solitons in the absence of an external field. *© 2001 MAIK “Nauka/Interperiodica”.*

1. INTRODUCTION

Investigations of the nonlinear dynamics of modulated media (whose parameters vary periodically with a spatial coordinate) resulted in the discovery of new types of soliton excitations. The existence of gap (Bragg) solitons was first predicted by Chen, Mills, and Trullinger [1, 2], who investigated the propagation of nonlinear waves in optical media with a modulated transmission coefficient. The frequency and wave number of these solitons lie in the gap of the linear-wave spectrum (LWS) of the system. Only the static optical gap solitons were found at first. More recently, analogous nonlinear solitons were found for other modulated media, such as crystals with a microscopic structure [3–7] and magnets with several magnetic sublattices [7]. In addition to gap solitons, another type of soliton can also exist in modulated media; they have a more complex structure and their frequency lies above or below the LWS gap. These solitons are called near-gap solitons and were first considered by Coste and Peyraud [8–10]. In [7], we gave a detailed classification of all types of static gap and near-gap solitons that can exist in nonlinear modulated optical media, diatomic anharmonic chains, and magnetic chains with two sublattices.

Traveling gap and near-gap solitons have a more complex structure. They are two-parametrical and are composed of two nonlinear waves of the same frequency, which propagate in opposite directions. As the two parameters characterizing a soliton solution, one can conveniently take the soliton velocity and the frequency of its constituent nonlinear waves. Dynamic gap solitons propagating in a modulated optical medium were analyzed by Wabnitz and Aceves [11, 12]. Later on, Gorshkov *et al.* [13] found solutions that describe traveling gap solitons in a diatomic chain with nonlinear interparticle interaction. Traveling optical near-gap solitons were considered in [14]. The possible existence of traveling three-parametric solitons in a modulated optical medium was discussed in [15].

This paper is devoted to a study of traveling elastic soliton excitations in crystals with an internal structure. The nonlinear dynamics of such systems has been investigated theoretically in many recent papers [3–7, 13, 16]. Most of these results were obtained using numerical methods within simple models (see, e.g., [17, 18]). Despite their simplicity, these models are of interest, because they allow one to understand the physical nature of complex nonlinear excitations in real crystals. These elementary excitations become strongly nonlinear when the amplitude of atomic oscillations is large. Some information on these excitations is required, in particular, in describing the thermodynamic and kinetic properties of real crystals.

It should be noted that the methods developed in this paper can also be employed to investigate the nonlinear dynamics of optical and magnetic modulated systems (see, e.g., [7, 19]). We consider a diatomic chain with two types of nonlinearity: the intrinsic nonlinearity of interparticle interaction and the extrinsic nonlinearity due to an external potential. We analyze all types of traveling gap and near-gap solitons existing in this system at different relative strengths of the intrinsic and extrinsic nonlinearities. It is shown that traveling gap and near-gap solitons of new types, not discussed in the literature, can exist in the system under study. At a certain relationship between the two competing nonlinearities, near-gap solitons can exist simultaneously above and below the gap of the LWS of the system. Some exact analytical expressions are derived for traveling near-gap solitons in a diatomic chain in the absence of an external potential.

2. STATEMENT OF THE PROBLEM AND BASIC DYNAMIC EQUATIONS

We consider a one-dimensional periodic diatomic chain of alternate atoms of masses M and m ($M > m$) whose interaction is characterized by an anharmonic potential,

$$U(\xi_n) = \frac{K_2}{2}(\xi_n - \xi_{n-1})^2 + \frac{K_4}{4}(\xi_n - \xi_{n-1})^4; \quad (1)$$

the chain is placed in an external anharmonic potential,

$$V(\xi_n) = \frac{\gamma_2}{2}\xi_n^2 + \frac{\gamma_4}{4}\xi_n^4. \quad (2)$$

Here, ξ_n is the displacement of the nth atom and K_2 and γ_2 are positive constants. The difference in the mass of atoms is assumed to be small, $(M - m) \ll m$, which implies that the LWS is narrow.

The equation of motion of the nth atom has the form

$$\mu[1 + \eta\cos(\pi n)]\frac{d^2\xi_n}{dt^2} + K_2(2\xi_n - \xi_{n-1} - \xi_{n+1}) \quad (3)$$
$$+ \gamma_2\xi_n + K_4[(\xi_n - \xi_{n-1})^3 + (\xi_n - \xi_{n+1})^3] + \gamma_4\xi_n^3 = 0,$$

where $\mu = (M + m)/2$ and $\eta = (M - m)/(M + m)$.

2.1. Analysis of Linear Waves

In order to analyze the properties of linear waves in the system indicated above, the general solution to the linearized equations (3) is represented as the sum of two fields that describe oscillations of light and heavy particles:

$$\begin{aligned} \xi_n &= F\exp(i\omega t - i\beta n), \quad n = \pm1, \pm3, \dots, \\ \xi_n &= G\exp(i\omega t - i\beta n), \quad n = 0, \pm2, \pm4, \dots, \end{aligned} \quad (4)$$

where β plays the role of a wave number. In this case, it is convenient to number particles of each type separately, that is, to label unit cells [3–7].

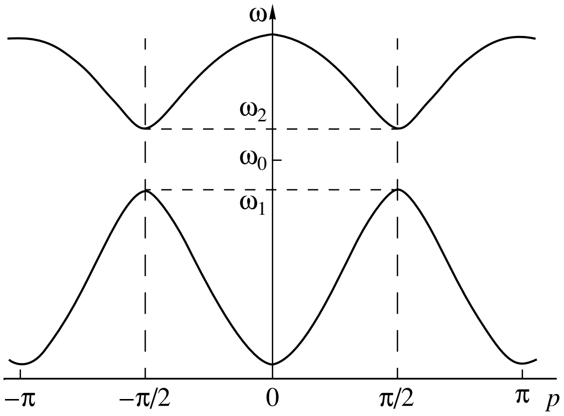

Fig. 1. Linear-wave spectrum of the set of equations (3) described by the characteristic equation (5). The vertical dashed lines are the boundaries of the first Brillouin zone.

The dispersion relation of linear waves in Eq. (4) is plotted in Fig. 1 and has the form

$$\omega^4 - (\omega_1^2 + \omega_2^2)\omega^2 + \omega_1^2\omega_2^2 - \tilde{\omega}_1^2\tilde{\omega}_2^2\cos^2(\beta a) = 0, \quad (5)$$

where $\omega_1^2 = (2K_2 + \gamma_2)/M$, $\omega_2^2 = (2K_2 + \gamma_2)/m$, $\tilde{\omega}_1^2 = 2K_2/M$, $\tilde{\omega}_2^2 = 2K_2/m$, and a is the lattice parameter (taken to be unity in what follows). At $\beta = \beta_0 = \pm\pi/2$, the LWS has a gap whose width is proportional to the mass difference ($\tilde{\omega}_2^2 - \tilde{\omega}_1^2 = (2K_2 + \gamma_2)(M - m)/Mm$) and is a small parameter.

The ratio of the oscillation amplitudes of heavy and light particles is a function of the frequency of linear waves [20]:

$$\frac{G}{F} = \mp\sqrt{\left(1 - \frac{\omega^2}{\omega_2^2}\right)\left(1 - \frac{\omega^2}{\omega_1^2}\right)^{-1}}. \quad (6)$$

Here, the upper and lower signs correspond to different ranges of the excitation spectrum, in which the frequency increases and decreases, respectively, with increasing modulus of the wave vector.

For the lower branch of the spectrum (i.e., for $\omega \le \omega_1$), the oscillation amplitude of heavy atoms G is larger than that of light atoms F. At $\omega = \omega_1$, the amplitude of light atoms becomes zero and the adjacent heavy atoms oscillate in counterphase. For the upper branch of the spectrum ($\omega \ge \omega_2$), the oscillation amplitude of light atoms is larger than that of heavy atoms; at $\omega = \omega_2$, the latter amplitude vanishes and the adjacent light atoms oscillate in counterphase. Therefore, the lower branch can conventionally be referred to as the branch of heavy particles and the upper branch as that of light particles.

In Eq. (5), the wave number β varies within the $(-\pi/2, \pi/2)$ range (bounded by the vertical dashed lines in Fig. 1), that is, within the first Brillouin zone (see, e.g., [21]).

It is more convenient, however, to represent the general solution of the linearized equations (3) in a form which is the same for heavy and light particles [13, 20]:

$$\xi_n = A\exp i(\omega t - \beta n) + B\exp i(\omega t - (\beta - \pi)n). \quad (7)$$

In this case, the general solution consists of two waves which have equal frequencies and group velocities but different amplitudes and phase velocities.

The amplitudes A and B are not independent: their ratio is determined by the wave frequency [13, 20],

$$\frac{B}{A} = \frac{\sqrt{|1 - \omega^2/\omega_2^2|} \pm \sqrt{|1 - \omega^2/\omega_1^2|}}{\sqrt{|1 - \omega^2/\omega_2^2|} \mp \sqrt{|1 - \omega^2/\omega_1^2|}}, \quad (8)$$

where the upper and lower signs correspond to those in Eq. (6), respectively.

The wave numbers of the two waves in Eq. (7) lie within the extended Brillouin zone $(-\pi, \pi)$. The first Brillouin zone is inadequate in this case, because all atoms of the chain are numbered sequentially without regard of the fact that there are two types of particles. The decrease in the unit-cell size leads to an extended Brillouin zone, which coincides with the Brillouin zone of a monatomic chain.

It is easy to verify that the amplitudes F and G in Eq. (4) are expressed through A and B as

$$\begin{aligned} G &= A + B, \\ F &= A - B. \end{aligned} \tag{9}$$

Thus, both representations are equivalent and appropriate for describing linear and nonlinear waves.

2.2. Nonlinear Excitations

The most interesting range of the spectrum of nonlinear waves is the vicinity of the $\beta_0 = \pi/2$ point, that is, the range of $\beta = \beta_0 + \kappa$ with $\kappa \ll \beta_0$, in which both branches of the LWS in Eq. (5) are described by a quadratic function.

In accordance with Eq. (7), we seek a solution to the set of nonlinear equations (3) in the form

$$\begin{aligned} \xi_n &= A_1(n, t)\exp i\left(\omega t - \frac{\pi}{2}n\right) \\ &+ A_2(n, t)\exp i\left(\omega t + \frac{\pi}{2}n\right). \end{aligned} \tag{10}$$

In the long-wavelength limit, in which $A_i(n, t)$ are slowly varying functions of the number n, one can replace the discrete atomic number n in $A_i(n, t)$ with a continuous coordinate x and use the expansion

$$(A_i(x \pm 1, t) = A_i(x, t)) \pm \frac{\partial A_i(x, t)}{\partial x} + O(\eta^2 A_i)$$

(as will be seen further on, $\partial A_i(x, t)/\partial x \sim \eta A_i$).

If the mass modulation of the chain is weak ($\eta \ll 1$), we have $\partial A_i/\partial t \ll (\omega_1 A_i, \omega_2 A_i)$ and $\partial A_i/\partial x \ll A_i$ over the LWS gap and in the vicinity of it. Therefore, when substituting Eq. (10) into Eq. (3), one can keep only the first-order derivatives $\partial A_i/\partial t$ and $\partial A_i/\partial x$ in the linear part of Eq. (3). Furthermore, since the amplitudes of atomic oscillations are small ($|K_4||A_i|^2/K_2 \ll 1$, $|\gamma_4||A_i|^2/\gamma_2 \ll 1$), one can discard all derivatives of amplitudes A_i in the nonlinear part of Eq. (3) when substituting Eq. (10). Thus, we arrive at the following set of differential equations of the first order for the amplitudes A_1 and A_2:

$$\begin{aligned} i\frac{2}{\omega_0}\frac{\partial A_1}{\partial t} + i\frac{2K_2}{2K_2+\gamma_2}\frac{\partial A_1}{\partial x} &= \frac{2\delta}{\omega_0}A_1 + \eta A_2 \\ &- \frac{3K_4}{2(2K_2+\gamma_2)}[(3p+1)|A_1|^2 A_1 \\ &+ 2(3p+1)|A_2|^2 A_1 + 3(p-1)A_2^2 A_1^*], \\ i\frac{2}{\omega_0}\frac{\partial A_2}{\partial t} - i\frac{2K_2}{2K_2+\gamma_2}\frac{\partial A_2}{\partial x} &= \frac{2\delta}{\omega_0}A_2 + \eta A_1 \\ &- \frac{3K_4}{2(2K_2+\gamma_2)}[(3p+1)|A_2|^2 A_2 \\ &+ 2(3p+1)|A_1|^2 A_2 + 3(p-1)A_1^2 A_2^*], \end{aligned} \tag{11}$$

where $\omega_0 = \sqrt{(2K_2+\gamma_2)/\mu}$ is the frequency corresponding to the midgap of the LWS, $\delta = \omega - \omega_0$ is the frequency detuning from the midgap, and $p = (1 + \gamma_4/2K_4)/3$ is a parameter characterizing the relationship between the intrinsic and extrinsic nonlinearities.

From Eq. (11), it follows that the spectrum of linear waves of the Eq. (7) type for wave numbers near $\beta_0 = \pi/2$ ($\beta = \beta_0 + \kappa$, $\kappa \ll \beta_0$) has the form

$$\omega = \omega_0 \pm \frac{\omega_0\eta}{2}\sqrt{1 + \left(\frac{2K_2\kappa}{\eta(2K_2+\gamma_2)}\right)^2}. \tag{12}$$

Introducing renormalized amplitudes $\sqrt{6|K_4|/(2K_2+\gamma_2)\eta}A_i = F_i$ and variables $(\omega_0\eta/2)t \longrightarrow t$ and $(\eta(2K_2 + \gamma_2)/2K_2)x \longrightarrow x$, we rewrite the set of equations (11) in a dimensionless form:

$$\begin{aligned} i\frac{\partial F_1}{\partial t} + i\frac{\partial F_1}{\partial x} &= \Omega F_1 + F_2 - \frac{\sigma}{4}[(3p+1)|F_1|^2 F_1 \\ &+ 2(3p+1)|F_2|^2 F_1 + 3(p-1)F_2^2 F_1^*], \\ i\frac{\partial F_2}{\partial t} - i\frac{\partial F_2}{\partial x} &= \Omega F_2 + F_1 - \frac{\sigma}{4}[(3p+1)|F_2|^2 F_2 \\ &+ 2(3p+1)|F_1|^2 F_2 + 3(p-1)F_1^2 F_2^*], \end{aligned} \tag{13}$$

where $\Omega = 2\delta/\omega_0\eta$ is the dimensionless frequency detuning from the midgap of the LWS and $\sigma = \operatorname{sgn} K_4$. In what follows, we consider only the case of rigid intrinsic nonlinearity ($\sigma = 1$); it is well known that, in nonlinear systems, there is a certain symmetry of soliton properties with respect to the change in sign of the nonlinearity (see, e.g., [22]).

We rewrite the LWS (12) in terms of the new variables in a coordinate frame moving at group velocity

$V = \partial\omega/\partial\kappa$, in which the solutions have the form $F_i \sim \exp[-i\kappa(x - Vt)]$. The result is

$$\Omega_L = \frac{2}{\eta} \pm \sqrt{1 - V^2}. \tag{14}$$

Putting $p = 1/3$ in Eq. (13), we obtain dynamic equations for the diatomic chain in the absence of an external potential [13]. In the case of $p = 1$, Eq. (13) is qualitatively similar to the dynamic equations describing the propagation of waves in a nonlinear optical medium with a modulated transmission coefficient [11, 12, 14, 15].

3. TRAVELING GAP AND NEAR-GAP SOLITONS

In order to analyze Eq. (13), we assume the coordinate and time dependence of the amplitudes F_i to have the form $F_i(x, t) = F_i(x - Vt)$ characteristic of envelope solitons moving at a velocity V. Let us introduce new real variables u_1, u_2, q, and s defined by

$$\begin{aligned} F_1 &= u_1 \exp(iq + is), \\ F_2 &= u_2 \exp(iq - is). \end{aligned} \tag{15}$$

These variables satisfy the set of differential equations

$$\begin{aligned}
\frac{\partial u_1}{\partial x} &= -\frac{u_2 \sin(2s)}{1 - V} + \frac{3}{4(1 - V)}(p - 1)u_1 u_2^2 \sin(4s), \\
\frac{\partial u_2}{\partial x} &= -\frac{u_1 \sin(2s)}{1 + V} + \frac{3}{4(1 + V)}(p - 1)u_2 u_1^2 \sin(4s), \\
\frac{\partial s}{\partial x} &= -\frac{\Omega}{1 - V^2} + \frac{3p + 1}{8}\frac{3(u_1^2 + u_2^2) + V(u_2^2 - u_1^2)}{1 - V^2} \\
&\quad - \frac{(1 - V)u_1^2 + (1 + V)u_2^2}{2u_1 u_2 (1 - V^2)}\cos(2s) \\
&\quad + \frac{3(p - 1)}{8}\frac{(1 - V)u_1^2 + (1 + V)u_2^2}{1 - V^2}\cos(4s), \\
\frac{\partial q}{\partial x} &= -\frac{V\Omega}{1 - V^2} + \frac{3p + 1}{8}\frac{(u_2^2 - u_1^2) + 3V(u_1^2 + u_2^2)}{1 - V^2} \\
&\quad + \frac{(1 - V)u_1^2 - (1 + V)u_2^2}{2u_1 u_2 (1 - V^2)}\cos(2s) \\
&\quad - \frac{3(p - 1)}{8}\frac{(1 - V)u_1^2 - (1 + V)u_2^2}{1 - V^2}\cos(4s).
\end{aligned} \tag{16}$$

From the first two equations of set (16), we find an integral of motion,

$$(1 - V)u_1^2 - (1 - V)u_2^2 = C, \tag{17}$$

which is analogous to the corresponding integral of motion for optical near-gap solitons [2, 14, 15]. The constant C characterizes the energy transfer in the nonlinear wave [2]; it determines the ratio of the two amplitudes in a wave of the Eq. (10) type and is equal to zero for gap solitons, because the field vanishes at infinity in these solitons [3–7, 13]. In near-gap solitons, the field does not tend to zero at infinity and these solitary waves have the form of so-called solitons on a pedestal; for them, the constant C can be nonzero and is another (third) parameter of the soliton. In this paper, we consider only traveling two-parametric near-gap solitons by analogy with the two-parametric gap solitons investigated in [13, 14]. A wider class of three-parametric solutions was considered in [15].

Putting $C = 0$ in Eq. (17), we obtain a relation between the fields u_1 and u_2:

$$u_2 = \sqrt{\frac{1 - V}{1 + V}}u_1. \tag{18}$$

Eliminating the variable u_2 between Eqs. (16), we arrive at effective dynamic Hamiltonian equations for u_1 and s:

$$\begin{aligned}
\frac{du_1}{dz} &= -u_1 \sin(2s) + \frac{3(p - 1)}{2}\beta(V)u_1^3 \sin(4s), \\
\frac{ds}{dz} &= -\nu - \cos(2s) + \frac{3p + 1}{2}\alpha(V)u_1^2 \\
&\quad + \frac{3(p - 1)}{2}\beta(V)u_1^2 \cos(4s),
\end{aligned} \tag{19}$$

where the variable $z = (x - Vt)/\sqrt{1 - V^2}$ plays the role of effective time, $\nu(\Omega, V) = \Omega/\sqrt{1 - V^2}$, $\alpha(V) = (3 - V^2)/2(1 + V)\sqrt{1 - V^2}$, and $\beta(V) = \sqrt{(1 - V)/(1 + V)}/2$. The Hamiltonian of this system is

$$\begin{aligned} H &= (\nu + \cos(2s))u_1^2 \\ &\quad - \frac{3p + 1}{4}\alpha u_1^4 - \frac{3(p - 1)}{4}\beta u_1^4 \cos(4s), \end{aligned} \tag{20}$$

where the variables u_1^2 and $2s$ play the roles of the canonically conjugate coordinate and the momentum, respectively.

The differential equation for variable q takes the form

$$\frac{dq}{dz} = -\nu V + \frac{(3p + 1)V}{2\sqrt{1 - V^2}(1 + V)}u_1^2. \tag{21}$$

Using the integral of motion (20), one can integrate the set of equations (19). However, it is instructive to make a qualitative analysis of this dynamic system and consider possible solutions to Eq. (19) in the (u_1, s) phase plane. Given the phase portrait of the system, one can find profiles of possible solutions of different types at given values of p and ν. Furthermore, a qualitative analysis of Eq. (19) enables one to determine the value of the integral of motion (20) that corresponds to a soliton solution.

4. QUALITATIVE ANALYSIS OF THE DYNAMIC EQUATIONS

In the general case, the phase portrait of the set of equations (19) is symmetric relative to the $u_1 = 0$ axis and periodic in variable s with a period of π. Therefore, it will suffice to consider the phase portrait of the system at hand in the region $u_1 > 0$ and $-\pi/2 \le s \le \pi/2$ (Fig. 3).

Analysis shows that, in the (u_1, s) plane, the fixed points of set (19) have the coordinates

$$\text{I. } u_1 = 0, \quad s = \pm\frac{1}{2}\arccos(-\nu);$$

$$\text{II. } u_1 = \pm\left\{\frac{2(1+\nu)(1+V)\sqrt{1-V^2}}{3p(2-V^2)+V^2}\right\}^{1/2}, \quad s = 0;$$

$$\text{III. } u_1 = \pm\left\{\frac{2(\nu-1)(1+V)\sqrt{1-V^2}}{3p(2-V^2)+V^2}\right\}^{1/2}, \quad s = \pm\frac{\pi}{2};$$

$$\text{IV. } u_1 = \pm\left\{\frac{2\nu(1+V)\sqrt{1-V^2}}{3p+3-2V^2}\right\}^{1/2},$$

$$s = \pm\frac{1}{2}\arccos\left(\frac{3p+3-2V^2}{3(p-1)\nu}\right). \qquad (22)$$

The type of fixed points and the conditions for their existence depend on the parameters p and ν. In order to investigate the evolution of the phase portrait of set (19), we conveniently consider the dependence of the position of the fixed points in the (u_1, s) phase plane on the frequency ν for a fixed value of parameter p. There are five ranges of p values in which the behavior of the system is different:

$$A.\ p > p_1 = 1,$$

$$B.\ -\frac{V^2}{3(2-V^2)} = p_2 < p < p_1,$$

$$C.\ \frac{-3+2V^2}{3} = p_3 < p < p_2, \qquad (23)$$

$$D.\ \frac{-6+5V^2}{3V^2} = p_4 < p < p_3,$$

$$E.\ p < p_4.$$

Figure 2 shows the evolution of the phase portrait of set (19) with variations in the nonlinear-excitation frequency ν and the nonlinearity parameter p. In all phase portraits presented, the abscissa is s and the ordinate is u_1 (as in Fig. 3).

In range A in Fig. 2, at frequencies $\nu < -1$, that is, below the lower branch of the LWS, there are no fixed points in the (u_1, s) phase plane and soliton solutions are absent. At such frequencies, only spatially periodic nonlinear (cnoidal) waves can occur. At $\nu = -1$, bifurcation takes place and new types of dynamic solutions to the set of equations (19) arise. In the frequency range $-1 < \nu < 1$, fixed points appear in the (u_1, s) phase plane; they are saddles at points I and centers at points II [see Eq. (22)]. The saddle points I connect two separatrices of the L type, each of which goes out of a saddle, skirts one of the center points II, and terminates at the other saddle. The phase portrait for this case is shown in Fig. 3a. Separatrices L correspond to two-parametric traveling gap solitons. The profiles of the fields u_1 and u_2 of these solitons have a typical bell shape and asymptotically approach zero at infinity ($z \longrightarrow \pm\infty$), while the phase s is changed by $\Delta_s = \arccos(-\nu)$ as the coordinate z varies from $-\infty$ to $+\infty$. For the particular case of $p = 1/3$, the soliton solutions were found analytically in [13]. At $\nu = 1$ (the upper branch of the LWS), another bifurcation occurs and, in the frequency range $1 < \nu < \nu_* = (3p + 3 - 2V^2)/3(p - 1)(1 - V^2)$, there are centers at points II and saddles at points III in the (u_1, s) phase plane (Fig. 3b). There are separatrices of two types, N and N', which correspond to two-parametric traveling near-gap solitons. The main difference between the near-gap solitons of the N and N' types and the gap solitons of type L is that the field amplitudes u_1 and u_2 do not tend to zero at infinity in the near-gap solitons (they are solitons on a pedestal) and the phase s is changed by $\Delta_s = \pi$ in them as the coordinate z varies from $-\infty$ to $+\infty$. In a soliton of the N type, the amplitude at its center is greater than at infinity, while in a type-N' soliton, on the contrary, the amplitude at its center is smaller than at infinity (dark soliton on a pedestal). Finally, at $\nu = \nu_*$, another (third) bifurcation occurs: each of the centers at points II is split into a saddle, which has the same coordinates, and two new centers at points IV. Thus, at frequencies $\nu > \nu_*$, separatrices of a new type K arise; they go out of a saddle point II, skirt one of the centers at points IV, and return to the same saddle point. In the near-gap solitons of type K, as well as in the solitons of types N and N', the limiting values of the amplitudes u_1 and u_2 at infinity are nonzero, but the overall change in the phase s with increasing coordinate z from $-\infty$ to $+\infty$ is equal to zero in near-gap solitons of type K.

At values of parameter p in range B, in the LWS gap and near the gap, the phase portraits and soliton solutions of the set of equations (19) are qualitatively similar to those in range A, but the third bifurcation, at the frequency $\nu = \tilde{\nu}_* = (3p + 3 - 2V^2)/3(1 - p)(1 - V^2) > 1$, differs from the bifurcation at $\nu = \nu_*$ in range A. Now, each of the saddle points III is split into a center with

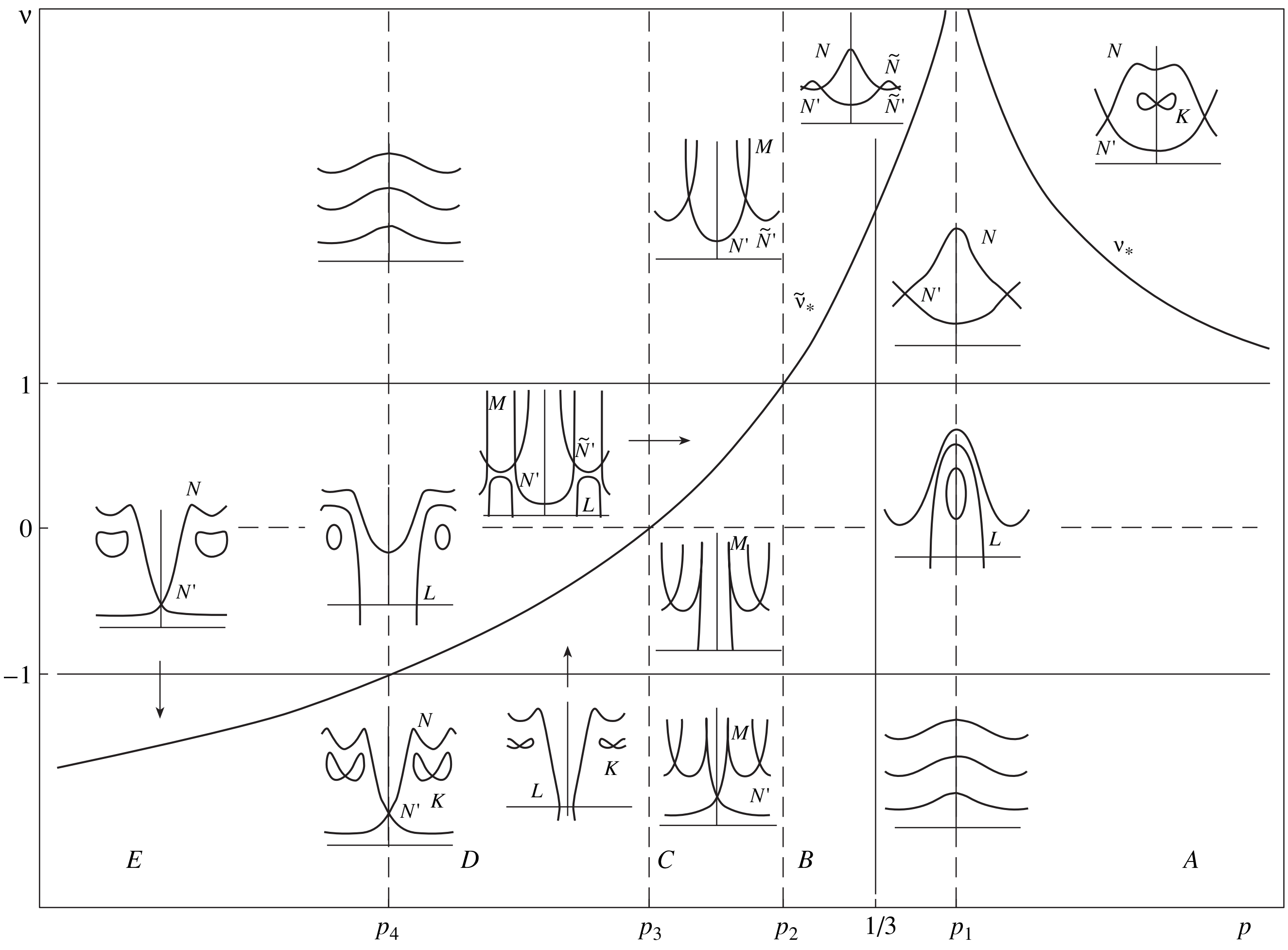

Fig. 2. Evolution of the phase portrait of set (19) with variations in the frequency ν of the nonlinear excitation and in the nonlinearity parameter p. In all phase portraits, the abscissa is s and the ordinate is u_1.

the same coordinates and two new saddle points IV. At frequencies $\nu > \tilde{\nu}_*$, there are four types of separatrices that connect the saddle points IV: N, N', $\tilde{N}$, and $\tilde{N}'$ (Fig. 3c). These separatrices correspond to two-parametric traveling near-gap solitons which are similar to near-gap solitons of type N and N' in the frequency range $1 < \nu < \tilde{\nu}_*$ described above. However, at $\nu > \tilde{\nu}_*$, as the coordinate z varies from $-\infty$ to $+\infty$, the phase s is changed by $\Delta_s = \arccos[(3p + 3 - 2V^2)/3(p-1)\nu]$ for solitons of types N and N' and by $\Delta_s = \pi - \arccos[(3p + 3 - 2V^2)/3(p-1)\nu]$ for solitons of the $\tilde{N}$ and $\tilde{N}'$ types.

The boundary point between ranges A and B corresponds to $p = 1$. At this value of p, as mentioned above, set (19) is qualitatively similar to the dynamic equations for a modulated nonlinear optical medium. In this case, only two bifurcations occur at the lower and upper branches of the LWS [14, 15].

Range B contains the point $p = 1/3$, which corresponds to the case of a diatomic chain in zero external potential. The exact soliton solutions corresponding to this case are considered separately in the next section, although this point does not stand out in the phase plane for range B.

Of special interest is range C, where the extrinsic soft nonlinearity begins to compete with the intrinsic rigid nonlinearity. At frequencies $\nu < -1$, i.e., below the lower branch of the LWS, there are fixed points II and III of the saddle type in the (u_1, s) phase plane. The saddle points II are connected by separatrices of the N' type. These separatrices correspond to two-parametric traveling near-gap solitons, which are qualitatively similar to solitons of the N' type in ranges A and B. In addition to the type-N' separatrices, there are also separatrices of the M type, which differ drastically from all separatrices considered before. The type-M separatrices leave the saddle points II and III and go to infinity ($u_1 \longrightarrow \infty$); they correspond to solutions that are physically meaningless. The first bifurcation occurs at $\nu = -1$ (the lower branch of the LWS), and in the frequency range $-1 < \nu < \tilde{\nu}_* < 1$, there are saddle points I and III in the (u_1, s) phase plane. At these frequencies, only separatrices of the M type exist and there are no soliton solutions. At $\nu = \tilde{\nu}_*$, another bifurcation occurs, with the consequence that each of the saddle points III is split into a center at point III and two saddle points IV. In addition to the type-M separatrices, separatrices of the L type arise; they connect the saddle points I. In this range, traveling gap solitons of the L type are similar to the traveling gap solitons in ranges A and B. The saddle points IV are connected to each other through separatrices of the N' and $\tilde{N}'$ types, which correspond to gap solitons similar to near-gap solitons of the N' and $\tilde{N}'$ types in range B. It should be noted that two-parametric traveling gap solitons in which the limiting values of the amplitudes u_1 and u_2 at infinity ($z \longrightarrow \pm\infty$) are nonzero appear for the first time in range C. Finally, the third (last) bifurcation occurs at $\nu = 1$ (the upper branch of the LWS). Above the LWS gap, there are saddle points IV in the (u_1, s) phase plane. At these frequencies, separatrices are of three types, N', $\tilde{N}'$ (solitons), and M (nonphysical solutions). These separatrices correspond to solutions that are similar to those associated with the analogous separatrices described above. The characteristic feature of range C is that, at these values of parameter p, the two-parametric traveling near-gap solitons exist both below and above the LWS gap. For all other possible values of parameter p, near-gap solitons can exist either strictly above the LWS gap (in ranges A and B) or strictly below this gap (in ranges D and E).

In ranges D and E, the extrinsic, soft nonlinearity is dominant. The phase portraits in these ranges are similar to those in ranges A and B, but they are shifted along the s axis by $\pi/2$. In addition, the bifurcations occur in the reverse order (i.e., as in the case of decreasing frequency ν). Above the LWS gap (at $\nu > 1$), there are no soliton solutions in ranges D and E, while below the gap (at $\nu < -1$), near-gap solitons exist. The bifurcation frequency $\tilde{\nu}_*$ lies within the LWS gap in range D and below the LWS gap in range E.

In the limit as $V \longrightarrow 0$, the boundary point between ranges B and C corresponds to $p = 0$, the boundary point between C and D is $p = -1$, and range E ceases to exist. Therefore, at $V = 0$, the evolution of the phase portrait of the set of equations (19) is the same as that considered in [7] for static gap and near-gap solitons in a diatomic chain with intrinsic and extrinsic nonlinearities. In the opposite extreme case, where the velocity V tends to its maximum absolute value, $V \longrightarrow \pm 1$, only ranges A, B, and E survive; the boundary point between ranges B and E is $p = -1/3$.

The change in sign σ of the intrinsic nonlinearity of the system does not lead to significantly new physical results. Only the consecutive order in which the bifurcations occur, as well as the regions of existence of near-gap solitons, is changed. In particular, the near-gap solitons will exist below the LWS gap in ranges A and B and above this gap in ranges D and E.

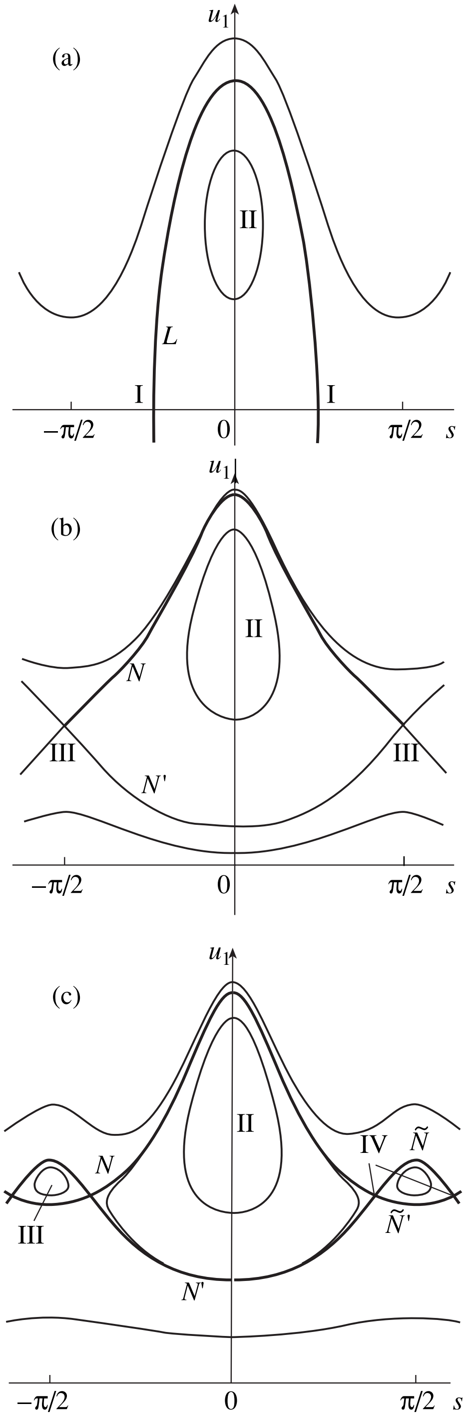

Fig. 3. Phase portraits of set (19) for different values of the parameters ν and p: (a) $-1 < \nu < 1$ and $p > 0$ (ranges A and B in Fig. 2); (b) $1 < \nu < \nu_*$ and $p > 1$ (range A in Fig. 2) and $1 < \nu < \nu_*$ and $0 < p < 1$ (range B in Fig. 2); and (c) $\tilde{\nu}_* < \nu$ and $0 < p < 1$ (range B in Fig. 2).

5. EXACT SOLITON SOLUTIONS

In order to integrate the set of equations (19), one has to introduce boundary conditions, i.e., to specify the value of the integral of motion in Eq. (20), which determines the type of solution. For this purpose, we use the results of the qualitative analysis of the set of differential equations performed above by constructing the phase portrait of the system. In particular, in order to obtain soliton solutions of different types, one should take the values of the integral in Eq. (20) that correspond to the separatrices in the phase portrait of set (19).

Analytical expressions for all types of soliton solutions of set (19) are derived using the same technique for any value of frequency ν and nonlinearity parameter p. Therefore, in this section, we consider only the particular case of a diatomic chain in the absence of an external potential ($p = 1/3$). Expressions for two-parametric dynamic gap solitons in this system were derived and analyzed in [13]. However, as shown in the preceding section, in addition to gap solitons in this system, there are also near-gap solitons of frequencies lying above the LWS gap.

In the frequency range $1 < \nu < \tilde{\nu}_* = (1 - V^2)/(1 - V^2)$ at $p = 1/3$, there are separatrices of two types, N and N', in the phase portrait of set (19) (Fig. 3b). For these separatrices, the integral of motion in Eq. (20) is equal to $H_0 = (\nu - 1)^2(1 + V)\sqrt{1-V^2}/2$. Substituting this expression into Eq. (20) and integrating the set of equations (19) yields the following expressions for the amplitude u_1 and phase s of solitons of the N and N' types:

$$u_1 = \left\{\sqrt{1-V^2}(1+V)(\nu-1)^2 \right.$$

$$\left. \times \frac{1+\gamma \sinh\zeta^2}{2(1 \pm \sqrt{\nu}\cosh\zeta) + (\nu-1)(1+\gamma\sinh\zeta)^2}\right\}^{1/2}, \quad (24)$$

$$s = \arctan(\sqrt{\gamma}\sinh\zeta),$$

where $\gamma = \nu/\{(\nu - 1)[1 - (1 - V^2)(\nu - 1)]\}$, $\zeta = 2z\sqrt{(\nu-1)[1-(1-V^2)(\nu-1)]}$, and the plus–minus sign corresponds to solitons of different types (the upper sign corresponds to solitons of the N type). From Eq. (21), the variable q is found to be

$$q = [\nu - (\nu-1)^2]Vz \pm \frac{V}{2\sqrt{\gamma(2-V^2)(1-V^2)^2}}$$

$$\times \left\{\frac{1-a_2}{\sqrt{1-a_1^2}}\arctan\left[\frac{\exp(-\zeta)+a_1}{\sqrt{1-a_1^2}}\right]\right. \quad (25)$$

$$\left. + \frac{a_1-1}{\sqrt{1-a_2^2}}\arctan\left[\frac{\exp(-\zeta)+a_2}{\sqrt{1-a_2^2}}\right]\right\},$$

where $a_n = [1 - (1 - V^2)(\nu - 1) - (-1)^n(\nu - 1) \times \sqrt{(2-V^2)(1-V^2)}]/\sqrt{\nu}$ with $n = 1, 2$.

The expression for solitons of the N and N' types can be rewritten in terms of the atomic displacements by using Eqs. (18), (15), and (10) and going over to the original variables (amplitudes, coordinate, and time) through the relations $x \longrightarrow [\eta(2K_2 + \gamma_2)/2K_2]x$, $t \longrightarrow (\eta\omega_0/2)t$, and $A_i = \sqrt{(2K_2+\gamma_2)\eta/6|K_4|}\,F_i$.

The solitons described above are localized excitations moving at a velocity V; each of them consists of two nonlinear waves of equal frequency propagating in opposite directions. The frequency and wave numbers of these nonlinear waves are related to two soliton parameters, its velocity V and the frequency of its internal oscillations Ω in a coordinate frame moving with the soliton:

$$\omega = \omega_0 + \frac{\omega_0\eta}{2}\left\{\Omega - \frac{V^2}{(1-V^2)^{3/2}}\right.$$

$$\left. \times [\Omega\sqrt{1-V^2} - (\Omega - \sqrt{1-V^2})^2]\right\}, \quad (26)$$

$$k_{1,2} = \pm\frac{\pi}{2} + \frac{\eta V}{(1-V^2)^{3/2}}$$

$$\times [(\Omega - \sqrt{1-V^2})^2 - \Omega\sqrt{1-V^2}].$$

The size of the soliton localization region is proportional to $1/\eta$, and the soliton amplitude is proportional to $\sqrt{\eta}$, where η is the small parameter introduced in Eq. (3). We note that, in a polyatomic chain, the relationship between the soliton amplitude a and the size of its localization region η is $a \sim 1/\eta$.

The amplitude of atomic displacements at the center of the soliton is

$$\xi^{(0)} = \sqrt{\frac{K_2\eta}{3K_4}}(\sqrt{\nu} \mp 1)(1-V^2)^{1/4}(\sqrt{1+V} + \sqrt{1-V}).$$

Depending on the soliton velocity V and frequency Ω, this amplitude can be both greater and smaller than the amplitude of atomic displacements at infinity:

$$\xi^{(\infty)} = \sqrt{\frac{K_2\eta}{3K_4}}\sqrt{\nu-1}(1-V^2)^{1/4}(\sqrt{1+V} + \sqrt{1-V}).$$

We also note that the phase of the nonlinear waves composing the soliton is changed by

$$\Delta = \pi \pm \frac{V}{2\sqrt{\gamma(2-V^2)(1-V^2)}} \times \left\{ \frac{1-a_2}{\sqrt{1-a_1^2}} \left[\frac{\pi}{2} - \arctan\left(\frac{a_1}{\sqrt{1-a_1^2}} \right) \right] + \frac{a_1-1}{\sqrt{1-a_2^2}} \left[\frac{\pi}{2} - \arctan\left(\frac{a_2}{\sqrt{1-a_2^2}} \right) \right] \right\} \tag{27}$$

as the coordinate $z = (x - Vt)/\sqrt{1-V^2}$ increases from $-\infty$ to $+\infty$.

At frequencies $\nu > \tilde{\nu}_*$, there are separatrices of four types, namely, N, N', $\tilde{N}$, and $\tilde{N}'$, in the phase portrait of the set of equations (19) (Fig. 3c). The traveling near-gap solitons corresponding to these separatrices are described by the expression

$$\begin{aligned} u_1^{(n)} &= \left\{ \frac{\nu_1\nu - 1}{\sqrt{1-V^2}}(1+V)\frac{\nu_1\cosh(2\zeta_1) - (-1)^n}{(\nu_1\nu - 1)\cosh(2\zeta_1) + c_n} \right\}^{1/2}, \\ s^{(n)} &= \arctan\left(\sqrt{\frac{\nu_1+1}{\nu_1-1}}\tanh^{-n}(\zeta_1) \right), \\ q^{(n)} &= -\nu_1 Vz + V\frac{(\sqrt{1/\tilde{\nu}_*} \mp \nu_1)\sqrt{\nu_1^2-1}}{(1-V^2\sqrt{(\nu_1^2-1)^2 - c_n^2}} \\ &\quad \times \arctan\left(\frac{(\nu_1\nu - 1)\exp(2\zeta_1) + c_n}{\sqrt{(\nu_1^2-1)^2 - c_n^2}} \right), \end{aligned} \tag{28}$$

where the superscript specifies the soliton solutions corresponding to separatrices N, N' ($n = 0$) and $\tilde{N}$, $\tilde{N}'$ ($n = 1$); $\nu_1 = \nu/\tilde{\nu}_*$; $\zeta_1 = z\sqrt{(\nu_1^2-1)\tilde{\nu}_*}$; and $c_n = (-1)^{n+1}\nu_1(\tilde{\nu}_* - 1) \pm (\nu_1^2 - 1)\sqrt{\tilde{\nu}_*}$ with $n = 0, 1$ (the upper sign corresponds to solitons of the N and $\tilde{N}$ types; the lower sign, to solitons of the N' and $\tilde{N}'$ types).

The frequency and wave numbers of the nonlinear waves composing these soliton excitations are given by

$$\begin{aligned} \omega &= \omega_0 + \frac{\eta\omega_0\Omega}{2-V^2}, \\ k &= \pm\frac{\pi}{2} + \frac{\eta V\Omega}{2-V^2}. \end{aligned} \tag{29}$$

The amplitudes of atomic oscillations at the center of a soliton and at infinity are

$$\begin{aligned} \xi^{(0)} &= \sqrt{\frac{K_2\eta}{3K_4}}\left\{ \frac{\nu_1\nu - 1}{\sqrt{1-V^2}} \frac{\nu_1 - (-1)^n}{\nu_1\nu - 1 + c_n} \right\}^{1/2} \\ &\quad \times (\sqrt{1+V} + \sqrt{1-V}), \\ \xi^{(\infty)} &= \sqrt{\frac{K_2\eta}{3K_4}}\frac{\sqrt{\nu_1}}{(1-V^2)^{1/4}}(\sqrt{1+V} + \sqrt{1-V}), \end{aligned}$$

respectively. The phase of the nonlinear waves composing a soliton is changed by

$$\begin{aligned} \Delta^{(n)} &= \pi n + (-1)^n 2\arctan\left(\sqrt{\frac{\nu_1+1}{\nu_1-1}} \right) \\ &\quad + V\frac{(\sqrt{1/\tilde{\nu}_*} \mp \nu_1)\sqrt{\nu_1^2-1}}{(1-V^2)\sqrt{(\nu_1^2-1)^2 - c_n^2}} \\ &\quad \times \left[1 - \arctan\left(\frac{c_n}{\sqrt{(\nu_1^2-1)^2 - c_n^2}} \right) \right] \end{aligned} \tag{30}$$

as the coordinate z increases from $-\infty$ to $+\infty$.

It should be noted that, in all cases, the degree of localization of traveling near-gap solitons is proportional to $(1 - V^2)$ and, therefore, the soliton excitations are delocalized as V tends to its maximum absolute value ($|V| \longrightarrow 1$). At the same time, the ratio of the amplitude at the soliton center to that at infinity tends to unity as $|V| \longrightarrow 1$. Therefore, traveling near-gap solitons are transformed into nonlinear waves at large velocities.

6. CONCLUSION

We considered a diatomic chain with nonlinear interparticle interaction placed in an external nonlinear potential. This is the most general model of a one-dimensional modulated nonlinear medium. In particular, at a certain relationship between the two nonlinearities, the dynamic equations (13) become similar to the dynamic equations describing the propagation of waves in a modulated nonlinear optical medium [11, 12, 14, 15]. We made a detailed classification of all types of two-parametric traveling gap and near-gap solitons in the system. Explicit analytical expressions are derived for two-parametric traveling near-gap solitons in the particular case of zero external potential. The evolution of the phase portrait of the system is investigated with variations in the frequency of the nonlinear soliton and in the relationship between intrinsic and extrinsic nonlinearities.

ACKNOWLEDGMENTS

This study was supported in part by the INTAS-99, grant no. 167, and by the MNOP, grant no. USU 082087.

REFERENCES

1. W. Chen and D. L. Mills, Phys. Rev. Lett. **58** (2), 160 (1987).
2. D. Mills and J. Trullinger, Phys. Rev. B **36** (2), 947 (1987).
3. O. Chubykalo, A. Kovalev, and O. Usatenko, Phys. Rev. B **47** (6), 3153 (1993).
4. A. S. Kovalev, K. V. Kladko, and O. V. Usatenko, J. Phys. Soc. Jpn. **64** (7), 2455 (1995).
5. O. V. Usatenko, A. S. Kovalev, and A. A. Vialov, in *Fluctuation Phenomena: Disorder and Nonlinearity*, Ed. by A. R. Bishop, S. Jimenez, and L. Vazquez (World Scientific, Singapore, 1994), pp. 286–291; O. V. Usatenko, A. S. Kovalev, and A. A. Vyalov, Fiz. Tverd. Tela (St. Petersburg) **37** (8), 2487 (1995) [Phys. Solid State **37**, 1362 (1995)].
6. O. Chubykalo and Yu. Kivshar, Phys. Rev. E **48** (5), 4128 (1993).
7. A. S. Kovalev, O. V. Usatenko, and A. V. Gorbatch, Phys. Rev. E **60** (2), 2309 (1999).
8. J. Coste and J. Peyraud, Phys. Rev. B **39** (18), 13086 (1989).
9. J. Coste and J. Peyraud, Phys. Rev. B **39** (18), 13096 (1989).
10. J. Peyraud and J. Coste, Phys. Rev. B **40** (18), 12201 (1989).
11. S. Wabnitz, Opt. Lett. **14** (19), 1071 (1989).
12. A. B. Aceves and S. Wabnitz, Phys. Lett. A **141** (1–2), 37 (1989).
13. A. S. Gorshkov, O. N. Ermakova, and V. F. Marchenko, Nonlinearity **10** (4), 1007 (1997).
14. A. S. Kovalev, O. V. Usatenko, and A. V. Gorbach, Fiz. Tverd. Tela (St. Petersburg) **42** (7), 1218 (2000) [Phys. Solid State **42**, 1253 (2000)].
15. A. S. Kovalev, O. V. Usatenko, and A. V. Gorbatch, submitted to Phys. Rev. E.
16. R. Lai and A. J. Sievers, Phys. Rep. **314** (3), 147 (1999).
17. S. A. Kiselev, S. R. Bickham, and A. J. Sievers, Phys. Rev. B **48** (18), 13508 (1993).
18. S. A. Kiselev, S. R. Bickham, and A. J. Sievers, Phys. Rev. B **50** (13), 9135 (1994).
19. C. Martijn de Sterke, Phys. Rev. E **48** (5), 4136 (1993).
20. P. S. Landa and V. F. Marchenko, Usp. Fiz. Nauk **161** (9), 201 (1991) [Sov. Phys. Usp. **34**, 830 (1991)].
21. A. M. Kosevich, *Theory of Crystal Lattice* (Khark. Univ., Kharkov, 1988).
22. A. M. Kosevich and A. S. Kovalev, *An Introduction to the Nonlinear Physical Mechanics* (Naukova Dumka, Kiev, 1989).

Translated by Yu. Epifanov

Physics of the Solid State, Vol. 43, No. 9, 2001, pp. 1675–1679. Translated from Fizika Tverdogo Tela, Vol. 43, No. 9, 2001, pp. 1609–1612.
Original Russian Text Copyright © 2001 by Gerasimov, Leushin, Falin.

SEMICONDUCTORS AND DIELECTRICS

EPR and Optical Spectroscopy of the Yb^{3+} Cubic Center in β-PbF_2

K. I. Gerasimov*, A. M. Leushin, and M. L. Falin***

**Zavoĭskiĭ Physicotechnical Institute, Kazan Scientific Center, Russian Academy of Sciences,*
Sibirskiĭ trakt 10/7, Kazan 29, 420029 Tatarstan, Russia
*** Kazan State University, ul. Lenina 18, Kazan, 420008 Tatarstan, Russia*
e-mail: falin@kfti.knc.ru

Received December 9, 2000

Abstract—Optical spectroscopy and EPR are employed to study a β-PbF_2 crystal doped with Yb^{3+} ions. The presence of only one paramagnetic center, the Yb^{3+} ion with cubic symmetry, is established. Its optical lines are identified, the empirical system of energy levels is constructed, and the phenomenological crystal field potential is determined. The information on the phonon spectrum of the β-PbF_2 crystal is obtained from the electron–vibrational structure of the optical absorption and luminescence spectra. *© 2001 MAIK “Nauka/Interperiodica”.*

1. INTRODUCTION

Lead fluoride (PbF_2) in the cubic β-phase, which is stable under ordinary conditions, has been drawing the attention of researchers. One of the simplest ionic compounds, it possesses some remarkable properties as regards technology. More specifically, β-PbF_2 is a superionic conductor with the lowest temperature of transition in the superionic state [1]. It also satisfies the largest number of criteria to become an ideal scintillation material in high-energy physics experiments [2]. In addition, all lead halogenides arouse considerable interest due to manifestations of the electron–lattice interaction in various physical phenomena [3]. Since superionic conduction and scintillation processes are essentially connected to the presence of natural defects in the PbF_2 crystal lattice, these characteristics can be varied by artificial doping of MeF_2 crystals with rare-earth ions (REI). The introduction of REI, for example, considerably lowered the superionic transition temperature of CaF_2, BaF_2, and $SrCl_2$ crystals [4], while the introduction of Cd ions into the PbF_2 lattice has made it possible to design a scintillation detector with a high energy resolution and a high counting rate, which can successfully operate at room temperature [5].

In spite of the fact that a considerable number of experimental and theoretical works have been devoted to the study of PbF_2, the chemistry of defect formation in it is not completely clear. It is normally assumed that the defect structure in PbF_2 is the same as in other fluorides of the fluorite type. However, the actual situation is quite different. For example, the introduction of Yb^{3+} ions into SrF_2 and BaF_2 crystals, whose lattice constants a_0 are closest to that of PbF_2 (a_0 = 5.80, 5.93, and 6.20 Å for SrF_2, PbF_2, and BaF_2 [6], respectively), leads to the formation of paramagnetic centers (PCs) with cubic and trigonal symmetries, while only PCs with cubic symmetry are observed in PbF_2 crystals [7] (the observation of trigonal PCs is reported only in one publication [8]).

Such a small number of rare-earth centers in PbF_2 crystals makes them very attractive for studying complexes of rare-earth defects in all fluorite structural-type crystals. Optical investigation of REI in these crystals is complicated by the presence of many PCs in them due to different mechanisms of excess-charge compensation, conditions of crystal growth, and methods of sample processing. The identification of the optical spectra of low-symmetry centers is especially difficult in view of the averaging effect over various orientations. The available data mainly correspond to fluorite itself (CaF_2). However, even cubic PCs of the Yb^{3+} ion, which are formed due to nonlocal compensation of the excess charge and have the simplest structure, are studied insufficiently in spite of the fact that the first results on these centers were reported by Feofilov [9] as early as in 1958. From the large number of contradictory publications devoted to CaF_2, the most comprehensive information is contained in [10, 11], where the energy levels of the cubic center are determined from the optical absorption and luminescence spectra and the parameters of the crystal field are established. However, the upper Stark level of the ground multiplet $^2F_{7/2}$ remains experimentally undetermined.

In the present work, we report the results of our study of cubic-symmetry PCs of the Yb^{3+} ion in a β-PbF_2 crystal by EPR and optical spectroscopy methods. This enabled us to completely determine the empirical Stark structure of the ground and excited multiplets and to determine the crystal field potential. The information obtained can be subsequently used to interpret the spectra of other PCs of the Yb^{3+} ion, as well as cubic PCs of other REI in fluorite-type crystals, which can help to solve the problem of defect formation in them.

2. EXPERIMENTAL RESULTS

Crystals of $PbF_2 : Yb$ were grown by the Bridgman–Stockbarger method in graphite crucibles in a fluorine atmosphere. The EPR measurements were made on a 3-cm spectrometer at $T = 4.2$ K. The optical spectra were recorded at $T = 2$ and 300 K on a multipurpose optical spectrometer [12].

Using the EPR spectra, it was found that PbF_2 crystals with various Yb^{3+} concentrations contain only one cubic PC of Yb^{3+} with $g = 3.434$. The value of the g-factor indicates that the doublet Γ_7 is the lower level of the ground multiplet. Experimental optical absorption and luminescence spectra of $PbF_2 : Yb^{3+}$ crystals recorded at various temperatures are presented in Fig. 1. It can be seen that the number of observed lines exceeds the number of electron transitions predicted for a cubic PC from symmetry considerations. This is due to the fact that the optical spectra of PCs of the Yb^{3+} ion are always of the clearly manifested electron–vibrational type, some of the lines being phonon satellites of purely electronic transitions. The narrow line observed at 2 K at a frequency of 10 344 cm^{-1} in the absorption and luminescence spectra apparently corresponds to the ${}^1\Gamma_7 \longleftrightarrow {}^2\Gamma_7$ transition between the lower Stark levels of the excited and ground multiplets and the luminescence level being doublet Γ_7, as in a CaF_2 crystal [10, 11]. In the luminescence spectrum recorded at 300 K (Fig. 1c), this line is slightly shifted to the long-wavelength region due to thermal expansion of the crystal. In addition, it also acquires anti-Stokes components along with Stokes vibrational satellites observed at 2 K. The frequencies of the anti-Stokes components exactly

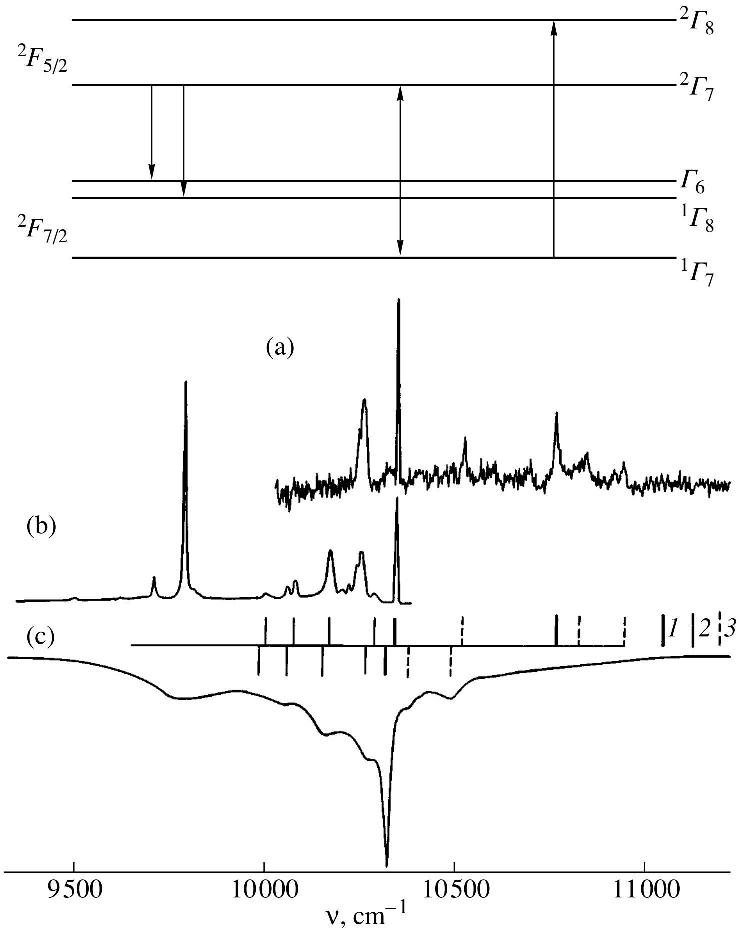

Fig. 1. (a) Absorption and (b, c) luminescence spectra of Yb^{3+} ions in a PbF_2 crystal at temperatures of (a, b) 2 and (c) 300 K. The upper diagram describes the energy levels of a cubic center of the Yb^{3+} ion; arrows mark the transitions corresponding to the experimental spectral lines; the middle diagram shows (*1*) the electron lines, (*2*) electron–phonon Stokes components corresponding to them, and (*3*) electron–phonon anti-Stokes components.

coincide with the frequencies of phonon replicas of the electron line observed in the absorption spectrum at $T = 2$ K (Fig. 1a) and corresponding to the $^1\Gamma_7 \longrightarrow {}^2\Gamma_8$ transition. The phonon frequencies appearing in the observed electron–vibrational absorption and luminescence spectra are presented in Table 1.

The most intense line at 9786 cm^{-1} in the low-temperature luminescence spectrum (Fig. 1b) exhibits the same concentration dependence as the resonance line discussed above. It is characterized by the same luminescence decay time as the latter line and can be attributed to the transition from the same $^2\Gamma_7$ level to the first excited level of the ground multiplet, which is apparently the $^2\Gamma_8$ quartet. The assumption that this level is the Γ_6 doublet was in all probability incorrect, because the $^2\Gamma_7 \longrightarrow \Gamma_6$ transition line must have a low intensity since it is forbidden altogether by the selection rules in view of the magnetic-dipole nature of the transitions. In the given case, however, the electric dipole transition between the levels of a cubic center with the symmetry of group O_h is also impossible due to the absence of odd-parity terms in the crystal field potential; this admix excited even-parity configuration states to the functions of odd-parity $4f^{13}$ ground-state configuration. Its emergence can be due to the electric dipole transition that occurs due to small distortions (caused by lattice vibrations) in the central symmetry of the center under investigation that have odd parity relative to inversion [13]. In addition, according to our theoretical calculations, the assumption that the Stark levels in the ground multiplet $^2F_{7/2}$ are arranged in increasing order of energy as Γ_7, Γ_6, Γ_8 leads to an inadequate description of the experimental spectra in the framework of the crystal-field theory. In this connection, the transition $^2\Gamma_7 \longrightarrow \Gamma_6$ should correspond to a weak line observed at 9704 cm^{-1} in the luminescence spectrum at the liquid helium temperature (Fig. 1b). The increase in its relative intensity compared to a similar line which was not observed in the CaF_2 crystal [11] is probably associated with the enhancement of the electron–lattice interaction in the PbF_2 crystal.

Table 1. Phonon frequencies appearing in the absorption and luminescence spectra of the cubic center of the Yb^{3+} ion in β-PbF_2

Temperature, K	Electron transitions	Phonon frequencies, cm^{-1}	Satellites
2	$^1\Gamma_7 \longrightarrow {}^2\Gamma_8$	77; 177	Anti-Stokes
	$^2\Gamma_7 \longrightarrow {}^1\Gamma_7$	55; 175; 267; 342	Stokes
	$^1\Gamma_7 \longrightarrow {}^2\Gamma_7$	175	Anti-Stokes
300	$^2\Gamma_7 \longrightarrow {}^1\Gamma_7$	46; 161; 268; 336	Stokes
		47; 166	Anti-Stokes

Table 2. Energy levels (cm^{-1}) and g-factor of the cubic center of the Yb^{3+} ion in β-PbF_2 (the data for CaF_2 are given for comparison)

J	Symmetry and g-factor of energy levels	Experiment	Theory	CaF_2
5/2	$^2\Gamma_8$	10766	10765	10845* [11]
	$^2\Gamma_7$	10344	10334	10390* [11]
	Γ_6	640	633	684 [16]
7/2	$^1\Gamma_8$	558	554	647* [11]
	$^1\Gamma_7$	0	0	0
	$g(^1\Gamma_7)$	$\lvert 3.434 \rvert$	3.476	$\lvert 3.438 \rvert$* [17]

* Experimental values.

3. THEORY AND DISCUSSION OF RESULTS

The electron ground-state configuration $4f^{13}$ of the Yb^{3+} ion, which is equivalent to a single $4f$ hole in the unfilled shell, has a single ^2F term split on account of the spin–orbit interaction into two multiplets, $^2F_{5/2}$ and $^2F_{7/2}$ (the latter being the ground multiplet), separated by an interval approximately equal to 10000 cm^{-1}. In a cubic crystal field, the upper multiplet splits into two (Γ_7 and Γ_8), while the lower multiplet splits into three (Γ_7, Γ_8, and Γ_6), energy levels. In order to explain the position of these levels determined from the experimental optical spectra and EPR data, we diagonalized the matrix of the Hamiltonian

$$H = -\xi(\mathbf{SL}) + B_4(V_4^0 + 5V_4^4) + B_6(V_6^0 - 21V_6^4) \qquad (1)$$

and calculated the theoretical energy levels and wave functions. In this expression, ξ is the spin–orbit interaction parameter; **S** and **L** are the operators of the spin and orbital angular momenta of the Yb^{3+} ions, respectively; B_4 and B_6 are the crystal field parameters; and V_k^q are the standard harmonic polynomials [14]. The wave functions of the ground-state Kramers doublet $^1\Gamma_7$ were subsequently used to calculate the g-factor of the spin Hamiltonian $g\beta\mathbf{H}\mathbf{S}'$, where **H** is the magnetic field and **S**' is the effective $S' = 1/2$ spin operator. Furthermore, the five theoretical quantities (four energy differences and the g-factor) were compared with the corresponding experimental values according to the procedure described in [15] in order to find the best parameters of the crystal field and spin–orbit interaction.

The results of our analysis are presented in Tables 2 and 3. It can be seen from Table 2 that the energy levels are described satisfactorily (the standard deviation σ

Table 3. Parameters of crystal field and spin–orbit interaction (in cm^{-1}) for a cubic center of the Yb^{3+} ion in *Me*F$_2$

Crystal	ξ	B_4	B_6
β-PbF$_2$	2907	–196	24
CaF$_2$ [11]	2909	–213	34

does not exceed 6 cm^{-1}) and the difference $\Delta g = g^t - g^e = 0.042$ between the theoretical g factor and its experimental value proved to be considerably larger than the experimental value. The value of the spin–orbit interaction constant ξ presented in Table 3 has a typical value for the Yb^{3+} ion in compounds for which fluorine ions are its ligands [18] and the crystal field parameters in a β-PbF$_2$ crystal are similar to those for a CaF$_2$ crystal [10, 11] and follow the general tendency to decrease with an increase in the lattice constant a_0.

The large value of Δg can be explained by taking into account the deviation from the purely ionic nature of the bond between the Yb^{3+} ion and the surrounding F$^-$ ions (assuming the existence of a small degree of covalence), which leads to a reduction of the orbital angular momentum. However, the difference Δg is not so large (0.033 [17]) for a CaF$_2$ crystal with a higher density, in which the covalence effects of the Yb^{3+}–F$^-$ bond must be stronger. It should also be kept in mind that the role of the orbital angular momentum in the Zeeman interaction Hamiltonian $H_z = \beta\mathbf{H}(\mathbf{L} + g_s\mathbf{S})$ can be reduced not only by the covalent nature of the chemical bond but also by the orbit–lattice interaction effects discussed in [19]. If, following Axe and Burns [20], we introduce two factors of orbital-momentum reduction (the factor k of orbital angular momentum reduction due to covalence effects and factor k^* of the orbital angular momentum reduction due to the orbit–lattice interaction) into our analysis, we can obtain the following expression for the theoretical value g^t of the g factor [6]:

$$\begin{aligned} g^t &= 3g_{7/2} + \frac{16\alpha}{7\sqrt{3}} - \frac{34\alpha^2}{7} \\ &- (1-k)\left(\frac{16}{7} - \frac{8\alpha}{7\sqrt{3}} - \frac{32\alpha^2}{7}\right) \\ &- (1-k^*)\left(\frac{2}{7} - \frac{8\alpha}{7\sqrt{3}} + \frac{2\alpha^2}{21}\right). \end{aligned} \tag{2}$$

Here, $g_{7/2}$ is the Landé g-factor of the ground multiplet and α is the coefficient of the admixture of the state $|^2F_{5/2}\Gamma_7\rangle$ of the upper multiplet to the states $|^2F_{7/2}\Gamma_7\rangle$ of the lower multiplet in the wave function of the ground-state Kramers doublet $|^1\Gamma_7\rangle$. Rewriting the functions $|^1\Gamma_7\rangle$

$$\begin{aligned} |^1\Gamma_7 \pm 1/2\rangle &= \pm 0.86528|^2F_{7/2} \pm 5/2\rangle \\ &\mp 0.49957|^2F_{7/2} \mp 3/2\rangle - 0.03779|^2F_{5/2} \mp 3/2\rangle \\ &+ 0.01689|^2F_{5/2} \pm 5/2\rangle, \end{aligned} \tag{3}$$

obtained by us in the form [21]

$$\begin{aligned} |^1\Gamma_7 \pm 1/2\rangle &= \pm\sqrt{\frac{3}{4}}|^2F_{7/2} \pm 5/2\rangle \mp \sqrt{\frac{1}{4}}|^2F_{7/2} \mp 3/2\rangle \\ &+ \alpha\left\{-\sqrt{\frac{5}{6}}|^2F_{5/2} \mp 3/2\rangle + \sqrt{\frac{1}{6}}|^2F_{5/2} \pm 5/2\rangle\right\}, \end{aligned} \tag{4}$$

we find the value of the admixture coefficient $\alpha = 0.04143$. The reduction factor k for a β-PbF$_2$ crystal can be estimated by assuming that it is proportional to the parameter of the isotropic component of the superhyperfine interaction (A_s) of REI with fluorine ions from the nearest neighbors, which characterizes the degree of covalence of the Yb^{3+}–F$^-$ bond. Using the values of A_s measured in the electron–nuclear double resonance (ENDOR) experiments [22, 23] and $(1 - k) = 0.016$ in CaF$_2$ [17], we find that $(1 - k) = 0.013$ for β-PbF$_2$. Substituting this value, the calculated value of α, and the Landé g-factor $g_{7/2} = 1.1412$ into Eq. (2), one can verify that approximately 0.013 of the deviation Δg in β-PbF$_2$ is due to the orbit–lattice interaction. For the corresponding reduction factor k^*, we obtain the value 0.950 $(1 - k^* = 0.050)$. The results of this analysis suggest that the orbital angular momentum in a PbF$_2$ crystal is suppressed by the orbit–lattice interaction more strongly than by covalence effects.

Thus, if the above considerations are correct, we may conclude that the orbit–lattice interaction plays an important role in interpreting the optical spectra and the g-factor of the Yb^{3+} ion in β-PbF$_2$.

It should also be noted that the phonon frequencies presented in Table 1 and in our experimental spectra agree well with the phonon density distribution function for the PbF$_2$ crystal calculated in [24].

ACKNOWLEDGMENTS

This work was supported by the Russian Foundation for Basic Research (project no. 99-02-17481) and the NIOKR RT Foundation (project no. 14-14/99).

REFERENCES

1. W. Schroter and J. Notting, J. Phys. Colloq. **41**, 20 (1980).
2. S. E. Derenzo, W. W. Moses, J. L. Cahoon, *et al.*, IEEE Trans. Nucl. Sci. **37**, 203 (1990).

3. V. Fujita, M. Itoh, H. Nakagawa, *et al.*, J. Phys. Soc. Jpn. **67** (9), 3320 (1998).
4. C. R. A. Catlov, J. D. Comins, F. A. Germano, *et al.*, Phys. Lett. A **71A** (1), 97 (1979); C. R. A. Catlov, J. D. Comins, F. A. Germano, *et al.*, J. Phys. C **14** (4), 329 (1981).
5. D. Z. Shen, G. H. Ren, Q. Deng, and Z. W. Yin, Sci. Sin. **28**, 46 (1998).
6. J. M. Baker, J. Phys. C **1** (6), 1670 (1968).
7. J. M. Baker, in *Crystal with Fluorine Structure*, Ed. by W. Hayes (Clarendon, Oxford, 1974), p. 341.
8. A. A. Antipin and I. N. Kurkin, Fiz. Tverd. Tela (Leningrad) **10** (4), 1248 (1968) [Sov. Phys. Solid State **10**, 994 (1968)].
9. P. P. Feofilov, Opt. Spektrosk. **5** (2), 216 (1958).
10. W. Low, Phys. Lett. A **26A** (6), 234 (1968); Yu. K. Voron'ko, V. V. Osiko, and I. A. Shcherbakov, Zh. Éksp. Teor. Fiz. **56** (1), 151 (1969) [Sov. Phys. JETP **29**, 86 (1969)].
11. D. Kiro and W. Low, in *Magnetic Resonance*, Ed. by C. K. Coogan, N. S. Ham, S. N. Stuart, J. R. Pilbrow, and G. V. H. Wilson (Plenum, New York, 1970), p. 247.
12. M. L. Falin, K. I. Gerasimov, B. N. Kazakov, and M. A. Yakshin, Appl. Magn. Reson. **17** (1), 103 (1999).
13. B. R. Judd, Phys. Rev. **127** (3), 750 (1962).
14. K. W. H. Stevens, Proc. Phys. Soc. London, Sect. A **65**, 209 (1952).
15. V. F. Bespalov, B. N. Kazakov, A. M. Leushin, and G. M. Safiullin, Fiz. Tverd. Tela (St. Petersburg) **39** (6), 1030 (1997) [Phys. Solid State **39**, 925 (1997)].
16. J. M. Baker and E. R. Davies, J. Phys. C **8** (12), 1869 (1975).
17. J. M. Baker, W. B. Blake, and G. M. Copland, Proc. R. Soc. London, Ser. A **309** (1496), 119 (1969).
18. V. F. Bespalov, B. N. Kazakov, A. M. Leushin, and G. M. Safiullin, Fiz. Tverd. Tela (St. Petersburg) **40** (11), 2029 (1998) [Phys. Solid State **40**, 1836 (1998)].
19. M. Inoue, Phys. Rev. Lett. **11** (5), 196 (1963).
20. J. D. Axe and G. Burns, Phys. Rev. **152** (1), 331 (1966).
21. A. M. Leushin, *Tables of Functions Transforming on Irreducible Representations Crystallographic Point Groups* (Nauka, Moscow, 1968).
22. U. Ranon and J. S. Hyde, Phys. Rev. **141** (1), 259 (1966).
23. R. Yu. Abdulsabirov, A. D. Gorlov, V. G. Stepanov, *et al.*, Fiz. Tverd. Tela (Leningrad) **20** (10), 3189 (1978) [Sov. Phys. Solid State **20**, 1842 (1978)].
24. M. H. Dickens and M. T. Hutchings, J. Phys. C **11** (3), 461 (1978).

Translated by N. Wadhwa

Physics of the Solid State, Vol. 43, No. 9, 2001, pp. 1680–1685. Translated from Fizika Tverdogo Tela, Vol. 43, No. 9, 2001, pp. 1613–1618.

DEFECTS, DISLOCATIONS, AND PHYSICS OF STRENGTH

Short-Lived Primary Radiation Defects in LiF Crystals

L. A. Lisitsyna*, T. V. Grechkina, V. I. Korepanov**, and V. M. Lisitsyn****

**Tomsk State Civil Engineering University, Solyanaya pl. 2, Tomsk, 634003 Russia*

***Tomsk Polytechnical University, Tomsk, 634034 Russia*

Received November 9, 2000

Abstract—The spectral and kinetic parameters of electron-pulse-initiated transient absorption and emission of LiF crystals were studied using pulsed spectrometry with a nanosecond time resolution. The measurements were performed in the spectral region of 6 eV, the temperature range of 11–150 K, and within 10^{-8}–10 s after the termination of an electron pulse. It is shown that the electron-pulse irradiation not only gives rise to F, V_k, and H centers in the LiF crystal but also to certain short-lived defects of two types that differ in the spectral positions of the absorptive and radiative transitions, the lifetime, and the temperature dependence of the production efficiency. Defects of type I feature absorptive transitions at 5.5 and 5.1 eV and a radiative transition at 5.8 eV, whereas the absorptive transitions at 5.3 and 4.75 eV and a radiative transition at 4.4 eV are characteristic of type-II defects. It is found that a variation in the ratio between the concentrations of the different types of short-lived centers in the range of 11–150 K does not affect the quantum efficiency of the F centers. It is assumed that the observed centers are self-trapped excitons of various types. *© 2001 MAIK "Nauka/Interperiodica".*

1. INTRODUCTION

In ionic crystals, the primary products of the relaxation of radiation-induced electronic excitations are the Frenkel defect pairs and self-trapped excitons (STEs). With time, the Frenkel pairs either recombine or transform into defects stable under experimental conditions. The STEs, the lifetime of which is controlled by the spin multiplicity and the degree of spatial overlap of electronic wave functions for the electron and hole components, decompose radiatively or nonradiatively.

In a series of alkali-halide crystals, the processes of formation and relaxation of primary radiation defects are well understood; the causes for the changes in the relation between various types of radiation defects have been determined. The sole exception is provided by the crystals of alkali-metal fluorides, the primary defects of which are poorly understood. The reasons for this are the extremely low intensity of intrinsic luminescence compared to other alkali-halide crystals, the appreciable effect of residual impurities on the above processes, and the difficulties encountered in obtaining ultrahigh-purity materials.

In this paper, we report the results of an experimental study on the primary radiation defects in high-purity LiF crystals. Information on the initial stages of the radiation-defect evolution can be obtained only if the methods with high time resolution are used. In this study, we used pulsed optical spectrometry with nanosecond resolution to gain insight into the spectral and kinetic characteristics of the radiation-induced luminescence and absorption in the crystals within the time interval of 10^{-8}–10 s. In the temperature range of 11–150 K, the crystals were subjected to irradiation with a single electron pulse, which gave rise to a volume excitation density no higher than 1 J cm^{-3} and had a mean electron energy of 350 keV, with pulse duration being equal to 10 ns.

We studied the ultrahigh-purity LiF crystals, which were transparent in the range of 12–0.5 eV and contained less than 1×10^{-3} mol % of Mg, Al, and Si impurities and less than 1×10^{-5} mol % of oxygen (according to the data of the proton-activation analysis).

2. RESULTS

2.1. Luminescence Initiated by a Single Electron Pulse in a LiF Crystal

An electron pulse initiates emission in an LiF crystal; the relation between bands in the spectrum of this emission is controlled by the crystal temperature during irradiation and by the elapsed time from the instant of the pulse termination. At 11 K, bands at 5.8, 4.4, and 3.5 eV are observed in the emission spectrum measured at the instant of electron-pulse termination; the intensity of emission in the region of 5.8 eV is more than an order of magnitude higher than those in the other two bands (Fig. 1). In the range of 50–80 K, the same bands are observed in the spectrum measured at the instant of electron-pulse termination; however, the intensities of the 5.8 and 4.4 eV bands are now comparable. At 80 K, the same bands are observed in the spectrum measured within 100 ns after electron-pulse termination; however, only the band at 4.4 eV can be distinguished in the spectrum measured with a delay of 300 ns. It is noteworthy that the emission spectra reported here were plotted with a allowance made for the spectral sensitivity of the photomultiplier and the transmittance of the optical channel.

For all the bands, the emission decay is multiexponential at low temperatures. The emission-decay kinetics for each of the bands at T = const can be described by a function $I(t) = \Sigma I_{0i} \exp(t/\tau_i)$, where I_{0i} is the amplitude value of intensity of the ith component (determined by decomposing the decay kinetics) characterized by the time constant τ_i.

At 11 K, we observed four decay components in the region of 3.5 eV (τ_1 = 50 ns, τ_2 = 30 μs, τ_3 = 700 μs, and τ_4 = 8 ms), three decay components for the band at 4.4 eV (τ_1 = 50 ns, τ_2 = 30 μs, and τ_3 = 700 μs), and two decay components for the band at 5.8 eV (τ_2 = 30 μs and τ_3 = 700 μs).

It was found that the low-intensity emission band at 3.5 eV is not elementary. The spectra of three decay components (700, 30 μs, and 50 ns) are the same and consist of the band at 3.5 eV, whereas the emission spectrum of the millisecond component involves the bands at 3.35 and 2.8 eV (see the inset in Fig. 1). The inference that the emission band in the region of 3.5 eV is not elementary at 4 K also follows from the data reported by Pooley *et al.* [1].

It was found by studying the effect of the irradiated-crystal temperature on the decay kinetic parameters that the decay constants are nearly temperature-independent in the range of 11–50 K (Fig. 2). A further increase in temperature causes the decay constants to decrease and intermix. The activation energy of a process resulting in changes in the decay constants is equal to 0.3 eV for the decay components of the emission at 5.8 and 3.5 eV in the range of 60–90 K and to 0.06 eV for the decay components of emission at 4.4 eV in the range of 70–150 K.

As follows from the data shown in Fig. 2, the distinction between the temperature dependences of characteristic decay times for the emission bands of differing spectral positions results in the fact that the emission at 3.5 eV is the most long lived in the range of 11–70 K, whereas the decay of the emission at 4.4 eV is the slowest in the range of 80–150 K.

From the studies of the effect of the crystal temperature during irradiation on the emission intensity, we found the following:

(1) The amplitude value of the total emission intensity in the band at 3.5 eV changes only slightly in the range of 11–80 K and decreases as temperature increases further. The amplitude intensities of emission described by the separate decay components depend on temperature in the following manner: I_{01} and I_{03} are temperature-independent in the range 11–60 K and decrease as temperature increases further; at the same time, I_{02} is constant in the range of 11–30 K, increases by a factor of 5 in the range of 30–80 K, and decreases as temperature is increased further. The intensity of the millisecond component is temperature-independent in the temperature range of 11–150 K.

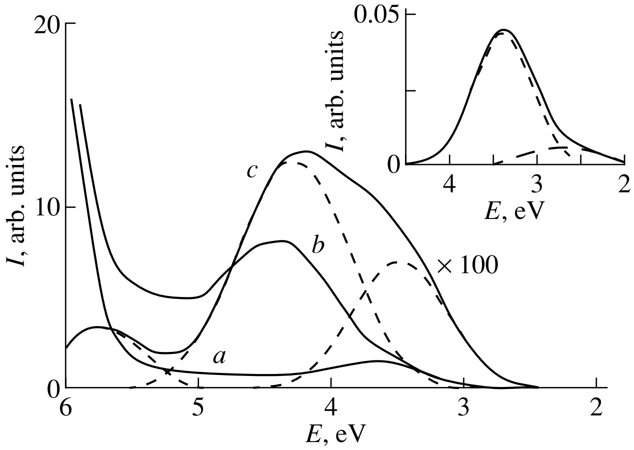

Fig. 1. Luminescence spectra initiated by irradiation of an LiF crystal with a single electron pulse at temperatures of (*a*) 20, (*b*) 50, and (*c*) 80 K and measured after a delay of (*a–b*) 10 and (*c*) 100 ns after electron-pulse termination. The spectrum of the millisecond component of emission at 22 K is shown in the inset.

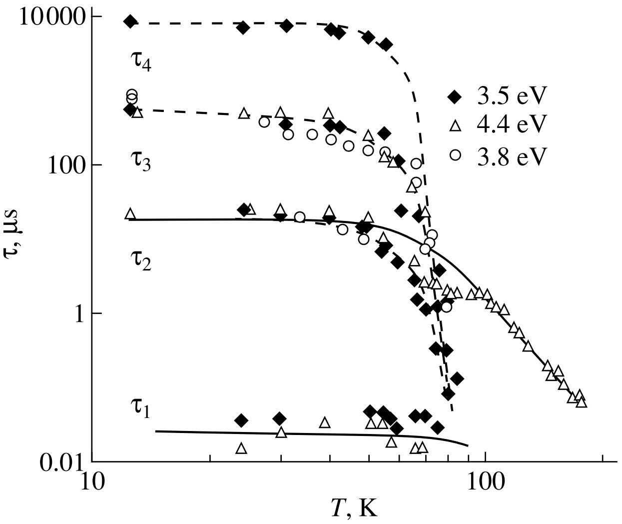

Fig. 2. Temperature dependences of decay constants for several components of emission initiated by irradiation of on LiF crystal with a single electron pulse.

(2) The dependence of the amplitude value of emission intensity in the 4.4-eV band on the crystal temperature during irradiation is described by a curve with a peak in the vicinity of 50 K. The amplitude intensities of emission with the decay components τ_1 and τ_2 are constant in the temperature range of 11–80 K and decrease as temperature is increased further. The amplitude intensity of emission described by the component τ_2 is constant in the range of 11–25 K, increases with temperature by more than an order of magnitude in the

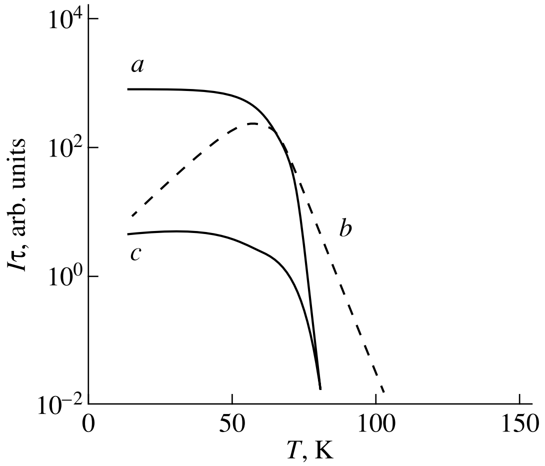

Fig. 3. Temperature dependences of the light sums ($I\tau$) emitted at (*a*) 5.8, (*b*) 4.4, and (*c*) 3.5 eV and initiated by irradiation of an LiF crystal with a single electron pulse.

range of 25–60 K, and then decreases as temperature is increased further.

(3) The amplitude value of the total intensity of the 5.8-eV emission, similar to amplitude values of the intensities of the separate components (I_{02} and I_{03}), is constant in the range of 11–60 K and decreases as temperature is increased further. At 11 K, the contributions of the separate components I_{02} and I_{03} to the total intensity amount to 90 and 10%, respectively.

In order to assess the effect of temperature on the occupancy of various radiative states, we studied the temperature dependences of the emitted light sums ($I\tau = \Sigma I_{0i}\tau_i$) in each of the observed spectral bands. It follows from the data shown in Fig. 3 that the following trends are found in the temperature dependences of the light sums:

(i) The light sums emitted at 3.5 and 5.8 eV are temperature-independent in the range of 11–60 K and decrease as the irradiated-crystal temperature is increased further. In all the LiF crystals we studied, the light sum emitted in the band peaked at 5.8 eV at 11 K exceeded the light sum emitted at 3.5 eV by two orders of magnitude and the light sum emitted by the millisecond component of emission with the spectrum represented in the inset in Fig. 1 (the bands at 3.35 and 2.8 eV) by an order of magnitude.

(ii) In the range of 11–150 K, the temperature dependence of the light sum emitted at 4.4 eV is represented by a curve with a peak in the vicinity of 50 K, which correlates with the temperature dependence of amplitude intensity for the emission that corresponds to the decay component τ_2 (I_{02}).

Thus, it follows from the data represented in Fig. 3 that occupancy of the radiative state at 5.8 eV is dominant at 11 K, whereas the occupancy of the radiative state at 4.4 eV is prevalent in the range of 75–140 K. Redistribution of occupancies of these radiative states occurs in the temperature range of 30–75 K: occupancy of the radiative state at 5.8 eV decreases, whereas the occupancy of the radiative state at 4.4 eV increases. The total number of radiative centers introduced by irradiation in the range of 11–70 K is virtually independent of the crystal temperature during irradiation.

2.2. Short-Lived Optical Absorption of LiF Crystals Initiated by the Impact of a Single Electron Pulse

An electron pulse gives rise to nonsteady optical absorption in the vicinity of 5 eV in LiF crystals. As reported previously [2, 3], the relaxation kinetics of absorption in the vicinity of 5 eV is multiexponential and is accompanied with changes in the band halfwidth. Thus, for example, only 15% of the electron-pulse-induced absorption is retained at 80 K one second after electron-pulse termination; it is only in the 0- to 1-s time interval that the absorption band has the halfwidth of 0.6 eV and the peak position at 5.05 eV, which are consistent with the corresponding parameters of the *F* band. The relaxation of the remaining 85% of the absorption induced in the region of 5 eV can be described by a combination of two exponential functions with characteristic relaxation times equal to 500 ns and 2 μs. It was found that the spectra of the components differ. The spectrum of the nanosecond component consists of overlapping bands peaked at 5.5 and 5.1 eV (the type-I spectrum). The spectrum of the microsecond component is comprised of bands peaked at 5.3 and 4.7 eV (the type-II spectrum).

A comparative analysis of spectral and kinetic parameters of short-lived absorptive and radiative transitions in the spectra of LiF crystals in a wide temperature range led to the following conclusions:

(I) Only a single type of the spectrum of short-lived absorption is observed in the range of 90–150 K; this is a spectrum belonging to type II and includes bands at 4.7 and 5.3 eV. Emission in the region of 4.4 eV is dominant in the same temperature region. The decay constants of the observed emission and short-lived absorption coincide throughout the entire temperature range of 90–150 K, as we have shown previously [4]. The coincidence of the characteristic relaxation times suggests that the above absorptive and radiative transitions are effected from a single energy level and belong to the same radiation defect, i.e., a defect of type II.

It follows from the shape of the temperature dependence of the light sum emitted in the band peaked at 4.4 eV that this short-lived defect is formed in the range of 11–150 K, with the highest formation efficiency being in the vicinity of 50 K.

There is a correlation between the temperature dependences of the production efficiency for the type II centers according to estimations performed by two different methods, i.e., from the value of the emitted light sum in the band at 4.7 eV and from the value of the emitted light sum at 4.4 eV; this correlation suggests that quenching of an emission at 4.4 eV at $T \geq 60$ K is caused by a decrease in the efficiency of formation of type-II centers with increasing temperature.

(II) The spectrum of short-lived absorption of type I consists of bands peaked at 5.5 and 5.1 eV and is not observed at temperatures higher than 90 K; under the same conditions, the emission in the vicinity of 5.8 eV is also not observed. It is assumed that the radiative transition at 5.8 eV and the type-I absorption spectrum are characteristic of the same center, i.e., a type-I center. It is evident from comparison of the light sums emitted at 4.4 and 5.8 eV that the defects of type I are predominantly formed in the temperature range of 11–30 K.

(III) In the higher temperature regions ($T \geq 160$ K), the absorption spectrum induced as a result of the impact of a single electron pulse includes only the F and V_k bands and also a low-amplitude H band. In the temperature range of 11–150 K, we studied the efficiency of buildup of the F centers; this efficiency was estimated from the concentration of the F centers in the crystal in a time interval several seconds after excitation with an electron pulse (by that time, all the short-lived components of the absorption relaxation within the F band ceased to exist completely). It is found that the yield of the buildup of the F centers per electron–hole pair in the range of 11–150 K is temperature-independent and is equal to 0.02. This is consistent with the F-center yield at 4 K [5]. We have shown previously that the buildup yield of F centers increases in the range of 150–300 K and may be as high as 0.15 [2].

3. DISCUSSION

The aforementioned experimental data indicate that the multiexponential kinetics of the absorption relaxation for the F band in the absorption spectrum of LiF crystals does not represent the function of the initial distribution of the Frenkel pairs in their separation; rather, it is the result of the superposition of absorptive transitions related to the F centers and to radiation defects which are more short lived than the F centers.

The two types of short-lived radiation defects in LiF crystals differ in their spectral–kinetic parameters of absorptive and radiative transitions, the activation energies for postirradiation relaxation, and the temperature dependences of their production under the effect of electron pulse. The defects of type I are involved in absorptive transitions at 5.5 and 5.1 eV and in radiative transition at 5.8 eV, are dominant at low temperatures (11 K), and are almost not produced by radiation at $T \geq 90$ K. The defects of type II are involved in absorptive transitions at 5.3 and 4.75 eV and in radiative transition at 4.4 eV and are produced in the range of 11–170 K, with the highest production efficiency being attained at about 60 K.

We may assume that the aforementioned short-lived defects are primary radiation defects; i.e., they are the products of decay of electronic excitations generated in the crystal by radiation and constitute the STEs in the triplet state.

In alkali halide crystals, a two-halide STE constitutes an excimer ($X_2^- + e^*$), where X_2^- is the hole component or the STE core ($X \equiv$ hal). The thermodynamically equilibrium type of STE is governed by the position of its hole component in the lattice. This component can occupy two neighboring halide lattice sites; a single halide site; or certain intermediate states without a center of symmetry, which are in the vicinity of a nascent vacancy. An STE of the "on" type is an excimer with point symmetry D_{2h} and the V_k center as its core (the V_k center is the X_2^- molecule that occupies two neighboring halide lattice sites in the $\langle 110 \rangle$ direction). An STE with the core displaced to the site with a lower symmetry constitutes an STE of the "off" type.

It is assumed that distinctions between the spectral–kinetic, temporal, and energy parameters of the two types of short-lived centers in LiF crystals are caused by difference in the STE-core structure. At low temperatures, the centers of type I are the triplet STEs of the on type (with the D_{2h} point symmetry); by contrast, at high temperatures, the equilibrium configuration of the type-II STE amounts apparently to an STE of the off type with the position of the F_2^- molecular ion displaced in the $\langle 111 \rangle$ direction.

The above assumption is supported by the following facts:

(1) The short-lived defects of both types are produced (as the F centers) during the exposure to an electron pulse; however, in contrast to the F centers, these defects do not accumulate in the crystals as a result of exposure to a series of electron pulses. As we have shown previously [4], the efficiency of production of short-lived radiation defects in LiF crystals (as in the case of other STEs in alkali halide crystals) decreases when introducing defects of radiation origin in the crystal. This circumstance gives rise to the density effect, i.e., to a sublinear dependence of the production efficiency for both types of defects on the volume excitation density in the LiF crystals [3].

(2) As in the case of STEs in other alkali halide crystals [6], the positions of radiative transitions for the observed short-lived defects of both types in LiF crystals are also located in the spectral range between the F and F_2^- bands. For alkali halide crystals, this fact is considered as evidence that the observed triplet–triplet (T–T) transitions occur in the electron component of an STE.

(3) It follows from the results of studies conducted by us using optical spectrometry that the short-lived defects of type I involved in radiative transition at 5.8 eV are predominantly produced during irradiation at 11 K. In the same temperature region, the signal of an optically detected ESR is observed in an irradiated

LiF crystal [7]; this signal is related to a triplet STE with the hole component in the form of a V_k center having the D_{2h} point symmetry.

(4) A multicomponent emission decay for the short-lived defects of both types in LiF crystals is related (as in the case of triplet STEs in other alkali halide crystals) to the splitting of the radiative level in the zero magnetic field and to the higher rate of transition to the ground state as compared to the rates of transitions between the sublevels [8, 9]. For low-temperature triplet STEs in LiF, the splitting constant D was determined to be 0.11 cm^{-1} at 4 K [10]. Small values of D observed in some of the alkali halide crystals are characteristic of STEs with a centrally symmetric position of the core [11].

(5) In a series of alkali halide crystals, the degree of spatial overlap of the wave functions of the electron and hole components in the triplet STE correlates with the Rabin–Click parameter and governs the lifetime and the type of point symmetry of the center; the degree of vibrational relaxation of the lattice in the vicinity of the center; and, correspondingly, the magnitude of the Stokes shift that controls the position of radiative transition in a triplet STE [8, 12, 13].

In the context of this approach, the longer lifetime of the type-II triplet STEs in LiF crystals compared to the type-I triplet STEs (for example, these lifetimes are equal to 2 μs and 500 ns for the type-I and type-II centers, respectively, at 80 K), in combination with the appreciable difference (by 1.5 eV) between the radiative-transition positions for the triplet STEs of types II and I, is indicative of a lesser degree of spatial overlap of the wave functions for the electron and hole components of the type-II STE compared to the type-I STE. In the alkali halide crystals, the processes leading to this effect are related to a change in the STE-core position (to its transfer to a site with lower point symmetry of the center). An appreciable vibrational relaxation of the lattice in the vicinity of such a center is caused by the nascence of vacancy and the formation of the wave function of an F center at this vacancy and is accompanied with a shift of the radiative-transition position to longer wavelengths, which is observed in the LiF crystals for the SETs of types I and II with the radiative-transition positions located at 5.8 and 4.4 eV, respectively.

(6) In the alkali halide crystals, the STEs of the on and off types differ in the point symmetry (the D_{2h} and C_{2v}, respectively), A displacement of the STE core along the $\langle 110\rangle$ direction and formation of the F-center wave function at the nascent vacancy make it possible to represent the off-type STE as an analogue of the F–H unseparated pair with the axis that is also oriented along the $\langle 110\rangle$ direction.

In fluorides with a rock salt lattice, the axis of the H center is oriented along the $\langle 111\rangle$ direction [14, 15]. Consequently, in an LiF crystal, the nascence of vacancy should be accompanied with a change in the spatial orientation of the axis of the STE hole core from the $\langle 110\rangle$ direction (the orientation at the stage of self-trapping of the electronic excitation) to the $\langle 111\rangle$ direction or close to it. The temperature corresponding to activation of such a process is about 50 K. In the range of 45–70 K, a correlation between the temperature variations in the production efficiency of the short-lived defects is observed: a decrease in the yield of type-I defects and an increase in the yield of type-II defects.

(7) In the alkali halide crystals, a coincidence of the spectral position of radiative T–T transitions in the electronic component for STEs of the on type and for the F_2 centers is observed; these excitons and centers are two types of defects with the same outer molecular orbital but with a radically different core structure (the STE core is the F_2^- molecular ion that occupies two halide lattice sites, whereas the core of an F_2 center is represented by two neighboring anionic vacancies). In the LiF crystals, a weak influence of the hole-component structure on the position of the absorptive T–T transition can also be expected for isoelectronic STEs of two types, which is in fact observed (5.5 and 5.1 eV and 5.3 and 4.7 eV for the triplet STEs of types I and II, respectively).

(8) For alkali halide crystals, the use of measuring equipment with picosecond-scale time resolution has made it possible to clearly demonstrate [17, 18] that the formation of an STE is an alternative process to the generation of a Frenkel pair in the course of autolocalization of electronic excitation. According to the results of our studies, neither of the types of STEs observed in LiF can be considered to start the formation of correlated Frenkel pairs. This inference is clearly supported, first, by the discrepancy between the production time of the F centers (≤10 ns) and the lifetime of the triplet STEs (700 μs at 11 K) and, second, by the fact that the yield of the F centers is not affected by the type of simultaneously produced STEs.

(9) According to the results of our studies, the formation efficiency for the type-II triplet STEs increases in LiF crystals in the range of 40–60 K; at the same time, the yield of Frenkel pairs with intercomponent distance exceeding the recombination-sphere radius remains unchanged, which is indicated by a constant yield of the F centers in the aforementioned temperature range. Apparently, only the reorientation of the H centers is activated in the region of 40 K, whereas the diffusive motion of these centers is observed at higher temperatures (120–155 K) (see [19, 20]). This assumption is also corroborated by previously reported data on an increase (near 150 K) in both the yield of the F centers [2] and the efficiency of decomposition of the F_2 centers produced preliminarily by an electron pulse [21]. These processes have the same activation energy (0.06 eV), which is close to the value of activation energy for diffusive motion of the H centers in alkali halide crystals (0.08 eV) [22].

Thus, on the basis of the obtained experimental data, we suggest the following model for production of primary radiation defects in LiF crystals. In the range of low temperatures (4–40 K), the *F* centers and the STEs (predominantly on type) having a core in the form of the V_k center at the position with a center of symmetry are formed in LiF crystals in the course of autolocalization of electronic excitation. The number of such STEs is controlled by the volume excitation density and by the degree of purification and the temperature of irradiated crystal. In this situation, the probability of forming off-type STEs is low.

In the range of 70–120 K, activation of reorientational motion of the *H* centers leads to preferential radiation-induced formation of the STEs of the off type at the expense of on-type STEs. The structure of an off-type STE can be conceived as an unseparated *F*–*H* pair with the axis orientated along the $\langle 111 \rangle$ direction.

The total yield of the triplet STEs of both types is nearly independent of the crystal temperature in the range of 11–80 K.

In the region of higher temperatures ($T \geq 120$ K), the activation of diffusive motion of the *H* centers leads to an increase in the production efficiency for spatially separated *F*–*H* pairs during an electron pulse, which is accompanied with a decrease in the STE production efficiency.

We cannot explain the origin of the low-intensity multicomponent emission in the band peaked at 3.5 eV (the ratio between the emitted light sums in the bands at 5.8 and 3.5 eV is 1 : 100 in the range of 11–90 K) in terms of the suggested model; the origin of the long-lived emission, the spectrum of which consists of the bands peaked at 3.35 and 2.8 eV, also remains unexplained. Most probably, the emission with the bands at 3.35 and 2.8 eV is related to impurities. This assumption is supported by the following facts: there are traces of divalent impurities in the material under consideration, the ratio between the intensities of the above two bands differs widely [1, 23, 24], the emission intensity is temperature-independent, and there is an emission in this spectral region in the crystals activated with Ti and Mg impurities [25].

ACKNOWLEDGMENTS

This study was supported by the Program "Universities of Russia." We thank V.M. Reĭterov for providing us with the samples for our studies.

REFERENCES

1. D. Pooley and W. Runciman, J. Phys. C **3**, 1815 (1970).
2. L. A. Lisitsyna, V. M. Lisitsyn, and E. P. Chinkov, Izv. Vyssh. Uchebn. Zaved., Fiz. **38** (1), 13 (1995).
3. L. A. Lisitsyna, Izv. Vyssh. Uchebn. Zaved., Fiz. **39** (11), 57 (1996).
4. L. A. Lisitsyna, V. A. Kravchenko, E. P. Chinkov, *et al.*, Fiz. Tverd. Tela (Leningrad) **32** (8), 2458 (1990) [Sov. Phys. Solid State **32**, 1425 (1990)].
5. R. T. Williams, Opt. Eng. **28** (10), 1024 (1989).
6. R. T. Williams and M. N. Kabler, Phys. Rev. B **9** (4), 1897 (1974).
7. P. G. Baranov, Izv. Akad. Nauk SSSR, Ser. Fiz. **45** (2), 253 (1981).
8. J. U. Fischbach, D. Frohlich, and M. N. Kabler, J. Lumin. **6**, 29 (1973).
9. H. Karasawa and M. Hirai, J. Phys. Soc. Jpn. **39**, 999 (1975).
10. D. Block and A. Wasiela, Solid State Commun. **28**, 455 (1978).
11. K. Song, C. Leung, and J. Spaeth, J. Phys.: Condens. Matter **2**, 6373 (1990).
12. K. Song and C. Leung, J. Phys.: Condens. Matter **1**, 8425 (1989).
13. K. Song and F. Chen, J. Phys. Soc. Jpn. **58** (8), 3022 (1989).
14. H. Chu and R. Mieher, Phys. Rev. **188** (3), 1311 (1969).
15. A. Ch. Lushchik, E. A. Vasil'chenko, V. G. Galaganov, *et al.*, Izv. Akad. Nauk Latv. SSR, Ser. Fiz. Tekh. Nauk **3**, 33 (1990).
16. L. A. Lisitsyna, Izv. Vyssh. Uchebn. Zaved., Fiz. **38** (8), 115 (1995).
17. Y. Suzuki, S. Wakita, H. Ohtani, *et al.*, J. Phys. Soc. Jpn. **49** (1), 207 (1980).
18. J. N. Bradford, R. T. Williams, and W. Fast, Phys. Rev. Lett. **35**, 300 (1975).
19. B. D. Lobanov, L. I. Smol'skaya, A. I. Nepomnyashchikh, and L. M. Georgievskaya, Izv. Akad. Nauk SSSR, Ser. Fiz. **38** (6), 1312 (1974).
20. P. D. Townsend, C. D. Clark, and P. W. Levy, Phys. Rev. **155**, 908 (1967).
21. L. A. Lisitsyna, Fiz. Tverd. Tela (St. Petersburg) **34** (9), 2694 (1992) [Sov. Phys. Solid State **34**, 1441 (1992)].
22. R. Williams, Radiat. Eff. Defects Solids **109**, 175 (1989).
23. V. G. Plekhanov and A. V. Emel'yanchenko, in *Proceedings of the VIII All-Union Conference on the Physics of Vacuum Ultraviolet Radiation and Its Interaction with Materials* (Irkutsk, 1989), p. 36.
24. A. I. Nepomnyashchikh, E. A. Radzhabov, and A. V. Egranov, *Color Centers and Luminescence in LiF Crystals* (Nauka, Novosibirsk, 1984).
25. V. K. Jain, J. Phys. D **19** (9), 1791 (1986).

Translated by A. Spitsyn

Physics of the Solid State, Vol. 43, No. 9, 2001, pp. 1686–1699. Translated from Fizika Tverdogo Tela, Vol. 43, No. 9, 2001, pp. 1619–1631.
Original Russian Text Copyright © 2001 by Zaĭnullina, Zhukov.

DEFECTS, DISLOCATIONS, AND PHYSICS OF STRENGTH

Defect Clusterization and Transport Properties of Oxide and Fluoride Ionic Conductors with Fluorite Structure: Quantum-Chemical Approach

V. M. Zaĭnullina and V. P. Zhukov

Institute of Solid-State Chemistry, Ural Division, Russian Academy of Sciences,
ul. Pervomaĭskaya 91, Yekaterinburg, 620219 Russia
e-mail: Veronika@ihim.uran.ru

Received November 17, 2000

Abstract—Systematic studies of the effect of point defects on the electronic structure, chemical bond, and ionic conduction of classical ionic conductors *Me*F_2 (*Me* = Ca, Sr, Ba, Pb), ZrO_2–CaO, ZrO_2–Y_2O_3, and δ-Bi_2O_3 are carried out using the nonempirical LMTO method in the tight-binding approximation and using Hückel’s semiempirical method. The energies of formation and interaction of anti-Frenkel defects are calculated. The effect of defect clusterization in these compounds is detected. This effect is responsible for the emergence of the superionic state and anomalous physicochemical properties of the given solid electrolytes. The nature of instability of the fluorite structure is studied, and methods of its stabilization are proposed. The mechanisms and energetics of ionic transport in oxide and fluoride conductors with fluorite structure are investigated. *© 2001 MAIK “Nauka/Interperiodica”.*

1. INTRODUCTION

Solid electrolytes that combine high ionic conductivity with the mechanical strength and elasticity of a solid form a large group of conductors of exceptional scientific and technological importance. Ionic conductors are widely used as chemical sources of electrical energy and electrochemical sensors and detectors [1–3] and are used in various optoionic devices [4].

Further prospects of practical application of materials based on solid electrolytes depend on the understanding of the nature of formation of physicochemical properties and the possibility of their purposeful modification. The solution of such problems requires a detailed investigation of the electronic structure and the chemical bond in these compounds. This type of investigation was carried out for several decades using experimental as well as theoretical methods [5–13]. Insight into the electronic structure of classical solid electrolytes was facilitated in many respects by the results of x-ray emission, x-ray electron, and photoelectron spectroscopy [5–7]. However, the description of the electronic structure of ionic conductors remains incomplete. The available quantum-chemical calculations are mainly aimed at studying the electron energy spectrum of conductors (PbF_2, ZrO_2–CaO, Bi_2O_3, CaF_2, etc.) [8–13] and do not clarify the origin of the superionic state.

The rapid development of computational methods over recent decades and the creation of a number of powerful computational programs considerably extended the potentialities of computational methods in solid-state physics as applied to analysis of not only electronic structure but also important physicochemical properties of solids. However, the above-mentioned methods are virtually not employed in analyzing transport phenomena and in studying the nature of conduction in superionic conductors. Only scarce examples of simulation of ionic conduction and diffusion in solid electrolytes on the basis of *ab initio* methods are known at present [14].

In the present work, the nonempirical linear muffin-tin orbital method in the tight-binding approximation [15, 16] and the extended Hückel method [17] are used for analyzing the peculiarities of the defect electronic structure and chemical bond in ionic conductors CaF_2, SrF_2, BaF_2, PbF_2, δ-Bi_2O_3, ZrO_2–Y_2O_3, ZrO_2–CaO, and $Ca_{1-x}L_xF_{2+x}$, where L = Yb and La, and for determining the characteristics of the ionic conduction (energy of formation and interaction of defects). The combined application of these methods makes it possible to study the effect of the electronic structure of defects and their interaction on the transport properties of solid electrolytes and to establish a correlation between the nature of chemical bonds, the features of defect formation, and the stability of the fluorite structure of fluoride and oxide conductors.

2. CRYSTAL STRUCTURE

High values of the ionic conductivity of solid electrolytes are determined by the peculiarities of their crystal structure. For example, the fluorite structure is convenient for fast ionic transport. This structure is a superposition of two cubic sublattices formed by cations and anions (Fig. 1) [18, 19]. Cations are located at the centers of cubes formed by eight anions and occupy sites only in half anionic cubes, forming a face-centered cubic lattice. A unit cell of fluorite consists of four structural units MF_2, where M stands for a cation. In the fluorite lattice, we can single out a face-centered cubic sublattice formed by empty lattice sites (interstices) V_i over which fast ionic transport can occur.

Typical representatives of compounds with the fluorite structure are fluorides of alkali-earth metals (AEM) and PbF_2. The presence of interstitial fluorine ions in the lattice of such compounds has been proved in neutron diffraction experiments [20, 21].

Among the oxide-type ionic conductors with fluorite structure, δ-Bi_2O_3 occupies a special place. Several structural models of this compound have been constructed to determine its structure more exactly. These models are based on the different positions of vacancies and the distribution of oxygen atoms in the fluorite lattice [22]. In accordance with the Sillen model [23], six possible oxygen positions are occupied, while two vacancies are ordered in the {111} direction. Another model developed by Gattow and Schutze [24] takes into account the high degree of disorder in the oxygen sublattice. These authors considered the statistical filling of all eight positions of oxygen with a filling factor of 3/4. In the Willis model [25], anharmonic vibrations of the anionic sublattice are considered and four oxygen atoms are localized in the $[x, x, x]$ positions, where $x = 1/4 + \delta$ ($\delta = 0.066$). As a result, anions are distributed statistically over the faces of the bismuth tetrahedron with a filling probability of 3/16. However, experiments cannot provide an unambiguous choice in favor of any of these models.

Another large class of compounds with fluorite structure are oxide electrolytes with impurity-induced disorder: MO_2–$M'O$ and MO_2–M''_2O_3, where M = Zr, Hf, and Ce; M' = Ca, Ba, and Sr; and M'' = Y, Sc, and rare-earth metals (REM). The high ionic conductivity of these compounds is due to the large concentration of oxygen vacancies emerging as a result of the introduction of ions activating the disorder of the fluorite structure [18, 19, 26].

3. COMPUTATIONAL METHODS

It is well known that the main factor determining the ionic conduction of solid electrolytes is the presence of point defects associated with intrinsic or impurity-induced disorder of the structure. The energies of formation and migration of such defects in a crystal are the most important characteristics of ionic transport [27–29]. For a high concentration of these defects, the interaction between them can considerably affect the ionic conductivity [18, 26]. Since the values of the energy of formation, migration, and interaction of defects for superionic conductors are relatively small (units or tenths of an electronvolt), accurate quantum-chemical methods are required for calculating the total energy of the electron–nuclear system. At present, the electron density functional (EDF) methods are the most suitable for such calculations.

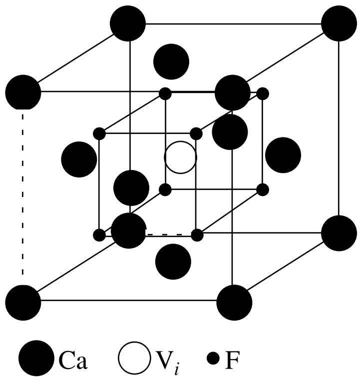

Fig. 1. Unit cell of fluorite (schematic) [7, 8].

In accordance with the EDF theory, the total energy of the electron–nuclear system in the ground state has the form [30]

$$E(\rho) = T(\rho) + \iint\limits_{r\,r'} \frac{\rho(\mathbf{r})\rho(\mathbf{r}')}{|\mathbf{r}-\mathbf{r}'|} d^3\mathbf{r}\, d^3\mathbf{r}' + E_{\mathrm{xc}}(\rho) + \int V_{\mathrm{ext}}(\mathbf{r})\rho(\mathbf{r}) d^3\mathbf{r}, \tag{1}$$

where $T(\rho)$ is the kinetic energy of the system without electron–electron interaction, E_{xc} is the exchange-correlation energy, and V_{ext} is the electrostatic potential of the nuclei (external potential).

However, such calculations encounter considerable difficulties.

First, the disorder of crystals with point defects complicates the calculations. On the basis of the EDF theory, a number of methods and programs have been developed for calculating the electronic structure of disordered solids [31], but no systematic attempts were made to calculate the total energy using these methods. Here, we use the supercell model, which makes it possible to apply the band methods of calculating the electronic structure, which were developed for periodic crystals.

Second, the motion of ions over a crystal is accompanied by crystal structure relaxation in the vicinity of a defect. The inclusion of this relaxation considerably complicates the estimation of the conduction parameters mentioned above. In our calculations, we disregard the relaxation of atoms around defects. This is justified by the fact that without taking relaxation into account, we obtain results that reproduce experimentally observed tendencies; i.e., the errors due to the disregard of relaxation are systematic.

Table 1. Parameters of LMTO calculations: composition of the computational cell and the set of atomic orbitals

Crystal (space group)	Lattice constants, Å	Composition of the computational cell	Atomic orbitals	N_k
CaF_2	$a = 5.45$	$Ca_8F_{16}E_8$	$4s(4p, 3d)$-Ca	64
($Fm3m$)	$\alpha = \beta = \gamma = 90°$		$2p(2s, 3d)$-F	
			$s(p, d)$-E	
SrF_2 ($Fm3m$)	$a = 5.78$	$Sr_8F_{16}E_8$	$5s(5p, 4d)$-Sr	64
BaF_2 ($Fm3m$)	$a = 6.18$	$Ba_8F_{16}E_8$	$6s(6p, 5d)$-Ba	64
PbF_2 ($Fm3m$)	$a = 5.93$	$Pb_8F_{16}E_8$	$6s, 6p(5d)$-Pb	64
δ-Bi_2O_3	$a = 5.66$	$Bi_4O_6E_4^*$	$6s, 6p(6d, 5f)$-Bi	64
($Fm3m$)	$\alpha = \beta = \gamma = 90°$	$Bi_4O_6E_6^{**}$	$2p(3s, 3d)$-O	
$0.875ZrO_2$–$0.125CaO$	$a = 5.129$	$Zr_7CaO_{15}E_9$	$5s, 5p, 4d(4f)$-Zr	64
($Fm3m$)	$\alpha = \beta = \gamma = 90°$		$2p(3s, 3d)$-O	
			$4s(4p, 3d)$-Ca	
$0.75ZrO_2$–$0.25YO_{1.5}$	$a = 5.129$	$Zr_6Y_2O_{15}E_9$	$5s, 5p, 4d(4f)$-Zr	64
	$\alpha = \beta = \gamma = 90°$		$2p(3s, 3d)$-O	
			$5s, 4d(5p)$-Y	

Note: Atomic orbitals not included in the basis of Bloch functions and taken into account while constructing the matrices of the Hamiltonian using the down-folding technique [36] based on the Löwdin perturbation theory [37] are given in parentheses; N_k is the number of k vectors per first Brilloun zone.

*Composition of the computational cell for δ-Bi_2O_3 in the Willis model.

**Composition of the computational cell for δ-Bi_2O_3 in the Sillen model.

While calculating the electronic structure and the total energy, we used one of the fastest and most sufficiently precise methods of the EDF theory, viz., the linear muffin-tin orbital method in the atomic-sphere approximation (LMTO–ASA) in the version of tight-binding orbitals (LMTO–TB) [15, 16, 32–35]. Publications [32–35] contain a detailed description of the mathematical foundations of the method. For this reason, we consider here only those details of computations which are presumed from the available computer programs and also determine the accuracy of the obtained results. The optimal parameters of computation are presented in Table 1.

In order to describe the electronic structure of crystals with defects, we used a rhombohedral supercell obtained through double translations of a primitive cell along the cell edge vectors of a fcc fluorite structure. The atomic basis of the Me_8F_{16} supercell (Me = Ca, Sr, Ba, Pb, Zr) is sufficiently large to make it possible to study the characteristics of ionic conduction as functions of the concentration of defects, their separation, and packing density. In our calculations, we introduced empty spheres (so-called extraspheres E) into the interstices with a self-consistently calculated basis of orbitals. The necessity of introducing extraspheres is dictated by the fact that the LMTO–ASA method was developed (and gives the most accurate results) for close-packed crystals. After the introduction of extraspheres, the composition of the computational supercell changes by eight empty spheres; that is, we have $Me_8F_{16}E_8$.

The accuracy of the LMTO computational methods is determined to a considerable extent by the supercell size and by the choice of the radii of atomic spheres. The initial radii of atomic spheres were determined from the conditions of filling of the volume of the perfect crystal with these spheres in accordance with the automatic procedure described in [38]. The appropriate choice of the radii of extraspheres and real atoms which change places, thus forming a defect, plays a significant role in obtaining sufficiently accurate results on the energy of defect formation. We assumed that a real atom occupying the position of an extrasphere acquires its radius, and vice versa, while the radii of atoms and extraspheres which are not involved in defect formation remain unchanged. The errors in the LMTO method associated with overlapping of atomic spheres are known to increase in proportion to the third power of overlapping [39]. Since we analyze here the difference between the total energy of a perfect crystal and that of a crystal with a defect, the application of the above-mentioned computational algorithm for calculating atomic radii allows us to minimize the errors associated with overlapping. The application of other methods of determining the atomic radii for crystals with defects leads to values of the defect formation energy that are 2–3 times higher than those presented below, although

Table 2. Atomic parameters used in calculations based on the Hückel method: ionization potentials H_{ii} of valence orbitals, exponents ξ_i, and weight factors C_i of the exponentials in the expression for Slater-type atomic orbitals

Atom	Orbital	H_{ii}, eV	$\xi_1(C_1)$	$\xi_2(C_2)$
O	2*s*	32.30	2.275	–
	2*p*	14.80	2.275	–
F	2*s*	40.00	2.425	–
	2*p*	18.10	2.425	–
Ca	4*s*	7.00	1.20	–
	4*p*	4.00	1.20	–
Sr	5*s*	6.62	1.214 (1.00)	–
	5*p*	3.92	1.214 (1.00)	–
Y	5*s*	8.94	1.63 (1.00)	–
	5*p*	6.00	1.61 (1.00)	–
	4*d*	10.26	3.59 (0.6114)	1.36 (0.6010)
Zr	5*s*	8.00	1.817 (1.00)	
	5*p*	5.40	1.777 (1.00)	
	4*d*	10.20	3.836 (0.6224)	1.506 (0.57822)
Pb	6*s*	15.00	2.35 (1.00)	–
		20.00*		
	6*p*	8.00	2.06 (1.00)	–
		13.00*		
Bi	6*s*	15.19	2.560 (1.0)	–
	6*p*	7.79	2.072 (1.0)	–

* Ionization potentials corrected in accordance with the LMTO calculations of the band structure of a PbF_2 crystal.

the tendency of variation in the experimental values of the energy of defect formation is reproduced correctly.

An analysis of the chemical-bond characteristics is carried out using the extended semiempirical Hückel method in the cluster and band approximations [40]. Standard values of the parameters used in our calculations are tabulated in [41] and presented in Table 2.

4. ELECTRONIC STRUCTURE, CHEMICAL BOND, AND TRANSPORT PROPERTIES OF AEM FLUORIDES AND LEAD FLUORIDE WITH ANTI-FRENKEL DEFECTS

4.1. Electronic Structure and Characteristics of Ionic Conduction

The electronic structure of AEM fluoride and PbF_2 (perfect and with Frenkel defects) was considered by us earlier in detail [42]. In accordance with our earlier results, the valence band is mainly formed by the 2*p* states of fluorine with small admixtures of virtual AEM *s* states. The valence band is separated from the empty conduction band mainly formed by the AEM *s* states by a forbidden gap. When the fluorine ion is transferred to an octahedral interstice (formation of an anti-Frenkel defect), the forbidden gap acquires a very narrow band of defect states. For a small shift of an interstitial fluorine atom towards one of the nearest fluorine atoms at a fluorite lattice site, this band splits into a number of quasi-molecular levels which determine the presence of optical and EPR spectra of the *H* centers (F_2^- molecular ion with orientation along the [111] direction) (Table 3). When an AEM atom moves to an octahedral interstice (formation of a Frenkel defect FD), no quasi-atomic levels are formed, but the widths of the valence and forbidden bands change.

Table 3. Energies of optical excitations for the *H* center on CaF_2 according to LMTO calculations

Calculated excitation energy, eV	Transition	Experimental excitation energy, eV [43]
1.77	$\pi_u \longrightarrow \sigma_u$	1.65
3.34, 3.20	$\pi_g \longrightarrow \sigma_u$	
3.78	$\sigma_g \longrightarrow \sigma_u$	3.87

The energy effects of formation of Frenkel and anti-Frenkel defects determined from the displacement of a single atom to an octahedral interstice are characterized by the data given in Table 4. The experimental data mainly compiled in [18] differ on account of the different experimental details used. However, the general tendency is a smooth lowering of the energy of anti-Frenkel defect (AFD) formation upon a transition from CaF_2 to BaF_2 and its abrupt decrease as we go over to PbF_2. The calculated values of AFD formation energy are higher, but they reproduce this tendency. The exaggerated theoretical value of the AFD formation energy for PbF_2 will be explained below. The value of the AFD formation energy in PbF_2, corrected taking into account the peculiarities of the chemical bond and given in parentheses, is also in line with the observed tendency. As regards the energy of FD formation, experimental results (6.0 eV) are available only for CaF_2 [18]. Both theoretical and experimental results indicate the dominating role of the AFD formation, which is in accord with the generally accepted concepts on the ionic transport in the given class of compounds [2, 3, 18].

4.2. Clusterization of Anti-Frenkel Defects

The combined application of the *ab initio* LMTO–TB method and the supercell model enabled us to observe the interaction between defects for high concentrations attainable in the superionic state. First, we studied the interaction between two AFDs at the shortest separation and with all possible orientations of anionic vacancies bonded with them. Second, we calculated the energy of AFD formation for some configuraions with three and five AFDs per cell.

Table 4. Energies of defect formation in crystals of CaF_2, SrF_2, BaF_2, and PbF_2

Energy, eV		CaF_2	SrF_2	BaF_2	PbF_2
FD formation	Theory	4.37	3.57	2.55	2.58 (1.82)
	Experiment	2.2–3.1	1.7–2.3	1.6–1.9	1.1
AFD formation	Theory	9.47	8.56	4.40	9.79
	Experiment	6.0	–	–	–

The minimum total energy of CaF_2 is observed for the minimum separation between the interstitial fluorine atom F_i from its vacancy V; i.e., the AFD exists in the form of a V–F_i dipole. On the other hand, the change in the total energy of the supercell for different configurations of the two AFD and a fixed V–F_i separation is relatively small. Consequently, the interaction between vacancies at lattice sites is of secondary importance. In all subsequent calculations, the observed effect of short-range attraction between an interstitial fluorine ion and a vacancy was taken into account *a priori*.

The results of our analysis of the change in the energy of interaction between AFDs as a function of the distance and the number of AFDs per superlattice in the case of CaF_2 are presented in Table 5. As the separation between two AFDs increases to the lattice parameter a, the energy of the AFD formation increases approximately by 1 eV, which can be regarded as an indication of the existence of a short-range attraction between AFDs (clusterization); this was observed experimentally in [44–46]. The short-range attraction between defects is also observed for three and five AFDs per cell. For the same number of defects per cell, the minimum of the energy of formation of a single AFD corresponds to the configuration with the densest packing of AFDs.

Table 5 shows that a decrease in the energy of AFD formation takes place not only at the minimum distance between defects but also upon an increase in the number of defects per supercell. We analyzed this effect for CaF_2, SrF_2, and PbF_2 for the densest defect configurations. Figure 2 shows the values of the total energy of defect formation as a function of the number n of defects. The curves were approximated by the second–degree polynomial $An^2 + Bn + C$. It can be seen from Fig. 2 that such a simple approximation is quite good and ensures a small standard deviation from the calculated results (0.5387 for CaF_2, 0.4890 for SrF_2, and 0.6273 for PbF_2). These curves indicate a decrease in the energy of defect formation with increasing defect number n. This effect was postulated earlier in the quasi-chemical theory of transition to the superionic state [1, 3, 4]. This effect is quite important since it is responsible for the fast increase in the number of defects upon attainment of the temperature of the onset of transition to the superionic state and the emergence of some anomalies in the physicochemical properties of fluoride conductors. This work is probably the first in which the existence of this effect is confirmed by *ab initio* calculations of the electronic structure.

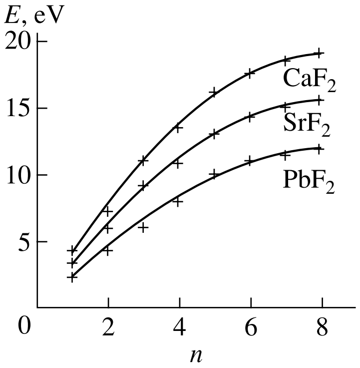

Fig. 2. Dependence of the total energy of defect formation $E(n)$ on the number n of defects per supercell. The curves are approximated by the second-degree polynomial $E = An^2 + Bn + C$.

In the Huberman–Gurevich quasi-chemical theory, it is assumed that the dependence of the energy of AFD formation on the relative concentration x of these defects has the form [47–50]

$$E = N(\omega x - \lambda x^2/2), \tag{2}$$

where $x = n/N$, $N = 16$ is the number of sites in the fluorine sublattice, and n is the number of interstitial positions equivalent from the energy point of view. Neglecting the small coefficient C in the approximation $E(n) = An^2 + Bn + C$, we find that $\omega = B$ and $\lambda = 2NA$.

Since the dependences of the energy $E(n)$ of AFD formation are successfully approximated by the polynomial $An^2 + Bn + C$, we can calculate the main parameters of the quasi-chemical theory of the transition to the superionic state: the energy ω of formation of an isolated defect and the interaction energy λ between a pair of defects (Table 6). Although the values of ω and λ are slightly higher than the experimental values, their ratio is nevertheless reasonable and makes it possible to determine the parameters χ and λ in the quasi-chemical theory from the equalities

$$\lambda/\omega = (\lambda_{calcd}/\omega_{calcd}), \tag{3}$$

$$\ln\chi = 13.066(\omega_{calcd}/\lambda_{calcd}) - 4.362, \tag{4}$$

Table 5. Dependence of the energy of AFD formation on the spatial configuration and the number of AFDs per supercell for CaF_2

Number of defects	Configuration*	Distance between defects*	Energy of AFD formation, eV
	(1/2, 1/2, 1/2)	$\sqrt{2}/2$	3.36
	(1/2, 0, 0)		
	(0, 1/2, 0)	1	4.26
	(0, –1/2, 0)		
Two AFDs	(1/2, 1/2, 1/2)	$\sqrt{6}/2$	4.47
	(–1/2, 0, 0)		
	(1/2, 1/2, 1/2)	$\sqrt{2}$	4.43
	(3/2, 1/2, 3/2)		
	(1/2, 1/2, 1/2)	$\sqrt{3}$	4.25
	(–1/2, –1/2, –1/2)		
	(0, 0, 1/2)(0, 1/2, 0)	$\sqrt{2}/2$	
Three AFDs	(1/2, 0, 0)		3.68
	(1/2, 0, 0)(0, 1/2, 0)	$\sqrt{2}/2$, $\sqrt{6}/2$ (2)**	
	(–1/2, –1/2, –1/2)		3.94
	(0, 0, 1/2)(0, 1/2, 0)	$\sqrt{2}/2$ (8), 1(2)	
	(–1/2, 0, 0)(0, 0, –1/2)		3.21
Five AFDs	(–1/2, 0, 0)		
	(–1/2, 0, 0)(0, –1/2, 0)	$\sqrt{2}/2$ (6), $\sqrt{6}/2$ (3)	
	(0, 0, –1/2)	$\sqrt{3}$	3.65
	(1/2, 1/2, 1/2)		
	(–1/2, –1/2, –1/2)		

* In units of the CaF_2 lattice parameter $a = 5.45$ Å.

** The multiplicity of the emergence of this separation between defects is shown in parentheses.

where the ratio $\lambda_{calcd}/\omega_{calcd}$ is calculated from the results of *ab initio* LMTO calculations and λ and χ are parameters of the quasi-chemical theory (the interaction energy and the function of the vibrational frequencies, respectively), which are difficult to determine experimentally. Taking into account the obtained parameters χ and λ of the theory ($\lambda = (\lambda_{calcd}/\omega_{calcd})\omega_{exp}$) and the basic equation in the Chebotin–Tsidil'kovskiĭ quasi-chemical theory adapted to compounds with fluorite structure [50],

$$G/N = (\omega x - \lambda x^2/2) + kT\{2x\ln x + (1-x)\ln(1-x) + (0.5-x)\ln(0.5-x) - x\ln\chi + 1/2\ln 2\}, \quad (5)$$

where G is the thermodynamic potential of the crystal, we calculated the temperatures of phase transitions to the superionic state in calcium and lead fluorides. The phase-transition temperature for PbF_2 is 731 K and that for CaF_2 lies in the interval from 1440 to 1450 K, which is in satisfactory agreement with the experimental values (705 and 1430 K, respectively) [51].

Our calculations also lead to certain conclusions concerning the nature of interaction between AFDs. The calculated values of energy ω for a solitary defect presented in Table 6 are 0.05–0.1 eV higher than the energy of formation of one AFD per supercell in Table 1. This proves that for $n = 1$, the defects located in neigh-

Table 6. The results of approximation of the dependence of the energy of defect formation on the number of defects

Parameters	CaF_2	SrF_2	PbF_2
$A = \lambda/2N$	–0.255	–0.214	–0.135
$B = \omega$, eV	4.43	3.67	2.60
C	–0.05	–0.21	–0.094
λ, eV	8.32	6.84	4.31

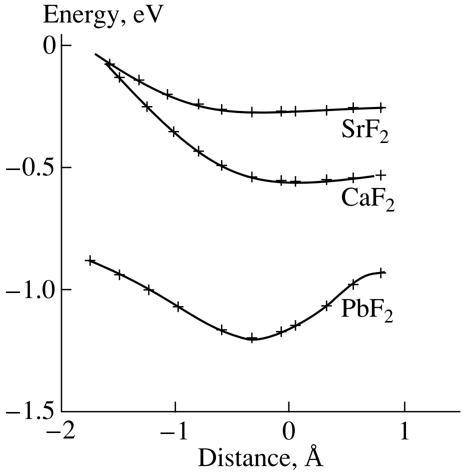

Fig. 3. Dependence of the total energy of the $(Me_4F)^{3+}$ cluster (Me = Ca, Sr, Pb) for the motion of a fluorine ion from the center of the Me_4 tetrahedron to an octahedral interstice in the fluorite structure.

boring supercells interact with each other with an energy not exceeding 0.1 eV. The smallness of this interaction implies that distant defects interact insignificantly and the main reason behind the lowering of the energy of AFD formation upon an increase in AFD concentration is the above-mentioned interaction between AFDs located at the shortest distance from one another. In order to clarify the nature of this interaction, we also calculated the covalent component of the chemical bond energy using the technique described in [52]. According to the scheme proposed in [52], the strength of the chemical bond is determined for a pair of atoms R and R' as

$$U_{RR'} = \int^{E_F} d\varepsilon \sum_{l,m \in R} \sum_{l'm' \in R'} H_{Rlm,R'l'm'} D_{Rlm,R'l'm'}(\varepsilon). \quad (6)$$

Here, $H_{Rlm,R'l'm'}$ are the matrix elements of the Hamiltonian and $D_{Rlm,R'l'm'}$ are the elements of the density matrix. Orbitals with quantum numbers l and m belong to atom R, while orbitals with quantum numbers l' and m' belong to atom R'. Integration is carried out over the entire energy range of valence states up to the Fermi level.

The value 0.0015 eV of the covalent component of the chemical bond obtained for CaF_2 indicates that this interaction cannot be regarded as a manifestation of a virtual chemical bond emerging between AFDs at high temperatures. On the other hand, while analyzing various components of the total energy, we could not single out a certain component (Madelung energy, Coulomb energy of the valence shell, etc.) whose variation would determine the interaction between nearest neighbor AFDs. This interaction is apparently due to the variation of the entire aggregate of Coulomb and exchange–correlation interactions as a result of the electron density polarization in the case when AFDs are separated by the shortest distance.

4.3. Peculiarities of the Chemical Bond

Analysis of the nature of the chemical bond allowed us to establish the peculiarities of defect formation in simple and double AEM fluorides and PbF_2. The results of calculations of the covalent component of the chemical bond in accordance with the above-mentioned algorithm (formula (6)) proved that the chemical bond in AEM fluorides is mainly ionic. The covalent component of the bonding energy of a pair (in particular, Sr–F) is equal to just 0.028 eV. The case of PbF_2 requires special attention. Although the covalent component of the Pb–Pb bond is insignificant, the covalent fraction of the energy of the Pb–F bond is 0.58 eV. The considerable contribution of the covalent component of the Pb–F chemical bond in PbF_2 affects the AFD geometry. This follows from the results obtained by Salamon [53], who used the neutron diffraction method for determining the change in the filling of sites and interstices by fluorine atoms at temperatures corresponding to the transition to the superionic state. It was proved that fluorine ions in PbF_2 predominantly occupy trigonal interstices, i.e., the centers of the faces of the FMe_4 tetrahedron and not octahedral interstices as in CaF_2 and SrF_2. The occupancy of trigonal interstices increases sharply with the onset of the transition to the superionic state at a temperature near 770 K and is anomalously high (0.38) at 1023 K. The occupancy of octahedral interstices is lower by a factor of 2–3. This leads to the conclusion that in the case of PbF_2, the energy of AFD formation with a fluorine atom at a trigonal interstice at the transition temperature to the superionic state must be lower by several hundredths of an electronvolt than that for a defect in an octahedral interstice.

In connection with the effects described above, it would be expedient to calculate the change in total energy upon the motion of fluorine atoms from their normal positions in the direction to octahedral interstices through trigonal positions. However, this cannot be done in the framework of the LMTO–ASA method in view of the poor convergence of self-consistent calculations for certain positions of fluorine atoms and also due to errors associated with the overlapping of atomic spheres. For this reason, we carried out model non-self-consistent calculations using the extended Hückel method. We studied the change in the total one-electron energy of clusters formed by nearest neighbors of a fluorine atom $(Pb_4F)^{3+}$ upon displacement of the fluorine atom from the center of the tetrahedron (0.9 Å) through the center of the Pb_3 face (0 Å) and further to the octahedral interstice (–1.7 Å) (Fig. 3). These rough calculations do not include a number of important interactions, such as the electrostatic interaction between ionic charges and the repulsion of atomic cores. Nevertheless, the calculations indicate the presence of a min-

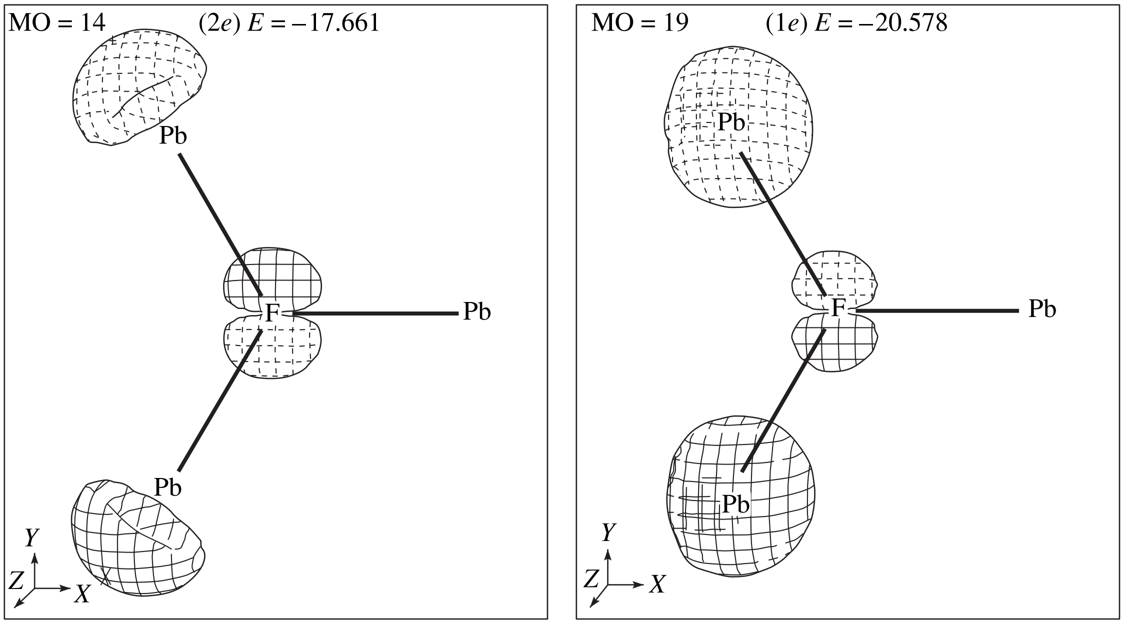

Fig. 4. Pseudospatial image of the bonding and antibonding MO of the FPb_4 cluster in the Pb_3 plane.

imum of total energy on the curve describing its dependence on the coordinate of motion along the indicated path in the vicinity of a trigonal interstice. These results are in qualitative agreement with the experimental data [54, 55]. For CaF_2 and SrF_2, this minimum is shallow, which corresponds to the presence of only anharmonic vibrations of fluorine atoms relative to their normal tetrahedral positions, while in the case of PbF_2, the minimum is much deeper, which corresponds to a shift to the trigonal position at high temperatures. Thus, the partial covalence of the chemical bond facilitates the observed shift, which is manifested much more strongly for PbF_2.

The partially covalent type of the chemical bond Pb–F realized for the trigonal position of the fluorine ion is manifested when we plot the molecular orbital (MO) maps. Figure 4 shows pseudospatial images of MOs of a FPb_4 cluster in the Pb_3 plane, which bind and antibind lead atoms with nearest fluorine atoms in a trigonal interstice. Orbital 1*e*, as well as its antibonding partner 2*e*, mainly contains contributions from the 2*p*F-atomic states and from the 6*s* orbitals of lead atoms. However, while 6*s* contributions to the 1*e* orbital preserve the spherical symmetry, the form of the 2*e* orbitals indicates admixture of the 6*p* orbitals, which reduces the effectiveness of 6*s*Pb–2*p*F antibonding. Thus, the chemical bond in the FPb_3 triangle can be described as *s*Pb–*p*F bonding–antibonding, which is not compensated due to 6*p*Pb–2*p*F hybridization.

Taking into account the peculiarities of defect formation for PbF_2 considered above, we recalculated the energy of AFD formation upon displacement of a fluorine atom to a trigonal position. It was found to be 1.82 eV, which is much lower than the initially calculated value 2.58 eV (Table 4). The new value of the energy of AFD formation is in good agreement with the experimentally observed tendency of decrease in this value in the series CaF_2, SrF_2, BaF_2, and PbF_2.

The covalence effects are found to be significant not only for simple fluorides. It is well known that alkali-earth fluorides doped with yttrium and REMs exhibit clusterization of trivalent impurities leading to the formation of defect regions. According to the results obtained in [44–46, 56], doping of alkali-earth fluorides with yttrium and heavy REMs leads to the formation of a number of clusters centered at an octahedral symmetry site, while the doping with light REM leads to the formation of a set of clusters centered at a tetragonal symmetry site. It follows from crystallographic studies [57, 58] that additional fluorine ions bonded with trivalent impurities do not occupy octahedral interstices after doping with yttrium and heavy REMs but are localized on binary symmetry axes, while in the case of doping with light REMs, they occupy positions on triad axes.

It may appear that these effects are due to the instability of interstitial fluorine atoms relative to the shift from an octahedral position to trigonal and binary positions in the presence of REM. We verified this assumption by carrying out a number of cluster calculations using the Hückel method and studied the change in the total energy of the clusters presented in Fig. 5 upon displacement of interstitial fluorine atoms along the indicated directions (Fig. 6). For the sake of comparison, similar calculations were also made for clusters containing only alkali-earth elements.

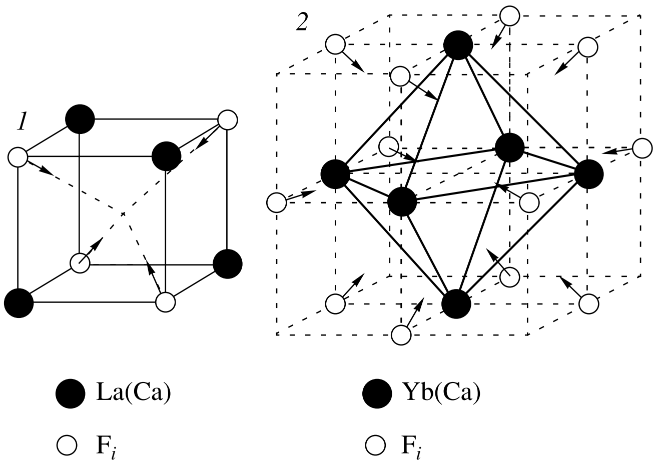

Fig. 5. Cluster *1* simulates the situation observed for light REMs; cluster *2*, for heavy REMs.

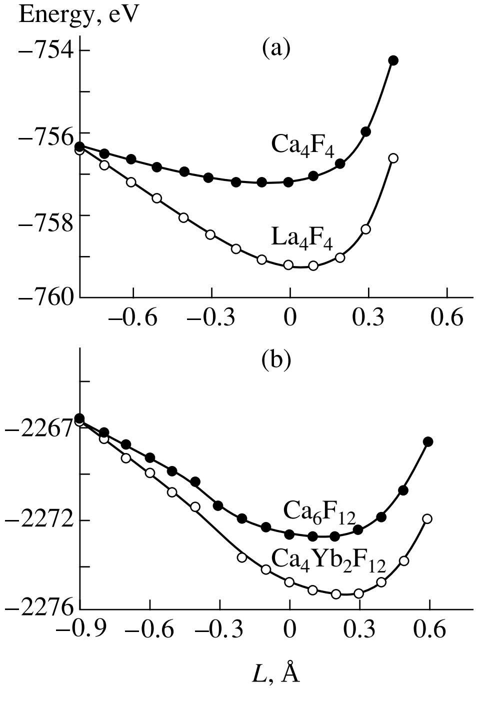

Fig. 6. Dependence of the total energy of clusters *1* and *2* in the case of displacement of interstitial fluorine atoms along (a) triad and (b) binary axes, respectively.

The curves describing the variation of the total energy of clusters during the motion of fluorine atoms along the directions indicated by the arrows in Fig. 5 show that when calcium atoms are replaced by lanthanum or REM atoms, the minimum on the curves in the vicinity of a binary or trigonal position becomes deeper, which is in accordance with the above-mentioned experimental data. The bond occupancies according to Mulliken for the Ca–F bonds are 0.08 for fluorine in the trigonal position and 0.134 for its position on the binary axis, which is noticeably lower than the analogous values for the La–F and Yb–F bonds (0.146 and 0.263, respectively). Thus, the effects of covalence in double fluorides of alkali-earth elements are also responsible for the experimentally observed coordination of interstitial fluorine ions.

5. QUANTUM-CHEMICAL SIMULATION OF THE ELECTRONIC STRUCTURE AND IONIC CONDUCTION OF δ-Bi_2O_3

The results of structural simulation of the well-known ionic conductor δ-Bi_2O_3 enabled us to analyze the peculiarities of its electronic structure and to choose a model that correctly describes its crystal structure.

In the nonempirical calculations carried out on the basis of the Sillen model, two oxygen vacancies were arranged along crystallographic axes {111}. In the Willis model, six oxygen atoms were randomly distributed over 32 vacant sites in the fluorite structure upon a displacement of oxygen atoms in directions to the centers of faces of the Bi_4 tetrahedra.

The total density of states in δ-Bi_2O_3 in the Sillen and Willis models is presented in Fig. 7. In the Willis model, the electron energy spectrum has three clearly manifested bands (Fig. 7b). The low-energy band (near –12.5 eV) corresponds to the 6*s* states of Bi. The density of states in the energy range from –8 to –3 eV is formed by the hybrid 2*p*O–6*p*Bi states. The conduction band is of the metallic type and is formed mainly by the *p* states of Bi. The valence band of bismuth oxide is filled completely. An analysis of the calculated data shows that the Willis model describes the crystalline structure of δ-Bi_2O_3 more accurately than the Sillen model. First, the electron energy spectrum of δ-Bi_2O_3 in the Willis model displays a semiconducting gap whose presence can be explained by the statistical distribution of oxygen over the lattice and by an enhancement of the hybridization of atomic orbitals of bismuth and oxygen upon a displacement of oxygen from the center of the Bi_4 tetrahedron to trigonal positions. Second, the total energy of the crystal with oxygen atoms in trigonal positions is considerably lower than the energy of the crystal with oxygen distributed over octahedral and tetrahedral interstices. The Willis model is also in accordance with the traditional concepts of superconducting phases. The high ionic conductivity of these phases is determined by the presence of a large number of vacant positions with low potential barriers for migration.

Along with the analysis of the electronic structure of cubic bismuth oxide, we analyzed the chemical bond for the δ-Bi_2O_3, α-Bi_2O_3, and β-Bi_2O_3 phases using the Hückel method. The estimates of average overlap population of Bi–Bi and Bi–O bonds according to Mulliken are presented in Table 7. The calculations show that the interaction in the phases of bismuth oxide mainly occur due to the covalent Bi–O bonds. The average occupancy of the Bi–O bond in the series α-Bi_2O_3, β-Bi_2O_3, and δ-Bi_2O_3 gradually decreases and has a minimum value for the fluorite-like structure of bismuth oxide. The minimum overlap population of the Bi–O bond in δ-Bi_2O_3 corresponds to oxygen mobility in the structure of the cubic bismuth oxide, i.e., to a high ionic conductivity. The covalent component of the Bi–Bi bond in all modifications of bismuth oxides is virtually equal to zero.

Results of the analysis of the electronic structure and chemical bond were used for studying the possible models of conduction in cubic bismuth oxide. In the fluorite-like structure δ-Bi_2O_3, two mechanisms of migration of oxygen ions are possible in accordance with the Willis model: through the centers of the Bi_4 tetrahedra and of the Bi_6 octahedra or through tetrahedra and trigonal pyramids, bypassing octahedral interstices. The preferability of either of the mechanisms was estimated from the difference in the total energies of a perfect crystal and a crystal with an oxygen atom shifted to octahedral or tetrahedral interstices. The results of analysis proved that the total energy of the crystal changes by 0.7 eV when an oxygen atom is shifted to a tetrahedral interstice and by 3.2 eV in the case of an octahedral interstice. We can assume that the migration of oxygen ions takes place through tetrahedral voids in the fluorite structure rather than through octahedral positions.

An analysis of the curves describing the overlap population of crystalline orbitals for the Bi–O bond (Fig. 8) and the scheme of formation of the chemical bond (Fig. 9) in δ-Bi_2O_3 made it possible to explain the instability of the fluorite structure of the solid electrolyte. The top of the upper filled band (Fig. 8) is determined by the uncompensated antibonding of the 6*s*Bi, 6*p*Bi, and 2*p*O states. The antibonding nature of the hybridization of the 6*s* and 6*p* states of the Bi and 2*p* states of O suppresses the Bi–O interactions. The introduction of double-charged cations (Ca^{2+}, Sr^{2+}, etc.) reduces the antibonding of 6*s*, 6*p*Bi–2*p*O. The addition of highly covalent ions without low-energy *s* states (V, Nb, Ta, Cr, Mo, W) and trivalent cations having no *s* level lower and close to the energy of the 2*p* state of oxygen (REMs and Y) does not lead to the splitting of the 2*p* state of oxygen in the 6*p*Bi field. The above-listed cations can be used as stabilizers of the crystalline structure of δ-Bi_2O_3. Small admixtures of lead, tin, and antimony oxides virtually do not change the band structure of pure δ-Bi_2O_3.

6. EFFECT OF INTERACTION BETWEEN DEFECTS ON THE ELECTRONIC STRUCTURE AND IONIC CONDUCTIVITY OF STABILIZED ZIRCONIUM OXIDE

Using the nonempirical LMTO method, we calculated the electronic structure of stabilized zirconium oxide, which corresponds to a phase with composition 0.875 ZrO_2–0.125 CaO (Fig. 10). The admixtures of CaO and $YO_{1.5}$ do not introduce considerable changes in the electron energy spectrum of purely cubic zirconium oxide. The total density of states for ZrO_2–CaO (Fig. 10) is characterized by two wide bands. The low-energy valence band is mainly formed by hybrid 2*p* states of oxygen and 4*d* states of zirconium. The conduction band is of the metal type and is mainly formed by the 4*d* states of zirconium atoms. The *d* band is split into t_{2g} and e_g subbands. The narrow peak observed in the region of the forbidden gap near the bottom of the conduction band is formed by the 4*d* states of zirconium atoms from the nearest neighborhood of oxygen vacancies and the *s* states of the vacancies themselves. After the formation of such states, the

Table 7. Average bond population by Mulliken for α-Bi_2O_3, β-Bi_2O_3, and δ-Bi_2O_3

Phase	Bond population	
	Bi–O	Bi–Bi
α-Bi_2O_3	0.15	0.05
β-Bi_2O_3	0.14	0.01
δ-Bi_2O_3	0.07	0.00

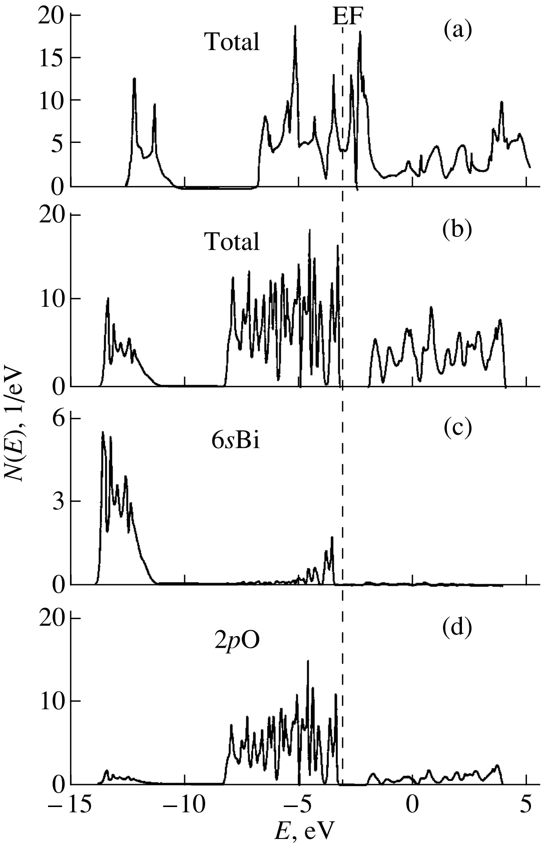

Fig. 7. Total and partial densities of states ($N(E)$) of δ-Bi_2O_3 according to (a) the Sillen and (b, c, d) Willis models.

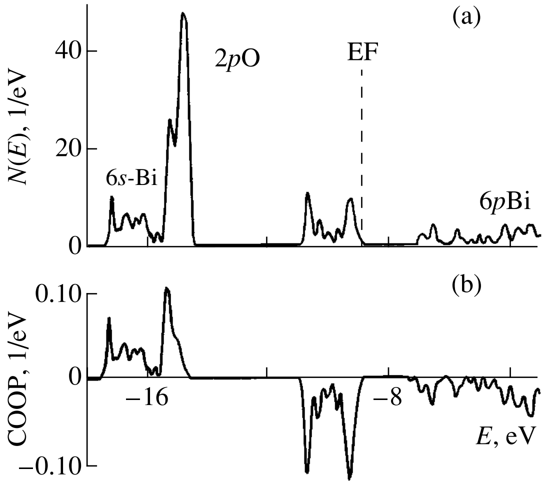

Fig. 8. (a) Total density of states ($N(E)$) and (b) Mulliken overlap population (COOP) of the Bi–O bond.

forbidden gap width between the filled valence band mainly formed by the 2p states of oxygen and the empty conduction band decreases. The electron energy spectrum of the ZrO_2–$YO_{1.5}$ phase virtually coincides with the electronic structure of the phase with composition 0.875 ZrO_2–0.125 CaO.

The Hückel band method was used for determining the main types of interaction and the chemical-bond strength in doped zirconium oxide. The results of analysis by Mulliken (Table 8) indicate that the covalent component of the Zr–O bond slightly increases in 0.875 ZrO_2–0.125 CaO and does not change in 0.75 ZrO_2–0.25 $YO_{1.5}$ as compared to pure ZrO_2. The Zr–O interactions are the strongest for Zr atoms from the first vacancy coordination shell. Strengthening of the Zr–O chemical bond is observed upon an increase in the number of vacancies per computational cell. The Ca–Zr and Zr–Zr interactions are virtually absent. An analysis of these results makes it possible to explain the increase in the structural stability of the cubic zirconium dioxide through the local strengthening of the Zr–O chemical bond upon the introduction of Ca atoms and through the emergence of the Y–O covalent bond as a result of the electron density redistribution upon the introduction of Y atoms.

Table 8. Analysis of bond population in ZrO_2 and in ZrO_2–CaO and ZrO_2–Y_2O_3 solid solutions

Phase	Average bond population			
	Zr–O	Zr–Zr	*Me*–O *Me* = Ca, Y	*Me*–Zr
ZrO_2	0.238	0.000	–	–
0.875ZrO_2–0.125CaO	0.247	0.000	0.071	−0.008
0.75ZrO_2–0.25CaO	0.253	0.000	0.080	−0.007
0.75ZrO_2–0.25$YO_{1.5}$	0.233	0.000	0.288	0.001

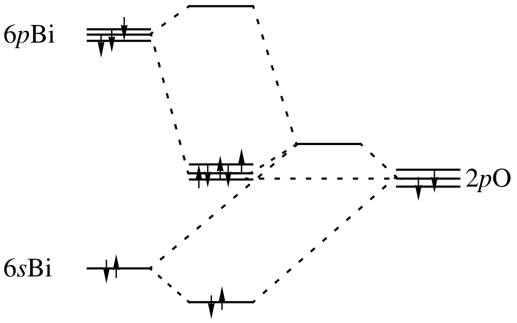

Fig. 9. Schematic diagram of formation of hybrid bonds in the three-level system of δ-Bi_2O_3.

On the basis of *ab initio* calculations, we could also explain the anomalous behavior of some physicochemical properties of doped zirconium oxide with fluorite structure.

In numerous publications [18, 19, 59–61], a peak on the electrical conductivity–composition isotherms for oxide electrolytes with fluorite structure was detected in the region of 15–20 mol %. While the ascending segment of the isotherm corresponds to the theory predicting a continuous increase in electrical conductivity with increasing impurity concentration [18], its descending segment contradicts this theory. Attempts to explain the extreme behavior of the ionic conductivity of solid cubic electrolytes were made by O'Keefe [62] and Carter and Roth [63]. However, the concepts put forth by O'Keefe concerning the existence of only the repulsion between identically charged vacancies in the anionic sublattice were not confirmed and contradict experimental data on the tendency to the formation of bivacancies [64]. The model of charge transport by associated defects proposed in [63] was not confirmed either.

On the basis of the nonempirical approach, we studied the clusterization of impurities presumed in the Carter and Roth models as the possible reason behind the decrease in conductivity for high dopant concentrations (exceeding 14 mol %) in the ZrO_2–$YO_{1.5}$ and ZrO_2–CaO systems.

We studied the dependence of the total energy of the crystal per computational cell on the number of defects and calculated the mean energy of interaction of a defect with its surroundings. In our calculations, we assumed that defects in the ZrO_2 structure (calcium cations and vacancies) exist in the form of Ca–V dipoles which are separated by the shortest possible distance (the Ca–Ca distance is equal to 3.726 Å). The difference between the calculated values of the total energy E_{tot} and its linear component equal to 5983.3608n (Ry) is presented in Fig. 11. The linear component was determined as the product of the number of dipoles and

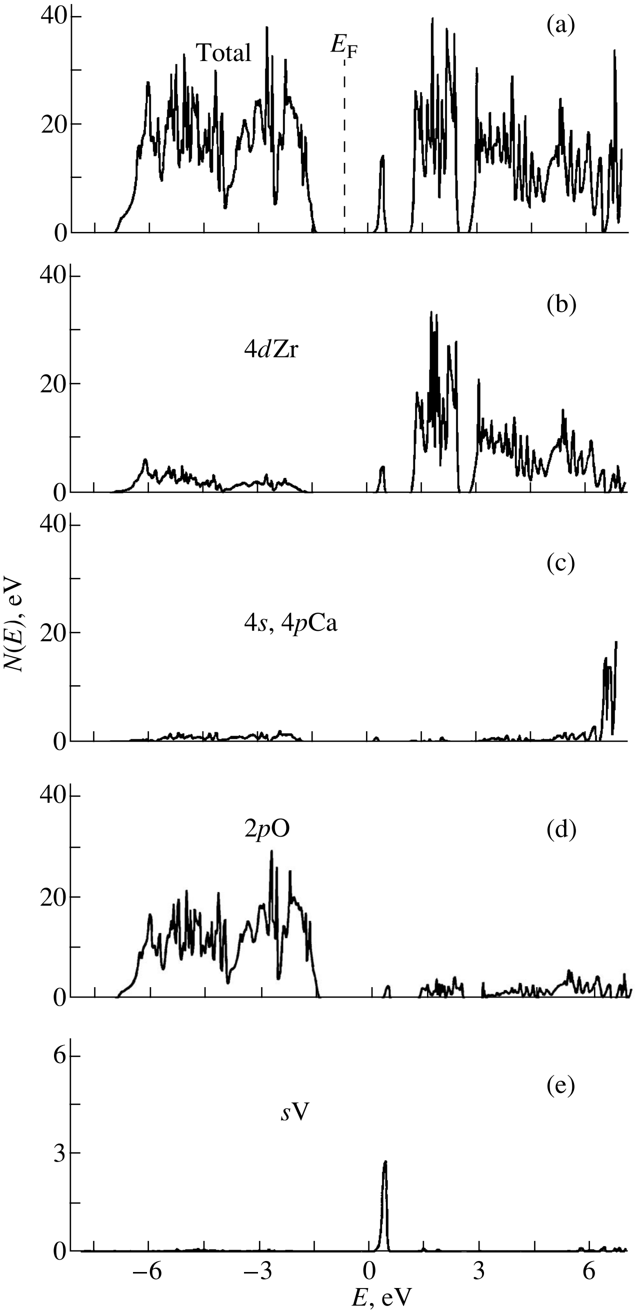

Fig. 10. (a) Total ($N(E)$) and (b–e) partial densities of states for a crystal of composition 0.875 ZrO_2–0.125 CaO.

the value of the total energy (per unit cell) of the crystal with a single dipole. In fact, we obtained the energy of interaction of defects as a function of their concentration n. In the entire range of n, the energy of interaction is negative, which indicates the existence of attraction between dipoles, thus lowering the value of the total energy. The used algorithm allows us to estimate the interaction energy between one dipole and all the remaining dipoles as $(E_{tot} – 5983.3608n)/n$. The calculated mean interaction energy per dipole was 1.1 eV.

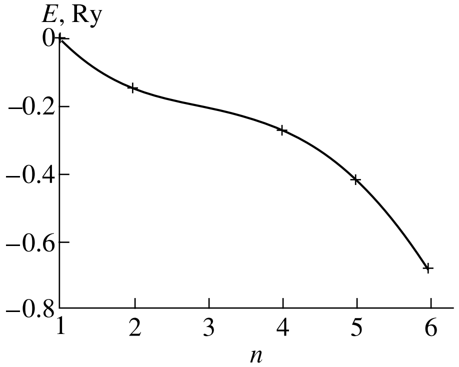

Fig. 11. Dependence of the interaction energy E between defects on their number n.

Thus, the strong interaction between Ca–V and Y–V–Y defects (clusterization) in the ZrO_2–CaO and ZrO_2–$YO_{1.5}$ systems reduces the concentration of charge carriers (mobile oxygen vacancies) and is a factor that determines the behavior of the transport properties (in particular, it lowers the ionic conductivity at high concentrations of the admixture).

7. CONCLUSIONS

The main results obtained by us here can be summarized as follows.

(1) The influence of defects on the electronic structure of a number of ionic conductors with fluorite structure, MeF_2 (Me = Ca, Sr, Ba, Pb), ZrO_2–CaO, ZrO_2–Y_2O_3, and δ-Bi_2O_3, is determined. The states responsible for the electron transport are analyzed. It is shown that in the case of δ-Bi_2O_3, the Willis model is preferable to the Sillen model.

(2) For fluorides of alkali-earth elements, a nonempirical scheme of calculation of the energy of formation and interaction of anti-Frenkel defects is developed. The obtained values of these quantities reproduce the experimentally observed tendency towards a decrease of the AFDs formation energy in the series CaF_2, SrF_2, BaF_2, and PbF_2.

(3) The interaction between point defects is studied. The clusterization of defects following from the results of nonempirical calculations is found to be responsible for the origin of the superionic state in fluorides of alkali-earth elements and PbF_2 and the extremal behavior of the ionic conductivity of doped zirconium oxide with fluorite structure.

(4) It is shown that the phenomenologically introduced approximation $E = N_2(\omega x - \lambda x^2/2)$ holds for fluorides of alkali-earth elements and PbF_2 to a high degree of accuracy. The calculated parameters (ω and λ) of this theory lead to reasonable values for the temperatures of transition to the superionic state.

(5) The influence of the covalence effects in the compounds CaF_2, SrF_2, BaF_2, PbF_2, δ-Bi_2O_3, and ZrO_2–CaO on the geometry of defects, the stability of conducting phases, and transport properties is considered.

(6) The possible ways of ionic transport in oxide and fluoride conductors with fluorite structure are analyzed.

The obtained results of investigations demonstrate broad prospects for the application of quantum-chemical computational methods in analysis of the physicochemical properties of solid electrolytes. These results can be used for calculating the parameters of ionic conduction of a number of solid electrolytes. The results of nonempirical calculations make it possible to analyze the effect of the processes of defect formation on the macroscopic properties of solid-phase compounds.

Further advances in the application of quantum-chemical methods in analyzing ionic transport can be made by improving the accuracy of the calculations of the ionic conduction parameters with the help of more accurate methods of calculation of the electronic structure: the full-potential LMTO method [65] and the Hartree–Fock method [66]. The dynamic characteristics of ionic conduction can be studied using the Car–Parrinello method [67], whose application is restricted at present due to the inadequate capacity of computers.

ACKNOWLEDGMENTS

This work was supported by the Russian Foundation for Basic Research, project no. 98-03-33188a.

REFERENCES

1. A. V. Chadwick, Solid State Ionics **8** (3), 209 (1983).
2. W. Hayes, *Crystals with the Fluorite Structure* (Clarendon, Oxford, 1974).
3. S. Geller, *Solid Electrolytes* (Springer-Verlag, New York, 1977).
4. P. Hagenmuller, *Inorganic Solid Fluorides. Chemistry and Physics* (Academic, New York, 1985).
5. M. Scrocco, Phys. Rev. B **32** (2), 1301 (1985).
6. W. Hayes, A. B. Kunz, and E. E. Koch, J. Phys. C **4** (10), 1200 (1971).
7. V. V. Nemoshkalenko, V. G. Aleshin, I. A. Brytov, *et al.*, Izv. Akad. Nauk SSSR, Ser. Fiz. **38** (3), 628 (1974).
8. J. Kudrnovsky, N. E. Christensen, and J. Masek, Phys. Rev. B **43** (15), 12597 (1991).
9. N. V. Starostin and V. A. Ganin, Fiz. Tverd. Tela (Leningrad) **15** (11), 3404 (1973) [Sov. Phys. Solid State **15**, 2265 (1973)].
10. N. I. Medvedeva, V. P. Zhukov, D. L. Novicov, *et al.*, J. Phys. Chem. Solids **57**, 1243 (1996).
11. E. V. Stefanovich, A. L. Shluger, and C. R. A. Catlow, Phys. Rev. B **49**, 11560 (1994).
12. G. A. Ol'khovic, I. I. Naumov, and O. I. Velikokhatnyi, J. Phys.: Condens. Matter **7**, 1273 (1995).
13. R. H. French, S. J. Glass, F. S. Ohuchi, *et al.*, Phys. Rev. B **49**, 5133 (1994).
14. R. W. Grimes, C. R. A. Catlow, and A. M. Stoneham, J. Phys.: Condens. Matter **1** (40), 7367 (1989).
15. O.-K. Andersen and O. Jepsen, Physica B (Amsterdam) **91**, 317 (1977).
16. O.-K. Andersen, Phys. Rev. B **12**, 3060 (1975).
17. R. Hoffman, *Manuals for Extended Huckel Calculations* (Cornell Univ., Ithaca, 1989).
18. V. N. Chebotin and M. V. Perfil'ev, *Electrochemistry of Solid Electrolytes* (Khimiya, Moscow, 1978).
19. U. A. Ukshe and N. G. Bukin, *Solid Electrolytes* (Nauka, Moscow, 1977).
20. A. K. Cheetham, B. E. F. Fender, and M. J. Cooper, J. Phys. C **4**, 3107 (1971).
21. D. Steele and P. E. F. Childs, J. Phys. C **5**, 2677 (1972).
22. H. A. Harwig, Z. Anorg. Chem. **44**, 151 (1978).
23. L. G. Sillen, Ark. Kemi, Mineral. Geol. A **12**, 1 (1937).
24. G. Gattow and H. Schutze, Z. Anorg. Allg. Chem. **328**, 44 (1964).
25. B. T. M. Willis, Proc. R. Soc. London, Ser. A **274**, 134 (1963).
26. Yu. Ya. Gurevich, A. K. Ivanov-Shits, and Yu. I. Kharkats, Usp. Khim. **50** (11), 1960 (1981).
27. *Transport Processes in Solid Electrolytes and in Electrodes*, Ed. by J. Hladik (Academic, London, 1974; Mir, Moscow, 1978).
28. A. B. Lidiard, in *Handbuch der Physik*, Ed. by S. Flugge (Springer-Verlag, Berlin, 1957), p. 246.
29. A. N. Murin, *Chemistry of Imperfect Crystals* (Leningr. Gos. Univ., Leningrad, 1975).
30. W. Kohn and L. J. Sham, Phys. Rev. A **140**, 1133 (1965).
31. J. Kudrnovsky, V. Drchal, and J. Masek, Phys. Rev. B **35**, 2487 (1987).
32. O.-K. Andersen, Z. Pawlowska, and O. Jepsen, Phys. Rev. B **34**, 5253 (1986).
33. O.-K. Andersen, O. Jepsen, and M. Sob, in *Electronic Band Structure and Its Applications* (Springer-Verlag, Berlin, 1987).
34. O.-K. Andersen, in *The Electronic Structure of Complex Systems* (Plenum, New York, 1984).
35. O.-K. Andersen and O. Jepsen, Phys. Rev. Lett. **53** (27), 2571 (1984).
36. W. R. L. Lambrecht and O.-K. Andersen, Phys. Rev. B **34**, 2439 (1986).
37. P.-O. Löwdin, J. Chem. Phys. **19** (11), 1396 (1951).
38. G. Krier, O. Jepsen, A. Burkhardt, and O.-K. Andersen, *The TB–LMTO–ASA Program* (MPI für Festkorperforshung, Stuttgart, 1996).
39. O.-K. Andersen, A. V. Postnikov, and S. Yu. Savrasov, Mater. Res. Soc. Symp. Proc. **253**, 37 (1992).
40. M. H. Whangbo and R. Hoffman, J. Am. Chem. Soc. **100**, 6093 (1978).
41. S. Alvarez, *Tables of Parameters for Extended Huckel Calculations* (Uversitat de Barcelona, Barcelona, 1989).
42. V. P. Zhukov and V. M. Zaĭnullina, Fiz. Tverd. Tela (St. Petersburg) **40** (11), 2019 (1998) [Phys. Solid State **40**, 1827 (1998)].

43. J. H. Beaumont, W. Hayes, D. L. Kirk, and G. P. Summers, Proc. R. Soc. London, Ser. A **315** (1520), 69 (1970); A. M. Stoneham, *Theory of Defects in Solids: The Electronic Structure of Defects in Insulators and Semiconductors* (Clarendon Press, Oxford, 1975; Mir, Moscow, 1978), Vol. 2.
44. A. K. Ivanov-Shits and N. I. Sorokin, Solid State Ionics **36**, 7 (1989).
45. A. K. Ivanov-Shits, N. I. Sorokin, P. P. Fedorov, and B. P. Solovev, Solid State Ionics **31**, 269 (1989).
46. A. K. Ivanov-Shits, N. I. Sorokin, P. P. Fedorov, and B. P. Solovev, Solid State Ionics **31**, 253 (1989).
47. B. A. Huberman, Phys. Rev. Lett. **32** (18), 1000 (1974).
48. Yu. Ya. Gurevich and Yu. I. Kharkats, Itogi Nauki Tekh., Ser. Khim. Tverd. Tela **4**, 3 (1987).
49. Yu. Ya. Gurevich and Yu. I. Kharkats, Usp. Fiz. Nauk **136** (4), 693 (1982) [Sov. Phys. Usp. **25**, 257 (1982)].
50. V. N. Chebotin and V. I. Tsidil’kovskiĭ, Élektrokhimiya **16** (5), 651 (1980).
51. J. Schoonman, Solid State Ionics **1** (1–2), 121 (1980).
52. R. Dronskowski and P. E. Blochl, J. Phys. Chem. **97**, 8617 (1993).
53. *Physics of Superionic Conductors*, Ed. by M. B. Salamon (Springer-Verlag, New York, 1979; Zinatne, Riga, 1982).
54. M. J. Cooper and K. D. Rouse, Acta Crystallogr., Sect. A: Cryst. Phys., Diffr., Theor. Gen. Crystallogr. **A27**, 622 (1971).
55. M. J. Cooper and K. D. Rouse, Acta Crystallogr., Sect. A: Cryst. Phys., Diffr., Theor. Gen. Crystallogr. **A24**, 484 (1968).
56. A. K. Ivanov-Shits, N. I. Sorokin, P. P. Fedorov, and B. P. Sobolev, Solid State Ionics **37**, 125 (1990).
57. V. B. Aleksandrov and L. S. Garashina, Dokl. Akad. Nauk SSSR **189**, 307 (1969) [Sov. Phys. Dokl. **14**, 1040 (1970)].
58. L. A. Muradyan, B. A. Maksimov, and V. I. Simonov, Koord. Khim. **12**, 1398 (1986).
59. T. H. Etsell and S. N. Flengas, Chem. Rev. **70**, 339 (1970).
60. J. M. Dixon, L. D. LaGrange, U. Merten, *et al.*, J. Electrochem. Soc. **110**, 276 (1963).
61. É. Kh. Kurumchin, Author’s Abstract of Doctoral Dissertation (Inst. Élektrokhimii Ural. Otd. Ross. Akad. Nauk, Yekaterinburg, 1997).
62. M. O’Keefe, in *The Chemistry of Extended Defects in Nonmetallic Solids*, Ed. by E. Le Roy and M. O’Keefe (North-Holland, Amsterdam, 1970).
63. R. E. Carter and W. L. Roth, in *Electromotive Force Measurements in High Temperature Systems* (Inst. of Mining and Metallurgy, London, 1968).
64. M. R. Thornber and D. J. Bevan, J. Solid State Chem. **1**, 536 (1970).
65. M. Methfessel, Phys. Rev. B **38**, 1537 (1988).
66. C. Pisani, R. Dovesi, and C. Roetti, in *Lecture Notes in Chemistry* (Springer-Verlag, Berlin, 1988), Vol. 48.
67. R. Car and M. Parrinello, Phys. Rev. Lett. **55**, 2471 (1985).

Translated by N. Wadhwa

Physics of the Solid State, Vol. 43, No. 9, 2001, pp. 1700–1702. Translated from Fizika Tverdogo Tela, Vol. 43, No. 9, 2001, pp. 1632–1634.

DEFECTS, DISLOCATIONS, AND PHYSICS OF STRENGTH

Magnetosensitive Intermediate States of Point-Defect Complexes Formed as a Result of Quenching of NaCl : Eu Single Crystals

R. B. Morgunov and A. A. Baskakov
Derzhavin State University, Tambov, 392622 Russia
e-mail: morgunov@tsu.tmb.ru

Received January 30, 2001

Abstract—A correlation between temporal variation in the optical and mechanical properties of quenched NaCl : Eu single crystals and the sensitivity of these crystals to a constant magnetic field was found. The results obtained make it possible to assess the atomic structure of magnetosensitive point-defect complexes. *© 2001 MAIK “Nauka/Interperiodica”.*

Recently, a number of phenomena related to the effect of a magnetic field with the induction $B \sim 1$ T on the state of point-defect complexes in crystals with various types of interatomic bonding have been discovered and actively discussed. Such magnetosensitive complexes have been observed in the ionic [1, 2], ionic–covalent [3], and covalent (Si and Ge) [4] crystals, in metal–oxide–semiconductor structures [5, 6], and so on. Modification of magnetosensitive complexes in a magnetic field affects many structure-sensitive microproperties of solids: mechanical [1–3], optical [3], and electrical [4–6]. We emphasize that residual variations in these properties are observed over a long period of time after the magnetic field has been turned off (over several days), which markedly differentiates the aforementioned phenomena from those in which variations in plasticity [7–9] or, e.g., photocurrent [10–12], are observed only during exposure to a magnetic field.

The main cause of the difficulties encountered in gaining insight into the mechanisms governing the effect of a magnetic field on magnetosensitive complexes and in explaining the corresponding magnetoplastic and other phenomena related to the influence of a magnetic field on physical properties of crystals is the lack of information on the atomic structure of these complexes. In our opinion, the key to solving this problem consists in identifying the stage of aggregation of impurities into complexes and the formation of magnetosensitive complexes. The results obtained should be compared with numerous experimental data on aggregation of impurities into defect complexes in the absence of a magnetic field [13–17].

Thus, the objective of this study was to provide experimental conditions for studying the kinetics of the initiation and disappearance of magnetosensitive complexes in a magnetic field and in its absence.

The most through studies of the various transformational stages of point-defect complexes as a result of quenching have been conducted on ionic crystals with an Eu impurity [15–22]. This is due to the fact that the appearance of different charge states of this impurity can be deduced from variations in the ESR spectra [16, 18], in the dielectric-loss tangent [17, 20], and in luminescence [17–19], which occur with the amount of time elapsed after quenching. Therefore, NaCl : Eu (0.1 wt %) crystals were used in this study. The crystals were quenched prior to each experimental; this was done by rapidly cooling the crystals in an air atmosphere from 920 K, at which temperature the crystals were preliminarily kept for 2 h.

We used the Vickers microhardness H as an indicator of the impurity state that can change under the effect of thermal treatment or a magnetic field. The microhardness was measured in all experiments, the load applied to the indenter amounted to 0.2 N, and the duration of loading was equal to 10 s. Each point in a plot of $H(t)$ is a result of averaging of 40–50 individual measurements. This made it possible to reduce the relative error for determining the value of H to 0.5%, which corresponded to a single mark on the scale of the microscrew in a conventional PMT-3 microhardness gage where the indentation-diagonal length was equal to 145 scale divisions. In addition, we assessed the variations in the state of impurity from changes in the spectra of photoluminescence excited with light with a wavelength of $\lambda = 350$ nm.

It was found that in the absence of a magnetic field, the microhardness of the crystals varied nonmonotonically with time t when the crystals were kept at $T = 293$ K after quenching (Fig. 1a, curve *1*). In a special run, it was verified that similar variations were also observed upon indentation of the crystals, which fractured only immediately before indentation of the freshly formed surface rather than immediately after quenching. Consequently, nonmonotonic variations in H are related to changes in the state of impurities in the bulk crystal and cannot be accounted for by random variations in the atmosphere-sensitive surface properties of the samples.

If the quenched crystals were subjected to a magnetic field pulse (with an amplitude of 7 T and a duration of 10 ms) after being kept for time t at $T = 293$ K after quenching and then were indented, the microhardness was found to be lesser (in a narrow time range of $30 < t < 100$ h) than in the experiments without a magnetic field (Fig. 1a, curve *2*). If the crystals were kept for a long time at $T = 293$ K after quenching, H tended asymptotically to the initial value H_0 (irrespective of whether the crystal were subjected to a magnetic field), which corresponds to the hardness of unquenched crystals (the dashed straight line in Fig. 1a).

The peak in the luminescence spectra I for NaCl : Eu was observed at $\lambda = 427$ nm irrespective of the thermal history of the crystals (see the inset in Fig. 1b). After quenching, nonmonotonic temporal variations in the peak luminescence intensity I_{max} were also observed (Fig. 1b). The highest sensitivity of H to a magnetic field for $t = 30$ h corresponded to a decrease in the luminescence intensity I_{max} to a minimum. For $t \gg 30$ h, the luminescence intensity first increased and then decreased to a level much lower than its value shortly after quenching.

We note that in the initial stage of relaxation in a subsystem of point defects (immediately after quenching), the Eu^{2+} impurity ions are, as a rule, in a disperse state in the form of isolated impurity–vacancy dipoles [16, 17].

Consequently, the variations in H and I_{max} after quenching are apparently caused by the formation of various complexes consisting of the impurity–vacancy dipoles Eu^{2+}–V. The observed luminescence at λ = 427 nm corresponds to electron transitions from the excited state $4f^65d$ to the ground state $4f^7(^8S_{7/2})$ in Eu^{2+} ions in isolated dipoles that are not incorporated in the complexes [17]. A change in the crystalline surroundings of these ions as the dipoles are combined into complexes leads to a shift of the peak in the band of optical absorption by the impurity and to changes in the luminescence intensity I [17, 18]. Therefore, the temporal variation in I represents the process of dipole transformation of the first aggregation products (dimers and trimers) into more involving complexes, of which the precipitates of the Na_2EuCl_4 second phase (with the CsCl lattice) and of the $EuCl_2$ phase (with the CaF_2 lattice) have only been studied adequately. However, these precipitates only form within several months or even years at $T = 293$ K [17]; therefore, the temporal variations in H and I_{max} observed in this study cannot be accounted for by the origination of new phases.

Thus, by comparing Figs. 1a and 1b, we may conclude that a magnetic field affects the intermediate unstable point-defect complexes that are formed at the initial stage of the impurity aggregation. The insensitivity of microhardness to a magnetic field within the first few hours after quenching (for $t < 20$ h) means that the isolated dipoles and dimers that exist at this stage are not affected by exposing the crystals to a magnetic field.

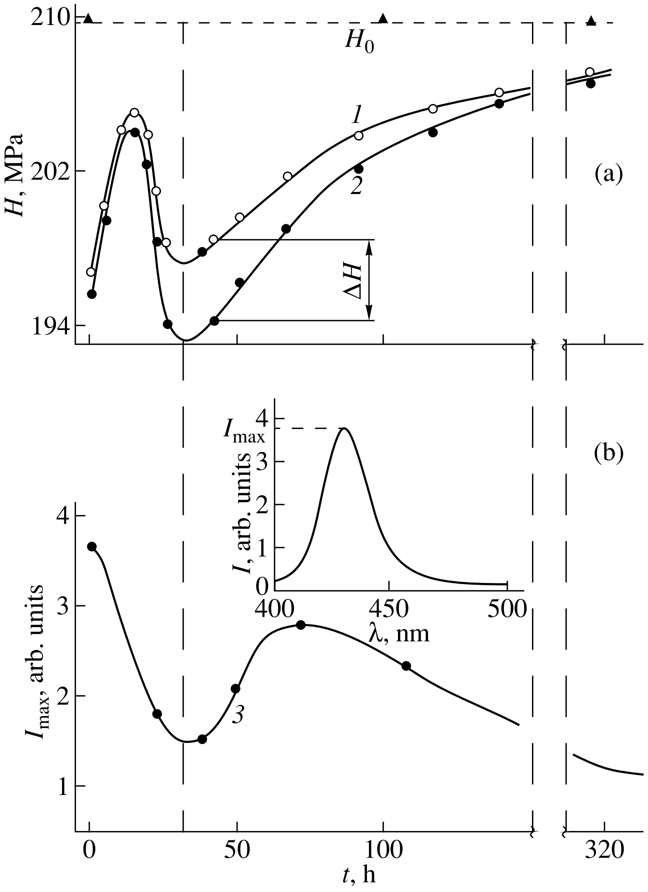

Fig. 1. (a) Dependences of microhardness H on time t elapsed from quenching of (*1*) the samples that were not subjected to a magnetic field and (*2*) the samples subjected before indenting to a single magnetic-field pulse with $B = 7$ T and duration of 10 ms. H_0 stands for the microhardness of the crystals that were not subjected to preliminary quenching or were kept for several years at room temperature after quenching, and ΔH stands for the change in microhardness caused by a magnetic-field pulse. (b) Dependence of the peak intensity I_{max} of luminescence excited with light with the wavelength λ_{ex} = 350 nm upon elapsed time from quenching (curve *3*). The dependence of the luminescence intensity I on the emission wavelength λ to which the photodetector is tuned is shown in the inset.

Thus, the data make it possible to formulate the following qualitative conclusions.

(1) A magnetic field does not affect isolated impurity–vacancy complexes and the primary aggregation products (dimers), which are present in the crystal in the initial stage of postquenching relaxation.

(2) A magnetic field affects the intermediate unstable Eu complexes that have their origin in dipoles, dimers, and trimers, and appears well before the precipitates and comparatively stable nuclei of the second phase are formed.

(3) The final result of the multistage relaxation process is independent of the magnetic field and merely enhances the rate of one of the intermediate reactions of relaxation in a subsystem of point defects, much the same as it occurs in the liquid- and solid-phase chemical reactions in organic materials [23].

Unambiguous identification of the intermediate point-defect complexes sensitive to a magnetic field and the determination of their atomic structure require further investigation.

ACKNOWLEDGMENTS

This study was supported by the Russian Foundation for Basic Research (project no. 00-02-16094) and the Program “Universities of Russia, Basic Research.”

REFERENCES

1. Yu. I. Golovin, R. B. Morgunov, and A. A. Dmitrievckii, Mater. Sci. Eng., A **288**, 261 (2000).
2. Yu. I. Golovin, R. B. Morgunov, V. E. Ivanov, *et al.*, Pis’ma Zh. Éksp. Teor. Fiz. **68** (5), 400 (1998) [JETP Lett. **68**, 426 (1998)].
3. Yu. I. Golovin, R. B. Morgunov, A. A. Baskakov, and M. V. Badylevich, Pis’ma Zh. Éksp. Teor. Fiz. **69** (2), 114 (1999) [JETP Lett. **69**, 127 (1999)].
4. M. N. Levin and B. A. Zon, Zh. Éksp. Teor. Fiz. **111** (4), 1373 (1997) [JETP **84**, 760 (1997)].
5. A. G. Kadmenskiĭ, S. G. Kadmenskiĭ, M. N. Levin, *et al.*, Pis’ma Zh. Tekh. Fiz. **19** (3), 41 (1993) [Tech. Phys. Lett. **19**, 86 (1993)].
6. M. N. Levin, Yu. O. Lichmanov, and V. M. Maslovskiĭ, Pis’ma Zh. Tekh. Fiz. **20** (4), 27 (1994) [Tech. Phys. Lett. **20**, 145 (1994)].
7. Yu. I. Golovin and R. B. Morgunov, Pis’ma Zh. Éksp. Teor. Fiz. **61** (7), 583 (1995) [JETP Lett. **61**, 596 (1995)].
8. V. I. Al’shits, E. V. Darinskaya, and E. A. Petrzhik, Fiz. Tverd. Tela (Leningrad) **33** (10), 3001 (1991) [Sov. Phys. Solid State **33**, 1694 (1991)].
9. V. I. Al’shits, N. N. Bekkauer, A. E. Smirnov, and A. A. Urusovskaya, Zh. Éksp. Teor. Fiz. **115** (3), 951 (1999) [JETP **88**, 523 (1999)].
10. E. L. Frankevich and A. I. Pristupa, Izv. Akad. Nauk SSSR, Ser. Fiz. **50** (2), 220 (1986).
11. E. L. Frankevich and E. I. Balabanov, Pis’ma Zh. Éksp. Teor. Fiz. **1** (6), 33 (1965) [JETP Lett. **1**, 169 (1965)].
12. Yu. A. Osip’yan, R. K. Nikolaev, S. Z. Shmurak, *et al.*, Fiz. Tverd. Tela (St. Petersburg) **41** (11), 2097 (1999) [Phys. Solid State **41**, 1926 (1999)].
13. M. Dubiel, G. Berg, and F. Fröhlich, Phys. Status Solidi B **89**, 595 (1978).
14. M. Dubiel, G. Berg, and F. Fröhlich, Phys. Status Solidi A **55**, 153 (1979).
15. J. Garcia, J. Hernandez, E. Carillo, and J. Rubio, Phys. Rev. B **21** (11), 5012 (1980).
16. A. Muňoz, E. Cabrera, H. Riveros, et al., Phys. Rev. B 31 (12), 8196 (1985).
17. J. Rubio, J. Phys. Chem. Solids **52** (1), 101 (1991).
18. E. Orozco, J. Soullard, C. Zaldo, and F. Agulló-López, Philos. Mag. A **50** (3), 425 (1984).
19. C. Zaldo, E. Orozco, A. Mendoza, and J. Rubio, J. Phys. D **18**, 247 (1985).
20. R. W. Dreyfus and R. B. Laibowitz, Phys. Rev. A **135** (5), 1413 (1964).
21. A. L. Guerrero, S. C. Jain, and P. L. Pratt, Phys. Status Solidi A **49**, 353 (1978).
22. J. Poźniak, G. Berg, and T. Galbatar, Phys. Status Solidi B **143**, 37 (1987).
23. Ya. B. Zel’dovich, A. L. Buchachenko, and E. L. Frankevich, Usp. Fiz. Nauk **155** (1), 3 (1988) [Sov. Phys. Usp. **31**, 385 (1988)].

Translated by A. Spitsyn

Physics of the Solid State, Vol. 43, No. 9, 2001, pp. 1703–1711. Translated from Fizika Tverdogo Tela, Vol. 43, No. 9, 2001, pp. 1635–1642.
Original Russian Text Copyright © 2001 by Al'shits, Darinskaya, Koldaeva.

Dislocation Dynamics in Pulse-Loaded NaCl Crystals

V. I. Al'shits, E. V. Darinskaya, and M. V. Koldaeva
Institute of Crystallography, Russian Academy of Sciences, Leninskiĭ pr. 59, Moscow, 117333 Russia
e-mail: alshits@ns.crys.ras.ru

Received December 22, 2000; in final form, February 14, 2001

Abstract—The mean path l of freshly introduced dislocations in NaCl crystals under the effect of triangular loading pulses $\tau(t)$ is shown to depend only on the pulse amplitude τ_m and be insensitive to the rate of stress growth. The replacement of triangular pulses with trapezoidal ones with a constant-load plateau (τ = const) extension of up to 60 min only insignificantly changes the $l(\tau_m)$ dependence. The data obtained are interpreted on the basis of the concept of quasi-static relaxation in a nonequilibrium system of dislocations subject to a combined effect of time-dependent applied stresses $\tau(t)$, coordinate-dependent internal stresses $\tau_i(x)$, and "dry friction" τ_p due to the pinning of dislocations by point defects. In such a model, the $l(\tau_m)$ dependence should saturate at $\tau_m > 2\tau_p$; this is in fact observed in the range of $0.2\tau_y < \tau_m < 0.3\tau_y$ (here, τ_y is the yield stress), which gives an estimate for the pinning stress $\tau_p \approx 0.1\tau_y$. Based on the model suggested, a series of experimentally confirmed predictions were obtained, e.g., a recipe of "switching-off" of anomalies. Thus, a preliminary treatment of the samples by a series of stress pulses or holding in a magnetic field, which transforms the system of fresh dislocations into a more equilibrium state, sharply decreases the density of mobile dislocations quasi-statically responding to a pulsed load. It is shown that the discussed anomalies of dislocation mobility should be observed only in sufficiently pure crystals, where $\tau_p \ll \tau_y$, and should be absent in contaminated crystals, where $\tau_p \sim \tau_y$. *© 2001 MAIK "Nauka/Interperiodica".*

INTRODUCTION

Usually, the dislocation motion in crystals under the effect of an applied stress τ is described in terms of their mean velocity v. The $v(\tau)$ dependence and the effects of the temperature, the type and concentration of impurities, and the shape and height of the Peierls relief on this dependence were studied experimentally and theoretically in various crystals in many hundreds of papers and were discussed at numerous scientific conferences. We here restrict ourselves to the first experimental work in this field performed by Johnston and Gilman [1] four decades ago on individual dislocations in LiF crystals. To date, that work is considered to be classical, since it attracted great attention to the field of dislocation dynamics, which has continued for more than twenty years.

Against this background, experimental evidences [2–6] of more complex behavior of dislocations, which could not be described in terms of the simple concept of the mean velocity v single-valuedly linked with the applied stress τ, remained almost unnoticed. For example, in experiments described in [4], the mean path of dislocations in LiF crystals under the action of trapezoidal stress pulses with a variable constant-load plateau was found to be independent of the pulse duration, since this path was "accumulated" mainly at the rise front of the pulse. Similar data were later obtained on crystals of KCl [5] and NaCl [6].

All this shows that the formal treatment of experimental data concerning the determination of the mean dislocation velocity v as the ratio of the mean path l to the duration of the stress pulse in some cases can lead to confusion. Even if such cases are considered as anomalies of dislocation behavior, we should understand the nature of these anomalies. Since until recently no complete clarity was reached in this question, the aim of this work was as follows. First of all, we had to check the real existence of these anomalies (using available pure NaCl crystals). Then (after these anomalies were revealed), we had to understand their nature, properties, and the possibilities of deriving physical information from the corresponding experimental dependences. Finally, we had to answer the main question: how the observed "specificity" of dislocation response to pulsed loading of a crystal correlates with the existing concepts of dislocation dynamics.

An essential factor that favored the realization of the purposes of our work was the technique of magnetically stimulated breaking-away of dislocations from point defects that was developed in our previous work [7] and ensured new possibilities for the choice of the strategy of the experimental study.

1. EXPERIMENTAL

For experiments, we used NaCl single crystals grown in LOMO (Leningrad. Optiko-Mekhanich. Ob"edinenie) with a yield stress $\tau_y \approx 0.5$ MPa and total concentration of impurities of no more than 10^{-3} wt %. Samples prepared by splitting along cleavage planes

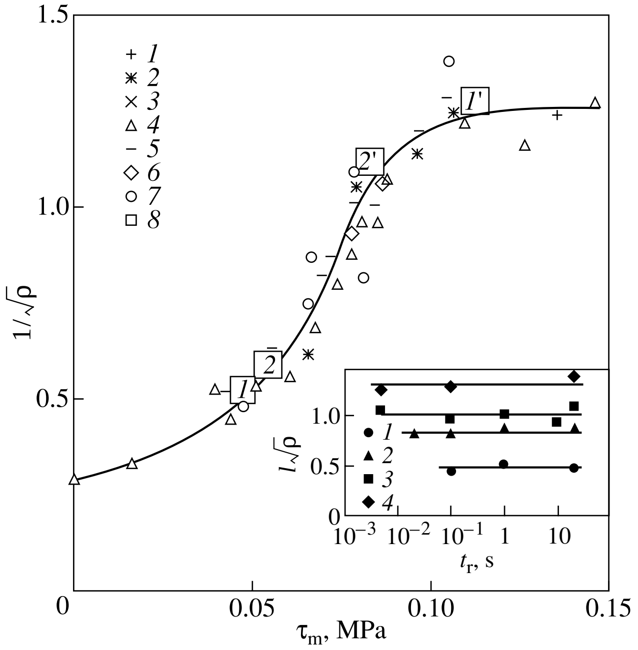

Fig. 1. Variation of the mean length of dislocation paths l referred to the mean spacing between dislocation $1/\sqrt{\rho}$ as a function of the amplitude τ_m of a triangular pulse for a series of pulse rise times t_r: (*1*) t_r = 1 ms, (*2*) 5 ms, (*3*) 20 ms, (*4*) 100 ms, (*5*) 1 s, (*6*) 10 s, and (*7*) 20 s. Points *8* are discussed in the main text. The inset displays the variation of $l\sqrt{\rho}$ as a function of the pulse rise time t_r for a series of amplitudes: (*1*) τ_m = 0.04, (*2*) 0.07, (*3*) 0.08, and (*4*) 0.11 MPa.

with dimensions of about 4 × 4 × 10 mm were subjected to prolonged annealing at 650°C followed by chemical polishing. Before the experiments, fresh dislocations were introduced by lightly striking the samples. The dislocations were detected by selective etching. The free path of individual edge dislocations and the local total density of dislocations ρ were measured in an optical microscope. From the histograms of the paths normalized to the average spacing between dislocations $1/\sqrt{\rho}$, the mean normalized path $l\sqrt{\rho}$ was calculated. Each histogram was based on 70–300 measurements of the paths.

The loading of the samples was performed in a special setup, which permitted us to create mechanical pulses with specified parameters [8]. Depending on the conditions of experiments, the control of the force that acted on a crystal was performed with the help of piezoelectric or strain gages located directly under the sample. The readings of the gages were recorded by either a storage oscilloscope or a chart recorder. For experiments, pulses were used with amplitudes τ_m = 0.015–0.35 MPa, rising times of the leading front t_r = 1 ms to 20 s, a constant-load plateau t_{f-t} = 0–60 min, and a constant time of the trailing edge of the pulse t_f = 1 s.

2. PRELIMINARY RESULTS

In the first series of experiments, we studied the displacement of dislocations under the action of triangular stress pulses with various amplitudes τ_m and various rising times of the pulse front t_r. The results are shown in Fig. 1. As is seen from this figure, with the small amplitudes used ($\tau_m < 0.3\tau_y$), the mean dislocation path l depends only on the pulse amplitude, being virtually insensitive to the variations in the steepness of the pulse edge. The latter fact is illustrated in the inset in Fig. 1; at a fixed amplitude τ_m, the variation of the duration t_r of the rising edge of the pulse within several orders of magnitude does not lead to noticeable effects on the magnitude of the path l. Thus, the previously noted [5, 6] dependence of the dislocation path on the rate of stress change[1] has not been confirmed in our experiments.

Note that the sensitivity of the path l to the pulse amplitude is traced only to not too high stresses. As is seen from Fig. 1, at $\tau_m > \tau_0 \approx 0.1$ MPa, a saturation of the paths is observed at a level of $l \approx l_m \sim 1/\sqrt{\rho}$, which corresponds in order of magnitude to the mean spacing between dislocations. With the real dislocation density in our samples being $\rho \sim 10^4$ cm^{-2}, the saturation mean path l_m is very high (~100 μm). The background path l_0 also is relatively high; it is mainly determined by the following two factors: by the method of observation (etching leads to the removal of near-surface stoppers and subsequent relaxation of the dislocation structure) and by the technology of mounting of the samples in the loading device.

In the second series of experiments, the samples were loaded using trapezoidal pulses with various amplitudes and various durations of the rising edges and constant-stress plateaus of the pulses. Figure 2 displays the results of loading the samples with pulses with a constant-stress plateau duration t_{f-t} = 5 min and various rising times t_r (from 5 ms to 1 s). The curve of the dependence of the mean normalized path $l\sqrt{\rho}$ on the loading amplitude τ_m again is independent (within the error) of the steepness of the rising edge of the leading front and only slightly differs from the curve for triangular pulses shown by the dashed line (transferred from Fig. 1). Thus, we may state that at the loads used in our experiments, the path is mainly accumulated during the rising front of the pulse and almost does not increase during the 5-min period of action of the constant load, in complete analogy with the results of [4]. Even when the duration of the constant-stress plateau

---

[1] Note, however, that, according to a private communication of the author of [6], the slope of the rising front of the pulse $\tau(t)$ in the experiments with NaCl was varied, with the time t_r being constant, i.e., an increase in $\dot{\tau}(t)$ corresponded to a proportional growth of the amplitude τ_m. With this refinement (which, unfortunately, is absent in [6]), no contradiction exists between his and our data.

increases to $t_{\text{f–t}} = 60$ min, the hardly noticeable growth of the path l virtually does not go out beyond the limits of the experimental error (see inset in Fig. 2).

Figure 3a demonstrates the growth of the relative density of mobile dislocations ρ_m/ρ_0 (here, ρ_0 is the density of freshly introduced dislocations) with increasing amplitude τ_m of the stress pulses. Note that, at sufficiently high amplitudes τ_m, more than 90% of the freshly introduced dislocations take part in dislocation motion. The curve for the pulses of trapezoidal shape increases somewhat faster than the corresponding dependence for the triangular pulses. The background values of ρ_m/ρ_0 at $\tau_m = 0$, which constitute about 15%, appear to be determined by the same processes as the background path l_0.

Separately, we studied the mobility of dislocations in samples loaded with series of identical triangular pulses ($t_r = 0.1$ s) of various amplitudes τ_m. Figure 4 shows the dependences of the relative path $l\sqrt{\rho}$ and of the relative density of mobile dislocations ρ_m/ρ_0 on the number of pulses n in a series. As is seen from this figure, at a sufficient magnitude of the amplitude τ_m, an isolated pulse ensures the same level of the mean path l and density ρ_m as a long series of such pulses. On the other hand, if series of pulses with a progressively increasing (from pulse to pulse) amplitude are used, it is natural to expect that the resulting mean dislocation path will correspond to the maximum pulse amplitude in this series. In Fig. 1, points *8* labeled by figures *1* and *2* in squares correspond to paths under the action of two successive pulses with an increasing amplitude. The first path was fixed by intermediate etching of the sample between the first and second pulses. Both paths are measured from the starting position and are plotted against the corresponding amplitudes of each pulse. Points *8* labeled by primed figures *1*' and *2*', corresponding to longer series, were obtained from measurements without intermediate etching and are plotted in Fig. 1 against the maximum stresses in each series. The fact that all the points (*1*, *2*, *1*', and *2*') fall well onto the main curve in Fig. 1 is more evidence of the sensitivity of the dislocation path in our crystals only to the amplitude rather than to the time structure of the loading stress.

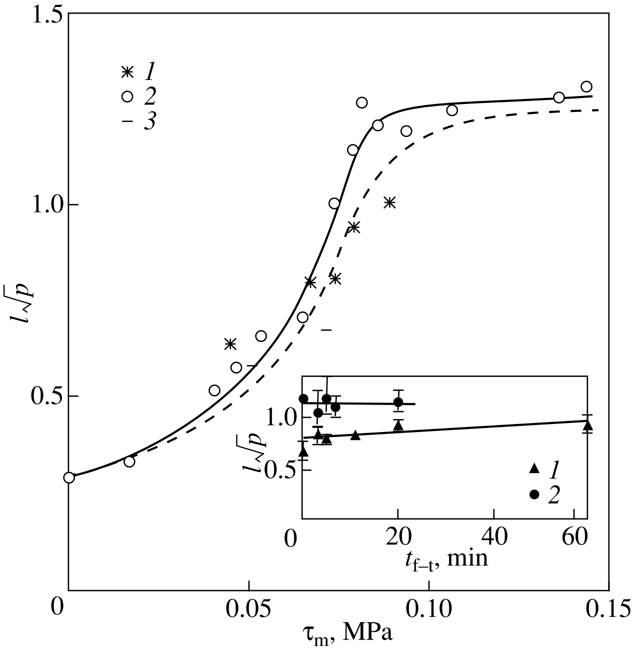

Fig. 2. Variation of the normalized path $l\sqrt{\rho}$ of dislocations as a function of the amplitude τ_m of a trapezoidal pulse of duration of 5 min for a series of pulse rise times: (*1*) $t_r = 5$ ms, (*2*) 0.1 s, and (*3*) 1 s. The inset shows the dependence of the path $l\sqrt{\rho}$ on the constant-load plateau extension $t_{\text{f–t}}$ ($t_r = 0.1$ s) for the amplitudes (*1*) $\tau_m = 0.07$ and (*2*) 0.10 MPa.

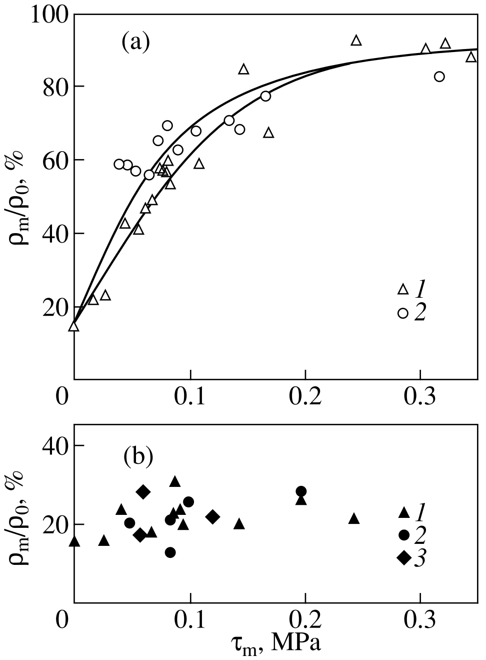

Fig. 3. Dependence of the relative density of mobile dislocations ρ_m/ρ_0 on the pulse amplitude τ_m: (a) conventional samples and (b) samples preliminarily treated with (*1*), (*2*) a magnetic field $B = 0.7$ T for 5 min or (*3*) a series of ten pulses with amplitudes 0.1–0.2 MPa; (*1*) in (a) and (b) and (*3*) in (b) triangular pulses, $t_r = 0.1$ s; (*2*) trapezoidal pulses, $t_r = 0.1$ s, $t_{\text{f–t}} =$ (a) 5 and (b) 20 min.

3. THEORETICAL MODEL

Thus, the experimental data obtained indicate that, with the low loads used in our experiments, the motion of dislocations occurs almost exclusively within the time of rising of the pulse amplitude. The dislocation path proves to be virtually insensitive to both the duration of this stage and the full duration of the pulse; it only depends on the stress amplitude τ_m. Such features of dislocation motion are characteristic of relaxational quasi-static displacements of objects in a potential relief with dry friction under the effect of a variable

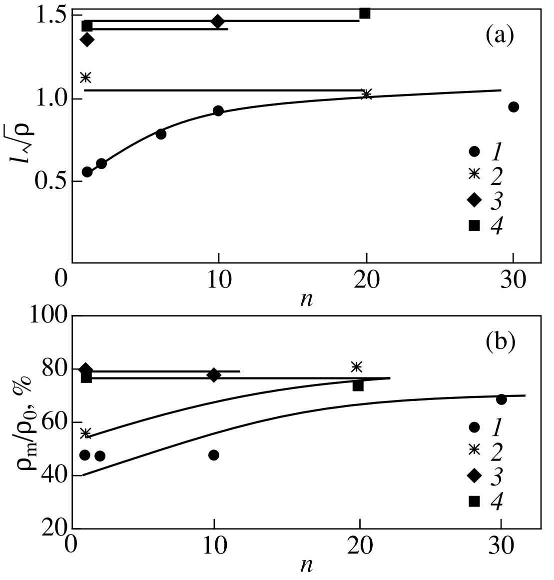

Fig. 4. Dependence of (a) the relative path $l\sqrt{\rho}$ and (b) relative density ρ_m/ρ_0 of mobile dislocations on the number of pulses in a series (t_r = 0.1 s) for various amplitudes: (*1*) t_m = 0.06, (*2*) 0.10, (*3*) 0.16, and (*4*) 0.20 MPa.

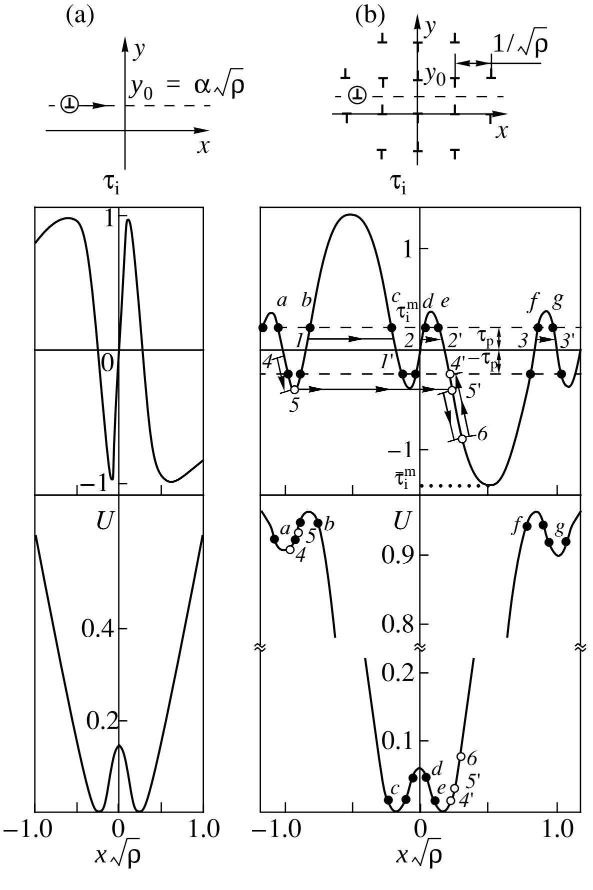

Fig. 5. Distribution of internal stresses $\tau_i(x)$ (in $AGb\sqrt{\rho}$ units) and the potential relief $U(x)$ (in AGb units) in the slip plane $y = y_0$ (a) stresses produced by an isolated edge dislocation and (b) by a regular lattice of edge dislocations.

load. The motion of the object is possible until the total force applied to the object exceeds the dry friction, and the final position of the object on the slope after removal of the load is determined from the condition of the stable equilibrium of the object at the instant at which the maximum load is applied.

Judging from the observed saturation of the paths l within lengths l_m of an order of the mean spacing $1/\sqrt{\rho}$ between dislocations (Figs. 1, 2), we deal in this case with the relaxation of the dislocation structure in the subsystem of dislocations freshly introduced before the experiment. At the rising edge of a stress pulse, such dislocations should move down from the "tops" of the potential relief corresponding to the field of internal long-range stresses $\tau_i(x)$ related to the entire dislocation ensemble. In this case, the role of dry friction is played by the force of dislocation pinning by point defects $f_p = b\tau_p$ (where b is the length of the Burgers vector), which, as any force of dry friction, has the direction opposite to the resultant of other operative forces. As is seen from Fig. 2, in the whole range of external stresses used in this work ($\tau_m < 0.3\tau_y$), the thermoactivation processes of breaking away of dislocations from individual local stoppers give no marked contribution to the mean path l. In other words, the introduction into the model of a dry-friction force f_p, whose overcoming is a necessary condition for a dislocation to move, seems to be well substantiated. In fact, the model suggested lies within the framework of the concept that was developed by Predvoditelev and his students [2, 9, 10]. This group of researchers were the first to perform a computer simulation of quasi-static displacements of dislocations in a random relief of internal stresses in a crystal under the action of a constant applied stress [10]. We only add a time-dependent external stress to the scheme that was used in [10].

It is assumed that the potential relief $U(x)$ responsible for the effects under discussion arises due to the fields of straight dislocations oriented along the z axis and parallel to the mobile dislocations studied in this work. Strictly speaking, the shape of the potential relief $U(x)$ should change in time in the process of motion of relaxing dislocations. However, we suppose that the density of freshly introduced dislocations ρ_0 is much smaller than the total dislocation density ρ and, to a first approximation (which is sufficient for the suggested qualitative model), neglect the rearrangement of the relief $U(x)$ resulting from the motion of fresh dislocations. For simplicity, we will not consider cases where several dislocations fall onto a given slope of the relief, and, as is well-known, a single "probe" straight dislocation exerts no self-action on itself.

Let us consider a straight edge dislocation whose axis coincides with the axis z of the Cartesian coordinate system and the related field of internal stresses $\tau_i(x)$, which lies in the slip plane parallel to the coordinate plane xz and is located a distance $y_0 \equiv \alpha/\sqrt{\rho}$ from the latter. In the isotropic approximation, the force of interaction (per unit length) of such a dislocation with a probe dislocation of the opposite (mechanical) sign located at the point (x, y_0) is described by the well-known formula [11]

$$f_{\mathrm{i}} = b\tau_{\mathrm{i}}(x) = -AGb^2\frac{x(x^2-y_0^2)}{(x^2+y_0^2)^2}, \qquad A = 1/2\pi(1-\nu), \tag{1}$$

where G is the shear modulus and ν is Poisson's ratio of the crystal. Figure 5a shows the graph of Eq. (1) in dimensionless coordinates $\tau_{\mathrm{i}}(x)/AGb\sqrt{\rho}$ vs. $x\sqrt{\rho}$ at $\alpha \equiv y_0\sqrt{\rho} = 0.25$ along with the corresponding potential relief $U(x)$ defined by the equation $\tau_i(x) = -\partial U/\partial x$. An interesting property of this relief is the equal maximum steepness of all four of its slopes: $\tau_{\mathrm{i}}^{\mathrm{m}} = AGb/4y_0$. It is natural that the presence of other randomly located dislocations will distort the above shape of the $\tau_{\mathrm{i}}(x)$ and $U(x)$ dependences. Figure 5b demonstrates these distortions for a model case, when a whole two-dimensional lattice of dislocation is attached to a single forest dislocation. As a result of such an attachment, the maximum steepness of the various slopes of the relief ceases to be the same, so that we should distinguish two corresponding amplitudes of internal stresses: $\tau_{\mathrm{i}}^{\mathrm{m}}$ and $\bar{\tau}_{\mathrm{i}}^{\mathrm{m}}$. However, the main topological motif of the function $U(x)$, which has the form of a double well with an additional peak near the bottom, is retained. Simply, such wells, when uniting with one another, prove to be separated with double hills that are antisymmetric with respect to the wells. Such a motif appears to be a sufficiently typical element of the potential relief produced by groups of parallel edge dislocations. Therefore, the subsequent semiqualitative considerations will be performed using the relief shown in Fig. 5b as an example.

Prior to the application of a stress pulse, the freshly introduced dislocations are located randomly on the slopes of the potential relief in those places where the "skating force" $f_{\mathrm{i}} = b\tau_{\mathrm{i}}(x)$ does not exceed the force of pinning $f_{\mathrm{p}} = b\tau_{\mathrm{p}}$. In Fig. 5b, the zones (a)–(g) in which starting positions of dislocations can exist are marked as solid segments in the curves. Consider the effect of a pulse of external stresses $\tau(t)$ on the displacement of one such dislocation at a given portion of a relief. For definiteness, we assume that the force $b\tau$ acting on the dislocation is directed from left to right. It is evident that, at sufficiently low amplitudes $\tau_{\mathrm{m}} < t_{\mathrm{p}}$, the stress pulse has a chance, adding to $\tau_{\mathrm{i}}(x)$, to displace only dislocations of the same mechanical sign on a given slope, which are pushed down along the relief. However, even such a dislocation cannot be displaced if $\tau_{\mathrm{m}} + \tau_{\mathrm{i}}^{\max} < \tau_{\mathrm{p}}$, where $\tau_{\mathrm{i}}^{\max} = \max\{\tau_{\mathrm{i}}(x)\}$ (as applied to the relief discussed above, shown in Fig. 5b; the latter quantity, depending on the slope, is equal to $\tau_{\mathrm{i}}^{\mathrm{m}}$ or $\bar{\tau}_{\mathrm{i}}^{\mathrm{m}}$). However, as we see, more typical of our crystals is the case where $\tau_{\mathrm{p}} < \tau_{\mathrm{i}}^{\max}$, when no threshold for dislocation motion exists at all. In any case, the motion of a dislocation located at the point $x = x_0$ starts at the instant when $\tau(t) = \tau_{\mathrm{p}} - \tau_{\mathrm{i}}(x_0)$ and stops when the pulse reaches its maximum. The dislocation stops at the point x_{f}, which is determined from the condition of equilibrium $\tau_{\mathrm{i}}(x_{\mathrm{f}}) = \tau_{\mathrm{p}} - \tau_{\mathrm{m}}$. It is important that the final position of the dislocation x_{f} is independent of the time characteristics of the pulse, being determined only by its amplitude. Note that the starting position $x = x_0$ can belong to both the convex and concave parts of the relief $U(x)$, whereas the final position $x = x_{\mathrm{f}}$, only to the concave part. Between the points belonging to the concave part of a given slope, the dislocation motion is completely quasi-static; i.e., the dislocation at each time moment and at each point of the relief is under the conditions of static equilibrium: $\tau(t) + \tau_{\mathrm{i}}(x) = \tau_{\mathrm{p}}$. If the starting position of the dislocation x_0 belongs to the convex part of the relief, the dislocation first loses its stability and "instantaneously falls" into an equivalent equilibrium position on the concave part of the slope (transitions of the types $1 \longrightarrow 1'$, $2 \longrightarrow 2'$, and $3 \longrightarrow 3'$ in Fig. 5b), after which it moves quasi-statically up to the final point x_{f}. Note also that it is just such processes of loss of stability of dislocations that can be responsible for the high level of background paths l_0.

The regime of motion discussed above should continue even after the amplitude τ_{m} reaches the level of the stress of pinning τ_{p}, when the dislocations quasi-statically pass through the corresponding minima of the potential relief. As the stress τ_{m} increases further up to a value of $2\tau_{\mathrm{p}}$, the dislocations lift the slope of the relief upward, remaining at a place after the pulse is switched off, since, according to the condition of force balance $\tau_{\mathrm{m}} + \tau_{\mathrm{i}}(x_{\mathrm{f}}) = \tau_{\mathrm{p}}$, the skating force of the relief at each of such final points x_{f} does not exceed the stress of pinning at $\tau_{\mathrm{m}} < 2\tau_{\mathrm{p}}$. The considered reserve of growth of paths proves to be exhausted at the right-hand side ends of the zones a, c, e, and g, where $\tau_{\mathrm{i}} = -\tau_{\mathrm{p}}$ (Fig. 5b). A further increase in the pulse amplitude in the range $2\tau_{\mathrm{p}} < \tau_{\mathrm{m}} < \tau_{\mathrm{p}} + \tau_{\mathrm{i}}^{\mathrm{m}}$ will only partly lift the dislocations up onto the hill on the leading front of the pulse, with their subsequent "backflow" after the stress is removed. The test experiments with an intermediate etching of the sample on the plateau of the trapezoidal pulse (i.e., directly in the device under the load) show that such reciprocating motions upon the unloading of the sample are sufficiently typical. Apparently, it is in such a manner that the saturation of paths occurs that is observed in Figs. 1 and 2 at a level of $l_{\mathrm{m}} \sim 1/\sqrt{\rho}$ beginning from stresses $\tau_{\mathrm{m}} = 2\tau_{\mathrm{p}} \approx 0.1$ MPa. Thus, the suggested model not only successfully describes the specific features in the behavior of dislocations under the conditions of our experiments but also permits one to obtain such an important physical characteristic of the dislocation system of the crystal as the stress of pinning,

$$\tau_p \approx 0.05 \text{ MPa}. \quad (2)$$

Note that, with increasing stress τ_m, a gradual activation of new portions of zones to which the starting positions of dislocations belong and the corresponding monotonic increase in the density of mobile dislocations occur. It is characteristic that the new portions of the zones correspond to progressively increasing paths. Thus, after the amplitude τ_m passes through the level of the pinning stress τ_p, new dislocation are involved into the motion on the ascending portions of the slopes of the relief $U(x)$ in the zones *b*, *d*, and *f*, which ensure the interzone transitions $b \longrightarrow c$, $d \longrightarrow e$, and $f \longrightarrow g$ and the longest paths. Possibly, it is these transitions that are responsible for the achievement of the maximum slope of the curve $l(\tau_m)$ in the range $\tau_p < \tau_m < 2\tau_p$ (Fig. 1). If we assume that the initial positions x_0 are equiprobably distributed over all allowed zones, then approximately one-half of the freshly introduced dislocations become mobile at $\tau_m = \tau_p$ and all 100% of such dislocations should be involved into dislocation motion at $\tau_m = 2\tau_p$. Despite the roughness of this model, we must recognize that the experimental data (Fig. 3a) quite satisfactorily correspond to this picture.

In summarizing this section, it is expedient to discuss the cause for, and the physical meaning of, the normalizing of the mean dislocation path *l* with respect to the mean local spacing between dislocations $1/\sqrt{\rho}$ that was used upon processing our experimental data. In essence, the parameter $l\sqrt{\rho}$ specifies the characteristic scale of length in the potential relief $U(x)$ in local portions of the crystal and, simultaneously, the scale of relaxation paths of dislocations measured in these regions. It is for this reason that the transition to a normalized path $l\sqrt{\rho}$ significantly decreases the scatter of experimental points in figures such as Figs. 1 and 2, which was first noticed empirically.

4. SOME PREDICTIONS AND THEIR EXPERIMENTAL TEST

The first consequence of the model suggested that admits an experimental test has a general character and is related to the principle itself of the interpretation of the results in terms of the relaxation of the dislocation structure. If this fundamental assumption is valid, then any preliminary treatment of samples that ensures the transformation of the dislocation system into a more equilibrium state should markedly decrease the concentration of dislocations that respond to the subsequent pulsed load. Upon experimental testing of this prediction, a series of ten triangular mechanical pulses with amplitudes $\tau_m = 0.1$–0.2 MPa and rising time of the leading front of the pulse $t_r = 0.1$ s were used as such a preliminary treatment; as an alternative, holding of the samples in a constant magnetic field $B = 0.7$ T for 5 min was also employed. As is seen from Fig. 3b, after such a treatment, the application to the sample of both a triangular and a trapezoidal pulse, irrespective of their amplitude, activates only 15–30% of the fresh dislocations, which is slightly above the usual level of the background. Keep in mind that on samples not subjected to a preliminary treatment, pulses with amplitudes $\tau_m = 0.15$–0.35 MPa led to motion of 80–90% of the freshly introduced dislocations (Fig. 3a). The dislocations that were not relaxed after a preliminary treatment appear to represent a standard part of the ensemble which is pinned at the surface by strong stoppers. They are freed only by etching of the surface rather than by a preliminary treatment of the surface. After the stoppers break away and still before a pulse is applied to the sample, these dislocations (at least, part of them) move jumpwise from unstable into stable positions in the potential relief (transitions of the $1 \longrightarrow 1'$ type in Fig. 5b). As was already noted, this ensures usual background values of the mean paths $l_0 \approx 0.3/\sqrt{p}$ (Fig. 1) and of the relative density of mobile dislocation $\rho_m/\rho_0 \approx 15\%$ (Fig. 3a). The subsequent pulse loading results in the displacement of dislocations broken-away after etching. As is shown by our measurements, the corresponding dependence $l(\tau_m)$ is analogous to that shown in Figs. 1 and 2.

Thus, the first conclusion that follows from the model was successfully tested experimentally. One more prediction of the theory is related to the continuation of the $l(\tau_m)$ dependence after it saturates in the range of stresses and beyond the range of measurements used in Figs. 1 and 2. In terms of our model, the extension of the saturation region should be determined by the range of amplitudes $2\tau_p < \tau_m < \tau_p + \tau_i^m$. When the amplitude τ_m exceeds the threshold value $\tau_p + \tau_i^m$ the system loses its stability. In terms of the scheme shown in Fig. 5b, the dislocations pass from zones *a*–*d* into zone *e*, where they concentrate on its right boundary. For example, under the action of a pulse $\tau(t)$ with an amplitude $\tau_m > \tau_p + \tau_i^m$, the dislocation first quasi-statically lifts the relief $U(x)$ upward from point *4* in the zone *a* to point *5*, corresponding to the maximum steepness between the zones *a* and *b*, then passes jumpwise into an equivalent stable position *5*' at the slope between the zones *e* and *f*, then quasi-statically lifts the same slope upward to point *6*, where $\tau_i(x) = -\tau_m$, and, finally, on the tailing edge of the pulse, it drops in the same quasi-static manner into point *4*', corresponding to the slope of the relief $\tau_i(x) = -\tau_p$. Thus, at $\tau_m > \tau_p + \tau_i^m$, there should be observed a serious increase in dislocation paths with a leveling out of the $l(\tau_m)$ dependence on a new level of saturation, whose extension in our model is determined by the interval $\tau_p + \tau_i^m < \tau_m < \tau_p + \bar{\tau}_i^m$. At $\tau_m > \tau_p + \bar{\tau}_i^m$, we should expect one more jump in the length of paths with the passage of dislocations onto steeper slopes. Naturally, with allowance for the statistical scatter (from place to place) of the parameters of the potential relief, we speak of a sufficiently sharp increase in the mean paths l by a magnitude that is comparable with the mean spacing between dislocations $1/\sqrt{\rho}$ rather than of a truly jumpwise increase.

Note that the prediction made is a more universal consequence of the suggested model than the concrete shape of the elementary potential well (Fig. 5) that was used as an example for the illustration. It seemed even more important to test this prediction, even though, with increasing amplitude of pulses, the experiments become more and more laborious because of the increase in the statistical scatter of the results and corresponding necessity of increasing the amount of measurements in order to decrease the level of experimental errors. Curve *1* in Fig. 6 demonstrates the continuation of the $l(\tau_m)$ dependence measured in the first series of experiments (Fig. 1) into the region of $0.15 < \tau_m < 0.35$ MPa. It is seen that in the region $0.16 < \tau_m < 0.22$ MPa, there indeed occurs a predicted increase in the dislocation paths with the passage of the $l(\tau_m)$ curve on a new level of saturation, which is higher than the preceding level by $\Delta l \approx 0.7/\sqrt{\rho}$. Thus, we may state that the suggested model, in spite of its simplified nature, satisfactorily describes the experiment in this case as well.

To the above-mentioned range of amplitudes τ_m in which the transition onto a new level of saturation of the paths occurs, there corresponds an interval of quasi-continuous distribution of the parameter $\tau_i^m = \tau_m - \tau_p$:

$$0.11 < \tau_i^m < 0.17 \text{ MPa}. \tag{3}$$

Since at the maximum amplitude $\tau_m = 0.35$ MPa used in the experiments we still did not reach the end of the current level of saturation, the magnitude of $\bar{\tau}_i^m$ can only be estimated from below:

$$\bar{\tau}_i^m > 0.3 \text{ MPa}. \tag{4}$$

As can be seen from Figs. 3a and 4, the degree of relaxation of the initial dislocation structure increases with increasing pulse amplitude τ_m: the density of mobile dislocations increases and the mean path l reaches its equilibrium value at a smaller number n of pulses in a series. Hence, one more prediction follows: if, after loading the crystal with a single triangular pulse, the crystal is subjected to a dc magnetic field, similar to how this was made during the preliminary treatment of samples to ensure relaxation of the dislocation structure in them (Fig. 3b), the paths corresponding to curve *1* in Fig. 6 should increase all the less, the higher the pulse amplitude. Curve *2* in Fig. 6 completely confirms this prediction.

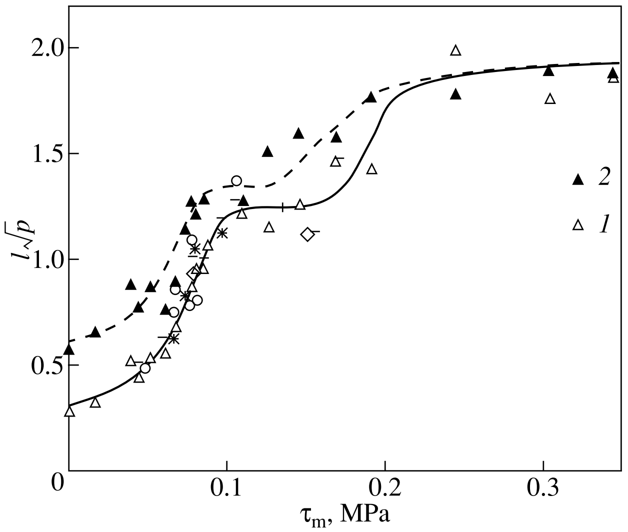

Fig. 6. (*1*) Continuation of the $l\sqrt{\rho}\,(\tau_m)$ dependence (Fig. 1) into the region of $\tau_m = 0.15$–0.35 MPa and (*2*) the analogous dependence for samples that were treated with a magnetic field $B = 0.3$ T for 5 min after loading with a triangular stress pulse ($t_r = 0.1$ s).

5. ON THE CONDITIONS OF THE OBSERVATION OF NORMAL DISLOCATION DYNAMICS

By the normal dislocation dynamics, we mean such motions in which a dislocation is characterized by a certain velocity dependent on the external stress and its mean path changes linearly in time as long as the load is applied. One feature of our crystals with low concentration of impurities is a relatively small pinning stress as compared to the characteristic maxima of the potential relief. Indeed, according to Eq. (2), τ_p is smaller than the yield stress τ_y by an order of magnitude, whereas, according to Eq. (4), the stress $\bar{\tau}_i^m$ has the same order of magnitude as τ_y. In such crystals, the normal dynamics of dislocations can be observed only at very high stresses that substantially exceed the yield stress, when dislocation motion has an overbarrier dynamic character and its velocity is limited by viscous friction due to the interaction of dislocations with the phonon subsystem of the crystal [12]. Such a regime of dislocation motion was studied in detail on crystals of precisely this series in [13].

On the other hand, the observation in these crystals of the motion of individual dislocations in the regime of thermoactivational overcoming of local barriers seems to be almost impossible. Indeed, such a motion can only be effected in the range of stresses $\tau - \tau_i < \tau_p$. At the same time, under our conditions, in the case of the experimentally significant values of dislocation paths (exceeding experimental error), the internal stresses τ_i change by a value that certainly exceeds τ_p.

Quite another situation is observed in impurity crystals, where $\tau_i^{max} \ll \tau_p \sim \tau_y$ and the above-noted methodical difficulties are absent. Here, on the contrary, we can expect large problems in the observation of the above-studied quasi-static displacements of dislocations, in distinction from the motion in the thermoactivation regime (in the interval of stresses $\tau_i^{max} \ll \tau < \tau_p$), which, indeed, was successfully studied in alkali-halide crystals of this type [1, 14–18].

It should be emphasized that the features of the dislocation mobility that were observed in our work and by other authors in pure crystals do not cast any doubt on the results of many years of research into the thermofluctuational dynamics of dislocations in impurity crystals, where the pinning stress is comparable with the yield stress.

CONCLUSION

Thus, the specific features of the dislocation dynamics in alkali-halide crystals noted previously in the literature [2–6] were indeed revealed in our experiments on the pulsed loading of NaCl crystals, although by no means were all these features reproduced in our experiments. Similar to our predecessors, we found that dislocations move only at the rising edge of the loading pulse and are almost immobile at the constant-load plateau. According to our data, the mean path of dislocations is sensitive only to the pulse amplitude and is independent of the rate of change of stresses.

The model suggested, based on the hypothesis of the relaxational nature of the observed displacements of dislocations, not only completely explains all features of the observed anomalies, but also permits us to experimentally determine the force of dislocation pinning and the main characteristics of the field of internal stresses in the crystal. However, the main argument in favor of the model is the fact that a whole series of predictions of the model was confirmed experimentally. In particular, the recipe of switching off of anomalies by means of a preliminary pulsed or magnetic treatment of samples was realized, which eliminates the strong nonequilibrium of the structure of freshly introduced dislocations in the crystal. Note that in this paper the magnetoplastic effect was for the first time used for purely application purposes as a very efficient, simple, and technological method of deep relaxation of the structure of freshly introduced dislocations in a crystal.

As was shown above, the anomalies found in the dislocation dynamics should be specific of pure crystals, where the total pinning of dislocations by point defects (the pinning stress τ_p) is small as compared to the characteristic maxima of the field of internal stresses τ_i^m, which are comparable with the yield stress of the crystal τ_y. In impurity crystals, where $\tau_p \sim \tau_y \gg \tau_i^m$, normal dislocation dynamics characterized by the mean path *l* proportional to the pulse duration should be observed. However, the existence of anomalies of dislocation mobility in pure crystals also does not eliminate the fundamental regularities of dislocation dynamics, but only reminds one of the necessity to more carefully regard the conditions of loading and accurately use the concept of the mean velocity of dislocations when studying these regularities. The investigation of the "anomalous dynamics" of nonequilibrium dislocations admits the derivation of unique information, which cannot be obtained by other methods.

ACKNOWLEDGMENTS

We are grateful to O.V. Klyavin, N.A. Tyapunina, and E.É. Glikman for fruitful discussions of the results and to V.P. Kisel' for his assistance in annealing crystals.

REFERENCES

1. W. G. Johnston and J. J. Gilman, J. Appl. Phys. **30**, 129 (1959).
2. A. A. Predvoditelev, N. K. Rakova, and Nan Hung-pin, Fiz. Tverd. Tela (Leningrad) **9** (1), 300 (1967) [Sov. Phys. Solid State **9**, 224 (1967)].
3. V. A. Makara, N. N. Novikov, and O. V. Rudenko, in *Dynamics of Dislocation* (Naukova Dumka, Kiev, 1975), p. 190.
4. A. V. Nikiforov, V. A. Shvetsova, O. V. Klyavin, and V. A. Likhachev, Fiz. Tverd. Tela (Leningrad) **18** (10), 3152 (1976) [Sov. Phys. Solid State **18**, 1841 (1976)].
5. G. N. Ermolaev, S. I. Ninenko, and A. A. Urusovskaya, Fiz. Tverd. Tela (Leningrad) **31** (4), 277 (1989) [Sov. Phys. Solid State **31**, 707 (1989)].
6. G. N. Ermolaev, Fiz. Tverd. Tela (St. Petersburg) **38** (11), 3375 (1996) [Phys. Solid State **38**, 1841 (1996)].
7. V. I. Alshits, E. V. Darinskaya, O. L. Kazakova, *et al.*, Mater. Sci. Eng. A **234–236**, 617 (1997).
8. M. V. Koldaeva, E. V. Darinskaya, and V. N. Sytin, Prib. Tekh. Éksp., No. 3, 151 (1998).
9. I. V. Stratan, A. A. Predvoditelev, and V. M. Stepanova, Fiz. Tverd. Tela (Leningrad) **12** (3), 766 (1970) [Sov. Phys. Solid State **12**, 594 (1970)].
10. I. V. Stratan and A. A. Predvoditelev, Fiz. Tverd. Tela (Leningrad) **12** (6), 1729 (1970) [Sov. Phys. Solid State **12**, 1367 (1970)].
11. J. P. Hirth and J. Lothe, *Theory of Dislocations* (McGraw-Hill, New York, 1967; Atomizdat, Moscow, 1972).

12. V. I. Alshits and V. L. Indenbom, in *Dislocations in Crystals*, Ed. by F. R. N. Nabarro (North-Holland, Amsterdam, 1986), Vol. 7, pp. 43–111.
13. E. V. Darinskaya, A. A. Urusovskaya, V. I. Al'shits, *et al.*, Fiz. Tverd. Tela (Leningrad) **25** (12), 3636 (1983) [Sov. Phys. Solid State **25**, 2092 (1983)].
14. É. Yu. Gutmanas, É. M. Nadgornyĭ, and A. V. Stepanov, Fiz. Tverd. Tela (Leningrad) **5** (4), 1021 (1963) [Sov. Phys. Solid State **5**, 743 (1963)].
15. V. B. Pariĭskiĭ, S. V. Lubenets, and V. I. Startsev, Fiz. Tverd. Tela (Leningrad) **8** (4), 1227 (1966) [Sov. Phys. Solid State **8**, 976 (1966)].
16. S. V. Lubenets and V. I. Startsev, Fiz. Tverd. Tela (Leningrad) **10** (1), 22 (1968) [Sov. Phys. Solid State **10**, 15 (1968)].
17. G. A. Ermakov and É. M. Nadgornyĭ, Fiz. Tverd. Tela (Leningrad) **13** (2), 513 (1971) [Sov. Phys. Solid State **13**, 410 (1971)].
18. É. M. Nadgornyĭ, in *Imperfection of Crystalline Structure and Martensite Transformations* (Nauka, Moscow, 1972), p. 151.

Translated by S. Gorin

Physics of the Solid State, Vol. 43, No. 9, 2001, pp. 1712–1714. Translated from Fizika Tverdogo Tela, Vol. 43, No. 9, 2001, pp. 1643–1645.
Original Russian Text Copyright © 2001 by Patrin, Ovchinnikov, Velikanov, Kononov.

MAGNETISM AND FERROELECTRICITY

Magnetic Properties of Fe/Si/Fe Trilayer Films

G. S. Patrin*, **, S. G. Ovchinnikov*, **, D. A. Velikanov, and V. P. Kononov****
**Krasnoyarsk State University, Krasnoyarsk, 660041 Russia*
***Kirensky Institute of Physics, Siberian Division, Russian Academy of Sciences,*
Akademgorodok, Krasnoyarsk, 660036 Russia
e-mail: pat@iph.krasnoyarsk.su

Received January 10, 2001

Abstract—The magnetization of Fe/Si/Fe trilayer films is experimentally investigated at low temperatures. It is found that the shape of the magnetization curves measured at $T < 30$ K depends on the thermomagnetic state of the system. The possible mechanisms of the interaction between iron layers are discussed. *© 2001 MAIK “Nauka/Interperiodica”.*

1. INTRODUCTION

In recent years, multilayer magnetic systems have attracted the particular attention of many researchers, because they can be successfully used in the preparation of magnetic materials with controlled properties [1]. This is achieved by the proper choice of the materials of the main magnetic and intermediate layers, their thicknesses, and packing modes. The use of a semiconductor material as an intermediate layer provides a means for controlling the properties of these layers through external factors (impurities, different types of radiation, temperatures, fields, etc.).

A distinctive feature of magnetic films with a silicon interlayer (of thickness t_{Si}) is that they can be rather easily obtained using different methods and, what is more important, possess unusual properties in readily attainable ranges of controlling parameters. In particular, Toscano *et al.* [2] found that, at $T > 40$ K, the exchange interaction parameter varies with temperature. Mattson *et al.* [3, 4] revealed a photoinduced change in the interlayer exchange parameter with the use of the Kerr effect. In our recent work [5], we studied the dependence of the internal effective magnetic field on the thickness of a silicon interlayer by electron magnetic resonance. It was demonstrated that, at $T \geq 80$ K, the photoinduced contribution to the magnetic interaction between the iron layers in films at $t_{\mathrm{Si}} > 10$ Å has an antiferromagnetic nature.

In the present work, we investigated the low-temperature behavior of the magnetization of Fe/Si/Fe films in weak magnetic fields by the superconducting quantum interference device (SQUID) method.

2. SAMPLE PREPARATION AND EXPERIMENTAL TECHNIQUE

The Fe/Si/Fe trilayer films were prepared by molecular beam epitaxy with an Angara setup, which was specially adapted for evaporation of magnetic materials [6]. Four samples with different thicknesses of the silicon interlayers were prepared in one evaporation cycle. For all the studied samples, the iron layer thickness t_{Fe} was equal to 50 Å. The thickness was checked against a quartz thickness meter and the growth rate of the film. One reference film with thickness $t_{\mathrm{Fe}} = 100$ Å was prepared in each evaporation cycle. The intensities of microwave absorption in the films were compared with the aim of revealing the difference between the masses of the magnetoactive materials. The magnetization was measured on a SQUID magnetometer [7]. The magnetic field was applied along the film plane.

3. RESULTS AND DISCUSSION

All the previous experiments [2–4] were performed in magnetic fields of the order of 1 kOe. In these works, it was assumed that the main mechanism responsible for the observed effects is associated with a change in the charge carrier concentration in a semiconductor interlayer either with a variation in temperature or under illumination. At the liquid-nitrogen temperature under equilibrium conditions, all conduction electrons in silicon are frozen. In this case, the signals taken from the iron layers indicated a nearly independent ferromagnetic behavior of these layers. According to our earlier measurements of the magnetic resonance parameters [5], the observed shift of the resonance field is caused by oscillations of the parameter of the exchange interaction between the iron layers and its value depends on the thickness of the silicon interlayer in the studied film (Fig. 1). The iron layers interact ferromagnetically at $t_{\mathrm{Si}} < 10$ Å and antiferromagnetically at $t_{\mathrm{Si}} > 10$ Å. This behavior is observed at temperatures of 300 and 80 K. Note that, although the effect in the latter case is considerably weaker, all the main features are well reproduced.

Figure 2 shows the temperature dependences of the difference between the magnetizations $\delta\sigma(T) = \sigma(T, 0) - \sigma(T, t_{Si})$ for the reference and studied Fe/Si/Fe films at different silicon interlayer thicknesses. These dependences were measured in a magnetic field of 250 Oe upon heating of samples preliminarily cooled under different conditions. The applied field (250 Oe) is high enough for the samples to be at saturation at all temperatures. First, it should be noted that, in the temperature range 30–300 K, the dependences of $\delta\sigma$ on t_{Si} at T = const correlate with the curves depicted in Fig. 1. These results do not depend on whether the samples were cooled with or without a magnetic field. Second, the curves obtained under different cooling conditions considerably differ at temperatures below 30 K. It is also worth noting that the dependence of $\delta\sigma(H_c = 250\text{ Oe}) - \delta\sigma(H_c = 0\text{ Oe})$ (where H_c is the magnetic field applied to the sample during its cooling) on the silicon interlayer thickness t_{Si} at a constant temperature correlates with the dependences displayed in Fig. 1.

For the film at t_{Si} = 20 Å, which is characterized by the maximum antiferromagnetic coupling between the iron layers, the magnetization curves obtained at 4.2 K upon an increase (curve *1*) and decrease (curve *2*) in the magnetic field are plotted in Fig. 3. In this experiment, we measured the signal from the film on a substrate, then removed the magnetic film, and measured the signal from the substrate. The difference between these signals was taken as the magnetization of the studied film. It is clearly seen from Fig. 3 that an increase in the magnetic field leads to the appearance of two characteristic points in the magnetization curve: $H_1 \approx 160$ Oe (the inflection point in the initial portion of the magnetization curve) and $H_2 \approx 240$ Oe (the point where the magnetization reaches saturation). In the case when the magnetic field decreases, no features are revealed at the field H_1. Since the magnetization in the given experimental geometry should be aligned with the film plane, curve *1* can be realized in the presence of crystalline magnetic anisotropy competing with the shape anisotropy. In the framework of the two-sublattice antiferromagnet model, this behavior becomes possible either in the case when the anisotropy axis is perpendicular to the film plane or in the presence of in-plane anisotropy. Therefore, the magnetic field H_1 can be considered a field of the spin-flop state and the field H_2 can be treated as a field attained after collapse of the sublattice. The magnetization behavior observed with a decrease in the magnetic field can be interpreted as a manifestation of either the ferromagnetism induced by the magnetic field or the magnetic-field-induced metastable state in which the magnetic anisotropy can be observed only after overcoming a certain energy barrier.

All these findings seem unexpected under the assumption that the interaction between the iron layers can be provided only by conduction electrons in the bulk of the silicon interlayer, because the carriers responsible for this interaction should not occur at low temperatures.

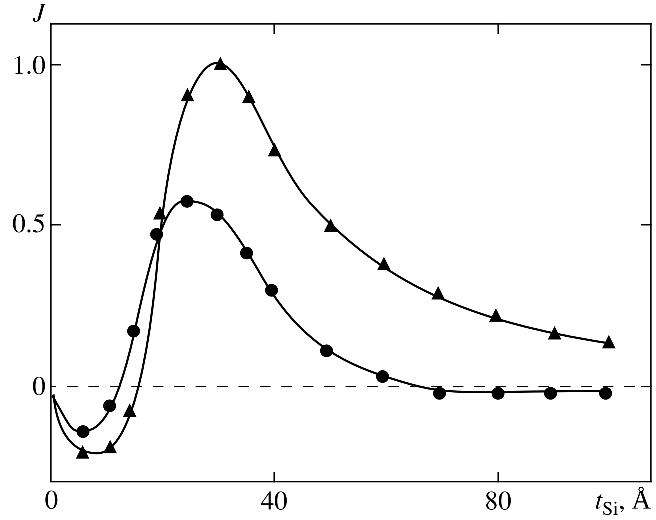

Fig. 1. Dependences of the normalized shift of the molecular field on the silicon interlayer thickness for Fe/Si/Fe films at T = (*1*) 80 and (*2*) 300 K.

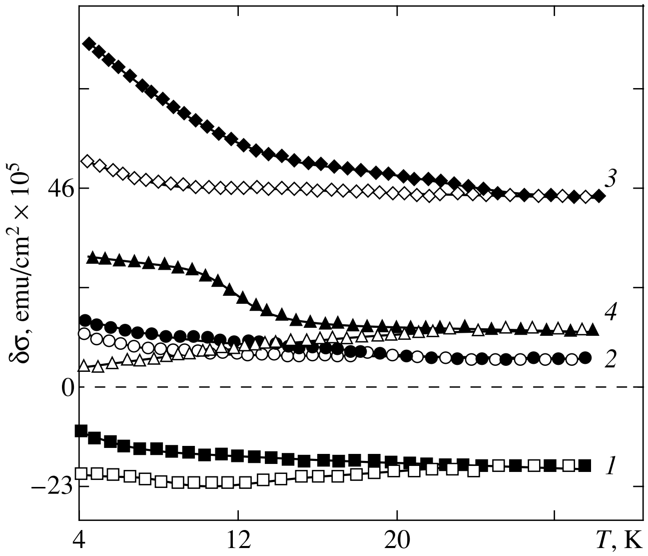

Fig. 2. Temperature dependences of the change in the magnetization per unit area $\delta\sigma(T, t_{Si}) = \sigma(T, 0) - \sigma(T, t_{Si})$ at different silicon interlayer thicknesses t_{Si}: (*1*) 5, (*2*) 10, (*3*) 20, and (*4*) 30 Å. The open and closed symbols correspond to cooling in magnetic fields H = 0 and 250 Oe, respectively.

In order to explain the low-temperature behavior of the magnetization of the Fe/Si/Fe films under investigation, it is necessary to reveal the carriers responsible for the interaction between the iron layers and to elucidate the mechanism of this interaction. It is known that a transition region of the metal silicide–silicon type is formed at the metal–semiconductor interface [8]. According to the data of Auger electron spectroscopy,

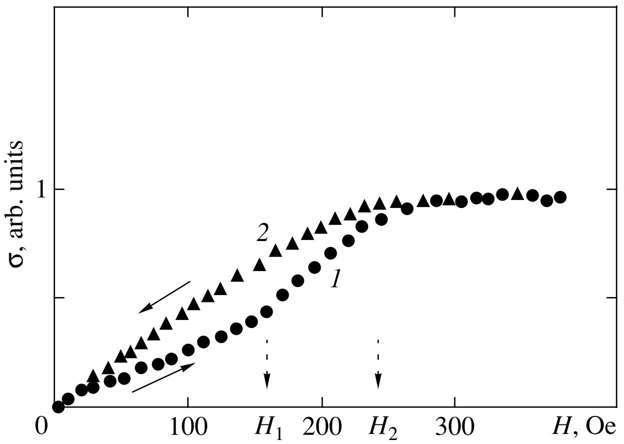

Fig. 3. Dependences of the reduced magnetization on the magnetic field upon (*1*) increase and (*2*) decrease in the field. $T = 4.2$ K.

silicon comes into contact with *d* elements when the thickness of this transition region lies in the range from several to twenty angstroms (for example, 7–14 Å for Ni and approximately 3 Å for Pd). Imada *et al.* [9] demonstrated that the FeSi compound is a nearly ferromagnetic semiconductor. This means that FeSi possesses both weak metallic properties according to the magnitude of the electrical conductivity and semiconductor properties as judged from the temperature dependence of the electrical conductivity. The point is that the density of states of FeSi is not high enough for this compound to possess highly ferromagnetic properties. However, owing to the electron transfer from the metal, a region enriched with electrons is formed at the metal–semiconductor interface on the semiconductor side. It is easy to estimate [8] that, in the case when the total thickness of the silicon interlayer is of the order of 10 Å, the overlapping transition regions formed at the boundaries with both iron layers should be located throughout the bulk of the interlayer. In this case, the electron density turns out to be high enough for the ferromagnetic order to arise in the system. When the order in the system is formed according to the spin-density wave scheme, a further increase in the interlayer thickness leads to a change in the magnetic order. Apparently, the interlayer thickness $t_{\mathrm{Si}} \sim 20$ Å can be treated as an oscillation period in the system with a low density of states. A further increase in t_{Si} results in disturbance of the long-range order in the system due to the low density of states.

At low temperatures, the possibility of the interaction occurring through the states of band tails in the semiconductor should not be ruled out. As was noted by Toscano *et al.* [2], the silicon interlayer prepared through evaporation is in an amorphous state and the short-range order region is approximately equal to 16 Å. In this situation, the silicon interlayer contains a large number of defects and the electron transfer processes should be considered with due regard for the band-tail states [10]. In amorphous silicon, the mobility of charge carriers increases at temperatures below 30 K. The activation energies of these processes fall in the range 1–2 meV. Consequently, the interaction between the iron layers can proceed through the band-tail states. A decrease in the concentration of carriers with a decrease in the temperature can be compensated for by an increase in their mean free path. This mechanism can provide a memory effect in the spin state of the layer already vacated by electrons. In order to determine the specific mechanism of formation of a long-range order in the trilayer system, it is necessary to investigate in more detail the electronic properties at the iron–silicon interface and to elucidate the role of the band-tail states in charge carrier transfer.

ACKNOWLEDGMENTS

This work was supported by the Scientific Program "Russian Universities—Basic Research."

REFERENCES

1. P. Grunberg, R. Schreiber, Y. Pang, *et al.*, Phys. Rev. Lett. **57**, 2442 (1986).
2. S. Toscano, B. Briner, H. Hopster, and M. Landolt, J. Magn. Magn. Mater. **114**, L6 (1992).
3. J. E. Mattson, S. Kumar, E. E. Fullerton, *et al.*, Phys. Rev. Lett. **71**, 185 (1993).
4. J. E. Mattson, E. E. Fullerton, S. Kumar, *et al.*, J. Appl. Phys. **75**, 6169 (1994).
5. G. S. Patrin, N. V. Volkov, and V. P. Kononov, Pis'ma Zh. Éksp. Teor. Fiz. **68**, 287 (1998) [JETP Lett. **68**, 307 (1998)].
6. E. G. Eliseeva, V. P. Kononov, V. M. Popel, *et al.*, Prib. Tekh. Éksp., No. 2, 141 (1986).
7. G. S. Patrin, D. A. Velikanov, and G. A. Petrakovskiĭ, Zh. Éksp. Teor. Fiz. **103**, 234 (1993) [JETP **76**, 128 (1993)].
8. T. Bechshtedt and R. Enderlein, *Semiconductor Surfaces and Interfaces: Their Atomic and Electronic Structures* (Academie-Verlag, Berlin, 1988; Mir, Moscow, 1990).
9. M. Imada, A. Fujimori, and Y. Tokura, Rev. Mod. Phys. **70**, 1039 (1998).
10. W. E. Spear, in *Advances in Disordered Semiconductors*, Vol. 1: *Amorphous Silicon and Related Materials*, Ed. by H. Fritzsche (World Scientific, Singapore, 1989; Mir, Moscow, 1991).

Translated by O. Borovik-Romanova

Physics of the Solid State, Vol. 43, No. 9, 2001, pp. 1715–1719. Translated from Fizika Tverdogo Tela, Vol. 43, No. 9, 2001, pp. 1646–1650.
Original Russian Text Copyright © 2001 by Zvezdin, Kostyuchenko.

MAGNETISM AND FERROELECTRICITY

Magnetic-Field-Induced Phase Transitions in Molecular Ferrimagnets with Two Compensation Points

A. K. Zvezdin* and V. V. Kostyuchenko**
**Institute of General Physics, Russian Academy of Sciences, ul. Vavilova 38, Moscow, 117942 Russia*
***Institute of Microelectronics and Informatics, Russian Academy of Sciences,*
ul. Universitetskaya 21, Yaroslavl, 150007 Russia

Received January 17, 2001

Abstract—Phase transitions induced by an external magnetic field in materials analogous to iron earth with two compensation points are studied for the first time. The *H*–*T* phase diagrams are plotted. The dependences of the magnetic properties of these materials on the composition are investigated. It is shown that the net magnetization in the region between the two compensation points is small for some compositions and at these compositions, the magnetic properties are similar to antiferromagnetic ones. *© 2001 MAIK "Nauka/Interperiodica".*

The possible existence of a compensation point, i.e., the temperature at which spontaneous magnetization of a ferrimagnet changes its sign, was indicated for the first time by Néel in 1948 [1]. In the past fifty years, a wealth of various ferrimagnets showing a compensation point have been investigated experimentally. There has also been a great many theoretical studies on the phase transitions in ferrimagnets with a compensation point (see [2] and references therein). However, it was not until 1999 that a four-sublattice molecular ferrimagnet with two compensation points was investigated [3]. Molecular-based ferrimagnets present a new group of promising magnetic materials. These materials offer major advantages over traditional magnets as they provide a high degree of control by changing their properties in sufficiently wide ranges when exposed to external effects (for instance, optical or electrochemical). For example, magnetic-moment inversion after exposure to light was discovered in [4]. In [5], the reversible paramagnet–ferromagnet phase transition induced by light was investigated.

In the present work, we investigate the molecular magnets known as analogs of iron earth [4, 6–16]. These materials are of interest for use in computer modeling of new materials. Magnetic interactions between *d* ions in these materials allow one to predict magnetic properties of the material with a high precision and, thus, to calculate the composition of the material with predetermined parameters. The magnetic properties of analogs of iron earth are very sensitive to changing illumination, temperature, and other factors, which makes them very promising materials for use in various practical purposes. The comparatively low density of these materials opens up the possibility of synthesizing transparent magnets on their basis. However, phase transitions induced by an external magnetic field in these materials have not been considered previously. Theoretical investigation of these phase transitions is the objective of the present article.

It is well known that the magnetic structure of a ferrimagnet can be noncollinear in a certain range of temperatures and magnetic fields. This structure results from competition between the exchange antiferromagnetic interactions of the sublattices, which tend to align the sublattice magnetizations antiparallel to each other, and an external field, which tries to align them parallel to each other. Phase transitions from the noncollinear phase to the collinear one, induced by an external magnetic field, have been thoroughly investigated in the physics of ferrimagnetic materials, as this is a direct method of investigating exchange interactions and magnetic anisotropy in these materials [2, 17]. These phase transitions and, correspondingly, *H*–*T* phase diagrams have been most widely investigated in rear-earth iron garnets and rear-earth–transition-metal intermetallic compounds [2].

We consider four-sublattice ferrimagnets described by a formula $(\mathrm{Ni}_{x_2}\mathrm{Mn}_{x_3}\mathrm{Fe}_{x_4})_{1.5}[\mathrm{Cr(CN)}_6] \cdot z\mathrm{H_2O}$ with $x_2 + x_3 + x_4 = 1$. Not all these compositions have two compensation points. Finding these compositions can be an arduous task unless there exists a possibility of predicting their properties theoretically. The relative simplicity of the theoretical approach in treating the analogs is based on two important presumptions: (1) only the exchange interaction between the nearest neighbors is accounted for and (2) the magnitudes and signs of the exchange integrals can be estimated with sufficient accuracy. This makes it possible to predict the magnetic properties of these materials on the basis of the molecular-field theory [3, 14]. In the present article, we generalized the model proposed in the articles cited above to take into consideration the effect of an external magnetic field.

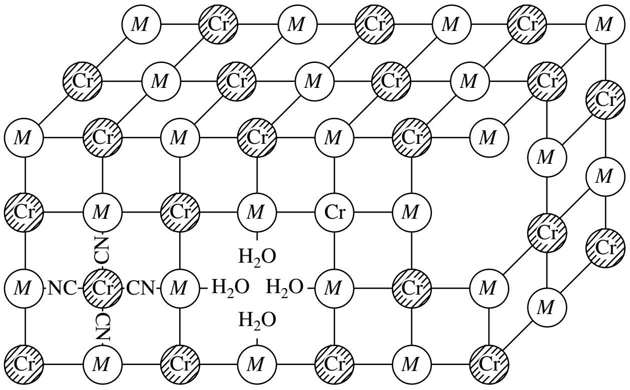

Fig. 1. Schematic representation of the crystalline structure: M = Ni, Mn, and Fe.

The crystalline structure is presented in Fig. 1. The dominant interaction is the superexchange interaction between Cr and M ions (M = Ni, Mn, Fe) via the cyanide ligands. The exchange interaction in the sublattices (Cr–Cr and M–M) can be neglected, as the distances between the corresponding ions are very large. Thus, the necessary condition for the use of the molecular-field approximation—the predominance of the exchange interaction between the sublattices over the exchange interaction in each of the sublattices—is fulfilled.

According to the molecular-field method, we approximate the interaction between spins using effective magnetic fields. The number of effective fields is equal to that of the sublattices.

The initial Hamiltonian has the form

$$\mathcal{H} = -\sum_{k=2}^{4}\sum_{i_1, i_k} I(i_1 - i_k)(\mathbf{S}_{i_1}\mathbf{S}_{i_k}) - \sum_{k=1}^{4}\sum_{i_k} g\mu(\mathbf{H}\mathbf{S}_{i_k}). \quad (1)$$

For definiteness, we assume that the indices that specify the sublattices take on the values 1–4, corresponding to Cr, Ni, Mn, and Fe ions, respectively. In accordance with the molecular field approximation [18], Hamiltonian (1) is conveniently represented as the sum of two parts:

$$\mathcal{H} = \mathcal{H}_0 + \{\mathcal{H} - \mathcal{H}_0\}, \quad (2)$$

$$\mathcal{H}_0 = -\sum_{k=1}^{4}\sum_{i_k} g\mu(\mathbf{h}_k\mathbf{S}_{i_k}). \quad (3)$$

Numerical values of the exchange integrals presented in [3]

J_{12}, cm^{-1}	J_{13}, cm^{-1}	J_{14}, cm^{-1}
5.6	–2.5	0.9

We assume that $\mathbf{h}_k = \boldsymbol{\gamma}_k h_k$, where $\boldsymbol{\gamma}_k$ is the unit vector defining the orientation of the mean field in the kth sublattice. The variation parameters h_k and $\boldsymbol{\gamma}_k$ are determined from the condition for a minimum of free energy F, where

$$F = \frac{1}{\beta}\ln \mathrm{Tr}[\exp(-\beta\mathcal{H}_0)]_0 + \frac{\mathrm{Tr}[(\mathcal{H} - \mathcal{H}_0)\exp(-\beta\mathcal{H}_0)]_0}{\mathrm{Tr}[\exp(-\beta\mathcal{H}_0)]}. \quad (4)$$

Minimizing the free energy in Eq. (4), one can obtain the following relationships, which determine the spin orientation in the sublattices, and expressions for the effective fields:

$$\boldsymbol{\gamma}_k = \frac{\mathbf{H} - \lambda_k\langle S_1\rangle\boldsymbol{\gamma}_1}{h_k}, \quad (5)$$

$$h_k = [H^2 + \lambda_k^2\langle S_1\rangle^2 + 2\lambda_k\langle S_1\rangle H\cos\theta]^{1/2}, \quad (6)$$

where θ is the angle between the spin direction in the Cr sublattice and the external magnetic field and λ_k is given by the expression

$$\lambda_k = \frac{1}{g\mu N_k}\sum_{i_1, i_k} I(i_1 - i_k), \quad k = 2, 3, 4.$$

If we allow only for the exchange interaction between nearest neighbors, the expression for λ_k can be represented in the form

$$\lambda_k = J_{1k}Z_{k1}/(g\mu), \quad (7)$$

where J_{1k} is the exchange interaction energy between neighboring ions in the first and kth sublattices. The factors Z_{k1} determining the number of nearest neighbors are equal to $Z_{21} = Z_{31} = Z_{41} = 4$. The average spin values in the Ni, Mn, and Fe sublattices are determined by the magnitudes of the effective fields and are equal to

$$\langle S_k\rangle = S_k B_{S_k}(\beta h_k S_k). \quad (8)$$

The magnetization orientation in the Cr sublattice is prescribed by the equation

$$\left(1 + \frac{3}{2}\sum_{k=2}^{4}\frac{\lambda_k x_k\langle S_k\rangle}{h_k}\right)\sin\theta = 0. \quad (9)$$

The effective field for the first sublattice (Cr) is

$$h_1 = \left|\mathbf{H} + \frac{3}{2}\sum_{k=2}^{4}\lambda_k\langle S_k\rangle x_k\boldsymbol{\gamma}_k\right|, \quad (10)$$

and allowing for Eq. (10), it can be represented in the form

$$h_1 = \sum_{k=2}^{4}\frac{\lambda_k^2\langle S_k\rangle x_k}{h_k}. \quad (11)$$

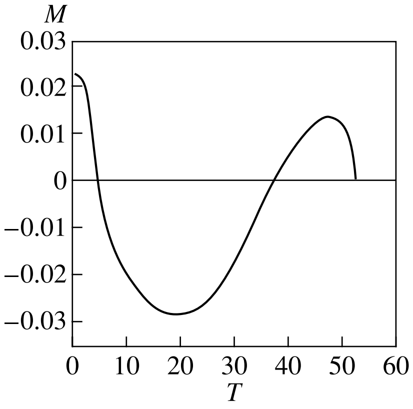

Fig. 2. Magnetization temperature dependence for the composition $(Ni_{0.24}Mn_{0.61}Fe_{0.15})_{1.5}[Cr(CN)_6]$.

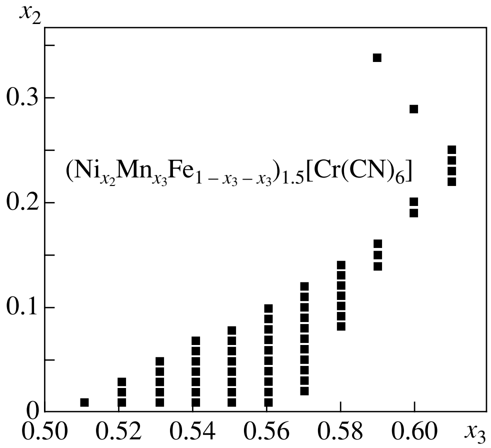

Fig. 3. Diagram for the compounds with two compensation points.

The magnitudes and orientations of spins in the sublattices are found by solving Eqs. (8), (9), and (11).

No possibility is offered to obtain exact analytical solutions to the system of Eqs. (9)–(12), and in this article, in order to calculate the magnetization magnitudes, the compensation temperatures, and *H*–*T* phase diagram, we applied numerical methods. In calculations, we used exchange integrals (table) obtained from experimental data on the Curie temperatures for various compositions of the analogs of iron earth (see, e.g., [3]).

Not all the compositions of this type show two compensation points. One should, therefore, initially find such compositions. If the external magnetic field is equal to zero, the net magnetization is

$$M = Ng\mu\left[\frac{3}{2}[x_2\langle S_2\rangle - x_3\langle S_3\rangle + x_4\langle S_4\rangle] + \langle S_1\rangle\right]. \quad (12)$$

Having calculated the *M*(*T*) dependence, one can also determine the number of compensation points. The typical *M*(*T*) dependence for a compound with two compensation points is presented in Fig. 2. The region of values of the parameters x_2 and x_3 corresponding to the compounds with two compensation points is shown in Fig. 3. A characteristic feature of these compounds is a strong dependence of the compensation temperatures on composition. In Figs. 4 and 5, the dependences of the first and second compensation temperatures on the

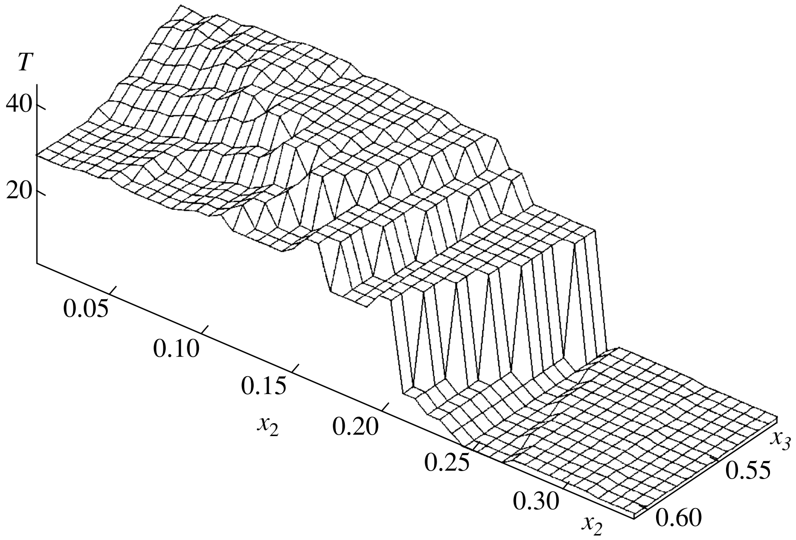

Fig. 4. First-compensation-point temperature dependence on the composition.

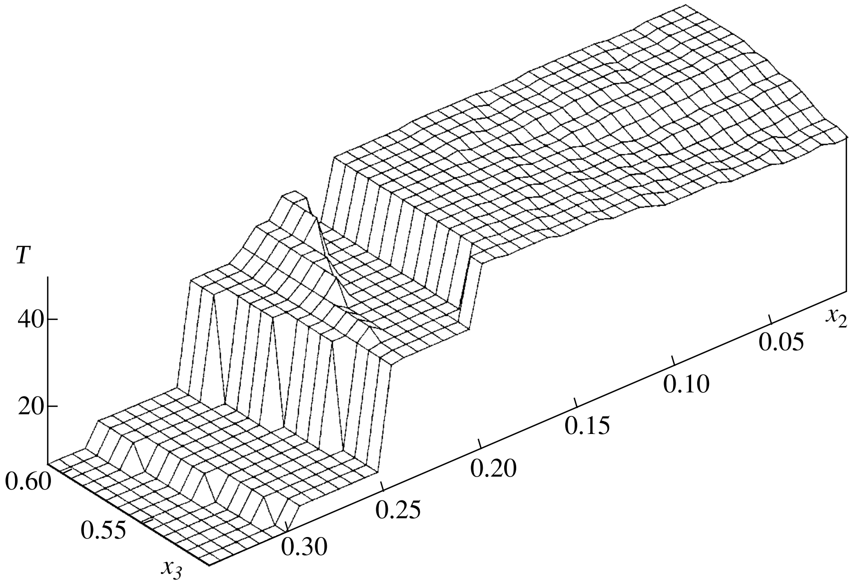

Fig. 5. Second-compensation-point temperature dependence on the composition.

composition are presented, respectively. It can be seen that these dependences have a sharp steplike character.

Having calculated the dependences $\langle S_k \rangle$ and θ on the temperature and external magnetic field, one can plot the *H*–*T* phase diagram for a given composition. A typical *H*–*T* phase diagram for a composition with two compensation points is presented in Fig. 6. As one would expect, the lower critical field H_{C_1} for the phase transition from the collinear to a noncollinear phase is equal to zero at the compensation points. Of course, for a more comprehensive understanding of the *H*–*T* phase diagram and of the physical properties of the material near the compensation points and in between, one should include magnetic anisotropy in the model, i.e., the crystal fields acting on the magnetic ions, and also, possibly, anisotropy of exchange interactions. As a result, one should expect the lower-field region of the *H*–*T* phase diagram to be very complicated because of the occurrence of lines of first-order phase transitions,

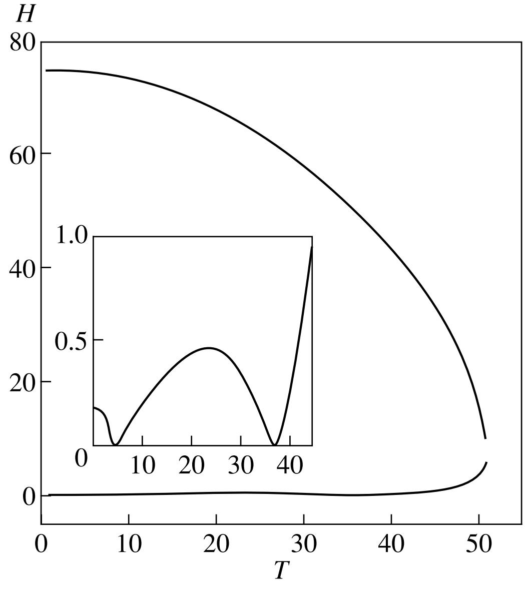

Fig. 6. *H*–*T* phase diagram for the $(Ni_{0.24}Mn_{0.61}Fe_{0.15})_{1.5}[Cr(CN)_6]$ composition.

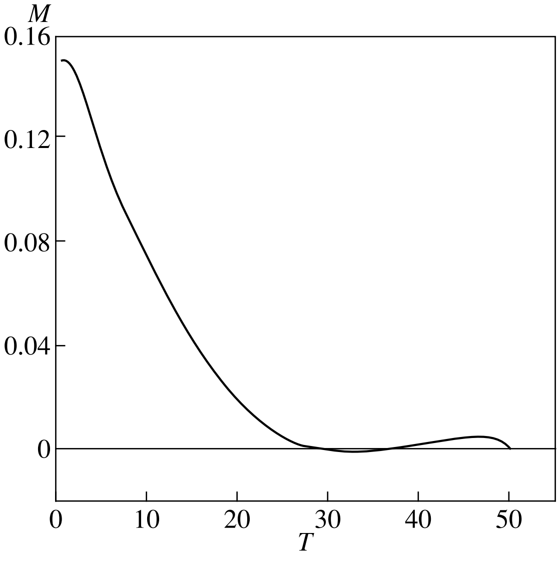

Fig. 7. Magnetization temperature dependence for the $(Ni_{0.2}Mn_{0.6}Fe_{0.2})_{1.5}[Cr(CN)_6]$ composition.

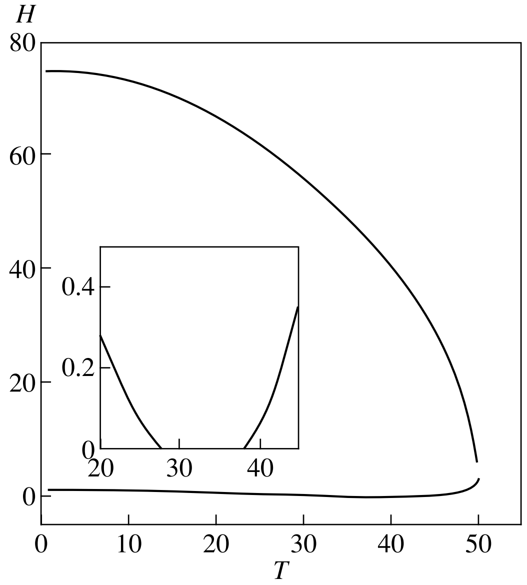

Fig. 8. *H–T* phase diagram for the $(Ni_{0.2}Mn_{0.6}Fe_{0.2})_{1.5}[Cr(CN)_6]$ composition.

tricritical points, and critical points of the gas–liquid type, which are always accompanied by characteristic anomalies in the physical properties, like heat capacity, magnetothermal effect, temperature magnetic hysteresis, magnetic susceptibility, magnetoelastic and magnetooptical properties, and domain structure [2, 17]. These issues as applied to molecular ferrimagnets will be considered elsewhere.

Some compounds with two compensation points reveal an intriguing feature. The net magnetization is small in a wide temperature range (in between the compensation points), and these compounds, as to their magnetic properties, are similar to antiferromagnets. The $M(T)$ dependence and the *H–T* phase diagram for the compound showing these properties are presented in Figs. 7 and 8. On this point, they can be compared to the ferromagnets with virtually zero magnetization discovered recently [19].

In concluding, the magnetic properties of the analogs of iron earth with two compensation points are investigated theoretically. The dependences of the compensation temperatures on the chemical composition are calculated, and the *H–T* phase diagrams are plotted. It is shown that some compositions, as to their properties, are similar to antiferromagnets in the temperature range between the compensation points.

ACKNOWLEDGMENTS

This work was supported by the Russian Foundation for Basic Research, project no. 99-02/17830, the Coordinational-Analytical Center of Innovation and Science/Engineering Programs, project no. 97-1071, and the International Association Program (INTAS), project no. 97-705. The calculations were supported by the Russian Foundation for Basic Research, project no. 98-07/90171.

REFERENCES

1. L. Neel, Ann. Phys. (Paris) **3** (2), 137 (1948).
2. A. K. Zvezdin, in *Handbook of Magnetic Materials*, Ed. by K. H. J. Buschow (Elsevier, Amsterdam, 1995), Vol. 9, p. 405.
3. S. Ohkoshi, Y. Abe, A. Fujishima, and K. Hashimoto, Phys. Rev. Lett. **82** (6), 1285 (1999).
4. S. Ohkoshi, S. Yorozu, O. Sato, *et al.*, Appl. Phys. Lett. **70** (8), 1040 (1997).
5. O. Sato, T. Iyoda, A. Fujishima, and K. Hashimoto, Science **272** (5262), 704 (1996).
6. A. Ludi and H. U. Güdel, in *Structure and Bonding*, Ed. by J. D. Dunitz, P. Hemmerich, J. A. Ibers, C. K. Jorgensen, J. B. Neilands, R. S. Neiholm, D. Reinen, and R. J. P. Williams (Springer-Verlag, Berlin, 1973), Vol. 14, p. 1.
7. W. D. Griebler and D. Babel, Z. Naturforsch. B **87** (7), 832 (1982).
8. T. Mallah, S. Thiebaut, M. Verdaguer, and P. Veillet, Science **262** (5139), 1554 (1993).
9. W. R. Entley and G. S. Girolami, Inorg. Chem. **33** (23), 5165 (1994).
10. W. R. Entley and G. S. Girolami, Science **268** (5209), 397 (1995).
11. S. Ferlay, T. Mallah, R. Ouahes, *et al.*, Nature **378** (6508), 701 (1995).
12. O. Sato, T. Iyoda, A. Fujishima, and K. Hashimoto, Science **271** (5245), 49 (1996).
13. W. E. Buschmann, S. C. Paulson, C. M. Wynn, *et al.*, Adv. Mater. **9** (8), 645 (1997).
14. S. Ohkoshi, T. Iyoda, A. Fujishima, and K. Hashimoto, Phys. Rev. B **56** (18), 11642 (1997).
15. S. Ohkoshi, O. Sato, T. Iyoda, *et al.*, Inorg. Chem. **36** (3), 268 (1997).
16. S. Ohkoshi, A. Fujishima, and K. Hashimoto, J. Am. Chem. Soc. **120** (21), 5349 (1998).
17. K. P. Belov, A. K. Zvezdin, A. M. Kadomtseva, and R. Z. Levitin, *Orientation Transitions in Rare-Earth Magnets* (Nauka, Moscow, 1979).
18. S. V. Tyablikov, *Methods in the Quantum Theory of Magnetism* (Nauka, Moscow, 1975, 2nd ed.; Plenum, New York, 1967).
19. H. Adachi and H. Ino, Nature **401** (6749), 148 (1999).

Translated by N. Kovaleva

Physics of the Solid State, Vol. 43, No. 9, 2001, pp. 1720–1727. Translated from Fizika Tverdogo Tela, Vol. 43, No. 9, 2001, pp. 1651–1657.
Original Russian Text Copyright © 2001 by Nikitin, I. Tereshina, Pankratov, E. Tereshina, Skourski, Skokov, Pastushenkov.

Magnetic Anisotropy and Magnetostriction in a Lu_2Fe_{17} Intermetallic Single Crystal

S. A. Nikitin*, **, I. S. Tereshina*, **, N. Yu. Pankratov*, E. A. Tereshina*, Yu. V. Skourski*, **, K. P. Skokov*, and Yu. G. Pastushenkov*****

** Moscow State University, Vorob'evy gory, Moscow, 119899 Russia*
*** International Laboratory of High Magnetic Fields and Low Temperatures, Wroclaw, 53-421 Poland*
**** Tver State University, ul. Zhelyabova 33, Tver, 170000 Russia*
e-mail: nikitin@rem.phys.msu.su

Received February 5, 2001

Abstract—The magnetic anisotropy and magnetostriction of a Lu_2Fe_{17} single crystal are investigated. The temperature dependence of the magnetic anisotropy constant K_1 is measured in the range 4.2–300 K. The results obtained are compared with the data calculated using the Callen theoretical formula. It is found that the temperature dependence of K_1 for the Lu_2Fe_{17} single crystal deviates from the temperature curve predicted by the localized single-ion model. The inference is drawn that a certain contribution to the magnetic anisotropy of the Lu_2Fe_{17} compound is made by the magnetic anisotropy of band electrons. The longitudinal, transverse, and volume magnetostrictions of the Lu_2Fe_{17} single crystal are studied, and the magnetostriction constants are calculated. It is demonstrated that the exchange integral of Lu_2Fe_{17}, as for the Y_2Fe_{17} compound, substantially depends on the atomic volume. This dependence is responsible for the considerable difference between the Curie temperatures of the Lu_2Fe_{17} and Y_2Fe_{17} compounds. It is revealed that the magnetostriction of the Lu_2Fe_{17} single crystal in the temperature range of the magnetic phase transition is determined by the two-ion exchange and single-ion contributions. *© 2001 MAIK "Nauka/Interperiodica".*

1. INTRODUCTION

Intermetallic compounds with the stoichiometric formula R_2Fe_{17} are ferromagnets (R is a rare-earth element of the cerium subgroup) or ferrimagnets (R is a rare-earth element of the yttrium subgroup) [1–3]. A characteristic feature of these compounds is that their magnetic properties strongly depend on the interatomic distance and atomic volume [4, 5]. This manifests itself in a substantial change in the magnetic ordering temperature T_C under pressure [5–8] and in a considerable magnetostriction of R_2Fe_{17} compounds [3, 9–11]. Undoubtedly, the most impressive effect associated with variations in the magnetic properties with an increase in the atomic volume consists in increasing the T_C temperature by approximately 200 K upon introduction of nitrogen atoms into the crystal lattice of Sm_2Fe_{17} [12], which is accompanied by the appearance of a strong uniaxial magnetic anisotropy. As a result, the $Sm_2Fe_{17}N$ compound becomes very promising in designing strong permanent magnets. From these facts, it is clear that the investigation into the magnetoelastic properties of R_2Fe_{17} compounds is an urgent problem.

Among these intermetallic compounds, Lu_2Fe_{17} is the least known metallide. A distinguishing feature of the Lu_2Fe_{17} compound is the zero magnetic moment of its rare-earth sublattice. For this compound, the temperature dependence of the magnetic anisotropy is unknown and the available data on the magnetostriction are fragmentary. As far as we know, Givord and Lacheisserie [9] analyzed only the temperature dependence of the magnetostriction susceptibility of Lu_2Fe_{17} crystals in a field of 3 kOe near the Curie temperature. However, investigation into the magnetic properties of the Lu_2Fe_{17} compound can provide a deeper insight into the nature of the magnetism of the iron sublattice.

In the present work, an attempt was made to fill the gap in the knowledge of the magnetism of this poorly understood compound. For this purpose, we studied the magnetic anisotropy and magnetostriction of a Lu_2Fe_{17} single crystal.

2. SAMPLE PREPARATION AND EXPERIMENTAL TECHNIQUE

Experiments were performed with single-crystal samples of the Lu_2Fe_{17} compound. The initial alloy was prepared by induction melting in an argon atmosphere in an alundum crucible. High-purity iron (99.9%) and lutetium (99.5%) served as the initial components. The weight of the melted ingot was 150 g. X-ray diffraction analysis was carried out on a DRON-3M diffractometer. A tube with a Co cathode was used as an x-ray source. According to x-ray diffraction analysis, the initial metallide was predominantly single-phase (the content of α-iron impurity was no more than 3%). The Lu_2Fe_{17} compound has a hexagonal crystal lattice of the

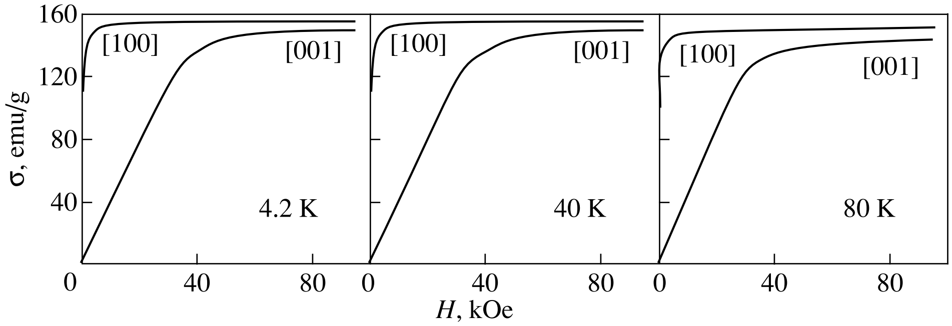

Fig. 1. Magnetization curves for the Lu_2Fe_{17} compound along the [100] and [001] crystallographic directions at temperatures of 4.2, 40, and 80 K.

Th_2Ni_{17} type. The lattice parameters determined from the experimental x-ray diffraction patterns are in good agreement with the data available in the literature [13].

Single crystals of Lu_2Fe_{17} were grown with the use of a resistance furnace. The samples were heated above the melting temperature, allowed to stand for 1 h, and were then slowly cooled under conditions specially chosen to increase the size of the crystal grains. The monocrystallinity of the samples was checked by the Laue method.

The surface finish quality of the single-crystal samples under investigation and their chemical composition were checked at the Institute of Low Temperatures and Structure Research (Wroclaw, Poland). According to the results obtained, the chemical composition of the single crystals prepared corresponds to the chemical formula Lu_2Fe_{17} to an accuracy of tenths of a percent. In the present work, all magnetic measurements were performed with single crystals or single-crystal aggregates with a misorientation angle of no more than two or three degrees.

The magnetic measurements were carried out on torque and capacitance magnetometers with single-crystal samples ~2 mm in size. The experimental curves of the mechanical torque were recorded on a torque magnetometer in the temperature range 77–350 K in magnetic fields up to 12 kOe with the use of disk-shaped samples ≈5 mm in diameter. The torque moments were measured in two degree intervals upon rotation of single crystals with respect to the magnetic field. The magnetization curves were obtained with a capacitance magnetometer at the International Laboratory of High Magnetic Fields and Low Temperatures (Wroclaw, Poland) in the temperature range from 4.2 to 80 K in magnetic fields up to 100 kOe.

The magnetostriction was measured by the tensometric technique. The strain gauges used in our measurements were fabricated from a strain-sensitive wire without any noticeable galvanomagnetic effect. The strain gauges were cemented to the surface of the single-crystal sample along the [001] and [100] crystallographic axes. The magnetostriction measurements were performed in the temperature range 80–300 K.

3. MAGNETIC PROPERTIES

The magnetic properties of the Lu_2Fe_{17} compound have been scarcely investigated. There is evidence that the magnetic ordering temperature of the Lu_2Fe_{17} metallide differs from that of the Y_2Fe_{17} compound by approximately 80 K and that the magnetic moment of Lu_2Fe_{17} is aligned with the basal plane at 4.2 K [4]. Moreover, the neutron diffraction data [4] have demonstrated that, in a certain temperature range below the Curie temperature, the Lu_2Fe_{17} compound has a helicoidal magnetic structure. However, no detailed analysis was performed to elucidate the behavior of the magnetization and magnetic anisotropy of the Lu_2Fe_{17} metallide over wide ranges of temperatures and magnetic fields, and hence, the magnetism of this compound calls for further investigation.

The magnetization curves for the Lu_2Fe_{17} single crystal were measured in strong magnetic fields in the range from 1 to 100 kOe. No transition to the helicoidal magnetic state was revealed in the field range covered. It is quite possible that this transition occurs in weaker fields. In this paper, we report our data on the magnetic properties necessary for determining the Curie temperature and magnetic anisotropy constants.

Figure 1 shows the magnetization curves measured along different crystallographic directions in fields up to 100 kOe at temperatures of 4.2, 40, and 80 K. It is seen that the [001] hexagonal axis is the hard magnetization axis, whereas the [100] axis lying in the basal plane is the easy magnetization axis (EMA). The effective magnetic anisotropy field H_A is equal to 40 kOe at $T = 4.2$ K and decreases to 36 kOe with an increase in the temperature to 80 K. These findings are in excellent agreement with the results obtained by Givord and Lemaire [4]: the magnetic anisotropy field H_A is also equal to 40 kOe at $T = 4.2$ K.

It can be seen from the torque curves (Fig. 2) that, in the temperature range 80–325 K, the Lu_2Fe_{17} com-

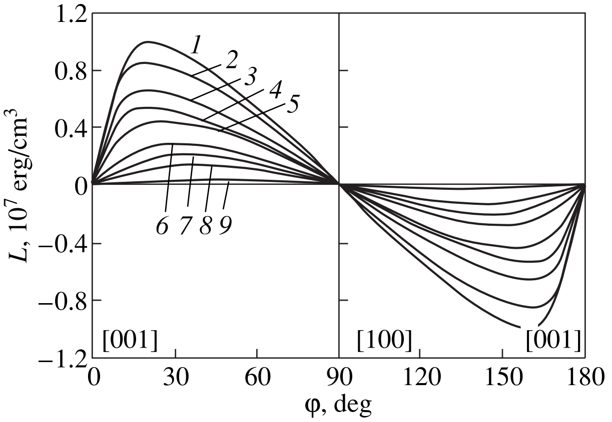

Fig. 2. Mechanical torque curves for the Lu_2Fe_{17} single crystal in a magnetic field of 12 kOe at different temperatures (K): (*1*) 80, (*2*) 140, (*3*) 150, (*4*) 200, (*5*) 225, (*6*) 260, (*7*) 280, (*8*) 290, and (*9*) 325.

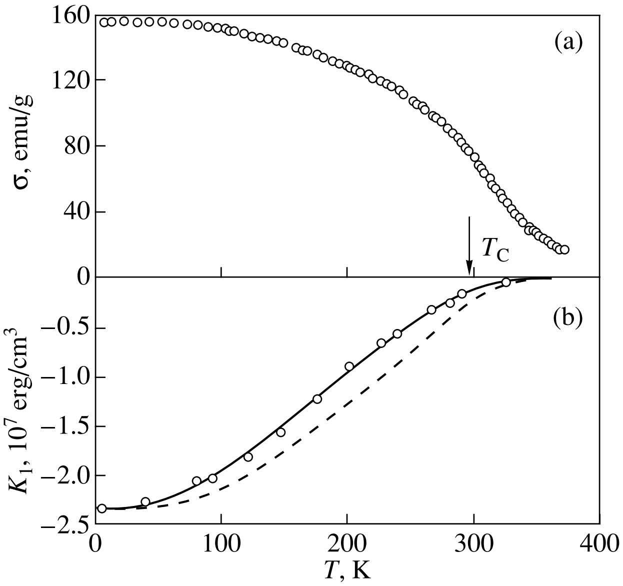

Fig. 3. (a) Temperature dependence of the magnetization in a magnetic field of 10 kOe and (b) experimental (solid line) and theoretical (dashed line) temperature dependences of the magnetic anisotropy constant K_1 for the Lu_2Fe_{17} single crystal.

pound is a ferromagnet with an easy-plane anisotropy. In this compound, the basal plane of the hexagonal crystal lattice is the easy plane. The [001] hexagonal axis is the hard magnetization axis over the entire temperature range. The results obtained from analysis of the magnetization and torque curves allowed us to conclude that easy-plane magnetic anisotropy occurs over the entire temperature range from 4.2 K to the Curie point.

Among the new results obtained in the present work are data on the temperature dependence of the magnetic anisotropy constant K_1. In the temperature range 4.2–80 K, the anisotropy constants were determined by the Sucksmith–Thompson method, which involved special mathematical processing of the experimental magnetization curves $M(H)$ measured along the hard magnetization direction (the [001] axis). It can readily be shown that, for a ferromagnet with the easy magnetization axis lying in the basal plane of a hexagonal crystal in an external magnetic field $H \parallel [001]$, the magnetization M and the external magnetic field H are related by the expression

$$\frac{H}{M} = \frac{2K_1}{M_S^2} + \frac{4K_2}{M_S^4}M^2, \tag{1}$$

where M_S is the spontaneous magnetization and K_1 and K_2 are the first-order and second-order magnetic anisotropy constants, respectively. By plotting H/M as a function of M^2 at different temperatures, we obtained the temperature dependence $K_1(T)$. The magnitude of K_2 was found to be negligibly small.

In the temperature range from 80 K to T_C, the K_1 constants were determined through mathematical processing of the torque curves $L(\theta)$ according to the least-squares procedure. The angular dependence $L(\theta)$ in the crystallographic plane $(01\bar{1}0)$ is defined by the relationship

$$L = K_1 \sin 2\theta + 2K_2 \sin 2\theta \sin^2\theta, \tag{2}$$

where θ is the angle between the **c** axis and the spontaneous magnetic moment $\mathbf{M}_S$. It was found that the $K_1(T)$ values are three orders of magnitude larger than the $K_2(T)$ values over the entire temperature range under investigation. Therefore, we can conclude that the K_1 anisotropy constant dominates over the K_2 constant.

The temperature dependences of the magnetic anisotropy constant and the magnetization in a field of 10 kOe are displayed in Fig. 3. The Curie temperature (T_C = 298 K) was determined from the specific magnetization curves $\sigma_S(H)$ in the magnetic transition range according to the Belov–Arrott method by plotting the curves $H/\sigma = f(\sigma^2)$. The curve $\sigma(T)$ in a field of 10 kOe falls off at a temperature higher than T_C, which can be explained by the contribution of the paraprocess to the magnetization. As a result, the magnetization becomes equal to the sum of the spontaneous magnetization σ_S and the magnetization induced by the paraprocess. This is responsible for the tail in the $\sigma(T)$ curve at $T > T_C$ (Fig. 3a).

As the temperature increases, the magnetic anisotropy constant (Fig. 3b) decreases more rapidly compared to the magnetization, which is consistent with the single-ion theory of crystalline magnetic anisotropy

[14]. However, the relationship following from this theory,

$$\frac{K_1(T)}{K_1(0)} = \left[\frac{M(T)}{M(0)}\right]^3, \tag{3}$$

should be considered an approximation. This can be associated with the contribution of the band 3*d* electrons to the magnetic anisotropy in addition to the main contribution of the iron 3*d* localized electrons.

It should be noted that the Lu_2Fe_{17} single crystal is characterized by the anisotropy of the saturation magnetization, i.e., by the difference ΔM_S between the saturation magnetizations M_S for the [100] and [001] directions. The value of ΔM_S at 4.2 K is of the order of ~4%, which is close in magnitude to ΔM_S for Y_2Fe_{17} crystals [15]. This effect can be explained by the fact that the anisotropic spin–orbit interaction affects the electronic states near the Fermi level [16, 17]. Note that, for the Lu_2Fe_{17} compound, the anisotropy ΔM_S per iron atom is equal to 0.087 μ_B and the magnetic moment M_S per iron atom is 1.99 μ_B. For the Y_2Fe_{17} compound, these magnetic characteristics per iron atom are as follows: $\Delta M_S = 0.016\ \mu_B$ [15] and $M_S = 2.01\mu_B$ [15] and $2.15\mu_B$ [8].

It is interesting that, at $T = 4.2$ K, the magnetic anisotropy constant $K_1 = -2.3 \times 10^7$ erg/cm^3 for Lu_2Fe_{17} coincides with the anisotropy constant $K_1 = -2.3 \times 10^7$ erg/cm^3 for Y_2Fe_{17} [15].

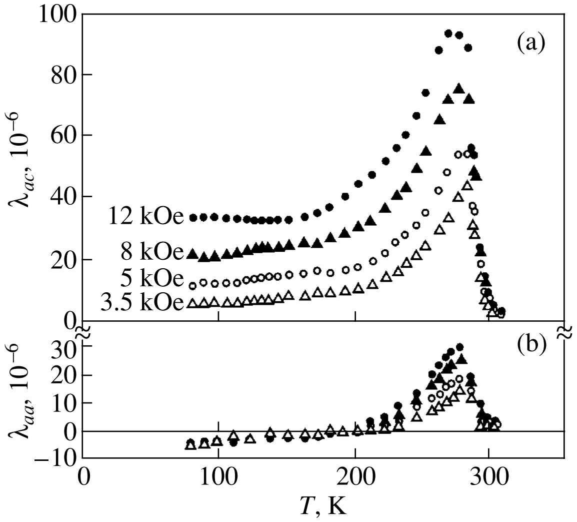

Fig. 4. Temperature dependences of the magnetostriction: (a) $\lambda_{ac}(T)$ and (b) $\lambda_{aa}(T)$.

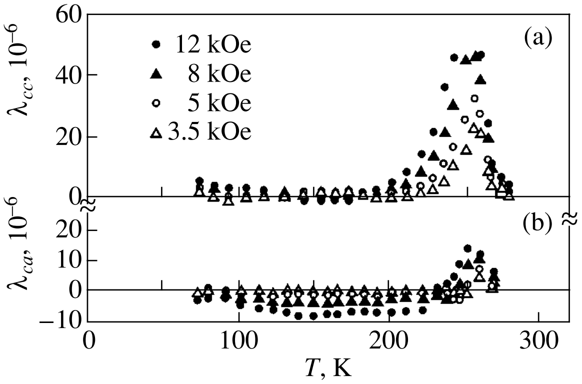

Fig. 5. Temperature dependences of the magnetostriction: (a) $\lambda_{cc}(T)$ and (b) $\lambda_{ca}(T)$.

4. MAGNETOSTRICTION

In order to elucidate the nature of the magnetostriction in Lu_2Fe_{17}, we examined in close detail the temperature and field dependences of the longitudinal and transverse magnetostrictions for the Lu_2Fe_{17} single crystal in the temperature range 78–300 K in magnetic fields (up to 12 kOe) parallel and perpendicular to the hexagonal axis **c** (the [001] direction). The single-crystal sample had the form of a disk whose plane coincided with the crystallographic plane passing through the **a** and **c** axes.

As follows from Figs. 4 and 5, the magnetostriction λ_{ac} (the first and second subscripts refer to the directions of the applied field and magnetostrictive strain measurement, respectively) considerably exceeds the magnetostriction in the basal plane. Consequently, the magnetic field applied in the basal plane induces an anisotropic strain of the crystal lattice: the interatomic distances along the **c** axis increase to a greater extent than those in the basal plane. Note that the magnetostrictive strains in both directions are positive, which indicates an increase in the sample volume in the magnetic field. The volume magnetostriction in the field along the **c** axis is defined by the relationship

$$\omega_c = \frac{\Delta V}{V} = \lambda_{cc} + 2\lambda_{ca}, \tag{4}$$

and the volume magnetostriction along the **a** axis is given by

$$\omega_a = \lambda_{ac} + 2\lambda_{aa}. \tag{5}$$

Figure 6 depicts the temperature dependences of ω_c and ω_a, which were determined from the experimental curves $\lambda_{cc}(H)$ and $\lambda_{ac}(H)$.

It is worth noting that, upon heating of the samples, the magnetostrictions $\lambda_{cc}(H)$, $\lambda_{ac}(H)$, and ω_c increase significantly as the Curie temperature T_C is approached (Figs. 4–6). The temperature of the maxima (T_{max}) in the $\lambda_{cc}(T)$, $\lambda_{ac}(T)$, $\omega_c(T)$, and $\omega_a(T)$ curves depends on the magnetic field strength. The higher the magnetic field strength *H*, the lower the T_{max} temperature (for example, $T_{max} = 275$ K at $H = 12$ kOe and $T_{max} = 280$ K at $H = 3$ kOe for the dependence $\lambda_{cc}(T)$). This behavior of the magnetostriction of the Lu_2Fe_{17} single crystal is anomalous compared to that of typical ferromagnets. It

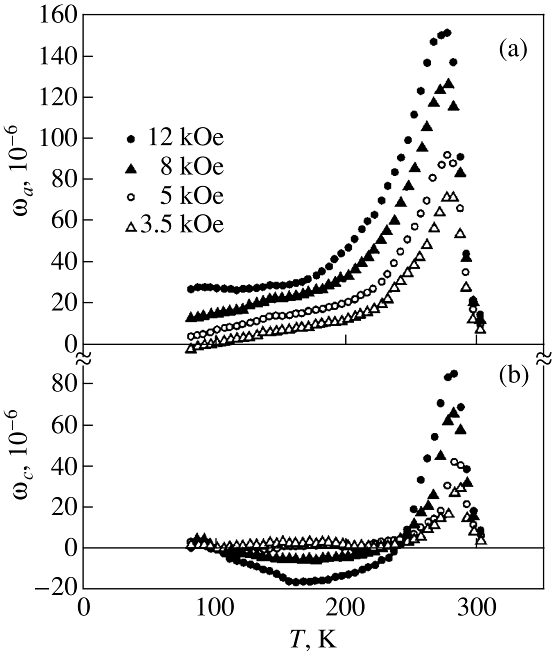

Fig. 6. Temperature dependences of the volume magnetostriction: (a) $\omega_a(T)$ and (b) $\omega_c(T)$.

seems likely that, in the temperature range from $T_{\max}$ to T_C, the Lu_2Fe_{17} single crystal has a helicoidal magnetic structure which is destroyed in relatively low fields $H <$ 2 kOe. The occurrence of this structure in Lu_2Fe_{17} is confirmed by the neutron diffraction data [4].

According to the theory [18], the volume magnetostrictions ω_a(**H** || **a**) and ω_c(**H** || **c**) can be represented as linear combinations of two magnetostriction constants λ_{11}^a and λ_{12}^a:

$$\omega_a = \lambda_{11}^a - \frac{1}{2\sqrt{3}}\lambda_{12}^a, \quad (6)$$

$$\omega_c = \lambda_{11}^a + \frac{1}{\sqrt{3}}\lambda_{12}^a. \quad (7)$$

Here, λ_{11}^a is the two-ion isotropic exchange constant and λ_{12}^a is the single-ion constant.

Furthermore, the magnetostriction brings about a change in the axial ratio c/a, which can be represented as a linear combination of two magnetostriction constants λ_{21}^a and λ_{22}^a for the two following cases. In the magnetic field **H** || **a**, we have

$$\frac{1}{2}\lambda_{ac} - \frac{1}{2}(\lambda_{aa} + \lambda_{ab}) = \lambda_{21}^a - \frac{1}{2\sqrt{3}}\lambda_{22}^a. \quad (8)$$

For **H** || **c**, we obtain

$$\frac{1}{2}(\lambda_{cc} - \lambda_{ca}) = \lambda_{21}^a + \frac{1}{\sqrt{3}}\lambda_{22}^a. \quad (9)$$

Here, λ_{21}^a is the two-ion exchange constant and λ_{22}^a is the single-ion constant.

The constants λ_{11}^a and λ_{21}^a account for the isotropic pair exchange and pseudodipole interactions of two neighboring magnetic ions. The constants λ_{12}^a and λ_{22}^a characterize the anisotropic interaction between the magnetic ion and the crystal field induced by the surrounding ions of the crystal lattice. The exchange interactions make isotropic contributions (independent of the direction cosines of the magnetization vector) to the magnetostrictive strain, whereas the single-ion interactions make anisotropic contributions (dependent on the direction of the magnetization vector).

By ignoring the orthorhombic distortions and shear strains, which are not observed in the temperature range studied, the magnetostrictive strain with due regard for the λ_{11}^a, λ_{12}^a, λ_{21}^a, and λ_{22}^a constants can be written in the following form [18]:

$$\lambda_{\alpha\beta} = \frac{1}{3}\lambda_{11}^a + 2\lambda_{21}^a\left(\beta_Z^2 - \frac{1}{3}\right) + \frac{1}{2\sqrt{3}}\lambda_{12}^a\left(\alpha_Z^2 - \frac{1}{3}\right) + \sqrt{3}\lambda_{22}^a\left(\alpha_Z^2 - \frac{1}{3}\right)\left(\beta_Z^2 - \frac{1}{3}\right), \quad (10)$$

where α_Z and β_Z are the direction cosines of the magnetization vector and the strain direction, respectively.

The temperatures dependences of the magnetostriction constants (Fig. 7) were calculated from the experimental data on the λ_{ac}, λ_{ca}, λ_{aa}, and λ_{cc} magnetostrictions according to formulas (4)–(9). In the magnetic transition range, the difference between λ_{aa} and λ_{ab} can be ignored.

It follows from Fig. 7 and relationship (6) that the exchange magnetostriction ω_a is determined by two nearly identical positive contributions, namely, by the two-ion exchange constant λ_{11}^a and the single-ion constant λ_{12}^a. The temperature at a maximum in the $\lambda_{11}^a(T)$ curve is ~20 K higher than that in the $\lambda_{12}^a(T)$ curve. The exchange constant λ_{21}^a and the single-ion constant λ_{22}^a also contribute to the change in the axial ratio c/a.

5. DISCUSSION

Trivalent ions Lu^{3+} do not possess paramagnetic moments, because the 4*f* electron subshell of lutetium ions is completely filled ($L = 0$ and $S = 0$). Therefore, the magnetic moment of the Lu_2Fe_{17} compound is determined only by the magnetic moments of the Fe ions. It is of interest to compare the properties of Lu_2Fe_{17} and Y_2Fe_{17}, because the latter compound has a similar crystal structure and its magnetism is governed by the iron sublattice. In the Y_2Fe_{17} compound, the yttrium ions Y^{3+} also do not exhibit magnetic moments. Since yttrium belong to the 4*d* transition elements, the question arises as to how the specific features of the electronic structures of lutetium and yttrium ions affect the magnetism of the Lu_2Fe_{17} and Y_2Fe_{17} compounds. These compounds have identical crystal structures and the same number of iron atoms per unit cell in their crystal lattices. At the same time, the electronic structures of lutetium ($4d^{10}4f^{14}5s^25p^65d^16s^2$) and yttrium ($4d^15s^2$) atoms differ significantly.

Tables 1 and 2 present the main crystal data (the *a* and *c* parameters of the hexagonal crystal lattice and the unit cell volume *V*) and some magnetic characteristics (magnetic moments μ_{Fe} per iron atom at 4.2 K, the Curie temperatures T_C, and the magnetic anisotropy constants at 4.2 K) for the Lu_2Fe_{17} and Y_2Fe_{17} compounds. A comparison of the results obtained shows that the magnetic moments μ_{Fe} and anisotropy constants K_1 for Lu_2Fe_{17} and Y_2Fe_{17} single crystals at 4.2 K are in close agreement. This suggests that these compounds have similar magnetic and electronic structures and the specific features of the electronic structures of Lu^{3+} and Y^{3+} ions do not substantially affect the magnetic anisotropy.

However, the Curie temperatures of these compounds differ by approximately 76 K. With the aim of elucidating the physical mechanisms responsible for the large difference in the Curie temperature, we considered some phenomena that provide information on the dependence of the exchange integral on the atomic volume. These are the change in the T_C temperature under pressure and the volume magnetostriction $\omega = dV/V$.

Table 1 lists the experimental data on the quantity $d\ln T_C/dp$ and the compressibility κ for the Y_2Fe_{17} compound. It is known that the compressibility κ is defined as

$$\kappa = -\frac{\Delta V/V}{p}. \qquad (11)$$

Table 1. Lattice parameters *a* and *c*, unit cell volumes *V*, changes in the Curie temperature T_C under pressure, and compressibilities κ for the Lu_2Fe_{17} and Y_2Fe_{17} compounds

Compound	*a*, Å	*c*, Å	*V*, Å	$d\ln T_C/dp$, kbar^{-1}	κ, kbar^{-1}
Y_2Fe_{17}	8.485	8.300	516.8	-12.6×10^{-3}	1.05×10^{-3}
Lu_2Fe_{17}	8.418	8.295	508.4	-8.4×10^{-3}	–

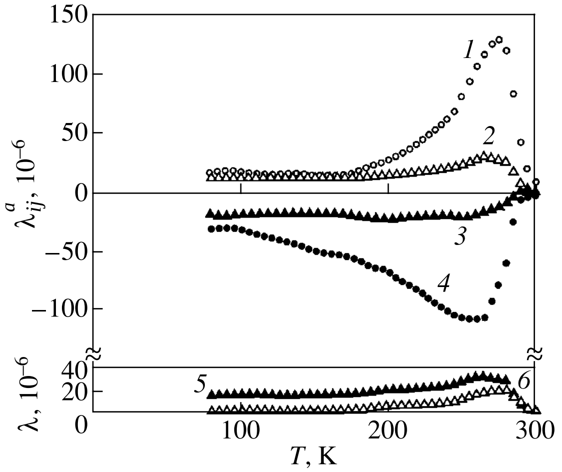

Fig. 7. Temperature dependences of the (*1*) λ^a_{11}, (*2*) λ^a_{21}, (*3*) λ^a_{22}, and (*4*) λ^a_{12} magnetostriction constants and the change in the axial ratio *c*/*a* at (*5*) **H** ∥ **c** and (*6*) **H** ∥ **a** in the magnetic field *H* = 12 kOe according to the calculation by formulas (8) and (9).

The change in T_C under pressure is related to the change in T_C under variation in the atomic volume by the expression

$$\frac{d\ln T_C}{dp} = -\frac{\kappa}{T_C}\frac{dT_C}{d\ln V} = -\kappa\frac{d\ln T_C}{d\ln V}. \qquad (12)$$

The difference between the unit cell volumes of Y_2Fe_{17} and Lu_2Fe_{17} single crystals is determined as follows (Table 1):

$$\frac{\Delta V}{V} = \frac{V_{Y_2Fe_{17}} - V_{Lu_2Fe_{17}}}{V_{Y_2Fe_{17}}} = 1.62 \times 10^{-2}. \qquad (13)$$

The change in Curie temperature due to a decrease in the unit cell volume *V* by the value $\Delta V/V = 1.6 \times 10^{-2}$ can be calculated from the experimental value of $\partial\ln T_C/\partial p = -12.6 \times 10^{-3}$ kbar^{-1}. From relationship (12) with the compressibility $\kappa = 1.05 \times 10^{-3}$ kbar^{-1} [8], we obtain

$$\Delta T_C = -\frac{T_C}{\kappa}\frac{\Delta V}{V}\frac{d\ln T_C}{dp} = 74\ \text{K}, \qquad (14)$$

Table 2. Curie temperatures, magnetic moments, magnetization anisotropies, and magnetic anisotropy constants for the Lu_2Fe_{17} and Y_2Fe_{17} compounds

Compound	T_C, K	$\mu_{Fe/at}$, μ_B	ΔM_S, μ_B	K_1, 10^7 erg/cm^3
Y_2Fe_{17}	374	2.01	0.016	–2.3 [14]
Lu_2Fe_{17}	298	1.99	0.087	–2.3

which is close to the difference between the Curie temperatures of Y_2Fe_{17} and Lu_2Fe_{17}. Therefore, it can be concluded that a decrease in the T_C temperature for Lu_2Fe_{17} as compared to that for Y_2Fe_{17} is associated with the decrease in the exchange integral due to the decrease in the atomic volume.

Let us now consider the dependence of the exchange integral on the atomic volume for Lu_2Fe_{17}. The change in the T_C temperature of this compound with variation in the pressure is unknown. However, the value of $d\ln T_C/dp$ can be calculated from the thermodynamic relationships under the assumption that the magnetization I in the paraprocess range is a function of T/T_C and H, that is,

$$\left(\frac{\partial\omega}{\partial H}\right)_p = -\left(\frac{\partial I}{\partial p}\right)_H = T\left(\frac{\partial I}{\partial T}\right)_H \frac{\partial \ln T_C}{\partial p}. \qquad (15)$$

From this relationship, we obtain

$$\frac{\partial \ln T_C}{\partial p} = \frac{1}{T\left(\frac{\partial I}{\partial T}\right)_H}\left(\frac{\partial\omega}{\partial H}\right)_p. \qquad (16)$$

By substituting the experimental values of $\partial\omega/\partial H = 15.4$ kOe^{-1} and $\partial I/\partial T = -7.1$ G/K into expression (16), we obtained $\partial \ln T_C/\partial p = -8.4 \times 10^{-3}$ kbar^{-1}, which only slightly differs from the corresponding value for Y_2Fe_{17} (Table 1). It was also of interest to determine the relative change α in the exchange integral A with a change in the atomic volume, that is,

$$\alpha = \frac{d\ln A}{d\ln V} = \frac{d\ln T_C}{d\ln V}. \qquad (17)$$

According to our calculations, the relative change $\alpha = 12$ for Y_2Fe_{17} (calculated from the experimental change in T_C under pressure) and $\alpha = 8$ for Lu_2Fe_{17} (determined from the volume magnetostriction of the paraprocess). Despite the difference between the values of α, the inference can be drawn that the exchange integral for both Y_2Fe_{17} and Lu_2Fe_{17} compounds strongly depends on the atomic volume. It should be noted that α for rare-earth metals and other rare-earth intermetallic compounds is substantially less (for example, $\alpha = 2$ and 1.8 for Gd and Tb, respectively [19]).

Now, we attempt to explain the large volume magnetostriction of the paraprocess in the vicinity of the Curie temperature. For this purpose, it should be taken into account that the hexagonal crystal structure of R_2Fe_{17} compounds (the Th_2Ni_{17}-type structure) involves alternating atomic basal planes which are normal to the hexagonal axis and are occupied by iron atoms in the four crystallographic positions 4*f*, 6*g*, 12*j*, and 12*k* [4]. Although the exchange force for Lu_2Fe_{17} is positive, there are the very short distances between iron atoms that occupy 4*f* positions and form a dumbbell perpendicular to a hexagon comprised of nearest-neighbor Fe atoms in 12*j* positions so that the exchange interaction constant for iron atoms in 4*f* positions is negative [4]. Most likely, this is the main reason for the maximum magnetostriction along the *c* axis, because the dumbbell axis is perpendicular to the atomic basal planes. According to the theory [20], the direct electron hopping between the iron atoms in 4*f* positions makes the main contribution to the two-ion exchange magnetostriction. Since these structural units are involved in crystal lattices of both Y_2Fe_{17} and Lu_2Fe_{17} compounds, they can contribute considerably to their magnetostrictions, which, according to the data obtained in [9] and our results, are close in magnitude to each other. This contribution is accounted for by the magnetostriction constant λ_{11}^{a}, which has a maximum value.

The aforementioned structural unit (the hexagon plus the 4*f*–4*f* dumbbell) is surrounded by three Lu (in Lu_2Fe_{17}) or three Y (in Y_2Fe_{17}) atoms. According to the data obtained by Givord and Lacheisserie [9] for Y_2Fe_{17} and our results for Lu_2Fe_{17}, the specific features of the electronic structures of Lu and Y atoms do not substantially affect the magnetostriction.

6. CONCLUSION

The measurements demonstrated that the magnetostriction itself and the magnetostriction constants for the Lu_2Fe_{17} compound are maximum in the temperature range of the magnetic phase transition in which the paraprocess makes the main contribution to the magnetization. The contributions from the rotation and displacement of domain boundaries to the magnetostriction in Lu_2Fe_{17} are insignificant in the temperature range studied. As follows from the calculated magnetostriction constants λ_{12}^{a} and λ_{11}^{a}, the anisotropic single-ion contributions to the field-induced magnetostriction are comparable in magnitude to the isotropic two-ion exchange contributions. The lack of saturation in the $\lambda(H)$ curves in the field aligned with the easy magnetization axis near the Curie point and at lower temperatures can be explained by the fact that the effective exchange field considerably affects the 3*d* electron band structure.

ACKNOWLEDGMENTS

This work was supported by the Russian Foundation for Basic Research, project nos. 99-02-17821 and 99-03-32824.

REFERENCES

1. D. Bonnenberg, E. Burzo, H. R. Kirchmayr, T. Nakamichi, and H. P. J. Wijn, in *Landolt–Börnstein: New Series III* (Springer-Verlag, Berlin, 1992), Vol. 19i2, p. 314.
2. B. Garcia-Landa, P. A. Algarabel, M. R. Ibara, *et al.*, J. Magn. Magn. Mater. **140–144**, 1085 (1995).

3. A. V. Andreev, A. V. Deryagin, S. M. Zadvorkin, N. V. Kudrevatykh, V. N. Moskalev, R. Z. Levitin, Yu. F. Popov, and R. Yu. Yumaguzhin, in *Physics of Magnetic Materials*, Ed. by D. D. Mishin (Kalinin. Univ., 1985), p. 21.
4. D. Givord and R. Lemaire, IEEE Trans. Magn. **10** (2), 109 (1974).
5. S. A. Nikitin, A. M. Tishin, M. D. Kuz'min, and Yu. I. Spichkin, Phys. Lett. A **153** (2), 155 (1991).
6. A. S. Andreenko, S. A. Nikitin, and Yu. S. Spichkin, Fiz. Tverd. Tela (St. Petersburg) **34** (6), 1823 (1992) [Sov. Phys. Solid State **34**, 972 (1992)].
7. A. S. Andreenko, S. A. Nikitin, and Yu. S. Spichkin, Vestn. Mosk. Univ., Ser. 3: Fiz., Astron. **3** (1), 55 (1993).
8. O. Mikulina, J. Kamarad, Z. Arnold, *et al.*, J. Magn. Magn. Mater. **196–197**, 649 (1999).
9. D. Givord and E. T. Lacheisserie, IEEE Trans. Magn. **12** (1), 31 (1976).
10. K. Mori, K. Hathaway, and A. Clark, IEEE Trans. Magn. **19** (5), 1961 (1983).
11. B. Garcia-Landa, M. R. Ibara, P. A. Algarabel, *et al.*, Physica B (Amsterdam) **177**, 227 (1992).
12. J. M. D. Coey, Hong Sun, and D. P. F. Hurley, J. Magn. Magn. Mater. **101**, 310 (1991).
13. Cz. Kapusta, M. Rosenberg, H. Figel, *et al.*, J. Magn. Magn. Mater. **104–107,** 1331 (1992).
14. H. B. Callen and E. R. Callen, J. Phys. Chem. Solids **2**, 1271 (1966).
15. M. T. Averbuch-Pouchot, R. Chevalier, J. Deportes, *et al.*, J. Magn. Magn. Mater. **68**, 190 (1987).
16. J. Deportes, B. Kebe, and R. Lemaire, J. Magn. Magn. Mater. **54–57**, 1089 (1986).
17. H. B. Callen and E. R. Callen, J. Phys. Chem. Solids **16**, 310 (1960).
18. E. R. Callen and H. B. Callen, Phys. Rev. B **96** (2), 302 (1954).
19. S. A. Nikitin, *Magnetic Properties of Rare-Earth Metals and Their Alloys* (Mosk. Gos. Univ., Moscow, 1989).
20. K. Kulakowski and A. del Moral, Phys. Rev. B **52** (22), 15943 (1995).

Translated by O. Borovik-Romanova

Physics of the Solid State, Vol. 43, No. 9, 2001, pp. 1728–1730. Translated from Fizika Tverdogo Tela, Vol. 43, No. 9, 2001, pp. 1658–1660.
Original Russian Text Copyright © 2001 by Chesnokov, Naĭden.

MAGNETISM AND FERROELECTRICITY

Influence of Diamagnetic Cations Sc^{3+} on the Magnetoelastic Energy of *M*-Type Hexaferrites

A. G. Chesnokov and E. P. Naĭden
Kuznetsov Physicotechnical Institute, pl. Revolyutsii 1, Tomsk, 634050 Russia
e-mail: Chesn@elefot.tsu.ru

Received February 13, 2001

Abstract—The field and temperature dependences of the magnetostriction constants of a single-crystal $BaFe_{10.9}Sc_{1.1}O_{19}$ hexaferrite sample are investigated. It is demonstrated that the substitution of scandium ions for iron ions leads to a significant increase in magnetostriction constants and to their abnormal dependences on temperature below 250 K. The magnetoelastic interaction constants are estimated. © *2001 MAIK “Nauka/Interperiodica”.*

It is well known that substitution of scandium cations for the ions of trivalent iron is an efficient method of varying the field strength and magnetocrystalline anisotropy constants of hexaferrites with *M*-type structure. Thus, for the $BaFe_{12-x}Sc_xO_{19}$ system, the first anisotropy constant decreases rapidly with increasing scandium content and even changes its sign at $x = 1.8$ [1]. The tendency of scandium cations to occupy $4e \times 1/2$ sites (bipyramid) determines the strong dependence of the anisotropy field on the concentration. These magnetoactive cations basically form the magnetocrystalline anisotropy of ferrimagnets of this structure type. The major contribution to the magnetoelastic energy of Ba–*M* also comes from cations occupying the bipyramid sites. In view of this circumstance, one might expect that the replacement of the Fe^{3+} cations occupying these sites would affect not only magnetocrystalline anisotropy but also the magnetoelastic energy and, as a consequence, the magnetostriction constants of the Ba–*M*-based hexaferrites.

There are only fragmentary data in the literature on the behavior of the magnetostriction constants of some simplest hexaferrites ($BaFe_{12}O_{19}$—Ba–*M*, $BaFe_{18}O_{27}$—Fe_2–*W*, etc.). These data were obtained mainly at room temperature [2–5]. To date, the problem of varying magnetostriction with the replacement of iron ions by diamagnetic (e.g., Sc^{3+}) or paramagnetic cations with a dissimilar electron structure remains unclear. On the other hand, by measuring the velocities of longitudinal and shear ultrasonic waves in a Ba–*M* single crystal and in scandium-substituted hexaferrite on its basis, it was demonstrated that the elastic constants C_{11} and C_{12} coincide within the limits of experimental error at temperatures above 250 K. However, with decreasing temperature, the behavior of the $C_{ij}(T)$ curves is substantially different. The temperature dependences of the C_{33} constants for the hexaferrites mentioned above differ over the whole temperature range investigated [6, 7]. The purpose of this work was to investigate experimentally the magnetostriction of an *M*-type hexaferrite with a partial substitution of scandium ions for the iron ions and to evaluate the influence of this substitution on the magnetoelastic interaction parameters.

Single-crystal samples of hexaferrites of the $BaFe_{12-x}Sc_xO_{19}$ system ($x = 1.6$ by charge) were grown from solution in melt using a boron–barium solvent. For magnetostriction measurements, a parallelepiped-shaped sample of size $a \times b \times c = 10 \times 2 \times 1$ mm was cut from a large single crystal. The crystallographic *a* axis was parallel to a long edge of the parallelepiped, whereas the *c* axis was normal to the *ab* plane. The chemical composition of this sample, which was determined using neutron activation analysis and x-ray fluorescent analysis, corresponds to the formula $BaFe_{10.9}Sc_{1.1}O_{19}$. Data on the distribution of cations over the sublattices were obtained by minimizing the discrepancy factor for the integral intensities of 11 reflections from the basis layer line. Scandium cations mainly occupy the octahedral sites of the spinel block (2*a*) and quasi-tetrahedral sites of the hexagonal block of the structure ($4e \times 1/2$ sublattice). In addition, a small amount of Sc^{3+} cations occupy the octahedral sites of the hexagonal block *R* and interblock octahedra. The saturation magnetization M_s and anisotropy field H_a measured for this sample correspond to their values determined for the chemical composition mentioned above from the concentration dependences of $M_s(x)$ and $H_a(x)$ and are presented in [1].

Magnetostriction constants were measured using a tensometric method. GDT-type germanium dendrite strain gauges with a strain gauge factor $S = +55$ and a base length of 10 mm were used as sensors. For the sample configuration mentioned above, the magnetostriction constants λ_a ($\alpha_1 = \beta_1 = 1$), λ_b ($\alpha_2 = \beta_1 = 1$), and

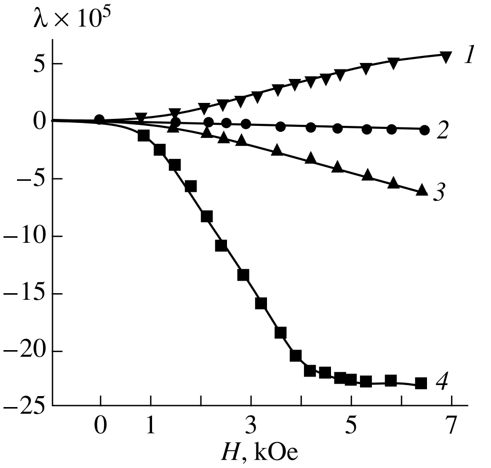

Fig. 1. Magnetostriction constants against an applied field at room temperature. (*1*) λ_b, (*2*) λ_a, (*3*) λ_{45}, and (*4*) $\lambda_\perp$.

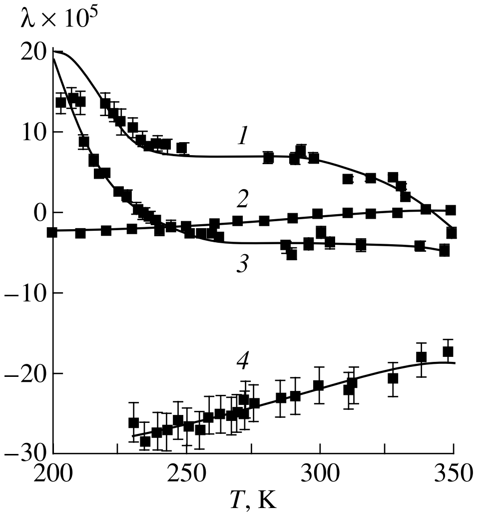

Fig. 2. Temperature dependences of the magnetostriction constants. (*1*) λ_b, (*2*) λ_a, (*3*) λ_{45}, and (*4*) $\lambda_\perp$.

$\lambda_\perp$ ($\alpha_3 = \beta_1 = 1$) can be measured immediately. Here, α_i and β_i are the direction cosines of the magnetization and of the axis of magnetostriction measurements, respectively. The magnetostriction constant λ_c was determined using x-ray dilatometry.

The dependences of the magnetostriction constants on the magnetizing field strength are shown in Fig. 1. For the constant $\lambda_\perp$, saturation is observed in a field of approximately 4 kOe. The effect observed is apparently determined by the presence of flux-closure domains on the sample surface. In the absence of the magnetizing field, the magnetic moments in these domains are parallel to the easy magnetization axis in the sample bulk. During magnetization, the moments in the flux-closure domains will turn until the field reaches the value at which the domain structure disappears. Thus, the field of 4 kOe corresponds to a field of technical saturation. The field dependences of magnetostriction constants λ_a, λ_b, and λ_{45} (magnetostriction along the *a* axis under magnetization at an angle of 45°) are monotonic with a tendency to saturation at $H > 7$ kOe. The largest magnetostriction value does not exceed 5×10^{-5}; i.e., it is of the same order as for unsubstituted Ba–*M*. The dependence of the magnetostriction constant λ_c differs only slightly from $\lambda_b(T)$, and it is not shown in Fig. 1.

The temperature dependences of the magnetostriction constants at a magnetizing field of 8 kOe are shown in Fig. 2. Linear portions in characteristics of germanium strain gauges restrict the temperature range of measurements. Magnetostriction constants vary only slightly in the temperature range 250–350 K. On decreasing the temperature below 250 K, the constants λ_b and λ_{45} increase rapidly. This is apparently related to the formation of a spiral-type noncollinear magnetic structure at these temperatures [8]. It should also be noted that the magnetostriction constants λ_b and λ_{45} change their sign at temperatures 330 and 230 K, respectively.

The lack of available data in the literature on the temperature dependences of λ_i for Ba–*M* precludes carrying out correct analysis of the effect of substitution of scandium cations for iron ions on these characteristics. However, one can make a comparison of the temperature dependences of the magnetostriction constant $\lambda^{\varepsilon 2} = \lambda_a - \lambda_b$. The data on this dependence for a single-crystal Ba–*M* hexaferrite sample in the temperature range of 80–300 K are presented in [9]. These data are shown in Fig. 3 for Ba–*M* (curve *2*) and for the scandium-substituted compound investigated by us (curve *1*). The magnetoelastic interaction constant $B^{\varepsilon 2}$ is related to the corresponding magnetostriction constant and elastic constants through a simple relationship [10]:

$$B^{\varepsilon 2} = -\lambda^{\varepsilon 2}(C_{11} - C_{12}).$$

Since C_{11} and C_{12} vary only slightly in the temperature range investigated, one can consider that the quantity ($C_{11} - C_{12}$) is constant and, therefore, the behavior

Elastic and magnetoelastic constants of Ba–*M* and BaSc–*M* compounds at room temperature

Material	C_{11}, 10^{10} N/m^2	C_{12}, 10^{10} N/m^2	C_{33}, 10^{10} N/m^2	C_{44}, 10^{10} N/m^2	B_{12}, 10^6 N/m^2	B_{22}, 10^6 N/m^2	$B^{\varepsilon 2}$, 10^6 N/m^2
Ba–*M* [7]	31.80	14.56	24.26	7.17	–1.03	–3.56	1.37
BaSc–*M*	30	15	18	6.5	–2.5	–8.8	7.4

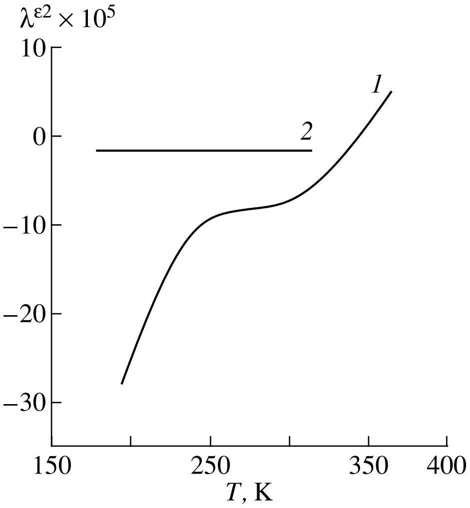

Fig. 3. Temperature dependence of the constant $\lambda^{\varepsilon 2}$. (*1*) BaSc–*M* and (*2*) Ba–*M*.

of the $B^{\varepsilon 2}(T)$ dependence is determined by that of $\lambda^{\varepsilon 2}(T)$. Our results and the data available in the literature on the temperature dependences of elastic constants allowed us to estimate some magnetoelastic constants for the BaSc–*M* compound. The computational procedure is similar to that used in [10]. The results of calculations are presented in the table. Incorporation of scandium ions insignificantly affects the ultrasound velocities and, correspondingly, the elastic moduli (except C_{33}) in the vicinity of room temperature. A noticeable distinction between the temperature dependences for the other elastic moduli is observed only at temperatures below 220 K. On the other hand, the magnetostriction constants of the scandium-substituted compound are significantly larger over the whole temperature range investigated, which is the consequence of increasing the magnetoelastic constants due to the substitution of scandium ions for iron ions. It seems likely that the microscopic reason for this phenomenon is the broken central symmetry of the crystal with statistically distributed Sc^{3+} cations. The broken symmetry brings about an increase in the contribution of the Dzyaloshinskiĭ–Moriya antisymmetric exchange to the anisotropic component of the magnetic energy.

ACKNOWLEDGMENTS

We thank L.N. Bezmaternykh for the single-crystal hexaferrite samples used in our investigations.

REFERENCES

1. T. M. Perekalina and V. P. Cheparin, Fiz. Tverd. Tela (Leningrad) **9** (11), 3205 (1967) [Sov. Phys. Solid State **9**, 2524 (1968)].
2. S. P. Kuntsevich, Yu. A. Mamaluĭ, and A. S. Mil’ner, Fiz. Met. Metalloved. **26** (4), 610 (1968).
3. S. P. Kuntsevich and V. P. Palekhin, Fiz. Tverd. Tela (Leningrad) **15** (11), 3460 (1973) [Sov. Phys. Solid State **15**, 2314 (1973)].
4. S. P. Kuntsevich and V. P. Palekhin, Fiz. Tverd. Tela (Leningrad) **20** (9), 2869 (1978) [Sov. Phys. Solid State **20**, 1661 (1978)].
5. S. P. Kuntsevich, Yu. A. Mamaluĭ, and A. S. Mil’ner, Ukr. Fiz. Zh. **16** (1), 67 (1971).
6. A. M. Kapitonov, in *Proceedings of the XV All-Union Conference on Physics of Magnetic Phenomena, Perm, 1981*, Vol. 1, p. 69.
7. T. P. Sorokina and A. M. Kapitonov, in *Proceedings of the XVIII All-Union Conference on Physics of Magnetic Phenomena, Kalinin, 1988*, Vol. 2, p. 291.
8. O. P. Aleshko-Ozhevskiĭ and R. A. Sizov, Pis’ma Zh. Éksp. Teor. Fiz. **7** (6), 207 (1968) [JETP Lett. **7**, 158 (1968)].
9. S. P. Kuntsevich, Yu. A. Mamaluĭ, and V. P. Palekhin, Fiz. Tverd. Tela (Leningrad) **22** (7), 2192 (1980) [Sov. Phys. Solid State **22**, 1278 (1980)].
10. H. Klimker and M. Rosen, Phys. Rev. B **7** (5), 2054 (1973).

Translated by N. Korovin

Physics of the Solid State, Vol. 43, No. 9, 2001, pp. 1731–1734. Translated from Fizika Tverdogo Tela, Vol. 43, No. 9, 2001, pp. 1661–1664.
Original Russian Text Copyright © 2001 by Kirste, Levitin, Ortenberg, Platonov, Puhlmann, Snegirev, Filippov, Tatsenko.

MAGNETISM AND FERROELECTRICITY

Induced Magnetic Phase Transitions in Rare-Earth Intermetallic Compounds $R\mathrm{Mn}_2\mathrm{Ge}_2$ in Ultrastrong Magnetic Fields

A. Kirste*, R. Z. Levitin, M. von Ortenberg*, V. V. Platonov***, N. Puhlmann*,**
V. V. Snegirev, D. A. Filippov**, and O. M. Tatsenko*****
**Humboldt University, D-10115 Berlin, Germany*
***Moscow State University, Vorob'evy gory, Moscow, 119899 Russia*
****Institute of Experimental Physics, Sarov, 607189 Russia*
e-mail: Levitin@plms.phys.msu.su

Received February 13, 2001

Abstract—The differential magnetic susceptibility of intermetallic compounds $R\mathrm{Mn}_2\mathrm{Ge}_2$ (R = Gd, Tb, Dy, Ho, Y) with a layered tetragonal structure is measured in pulsed magnetic fields up to 130 T. It is found that all these compounds undergo a first-order magnetic phase transition in strong magnetic fields. The nature of this transition is discussed, and it is found that a change in the magnetic state of the manganese sublattice is responsible for the transition. *© 2001 MAIK "Nauka/Interperiodica".*

The intermetallic compounds $R\mathrm{Mn}_2\mathrm{Ge}_2$ (R stands for rare-earth metals (REMs), yttrium, uranium, etc.) have a tetragonal crystal structure (space group *I*4/*mmm*) consisting of alternating atomic layers *R*–Ge–Mn–Ge–*R*– … normal to the tetragonal axis [1]. From the magnetic point of view, these compounds have two magnetic subsystems, one of which is formed by REM atoms and the other by Mn atoms. Numerous investigations (see [1] and the references therein) have shown that the Mn–Mn ferromagnetic exchange in a layer is the strongest in $R\mathrm{Mn}_2\mathrm{Ge}_2$. The interlayer Mn–Mn exchange interaction is approximately an order of magnitude weaker than the exchange in an Mn layer. The exchange interaction between the manganese and the rare-earth subsystems has nearly the same order of magnitude. The exchange within the rare-earth subsystems is still weaker by an order of magnitude. The exchange interaction between the Mn layers and between Mn and REM layers are both antiferromagnetic in intermetallic compounds with heavy REMs and yttrium.

The hierarchy of the exchange interactions described above determines the peculiarities of the magnetic properties of the $R\mathrm{Mn}_2\mathrm{Ge}_2$ compounds with heavy REM. The manganese subsystem in these compounds becomes ordered at temperatures of 350–450 K. This ordering is antiferromagnetic; the magnetic moments in adjacent ferromagnetic layers of manganese are antiparallel [1]. The magnetic rare-earth subsystem remains paramagnetic in this case, because the effective fields of the two adjacent manganese layers acting on this subsystem neutralize each other.

With decreasing temperature, the rare-earth subsystem of certain intermetallic compounds (with gadolinium, terbium, dysprosium) undergoes a first-order phase transition to the ferromagnetic state [1]. In this case, the manganese subsystem is also transformed to the ferromagnetic state due to the REM–manganese exchange interaction. Since this interaction is antiferromagnetic, the magnetic moments of the rare-earth and the manganese subsystems are antiparallel, and hence the magnetic structure on the whole is ferrimagnetic. In intermetallic compounds with holmium, erbium, and tulium, the REM–Mn exchange interaction is weaker and, hence, the manganese subsystem in these compounds remains in the antiferromagnetic state to the lowest temperatures [1].

The behavior of $R\mathrm{Mn}_2\mathrm{Ge}_2$ compounds in a magnetic field has been studied much more sparingly. Phase transitions induced by a magnetic field were detected in a number of intermetallic compounds (with dysprosium and gadolinium in Gd–Y and Gd–La systems) [2–6] and attributed to a change in the nature of magnetic ordering in the manganese subsystem. However, the nature of these transitions has not been established unambiguously so far. It should be emphasized that even in the strongest magnetic fields (up to 40 T) employed in those experiments, the magnetization of the investigated compounds was considerably lower than the theoretical saturation magnetization for a parallel orientation of the magnetic moments of the rare-earth and manganese subsystems, leading to the assumption that additional field-induced magnetic phase transitions can be observed in stronger fields.

In this work, we report on the attempts to detect these transitions by measuring the magnetic properties of the intermetallic compounds $R\mathrm{Mn}_2\mathrm{Ge}_2$ in ultrastrong magnetic fields.

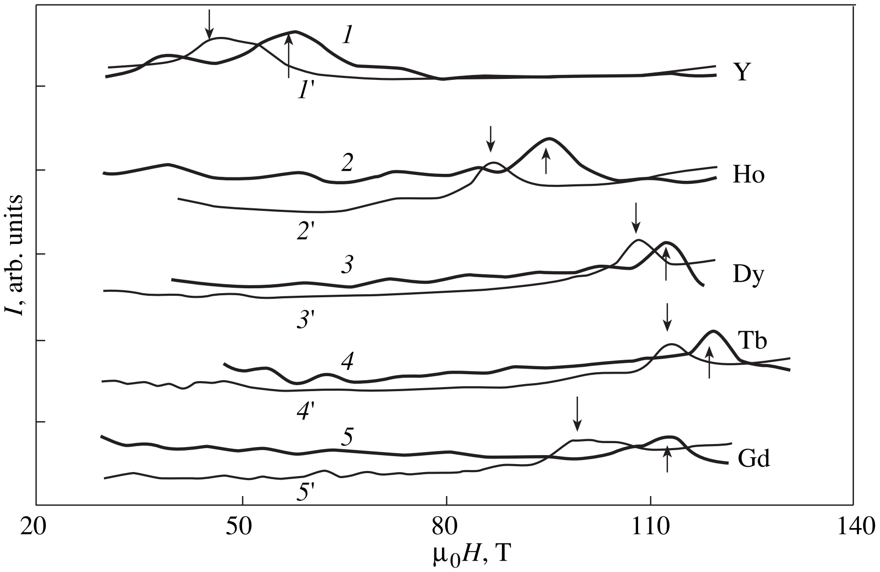

Fig. 1. Induced signal *I* for the investigated intermetallic compounds in the experiments in one-turn solenoids: curves *1*–*5* correspond to the increasing fields; *1*'–*5*', to the decreasing fields. Arrows indicate the increase (upwards) and decrease (downwards) in the critical field for the induced phase transition.

Polycrystalline samples of compounds $R\mathrm{Mn}_2\mathrm{Ge}_2$ (R = Gd, Tb, Dy, Er) were smelted from constituent elements in an induction furnace in an argon atmosphere under quasi-levitation conditions. For better homogenization, the samples were remelted three times and annealed in a dynamic vacuum at 750°C for 170 h. X-ray diffraction analysis was carried out to verify the single-phase nature of the samples.

Measurements were made on powdered samples with a particle size of about 10 μm at 5–7 K in pulsed magnetic fields up to 150 T generated by the inductive discharge of a bank of capacitors through a one-turn solenoid (the duration of the first half-period of the pulse was 6 μs). Note that considerable spurious signals are generated in this technique due to the noise of the capacitor bank discharge, decompensation of the measuring coils, mechanical vibrations of the system of measuring coils, etc. This makes it difficult to isolate the desired signal. For the small magnitudes of this signal, we made repeated measurements. The criterion for the correct isolation of the desired signal was its detection in both increasing and decreasing fields. Detection was impossible for most spurious signals. Finally, we made auxiliary measurements using the explosive compression technique to obtain an ultrastrong field [7] in the case of the gadolinium intermetallic compound, which produced the weakest signal during the phase transition in our experiments. All these measures enabled us to reliably determine the fields H_c for the induced magnetic phase transitions in the investigated compounds.

The signal induced in the measuring coils can be described by the formula

$$V = (a + B\chi)dH/dt. \qquad (1)$$

Here, dH/dt is the time derivative of the field; the first term in parentheses describes the decompensation signal from the measuring coils and the second, the signal from the sample; χ is the differential magnetic susceptibility of the sample; and a and b are constants associated with the parameters of the coils (number of turns and cross-sectional areas) and of the sample (mass and geometrical size), respectively. In the critical magnetic field H_c for the first-order magnetic phase transition, the susceptibility χ passes through a maximum. Consequently, a peak in the voltage V induced in the measuring coils is observed in this region. Note that the fields corresponding to the peaks of the dependences $V(H)$ and $\chi(H)$ will coincide only in the case of dH/dt = const. Estimates show that this condition is fulfilled in comparatively weak fields (for a sinusoidal time dependence of the field pulse, for approximately $H < 0.5H_{\max}$). Appropriate corrections must be made for transitions occurring in stronger fields. For this reason, we determined the value of H_c from the field dependence of the quantity $V/(dH/dt)$ in the region where no such correction was required. The corresponding dependences are shown in Fig. 1. It can be seen that the magnetization of all the investigated compounds undergoes a diffuse metamagnetic transition in strong fields. The values of the critical fields are different for transitions in increasing and decreasing fields, which is characteristic of first-order phase transitions. Note that the width of the hysteresis loop is apparently affected by relaxation effects associated with the pulsed nature of

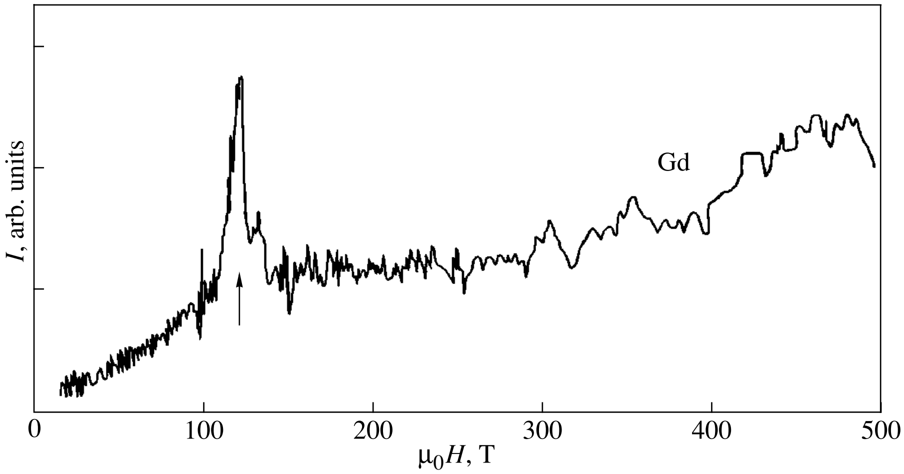

Fig. 2. Induced signal I for $GdMn_2Ge_2$ in experiments with explosive magnetic flux compression. The notation is the same as in Fig. 1.

magnetization. Such effects were observed recently [6] in $DyMn_2Ge_2$ at low temperatures. Table 1 contains the mean values in increasing and decreasing fields of the critical fields H_c and the half-width of the hysteresis loop $\Delta H_c/2$ (ΔH_c is the difference in the values of the critical fields for transitions in increasing and decreasing fields) for the investigated compounds.

Figure 2 shows the data for $GdMn_2Ge_2$ obtained from the experimental setup with explosive compression of the magnetic flux (in this case, the field dependence of the signal is presented only in increasing fields, since the sample and the measuring system are destroyed when the maximum field is attained). It can be seen that these data confirm the experimental results for a one-turn solenoid, indicating the occurrence of an induced magnetic phase transition in this intermetallic compound. In both experiments, the values of the critical field H_c coincide within the admissible error limits (±3% for measurements in a one-turn solenoid and ±5% for measurements in the explosive field generation setup).

The magnetic properties of the gadolinium–yttrium and gadolinium–lanthanum intermetallic systems were interpreted by us earlier [4, 5] using the Yafet–Kittel model [8] for a ferrimagnet with antiferromagnetic exchange interaction in one of the sublattices and were modified by taking the magnetic anisotropy into consideration. In this model, it was assumed that the sublattice is unstable and is bifurcated into two equivalent subsublattices. In addition to the collinear ferrimagnetic (Fi) and ferromagnetic (F) phases, as well as the noncolinear (NC) phase, all of which can exist in ferrimagnets with intrasublattice ferromagnetic interactions, new magnetic phases can also emerge in such a ferrimagnet: a phase in which the unstable sublattice is in the antiferromagnetic state (AF phase) and a trigonal (T) phase in which the magnetic moments of the sublattices are not parallel to one another or to the magnetic moment of the stable sublattice (in the case of the intermetallic compounds RMn_2Ge_2, the rare-earth subsystem is stable while the manganese subsystem is unstable). It was shown that this model provides a fairly correct description of the magnetic properties of $GdMn_2Ge_2$ in the fields used in our experiments (approximately up to 40 T) [4]. It was also predicted within the framework of the Yafet–Kittel model that one more first-order magnetic phase transition will occur from the AF phase to the T phase in this compound in stronger fields. Apparently, it is exactly this kind of transition that is associated with a change in the magnetic state of the manganese magnetic subsystem, as observed in our experiments on gadolinium and other magnetic-REM intermetallic compounds. The fact that the observed transitions are associated only with a change in the magnetic structure of the manganese subsystem is confirmed by the results of our investigations of the YMn_2Ge_2 compound, which also exhibits a field-induced phase transition. Since yttrium is nonmagnetic, this compound has only an antiferromagnetic manganese subsystem, which undergoes a spin-flop transition to the noncolinear phase or a metamagnetic transition to the ferromagnetic state in a magnetic field.

However, the theoretical value of the critical field for the magnetic transition from the AF to the T phase

Critical fields H_c for induced magnetic phase transitions and the half-width $\Delta H_c/2$ of the hysteresis loop for the intermetallic compounds RMn_2Ge_2 at a temperature of 5 K

R	Gd	Tb	Dy	Ho	Y
H_c, T	105	116	110	91	51
ΔH_c, T	7	2	2	3	5

in $GdMn_2Ge_2$ (70 T at 5 K) calculated in the Yafet–Kittel model [9] was found to be much smaller than the experimentally determined value at this temperature (105 T). This points out the approximate nature of the Yafet–Kittel model and the need to move away from this model towards a more adequate description of the experiment. Analysis of the experimental data obtained in [2, 3] for a $DyMn_2Ge_2$ single crystal also leads to a similar conclusion [10]. In our opinion, the approximate nature of the Yafet–Kittel model is due to the fact that it only takes into consideration the exchange interaction between adjacent planes containing magnetic ions (this is the nearest neighbor approximation), which is undoubtedly too rough a description, especially if we consider the long-range nature of the exchange interaction through conduction electrons (of the Ruderman–Kittel–Kasuya–Yosida type), which, along with the indirect exchange through germanium, determines the magnetic properties of the intermetallic compounds RMn_2Ge_2 [1].

ACKNOWLEDGMENTS

This study was partly supported by the Russian Foundation for Basic Research, project no. 99-02-17358, and by grant no. 00-15-96695 for the promotion of research schools.

REFERENCES

1. A. Szytula and J. Leciejevicz, in *Handbook of Physics and Chemistry of Rare Earths*, Ed. by K. A. Gschneidner, Jr. and LeRoy Eyring (North-Holland, Amsterdam, 1989), Vol. 12, p. 133.
2. H. Kobayashi, H. Onodera, Y. Yamaguchi, and H. Yamamoto, Phys. Rev. B **43**, 728 (1991).
3. H. Wada, Y. Tanabe, K. Hagivara, and M. Shiga, J. Magn. Magn. Mater. **123**, 203 (2000).
4. A. Yu. Sokolov, Guo Guanghua, S. A. Granovskiĭ, *et al.*, Zh. Éksp. Teor. Fiz. **116**, 1346 (1999) [JETP **89**, 723 (1999)].
5. Guo Guanghua, R. Z. Levitin, V. V. Snegirev, *et al.*, Zh. Éksp. Teor. Fiz. **117**, 1127 (2000) [JETP **90**, 979 (2000)].
6. A. S. Lagutin, R. Z. Levitin, and J. Vanacken, J. Magn. Magn. Mater. (in press).
7. A. I. Pavlovski, N. P. Kolokolchikov, and O. M. Tatsenko, *Megagauss Physics and Techniques*, Ed. P. Tachi (Plenum, New York, 1980).
8. Y. Yafet and C. Kittel, Phys. Rev. **87**, 290 (1952).
9. Guo Guanghua, N. P. Kolmakova, R. Z. Levitin, *et al.*, in *Proceedings of the Moscow International Symposium on Magnetism, 1999*, Ed. by A. Granovsky and N. Perov (Moscow, 2000), Part 2, p. 133.
10. Guo Guanghua, N. P. Kolmakova, R. Z. Levitin, *et al.*, in *Abstracts of 8th European Magnetic Materials and Applications Conference, Kiev, 2000*, p. 301.

Translated by N. Wadhwa

Physics of the Solid State, Vol. 43, No. 9, 2001, pp. 1735–1738. Translated from Fizika Tverdogo Tela, Vol. 43, No. 9, 2001, pp. 1665–1668.
Original Russian Text Copyright © 2001 by Gridnev, Biryukov, Ivanov.

MAGNETISM AND FERROELECTRICITY

The Decay of Low-Frequency Elastic Oscillations in a $Ba_2NaNb_5O_{15}$ Crystal

S. A. Gridnev, A. V. Biryukov, and O. N. Ivanov
Voronezh State Technical University, Voronezh, 394026 Russia
e-mail: gridnev@nsl.vstu.ac.ru

Received February 6, 2001

Abstract—The internal friction and shear modulus of a barium sodium niobate crystal were studied using the torsion pendulum technique at a frequency of ~25 Hz in the temperature range from 80 to 800 K. An internal friction relaxation peak of the domain nature was observed at 228 K. A relaxation process responsible for this internal friction peak is explained through compensation of the electric charge (induced by a piezoelectric effect at the 180° domain walls) by charged point defects diffusing toward the domain walls. © *2001 MAIK "Nauka/Interperiodica".*

$Ba_2NaNb_5O_{15}$ crystals possessing a tetragonal potassium– tungsten bronze structure occur in a broad (about 460-K-wide) temperature range in the form of a ferroelastic phase belonging to the point symmetry group *mm*2, which is intermediate between two ferroelectric phases of the lower symmetry 4*mm* [1–3]. Phase transitions with a change in the symmetry ($4mm \rightleftarrows mm2$) observed at 115 and 553 K are the so-called improper ferroelastic phase transitions. The ferroelastic properties of $Ba_2NaNb_5O_{15}$ crystals are described in terms of the spontaneous shear deformation x_6 [4].

Previously [5, 6], we studied the low-frequency internal friction Q^{-1} and the shear modulus G of $Ba_2NaNb_5O_{15}$ crystals using the inverse torsion pendulum technique and observed for the first time two clearly pronounced Q^{-1} peaks at the temperatures of ferroelectric phase transitions and a broad intermediate Q^{-1} peak near 228 K (Fig. 1). The peaks at 115 and 553 K were accompanied by the corresponding changes in the shear modulus G manifested in the $G(T)$ curves, which are characteristic of improper phase transitions [7]. A combination of the experimental data obtained in [5, 6] allowed us to explain the Q^{-1} peak corresponding to the first-order phase transition at 115 K in terms of fluctuational nucleation of a new phase and in terms of the motion of interphase boundaries through a system of obstacles under the action of oscillating mechanical stresses [8], while the peak at 553 K was explained in terms of the formation of a dislocation-initiated small-domain structure at the second-order phase transition temperature and in terms of features of the domain wall dynamics in a real ferroelastic crystal containing crystal lattice defects [8]. Since the Q^{-1} peak at 228 K remained insufficiently studied, the purpose of this study was to elucidate the factors responsible for the anomalous mechanical losses observed in this temperature region.

1. SAMPLE PREPARATION AND MEASUREMENT METHODS

The samples were cut from a Czochralski-grown $Ba_2NaNb_5O_{15}$ single crystal and had the dimensions 2 × 2 × 18 mm, with their long edges parallel to the X or Z axes of the tetragonal crystal structure (below the X- and Z-oriented samples, respectively). The experiments were performed in a setup employing the inverse torsion pendulum technique [9] with a relative deformation amplitude of 2×10^{-5}. The dielectric measurements were conducted on the Z-cut samples with the aid of an automated E-7-12 capacitance bridge (operating at 1 MHz) and a high-precision BM-400G capacitance bridge (120 and 800 Hz). The probing field strength amplitude was 25 V/cm. Prior to measurements, silver

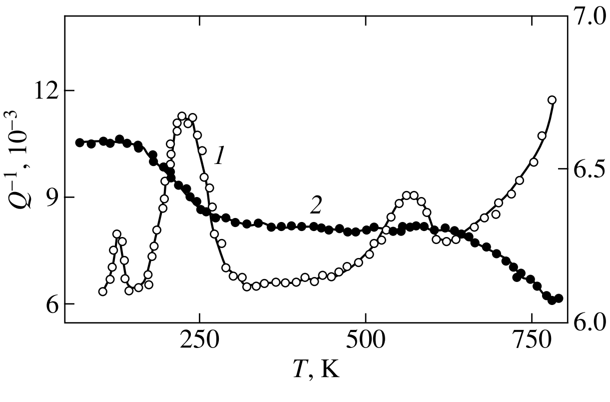

Fig. 1. The plots of (*1*) Q^{-1} and (*2*) $G \sim f^2$ for an X-oriented $Ba_2NaNb_5O_{15}$ crystal.

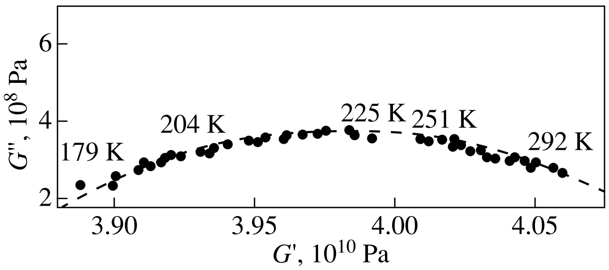

Fig. 2. The Cole–Cole pseudo-digram for an *X*-oriented $Ba_2NaNb_5O_{15}$ crystal.

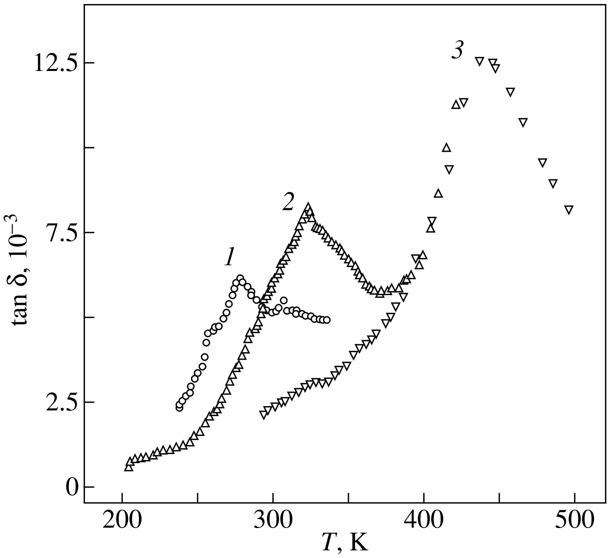

Fig. 3. The plots of $\tan\delta$ versus temperature measured at the frequencies f = (*1*) 120, (*2*) 800 Hz, and (*3*) 1 MHz.

contacts were applied to the sample crystals through thermal deposition in vacuum. The dielectric measurements were carried out in the course of continuous slow heating of the samples at a rate of 1 K/min. The sample temperature was monitored with a differential chromel–alumel thermocouple ensuring an accuracy no worse than 0.5 K.

RESULTS AND DISCUSSION

A relaxation character of the intermediate Q^{-1} peak observed at 228 K was evidenced by a characteristic temperature variation of the elastic modulus (Fig. 1) and by the shape of the Cole–Cole pseudo-diagram (Fig. 2). The flattened Cole–Cole curve is indicative of a broad spectrum of the relaxation times. In order to determine the mechanism or relaxation responsible for the intermediate Q^{-1} peak, we evaluated the relaxation activation energy H from analysis of the Q^{-1} peak shape [10], which gave an estimate of $H \sim 0.5$ eV. Using this activation energy and the relationship $\tau = \tau_0\exp(H/kT)$, we estimated the preexponential factor as $\tau_0 \sim 10^{-14}$ s.

Assuming that the mechanical and dielectric losses in the temperature range under consideration are of the same nature, we performed dielectric measurements at 120 Hz, 800 Hz, and 1 MHz. The $\tan\delta$ versus temperature curves (Fig. 3) showed a peak analogous to those in the Q^{-1} curves. It was found that the temperature position of this peak strongly depends on the probing field frequency: as the frequency decreases, the $\tan\delta$ peak shifts toward lower temperatures.

Assuming that the process is characterized by a single relaxation time, we used data on the $\tan\delta$ peak temperature shift with the frequency and evaluated the relaxation activation energy at 0.7 eV. Since the temperature dependence of the relaxation time is rather well described by the Arrhenius equation $\tau = \tau_0\exp(H/kT)$ (as evidenced by the linearity of the experimental plot of $\ln\tau(1/T)$ versus $1/T$), this experiment yields an estimate of $\tau_0 \sim 10^{-14}$ s. Note that the H and τ_0 values estimated from the shape of the Q^{-1} peak coincide in order of magnitude with those obtained from analysis of the frequency shift of the $\tan\delta(T)$ peak.

Taking into account that (i) the experiments revealed a significant dependence of the height and temperature position of the Q^{-1} peak on the static torsion stress $\sigma_=$ (Fig. 4) capable of changing the number and size of domains and (ii) the estimated H value is close to the energy of interaction of the domain walls with point defects [11–14], we may suggest that the Q^{-1} peak is related to the presence and state of the domain structure. Apparently, the internal friction peak is due to the interaction of point defects (predominantly, oxygen vacancies readily formed in the sample during thermal treatment [15]) with 180° domain walls [16].

The nature of the Q^{-1} peak at 228 K can be explained in terms of the model of interaction between immobile domain walls and charged point defects [17]. The model was originally developed for a 90° domain structure, but later [18] we demonstrated that this approach is applicable to the 180° domain walls as well. According to this mechanism, a charge on the domain walls appears due to the piezoelectric effect. The magnitude and sign of this charge vary during the oscillation period. For this reason, relaxation may also take place with immobile domain walls. In the very first moment of application of mechanical stress, an electric field appears in the domain. The field stress, determined by the piezoelectric charge induced at the domain walls, decreases with time as a result of the diffusion redistribution of charged point defects. The electric field variation is accompanied by additional inelastic deformation of the crystal, which gives rise to internal friction.

Since relaxation in the sample is characterized by a set of relaxation times, the estimates of the corresponding relaxation process parameters within the framework of the domain wall–point defect interaction model will be obtained for the average relaxation time τ_{av} entering into the Debye equation for the internal friction [10]. Calculations using this model lead to the following expression for the $Q^{-1}_{\max}$ peak height:

$$Q^{-1}_{\max} = \frac{2(d_{33}-d_{31})^2 q^2 C_0 L^2}{\pi^4 \varepsilon^2 \varepsilon_0^2 kTS}, \tag{1}$$

where d_{31} and d_{33} are the piesoelectric moduli, q is the charge of the point defect, C_0 is the concentration of point defects, L is the distance between the domain walls, S is the nonrelaxed shear compliance coefficient, ε is the dielectric permittivity, $\varepsilon_0 = 8.85 \times 10^{-12}$ F/m is the permittivity of vacuum, and k is the Boltzmann constant. The relaxation time is determined as

$$\tau = \frac{1}{D}\left(\frac{\pi^2}{L^2} + \frac{q^2 C_0}{\varepsilon\varepsilon_0 kT}\right)^{-1}, \tag{2}$$

where D is the diffusion coefficient. Taking into account that the $Ba_2NaNb_5O_{15}$ crystals possess a ferroelectric 180° (rather than 90°) domain wall structure [16], the factor $(d_{33} - d_{31})$ in formula (1) must be replaced by $2d_{15}$ [18].

The above relationships are valid in the case of small defect concentration, when the energy of interaction between a point defect and a domain wall is much smaller than kT, that is, under the condition that

$$\frac{q\rho L}{kT\varepsilon\varepsilon_0} \ll 1, \tag{3}$$

where ρ is the density of a bound charge induced in the domain wall.

Substituting experimental values ($L \sim 10^{-6}$ m [16], $q = 3.2 \times 10^{-19}$ C, $T = 228$ K, $\varepsilon = 240$, $d_{15} = 4.2 \times 10^{-11}$ C/N [16], and $\sigma = 2 \times 10^5$ N/m^2) into formula (3) and taking into account that $\rho = \sqrt{2}\, d_{15}\sigma$, we arrive at the inequality $0.4 < 1$. In the case of a large defect concentration C_0, the sense of inequality (3) would change to its opposite. The obtained estimate ($0.4 < 1$) allows us to conclude that the concentration of defects in the samples studied is small but still rather close to the intermediate case from small to large concentrations. This conclusion is also confirmed by the change in the internal friction peak height caused by high-temperature annealing. According to Eq. (1), $Q^{-1}_{\max}$ at small defect concentrations is proportional to C_0. In contrast, the internal friction at a large concentration of point defects is independent of C_0.

The samples of $Ba_2NaNb_5O_{15}$ crystals have a pale-pink color. Defects responsible for the appearance of a broad absorption band in the visible spectral range are nonstoichiometric oxygen vacancies, the concentration of which amounts to $C_0 \approx 10^{24}$ m^{-3} [15]. Using this C_0 value and the experimental data, we can estimate the Q^{-1} peak in formula (1). Substituting $d_{15} = 4.2 \times 10^{-11}$ C/N [16], $q = 3.2 \times 10^{-19}$ C, $L \sim 10^{-6}$ m, $\varepsilon = 240$, $S = 0.5 \times 10^{-10}$ m^2/N, and $T = 228$ K into formula (1), we obtain $Q^{-1}_{\max} = 13 \times 10^{-3}$, which is good agreement with the experimental peak height $Q^{-1}_{\max} = 11.8 \times 10^{-3}$.

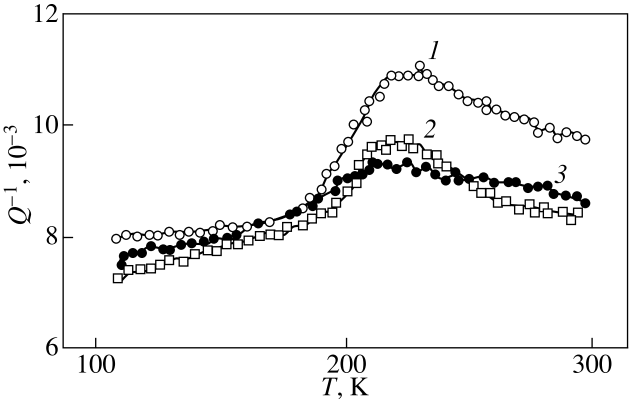

Fig. 4. The plots of Q^{-1} for an X-oriented $Ba_2NaNb_5O_{15}$ crystal measured at various $\sigma_=$ (MPa): (*1*) 0; (*2*) 10; and (*3*) 45.

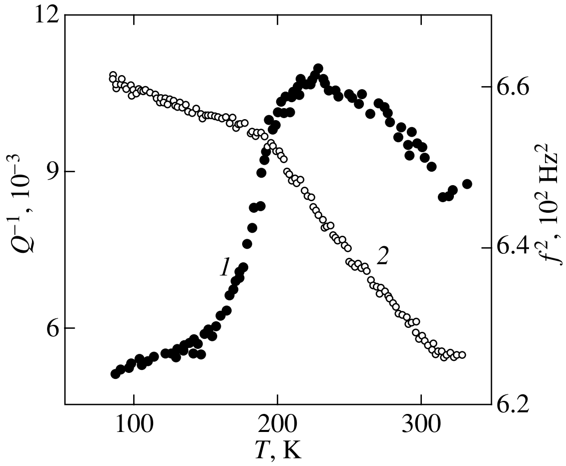

Fig. 5. The plots of (*1*) Q^{-1} and (*2*) $G \sim f^2$ for a Z-oriented $Ba_2NaNb_5O_{15}$ crystal.

According to formula (2), the temperature dependence of τ is determined by the T value proper, ε, and D. Under the experimental conditions studied, τ depends primarily on $D = D_0\exp(-H/kT)$ because $H/kT \gg 1$, while the dielectric permittivity ε of $Ba_2NaNb_5O_{15}$ crystals in the given temperature interval varies rather insignificantly [19]. Thus, we may take $\tau = \tau_0\exp(H/kT)$, where H is the diffusion activation energy. It should be noted that the results of $\tan\delta$ measurements at various frequencies confirm this behavior of $\tau(T)$. Thus, based on the model adopted, we can explain the observed variation of the temperature position of the Q^{-1} peak ($Q^{1}_{\max}$) in terms of the effect of the static torsion stress $\sigma_=$ applied to the sample.

According to formula (1), the Q^{-1} peak height is proportional to the squared domain wall spacing (L^2), which varies under the action of mechanical stresses. An increase in $\sigma_=$ in the $Ba_2NaNb_5O_{15}$ crystal leads to a decrease in domain size (i.e., in L), which results in the decrease of $Q^{-1}_{\max}$. A shift of the Q^{-1} peak toward lower temperatures with increasing static torsion stress can be explained by the fact that a decrease in the domain wall spacing leads to a decrease in the relaxation time. According to the above considerations, this results in displacement of the Q^{-1} peak toward lower temperatures.

The above model indicates that a Q^{-1} relaxation peak must also be observed in samples of the Z-orientation, where the applied external stress induceds the x_5 deformation component. Thus, the bound charges induced at the domain walls of the X- and Z-oriented samples under the action of external shear stresses are caused by the same piezoelectric modulus d_{15}. The experimental data on the temperature dependence of Q^{-1} in samples of the Z-orientation (Fig. 5) confirm the independence of the Q^{-1} peak of the sample orientation.

ACKNOWLEDGMENTS

This study was supported by the Russian Foundation for Basic Research, project no. 98-02-16055.

REFERENCES

1. J. C. Toledano and L. Pateau, J. Appl. Phys. **45** (4), 1611 (1974).
2. S. Mori, N. Yamamoto, Y. Koyama, and Y. Uesu, Ferroelectrics **190**, 13 (1997).
3. J. Schneck and D. Paquet, Ferroelectrics **21**, 577 (1978).
4. T. Yamada, H. Iwasaki, and N. Niizeki, J. Appl. Phys. **41**, 4141 (1970).
5. S. A. Gridnev, A. V. Biryukov, and O. N. Ivanov, Ferroelectr. Lett. Sect. **25** (1/2), 11 (1998).
6. S. A. Gridnev, A. V. Biryukov, and O. N. Ivanov, Ferroelectrics **219**, 1 (1998).
7. J.-C. Tolédano and P. Tolédano, *The Landau Theory of Phase Transitions* (World Scientific, Singapore, 1987; Mir, Moscow, 1994).
8. S. A. Gridnev, Ferroelectrics **112**, 107 (1990).
9. S. A. Gridnev, V. I. Kudryash, and L. A. Shuvalov, Izv. Akad. Nauk SSSR, Ser. Fiz. **43** (8), 1718 (1979).
10. V. S. Postnikov, *Internal Friction in Metals* (Metallurgiya, Moscow, 1974).
11. B. A. Strukov and A. P. Livanyuk, *Physical Principles of Ferroelectric Phenomena in Crystals* (Nauka, Moscow, 1995).
12. S. A. Gridnev, Izv. Akad. Nauk, Ser. Fiz. **64** (9), 1688 (2000).
13. A. S. Sidorkin and V. N. Fedosov, Fiz. Tverd. Tela (Leningrad) **19** (6), 1756 (1977) [Sov. Phys. Solid State **19**, 1024 (1977)].
14. S. A. Gridnev, L. A. Shuvalov, and V. I. Kudryash, Izv. Akad. Nauk SSSR, Ser. Fiz. **47** (3), 497 (1983).
15. V. P. Yarunichev, in *Ferroelectrics and Piezoelectrics* (Tvers. Univ., Tver', 1990), p. 64.
16. Yu. S. Kuz'minov, *Ferroelectric Crystals for Laser Radiation Control* (Nauka, Moscow, 1982).
17. V. S. Postnikov, V. S. Pavlov, S. A. Gridnev, and S. K. Turkov, Fiz. Tverd. Tela (Leningrad) **10** (6), 1599 (1968) [Sov. Phys. Solid State **10**, 1267 (1968)].
18. S. A. Gridnev, V. S. Pavlov, V. S. Postnikov, and S. K. Turkov, in *Analytical Possibilities of Internal Friction Methods* (Nauka, Moscow, 1973).
19. J. Shneck, J. Primot, R. von der Muhll, and J. Ravez, Solid State Commun. **21**, 57 (1977).

Translated by P. Pozdeev

Physics of the Solid State, Vol. 43, No. 9, 2001, pp. 1739–1742. Translated from Fizika Tverdogo Tela, Vol. 43, No. 9, 2001, pp. 1669–1673.
Original Russian Text Copyright © 2001 by Zalesskii, Sherman, Fregatov.

MAGNETISM AND FERROELECTRICITY

Study of the Local Repolarization Currents and Charge Carrier Injection on an $LiNbO_3$ Surface Scanned with a Mobile Point Electrode

V. G. Zalesskii*, A. B. Sherman, and S. O. Fregatov**
Ioffe Physicotechnical Institute, Russian Academy of Sciences, St. Petersburg 194021 Russia
**e-mail: nsh@pop.ioffe.rssi.ru*
***e-mail: asherman@pop.ioffe.rssi.ru*

Received February 8, 2001

Abstract—A method of the potential relief recording and reading in a subsurface region of *Z*-cut monodomain lithium niobate crystals of congruent composition was developed. The method is based on scanning the crystal surface with a point (needle-like) electrode. The injection and polarization switching currents were measured in the course of scanning. It was found that the characteristic time of the potential relief formation during the injection of carriers into the subsurface crystal region is on the order of 10^{-1} s. The process of polarization switching and the related potential relief formation is about ten times faster. For a dot recording, a characteristic distance on which a significant change in the recorded potential relief takes place is on the order of 10^2 μm. The carrier injection current in the +*Z* direction is smaller than that in the opposite direction. *© 2001 MAIK “Nauka/Interperiodica”.*

At a sufficiently large applied potential difference, a metal–insulator contact can serve as a source of free charge carriers injected into an insulator [1]. The charge injection efficiency of the contact significantly increases in the case of electrodes possessing micron and submicron dimensions, for which the electric field strength in the near-contact region is large even at relatively small applied voltages. The charge injection into the insulator is accompanied by the drift, diffusion, and trapping of injected carriers. As a result, a space charge of certain configuration is formed in the crystal. If the insulator represents a ferroelectric crystal and the field strength at the electrode is sufficient to induce a local repolarization in the crystal [2, 3], charges induced on the surface and on the domain walls will also contribute to the space charge [2–6].

Previously [2, 3], the injection of charge carriers from a needle electrode into $LiNbO_3$ crystals was studied using an optical technique. These investigations have been continued using a method based on the measurement of small currents passing through the electrode (Fig. 1). For this purpose, the experimental setup used previously [2, 3] was equipped with a device capable of scanning over a crystal sample surface with a point (needle-like) electrode moving at a given velocity. The small currents passing through the electrode were measured with the aid of an V7-30 electrometer possessing a sensitivity of 10^{-15} A in the working frequency band from 0 to 200 Hz. The electrometer was connected in series with a high-voltage source producing a voltage applied between the mobile point and the second (grounded) electrode pressed to the rear side of the sample. In order to prevent electric breakdown during experiments, the samples were placed into a cell with oil. Below, we present results for the +*Z*-cut samples of a congruent monodomain single $LiNbO_3$ crystal.

Scanning the sample surface with a needle-like electrode at a given potential led to the formation of a potential relief in the subsurface region of the crystal. Simultaneously with the potential relief recording, we measured the current passing through the moving electrode. The current measurements were also employed for reading the surface potential distribution during

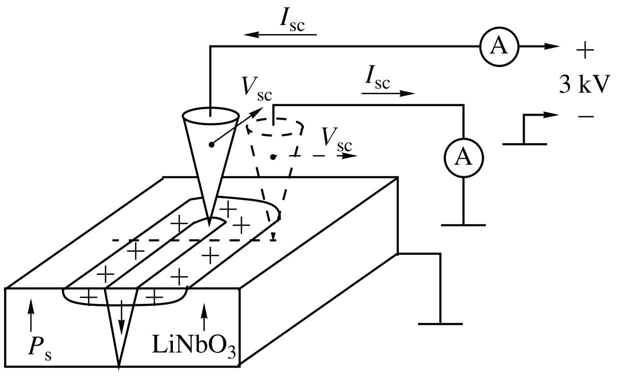

Fig. 1. A schematic diagram of the experimental arrangement for recording and reading potential profiles with the aid of a needle-like electrode.

1063-7834/01/4309-1739$21.00 © 2001 MAIK “Nauka/Interperiodica”

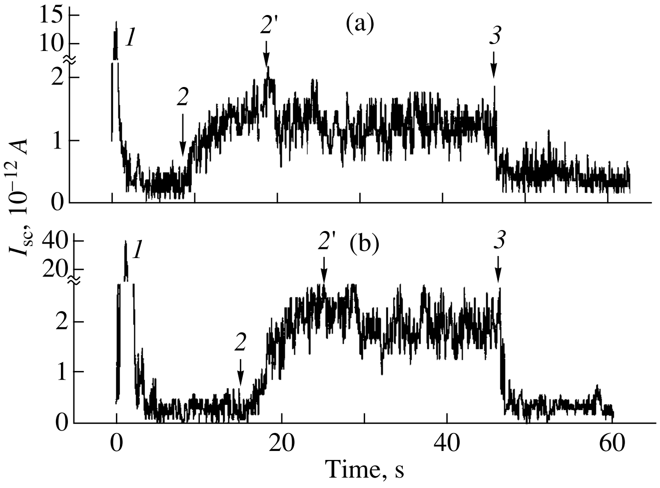

Fig. 2. Time variation of the current during scanning over an $LiNbO_3$ crystal surface with an needle-like electrode recording the potential relief at an electrode potential of (a) –0.6 and (b) +0.6 kV. Figures *1–3* on the curves indicate the time instants when the needle first touches the crystal surface, begins to move, and stops, respectively (point *2*' corresponds to attaining a stationary current level).

repeated scans. In the readout regime, the point electrode was connected to a ground via the electrometer.

Preliminary experiments showed that, in the case of contact between the electrode tip and the crystal surface, the main contribution to the measured signal is due to the current passing through the electrode–crystal surface contact. Therefore, the shorting effect of oil in this experiment could be ignored.

In the course of record and read scans, the crystal surface was optically monitored so as to determine local changes in the birefringence indicative of local polarization switching [3]. The absolute value of the threshold potential on the mobile electrode at which the local polarization switching was observed in the crystals studied was 1 kV. For studying the process of potential relief formation in a subthreshold regime (without polarization switching), the potential at the needle-like electrode was set equal to 0.6 kV (absolute value), while the overthreshold regime (with polarization switching) was studied at 3 kV.

The process of potential relief recording was conducted as follows. The needle-like electrode was brought into contact with the crystal surface (point *1* in Figs. 2 and 4) and kept immobile until a preset time instant (point *2*). Starting with moment *2*, the electrode was moved along the crystal surface at a velocity of 16 μm/s until being stopped at point *3*.

Figure 2 shows the time variation of the electrode current measured on scanning the crystal surface in a subthreshold regime. The curves of $I_{sc}(t)$ obtained for different polarities of the electrode potential are similar, but the absolute value of the current may differ, being smaller in the +*Z* than in the –*Z* direction. The electrode touching the crystal is accompanied by a sharp pulse of current. Then, the current drops at a slower rate (the decay time constants being close for the opposite voltage polarities: τ_+, $\tau_- \approx 0.5$ s). When the electrode was set to move along the crystal surface, the current increased during the first 10–15 s (the interval between points *2* and *2*' in Fig. 2) to reach a value that remained unchanged during the subsequent motion. In a subthreshold regime, observation of the crystal surface with a polarization microscope reveals no changes in the optical properties.

An analysis of the experimental results must take into account that the value of electric current through the point electrode is determined by the potential difference between the electrode and insulator at the point of contact. This potential difference depends both on the voltage applied to the metal electrodes and on the potential relief already existing in the crystal (i.e., on the sample prehistory), for example, that created in the course of preliminary recording.

When the mobile electrode touches the crystal surface, nonequilibrium charge carriers are injected into the subsurface region of the crystal [1, 3]. Drifting in the electric field of the point electrode and trapped on the impurity centers (e.g., oxygen vacancies, uncontrolled impurities of iron, chromium, etc. [7–9]), these charge carriers create a spatial bound charge relief $\sigma(\mathbf{r})$. This charge density accounts for the corresponding potential profile $\varphi(\mathbf{r})$ formed in the subsurface crystal region. As the charge is accumulated, the potential difference between the electrode and surface decreases. This results in the current decay in the interval between points *1* and *2* (Figs. 2a, 2b) by a nearly exponential law.

It is naturally expected that, on reaching an equilibrium level, the absolute value of the potential $\varphi(\mathbf{r})$ monotonically decreases with distance from the contact point. Accordingly, an increase in the potential difference between the electrode (set to move at point *2* in Fig. 2) and the crystal surface has to be accompanied by the current buildup. This explains the current growth observed in the initial stage of electrode motion (the interval between points *2* and *2*'). The electrode position in which the current ceases to grow (point *2*') can be considered conventionally as a boundary of the region of sharp variation of the potential $\varphi(\mathbf{r})$. Taking into account the electrode velocity ($V = 16$ μm/s) and the time of its motion ($t \approx 10$ s), we can estimate the distance to this boundary as $\rho \approx 160$ μm. The constancy of the electrode current in the interval between points *2*' and *3* indicates that $\varphi(\mathbf{r})$ weakly varies at $r > \rho$. The current decay observed after stopping the electrode is probably explained by the saturation of the subsurface crystal region with injected charge carriers.

Elucidating reasons for the difference in absolute values of the current through the electrode observed for opposite voltage polarities (Figs. 2a, 2b) requires additional investigation. This dependence of the injected current value on the electrode polarity can be related to a difference in parameters of nonequilibrium charge carriers of opposite signs injected into the crystal, to asymmetric conductivity of the contact between the electrode and polarized ferroelectric, and to certain features of the current passage in a medium containing no center of inversion [7, 9].

The potential profile formed in the course of recording was analyzed by the reading process. As indicated above, this was achieved by repeated scanning of the crystal surface with a grounded electrode moving in the direction perpendicular to the record line. The line was crossed at the site where the current reached a stationary level in the course of the recording electrode motion (Fig. 2). The reading scan was performed at the same electrode velocity as that during recording.

Figures 3a and 3b show the readout current profiles $I_{sc}(\mathbf{r})$ obtained in the course of single scanning of the potential relieves recorded with opposite polarities in a subthreshold regime. The two curves are similar, differing only in sign of the current. The profiles exhibit a maximum at the point of crossing the recorded line, which indicates the position of the peak of the preliminarily recorded potential profile $\varphi(\mathbf{r})$. The readout current drops with increasing distance from the recorded line, decreasing down to a noise level at a distance close to that ($\rho \approx 160$ μm) estimated above.

Figure 4 presents the results obtained for recording in an overthreshold regime. The $I_{sc}(t)$ curve measured for the negative polarity of voltage applied to the scanning electrode (Fig. 4a) is generally similar in shape to the curves depicted in Fig. 2. The amplitude of the initial current pulse observed upon the first touch increases in proportion to the electrode potential. The decay time constant of this current pulse is also on the same order of magnitude ($\tau_- \approx 0.3$ s). The stationary current level, reached upon monotonic increase at point *2*' and then retained between points *2*' and *3*, is proportional to the electrode potential. The radius ρ of the region of sharp potential variation in this case is also the same (approximately 160 μm) as that observed for a low voltage between electrodes.

Significant differences are observed in the curve of $I_{sc}(t)$ measured for the positive electrode polarity in the overthreshold regime (Fig. 4b). Here, the amplitude of the initial current pulse observed upon the first touch (point *1*) markedly increases, while the decay time constant of this current pulse significantly decreases (to $\tau_+ \approx 0.05$ s). When the electrode starts moving (point *2*), the current rapidly increases up to a level significantly exceeding the stationary current value in Fig. 4a. Also markedly increased is the noiselike signal component. Simultaneous observation of the crystal birefringence showed evidence of local polarization switching at the point of the first needle contact with the crystal surface and along the entire electrode path. Therefore, the features of the $I_{sc}(t)$ signal behavior in Fig. 4b are related to local domain structure formation in the crystal.

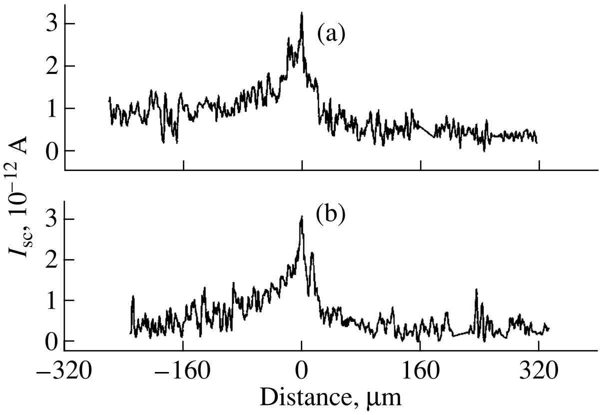

Fig. 3. Current profiles obtained during readout of a potential profile preliminarily recorded on an $LiNbO_3$ crystal surface at a recording electrode potential of (a) +0.6 and (b) –0.6 kV.

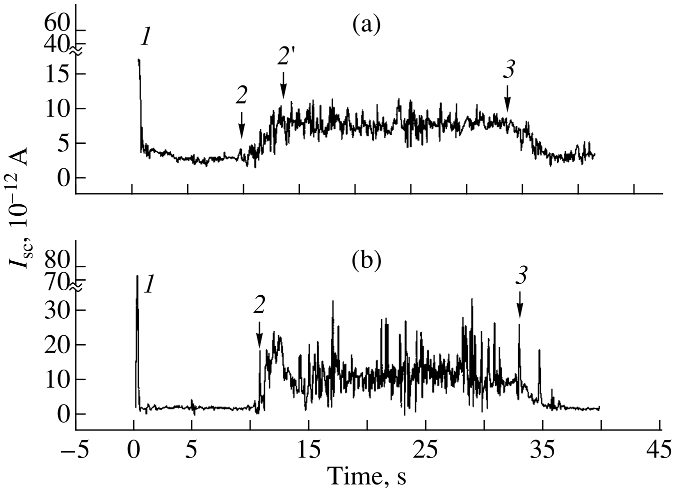

Fig. 4. Time variation of the current during scanning over an $LiNbO_3$ crystal surface with an needle-like electrode recording the potential relief at an electrode potential of (a) –3 and (b) +3 kV. Notations are the same as in Fig. 2.

The readout curves obtained for a potential relief recorded by a needle electrode at an applied voltage of +3 kV (Fig. 5a) show that the conventional boundary of the region of sharp potential variation is at a distance of about 160 μm from the recorded line (the same as that observed with a +0.6 kV subthreshold recording potential).

A distinctive feature of the signal profile obtained on reading a potential relief recorded at a negative voltage polarity in the overthreshold regime (Fig. 5b) is the presence of intense readout current peaks similar to those of the current recording the domain structure (Fig. 4b). These peaks are observed when the needle moves in the vicinity of the recorded line. The optical observations showed that the appearance of these current peaks is accompanied by the formation of a quasi-

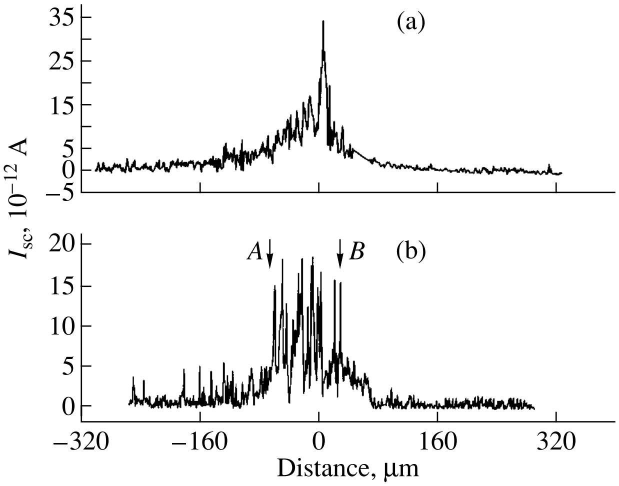

Fig. 5. Current profiles obtained during readout of a potential profile preliminarily recorded on an $LiNbO_3$ crystal surface at a recording electrode potential of (a) +3 and (b) −3 kV. Arrows indicate the onset (*A*) and termination (*B*) of the domain structure formation during motion of the recording electrode.

periodic needle-like domain structure in this region of the crystal [3]. Therefore, the potential difference between the grounded reading electrode and the crystal surface with a previously recorded negative potential profile exceeds the threshold value. The length of the domain structure is determined by the distance between the points on both sides of the record line, in which the potential difference between the reading electrode and the crystal surface reaches the threshold. As is seen from Fig. 5b, this distance amounts to approximately 80 μm.

According to our experimental data, all current profiles exhibit a relatively large noise level. It was established that this noise is related to processes occurring in the crystal, rather than to the method employed for measuring small currents at high voltages. When the needle electrode moves, the noise level is somewhat greater as compared to that observed with immobile needle. This effect is especially pronounced in an overthreshold regime. It should also be noted that the frequency characteristics of noise are close in all cases studied. Establishing the nature of this noise requires special investigation. Possible factors include crystal growth inhomogeneity, crystal surface quality, and contact instability.

We have also performed preliminary measurements of the injection currents and polarization switching with the –*Z*-cut crystal samples. It was found that, similar to the +*Z*-cut samples, the injection current in the +*Z* direction is smaller than that in the opposite direction. In the overthreshold regime, the currents corresponding to the polarization switching in the –*Z*- and +*Z*-cut samples had the same order of magnitude. The shapes of the record and readout profiles of the potential relief on the –*Z*-cut crystal surface were analogous to those observed for the +*Z*-cut samples.

The experimental results presented above allow us to formulate qualitative notions about the formation and shape of the potential relief in the subsurface region of a ferroelectric crystal: (i) the time of a potential relief formation as a result of the charge carrier injection (without spontaneous polarization switching) into the subsurface region of a monodomain $LiNbO_3$ crystal is 0.3–0.5 s; (ii) with a local spontaneous polarization switching, the time of a potential relief formation in a near-contact region of the crystal decreases by one order of magnitude (down to 0.05 s); (iii) a potential relief formed as a result of the point contact between a needle-like electrode and the $LiNbO_3$ crystal surface exhibits a maximum at the touch point and smoothly decays over a characteristic distance on the order of 10^2 μm; and (iv) during the charge carrier injection, the absolute current value depends on the mutual orientation of the current direction and the *Z* axis: the current in the +*Z* direction is smaller than that in the opposite direction.

ACKNOWLEDGMENTS

This study was supported by the Ministry of Science of the Russian Federation, project no. 99-2041.

REFERENCES

1. M. A. Lampert and P. Mark, *Current Injection in Solids* (Academic, New York, 1970; Mir, Moscow, 1973).
2. S. O. Fregatov and A. B. Sherman, Pis'ma Zh. Tekh. Fiz. **24** (6), 52 (1998) [Tech. Phys. Lett. **24**, 229 (1998)].
3. S. O. Fregatov and A. B. Sherman, Fiz. Tverd. Tela (St. Petersburg) **41** (3), 510 (1999) [Phys. Solid State **41**, 457 (1999)].
4. A. K. Tagantsev and I. A. Stolichnov, Appl. Phys. Lett. **74** (9), 1326 (1999).
5. A. V. Golenishchev-Kutuzov, V. A. Golenishchev-Kutuzov, and R. I. Kalimullin, Usp. Fiz. Nauk **170** (7), 697 (2000).
6. V. Ya. Shur, E. D. Rumyantsev, R. G. Batchko, *et al.*, Fiz. Tverd. Tela (St. Petersburg) **41** (10), 1831 (1999) [Phys. Solid State **41**, 1681 (1999)].
7. M. E. Lines and A. M. Glass, *Principles and Applications of Ferroelectrics and Related Materials* (Oxford Univ. Press, Oxford, 1977; Mir, Moscow, 1981).
8. Yu. S. Kuz'minov, *Electrooptical and Nonlinear-Optical Crystal of Lithium Niobate* (Nauka, Moscow, 1987).
9. B. I. Sturman and V. M. Fridkin, *Photovoltaic Effect in Media without Center of Symmetry and Related Phenomena* (Nauka, Moscow, 1992).

Translated by P. Pozdeev

Physics of the Solid State, Vol. 43, No. 9, 2001, pp. 1743–1749. Translated from Fizika Tverdogo Tela, Vol. 43, No. 9, 2001, pp. 1674–1679.
Original Russian Text Copyright © 2001 by N. Sirota, I. Sirota, Soshnina, Sokolovskiĭ.

LATTICE DYNAMICS AND PHASE TRANSITIONS

Cohesive Energy, Phonon Spectra, and Thermodynamic Properties of Elements with the Structures A_1, A_2, A_3, A_4—Al, Cu, V, Ti, Mg, Si, and Sn

N. N. Sirota*, I. M. Sirota, T. M. Soshnina*, and T. D. Sokolovskiĭ*****

**Moscow State University of Environmental Engineering, ul. Pryanishnikova 19, Moscow, 127550 Russia*
***Institute of Control Studies (Automation and Telemechanics), Russian Academy of Sciences,*
ul. Profsoyuznaya 65, Moscow, 117806 Russia
****Institute of Physics of Solids and Semiconductors, Belarussian Academy of Sciences,*
ul. Brovki 17, Minsk, 220072 Belarus

Received October 10, 2000; in final form, January 26, 2001

Abstract—The dependences of the cohesive (atomization) energy on the interatomic distance for elements Al, Cu, Ti(A_2), V, Mg, Ti(A_3), Si, and Sn are calculated using methods based on the Thomas–Fermi–Dirac–Gambosh statistical atomic theory. The obtained dependences are approximated by the Mie–Grüneisen potential. The phonon spectra calculated on the basis of the Born–Kärmän model and the Born–Kärmän–Blackman–de Lunay approach are used to determine the temperature dependences of the specific heat, free energy, and internal energy of the elements under investigation. The calculated cohesive energy, equilibrium interatomic distances, and temperature dependences of the specific heat agree with the experimental data. *© 2001 MAIK “Nauka/Interperiodica”.*

Quantitative analysis of the cohesive energy, phonon spectra, and thermodynamic properties of elements with different structures from the atomic constants is one of the most important issues in solid-state physics. Along with quantum-mechanical methods based on the Hartree–Fock relations, the computational methods using expressions from the theory of an inhomogeneous electron gas, the electron density functional, and the Coulson–Hohenberg–Kohn–Sham theorem are being developed intensively at present. Some of these methods are described in [1].

It was found that the methods based on the Thomas–Fermi–Dirac–Gombás statistical atomic theory [2–4] lead to similar results with much less cumbersome calculations.

The bond energy between two atoms is the sum of the Coulomb interaction u_c between atomic cores, the energy u_e of electrostatic interaction between electrons, the correlation energy u_ω due to the interaction of electrons with antiparallel spins, the ion-screening energy u_n, and the kinetic u_k and exchange energy u_a of electrons in the atomic bond:

$$u = u_c + u_e + u_\omega + u_n + u_k + u_a + \dots . \tag{1}$$

For the interaction between neutral atoms of the same species, the first term on the right-hand side of Eq. (1) is equal to zero. It was clearly demonstrated by Gombás [2] that the magnitude of the sum $u_e + u_n = u_s$ is approximately equal to half the kinetic energy of electrons forming a bond $|u_s| = u_k/2$. In contrast to the positive kinetic energy, the exchange energy u_a, as well as energy u_s, is negative. In this case, the energy of a pair bond between atoms of the same species can be expressed as $u = (1/2)u_k - u_a$.

The Dirac exchange energy and the kinetic energy of an electron gas can be expressed in terms of the electron density ρ in the bond. It was proved in [1, 5] that the gradient corrections due to the inhomogeneous electron cloud of the bond are small and can be neglected.

In the Thomas–Fermi–Dirac–Gombás approximation, the A–B pair atomic bond energy associated with the kinetic (u_k), exchange (u_a), and correlation (u_ω) energies of the electron gas in the bond is given by

$$\begin{aligned} u = {} & \frac{1}{2}\kappa_k \int [(\rho_A + \rho_B)^{5/3} - \rho_A^{5/3} - \rho_B^{5/3}]dV \\ & - \kappa_a \int [(\rho_A + \rho_B)^{4/3} - \rho_A^{4/3} - \rho_B^{4/3}]dW, \end{aligned} \tag{2}$$

where $\kappa_k = 2.871$ au, $\kappa_a = 0.7381$ au (in the absence of u_ω), and $\kappa_{a'} = 0.8349$ au (in the presence of u_ω).

It should be noted that at a half-length δ/2 of the pair bond between A and B atoms we have $\rho_{A_{1/2}} = \rho_{B_{1/2}} = \rho_{1/2}$ at points equidistant from the centers of these atoms.

The volume density of the total energy at a given point at the half-length of the bond is defined as

$$\left(\frac{du}{dV}\right)_{1/2} = -0.52\kappa_a\rho_{1/2}^{4/3} + 0.587\kappa_k\rho_{1/2}^{5/3}. \tag{3}$$

1063-7834/01/4309-1743$21.00 © 2001 MAIK “Nauka/Interperiodica”

Table 1. Coordination numbers z_i and the ratio of the radii of the *i*th and first coordination shells $K_i = \delta_i/\delta_1$ for structures of types A_1, A_2, A_3, and A_4

Structure type	Shell	I	II	III	IV	V	VI	VIII
A_1	z_i	12	6	24	12	24	8	48
	K_i	1	1.4142	1.7320	2.0	2.2361	2.4495	2.6457
A_2	z_i	8	6	12	24	8	6	24
	K_i	1	1.1547	1.6330	1.9148	2.0	2.3094	2.5166
A_3	z_i	12	6	2	18	12	6	12
	K_i	1	1.4142	1.6330	1.7321	1.9149	2.0	2.2361
A_4	z_i	4	12	12	6	12	24	16
	K_i	1	1.6330	1.9149	2.3094	2.5166	2.8284	3.0

The resultant electron densities of orbitals forming the bond can be described either by Slater expressions or by as is often used, Gaussian functions. In the latter case, the electron density can be represented as a function of distance r from the center of the atom in the form $\rho = A\exp(-\gamma r^2)$ (coefficient γ is inversely proportional to the square of the radius of the bonding orbital). If the bond is formed by N atomic electrons, the preexponential factor A is determined by the normalization condition:

$$A = \frac{N\gamma^{1.5}}{2\pi\Gamma(1.5)} = 0.1796N\gamma^{1.5}. \tag{4}$$

The distance r to any point (in the electron cloud) that lies on the perpendicular erected to the bond length at its midpoint and located at a distance y from it is determined from the condition $r^2 = (\delta/2)^2 + y^2$.

In this case, the linear density of the bond energy at its half-length $\delta/2$ is

$$\begin{aligned}\left(\frac{du}{d\delta}\right)_{1/2} &= -0.52\kappa_a A^{4/3}\exp\left[-\frac{4}{3}\gamma\left(\frac{\delta}{2}\right)^2\right] \\ &\times 2\pi\int_0^\infty y\exp\left(-\frac{4}{3}\gamma y^2\right)dy + 0.587\kappa_k A^{5/3} \\ &\times \exp\left[-\frac{5}{3}\gamma\left(\frac{\delta}{2}\right)^2\right]2\pi\int_0^\infty y\exp\left(-\frac{5}{3}\gamma y^2\right)dy \\ &= -0.52\kappa_a A^{4/3}\exp\left[-\frac{4}{3}\gamma\left(\frac{\delta}{2}\right)^2\right] \\ &\times\frac{3\pi}{4\gamma}\left\{1-\frac{4}{5}\frac{0.587\kappa_k}{0.52\kappa_a}A^{1/3}\exp\left[-\frac{1}{3}\gamma\left(\frac{\delta}{2}\right)^2\right]\right\}.\end{aligned} \tag{5}$$

The distribution of the linear bond energy density along the bond line l can be approximated by a function of the form of $\sin^2\varphi$, in which $\varphi = 2\pi l/\delta$. In this case, the pair bond energy u_i is determined by integrating the linear density along the bond line:

$$u_i = \int\left(\frac{du}{d\delta}\right)_{1/2}\sin^2\varphi d\varphi. \tag{6}$$

After introducing the coefficient $1.06 = (1/2)(\kappa'_a - \kappa_a)/\kappa_a$, which partially takes into account the role of U_ω, we obtain the total energy of a pair bond in a given coordination shell i of the crystal of element j in the form

$$\begin{aligned}u_{ji} &= -0.152\gamma N^{4/3}\exp\left[-\frac{4}{3}\gamma\left(K_i\frac{\delta}{2}\right)^2\right] \\ &\times\left\{1-1.982N^{1/3}\gamma^{1/2}\exp\left[-\frac{1}{3}\gamma\left(K_i\frac{\delta}{2}\right)^2\right]\right\}.\end{aligned} \tag{7}$$

When the correlation energy u_ω is taken into account completely, we have

$$\begin{aligned}u_{ij} &= -0.172\gamma N^{4/3}\exp\left[-\frac{4}{3}\gamma\left(K_i\frac{\delta}{2}\right)^2\right] \\ &\times\left\{1-1.752N^{1/3}\gamma^{1/2}\exp\left[-\frac{1}{3}\gamma\left(K_i\frac{\delta}{2}\right)^2\right]\right\}.\end{aligned} \tag{8}$$

Here, δ_1 is the bond length between the given atom and atoms from the first coordination shell and K_i is the ratio of the radius of the *i*th coordination shell to the radius r_1 of the first shell; $K_{ij} = (r_i/r_1)_j$ for element j.

In fact, the numerical coefficients in the expression for u_{ij} are variational parameters (α, η),

$$\begin{aligned}u_{ij} &= \alpha N^{4/3}\gamma\exp\left[-\frac{4}{3}\gamma\left(K\frac{\delta_1}{2}\right)^2\right] \\ &\times\left[1-\eta N^{1/3}\gamma^{1/2}\exp\left[-\frac{1}{3}\gamma\left(K_i\frac{\delta_1}{2}\right)^2\right]\right].\end{aligned} \tag{9}$$

Each atom of element j interacts with $z_{ij_{\text{eff}}}$ atoms of the ith coordination shell. In this case, $z_{ij_{\text{eff}}}$ is smaller than z_{ij} by a factor equal to the screening coefficient,

$$\xi = \left[1-\sigma\left(\frac{z_i-1}{K_{i-1}^2}+\ldots+\frac{z_2}{K_2^2}+\frac{z_1}{K_1^2}\right)\right], \qquad (10)$$

$$z_{ij_{\text{eff}}} = z_{ij}\left[1-\sigma\left(\frac{z_{i-1}}{K_{i-1}^2}+\ldots+\frac{z_2}{K_2^2}+\frac{z_1}{K_1^2}\right)\right], \quad K_1 \equiv 1, \qquad (11)$$

where σ is the relative effective cross section of the atom ($\sigma \approx 1/40$).

The total cohesive energy of the crystal per atom of element j is

$$U_j = \sum z_{ij_{\text{eff}}} u_{ij}. \qquad (12)$$

Table 1 contains the coordination numbers and the ratio of radii of the ith coordination shells to the radius of the first coordination shell $K_i = r_i/r_1$ for crystals with structures of types A_1 (fcc), A_2 (bcc), A_3 (hcp), and A_4 (diamond). Figure 1 shows the $U(\delta)$ dependences for the elements under investigation. The results of these calculations are presented in Table 2.

For cohesive energy of the crystals of a given structural type as a function of the spacing between nearest neighbor atoms, the radius of the first coordination shell in the range $\delta > \delta_i$ can be successively approximated by the Mie–Grüneisen potential:

$$U = \frac{a}{r^m} + \frac{b}{r^n}, \qquad (13)$$

$$U = \frac{U_0^{mn}}{n-m}\left[\frac{1}{m}\left(\frac{r_1}{r}\right)^m - \frac{1}{n}\left(\frac{r_1}{r}\right)^n\right]. \qquad (14)$$

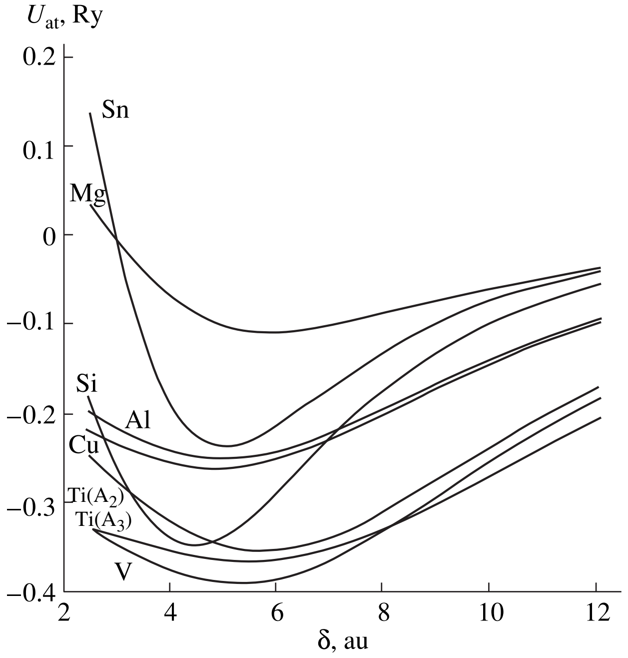

Fig. 1. Atomization energy as a function of the separation between nearest neighbor atoms.

We will use this expression to calculate the phonon spectra and thermodynamic properties of elements having structures of the type A_1 (Al, Cu), A_2 (V, Ti_α), A_3 (Mg, Ti_β), and A_4 (Si, βSn).

The curves describing the dependences $U_{\text{at}}(\delta)$ of the atomization energy are used for determining the exponents m and n in the range of variation of $U(\delta)$ for $\delta > \delta_1$.

Table 2. Structure types, number N of bonding electrons, atomization energy U_{at}, atomization energy per unit volume U_0, atomic mass A, molar volume V, separation between nearest neighbor atoms δ, coefficient γ, and exponents m and n used in the calculations of elements Al, Cu, V, Ti(A_2), Mg, Ti(A_3), Si, and Sn

Z	Element	Structure type	N	$-U_{\text{at}}$, kJ mol^{-1} [7]	A	V, cm^3 [7]	Experiment		Theory		Values adopted in calculations			[6]	
							$-U_{\text{at}}$, Ry	δ, au	$-U_{\text{at}}$, Ry	δ, au	γ	m	n	m	n
13	Al	A_1	3	326.4	26.98	10.00	0.2491	5.4122	0.252	5.1	0.110	4	7	4	7
29	Cu	A_1	3	338.32	95.54	7.11	0.2582	4.831	0.262	4.9	0.107	3.5	7	4	7
22	Ti	A_2	5	469.9	47.88	10.63	0.3587	5.5786	0.355	5.7	0.08	5	10	–	–
23	V	A_2	5	514.21	50.94	8.36	0.3925	5.0648	0.392	5.3	0.075	4	8	4	7
12	Mg	A_3	2	147.7	24.305	14.00	0.1127	6.0669	0.110	5.9	0.185	3	9.5	4	6
22	Ti	A_3	5	469.9	47.88	10.63	0.3587	5.5378	0.366	5.5	0.071	3.2	5.1	–	–
14	Si	A_4	4	455.6	28.08	12.04	0.3478	4.5478	0.348	4.5	0.106	3.2	5.1	(8)	(12)
50	Sn	A_4	4	302.1	118.72	16.29	0.2306	5.4342	0.238	5.1	0.126	3	10.5	3	10

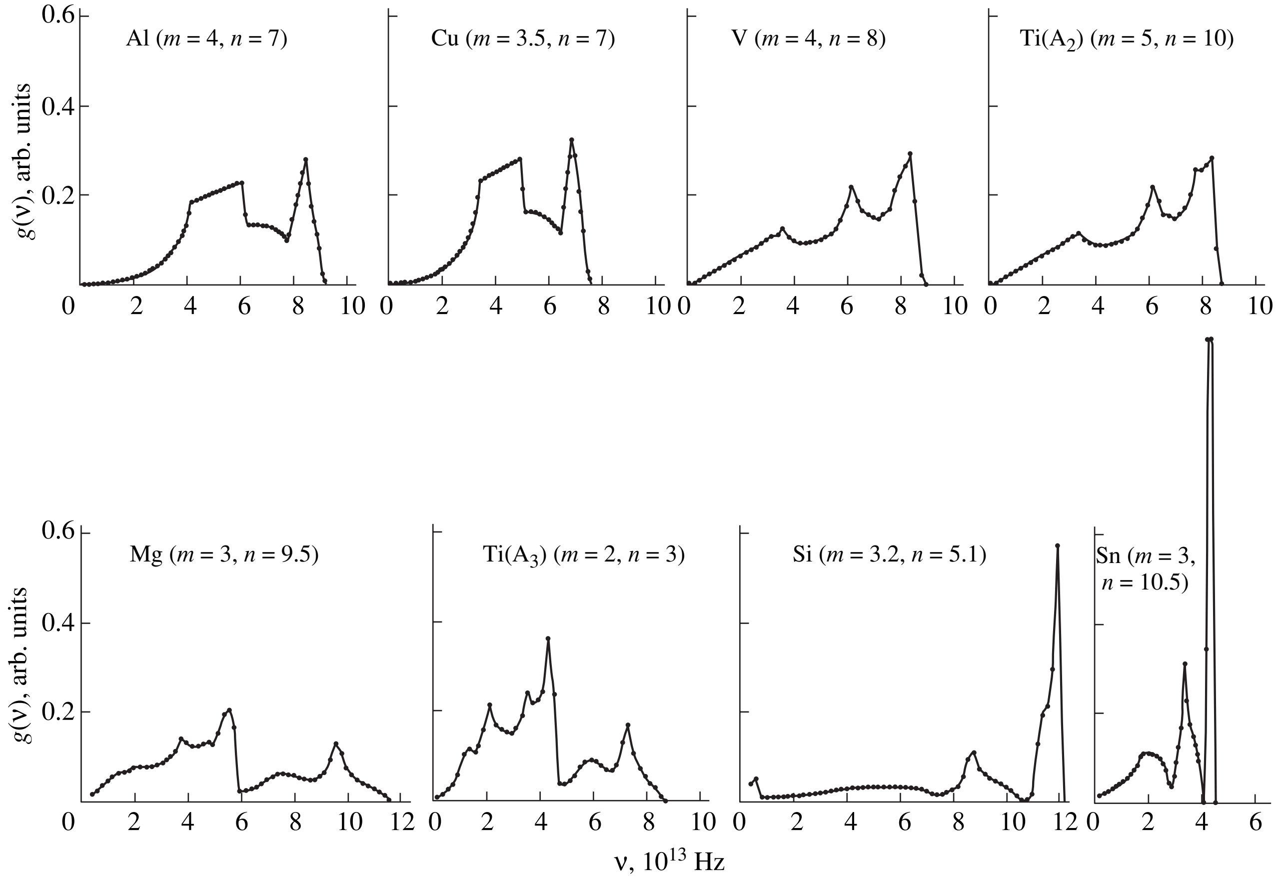

Fig. 2. Phonon spectra $g(\nu)$ for elements.

The values of exponents m and n were calculated earlier by Fürth [6] from empirical elastic and thermal constants for a large number of elements. The values of these indices used by us to calculate the phonon spectra and thermodynamic properties of elements (Table 2) slightly differ from the results obtained in [6].

Table 2 contains the experimental [7] and calculated values of U_{at}, $U_0 = U_{at}/V$, δ_1, as well as the values of m and n obtained in [6] and those used in our calculations.

An analysis of the phonon spectra of the elements under investigation was carried out in the approximation of the Born–Kärmän model of a solid [8, 9] using the Born–Kärmän–Blackman–de Launay method by solving the secular equation with the Born–Kärmän dynamic matrix

$$|D(q) - mw^2L| = 0, \tag{15}$$

where $D(q)$ is the dynamic matrix and L is the unit matrix.

A solution is stable if all frequencies are positive, i.e., if the principal minors of the matrix are positive ($D > 0$).

Proceeding from symmetry conditions, the dynamic equation was solved for a 1/48 part of the first Brillouin zone. The contribution of the wave vectors q at 10^6 points of the reciprocal unit cell was taken into account. The points were chosen by the Monte Carlo method [10]. No correcting changes were made in the region of extreme low frequencies of the spectrum.

The de Launay force constants α_{ij} and β_{ij} were determined from the functional dependence $U(r)$ calculated using the Mie–Grüneisen approximating expression. According to de Launay [11, 12], these constants are given by

$$\alpha_{ij} = \left(\frac{d^2U_j}{dr^2}\right)_{r_i}, \tag{16}$$

$$\beta_{ij} = \frac{1}{r_i}\left(\frac{dU_j}{dr}\right)_{r_i}. \tag{17}$$

The derivatives of the cohesive energy with respect to the atomic spacing are taken at the points corresponding to the radii of the *i*th coordination shells.

The approximation of $U(r)$ by the Mie–Grüneisen potential makes it possible to obtain analytical expressions for the force constants [13]:

$$\alpha_{ij} = \frac{mn(m+1)}{n-m}\frac{U_0}{r_{0j}}K_{ij}^{-(m+2)}\left[1-\frac{(n+m)}{(m+1)}K_{ij}^{-(n-m)}\right], \quad (18)$$

$$\beta_{ij} = \frac{-mn}{(n-m)}\frac{U_{0j}}{r_{0j}}K_{ij}^{-(m+2)}[1-K_{ij}^{-(n-m)}]. \quad (19)$$

Here, U_{0j} is the atomization energy of the element per molar volume, $r_{0j} \equiv r_{1j}$ is the separation between the nearest neighbor atoms in a unit cell of the crystal, m and n are the exponents in the Mie–Grüneisen potential of the given element, and $K = r_i/r_1$.

Figure 2 shows the phonon spectra $g_j(\nu)$ calculated for the elements under investigation. These spectra agree with the spectra of the elements obtained earlier [12, 14].

The results obtained for the phonon spectra calculated by us were used to determine the standard values and temperature dependences of thermodynamic properties of elements (heat capacity $C_V(T)$, internal energy $U(T)$, and the Helmholtz free energy $F(T)$) for the modifications indicated in Fig. 2.

Figure 3 shows the calculated values of the heat capacity $C_V(T)$. The experimental points [7, 15, 16] are plotted on the theoretical curves. The theoretical temperature dependences $U(T)$ and $F(T)$ are presented in Fig. 4. From the figures, it can be seen that the theoretical and experimental values of $C_V(T)$ are in good agreement.

Figure 5 illustrates the correlation between the experimental and calculated values of C_V in the range of C_V values from 0 to 24 J mol^{-1} K^{-1}. It can be seen from Figs. 3 and 5 that the calculated and experimental values of C_V match over a wide intermediate range of C_V values. Some deviations are observed at low and high values of C_V. The deviations corresponding to small values of C_V (i.e., at low temperatures) may be due to the inaccuracy of calculations in the long-wave length range. As a rule, the extreme left part of the phonon spectra calculated in the Born–Kärmän model of a crystal is approximated by a Debye parabola. In the spectra presented here, this approximation was not used; the contributions of the electronic and magnetic components to the thermodynamic functions were also disregarded in view of their relative smallness. The insignificant deviations at temperatures above 280 K require further analysis. These deviations are apparently associated with the discarded anharmonicity of vibrations, which is manifested at elevated temperatures.

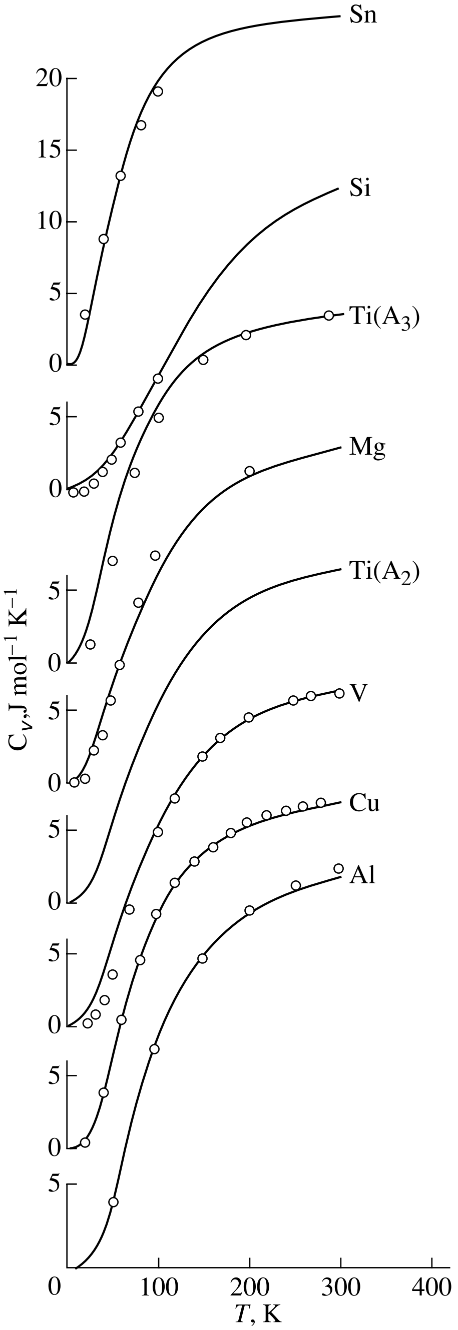

Fig. 3. Temperature dependences of heat capacity $C_V(T)$, J mol^{-1} K^{-1}. Experimental points are plotted on the $C_V(T)$ curves.

The results obtained indicate the effectiveness of the new method of calculations of $U(\delta)$ on the basis of the statistical atomic theory and the expedience of approximating $U(T)$ by the Mie–Grünaisen potential with appropriate values of m and n. However, this approximation in its simplest form must be refined for substances with negative thermal expansion coefficients.

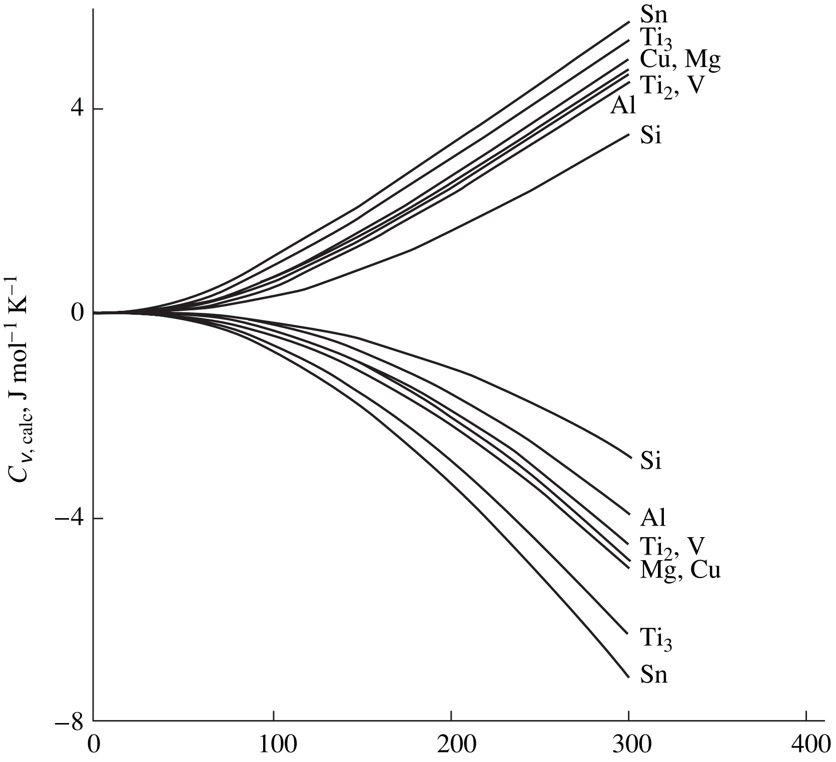

Fig. 4. Temperature dependences of the Helmholtz free energy $F(T)$ (descending curves) and internal energy $U(T)$ (ascending curves).

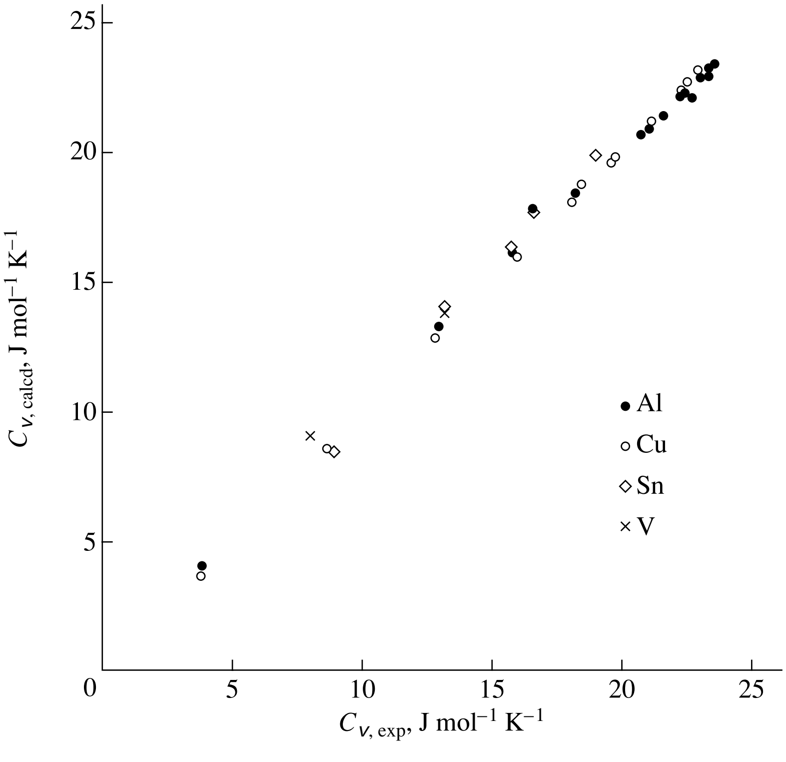

Fig. 5. Calculated and experimental values of $C_V(T)$.

REFERENCES

1. *Theory of the Inhomogeneous Electron Gas*, Ed. by S. Lundqvist and N. H. March (Plenum, New York, 1983; Mir, Moscow, 1987).
2. P. Gombás, *Die statistische Theorie des Atoms und ihre Anwendungen* (Springer-Verlag, Vienna, 1949; Inostrannaya Literatura, Moscow, 1951).
3. I. K. Dmitrieva and G. I. Plindov, *Properties of Atoms and Ions from the Point of Statistical Theory* (Nauka i Tekhnika, Minsk, 1991).
4. N. N. Sirota and I. M. Sirota, Cryst. Res. Technol. **32** (1), 143 (1997).
5. W. Kohn and P. Vashishta, in *Theory of the Inhomogeneous Electron Gas*, Ed. by S. Lundqvist and N. H. March (Plenum, New York, 1983; Mir, Moscow, 1987), p. 86.
6. R. Fürth, Proc. R. Soc. London, Ser. A **193** (922), 87 (1944).
7. J. Emsley, in *The Elements* (Clarendon, Oxford, 1989; Mir, Moscow, 1993), p. 256.
8. M. Born and K. Huang, *Dynamical Theory of Crystal Lattices* (Clarendon, Oxford, 1954; Inostrannaya Literatura, Moscow, 1958).
9. A. A. Maradudin, E. W. Montroll, and G. H. Weiss, in *Solid State Physics*, Suppl. 3 (Academic, New York, 1963; Mir, Moscow, 1965).
10. N. N. Sirota and T. D. Sokolovcky, in *Chemical Bond in Semiconductor and Solids* (Consultants Bureau, New York, 1967), p. 139.
11. De Launay, Solid State Phys. **2**, 219 (1956).
12. S. C. Upadhyaya, J. C. Upadhyaya, and R. Shyam, Phys. Rev. B **44** (1), 122 (1991).
13. N. N. Sirota, I. M. Sirota, T. M. Soshnina, and T. D. Sokolovskiĭ, Dokl. Akad. Nauk **373** (6), 750 (2000) [Dokl. Phys. **45** (8), 380 (2000)].
14. *Landolt–Börnstein: Numerical Data and Functional Relationships in Science and Technology* (Springer-Verlag, Berlin, 1981), Group III B, Vol. 13.
15. H. Zeise, *Thermodynamik. Tabellen* (S. Hirzel, Leipzig, 1954), Vol. 3/1.
16. *Physical Quantities: Handbook*, Ed. by I. S. Grigor'ev and E. Z. Meĭlikhov (Énergoizdat, Moscow, 1991).

Translated by N. Wadhwa

Physics of the Solid State, Vol. 43, No. 9, 2001, pp. 1750–1758. Translated from Fizika Tverdogo Tela, Vol. 43, No. 9, 2001, pp. 1680–1687.
Original Russian Text Copyright © 2001 by Shipitsyn.

LATTICE DYNAMICS AND PHASE TRANSITIONS

Magnetic and Electric Phase Transitions in the Hubbard Model

E. V. Shipitsyn
Bogdanov International Institute, Yekaterinburg, 620062 Russia
e-mail: ibi@uvtb.ru

Received January 9, 2001

Abstract—Within the Hubbard model, two boson Green’s functions that describe the propagation of collective excitations of the electronic system—magnons (states with a single electron spin flip) and doublons (states with two electrons at one site of the crystal lattice)—are calculated for a Coulomb interaction of arbitrary strength and for an arbitrary electron concentration by applying a decoupling procedure to the double-time *X*-operator Green’s functions. It is found that the magnon and doublon Green’s functions are similar in structure and there is a close analogy between them. Instability of the paramagnetic phase with respect to spin ordering is investigated using the magnon Green’s function, and instability of the metallic phase to charge ordering is analyzed with the help of the doublon Green’s function. Criteria for the paramagnet–ferromagnet and metal–insulator phase transitions are found. *© 2001 MAIK “Nauka/Interperiodica”.*

1. INTRODUCTION

One of the basic theoretical models in solid-state physics is the Hubbard model [1]. In this model, electrons are assumed to move through a crystal lattice by hopping between adjacent sites. It is also assumed that each site has only one electron energy level, and, therefore, according to the Pauli exclusion principle, it can be simultaneously occupied by no more than two electrons and they must be opposite in spin; in this case, there will be Coulomb (electrostatic) repulsion between two electrons occupying the same site. Electron transitions between sites are characterized by the kinetic energy t, and the Coulomb interaction between electrons is characterized by the Coulomb energy U. Another parameter of this model is the electron concentration n, which is the average number of electrons at one site,

$$n = \frac{N_e}{N}, \tag{1}$$

where N and N_e are the numbers of atoms and electrons in the crystal, respectively.

The second-quantized Hamiltonian of the Hubbard model has the form [1]

$$H = t\sum_{\langle ll'\rangle\sigma} a^*_{l\sigma}a_{l'\sigma} + U\sum_{l} n_{l+}n_{l-}, \tag{2}$$

where $a_{l\sigma}$ and $a^*_{l\sigma}$ are the annihilation and creation operators, respectively, for an electron of spin σ ($\sigma = \uparrow, \downarrow$ or, identically, +, –) at site l; $n_{l\sigma} = a^*_{l\sigma}a_{l\sigma}$ is the number operator of electrons of spin σ at site l; and $\langle ll'\rangle$ indicates summation over nearest neighbors in the lattice.

When $U \ll t$, the Hubbard model describes a Fermi liquid; at $U \gg t$, we have a strongly correlated system; in the intermediate region between these two extreme cases, we have a complicated system which shows two opposite tendencies, toward localization and toward delocalization of electronic states (characterized by the parameters U and t, respectively). The magnetic and electrical properties of the systems described by the Hubbard model are determined by a delicate balance between these two tendencies.

The Hubbard model has been studied in a wide range of U values using various methods (see, e.g., reviews [2–4] and references therein). However, none of them is universal or more adequate; the choice of the appropriate method is completely dictated by the physical problem under consideration. In this paper, we investigate the dynamic response functions of a system to external magnetic and electric fields in a wide range of values of n ($0 \le n \le 1$) and U ($U > t$), including the region of strong ($U \gg t$) and moderate ($U \sim t$) electron correlations.

In the theory of systems with weak Coulomb interaction ($U \ll t$), the random-phase approximation (RPA) [5] is used in a wide range of electron concentrations ($0 \le n \le 1$). Formally, the RPA corresponds to summation of electron loop diagrams of a series expansion in parameter U/t. Although this summation is justified only for systems with strongly degenerate electronic states, the application of the RPA to Hamiltonian (2) gives a physically reasonable description for Hubbard model parameters varied over a wide range [6].

In this paper, we consider the case of strong and moderate Coulomb interaction, starting from the limit of large values of U ($U > t$), which is commonly referred to as the atomic limit in order to distinguish it from the case of small U values ($U < t$), which is called the band limit. In the atomic limit, the most convenient dynamic variables are the Hubbard X operators [7], which operate in single-site electron state space. The X-operator formalism has been repeatedly employed to advantage in the theory of strongly correlated electron systems [8–23]; its detailed description can be found, e.g., in [24, 25].

In order to calculate the double-time X-operator Green's functions, we will employ a decoupling technique developed for infinite chains of the equations of motion of these functions [26, 27]. Thus, we will find two boson Green's functions, which are dynamic responses of the electron system. They describe propagation of collective bosonic excitations—magnons (states with a single electronic spin flip) and doublons (states with two electrons at one site)—in this system. The general expressions derived for the magnon and doublon Green's functions will be used to find the conditions for the occurrence of magnetic and insulating ordering of the electron system.

The approximations that we use to simplify the equations of motion of the Green's functions mentioned above can be classified as the RPA for the Hubbard model near the atomic limit. The results obtained for the dynamic response functions formally resemble usual RPA calculations near the band limit, with the difference that now, instead of band electron states, strongly correlated electronic states appear in them. The latter states are described in the Hubbard-1 approximation [1], which allows for the most important correlation effect, the splitting of the initial electron band into two Hubbard subbands. Although the Hubbard-1 approximation overestimates correlation effects, this does not lead to any problems in our case, because the objective of this paper is to investigate the effect of strong correlations on the dynamic response function of the electron system.

2. CALCULATION OF THE MAGNON AND DOUBLON GREEN'S FUNCTIONS

It will be recalled that, in the Hubbard model, there are only four possible electronic states at a lattice site [7, 28],

$$|0\rangle,\ |+\rangle,\ |-\rangle,\ |2\rangle, \tag{3}$$

which are the empty state, the singly occupied states of spin $\sigma = +$ and $-$ (i.e., of a spin aligned with the external field and opposite to it), and the doubly occupied state with electrons of opposite spin ($\sigma = +$ and $-$), respectively.

In accordance with (3), one can introduce Hubbard X operators X_l^{pq}, which take site l from the $|q\rangle$ to the $|p\rangle$ state [7]. Among these sixteen single-site Hubbard operators X_l^{pq} ($p, q = 0, +, -, 2$) are eight fermionlike ($X_l^{0\sigma}$, $X_l^{\sigma 2}$ and their adjoints $X_l^{\sigma 0}$, $X_l^{2\sigma}$), four bosonlike (X_l^{+-}, X_l^{02} and their adjoints X_l^{-+}, X_l^{20}), and four diagonal (X_l^{00}, $X_l^{\sigma\sigma}$, X_l^{22}) operators. Instead of the fermionlike operators, we conveniently introduce two-component spinors composed of them [28]:

$$\Psi_{\sigma l} = \begin{pmatrix} X_l^{0\sigma} \\ \sigma X_l^{\bar{\sigma}2} \end{pmatrix} \tag{4}$$
$$\text{and}\ \ \Phi^*_{\sigma l} = (X_l^{\sigma 0}\sigma X_l^{2\bar{\sigma}}),$$

where $\bar{\sigma} = -\sigma$ ($\sigma = +, -$). In terms of the Hubbard operators, the Hamiltonian of the Hubbard model is represented as the sum of a linear and a quadratic form [28]:

$$H = \sum_l \sum_{p\,=\,0,\,+,\,-,\,2} \varepsilon_p X_l^{pp} + t\sum_{\langle ll'\rangle} \sum_{\sigma\,=\,+,\,-} \Psi^*_{\sigma l} R \Phi_{\sigma l'}. \tag{5}$$

Here,

$$\varepsilon_0 = 0, \quad \varepsilon_\pm = \mp\frac{h}{2} - \mu, \quad \varepsilon_2 = U - 2\mu, \tag{6}$$

$$R = r_0 + r_1 \equiv \begin{pmatrix} 1 & 1 \\ 1 & 1 \end{pmatrix}, \tag{7}$$

where h is an external magnetic field, μ is the one-electron chemical potential, and r_j ($j = 0, 1, 2, 3$) are the Pauli matrices

$$r_0 = \begin{pmatrix} 1 & 0 \\ 0 & 1 \end{pmatrix}, \quad r_1 = \begin{pmatrix} 0 & 1 \\ 1 & 0 \end{pmatrix},$$
$$r_2 = \begin{pmatrix} 0 & -i \\ i & 0 \end{pmatrix}, \quad r_3 = \begin{pmatrix} 1 & 0 \\ 0 & -1 \end{pmatrix}. \tag{8}$$

We use the double-time retarded Green's function method [26, 27] and introduce three such functions: a matrix (anticommutator) function and two scalar (commutator) functions:

$$G_\sigma = (l - l', \tau - \tau') = \langle\langle \Psi_{\sigma l}(\tau) | \Psi^*_{\sigma l'}(\tau') \rangle\rangle, \tag{9}$$

$$F_{+-}(l - l', \tau - \tau') = \langle\langle X_l^{+-}(\tau) | X_{l'}^{-+}(\tau') \rangle\rangle, \tag{10}$$

$$F_{02}(l - l', \tau - \tau') = \langle\langle X_l^{02}(\tau) | X_{l'}^{20}(\tau') \rangle\rangle, \tag{11}$$

where the standard notation is used [26, 27]; τ and τ' are the initial and final instants of time, respectively. The function in Eq. (9) describes the motion of electrons, and the functions in Eqs. (10) and (11) describe the propagation of collective bosonic excitations of the electron system, magnons (states with a single electron spin flip) and doublons (states with two electrons at one site), respectively.

We note that the Hubbard operators involved in the magnon Green's function (10) are associated with processes in which the spin is changed but the electric charge is conserved, whereas the Hubbard operators involved in the doublon Green's function (11), on the contrary, change the charge but preserve the spin. Therefore, the former function describes the magnetic properties of the solid; the latter, the electrical ones. In other words, from the magnon and doublon Green's functions, one can derive criteria for magnetic and electric phase transitions, respectively [29].

For each of the Green's functions (9)–(11), one can write an infinite chain of equations of motion [by differentiating the function with respect to time τ and using Hamiltonian (5)] [26, 27]. We calculate all three (electron, magnon, and doublon) Green's functions in the same approximation, that in which the infinite chain of equations of motion is decoupled at the first equation among those in which newly arising functions are reduced, by decoupling to the functions that have arisen before; therefore, instead of an infinite chain of equations, we obtain a finite closed set of equations.

In the case of the electron Green's function (which is auxiliary in our investigation), the chain can be decoupled even at the first equation, which can be represented in the following form by taking the four-dimensional Fourier transform (i.e., by going from the spatial coordinates and time to the momentum and frequency, respectively) [26, 27]:

$$L_\sigma(\mathbf{k}, \omega) G_\sigma(\mathbf{k}, \omega) = M_\sigma. \tag{12}$$

Here,

$$L_\sigma(\mathbf{k}, \omega) = \begin{pmatrix} \omega - \varepsilon_\sigma - (1 - n_{\bar\sigma})\varepsilon(\mathbf{k}) & -(1 - n_{\bar\sigma})\varepsilon(\mathbf{k}) \\ -n_{\bar\sigma}\varepsilon(\mathbf{k}) & \omega - \varepsilon_\sigma - n_{\bar\sigma}\varepsilon(\mathbf{k}) - U \end{pmatrix}, \tag{13}$$

$$M_\sigma = \begin{pmatrix} 1 - n_{\bar\sigma} & 0 \\ 0 & n_{\bar\sigma} \end{pmatrix}, \tag{14}$$

where k is the wave vector (momentum); ω is the frequency; $\varepsilon(\mathbf{k})$ is the bare spectrum of free electrons in the lattice (for $U = 0$),

$$\varepsilon(\mathbf{k}) = t\sum_{\boldsymbol{\Delta}} \exp(i\mathbf{k}\boldsymbol{\Delta}) \tag{15}$$

($\boldsymbol{\Delta}$ specifies the nearest neighbors of an arbitrary fixed lattice site); and n_σ is the average number of electrons of spin σ at one site, such that

$$n_+ + n_- = n. \tag{16}$$

A solution to Eq. (12) can be written as

$$G_\sigma(\mathbf{k}, \omega) = \frac{P^{\sigma 1}(\mathbf{k})}{\omega + \mu - E_1^\sigma(\mathbf{k})} + \frac{P^{\sigma 2}(\mathbf{k})}{\omega + \mu - E_2^\sigma(\mathbf{k})}, \tag{17}$$

where the elements of matrices $P^{\sigma 1}(\mathbf{k})$ and $P^{\sigma 2}(\mathbf{k})$ are

$$P_{11}^{\sigma 1,2}(\mathbf{k}) = \frac{(1 - n_{\bar\sigma})}{2}\left[1 \mp \frac{(1 - 2n_{\bar\sigma})\varepsilon(\mathbf{k}) - U}{Y_\sigma(\mathbf{k})}\right],$$

$$P_{22}^{\sigma 1,2}(\mathbf{k}) = \frac{n_{\bar\sigma}}{2}\left[1 \pm \frac{(1 - 2n_{\bar\sigma})\varepsilon(\mathbf{k}) - U}{Y_\sigma(\mathbf{k})}\right], \tag{18}$$

$$P_{12}^{\sigma 1,2}(\mathbf{k}) = P_{21}^{\sigma 1,2}(\mathbf{k}) = \mp\frac{n_{\bar\sigma}(1 - n_{\bar\sigma})\varepsilon(\mathbf{k})}{Y_\sigma(\mathbf{k})}$$

and the electron energy bands $E_1^\sigma(\mathbf{k})$ and $E_2^\sigma(\mathbf{k})$ are given by

$$E_{1,2}^\sigma(k) = \frac{1}{2}[\varepsilon(\mathbf{k}) + U - \sigma h \mp Y_\sigma(\mathbf{k})] \tag{19}$$

with

$$Y_\sigma(\mathbf{k}) = [\varepsilon^2(\mathbf{k}) - 2(1 - 2n_{\bar\sigma})\varepsilon(\mathbf{k})U + U^2]^{1/2}. \tag{20}$$

We note that Eq. (17) corresponds to the Hubbard-1 approximation [1].

The infinite chains of equations for the magnon and doublon Green's functions can be decoupled only at the second equations, and, therefore, each of these functions is found by solving a set of two equations (one is scalar and the other is a matrix equation). The corresponding set of equations for the Fourier transform of the magnon Green's function $F_{+-}(\mathbf{k}, \omega)$ has the form

$$[\omega + (\varepsilon_+ - \varepsilon_-)]F_{+-}(\mathbf{k}, \omega) = [\langle X^{++}\rangle - \langle X^{--}\rangle] - \frac{1}{N}\sum_{\mathbf{p}}[\varepsilon(\mathbf{k} + \mathbf{p}) - \varepsilon(\mathbf{p})]\mathrm{Tr}\{R\Gamma_{+-}(\mathbf{k}, \omega|\mathbf{p})\}, \tag{21}$$

$$\begin{aligned} \omega\Gamma_{+-}(\mathbf{k}, \omega|\mathbf{p}) &= [K_+(\mathbf{k} + \mathbf{p})r_0 - r_0 K_-(\mathbf{p})] \\ &+ [\varepsilon(\mathbf{k} + \mathbf{p})K_+(\mathbf{k} + \mathbf{p})Rr_3 - \varepsilon(\mathbf{p})\tilde{r}_3 R K_-(\mathbf{p})]F_{+-}(\mathbf{k}, \omega) \\ &+ [L_+(\mathbf{k} + \mathbf{p})\Gamma_{+-}(\mathbf{k}, \omega|\mathbf{p}) - \Gamma_{+-}(\mathbf{k}, \omega|\mathbf{p})\tilde{L}_-(\mathbf{p})], \end{aligned} \tag{22}$$

and the set of equations for the Fourier transform of the doublon Green's function $F_{02}(\mathbf{k}, \omega)$ is

$$[\omega + (\varepsilon_0 - \varepsilon_2)]F_{02}(\mathbf{k}, \omega) = [\langle X^{00}\rangle - \langle X^{22}\rangle] - \frac{1}{N}\sum_{\mathbf{p}}[\varepsilon(\mathbf{k} + \mathbf{p}) + \varepsilon(\mathbf{p})]\mathrm{Tr}\{R\Gamma_{02}(\mathbf{k}, \omega|\mathbf{p})\}, \tag{23}$$

$$\begin{aligned}\omega\Gamma_{02}(\mathbf{k}, \omega|\mathbf{p}) &= -[K_+(\mathbf{k}+\mathbf{p})r_1 + r_1K_-(\mathbf{p})] \\ &- [\varepsilon(\mathbf{k}+\mathbf{p})K_+(\mathbf{k}+\mathbf{p})R(ir_2) + \varepsilon(\mathbf{p})(i\tilde{r}_2)RK_-(\mathbf{p})] \\ &\times F_{02}(\mathbf{k}, \omega) \\ &- [L_+(\mathbf{k}+\mathbf{p})\Gamma_{02}(\mathbf{k}, \omega|\mathbf{p}) + \Gamma_{02}(\mathbf{k}, \omega|\mathbf{p})\tilde{L}_-(\mathbf{p})].\end{aligned} \tag{24}$$

Here, $K_\sigma(\mathbf{k})$ is the Fourier transform of the electron correlator $\langle \Psi^*_{\sigma l}\Psi_{\sigma l'}\rangle$, which is expressed through the electron Green's function as [26, 27]

$$\begin{aligned}K_\sigma(\mathbf{k}) &= -\frac{1}{\pi} \\ &\times \int_{-\infty}^{+\infty} f(\omega+\mu)\lim_{\delta\to 0}[\mathrm{Im}G_\sigma(\mathbf{k}, \omega+i\delta)]d\omega,\end{aligned} \tag{25}$$

where

$$f(x) = \left[1 + \exp\left(\frac{x-\mu}{T}\right)\right]^{-1} \tag{26}$$

is the Fermi function and T is the absolute temperature; $\Gamma_{+-}(\mathbf{k}, \omega|\mathbf{p})$ and $\Gamma_{02}(\mathbf{k}, \omega|\mathbf{p})$ are auxiliary unknown functions; taking the trace is summation of the diagonal matrix elements; tilde ~ designates a transposed matrix; and $\langle\ldots\rangle$ represents the statistical average for the system with Hamiltonian (5) [26–28].

By solving the sets of equations (21), (22) and (23), (24) in combination with Eqs. (6)–(8), (13), (16), (17), and (25) and the relations [25, 28]

$$\begin{aligned}\langle X^{\sigma\sigma}\rangle &= n_\sigma, \quad \langle X^{00}\rangle = (1-n_+)(1-n_-), \\ \langle X^{22}\rangle &= n_+n_-,\end{aligned} \tag{27}$$

we arrive at the final expressions for the magnon and doublon Green's functions:

$$F_{+-}(\mathbf{k}, \omega) = \frac{[n_+ - n_-] + \dfrac{1}{N}\displaystyle\sum_{\mathbf{p}}[\varepsilon(\mathbf{k}+\mathbf{p}) - \varepsilon(\mathbf{p})]\sum_{\alpha=1}^{4}\frac{A_\alpha}{\omega + x_\alpha}}{[\omega - h] - \dfrac{1}{N}\displaystyle\sum_{\mathbf{p}}[\varepsilon(\mathbf{k}+\mathbf{p}) - \varepsilon(\mathbf{p})]\sum_{\alpha=1}^{4}\frac{B_\alpha}{\omega + x_\alpha}}, \tag{28}$$

$$F_{02}(\mathbf{k}, \omega) = \frac{[1-n] + \dfrac{1}{N}\displaystyle\sum_{\mathbf{p}}[\varepsilon(\mathbf{k}+\mathbf{p}) + \varepsilon(\mathbf{p})]\sum_{\alpha=1}^{4}\frac{C_\alpha}{(\omega+2\mu) - y_\alpha}}{[(\omega+2\mu) - U] - \dfrac{1}{N}\displaystyle\sum_{\mathbf{p}}[\varepsilon(\mathbf{k}+\mathbf{p}) + \varepsilon(\mathbf{p})]\sum_{\alpha=1}^{4}\frac{D_\alpha}{(\omega+2\mu) - y_\alpha}} \tag{29}$$

---

where

$$A_\alpha = u_\alpha\sum_{\beta=0}^{3}a_\beta x_\alpha^\beta, \quad B_\alpha = u_\alpha\sum_{\beta=0}^{2}b_\beta x_\alpha^\beta, \tag{30}$$

$$C_\alpha = v_\alpha\sum_{\beta=0}^{3}c_\beta y_\alpha^\beta, \quad D_\alpha = v_\alpha\sum_{\beta=0}^{2}d_\beta y_\alpha^\beta, \tag{31}$$

$$\begin{aligned}u_{1,4} &= \pm[(x_1-x_4)(x_1x_4-x_2x_3)]^{-1}, \\ u_{2,3} &= \mp[(x_2-x_3)(x_1x_4-x_2x_3)]^{-1},\end{aligned} \tag{32}$$

$$\begin{aligned}v_{1,4} &= \pm[(y_1-y_4)(y_1y_4-y_2y_3)]^{-1}, \\ v_{2,3} &= \mp[(y_2-y_3)(y_1y_4-y_2y_3)]^{-1},\end{aligned} \tag{33}$$

$$\begin{aligned}x_{1,4} &= E^+_{1,2}(\mathbf{k}+\mathbf{p}) - E^-_{1,2}(\mathbf{p}), \\ x_{2,3} &= E^+_{1,2}(\mathbf{k}+\mathbf{p}) - E^-_{2,1}(\mathbf{p}),\end{aligned} \tag{34}$$

$$\begin{aligned}y_{1,4} &= E^+_{1,2}(\mathbf{k}+\mathbf{p}) + E^-_{1,2}(\mathbf{p}), \\ y_{2,3} &= F^+_{1,2}(\mathbf{k}+\mathbf{p}) + E^-_{2,1}(\mathbf{p}),\end{aligned} \tag{35}$$

$$\begin{aligned}a_0 &= -U(n_+-n_-)\varepsilon(\mathbf{k}+\mathbf{p})\varepsilon(\mathbf{p})[\lambda_0^+(\mathbf{k}+\mathbf{p}) - \lambda_0^-(\mathbf{p})] \\ &-\frac{U^2}{2}\{[\varepsilon(\mathbf{k}+\mathbf{p}) - \varepsilon(\mathbf{p})][\lambda_1^+(\mathbf{k}+\mathbf{p}) - \lambda_1^-(\mathbf{p})] \\ &- [(1-2n_-)\varepsilon(\mathbf{k}+\mathbf{p}) - (1-2n_+)\varepsilon(\mathbf{p})] \\ &\times[\lambda_2^+(\mathbf{k}+\mathbf{p}) - \lambda_2^-(\mathbf{p})]\}, \\ a_1 &= -\varepsilon(\mathbf{k}+\mathbf{p})\varepsilon(\mathbf{p})[\lambda_0^+(\mathbf{k}+\mathbf{p}) - \lambda_0^-(\mathbf{p})] \\ &+ U\{[\varepsilon(\mathbf{k}+\mathbf{p}) + \varepsilon(\mathbf{p})][\lambda_3^+(\mathbf{k}+\mathbf{p}) - \lambda_3^-(\mathbf{p})] \\ &- [n_-\varepsilon(\mathbf{k}+\mathbf{p}) + n_+\varepsilon(\mathbf{p})][\lambda_0^+(\mathbf{k}+\mathbf{p}) - \lambda_0^-(\mathbf{p})]\} \\ &- U^2[\lambda_1^+(\mathbf{k}+\mathbf{p}) - \lambda_1^-(\mathbf{p})], \\ a_2 &= [\varepsilon(\mathbf{k}+\mathbf{p}) - \varepsilon(\mathbf{p})][\lambda_0^+(\mathbf{k}+\mathbf{p}) - \lambda_0^-(\mathbf{p})], \\ a_3 &= \lambda_0^+(\mathbf{k}+\mathbf{p}) - \lambda_0^-(\mathbf{p}),\end{aligned} \tag{36}$$

$$\begin{aligned}b_0 &= U^2\{[\varepsilon(\mathbf{k}+\mathbf{p}) - \varepsilon(\mathbf{p})][\varepsilon(\mathbf{k}+\mathbf{p})\lambda_4^+(\mathbf{k}+\mathbf{p}) \\ &- \varepsilon(\mathbf{p})\lambda_4^-(\mathbf{p})] - [n_-\varepsilon(\mathbf{k}+\mathbf{p}) - n_+\varepsilon(\mathbf{p})]\end{aligned}$$

$$
\begin{aligned}
&\times [\varepsilon(\mathbf{k}+\mathbf{p})\lambda_0^+(\mathbf{k}+\mathbf{p}) - \varepsilon(\mathbf{p})\lambda_0^-(\mathbf{p})]\}, \qquad (37)\\
b_1 &= U\varepsilon(\mathbf{k}+\mathbf{p})\varepsilon(\mathbf{p})[\lambda_0^+(\mathbf{k}+\mathbf{p}) - \lambda_0^-(\mathbf{p})]\\
&\quad - U^2[\varepsilon(\mathbf{k}+\mathbf{p})\lambda_2^+(\mathbf{k}+\mathbf{p}) - \varepsilon(\mathbf{p})\lambda_2^-(\mathbf{p})],\\
b_2 &= -U[\varepsilon(\mathbf{k}+\mathbf{p})\lambda_0^+(\mathbf{k}+\mathbf{p}) - \varepsilon(\mathbf{p})\lambda_0^-(\mathbf{p})],\\
c_0 &= -U(2-n)\varepsilon(\mathbf{k}+\mathbf{p})\varepsilon(\mathbf{p})[\lambda_0^+(\mathbf{k}+\mathbf{p}) - \lambda_0^-(\mathbf{p})]\\
&\quad - \frac{U^2}{2}\{[(1-n_-)\varepsilon(\mathbf{k}+\mathbf{p}) + (1-n_+)\varepsilon(\mathbf{p})]\\
&\quad \times ([\lambda_0^+(\mathbf{k}+\mathbf{p}) + \lambda_0^-(\mathbf{p})] - [\lambda_1^+(\mathbf{k}+\mathbf{p}) + \lambda_1^-(\mathbf{p})])\\
&\quad + 4((1-n_-)\varepsilon(\mathbf{k}+\mathbf{p})[\lambda_3^+(\mathbf{k}+\mathbf{p}) + \lambda_4^-(\mathbf{p})]\\
&\quad + (1-n_+)\varepsilon(\mathbf{p})[\lambda_4^+(\mathbf{k}+\mathbf{p}) + \lambda_3^-(\mathbf{p})])\}\\
&\quad - U^3\{[\lambda_0^+(\mathbf{k}+\mathbf{p}) + \lambda_0^-(\mathbf{p})] - [\lambda_1^+(\mathbf{k}+\mathbf{p}) + \lambda_1^-(\mathbf{p})]\},\\
c_1 &= \varepsilon(\mathbf{k}+\mathbf{p})\varepsilon(\mathbf{p})[\lambda_0^+(\mathbf{k}+\mathbf{p}) + \lambda_0^-(\mathbf{p})]\\
&\quad + U\{[(1-2n_-)\varepsilon(\mathbf{k}+\mathbf{p}) + (1-2n_+)\varepsilon(\mathbf{p})]\\
&\quad \times [\lambda_0^+(\mathbf{k}+\mathbf{p}) + \lambda_0^-(\mathbf{p})]\\
&\quad + \varepsilon(\mathbf{k}+\mathbf{p})[\lambda_3^+(\mathbf{k}+\mathbf{p}) + \lambda_4^-(\mathbf{p})]\\
&\quad + \varepsilon(\mathbf{p})[\lambda_4^+(\mathbf{k}+\mathbf{p}) + \lambda_3^-(\mathbf{p})]\}\\
&\quad + U^2\{3[\lambda_0^+(\mathbf{k}+\mathbf{p}) + \lambda_0^-(\mathbf{p})] - [\lambda_1^+(\mathbf{k}+\mathbf{p}) + \lambda_1^-(\mathbf{p})]\},\\
c_2 &= -[\varepsilon(\mathbf{k}+\mathbf{p}) + \varepsilon(\mathbf{p})][\lambda_0^+(\mathbf{k}+\mathbf{p}) + \lambda_0^-(\mathbf{p})]\\
&\quad - 3U[\lambda_0^+(\mathbf{k}+\mathbf{p}) + \lambda_0^-(\mathbf{p})],\\
c_3 &= \lambda_0^+(\mathbf{k}+\mathbf{p}) + \lambda_0^-(\mathbf{p}), \qquad (38)\\
d_0 &= -U^2\{\varepsilon(\mathbf{k}+\mathbf{p})\varepsilon(\mathbf{p})\\
&\quad \times ((1-n_-)[2\lambda_0^+(\mathbf{k}+\mathbf{p}) - \lambda_4^+(\mathbf{k}+\mathbf{p})]\\
&\quad + (1-n_+)[2\lambda_0^-(\mathbf{p}) - \lambda_4^-(\mathbf{p})])\\
&\quad - ((1-n_-)\varepsilon^2(\mathbf{k}+\mathbf{p})\lambda_4^+(\mathbf{k}+\mathbf{p})\\
&\quad + (1-n_+)\varepsilon^2(\mathbf{p})\lambda_4^-(\mathbf{p}))\}\\
&\quad - 2U^3[\varepsilon(\mathbf{k}+\mathbf{p})\lambda_3^+(\mathbf{k}+\mathbf{p}) + \varepsilon(\mathbf{p})\lambda_3^-(\mathbf{p})],\\
d_1 &= U\varepsilon(\mathbf{k}+\mathbf{p})\varepsilon(\mathbf{p})[\lambda_0^+(\mathbf{k}+\mathbf{p}) + \lambda_0^-(\mathbf{p})]\\
&\quad + U^2\{\varepsilon(\mathbf{k}+\mathbf{p})[\lambda_0^+(\mathbf{k}+\mathbf{p}) + 2\lambda_3^+(\mathbf{k}+\mathbf{p})]\\
&\quad + \varepsilon(\mathbf{p})[\lambda_0^-(\mathbf{p}) + 2\lambda_3^-(\mathbf{p})]\},\\
d_2 &= -U[\varepsilon(\mathbf{k}+\mathbf{p})\lambda_0^+(\mathbf{k}+\mathbf{p}) + \varepsilon(\mathbf{p})\lambda_0^-(\mathbf{p})], \qquad (39)
\end{aligned}
$$

$$\lambda_\gamma^\sigma(\mathbf{k}) = \sum_{\nu = 1, 2} V_\gamma^{\sigma\nu}(\mathbf{k}) f[E_\nu^\sigma(\mathbf{k})], \tag{40}$$

$$V_0^{\sigma\nu}(\mathbf{k}) = \sum_{\alpha, \beta = 1, 2} P_{\alpha\beta}^{\sigma\nu}(\mathbf{k}),$$

$$V_{1,2}^{\sigma\nu}(\mathbf{k}) = \sum_{\alpha = 1, 2} (\pm 1)^{\alpha - 1} P_{\alpha\alpha}^{\sigma\nu}(\mathbf{k}), \tag{41}$$

$$V_3^{\sigma\nu}(\mathbf{k}) = \sum_{\alpha = 1, 2} P_{1\alpha}^{\sigma\nu}(\mathbf{k}), \quad V_4^{\sigma\nu}(\mathbf{k}) = \sum_{\alpha = 1, 2} P_{2\alpha}^{\sigma\nu}(\mathbf{k}).$$

Equations (28) and (29) should be supplemented by an equation for the chemical potential μ [24, 27],

$$n = \frac{1}{N}\sum_{\mathbf{k}\sigma} \mathrm{Tr}\{RK_\sigma(\mathbf{k})\}, \tag{42}$$

which, when combined with Eqs. (7), (17), (25), (40), and (41), takes the form

$$n = \frac{1}{N}\sum_{\mathbf{k}\sigma} \lambda_0^\sigma(\mathbf{k}). \tag{43}$$

In Eq. (28), the quantities x_α are the energy differences for intraband ($\alpha = 1, 4$) and interband ($\alpha = 2, 3$) electron transitions with a spin flip and the quantities A_α and B_α determine the intensities of these transitions. In Eq. (29), the quantities y_α are the energy sums corresponding to two-particle states in the electronic spectrum (19) and C_α and D_α characterize the probabilities of these states.

From Eqs. (28) and (29), it follows that both calculated quasiparticle Green's functions describing different collective excitations (magnons and doublons) are determined by complicated combinations of one-particle characteristics of the bound electrons (of spin + and –) that compose these excitations. In addition, there is a close analogy (and even identity in some respects) between the final expressions for the magnon and doublon Green's functions (28) and (29), which is the consequence of the close analogy between the sets of equations (21), (22) and (23), (24) that define these functions.

As for the distinctions between the magnon and doublon Green's functions (and between the sets of equations that define them), most of them are due to the difference in physical interpretation of these functions (which follows from their different mathematical definitions) and are easy to understand. Indeed, many distinctions between Eqs. (28) and (29) [and between the sets of equations (21), (22) and (23), (24)] can easily be predicted by comparing the definitions in Eqs. (10) and (11). Furthermore, the following difference is also obvious. A magnon is associated with the process in which an electron leaves a site and then another electron occupies this site, these two electrons having opposite spins, whereas a doublon corresponds to the process in which two electrons of opposite spin simultaneously leave or occupy a site. Therefore, the magnon

Green’s function describes a collective excitation whose two constituents move in opposite directions, whereas the doublon Green’s function corresponds to a collective excitation whose two components move in the same direction. This is the reason for the main difference between Eqs. (28) and (29) [and between the sets of equations (21), (22) and (23), (24)]: in the expression (and equations) for the magnon Green’s function, the two one-electron characteristics differing in spin are subtracted (they have a minus sign between them), whereas in the expression (and equations) for the doublon Green’s function, these two characteristics are added (they have a plus sign between them). This last difference can be illustrated by comparing Eqs. (21), (22), (34), (36), and (37) with Eqs. (23), (24), (35), (38), and (39), respectively.

Therefore, given an expression for the magnon Green’s function, one can find the corresponding expression for the doublon Green’s function (or its general structure) and vice versa; that is, there is a certain relation between the magnon and doublon Green’s functions.

We note that the decoupling scheme that we employed in deriving Eqs. (28) and (29) is analogous to the RPA [5, 6] used in the Fermi liquid theory. Therefore, Eqs. (28) and (29) can be viewed, in a sense, as RPA calculations for strongly correlated electron systems.

In the specific case of the paramagnetic phase ($n_+ = n_- = n/2$) and strong Coulomb interaction ($U \gg t$), the general expressions for the magnon and doublon Green’s functions (28) and (29) can be written as

$$F_{+-}(\mathbf{k}, \omega) = \frac{\Pi(\mathbf{k}, \omega) + \frac{1}{U}\frac{n}{2}\left[Q(\mathbf{k}, \omega) + \Lambda(\mathbf{k}, \omega) + \left(1 - \frac{n}{2}\right)S_2(\mathbf{k}, \omega)\right]}{1 - R(\mathbf{k}, \omega) - \frac{1}{U}\left[\Phi(\mathbf{k}, \omega) + \frac{n}{2}\left(1 - \frac{n}{2}\right)S_3(\mathbf{k}, \omega)\right]}, \tag{44}$$

$$F_{02}(\mathbf{k}, \omega) = \frac{[1 - n] + \frac{1}{U}X(\mathbf{k}, \omega)}{[\omega + 2\mu] - U + Y(\mathbf{k}, \omega) - \frac{1}{U}Z(\mathbf{k}, \omega)}, \tag{45}$$

where

$$\begin{bmatrix} \Pi(\mathbf{k}, \omega) \\ Q(\mathbf{k}, \omega) \\ \Lambda(\mathbf{k}, \omega) \\ \Phi(\mathbf{k}, \omega) \end{bmatrix} = \frac{1}{N}\sum_{\mathbf{p}} \begin{bmatrix} 1 \\ \varepsilon(\mathbf{p}) \\ \varepsilon(\mathbf{k} + \mathbf{p}) \\ \varepsilon(\mathbf{p})\varepsilon(\mathbf{k} + \mathbf{p}) \end{bmatrix} \frac{f[E(\mathbf{k} + \mathbf{p})] - f[E(\mathbf{p})]}{\omega + E(\mathbf{k} + \mathbf{p}) - E(\mathbf{p})}, \tag{46}$$

$$R(\mathbf{k}, \omega) = \frac{1}{N} \times \sum_{\mathbf{p}} \frac{\varepsilon(\mathbf{k} + \mathbf{p}) f[E(\mathbf{k} + \mathbf{p})] - \varepsilon(\mathbf{p}) f[E(\mathbf{p})]}{\omega + E(\mathbf{k} + \mathbf{p}) - E(\mathbf{p})}, \tag{47}$$

$$S_\nu(\mathbf{k}, \omega) = \frac{1}{N} \times \sum_{\mathbf{p}} \frac{\varepsilon^\nu(\mathbf{k} + \mathbf{p}) f'[E(\mathbf{k} + \mathbf{p})] - \varepsilon^\nu(\mathbf{p}) f'[E(\mathbf{p})]}{\omega + E(\mathbf{k} + \mathbf{p}) - E(\mathbf{p})}, \tag{48}$$

$$X(\mathbf{k}, \omega) = \frac{1}{N} \times \sum_{\mathbf{p}} \frac{[E(\mathbf{k} + \mathbf{p}) + E(\mathbf{p})]^2 \{ f[E(\mathbf{k} + \mathbf{p})] + f[E(\mathbf{p})]\}}{[\omega + 2\mu] - [E(\mathbf{k} + \mathbf{p}) + E(\mathbf{p})]}, \tag{49}$$

$$Y(\mathbf{k}, \omega) = \frac{1}{N}\sum_{\mathbf{p}} \frac{E(\mathbf{k} + \mathbf{p}) + E(\mathbf{p})}{[\omega + 2\mu] - [E(\mathbf{k} + \mathbf{p}) + E(\mathbf{p})]} \times \{\varepsilon(\mathbf{k} + \mathbf{p}) f[E(\mathbf{k} + \mathbf{p})] + \varepsilon(\mathbf{p}) f[E(\mathbf{p})]\}, \tag{50}$$

$$Z(\mathbf{k}, \omega) = \frac{1}{N}\sum_{\mathbf{p}} \frac{E(\mathbf{k} + \mathbf{p}) + E(\mathbf{p})}{[\omega + 2\mu] - [E(\mathbf{k} + \mathbf{p}) + E(\mathbf{p})]} \times \left\{ \frac{n}{2}(\varepsilon^2(\mathbf{k} + \mathbf{p}) f[E(\mathbf{k} + \mathbf{p})] + \varepsilon^2(\mathbf{p}) f[E(\mathbf{p})]) - \left(1 - \frac{n}{2}\right)\varepsilon(\mathbf{k} + \mathbf{p})\varepsilon(\mathbf{p})(f[E(\mathbf{k} + \mathbf{p})] + f[E(\mathbf{p})]) \right\}, \tag{51}$$

$$E(\mathbf{k}) = \left(1 - \frac{n}{2}\right)\varepsilon(\mathbf{k}), \tag{52}$$

and $f'(x)$ is the derivative of the function $f(x)$ with respect to its argument x. In the specific case indicated above, Eq. (43) for the chemical potential can be written as

$$\frac{n}{2} = \left(1 - \frac{n}{2}\right)\frac{1}{N}\sum_{\mathbf{p}} f[E(\mathbf{p})] + \frac{1}{U}\frac{n}{2}\left(1 - \frac{n}{2}\right)^2 [2\Phi(\mathbf{k}_0, 0) - \Phi(\mathbf{0}, 0)], \tag{53}$$

where

$$\mathbf{k}_0 = (\pi, \pi, \pi). \tag{54}$$

It should be noted that expressions (46) were already derived in our papers [24, 29], where it was shown that they correspond to different electron loops that appear when the Hubbard model with strong electron correlations is treated by the X-operator diagram technique.

In the limit of infinitely strong Coulomb interaction ($U \longrightarrow \infty$), Eq. (44) has the form

$$F_{+-}(\mathbf{k}, \omega) = \frac{\Pi(\mathbf{k}, \omega)}{1 - R(\mathbf{k}, \omega)}, \tag{55}$$

which coincides with the corresponding expression derived in [30, 31]. Equation (55) is similar to the RPA expression for the dynamic magnetic susceptibility of a system with weak Coulomb interaction ($U \ll t$) [5, 6]. There are only two distinctions between them: Eq. (55) is obtained from the RPA expression by replacing, first, the free-electron spectrum $\varepsilon(\mathbf{k})$ with the spectrum of strongly correlated electrons $E(\mathbf{k})$ and, second, the parameter U, with the quantity $\varepsilon(\mathbf{k})$ [which, according to Eq. (15), is proportional to the parameter t].

3. MAGNETIC AND INSULATING INSTABILITIES

The expressions for the magnon and doublon Green's functions derived above allow one to find the criteria for the paramagnet–ferromagnet and metal–insulator phase transitions. The condition for instability of the paramagnetic phase with respect to ferromagnetic ordering has the form [25, 29]

$$[F_{+-}(\mathbf{0}, 0)]^{-1} > 0, \tag{56}$$

and the condition for instability of the metallic phase to insulating (charge) ordering is [25, 29]

$$[F_{02}(\mathbf{k}_0, 0)]^{-1} > 0. \tag{57}$$

Substituting Eq. (44) into Eq. (56), we obtain the criterion for the occurrence of ferromagnetism (at $T = 0$):

$$\begin{gathered}\left(1-\frac{n}{2}\right)^2 - \frac{n}{2} + \left(1-\frac{n}{2}\right)\bar{\mu}\bar{\rho}(\bar{\mu}) \\ + \nu\left(1-\frac{n}{2}\right)\left\{\left[1+\frac{n}{2}\left(1+3\frac{n}{2}\right)\right]\bar{\mu}^2\bar{\rho}(\bar{\mu}) \right. \\ \left. - \frac{n}{2}\left(1-\frac{n}{2}\right)\bar{\mu}^3\bar{\rho}'(\bar{\mu}) - nI_1(\bar{\mu})\right\} < 0.\end{gathered} \tag{58}$$

Equation (53) for the chemical potential can be written as

$$\frac{n}{2} = \left(1-\frac{n}{2}\right)I_0(\bar{\mu}) + \nu\frac{n}{2}\left(1-\frac{n}{2}\right)\{\bar{\mu}^2\bar{\rho}(\bar{\mu}) - 2I_1(\bar{\mu})\}, \tag{59}$$

where we have introduced the dimensionless quantities

$$\nu = \frac{W}{U}, \tag{60}$$

$$\bar{\mu} = \frac{\mu}{W\left(1-\frac{n}{2}\right)}, \quad \bar{\rho}(x) = W\rho(x), \tag{61}$$

$$I_\kappa(x) = \int_{-1}^{x} y^\kappa \bar{\rho}(y)dy. \tag{62}$$

Here, $\rho(x)$ is the bare electron density of states of the $\varepsilon(\mathbf{k})$ spectrum, $\rho'(x)$ is its derivative with respect to its argument x, and W is the half-width of the bare electron energy band:

$$W = zt, \tag{63}$$

where z is the coordination number of the crystal lattice.

In the case of the elliptic electron density of states

$$\rho(x) = \frac{2}{\pi W^2}[W^2 - x^2]^{1/2} \tag{64}$$

and

$$1 - n \ll 1 \tag{65}$$

(i.e., near the half-filling of the electron band), Eq. (59) for the chemical potential $\bar{\mu}$ can be solved exactly. Substituting this solution into Eq. (58) and taking into account Eqs. (61), (62), (64), and (65), we obtain an equation that describes the boundary for the ferromagnetic phase in the (ν, n) plane:

$$\nu = [3\pi(1-n)]^{1/3}\{\pi - 4[3\pi(1-n)]^{1/3}\}. \tag{66}$$

From Eq. (66), it follows that the condition for the existence of ferromagnetism $\nu > 0$ is fulfilled over the range $n_c < n < 1$, where

$$n_c = 1 - \frac{\pi^2}{192} \approx 0.95 \tag{67}$$

at the end points of this range ($n = n_c$, 1) and the function in Eq. (66) vanishes ($\nu = 0$), while at the internal point of this range

$$n_f = 1 - \frac{\pi^2}{1536} \approx 0.99, \tag{68}$$

this function reaches its maximum value

$$\nu_f = \frac{\pi^2}{16} \approx 0.62. \tag{69}$$

Therefore, for $\nu > \nu_f$, ferromagnetism does not occur for any value of n within the range $0 \le n \le 1$; that is, ν_f is the point at which ferromagnetism disappears everywhere in the range of possible values of the electron concentration.

Substituting Eq. (45) into Eq. (57) and taking into account the relation [25]

$$\varepsilon(\mathbf{k} + \mathbf{k}_0) = -\varepsilon(\mathbf{k}), \tag{70}$$

we find that, for $0 \le n < 1$, the metallic phase is stable for any value of ν and T. At $n = 1$, putting $\mu = U/2$ [28], the criterion for instability of this phase with respect to insulating (charge) ordering (at $T = 0$) can be written in the form

$$1 - \nu^2 \frac{J_2}{J_0} > 0, \tag{71}$$

where

$$J_\kappa = \int_{-1}^{1} y^\kappa I_1(y) dy. \tag{72}$$

In the case of the elliptic electron density of states (64), from Eq. (71), combined with Eqs. (60)–(62) and (72), it follows that for $n = 1$, $T = 0$, and

$$U > U_c, \tag{73}$$

where

$$U_c = \frac{W}{\sqrt{6}} \approx 0.41 W, \tag{74}$$

the system is in an insulating (charge-ordered) state. Therefore, U_c is the metal–insulator phase transition point.

For a simple cubic lattice, numerical calculations using Eqs. (58), (59), and (71) show that the magnetic and electrical properties of the Hubbard model are qualitatively similar to those in the case of the elliptic density of states (64) investigated above. The critical points for a simple cubic lattice are

$$n_c \approx 0.89, \tag{75}$$

$$n_f \approx 0.96, \tag{76}$$

$$\nu_f \approx 0.74, \tag{77}$$

$$U_c \approx 0.33 W. \tag{78}$$

4. DISCUSSION OF RESULTS

The general formulas (28) and (29) derived in this paper describe the propagation of two bosonlike collective excitations of an electron system, magnons and doublons. The former excitation corresponds to the state with a single electron spin flip propagating in the lattice, while the latter is a pair of electrons of opposite spin moving through a crystal. There is a close analogy between Eqs. (28) and (29). In both cases, the contribution to the dynamics is determined by a sum over α, consisting of four terms, in the numerators and denominators of these expressions. These terms describe intraband and interband electron transitions. These transitions occur in the particle–hole channel in the case of a magnon and in the particle–particle channel in the case of a doublon. The poles of the Green's functions $F_{+-}(\mathbf{k}, \omega)$ and $F_{02}(\mathbf{k}, \omega)$ give the magnon and doublon spectra, respectively. The damping of these quasiparticles is due to their decay into a particle (electron) and a hole in the former case and into two particles (electrons) in the latter.

It should be noted that, according to Eqs. (28) and (29), the self-energies in the magnon and doublon Green's functions vanish at the wave vectors $\mathbf{k} = 0$ and $\mathbf{k}_0$, respectively. This is indicative of the instabilities at these wave vectors.

The magnon Green's function is equal (except for the sign) to the dynamic magnetic susceptibility and, therefore, describes the response of the system to an external magnetic field. The dynamic response to an external electric field is determined by the dielectric permittivity, which is related to the Fourier transform $F_e(\mathbf{k}, \omega)$ of the diagonal-X-operator Green's function:

$$\begin{aligned} &F_e(l - l', \tau - \tau') \\ &= \langle\langle X_l^{22}(\tau) - X_l^{00}(\tau) \big| X_{l'}^{22}(\tau') - X_{l'}^{00}(\tau') \rangle\rangle. \end{aligned} \tag{79}$$

The doublon Green's function $F_{02}(\mathbf{k}, \omega)$, which involves off-diagonal Hubbard operators X_l^{02} and $X_{l'}^{20}$, is difficult to interpret as the response function of the system to an electric field; however, it is obvious that this Green's function describes charge redistribution in the system and can be used to reveal insulating instability.

Analysis of the doublon Green's function in the case of a half-filled electron band ($n = 1$) shows that, when $U > U_c$, the metallic phase becomes unstable with respect to insulating (charge) ordering, where U_c is of the order of the band width W. This conclusion agrees qualitatively with the findings of [4, 28, 32–34], in which the metal–insulator transition was investigated using the electron Green's function method.

As for the magnetic properties of the Hubbard model described by the magnon Green's function, the results of our investigation of the ferromagnetic instability of the paramagnetic phase are in good agreement with many findings obtained using various methods [3, 29, 35–40]: (i) in the case of strong Coulomb interaction ($U \gg W$), ferromagnetism exists in a relatively narrow range of values of the electron concentration n near the half-filling ($n < 1$); (ii) ferromagnetism is the stablest when $U \longrightarrow \infty$ (it becomes progressively weaker with decreasing U); (iii) the size and shape of the region of existence of ferromagnetism in the (W/U, n) plane depend quantitatively (rather than critically) on the shape of the bare electron density of states, i.e., on the crystal lattice type.

ACKNOWLEDGMENTS

The author is grateful to Yu.A. Izyumov.

REFERENCES

1. J. Hubbard, Proc. R. Soc. London, Ser. A **276** (1365), 238 (1963).

2. D. I. Khomskiĭ, Fiz. Met. Metalloved. **29** (1), 31 (1970).
3. Yu. A. Izyumov, Usp. Fiz. Nauk **161** (11), 1 (1991) [Sov. Phys. Usp. **34**, 935 (1991)].
4. Yu. A. Izyumov, Usp. Fiz. Nauk **165** (4), 403 (1995) [Phys. Usp. **38**, 385 (1995)].
5. T. Izuyama, D. Kim, and R. Kubo, J. Phys. Soc. Jpn. **18** (7), 1025 (1963).
6. T. Moriya, *Spin Fluctuation in Itinerant Electron Magnetism* (Springer-Verlag, Heidelberg, 1985; Mir, Moscow, 1988).
7. J. Hubbard, Proc. R. Soc. London, Ser. A **285** (1403), 542 (1965).
8. P. M. Slobodyan and I. V. Stasyuk, Teor. Mat. Fiz. **19** (3), 423 (1974).
9. R. O. Zaĭtsev, Zh. Éksp. Teor. Fiz. **70** (3), 1100 (1976) [Sov. Phys. JETP **43**, 574 (1976)].
10. R. O. Zaĭtsev, Zh. Éksp. Teor. Fiz. **75** (6), 2362 (1978) [Sov. Phys. JETP **48**, 1193 (1978)].
11. A. V. Vedyaev and M. Yu. Nikolaev, Teor. Mat. Fiz. **59** (2), 293 (1984).
12. A. V. Vedyaev and M. Yu. Nikolaev, Pis'ma Zh. Éksp. Teor. Fiz. **41** (1), 18 (1985) [JETP Lett. **41**, 20 (1985)].
13. E. G. Goryachev and E. V. Kuzmin, Phys. Lett. A **131** (7), 481 (1988).
14. E. G. Goryachev and E. V. Kuz'min, Zh. Éksp. Teor. Fiz. **98** (5), 1705 (1990) [Sov. Phys. JETP **71**, 957 (1990)].
15. N. M. Plakida, V. Yu. Yushankhai, and I. V. Stasyuk, Physica C (Amsterdam) **160** (1), 80 (1989).
16. V. Yu. Irkhin and M. I. Katsnel'son, Fiz. Tverd. Tela (Leningrad) **25** (11), 3383 (1983) [Sov. Phys. Solid State **25**, 1947 (1983)].
17. V. Yu. Irkhin and M. I. Katsnel'son, Fiz. Met. Metalloved. **66** (1), 41 (1988).
18. V. Yu. Irkhin and M. I. Katsnelson, J. Phys. C **18** (21), 4173 (1985).
19. Yu. A. Izyumov, B. M. Letfulov, E. V. Shipitsyn, and K. A. Chao, Int. J. Mod. Phys. B **6** (21), 3479 (1992).
20. Yu. A. Izyumov, B. M. Letfulov, and E. V. Shipitsyn, J. Phys.: Condens. Matter **6** (27), 5137 (1994).
21. Yu. A. Izyumov, B. M. Letfulov, and E. V. Shipitsyn, Zh. Éksp. Teor. Fiz. **105** (5), 1357 (1994) [JETP **78**, 731 (1994)].
22. E. V. Shipitsyn, Fiz. Tverd. Tela (St. Petersburg) **38** (9), 2797 (1996) [Phys. Solid State **38**, 1532 (1996)].
23. E. V. Shipitsyn, Fiz. Tverd. Tela (St. Petersburg) **39** (9), 1609 (1997) [Phys. Solid State **39**, 1433 (1997)].
24. Yu. A. Izyumov, B. M. Letfulov, E. V. Shipitsyn, *et al.*, Phys. Rev. B **46** (24), 15697 (1992).
25. Yu. A. Izyumov, M. I. Katsnel'son, and Yu. N. Skryabin, *Magnetism of Collective Electrons* (Fizmatlit, Moscow, 1994).
26. D. N. Zubarev, Usp. Fiz. Nauk **71** (1), 71 (1960) [Sov. Phys. Usp. **3**, 320 (1960)].
27. A. A. Abrikosov, L. P. Gor'kov, and I. E. Dzyaloshinskii, *Methods of Quantum Field Theory in Statistical Physics* (Fizmatgiz, Moscow, 1962; Prentice-Hall, Englewood Cliffs, 1963).
28. Yu. A. Izyumov and Yu. N. Skryabin, *Statistical Mechanics of Magneto-Ordered Systems* (Nauka, Moscow, 1987).
29. Yu. A. Izyumov, B. M. Letfulov, and E. V. Shipitsyn, J. Phys.: Condens. Matter **4** (49), 9955 (1992).
30. M. I. Auslender, V. Yu. Irkhin, and M. I. Katsnel'son, Fiz. Met. Metalloved. **65** (1), 57 (1988).
31. M. I. Auslender, V. Yu. Irkhin, and M. I. Katsnelson, J. Phys. C **21** (32), 5521 (1988).
32. J. Habbard, Proc. R. Soc. London, Ser. A **281** (1386), 401 (1964).
33. A. O. Anokhin and V. Yu. Irkhin, Phys. Status Solidi B **165** (1), 129 (1991).
34. A. O. Anokhin, V. Yu. Irkhin, and M. I. Katsnelson, J. Phys.: Condens. Matter **3** (11), 1475 (1991).
35. L. M. Roth, Phys. Rev. **184** (2), 451 (1969).
36. W. Nolting and W. Borgiel, Phys. Rev. B **39** (10), 6962 (1989).
37. M. Yu. Nikolaev, N. V. Ryzhanova, A. V. Vedyaev, and S. M. Zubritskii, Phys. Status Solidi B **128** (2), 513 (1985).
38. Yu. A. Izyumov, B. M. Letfulov, and E. V. Shipitsyn, Fiz. Met. Metalloved. **77** (1), 47 (1994).
39. Yu. A. Izyumov, B. M. Letfulov, and E. V. Shipitsyn, Fiz. Met. Metalloved. **79** (4), 3 (1995).
40. A. V. Zarubin and V. Yu. Irkhin, Fiz. Tverd. Tela (St. Petersburg) **41** (6), 1057 (1999) [Phys. Solid State **41**, 963 (1999)].

Translated by Yu. Epifanov

Physics of the Solid State, Vol. 43, No. 9, 2001, pp. 1759–1764. Translated from Fizika Tverdogo Tela, Vol. 43, No. 9, 2001, pp. 1688–1692.
Original Russian Text Copyright © 2001 by V. Prudnikov, P. Prudnikov, Fedorenko.

LATTICE DYNAMICS AND PHASE TRANSITIONS

Stability of the Critical Behavior of Weakly Disordered Systems with Respect to the Introduction of an Interaction Potential Breaking Replica Symmetry

V. V. Prudnikov, P. V. Prudnikov, and A. A. Fedorenko
Omsk State University, Omsk, 644077 Russia
e-mail: prudnikov@univer.omsk.su

Received December 5, 2000; in final form, February 7, 2001

Abstract—The critical behavior of weakly disordered systems with a *p*-component order parameter is described using field-theoretic methods. A renormalization-group analysis of the effective model replica Hamiltonian with an interaction potential breaking replica symmetry is performed directly for three-dimensional systems in the two-loop approximation. For the case of a one-step replica symmetry breaking, fixed points of renormalization group equations are found using the Padé–Borel summation technique. It is established that the critical behavior of weakly disordered systems is stable with respect to replica symmetry breaking and that the former scenario of the influence of structural defects on the critical behavior of these systems is realized. *© 2001 MAIK “Nauka/Interperiodica”.*

When the critical behavior of disordered systems with frozen disorder is described by the renormalization group theory, a replica method is used [1–3] to restore the translational symmetry of the effective Hamiltonian describing fluctuation interaction. However, it has been proposed [4–6] that replica symmetry can be broken in systems with frozen disorder. The available experimental data neither provide support nor argue against this hypothesis for systems with a weak frozen disorder.

Based on the assumption of multiple local energy minima existing in disordered systems that show random transition temperature effects, Dotsenko *et al.* [4, 5] considered the ϕ^4 model with an interaction potential breaking replica symmetry in the framework of the renormalization group theory. The critical behavior of three-dimensional systems was described using the ϵ-expansion method in the lowest order approximation. It was found that if the number of order parameter components p is less than four, the critical behavior of such systems is drastically affected by the replica symmetry breaking (RSB). For p values larger than unity but less than four, it was shown that the behavior of the system can be of two types. One of them is nonuniversal critical behavior, which depends on the bare model parameters and, in the final analysis, on the impurity concentration in the system; in the other case, the system shows no stable critical behavior, as in the most interesting case of Ising systems (p = 1). Although these findings are very interesting, it should be noted that analysis of the stability of different types of critical behavior to the first order in the ϵ expansion gives only a rough estimate, especially in the case of statistical multivertex models [8], as shown in our earlier field-theoretic study [7] of homogeneous and disordered systems in the two-loop and higher order approximations using methods for summation of asymptotic series. That the ϵ-expansion method is inadequate for describing the critical behavior of weakly disordered three-dimensional systems was clearly demonstrated in [9]. Therefore, the findings of investigations into the RSB effects in [4, 5] should be thoroughly revised using a more rigorous approach. We note that investigations into the critical behavior of the two-dimensional disordered Ising, Baxter [10], and Potts models (see, e.g., [11] and references therein) using analytical and numerical methods showed that the RSB effects are insignificant in these models.

In this paper, we perform a renormalization-group treatment of a weakly disordered system in which the RSB is associated with fourth-order interaction in the order-parameter fluctuations. In the framework of a field-theoretic approach, the renormalization-group equations are solved directly for three-dimensional systems (without resorting to ϵ expansion) in the two-loop approximation, consistently using summation methods, and the stability of various types of critical behavior is analyzed with respect to RSB.

The Ginzburg–Landau model Hamiltonian describing the behavior of a *p*-component spin system with a weak frozen disorder near a critical point has the form

$$H = \int d^d x \left\{ \frac{1}{2}\sum_{i=1}^{p}[\nabla\phi_i(x)]^2 + \frac{1}{2}[\tau - \delta\tau(x)]\sum_{i=1}^{p}\phi_i^2(x) + \frac{1}{4}g\sum_{i,\,l=1}^{p}\phi_i^2(x)\phi_j^2(x) \right\}. \tag{1}$$

Here, the random phase transition temperature $\delta\tau(x)$ is characterized by a Gaussian distribution with standard deviation $\langle\langle[\delta\tau(x)]^2\rangle\rangle \sim u$, where u is a positive constant proportional to the concentration of structural defects. Using the standard replica method, one can take the average over fluctuations of the temperature $\delta\tau(x)$, thereby reducing the problem of statistical description of the weakly disordered system to the problem of statistical description of a homogeneous system with an effective Hamiltonian

$$H_n = \int d^d x\left\{\frac{1}{2}\sum_{i=1}^{p}\sum_{a=1}^{n}[\nabla\phi_i^a(x)]^2 + \frac{1}{2}\tau\sum_{i=1}^{p}\sum_{a=1}^{n}[\phi_i^a(x)]^2 + \frac{1}{4}\sum_{i,l=1}^{p}\sum_{a,b=1}^{n} g_{ab}[\phi_i^a(x)]^2[\phi_j^b(x)]^2\right\}, \qquad (2)$$

where index a enumerates replicas (images) of the original homogeneous component of Hamiltonian (1). An additional vertex u, which arises in the interaction matrix $g_{ab} = g\delta_{ab} - u$, represents the effective interaction of $(n \times p)$-component order parameter fluctuations through the defect field. This statistical model is thermodynamically equivalent to the original disordered model in the limit as $n \longrightarrow 0$. Long-wavelength fluctuations of the order parameter from the ground state of a system with configuration $\phi(x) = 0$ (at $T \geq T_c$) are statistically taken into account by the subsequent renormalization-group procedure performed on the correlation-length scale, which tends to infinity as the phase transition temperature T_c is approached. This procedure allows one to analyze the possible types of critical behavior of the system and the conditions for their realization and to calculate the critical exponents.

As shown in [4–6], fluctuations of the random transition temperature at $[\tau - \delta\tau(x)] < 0$ lead to the formation of a macroscopically large number of spatial regions with $\phi(x) \neq 0$, which are separated from the ground state by potential barriers. The statistical properties of systems possessing multiple local energy minima were described in [4–6], by analogy with spin glasses, using Parisi RSB formalism [12]. It was shown in [4–6] that, when the contributions of the degrees of freedom associated with frozen order parameter fluctuations from the $\phi(x)$ field configurations corresponding to the local energy minima are statistically taken into account and the replica procedure is performed in the case of a weak disorder, additional interactions of the type $\sum_{a,b} g_{ab}\phi_a^2\phi_b^2$ appear in the effective replica Hamiltonian, where the ultimate matrix g_{ab} does not possess the replica-symmetric form $g_{ab} = g\delta_{ab} - u$ but has a Parisi RSB structure [12]. In the limit of $n \longrightarrow 0$ according to [4–6, 12], the matrix $g_{ab}$with an RSB structure has diagonal elements $\tilde g$ and off-diagonal elements characterized by a function $g(x)$, which is defined in the range $0 < x < 1$: $g_{ab} \longrightarrow (\tilde g, g(x))$. Mathematical operations are performed on the matrices g_{ab} in accordance with the following rules:

$$g_{ab}^k \longrightarrow (\tilde g^k; g^k(x)),\ (\hat g^2)_{ab} = \sum_{c=1}^{n} g_{ab}g_{cb} \longrightarrow (\tilde c; c(x)),$$
$$(\hat g^3)_{ab} = \sum_{c,d=1}^{n} g_{ac}g_{cd}g_{db} \longrightarrow (\tilde d; d(x)), \qquad (3)$$

where

$$\tilde c = \tilde g^2 - \int_0^1 dx g^2(x),$$

$$c(x) = 2\left[\tilde g - \int_0^1 dy g(y)\right]g(x) - \int_0^x dy[g(x)-g(y)]^2,$$

$$\tilde d = \tilde c\tilde g - \int_0^1 dx c(x)g(x), \qquad (4)$$

$$d(x) = \left[\tilde g - \int_0^1 dy g(y)\right]c(x) + \left[\tilde c - \int_0^1 dy c(y)\right]g(x)$$
$$\times\int_0^x dy[g(x)-g(y)][c(x)-c(y)].$$

In the replica-symmetric case, we have $g(x) = \text{const}$ (independent of x).

We performed a renormalization-group description of the model with the replica Hamiltonian (2) directly for the three-dimensional case using field-theoretic methods in the two-loop approximation. Possible types of critical behavior and their stability in the fluctuation region are determined by renormalization-group equations for the matrix elements g_{ab}. In order to find these equations, we used a standard method based on the Feynman diagram technique for the vertex parts of irreducible Green's functions and on the renormalization procedure. For example, in the two-loop approximation, we obtained the following expressions for the two-leg vertex function $\Gamma^{(2)}$ and four-leg vertex function $\Gamma_{ab}^{(4)}$:

$$\left.\frac{\partial\Gamma^{(2)}}{\partial k^2}\right|_{k^2=0} = 1 + 4fg_{aa}^2 + 2pf\sum_{c=1}^{n} g_{ac}g_{ca}, \qquad (5)$$

$$\Gamma_{ab}^{(4)}\Big|_{k_i=0} = g_{ab} - p\sum_{c=1}^{n} g_{ac}g_{cb} - 4g_{aa}g_{ab} - 4g_{ab}^2$$
$$+ (8+16h)g_{ab}^3 + (24+8h)g_{aa}^2 g_{ab} + 48hg_{aa}g_{ab}^2$$

$$+4g_{aa}g_{bb}g_{ab}+8ph\sum_{c=1}^{n}g_{ac}g_{cb}^{2}+8phg_{ab}\sum_{c=1}^{n}g_{ac}g_{cb} \quad (6)$$

$$+4phg_{ab}\sum_{c=1}^{n}g_{ac}^{2}+2p\sum_{c=1}^{n}g_{ac}g_{cc}g_{cb}$$

$$+4pg_{aa}\sum_{c=1}^{n}g_{ac}g_{cb}+p^{2}\sum_{c,d=1}^{n}g_{ac}g_{cd}g_{db},$$

where we have introduced the notation

$$f(d) = -\frac{1}{J^{2}}\frac{\partial}{\partial k^{2}} \times\int\frac{d^{d}k_{1}d^{d}k_{2}}{(k_{1}^{2}+1)(k_{2}^{2}+1)((k_{1}+k_{2}+k)^{2}+1)}\bigg|_{k^{2}=0}, \quad (7)$$

$$h(d) = \frac{1}{J^{2}}\int\frac{d^{d}k_{1}d^{d}k_{2}}{(k_{1}^{2}+1)(k_{2}^{2}+1)((k_{1}+k_{2})^{2}+1)}, \quad J = \int d^{d}k/(k^{2}+1)^{2}, \quad (8)$$

$$f(d=3) = \frac{2}{27}, \quad h(d=3) = \frac{2}{3} \quad (9)$$

and redefined the matrix $g_{ab} \longrightarrow g_{ab}/J$. However, the subsequent renormalization of the vertex functions and the determination of β functions, which characterize the renormalization-group transformations of the interaction constants, are difficult to perform because of the intricate form of Eqs. (3) and (4) for matrices g_{ab}. In [4–6], it was found that the function $g(x)$ has a steplike form, which makes the renormalization procedure much easier. In this paper, we consider the case where the function $g(x)$ has one step,

$$g(x) = \begin{cases} g_{0}, & 0 \le x \le x_{0} \\ g_{1}, & x_{0} < x \le 1, \end{cases} \quad (10)$$

where the coordinate of the step lies in the interval $0 \le x_0 \le 1$ and is an arbitrary parameter, which is not affected by scale transformations and has the same value as in the bare function $g_0(x)$. Therefore, the renormalization-group transformations are determined by three parameters, namely, $\tilde{g}$, g_0, and g_1. In this case, the β functions in the two-loop approximation are calculated to be

$$\begin{aligned}\beta_{1} = {} & -\tilde{g}+(p+8)\tilde{g}^{2}-px_{0}g_{0}^{2}-p(1-x_{0})g_{1}^{2} \\ & -\frac{4}{27}(41p+190)\tilde{g}^{3}+\frac{92}{27}px_{0}\tilde{g}g_{0}^{2} \\ & +\frac{92}{27}p(1-x_{0})\tilde{g}g_{1}^{2}-\frac{8}{3}px_{0}g_{0}^{3}-\frac{8}{3}p(1-x_{0})g_{1}^{3},\end{aligned}$$

$$\begin{aligned}\beta_{2} = {} & -g_{0}-(4-2px_{0})g_{0}^{2}+(4+2p)\tilde{g}g_{0} \\ & +2p(1-x_{0})g_{0}g_{1}+\frac{16}{3}\left(\frac{77}{36}px_{0}-1\right)g_{0}^{3} \\ & -\frac{92}{27}(p+2)\tilde{g}^{2}g_{0}-\frac{8}{3}(2px_{0}-5p-6)\tilde{g}g_{0}^{2} \\ & +\frac{40}{3}p(1-x_{0})g_{0}^{2}g_{1}-\frac{52}{27}p(1-x_{0})g_{0}g_{1}^{2} \\ & -\frac{16}{3}p(1-x_{0})\tilde{g}g_{0}g_{1},\end{aligned} \quad (11)$$

$$\begin{aligned}\beta_{3} = {} & -g_{1}-(px_{0}-2p+4)g_{1}^{2}+px_{0}g_{0}^{2} \\ & +(4+2p)\tilde{g}g_{1}-\left(\frac{92}{27}px_{0}-\frac{308}{27}p+\frac{16}{3}\right)g_{1}^{3} \\ & +\frac{8}{3}px_{0}g_{0}^{3}-\frac{92}{27}(p+2)\tilde{g}^{2}g_{1}+\frac{8}{3}px_{0}\tilde{g}g_{0}^{2} \\ & +\left(\frac{8}{3}px_{0}+8p+16\right)\tilde{g}g_{1}^{2}+\frac{20}{27}px_{0}g_{0}^{2}g_{1}.\end{aligned}$$

In order to correlate our results with those of [4–6], we have conveniently reversed the sign of the off-diagonal matrix elements, $g_{a\neq b} \longrightarrow -g_{a\neq b}$, in Eq. (11) for the β functions, as in [4–6], with the result that the parameters g_0 and g_1 become positive.

It is well known that, in the problem under study, the perturbation series are asymptotic and the magnitudes of the interaction vertices of the order parameter fluctuations in the fluctuation region $\tau \longrightarrow 0$ are too large for Eq. (11) to be immediately applicable. For this reason, in order to extract physical information from the expressions derived above, we apply the Padé–Borel method (generalized to the three-parametric case), which is used to find the sum of asymptotic series. The direct and inverse Borel transformations have the form

$$f(\tilde{g},g_{0},g_{1}) = \sum_{i,j,k}c_{ijk}\tilde{g}^{i}g_{0}^{j}g_{1}^{k} = \int_{0}^{\infty}e^{-t}F(\tilde{g}t,g_{0}t,g_{1}t)dt, \quad (12)$$

$$F(\tilde{g},g_{0},g_{1}) = \sum_{i,j,k}\frac{c_{ijk}}{(i+j+k)!}\tilde{g}^{i}g_{0}^{i}g_{1}^{k}.$$

In order to perform analytic continuation of the Borel transform, we introduce a power series in an auxiliary variable θ,

$$\tilde{F}(\tilde{g},g_{0},g_{1},\theta) = \sum_{k=0}^{\infty}\theta^{k}\sum_{i=0}^{k}\sum_{j=0}^{k-i}\frac{c_{i,j,k-i-j}}{k!}\tilde{g}^{i}g_{0}^{i}g_{1}^{k-i-j}, \quad (13)$$

and take the Padé approximant $[L/M]$ at the point $\theta = 1$. This technique was proposed and applied in [8] for describing the critical behavior of systems that are characterized by several interaction vertices of the

Table 1. Fixed points and eigenvalues for $p = 1$

Type	x_0	$\tilde{g}^*$	g_0^*	g_1^*	λ_1	λ_2	λ_3
1		0.1774	0	0	0.6536	–0.1692	–0.1692
2		0.1844	0.0812	0.0812	0.5253	$\pm$ 0.0893i	0.2112
3	0.0	0.1844	0	0.0812	0.5253	$\pm$ 0.0893i	–0.0392
	0.1	0.1840	0	0.0829	0.5352	$\pm$ 0.0983i	–0.0492
	0.2	0.1835	0	0.0846	0.5471	$\pm$ 0.1067i	–0.0599
	0.3	0.1830	0	0.0863	0.5607	$\pm$ 0.1133i	–0.0712
	0.4	0.1824	0	0.0880	0.5765	$\pm$ 0.1180i	–0.0832
	0.5	0.1817	0	0.0895	0.5951	$\pm$ 0.1203i	–0.0959
	0.6	0.1810	0	0.0910	0.6172	$\pm$ 0.1189i	–0.1093
	0.7	0.1802	0	0.0924	0.6439	$\pm$ 0.1114i	–0.1234
	0.8	0.1793	0	0.0936	0.6760	$\pm$ 0.0921i	–0.1381
	0.9	0.1784	0	0.0947	0.7135	$\pm$ 0.0353i	–0.1534
	1.0	0.1774	0	0.0957	0.8573	0.6536	–0.1692

Table 2. Fixed points and eigenvalues for $p = 2$

Type	x_0	$\tilde{g}^*$	g_0^*	g_1^*	λ_1	λ_2	λ_3
1		0.1558303	0	0	0.667315	–0.001672	–0.001672
2		0.1558310	0.0005837	0.0005837	0.667312	0.001682	0.000004
3	0.0	0.1558310	0	0.0005837	0.667313	0.001683	–0.000001
	0.1	0.1558310	0	0.0006143	0.667313	0.001684	–0.000088
	0.2	0.1558310	0	0.0006483	0.667313	0.001685	–0.000186
	0.3	0.1558310	0	0.0006863	0.667313	0.001686	–0.000296
	0.4	0.1558310	0	0.0007291	0.667313	0.001687	–0.000419
	0.5	0.1558310	0	0.0007775	0.667313	0.001687	–0.000559
	0.6	0.1558309	0	0.0008327	0.667313	0.001688	–0.000717
	0.7	0.1558308	0	0.0008964	0.667314	0.001690	–0.000901
	0.8	0.1558307	0	0.0009707	0.667314	0.001692	–0.001116
	0.9	0.1558306	0	0.0010583	0.667315	0.001694	–0.001369
	1.0	0.1558303	0	0.0011633	0.667316	0.001696	–0.001672

order parameter fluctuations. In [8], it was shown that taking a Padé approximant in the variable θ does not change the symmetry of the system. This result is significant in treating multivertex models.

We used the [2/1] approximant to calculate the β functions in the two-loop approximation. The critical behavior is determined by the stable fixed points, which satisfy the set of equations

$$\beta_k(\tilde{g}^*, g_0^*, g_1^*) = 0, \quad k = 1, 2, 3. \qquad (14)$$

By solving set (14) for the order parameter with $p = 1$, 2, 3 components, we found three types of nontrivial fixed points in the physically interesting range of parameter values $\tilde{g}^*$, g_0^*, $g_1^* \geq 0$ (Tables 1–3). For example, the fixed point at $\tilde{g}^* \neq 0$, $g_0^* = g_1^* = 0$ corresponds to the critical behavior of a homogeneous system; the fixed point $\tilde{g}^* \neq 0$, $g_0^* = g_1^* \neq 0$ is characteristic of the critical behavior of a replica-symmetric disordered system; and the point $\tilde{g}^* \neq 0$, $g_0^* = 0$, $g_1^* \neq 0$ corresponds to the critical behavior of a replica-symmetry-breaking disordered system. In the case of an RSB fixed point, its parameters $\tilde{g}^*$ and g_0^* depend on the step coordinate x_0; in the tables, we presented the calculated values of $\tilde{g}^*$ and g_1^* for $0 \leq x_0 \leq 1$ with a step of $\Delta x_0 = 0.1$.

Table 3. Fixed points and eigenvalues for $p = 3$

Type	x_0	$\tilde{g}^*$	g_0^*	g_1^*	λ_1	λ_2	λ_3
1		0.1383	0	0	0.6814	0.1315	0.1315
2		0.2744	0.2679	0.2679	1.0921	–14.9992	–18.3081
3	0.0	0.2744	0	0.2679	1.0921	–14.9992	1.7453
	0.1	0.2578	0	0.2563	1.0508	–13.8668	1.5640
	0.2	0.2417	0	0.2448	1.0077	–12.8086	1.3849
	0.3	0.2262	0	0.2333	0.9631	–11.8221	1.2087
	0.4	0.2112	0	0.2218	0.9177	–10.9054	1.0358
	0.5	0.1969	0	0.2105	0.8673	–10.0568	0.8722
	0.6	0.1834	0	0.1992	0.7042	–9.2751	0.8275
	0.7	0.1706	0	0.1881	0.5477	–8.5594	0.7848
	0.8	0.1588	0	0.1772	0.3991	–7.9084	0.7455
	0.9	0.1480	0	0.1667	0.2600	–7.3207	0.7106
	1.0	0.1383	0	0.1566	0.1315	–6.7938	0.6814
2		0.1419	–0.0359	–0.0359	0.6727	–0.0891	–0.0058
3	0.0	0.1419	0	–0.0359	0.6727	–0.0891	–0.0058
	0.1	0.1420	0	–0.0382	0.6727	–0.0865	0.0011
	0.2	0.1420	0	–0.0408	0.6728	–0.0836	0.0088
	0.3	0.1421	0	–0.0439	0.6730	–0.0802	0.0175
	0.4	0.1420	0	–0.0474	0.6734	–0.0764	0.0273
	0.5	0.1420	0	–0.0516	0.6738	–0.0719	0.0385
	0.6	0.1418	0	–0.0565	0.6745	–0.0668	0.0515
	0.7	0.1415	0	–0.0625	0.6755	–0.0606	0.0667
	0.8	0.1409	0	–0.0699	0.6768	–0.0533	0.0845
	0.9	0.1400	0	–0.0793	0.6787	–0.0443	0.1058
	1.0	0.1383	0	–0.0915	0.6814	–0.0331	0.1315

The realization of a specified type of critical behavior for each value of p is determined by the stability of the corresponding fixed point. A fixed point will be stable if the real parts of the eigenvalues λ_i of the matrix

$$B_{i,j} = \frac{\partial\beta_i(\tilde{g}^*, g_0^*, g_1^*)}{\partial g_i} \tag{15}$$

are positive. Calculations of λ_i for each type of fixed point (Tables 1–3) allow the following conclusions. For the Ising model ($p = 1$), the replica-symmetric fixed point, corresponding to a disordered system, is stable. For the *XY* model ($p = 2$), the positive values of λ_i are indicative of weak stability of the replica-symmetric fixed point; however, we are inclined to believe that, in higher order approximations, the fixed point corresponding to the critical behavior of a homogeneous system will become stable, as is the case when the RSB effects in disordered systems are ignored [13, 14]. For the isotropic Heisenberg model ($p = 3$), the fixed point corresponding to a homogeneous system is stable. It should be noted that, although the fixed points of the Heisenberg model with $g_1 \neq 0$ listed in the upper half of Table 3 lie in the physical range of parameter values, they are not infrared fixed points, i.e., those closest to the origin of parametric ($\tilde{g}$, g_0, g_1) space and determining the critical behavior of the system. Indirect evidence of this is the relatively large absolute values of λ_2 and λ_3. Calculations revealed that possible infrared fixed points are unstable and characterized by nonphysical, negative values of parameters: $g_0^* = g_1^* < 0$ for the replica-symmetric fixed point and $g_0^* = 0$, $g_1^*(x_0) < 0$ for the RSB fixed point (the lower half of Table 3).

Thus, our investigation of three-dimensional weakly disordered systems using the renormalization-group method in the two-loop approximation showed that the critical behavior is stable with respect to the RSB effects. The systems with a single-component order parameter exhibit critical behavior characteristic of a structural disorder with a replica-symmetric fixed point. The presence of a weak disorder in systems with a multicomponent order parameter does not affect their critical behavior, although, in the case of $p = 2$, calculations in higher order approximations should be carried out to support this conclusion [14]. The possible effect of RSB on the critical behavior of highly disordered systems can be investigated by determining the distribution function of the order parameter fluctuations and the spectrum of random phase transition temperature fluctuations using computer simulation techniques without invoking perturbation theory [15].

ACKNOWLEDGMENTS

This study was supported by the Russian Foundation for Basic Research, project no. 00-02-16455.

REFERENCES

1. S. F. Edwards and P. W. Anderson, J. Phys. F **5** (5), 965 (1975).
2. J. Emery, Phys. Rev. B **11** (1), 239 (1975).
3. G. Grinstein and A. Luther, Phys. Rev. B **13** (3), 1329 (1976).
4. Vik. S. Dotsenko, A. B. Harris, D. Sherrington, and R. B. Stinchcombe, J. Phys. A **28** (11), 3093 (1995).
5. Vik. S. Dotsenko and D. E. Feldman, J. Phys. A **28** (18), 5183 (1995).
6. Vik. S. Dotsenko, Usp. Fiz. Nauk **165** (5), 481 (1995) [Phys. Usp. **38**, 457 (1995)].
7. V. V. Prudnikov, A. V. Ivanov, and A. A. Fedorenko, Pis'ma Zh. Éksp. Teor. Fiz. **66** (12), 793 (1997) [JETP Lett. **66**, 835 (1997)]; V. V. Prudnikov, S. V. Belim, A. V. Ivanov, *et al.*, Zh. Éksp. Teor. Fiz. **114** (3), 972 (1998) [JETP **87**, 527 (1998)]; V. V. Prudnikov, P. V. Prudnikov, and A. A. Fedorenko, Zh. Éksp. Teor. Fiz. **116** (2), 611 (1999) [JETP **89**, 325 (1999)]; V. V. Prudnikov, P. V. Prudnikov, and A. A. Fedorenko, Phys. Rev. B **62** (13), 8777 (2000).
8. S. A. Antonenko and A. I. Sokolov, Phys. Rev. B **49**, 15901 (1994); K. B. Varnashev and A. I. Sokolov, Fiz. Tverd. Tela (St. Petersburg) **38** (12), 3665 (1996) [Phys. Solid State **38**, 1996 (1996)]; A. I. Sokolov, K. B. Varnashev, and A. I. Mudrov, Int. J. Mod. Phys. B **12** (12/13), 1365 (1998); A. I. Sokolov and K. B. Varnashev, Phys. Rev. B **59** (13), 8363 (1999).
9. B. N. Shalaev, S. A. Antonenko, and A. I. Sokolov, Phys. Lett. A **230** (1–2), 105 (1997).
10. D. E. Feldman, A. V. Izyumov, and Vik. Dotsenko, cond-mat/9512158 (1995).
11. C. Chatelain and B. Berche, Nucl. Phys. B **572** (3), 626 (2000).
12. G. Parisi, J. Phys. A **13** (3), 1101 (1980); G. Parisi, J. Phys. A **13** (4), L115 (1980); G. Parisi, J. Phys. A **13** (5), 1887 (1980); M. Mezard, G. Parisi, and M. Virasoro, *Spin-Glass Theory and Beyond* (World Scientific, Singapore, 1987); Vik. Dotsenko, Usp. Fiz. Nauk **163** (6), 1 (1993) [Phys. Usp. **36**, 455 (1993)].
13. G. Jug, Phys. Rev. B **27** (1), 609 (1983).
14. I. O. Mayer, A. I. Sokolov, and B. N. Shalaev, Ferroelectrics **95** (1), 93 (1989); R. Folk, Yu. Holovatch, and T. Yavorskii, Phys. Rev. B **61** (22), 15114 (2000); D. V. Pakhnin and A. I. Sokolov, Phys. Rev. B **61** (22), 15130 (2000); A. Pelissetto and E. Vicari, Phys. Rev. B **62**, 6393 (2000).
15. M. M. Tsypin, Phys. Rev. B **55** (14), 8911 (1997).

Translated by Yu. Epifanov

Physics of the Solid State, Vol. 43, No. 9, 2001, pp. 1765–1769. Translated from Fizika Tverdogo Tela, Vol. 43, No. 9, 2001, pp. 1693–1697.
Original Russian Text Copyright © 2001 by Belogorokhov, Belogorokhova.

LOW-DIMENSIONAL SYSTEMS AND SURFACE PHYSICS

Optical Phonons of Circular Wires in Porous GaP

A. I. Belogorokhov* and L. I. Belogorokhova**

**State Research Institute for the Rare-Metal Industry, Moscow, 109017 Russia*
***Moscow State University, Vorob'evy gory, Moscow, 119899 Russia*

Received November 22, 2000

Abstract—The reflection spectra of porous gallium phosphide samples are investigated in the far infrared region of wave numbers (10–700 cm^{-1}). In addition of the longitudinal and transverse optical phonon modes corresponding to the bulk material, additional vibrational modes are detected. Their number and spectral position are correctly described by a model of a dispersive dielectric medium under the assumption that porous gallium phosphide is formed by crystallites whose shape is close to cylindrical. It is concluded that such vibrational modes are optical phonons confined by the volume of the quantum wire. The experimental optical reflection spectra are used to obtain estimates of the average diameter of nanocrystallites forming the porous GaP layer. *© 2001 MAIK "Nauka/Interperiodica".*

1. INTRODUCTION

The interest of researchers in the influence of quantum size effects on the optical properties of nanocrystallites that form a porous semiconductor layer has extended beyond the class of silicon structures for a long time [1]. This is due to both purely academic interest [2] and the practical need for such materials [3]. The properties of monocrystalline gallium phosphide have been studied in detail. Like silicon, this material is an indirect-gap semiconductor. The process of obtaining porous GaP using the electrochemical etching method is quite similar to that for porous silicon. For this reason, information concerning the change in the properties of gallium phosphide on its transition from a bulk semiconductor to a low-dimensional phase is interesting in and of itself, and also for the possible comparison of the properties of porous GaP and Si.

Obtaining porous GaP and the analysis of its properties have been considered in several publications. Different luminescence properties of samples obtained by electrochemical etching using electrolytes with different compositions have been reported [1, 4–6]. Tiginyanu *et al.* [6] analyzed the typical features appearing in Raman spectra (RS) on the transition from monocrystalline GaP samples to its porous modification, which were observed for the first time in [1]. To our knowledge, no information is available regarding investigations of the vibrational properties of GaP nanocrystallites using the Fourier-transform infrared (FTIR) spectroscopy methods. Nevertheless, as was noted in [1], the spectral dependences of optical parameters change significantly upon the transition from crystallite GaP to its porous low-dimensional modification. It should be specified that the term low-dimensional can be applied to a semiconducting layer consisting of nanocrystallites with the same characteristic average diameter (under the assumption that the shape of the crystallites is close to spherical, cylindrical, spheroidal, etc.), when the size-quantization effects are manifested significantly. For the critical diameter, we can choose the exciton radius in the conductor being used.

A theoretical analysis of the dependence of the properties of phonons in GaP quantum dots on their size is given in [7], while a similar analysis for GaP quantum wires surrounded by the space filled with GaAs is presented in [8]. In the latter case, the theoretical analysis was confirmed experimentally [8]. Nevertheless, no calculations have been made so far for the frequencies of IR-active phonon modes in porous GaP in order to interpret the experimental results.

2. CONFINED PHONON MODES IN GaP QUANTUM WIRES

A dielectric medium model can be used to obtain dispersion relations for optical and acoustic phonon modes of an infinite wire with a definite diameter made, e.g., of a semiconducting material with zinc blend structure. Suppose that the wire is surrounded by a space characterized by a different permittivity or by another semiconducting medium. In the macroscopic approach, when studying crystal lattice vibrations (including the normal vibrations or optical phonons), one deals with the mechanical displacements $\mathbf{u}(\mathbf{x}, t)$ of ions. In the range of large wavelengths, $\mathbf{u}(\mathbf{x}, t)$ is the relative displacement of two atoms constituting a unit cell. The center of gravity of the cell has the coordinate $\mathbf{x}$, which varies monotonically within the crystal. Relative displacements of atoms of various species leads to a change in the lattice polarizability with the polarization vector $\mathbf{P}(\mathbf{x}, t)$, which can be expressed as

$$\mathbf{P}(\mathbf{x}, t) = N(\mathbf{x})e^*(\mathbf{x})\mathbf{u}(\mathbf{x}, t). \quad (1)$$

Here, $e^*(\mathbf{x})$ is the effective charge and $N(\mathbf{x})$ is the number of unit cells occupying position $\mathbf{x}$ in the lattice. We assume that $e^*(\mathbf{x}) = e_j^*$ and $N(\mathbf{x}) = N_j$, where $j = 1, 2$ depending on the atomic species under investigation. The polarization of the material can be expressed in terms of the electric field strength $E(\mathbf{x}, t)$. The quantities $\mathbf{u}(\mathbf{x}, t)$, $\mathbf{P}(\mathbf{x}, t)$, and $\mathbf{E}(\mathbf{x}, t)$ are connected through the system of Maxwell's equations. For the Fourier transforms of these functions, the Newton relations [9] are valid:

$$\begin{aligned}\omega_T^2(\mathbf{x}) - c_T^2(\mathbf{x})\nabla\times\nabla + c_L^2(\mathbf{x})\nabla\nabla - \omega^2\mathbf{u}(\mathbf{x})\\ - [e^*(\mathbf{x})/m^*(\mathbf{x})]E(\mathbf{x}) = 0,\end{aligned} \quad (2)$$

where $\omega_T(\mathbf{x})$ is the frequency of a transverse optical (TO) phonon; m^* is the reduced mass of the atoms constituting the unit cell; and $c_T(\mathbf{x})$ and $c_L(\mathbf{x})$ are the transverse and longitudinal velocities of the propagation of lattice vibrations, respectively, which are in turn proportional to the elastic constants appearing in the dispersion relations for the wave vectors of optical phonons. Equation (2) is valid in the entire space except at the boundary of the wire, because the first derivatives of the functions describing the internal field can be discontinuous at this boundary. However, this does not mean that elastic forces obeying Eq. (2) do not act at this boundary. These forces are transformed into short-range mechanical forces [9]. Microscopically, these discontinuities of the function $\partial\mathbf{u}(\mathbf{x}, t)/\partial\mathbf{x}$ indicate that local changes in the vibrational properties of surface atoms take place. In contrast, macroscopically, short-range elastic forces are disregarded while describing the behavior of $\mathbf{u}(\mathbf{x}, t)$, thus precluding an analysis of local variations in the vibrational properties of surface atoms.

A detailed theoretical analysis of circular quantum wires in the dielectric medium model was carried out in [7]. The generalized Huang–Born equation with a Hermitian dynamic operator was used. The dispersion relations obtained for transverse and longitudinal optical (LO) phonons have the forms

$$\omega^2_{T(s/p)Kmq} = \omega_T^2 - c_T^2(q^2 + K^2_{T(s/p)m}), \quad (3)$$

$$\omega^2_{LKm} = \omega_L^2 - c_L^2(q^2 + K^2_{LKm}). \quad (4)$$

Here, K_{Lm} is the radial wave number which is quantized as

$$K_{Lm} = (z_{Km}/R), \quad K = 1, 2, \ldots, 8, \quad (5)$$

where z_{Km} is the Kth zero of the Bessel function $J_m(z)$ and R is the radius of the quantum wire.

While deriving Eqs. (3) and (4), it was assumed that the medium outside the wire is a vacuum. It can be seen from Eq. (3) that in the case of transverse modes, two vibrational branches (s and p, respectively) exist. These branches are usually denoted by T_s and T_p. By virtue of the axial symmetry of the problem (the cylindrical system of coordinates), it is impossible to find a transformation converting T_s into T_p. For $q \simeq 0$ (q is the quasi-momentum), mode T_s is perpendicular to the wire surface, while T_p is parallel to the wire axis. Confined longitudinal vibrations propagate along the third direction perpendicular to the wire interface. Microscopically, the normal components of transverse vibrations at the wire interface must be continuous [7]. This leads to the equations

$$J_m(K_{Tsm}R) = 0, \quad (6)$$

$$J'_m(K_{Tpm}R) = 0. \quad (7)$$

Here, $J(z)$ is the Bessel function; the quantization conditions for K_{Tsm} are the same as for the LO vibrations in Eq. (5):

$$K_{Tsm} = K_{Lm} = (z_{Km}/R), \quad (8)$$

$$K_{Tpm} = (z'_{Km}/R). \quad (9)$$

From Eqs. (8) and (9), it can be seen that different values are obtained on the left-hand sides; i.e., the degeneracy which takes place in bulk isotropic semiconducting media is removed from the two transverse vibrations in the wire. In the general case, assuming that the transcendental equations (6) and (7) have an infinitely large number of real roots, we formally obtain an infinitely large number of eigenvalues given by Eqs. (8) and (9), which correspond to the eigenfunctions of the boundary-value problem formulated by us. Thus, the degeneracy is removed for the vibrational modes described by various values of m. This degeneracy takes place in an isotropic medium in view of the complete spherical symmetry of such a medium. In the analysis of a quantum wire, we must carry out a transition from the spherical to axial symmetry, which removes the degeneracy.

3. DISCUSSION OF EXPERIMENTAL RESULTS

The samples of porous GaP were obtained by electrochemical etching of monocrystalline (100) gallium phosphide doped with tellurium with n-type conductivity ($n = 3–5 \times 10^{17}$ cm^{-3}). The composition of the electrolyte was identical to that normally used in the process of obtaining porous Si layers, specifically, 49% hydrofluoric acid HF and ethanol in a 1 : 1 ratio. The density of the current flowing through the electrolyte solution was 10–20 mA/cm^2 and the etching time was varied from 5 to 15 min. The layers of porous GaP had a thickness of 1–10 μm. The results obtained using the photoelectron spectroscopy method led to the conclusion that the compound Ga_2O_3 is sometimes present in the bulk of porous GaP. In this case, the Raman spectrum (RS) exhibits an additional low peak at a frequency of 201 cm^{-1}. Such samples are not considered here. The layers of porous GaP exhibit intense luminescence in the blue–green spectral region at room temperature, while the shapes of peaks in the RS was similar to that observed in [1, 6].

A comparison of the results of theoretical calculations with the experimental FTIR spectroscopic data, which was also carried out in [10], led to the conclusion that the layers of porous GaP obtained using the method described above were arrays of GaP crystallites. Otherwise, the structure of such materials would have the form of a crystalline skeleton with a network of extended pores of various diameters separated from one another by considerable distances.

The reflection spectra $R(\omega)$ at room temperature were obtained on a Fourier spectrometer IFS-113v (Bruker, Germany) over a range of wave numbers from 10 to 700 cm^{-1} with a spectral resolution greater than 0.1 cm^{-1}. The low-temperature spectral dependences $R(\omega)$ (at liquid nitrogen temperature) did not exhibit considerable differences compared to the high-temperature optical spectra; for this reason, the experimental data are not presented in this paper.

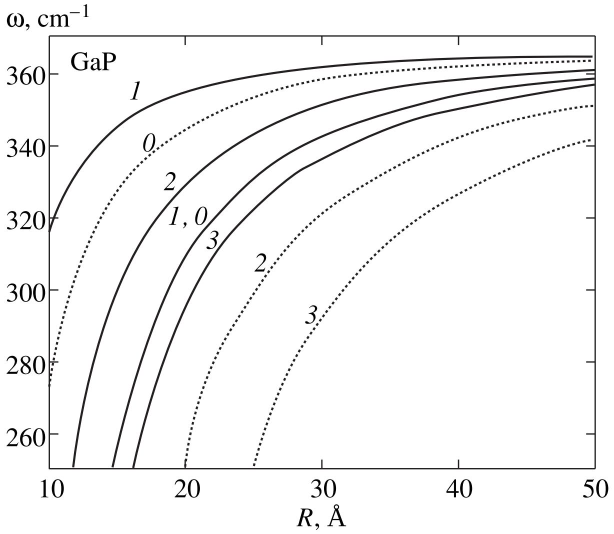

Fig. 1. Dependence of the frequencies of transverse optical phonons in GaP crystallites on their average radius R(Å) for various values of m ($K = 1$). Solid curves correspond to TO$_s$ phonons and dotted curves to TO$_p$ phonons.

The $R(\omega)$ dependences obtained were processed using a combined approach including the Kramers–Kronig relations and dispersion relations [11]. A successful example of the application of such an approach in the case when the experimental spectrum consists of a large number of vibrational modes of various origin was demonstrated by us in [12] for $Cd_{3-x}Zn_xAs_2$ crystals with a low-symmetry crystal lattice.

Figure 1 shows the results of the calculation of the frequencies of confined TO phonon modes in a GaP

Table 1. Experimental (sample 1) and theoretical values of optical phonon frequencies ($q \sim 0$) in quantum wires of GaP with radius $R = 22$ Å

	$K = 1$				$K = 2$			
m	0	1	2	3	0	1	2	3
TO$_s$	348.2	319.5	276.7	208.8	259.3	160.8	–	–
TO$_p$	319.5	356.1	335.8	308.3	160.8	268.3	186.9	–
LO	386.2	360.5	323.2	267.4	308.4	231.8	78.6	–
TO$_{s,\,\mathrm{exp}}$	347.6	322.2	275.9	205.3	255.0	162.2	–	
TO$_{p,\,\mathrm{exp}}$	321.9	356.5	337.5	304.7	159.9	266.1	181.8	–
LO$_{\mathrm{exp}}$	385.2	362.9	322.2	265.4	312.2	232.3	–	–

Note: The values of frequencies are given in inverse centimeters.

Table 2. Experimental (sample 2) and theoretical values of optical phonon frequencies in quantum wires of GaP with a radius of 34 Å

	$K = 1$				$K = 2$			
m	0	1	2	3	0	1	2	3
TO$_s$	358.7	347.3	331.6	310.0	325.6	297.8	262.3	212.7
TO$_p$	347.3	361.9	353.7	343.0	297.8	328.6	304.1	273.6
LO	395.6	385.4	371.2	352.2	365.9	341.4	310.9	270.4
TO$_{s,\,\mathrm{exp}}$	358.1	347.8	331.9	312.0	324.3	292.7	265.5	212.8
TO$_{p,\,\mathrm{exp}}$	347.6	356.3	356.0	337.5	292.7	328.9	304.7	275.9
LO$_{\mathrm{exp}}$	395.4	384.9	373.9	353.2	365.9	338.4	313.2	275.1

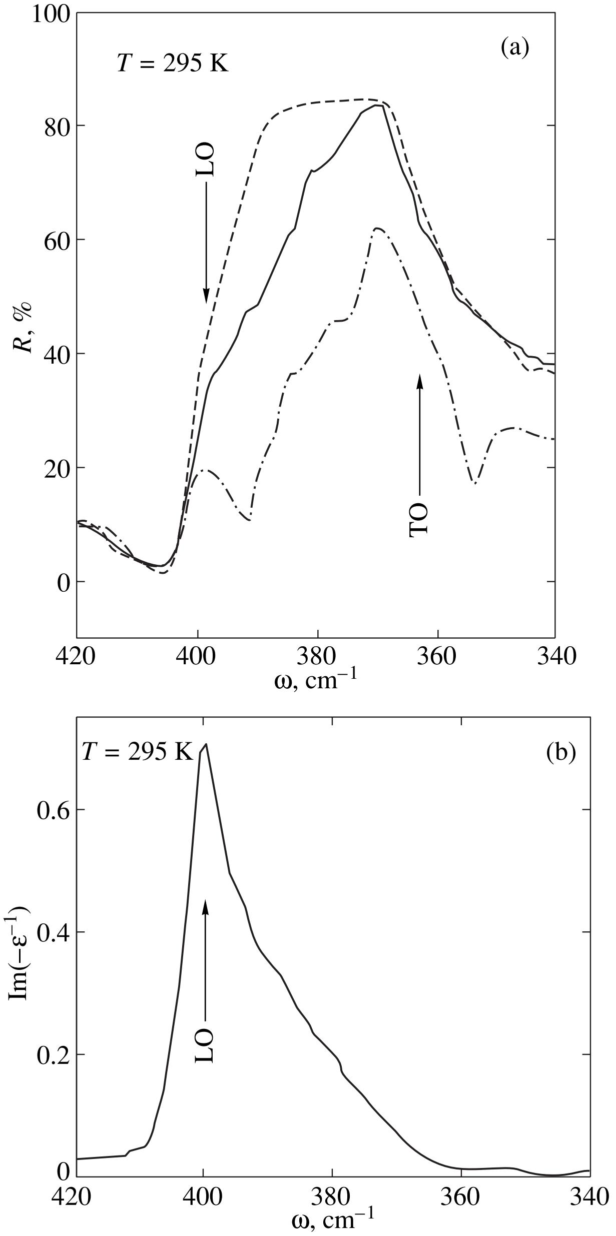

Fig. 2. (a) Reflection spectra for samples 1 and 2 of porous (curves *1* and *2*, respectively) and bulk (dashed curve) GaP and (b) the frequency dependence of the function $\mathrm{Im}(-\varepsilon^{-1})$ for porous GaP (sample 2).

quantum wire as a function of its radius [in accordance with Eq. (3)]. It can be seen from the figure that in the region of one-phonon resonance, for a certain value of the average wire diameter, additional vibrational modes associated with the spatial confinement of bulk phonon modes at the center of the Brillouin zone must take place.

Figure 2a shows the experimental reflection spectra for monocrystalline GaP (dashed curve) and for two samples of porous gallium phosphide. It can be seen that the one-phonon resonance band in a layer of porous material experiences considerable changes compared to the case of bulk GaP. First of all, this is observed in the region of wave numbers $\omega = 370–400\ \mathrm{cm}^{-1}$ lying between the frequencies of LO and TO phonons of GaP. The specific structure of the $R(\omega)$ spectrum consisting of auxiliary peaks is clearly manifested. Figure 2b shows the dependence of the function $\mathrm{Im}(-\varepsilon^{-1})$ on the photon wave vector for porous GaP sample 2, whose $R(\omega)$ spectrum is shown in Fig. 1. It can be clearly seen that the narrow peak corresponding to the frequency $\omega = 400.5\ \mathrm{cm}^{-1}$ has a typical asymmetric shape on the low energy side, which is due to the presence of the above-mentioned auxiliary peaks. The positions of these peaks can easily be determined using the procedure of its decomposition into several Gaussians. It should be noted that the frequency of an LO phonon in this porous GaP sample is displaced by ~2 cm^{-1} towards lower energies, which agrees with the predictions of the size-quantization theory [2].

The application of the equation

$$\begin{aligned}\omega_S^2 &= \omega_T^2 + \omega_p^2\frac{\varepsilon_\infty}{\varepsilon_\infty + \eta_m(R)},\\ \eta_m(R) &= -\frac{I'_m(R)K_m(R)}{I_m(R)K'_m(R)},\end{aligned} \qquad (10)$$

derived in [7], made it possible to calculate the frequency of a surface phonon in GaP crystallites. Here, $I_m(R)$ is a cylindrical function. The value of ω_S was found to be 396.0 cm^{-1}, which agrees well with the experimental results discussed in this section ($\omega_{S\mathrm{exp}}$ = 396.7 cm^{-1}), as well as with those obtained from the Raman scattering data for samples of porous GaP [4]. Similar results were obtained later by the authors of [6] for GaP nanocrystallites (ω_S = 398.0, 394.3 cm^{-1}) prepared using a similar technology. The theoretical value of ω_S in GaP quantum dots was found to be ~380 cm^{-1} [2]. In the latter case, the difference from our results can be explained by the fact that the spherical geometry of nanocrystallites was used in the calculations.

Tables 1 and 2 contain the values of frequencies of confined lattice vibrational modes obtained from the experimental optical spectra and calculated using the above algorithm for porous GaP samples, whose optical spectra are presented in Fig. 1. A comparison of the experimental results with the theoretically calculated values makes it possible to estimate the average radius of nanocrystallites that form a porous layer. If this radius tends to infinity, there will be no difference between the vibrational modes attributed to different values of the quantum number *m*. In other words, we will have the case of a 2D semiconductor. In this case, only the modes corresponding to surface phonons must appear in its reflection spectrum (see [9] for details).

The results presented here indicate good agreement between the experimental and calculated results. On the one hand, this confirms the correctness of the approach used for the calculations and, on the other hand, makes it possible to estimate the average radius of crystallites composing a porous GaP layer from the results of FTIR spectroscopic data. In addition, we can determine their preferred geometry. Moreover, since we are dealing with nanocrystallites of a diameter comparable with the exciton radius (the Bohr radius of an exciton in GaP is ~17 Å), we observe manifestations of size quantization effects in the bulk of these structures. It was mentioned above that Ga_2O_3 crystallites with luminescence in the green region of the spectrum are not observed in the porous GaP samples under investigation. There are no other factors that should be taken into account in this case. Consequently, we can state with confidence that the above-mentioned effects are mainly responsible for the emergence of visible luminescence signals in the matrix of porous gallium phosphide.

ACKNOWLEDGMENTS

The authors are grateful to Prof. R. Enderlein for fruitful discussions and critical remarks. This work was supported by the Russian Foundation for Basic Research, project no. 00-02-17104.

REFERENCES

1. A. I. Belogorokhov, V. A. Karavanskiĭ, A. N. Obraztsov, and V. Yu. Timoshenko, Pis’ma Zh. Éksp. Teor. Fiz. **60**, 262 (1994) [JETP Lett. **60**, 274 (1994)].
2. H. Fu, V. Ozolinš, and A. Zunger, Phys. Rev. B **59**, 2881 (1999).
3. V. V. Mamutin, V. P. Ulin, V. V. Tret’yakov, *et al.*, Pis’ma Zh. Tekh. Fiz. **25** (1), 3 (1999) [Tech. Phys. Lett. **25**, 1 (1999)].
4. A. Anedda, A. Serpi, V. A. Karavanskii, *et al.*, Appl. Phys. Lett. **67**, 3316 (1995).
5. A. Meijerink, A. A. Bol, and J. J. Kelly, Appl. Phys. Lett. **69**, 2801 (1996).
6. I. M. Tiginyanu, G. Irmer, J. Monecke, and H. L. Hartnagel, Phys. Rev. B **55**, 6739 (1997).
7. R. Enderlein, Phys. Rev. B **47**, 2162 (1993).
8. B. H. Bairamov, A. Aydinli, B. Tanatar, and S. Gurevich, in *Proceedings of the 1st International Conference on Materials for Microelectronics, Barcelona, Spain, 1994.*
9. R. Enderlein, Phys. Rev. B **43**, 14513 (1991).
10. A. I. Belogorokhov, Yu. A. Pusep, and L. I. Belogorokhova, J. Phys.: Condens. Matter **12**, 3897 (2000).
11. E. A. Vinogradov and I. I. Khammadov, *Spectroscopy of Bulk and Surface Phonons of Crystals* (Fan, Tashkent, 1989).
12. A. I. Belogorokhov, I. S. Zakharov, A. V. Kochura, and A. F. Knjazev, Appl. Phys. Lett. **77**, 2121 (2000).

Translated by N. Wadhwa

Physics of the Solid State, Vol. 43, No. 9, 2001, pp. 1770–1773. Translated from Fizika Tverdogo Tela, Vol. 43, No. 9, 2001, pp. 1698–1701.
Original Russian Text Copyright © 2001 by Valov, Leĭman, Semenov.

LOW-DIMENSIONAL SYSTEMS AND SURFACE PHYSICS

Initial Nucleation Stages and Properties of CuCl Nanoparticles in Glasses

P. M. Valov, V. I. Leĭman, and K. S. Semenov
St. Petersburg State University of Plant Polymer Technology, St Petersburg, 198095 Russia
e-mail: valeri_leiman@ip.com.ru

Received December 26, 2000

Abstract—The time variation and temperature dependence of a CuCl phase nucleation in a glass was studied by exciton spectroscopy. The phase formation kinetics at three temperatures was measured. A time delay in attaining a stationary rate of the new phase growth was observed at all temperatures, in agreement with the Zeldovich theory. The kinetic parameters of the CuCl phase formation were determined in the initial stage, when the critical nuclei possessing a zero surface energy (and an effective radius below 1.3 nm) appear in the glass matrix. The first-order phase transition in the new phase is 200 K below the melting temperature of CuCl single crystals. The temperature dependence of the CuCl phase nucleation rate reveals the second and third stages of the new phase formation. The activation energies for diffusion of the CuCl phase components in the glass matrix are determined. *© 2001 MAIK “Nauka/Interperiodica”.*

The formation of a new phase must exhibit three stages [1]. In the first stage, called nucleation, the degree of oversaturation remains virtually unchanged. In the second stage, normal growth, the new phase particles increase in size and the oversaturation decreases, while the number of particles exhibits no significant variations. The third stage, recondensation [2], features competitive growth of the new phase particles, while both oversaturation and the total amount of the new phase remain unchanged.

Golubkov *et al.* [3] observed the third stage of formation of a semiconducting CuCl phase in a glass matrix [3] over a sufficiently long time. The first two stages of this process were not observed experimentally until now. These initial stages were theoretically studied in [4, 5], where equations describing the time variation of the particle size and the total amount of the new phase were derived. The physical properties of the ultradisperse phase are determined to a considerable extent by the size dependence of the surface energy. There are many theoretical calculations (see, e.g., [6–8]) in which the surface tension of a new phase is assumed to tend to zero with decreasing particle size, which makes possible the loss of stability of the new phase. A decrease in the average particle radius leads to a “blue” shift in the energy of electron states [9] and to a significant decrease in the first-order phase transitions [10].

This study is a continuation of our previous investigations [11–14] of the ultradisperse CuCl phase in a glass matrix. The initial stages of the CuCl phase formation in the glass were studied using the method of exciton thermal analysis (exciton spectroscopy). We experimentally revealed three stages in the new phase formation and determined the activation energies for diffusion of the CuCl phase components in the glass matrix. It is demonstrated that the new phase can be stable even at an extremely small particle size, when the surface energy is virtually vanishing.

1. KINETICS OF THE CuCl PHASE NUCLEATION IN A GLASS MATRIX

An ultradisperse phase appears in liquid glass annealed at a temperature T_a above 500°C. On cooling the melt, the ultradisperse phase exhibits crystallization with the formation of copper halogenide nanocrystals. In this way, a glass matrix containing CuCl nanoparticles can be obtained. The spectrum of initial glass containing the necessary impurities exhibits a structureless absorption decay in a wavelength range from 300 to 370 nm related to the longwave absorption band edge of Cu^+ ions distributed in the glass matrix. Annealing of the sample at a temperature of $T_a = 500°C$ or above leads initially to a structureless increase of the optical absorption in the entire spectral range, after which an exciton absorption band (due to the $Z_{1,2}$ exciton of CuCl crystals in the glass matrix) begins to form as manifested by an absorption maximum in the region of 350–370 nm. The intensity of optical absorption in this wavelength interval was used to determine the amount of the CuCl phase formed in the glass matrix.

The experiments were performed with three samples (0.65, 0.64, and 0.63 mm thick) of a glass with the same initial composition annealed stepwise at three temperatures (T_a = 710, 612, and 500°C). After every exposure at a given temperature, the sample was extracted from the furnace and the absorption spectrum was measured in the 310–400 nm range. Then, absorption K_{ex} in the region of the $Z_{1,2}$ exciton (proportional to the overall amount of CuCl phase formed in the glass matrix during the total annealing time was determined. The results of these measurements are presented in Fig. 1 as a semilogarithmic scale of K_{ex} versus ln$t$, where t is the total time of the sample exposure at a given temperature.

As is seen from Fig. 1, the kinetic curves reflecting a buildup of the amount of CuCl phase formed in the glass matrix exhibit two regions apparently corresponding to the first (see [4]) and second stages of a new phase formation. An analysis of the absorption spectra showed that an absorption band related to the formation of energy states of the $Z_{1,2}$ excitons of the CuCl phase appears only in the second stage. It must be emphasized that a straight portion in the absorption buildup kinetics of the CuCl phase in the second stage is observed for all three annealing temperatures and that the slope of these linear regions is independent of the temperature of the new phase formation. This feature of the CuCl phase formation in the second stage disagrees with the model proposed in [5].

Note also that, at any annealing temperature, the process is characterized by a certain time τ from the start of annealing to attainment of the straight portion of the kinetic curve corresponding to the CuCl phase formation. According to the Zeldovich theory [4] of new phase formation, the delay time τ is determined by the critical nucleus size x_{cr} and the diffusion coefficient D of the new phase components:

$$\tau = \frac{x_{cr}^2}{4D}, \quad D = D_0 \exp\left(-\frac{U}{kT}\right). \tag{1}$$

Here, D_0 is the diffusion parameter, U is the diffusion activation energy, k is the Boltzmann constant, and T is the absolute temperature. Using the τ values determined for each annealing temperature from Fig. 1, we obtain the following values of parameters in relationship (1): $x_{cr}^2/D_0 = 3.6 \times 10^{-3}$ s and the effective activation energy $U = 1.1$ eV. The critical nucleus size x_{cr} depends on the surface energy σ [4] of the nucleus–glass interface. Since σ may strongly depend on the temperature [15], there is some uncertainty in the values of parameters determined for relationship (1).

The parameters of diffusion of the CuCl phase components in the glass can be evaluated using an alternative method. As the glass sample thicknesses were decreased to approximately one-tenth of the initial thickness, the amount of the CuCl phase formed at 710 and 612°C dropped by a factor of 7 and 1.8, while that at 500°C remained unchanged. We can estimate the parameters of diffusion of the ultradisperse phase components by assuming that a decrease in the amount of CuCl formed in the bulk is caused by the surface loss of components and using a formula for the mean square displacement $x^2 = 2Dt$ (where t is the diffusion time and $D = D_0\exp(-U/kT)$) from the diffusion theory. For a sample annealed for one hour at 600°C, the mean square displacement is about half of the sample thickness ($x \sim 0.04$ mm). According to the formula for x^2, this yields $D = 2 \times 10^{-7}$ mm^2/s. For $T_a = 710$°C, the analogous calculation yields an estimate of $D = 600 \times 10^{-7}$ mm^2/s. Evaluated from these estimates, the average activation energy for diffusion of the CuCl phase components in the glass is $U = 3.7$ eV and the corresponding preexponential factor is $D_0 = 2.7 \times 10^{15}$ mm^2/s.

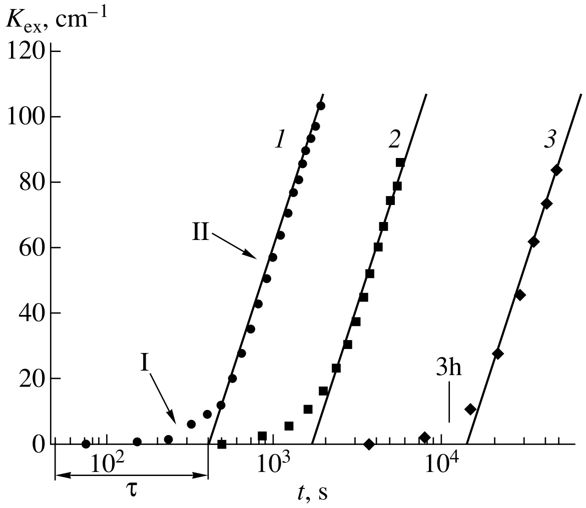

Fig. 1. Optical absorption buildup kinetics at the maximum of the absorption band of the $Z_{1,2}$ excitons of CuCl nanocrystals formed in a glass matrix annealed at (*1*) 710, (*2*) 612, and (*3*) 500°C. Regions I and II correspond to the first and second stages of the CuCl particle growth.

2. TEMPERATURE DEPENDENCE OF THE CuCl PHASE FORMATION IN THE GLASS MATRIX

The glass samples were treated for 3 h in a gradient furnace in the region of temperature variation from T_a = 506 to 720°C. After a 3-h annealing, the low-temperature end of the sample features the onset of the second stage of the CuCl phase formation (as indicated by arrow in Fig. 1). As was demonstrated previously [11], the crystalline CuCl phase particles formed at T_a = 506°C possess zero surface energy and have an average radius of about 1.3 nm. The first-order phase transition in this phase is 200 K below the melting temperature of CuCl single crystals. The opposite end of the sample treated during the same time at T_a = 720°C exhibited the third (recondensation growth) stage of the CuCl phase particles [3]. Figure 2 shows the absorption spectra (measured at 300 K) of CuCl nanocrystals grown at the low-temperature end of a sample annealed in the gradient furnace. Curve *0* represents the optical absorption spectrum of unannealed sample (containing no CuCl phase). Marks on each curve indicate the position of the maximum (E_m) of the $Z_{1,2}$ exciton band and the charac-

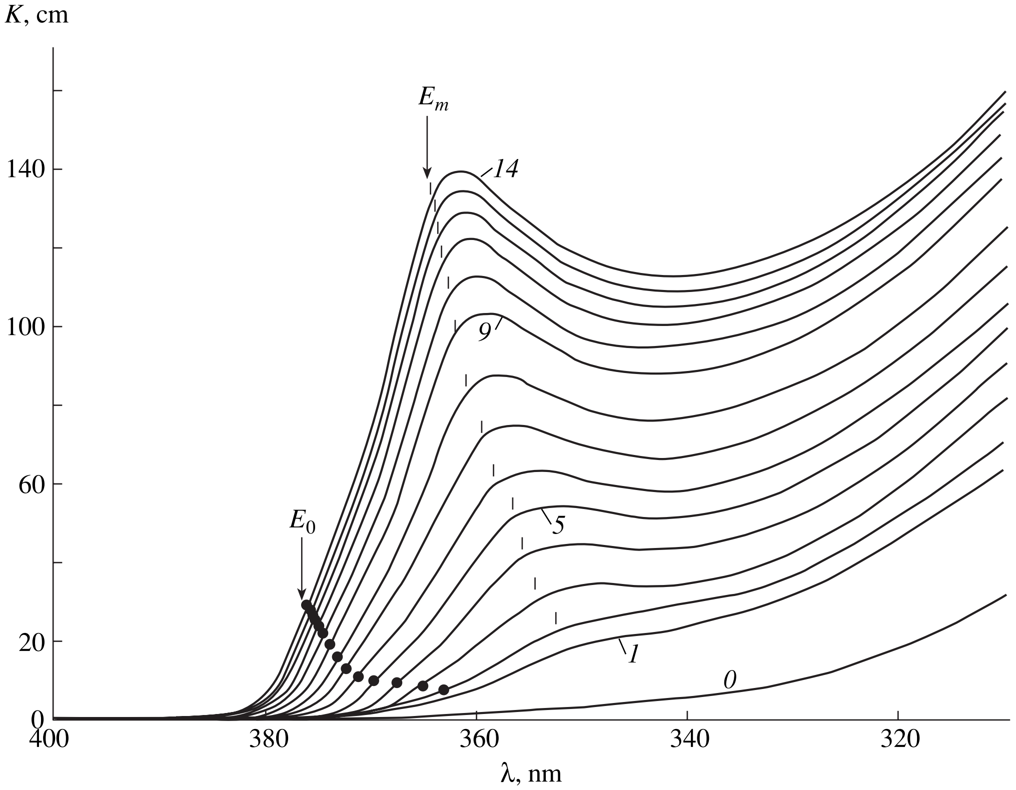

Fig. 2. The absorption spectra (measured at 300 K) of CuCl nanocrystals grown in various regions of a sample annealed in a gradient furnace. Figures on the curves indicate distance from the cold sample end (in mm). E_m is the energy of maximum of the $Z_{1,\,2}$ exciton band (determined by the second derivative peak); E_0 is the energy parameter [11] of the $Z_{1,\,2}$ exciton absorption band. The average CuCl nanocrystal dimensions are R = (*1*) 1.15, (*5*) 1.34, (*9*) 1.8, and (*14*) 2.1 mm.

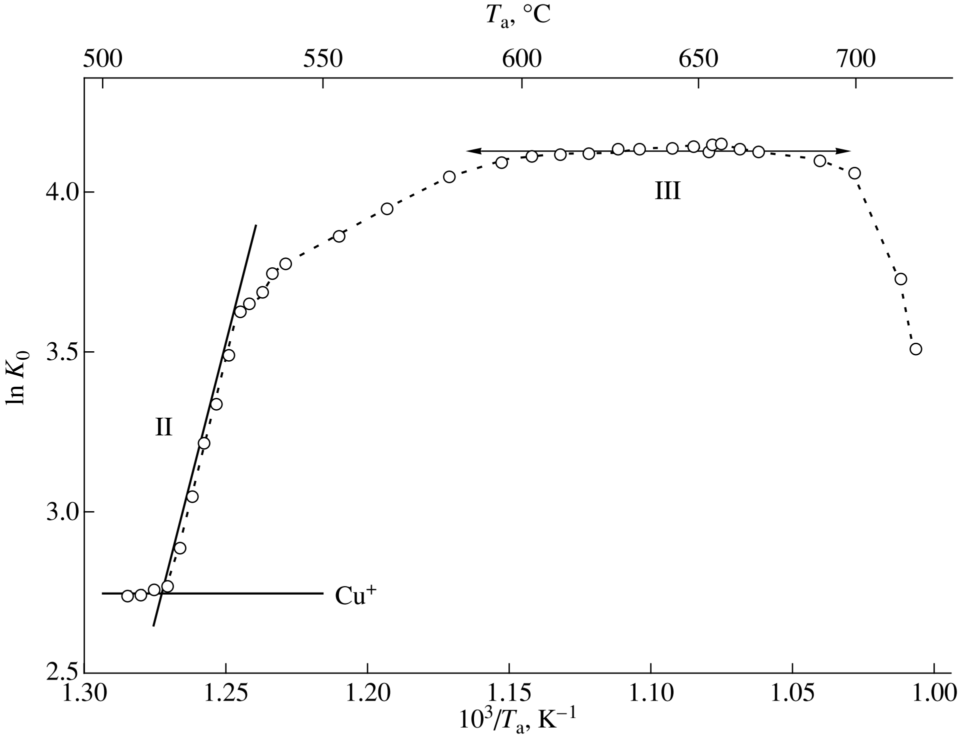

Fig. 3. The profile of absorption $K(E_0)$ at the energy E_0 measured at 300 K for CuCl nanocrystals grown in a glass matrix annealed in the gradient furnace. T_a is the annealing temperature in a given sample region. Regions II and III correspond to the second and third stages of the CuCl phase particle growth.

teristic point (E_0) where the absorption intensity is independent of the temperature in the entire range from 300 K up to the crystal melting temperature [11]. As the number of the spectrum ion in Fig. 2 increases, the average size R of CuCl nanocrystals decreases and the E_m and E_0 values shift toward higher energies as a result of the dimensional quantization [9, 11].

Figure 3 shows the plot of $\ln K(E_0)$ (optical absorption logarithm at the energy E_0) versus reciprocal absolute temperature T^{-1} in various regions of the sample treated for 3 h in the gradient furnace. The $K(E_0)$ value is proportional to the total amount of the CuCl phase formed in a given region of the glass matrix. In the interval of T_a = 500–530°C, the amount of the CuCl phase formed in the sample sharply increases. In this region, the $\ln K(E_0)$ versus $1/T_a$ plot is linear. The slope of this line can be used to determine the diffusion activation energy U_2 in the second stage of the CuCl phase formation in the glass matrix. The obtained value (U_2 = 2.89 eV) is somewhat lower than the estimate obtained as described above. At annealing temperatures above 530°C, a decease in the degree of oversaturation becomes significant and the growth of the CuCl phase slows down. In the range from 580 to 700°C, the third (recondensation [2]) stage takes place, where the CuCl particles grow without an increase in the total amount of the new phase. Above 700°C, the total amount of the CuCl phase in the glass matrix starts decreasing because of a loss at the sample boundaries.

ACKNOWLEDGMENTS

This study was supported by the Russian Foundation for Basic Research, project no. 00-15-96750.

REFERENCES

1. S. V. Gaponenko, Fiz. Tekh. Poluprovodn. (St. Petersburg) **30** (4), 577 (1996) [Semiconductors **30**, 315 (1996)].
2. I. M. Lifshits and V. V. Slezov, Zh. Éksp. Teor. Fiz. **35** (2), 479 (1958) [Sov. Phys. JETP **8**, 331 (1959)].
3. V. V. Golubkov, A. I. Ekimov, A. A. Onushchenko, and V. A. Tsekhomskiĭ, Fiz. Khim. Stekla **7** (4), 397 (1981).
4. Ya. B. Zel'dovich, Zh. Éksp. Teor. Fiz. **12** (11–12), 525 (1942).
5. L. C. Lin and S. H. Risbud, J. Appl. Phys. **68** (1), 28 (1990).
6. *The Collected Works of J. Willard Gibbs* (Longmans, Green and Co, New York, 1928; Goskhimizdat, 1950), Vol. 1, p. 434.
7. R. C. Tolman, J. Chem. Phys. **17** (3), 333 (1949).
8. A. I. Rusanov, *Phase Equilibrium and Surface Phenomena* (Khimiya, Leningrad, 1967).
9. A. I. Ekimov, Phys. Scr. T **39** (1), 217 (1991).
10. A. A. Onushchenko and G. T. Petrovskii, J. Non-Cryst. Solids **196** (1), 73 (1996).
11. P. M. Valov, L. V. Gracheva, V. I. Leĭman, and T. A. Negovorova, Fiz. Tverd. Tela (St. Petersburg) **36** (6), 1743 (1994) [Phys. Solid State **36**, 954 (1994)].
12. P. M. Valov, L. V. Gracheva, and V. I. Leĭman, Fiz. Khim. Stekla **23** (2), 187 (1997).
13. P. M. Valov and V. I. Leĭman, Pis'ma Zh. Éksp. Teor. Fiz. **66** (7), 481 (1997) [JETP Lett. **66**, 510 (1997)].
14. P. M. Valov and V. I. Leĭman, Fiz. Tverd. Tela (St. Petersburg) **41** (2), 310 (1999) [Phys. Solid State **41**, 278 (1999)].
15. N. T. Gladkikh, L. K. Grigor'eva, S. V. Dukarov, *et al.*, Fiz. Tverd. Tela (Leningrad) **31** (5), 13 (1989) [Sov. Phys. Solid State **31**, 728 (1989)].

Translated by P. Pozdeev

Physics of the Solid State, Vol. 43, No. 9, 2001, pp. 1774–1782. From Fizika Tverdogo Tela, Vol. 43, No. 9, 2001, pp. 1702–1709.
Original English Text Copyright © 2001 by Evarestov, Bredow, Jug.

LOW-DIMENSIONAL SYSTEMS AND SURFACE PHYSICS

Connection between Slab and Cluster Models for Crystalline Surfaces[1]

R. A. Evarestov*, Th. Bredow, and K. Jug****
**St. Petersburg State University, Stary Peterhof, St. Petersburg, 198904 Russia*
***Universität Hannover, 30167 Hannover, Germany*
e-mail: robert@hq.pu.ru

Received January 25, 2001

Abstract—Different models for the theoretical description of bare crystalline surfaces are compared and discussed in terms of stoichiometry and conservation of point symmetry. While infinite models such as the semi-infinite model or the slab model generally preserve the symmetry of the perfect crystal surface, special care has to be taken when finite cluster models are considered. The connection between the molecular cluster choice and surface unit cell of the slab model is demonstrated for metal oxides such as MgO, TiO_2, V_2O_5, and Al_2O_3 by analyzing how atoms of the primitive unit cell of the parent three-dimensional crystal are distributed in different planes of the slab and cluster models. General rules for the construction of finite cluster models based on stoichiometry and symmetry considerations are given and illustrated with calculations on water adsorption in rutile (110). *© 2001 MAIK “Nauka/Interperiodica”.*

1. INTRODUCTION

Crystalline surfaces are of great importance in many chemical and physical processes [1, 2]. They are therefore the subject of an increasing number of studies, both experimental and theoretical [3]. In recent decades, quantum-chemical calculations have become an important tool for investigating the structural, electronic, and catalytic properties of surfaces. Methodological developments and the rapid improvement of computer hardware have enabled theorists to work with systems of increasing complexity. Thereby, it is possible not only to reproduce experimental findings with increasing accuracy, but it is also possible to help in the interpretation of experimental results.

For simulations of the electronic structure of the surfaces of crystalline solids, three basic models are used: cluster, slab, and semi-infinite crystal models [4]. The last model is the most appropriate, because it takes into account an infinite number of atoms in the crystal below the surface [5]. Slab and cluster models are nevertheless more popular, since they are more feasible from the computational point of view. The cyclic cluster model [4] is intermediate between the slab and molecular cluster models. It takes into account the translational symmetry of the surface but considers only a finite number of interatomic interactions within a strictly defined region.

The choice of the cluster model (both molecular and cyclic) for a surface allows one to employ all quantum chemical techniques that have been developed for molecular systems. It is also possible to study defects or adsorption reactions in the limit of low coverage. Care must be taken in the selection of cluster size and shape because of the unavoidable presence of boundary effects. Different schemes have been developed to reduce boundary effects in the cluster model, either by using an embedding procedure or by the introduction of cyclic boundary conditions. Slab models eliminate two-dimensional boundary effects and are widely used for the study of periodic surface structures.

In the present work, the connection between the slab and cluster models is considered by performing a symmetry analysis of the crystalline surface. As far as we know, this connection has not been investigated explicitly before, although it is implied in many surface studies using molecular clusters as a model.

For some metal oxides, we compared how atoms in the primitive unit cell of a three-dimensional crystal are arranged in different atomic planes of slab models and clusters. General rules for the construction of molecular cluster models for surface simulations based on considerations of stoichiometry and symmetry are suggested.

In Section 2, infinite models of surfaces, the semi-infinite crystal model, and the slab model are briefly discussed. The relationship between unit cells of two-dimensional (2D) slab models and the three-dimensional (3D) bulk unit cell is investigated. Section 3 describes finite models (the cyclic cluster and the molecular cluster model) and discusses their connection with the slab model. The results of calculations of molecular clusters with the same stoichiometry but different arrangements of atoms are compared for the case of adsorption of water at rutile (110).

---

[1] This article was submitted by the authors in English.

Table 1. Distribution of the bulk primitive unit cell atoms over planes in the one-layer slab model of surfaces

Labeling of atoms in the bulk unit cell	Surface	Plane lattice	Atomic distribution in planes	Symmetry croup
MgO (primitive) 1—Mg, 2—O	(001)	Square	(1) 1, 2	$DG61$–$P4/mmm$ (D^1_{4h}–$G123$)
MgO (conventional) 1–4—Mg 5–8—O	(001)	Square	(1) 1, 2, 5, 6 (2) 3, 4, 7, 8	$DG61$–$P4/mmm$ (D^1_{4h}–$G123$)
TiO_2 (rutile) 1, 2—Ti 3–6—O	(110)	Rectangular	(1) 3 (2) 1, 2, 5, 6 (3) 4	$DG37$–$Pmmm$ (D^1_{2h}–$G47$)
TiO_2 (anatase) 1, 2—Ti 3–6—O	(001)	Square	(1) 3 (2) 1 (3) 4 (4) 5 (5) 2 (6) 6	$DG55$–$P4mmm$ (C^1_{4v}–$G99$)
V_2O_5 1–4—V 5–8—O 9–12—O 13, 14—O	(001)	Rectangular	(1) 7, 8 (2) 3, 4 (3) 9, 10, 11, 12, 13, 14 (4) 1, 2 (5) 5, 6	$DG37$–$Pmmm$ (D^1_{2h}–$G47$)
Al_2O_3 1–4—Al 5–10—O	(111)	Hexagonal	(1) 1 (2) 8, 9, 10 (3) 2 (4) 4 (5) 5, 6, 7 (6) 3	$DG66$–$P\bar{3}$ (C^1_{3i}–$G147$)

2. INFINITE MODELS OF SURFACES

2.1. Semi-Infinite Crystal Model

The symmetry group of the semi-infinite crystal model contains, in addition to translations in the surface plane, only those rotations and mirror reflections which keep the atoms in the planes parallel to the surface.

The model of a semi-infinite crystal turns out to be very difficult to calculate for real systems. Simplification of this model should take into account the finite number of interacting layers parallel to the surface. In this case, the 2D translation symmetry in the surface plane is maintained. This simplified model is known as the slab model of the surface [6].

2.2. Slab Model

The symmetry group of a slab of a finite thickness includes symmetry operations that move atoms out of the surface plane and bring them into equivalent positions. Such a group belongs to diperiodic space groups *DG* in three dimensions (layer groups).

The slab model is now widely used in Hartree–Fock LCAO calculations for crystalline surfaces [6] and also in DFT calculations [7, 8].

The layer group contains a subgroup of 2D translations $T^{(2)}$ with elements $(E|\mathbf{a}_n)$, where $\mathbf{a}_n = n_1\mathbf{a}_1 + n_2\mathbf{a}_2$ is an arbitrary translation vector of a 2D (plane) lattice

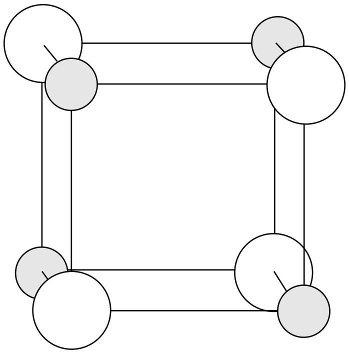

Fig. 1. Unit cell of an MgO (001) surface slab derived from the conventional unit cell of the 3D lattice. Gray spheres are Mg and white spheres are O.

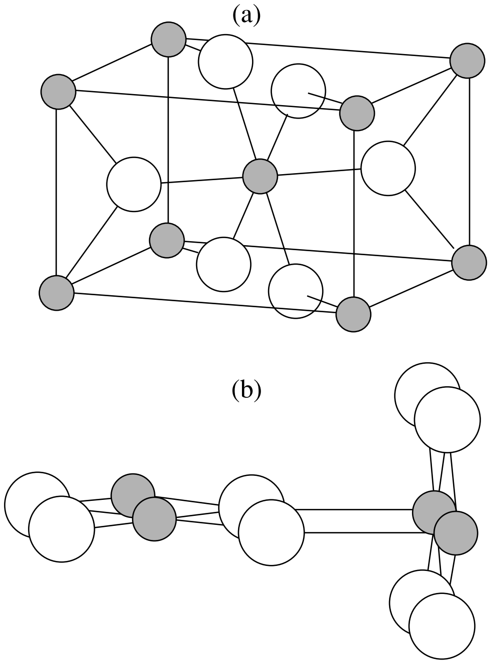

Fig. 2. (a) Conventional 3D rutile unit cell and (b) two unit cells of a rutile (110) surface slab derived from the primitive unit cell of the 3D lattice. Gray spheres are Ti and white spheres are O.

and $\mathbf{a}_1$ and $\mathbf{a}_2$ are primitive unit cell translation vectors defining a 2D Bravais lattice.

Let us consider the layer groups for the slab models of the following surfaces: (001) in MgO ($G = Fm\bar{3}m$), (110) in the rutile structure of TiO_2 ($P4_2/mnm$), (001) in the anatase structure of TiO_2 ($I4_1/amd$), (001) in a V_2O_5 crystal ($Pmmn$), and the (111) plane of Al_2O_3 ($P\bar{3}$).

In the slab model, the surface plane has a fixed orientation under the bulk symmetry group operations. All the atoms of the bulk primitive unit cell are distributed within one or several planes with the same 2D translation symmetry. These planes of atoms form a layer which is, by definition, stoichiometric. Of practical importance for surface studies using slab models is the dependence of the calculated properties on the number of layers in the slab. The point symmetry group of a slab generally depends on the number of layers included.

In Table 1, the distribution of the bulk primitive unit cell atoms over the atomic planes in one-layer slab models is given. For an MgO crystal, one can use not only the bulk primitive unit cell of two atoms, but also the conventional cell consisting of an 8-atom cubic cell with two planes of atoms (Fig. 1). The rutile (110) surface layer consists of three planes of atoms (Fig. 2a). When choosing the one-layer slab model in this case, the following order of planes is chosen: an oxygen plane, a mixed oxygen–titanium plane, and an oxygen plane (Fig. 2b). This layer choice ensures a zero dipole moment in the slab [6]. For the anatase (001) surface, the six atoms of the primitive bulk unit cell are distributed over six different planes (Fig. 3a), so that one layer consists of six atomic planes (Fig. 3b). The representative atoms are labeled in Table 1. In the case of the (001) surface of the V_2O_5 crystal (Fig. 4a), the layer consists of five atomic planes (Fig. 4b, Table 1). In the V_2O_5 bulk structure, there are three types of nonequivalent oxygen atoms with different coordinations. In the one-layer slab model, these atoms appear to be equally distributed over three planes of atoms. The primitive bulk unit cell of corundum Al_2O_3 (rhombohedral lattice) is shown in Fig. 5a. This unit cell contains two formula units. If the (111) surface is considered, the ten atoms are distributed over six different atomic planes as shown in Fig. 5b and Table 1. Alternatively, it is also possible to choose the hexagonal unit cell, which contains six formula units. The same surface is then labeled (0001) and the 30 atoms of the bulk unit cell are distributed over 12 atomic planes. The slab model is, in fact, an infinite model of a surface since the 2D periodicity of the system is maintained. For the computational schemes based on the use of plane waves, the 3D periodicity is restored in so-called multislab models that consider an infinite number of identical slabs regularly spaced along the normal to the surface (a typical separation is 10 a.u.) [6].

The most common application of the slab model is the study of regular adsorption phenomena. Both the monolayer of the adsorbed species (with the same 2D periodicity as the slab) and lower coverages can be studied in the slab model. In the latter case, the 2D supercell approach is used: the two translation vectors $\mathbf{a}_1$ and $\mathbf{a}_2$ defining the plane lattice are transformed with the integer matrix $\mathbf{l}$:

$$\mathbf{A}_j = \sum_{i=1}^{2} l_{ji}\mathbf{a}_i, \quad \det\mathbf{l} = L > 1. \tag{1}$$

The 2D supercell size is defined by the number of primitive unit cells L in the 2D supercell. The transformation in Eq. (1) is called symmetric if the point symmetry of the supercell 2D lattice is the same as that of the original 2D lattice [9]. The slab–supercell approach introduces a new 2D periodic system and can be treated by the same band theory tools as the slab itself. The supercell model is now popular for describing 3D periodic crystals when local defects are studied [10, 11]. There are no fundamental differences in the supercell use in 2D and 3D periodic systems. The transformation in Eq. (1) in the direct lattice generates a transformation of the reciprocal lattice:

$$\mathbf{b}_j = \sum_{i=1}^{2} (\mathbf{l}^{-1})_{ij} \mathbf{B}_i, \quad (2)$$

where $\mathbf{B}_i$ and $\mathbf{b}_j$ are the translation vectors of the original and transformed reciprocal lattices, respectively. The new 2D Brillouin zone (BZ) turns out to be L times smaller, such that L points in the initial BZ coincide:

$$\mathbf{K}_l^{(\mathbf{k})} = \mathbf{k} + \sum_{j=1}^{2} q_{lj} \mathbf{b}_j, \quad (3)$$

where q_{lj} are integers and $\mathbf{k}$ is an arbitrary vector in the small BZ.

Thus, in the slab–supercell model, a folding of BZ is used, corresponding to a 2D direct lattice, but the system under consideration remains infinite. The adsorbed species in this model are repeated periodically, and their distance and interaction with each other depends on the supercell size. Some examples of the band structure for the slab–supercell model are considered, for example, in [6].

In surface simulations, other models based on the consideration of finite systems are also used.

3. FINITE MODELS OF SURFACES

3.1. Cyclic Clusters

The cyclic cluster (CC) model of surfaces [12–20] is connected to the slab–supercell approach, but it is different due to the different introduction of cyclic boundary conditions (CBC). In the slab–supercell approach, these conditions are, in fact, introduced for a very large system, e.g., for the main region of the 2D periodic plane, so that band theory methods are used in the slab calculations. In the CC model, the CBC are introduced for the cluster itself, so that the model turns out to be finite. The convergence of the results to the slab values must be investigated by increasing the CC. However, the CC approach offers evident advantages:

(a) the spurious boundary effects of molecular clusters (to be discussed in Section 3.2) are absent;

(b) the periodicity of adsorbed species or of defects is excluded because the CC is a finite system;

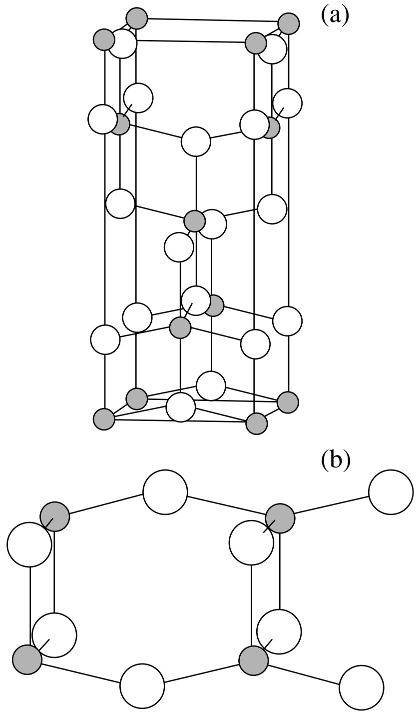

Fig. 3. (a) Conventional 3D anatase unit cell and (b) two unit cells of an anatase (001) surface slab derived from the primitive unit cell of the 3D lattice. Gray spheres are Ti and white spheres are O.

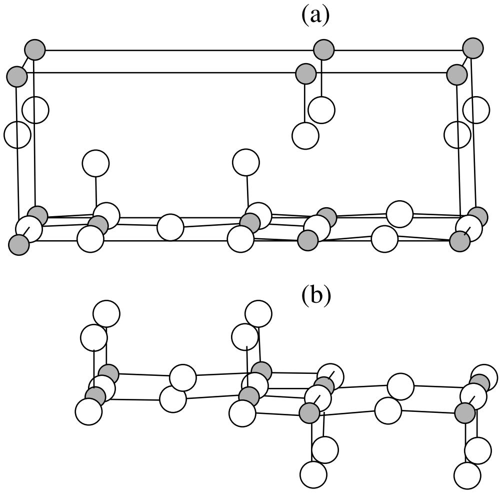

Fig. 4. (a) Conventional 3D V_2O_5 unit cell and (b) two unit cells of a V_2O_5 (001) surface slab derived from the primitive unit cell of the 3D lattice. Gray spheres are V and white spheres are O.

(c) there is a one-to-one symmetry correspondence between the electronic states of the 2D CC and the band states of the corresponding slab model.

Let us consider this correspondence in more detail. The CC model is based on the use of the transformation in Eq. (1) in the 2D direct lattice. However, the CBC are

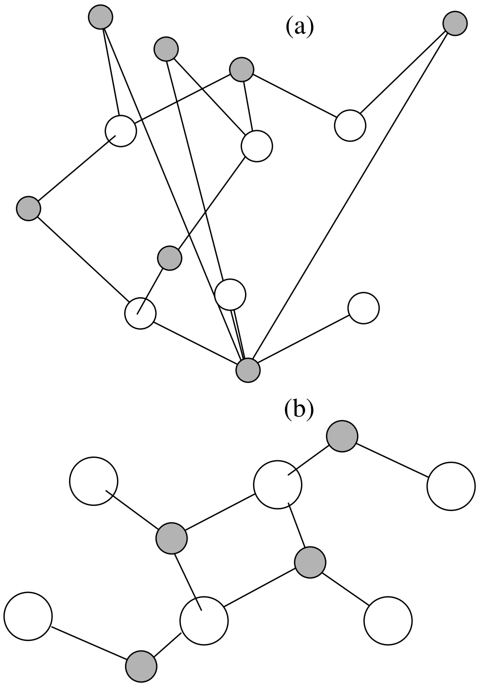

Fig. 5. (a) Rhombohedral 3D Al_2O_3 unit cell and (b) unit cell of an Al_2O_3 (111) surface slab derived from the primitive unit cell of the 3D lattice. Gray spheres are Al and white spheres are O.

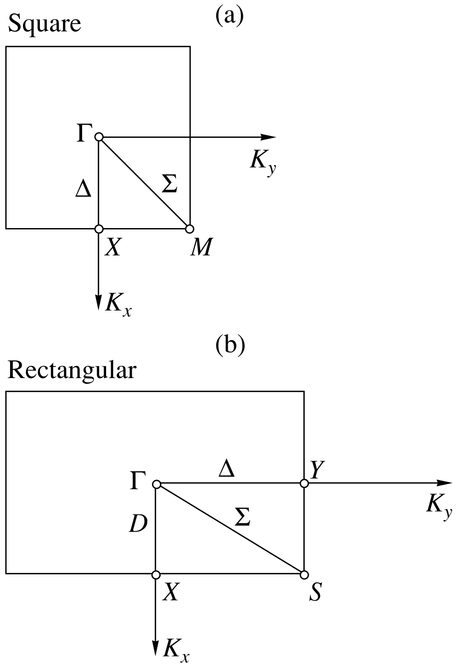

Fig. 6. Brillouin zones of (a) square and (b) rectangular 2D lattices.

introduced with the translation vectors $\mathbf{A}_j$ ($j = 1, 2$). For the one-electron Bloch function $\Psi_{n\mathbf{k}}(\mathbf{r})$, it is assumed that relation $\Psi_{n\mathbf{k}}(\mathbf{r}) = \Psi_{n\mathbf{k}}(\mathbf{r} + \mathbf{A}_j) = \exp(+i\mathbf{k}\mathbf{A}_j)\Psi_{n\mathbf{k}}(\mathbf{r})$ is satisfied. Therefore, the introduction of CBC defines those irreducible representations $\mathbf{K}$ of the 2D translation group for which

$$\exp(+i\mathbf{K}^{(0)}\mathbf{A}_j) = 1, \quad j = 1, 2, \tag{4}$$

i.e., for those $\mathbf{K}^{(0)}$ that satisfy Eq. (3) for $\mathbf{k} = 0$. Using Eqs. (1) and (4) and the expression $\mathbf{K}^{(0)} = \sum_{i=1}^{2} K_i^{(0)}\mathbf{B}_i$, one obtains

$$\sum_{i=1}^{2}\sum_{i'=1}^{2} K_i^{(0)}\mathbf{l}_{ji'}(\mathbf{a}_{i'}\mathbf{B}_i) = \sum_{i=1}^{2}\sum_{i'=1}^{2} K_i^{0}\mathbf{l}_{ji'}2\pi\delta_{i,i'} = 2\pi\sum_{i=1}^{2} K_i^{(0)}\mathbf{l}_{ji}, \quad j = 1, 2. \tag{5}$$

To satisfy Eq. (4), the 2D wave vector components are defined by the relation

$$\sum_{i=1}^{2} k_i\mathbf{l}_{ji} = m_j, \quad j = 1, 2, \tag{6}$$

where m_j are integers.

Equation (6) is always satisfied for the Γ point of the BZ ($\mathbf{K} = 0$) so that the CC reproduces states at the Γ point of the 2D BZ independently of its choice. However, for $\mathbf{K} \neq 0$, the points of a given 2D lattice, the set of the electronic states reproduced in the CC model depends on the choice of the $\mathbf{l}$ matrix in Eq. (1).

As examples, let us consider the following: two plane lattices, a square [MgO (100) and anatase TiO_2 (001) surfaces], and a rectangle [TiO_2 rutile (110) and V_2O_5 (001) surfaces].

The corresponding 2D BZs are given in Fig. 6. Let us choose a 2D CC for the square lattice in such a way that the C_{4v} point symmetry is not broken. The smallest CC corresponds to

$$\mathbf{l} = \begin{pmatrix} 1 & -1 \\ 1 & 1 \end{pmatrix}, \quad L = 2, \tag{7}$$

so that Eq. (6) is satisfied for the Γ(0, 0) and $M\left(\frac{1}{2}\ \frac{1}{2}\right)$ points of the 2D BZ. The corresponding point groups of these two $\mathbf{k}$ points are the same, C_{4v}. The 2D unit cell is two times larger than the primitive one. For transformation in Eq. (1) with matrix

$$\mathbf{l} = \begin{pmatrix} 2 & 0 \\ 0 & 2 \end{pmatrix}, \quad L = 4, \tag{8}$$

the corresponding CC reproduces the states at Γ, M, and X (two-ray) $\mathbf{k}$-vector stars. Further increase of the CC allows one to reproduce not only the symmetry points of the 2D BZ, but also points on the symmetry lines. In particular, for

$$\mathbf{l} = \begin{pmatrix} 3 & 0 \\ 0 & 3 \end{pmatrix}, \quad L = 9, \tag{9}$$

the following $\mathbf{k}$ points satisfy Eq. (6): $\Gamma(0, 0)$, $4\Delta\left(\frac{1}{3}\,0, -\frac{1}{3}\,0, 0\,\frac{1}{3}, 0\,-\frac{1}{3}\right)$, and $4\Sigma\left(\frac{1}{3}\,\frac{2}{3}, \frac{2}{3}\,\frac{1}{3}, \frac{1}{3}\,\frac{1}{3}, \frac{2}{3}, \frac{2}{3}\right)$. When the $\mathbf{k}$ points of the 2D BZ satisfying Eq. (6) are found, the induced representations (IRs) of DG space groups must be used to find the symmetry of the CC electron states. To construct the IR table of a given DG, the table of the IR for the corresponding triperiodic group can be used [5]. In particular, to obtain the table of IRs for $DG61$ (the symmetry group of cyclic clusters of the MgO (001) surface), the table of IRs for the related space group $G123(D_{4h}^1)$ has to be used. This table provides the connection between the irreducible representations of site-symmetry point groups of $DG61$ and those of the space group itself. For the symmetry directions Δ, Σ, and Y, compatibility relations must be used.

For the rectangular lattice, the transformation matrix in Eq. (7) leads to a CC reproducing the $\Gamma(0, 0)$ and $S\left(\frac{1}{2}\,\frac{1}{2}\right)$ points of the 2D BZ (Fig. 6). The corresponding CC for transformation (8) reproduces states at $\Gamma(0, 0)$, $X\left(\frac{1}{2}\,0\right)$, $Y\left(0\,\frac{1}{2}\right)$, and $S\left(\frac{1}{2}\,\frac{1}{2}\right)$. Further increase of the CC using transformation (9) allows one to reproduce the symmetry point $\Gamma(0, 0)$ and symmetry directions $D\left(\frac{1}{3}\,0, -\frac{1}{3}\,0\right)$, $\Delta\left(0\,\frac{1}{3}, 0\,-\frac{1}{3}\right)$, and $\Sigma\left(\frac{1}{3}\,\frac{1}{3}, -\frac{1}{3}\,\frac{1}{3}, \frac{1}{3}\,-\frac{1}{3}, -\frac{1}{3}\,-\frac{1}{3}\right)$. This consideration clarifies the symmetry connection between the CC model and supercell–slab models.

The CC choice scheme under consideration was applied [21] to calculate the adsorption geometry for organic adsorbates on a rutile (110) surface. The INDO parametrization scheme was modified to reproduce the experimental results for geometries of carbon- and nitrogen-containing molecules. The CC representing the rutile (110) surface [21] consists of 120 atoms. It includes two layers of 5×2 2D unit cells with six atoms in each 2D unit cell.

3.2. Molecular Clusters

The molecular cluster (MC) model is extremely popular in surface simulations because of its simplicity and flexibility and the possibility of its use in the standard techniques of molecular quantum chemistry [4, 22–25]. In the MC approach, a crystal with a surface is modeled by a finite (molecular) system consisting of atoms on the surface and of some atomic planes nearest to it. The 2D periodicity of the surface is disregarded so that the symmetry of such a model is described by one of the crystallographic point groups. In adsorption studies, the adsorbed species are included in the cluster–adsorbate systems.

An MC is cut out of the slab to simulate a portion of the surface so that spurious effects arise that are related to the limited cluster size and to the presence of the boundary. To eliminate these effects, the dangling bonds are saturated either by hydrogen atoms or pseudoatoms or the whole cluster is placed in an external field simulating the influence of the bulk crystal [24, 26, 27].

In the MC model, the results critically depend on the choice of the cluster size, stoichiometry, and shape. Nevertheless, the MC model can provide useful information if the cluster is properly chosen and the influence of its size is investigated.

In what follows, we suggest a number of general rules for the generation of an MC suitable for surface simulations based on the connection between the MC and the slab model.

We are aware of the fact that these rules have been intuitively applied in previous studies, in most cases without explicitly considering the relationship between periodic and molecular models. Nevertheless, we believe that it might be useful for future surface studies to consider these rules in order to minimize artefacts of the models:

(a) the clusters correctly reflect the stoichiometry of the bulk crystal and are electroneutral;

(b) atoms on the crystal surface should be equivalent to those on the cluster surface except for corners and edges;

(c) the average coordination of all cluster atoms is as close as possible to that of atoms on the crystal surface;

(d) as many symmetry elements of the crystal surface as possible are retained in the cluster; and

(e) an extension to rule (a) is that each layer of the cluster should have the stoichiometry of the crystal.

In fact, such principles of the MC choice ensure the simulation of the crystal surface as closely as possible and are directly connected with the 2D periodic slab model. By using 2D unit cells as basic units of the model clusters, it is possible to increase the cluster size in a systematic way and, thereby, to study the convergence behavior of calculated surface properties. As examples of MC model applications to surface studies using some of the above-mentioned rules, calculations

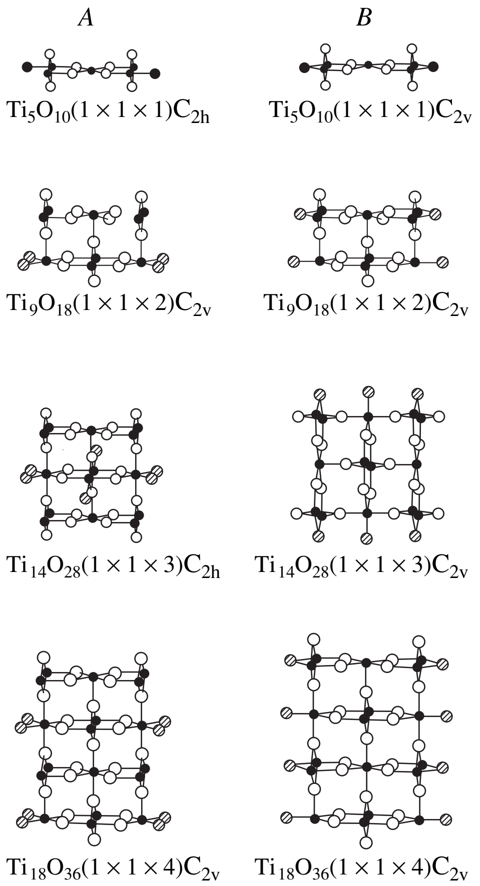

Fig. 7. Rutile (110) surface of size 1 × 1 simulated with 1–4-layer clusters of types *A* and *B*. Black spheres are Ti and white spheres are O; shaded spheres are additional O added to achieve stoichiometry.

of MgO, TiO_2 (rutile, anatase structures), and Cr_2O_3 (corundum structure) surfaces and adsorption of small molecules on them can be considered [23–25, 28–37]. However, it is also possible to find examples in the literature where these rules have not been applied [38, 39] and, in part, unphysical results were obtained.

Table 2. MSINDO adsorption energies (kJ/mol) for molecular and dissociative water adsorption on rutile (110) calculated with relaxation. The clusters correspond to those presented in Figs. 7 and 8

Cluster	Type *A*		Type *B*	
	molecular	dissociative	molecular	dissociative
Ti_5O_{10}	51	39	70	201
Ti_9O_{18}	139	–24	94	107
$Ti_{14}O_{28}$	66	8	92	143
$Ti_{18}O_{36}$	157	192	129	162
$Ti_{49}O_{98}$	120	151	119	157

In MgO and NaCl crystals, the MCs were chosen [33] so that they simulated the supercell of the surface and included several layers of the bulk crystal. For these crystals, the stoichiometry of the chosen MC was ensured by this choice.

For more complicated systems, e.g., TiO_2 structures, the stoichiometry of the MC is only ensured when several additional oxygen atoms are added. There are two principle ways to add these additional atoms. They can be placed on the regular surface around the cluster. This is denoted as type *A* in Figs. 7 and 8. In some cases, this procedure leads to clusters that do not correspond to rules (d) and (e). Another possibility is to place the additional atoms for saturation at irregular positions of the crystalline lattice so that rules (d) and (e) will be fulfilled. Examples of this second type (*B*) of cluster generation are presented in Figs. 7 and 8. If all layers of a multilayer cluster have the same stoichiometry, artificial polarization, which can affect the calculated surface properties, is reduced. This effect is investigated in the next section.

3.3. Numerical Results

To study the effect of the distribution of saturation atoms on the calculated properties of crystalline surfaces, we have selected the rutile (110) surface for the new MSINDO calculations. A large number of theoretical studies have been performed using the MC model for the simulation of this surface [28, 30–32, 34–39]. We used the semiempirical MSINDO SCF MO method [40], the successor of the SINDO1 method which was successfully applied in studies of metal oxide surfaces [23–25, 28, 29]. Water was adsorbed in the molecular and dissociated form on clusters of Ti_5O_{10}, Ti_9O_{18}, $Ti_{14}O_{28}$, and $Ti_{18}O_{36}$ (Fig. 7) chosen according to the rules suggested here. Nevertheless, even if these rules are applied, several different types of clusters can be constructed. Two types of possible cluster models were used. In type *A* clusters, which already have been used previously [28], additional oxygen atoms, necessary to ensure total stoichiometry (shaded in Fig. 7), were placed at regular lattice positions. In type *B* clusters, which were considered by us for the first time, additional oxygen atoms were placed at nonlattice positions to maximize the symmetry of the clusters and to reduce polarization, as discussed in the previous section. The adsorption energies calculated with these small cluster models are presented in Table 2. The geometries of the clusters were optimized within the symmetry of the rutile structure. In model *B*, there are one or two more degrees of freedom for oxygen atoms in nonlattice positions. For the cluster–water systems, the Cartesian coordinates of all water atoms, the two surface atoms close to the oxygen atom, and the hydrogen atom of water are optimized. The adsorption energy is calculated as the difference in the total energies of the isolated systems and the cluster–H_2O system. Therefore, positive values indicate stabilization.

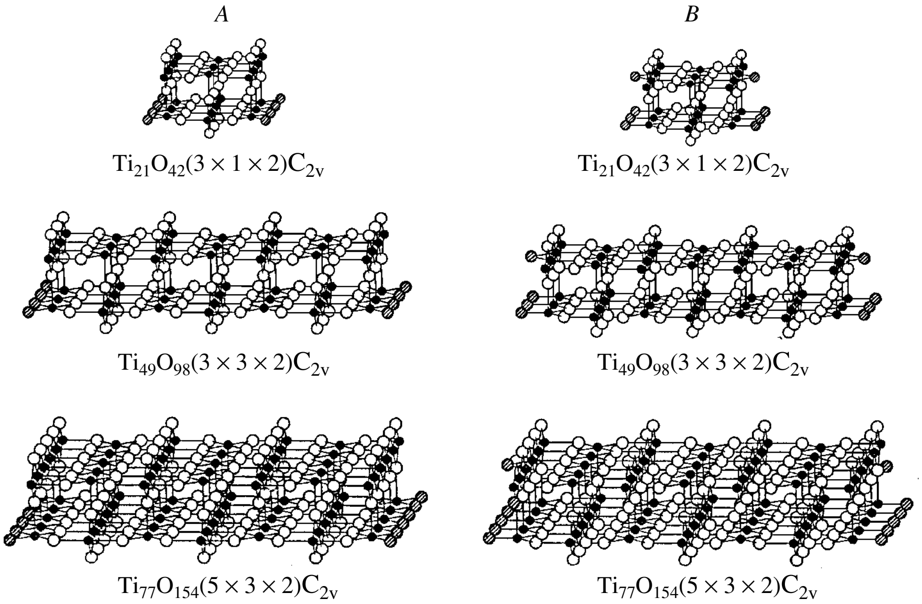

$Ti_{21}O_{42}(3 \times 1 \times 2)C_{2v}$ $Ti_{21}O_{42}(3 \times 1 \times 2)C_{2v}$

$Ti_{49}O_{98}(3 \times 3 \times 2)C_{2v}$ $Ti_{49}O_{98}(3 \times 3 \times 2)C_{2v}$

$Ti_{77}O_{154}(5 \times 3 \times 2)C_{2v}$ $Ti_{77}O_{154}(5 \times 3 \times 2)C_{2v}$

Fig. 8. Rutile (110) surfaces of size 3 × 1, 3 × 3, and 5 × 3 simulated with two-layer clusters of types *A* and *B*. Black spheres are Ti and white spheres are O; shaded spheres are additional O added to achieve stoichiometry. The structure drawings were performed with SCHAKAL97.

A comparison is made with the results of the calculations on a much larger cluster, $Ti_{49}O_{98}$ (Fig. 8), which is a better representation of the surface. From Table 2, it can be seen that the different distribution of additional oxygen atoms in clusters *A* and *B* has a substantial influence on the calculated adsorption energies. The variation of adsorption energy with an increasing number of layers is significantly reduced if model *B* is considered. Even for rather small systems, the adsorption energies are relatively close to that of the largest cluster, $Ti_{49}O_{98}$. The most important difference between the two models is that only for model *B* is the dissociative adsorption always more stable than that of the molecular form. The relative stability of the two forms of water on the rutile (110) surface is still a matter of debate [36]. We do not want to engage ourselves in this controversy here and instead focus on the convergence of results obtained for clusters with increasing sizes.

A comparison of models *A* and *B* of the largest model ($Ti_{49}O_{98}$) shows that the influence of additional atoms is negligible due to their large distance from the adsorption position. This indicates that, in this case, it is the description of the local environment near the adsorption site rather than the effect of the global polarization of the cluster that is responsible for the differences observed for the smaller clusters.

4. CONCLUSION

The consideration of symmetry in models of crystalline surfaces (infinite slab model and finite MC and CC models) allows us to provide the general criteria for the choice of the MC used to simulate the crystalline surface. Based on the atom distribution in the bulk primitive unit cell over the atomic planes for a given surface orientation, stoichiometric and electroneutral clusters are chosen. As many point symmetry elements of the slab model as possible are retained in the cluster. Surface atoms of the cluster have an equivalent surrounding if they are equivalent in the slab or the CC, except for corners and edges. If the cluster contains several layers, each of them must have the same stoichiometry.

The numerical results for the adsorption behavior of rutile (110) towards water with different clusters demonstrate that convergence to the methodological limit is significantly improved if the criteria suggested are taken into account. Since the underlying considerations are of a general nature, they can also be applied to cluster models of surfaces in other systems.

ACKNOWLEDGMENTS

R.A. Evarestov would like to thank Alexander von Humboldt-Stiftung for the Humboldt Award.

This work was partially supported by the Deutsche Forschungsgemeinschaft.

REFERENCES

1. G. A. Somorjai, *Introduction to Surface Chemistry and Catalysis* (Wiley, New York, 1994).
2. V. E. Henrich and P. A. Cox, *The Surface Science of Metal Oxides* (Cambridge Univ. Press, Cambridge, 1994).

3. J. Sauer, Chem. Rev. **89**, 199 (1989).
4. P. Deák, Phys. Status Solidi B **217**, 9 (2000).
5. R. A. Evarestov and V. P. Smirnov, *Site Symmetry in Crystals: Theory and Applications* (Springer-Verlag, Berlin, 1997, 2nd ed.).
6. C. Pisani, in *Quantum-Mechanical Ab-Initio Calculation of the Properties of Crystalline Materials*, Ed. by C. Pisani (Springer-Verlag, Berlin, 1996).
7. T. Bredow and G. Pacchioni, Surf. Sci. **426**, 106 (1999).
8. P. J. D. Lindan, J. Muscat, S. Bates, *et al.*, Faraday Discuss. **106**, 135 (1997).
9. R. A. Evarestov and V. P. Smirnov, J. Phys.: Condens. Matter **9**, 3023 (1997).
10. A. Lichanot, C. Zarrieu, C. Zicovich-Wilson, *et al.*, J. Phys. Chem. Solids **59**, 1119 (1998).
11. W. C. Mackrodt and E. A. Williamson, Philos. Mag. B **77**, 1077 (1998).
12. A. J. Bennet, B. McCarrol, and R. P. Messmer, Surf. Sci. **24**, 191 (1971); Phys. Rev. B **3**, 1397 (1971).
13. A. M. Dobrotvorskii and R. A. Evarestov, Phys. Status Solidi B **66**, 83 (1974).
14. A. Zunger, J. Chem. Phys. **62**, 1861 (1975); **63**, 1713 (1975).
15. R. A. Evarestov, M. I. Petrashen, and E. M. Ledovskaya, Phys. Status Solidi B **76**, 377 (1976).
16. P. Deák, Acta Phys. Acad. Sci. Hung. **50**, 247 (1981).
17. R. A. Evarestov, A. V. Leko, and V. P. Smirnov, Phys. Status Solidi B **128**, 275 (1985).
18. J. Stewart, J. Comput. Chem. **19**, 168 (1998).
19. J. Noga, P. Bańacký, S. Biskupič, *et al.*, J. Comput. Chem. **20**, 253 (1999).
20. T. Bredow and R. A. Evarestov, Phys. Status Solidi B **220**, R5 (2000).
21. P. Persson, A. Stashans, R. Bergström, and S. Lunell, Int. J. Quantum Chem. **70**, 1055 (1998).
22. C. Pisani, J. Mol. Struct.: THEOCHEM **463**, 125 (1999).
23. K. Jug, Int. J. Quantum Chem. **58**, 283 (1996).
24. T. Bredow, G. Geudtner, and K. Jug, J. Chem. Phys. **105**, 6395 (1996).
25. V. A. Tikhomirov, G. Geudtner, and K. Jug, J. Phys. Chem. B **101**, 10398 (1997).
26. U. Gutdeutsch, U. Birkenheuer, S. Krüger, and N. Rösch, J. Chem. Phys. **106**, 6020 (1997).
27. C. Pisani, S. Casassa, and F. Corà, Comput. Phys. Commun. **82**, 139 (1994).
28. T. Bredow and K. Jug, Surf. Sci. **327**, 398 (1995).
29. T. Bredow, Surf. Sci. **401**, 82 (1998).
30. A. Hagfeldt, H. Siegbahn, S.-E. Lindquist, and S. Lunell, Int. J. Quantum Chem. **44**, 477 (1992).
31. G. Pacchioni, A. M. Ferrari, and P. S. Bagus, Surf. Sci. **350**, 159 (1996).
32. P. Reinhardt, M. Causà, C. M. Marian, and B. A. Heβ, Phys. Rev. B **54**, 14812 (1996).
33. K. Jug and G. Geudtner, J. Mol. Catal. A: Chem. **119**, 143 (1997).
34. F. Rittner, R. Fink, B. Boddenberg, and V. Staemmler, Phys. Rev. B **57**, 4160 (1998).
35. M. A. San Miguel, C. J. Calzado, and J. F. Sanz, Int. J. Quantum Chem. **70**, 351 (1998).
36. E. V. Stefanovich and T. N. Truong, Chem. Phys. Lett. **299**, 623 (1999).
37. M. Casarin, C. Maccato, and A. Vittadini, Appl. Surf. Sci. **142**, 196 (1999).
38. H. Kobayashi and M. Yamaguchi, Surf. Sci. **214**, 466 (1989).
39. K. D. Schierbaum and W.-X. Xu, Int. J. Quantum Chem. **57**, 1121 (1996).
40. B. Ahlswede and K. Jug, J. Comput. Chem. **20**, 563 (1999).

Physics of the Solid State, Vol. 43, No. 9, 2001, pp. 1783–1787. Translated from Fizika Tverdogo Tela, Vol. 43, No. 9, 2001, pp. 1710–1714.
Original Russian Text Copyright © 2001 by Davydov.

Electron-Stimulated Desorption of Europium Atoms from the Surface of Oxidized Tungsten

S. Yu. Davydov
St. Petersburg State Electrotechnical University, St. Petersburg, 197376 Russia

Received January 30, 2001

Abstract—An analysis of the yield q of europium atoms is made, and scenarios of electron-stimulated desorption are put forward. Expressions are obtained for the dependence of q on the coverage of oxidized tungsten by europium atoms. © *2001 MAIK “Nauka/Interperiodica”.*

1. INTRODUCTION

Electron-stimulated desorption (ESD) of europium atoms from an oxidized (oxygen-monolayer-covered) tungsten (O/W) surface was studied earlier [1]. It was found that, in contrast to the previously well-investigated ESD of alkali metals from the O/W surface [2, 3], the dependence of the europium atom yield q on the incident electron energy E_e exhibits a clearly pronounced resonant character. To account for the features revealed in the study, an energy diagram of the Eu–O/W system was proposed for low and high europium adatom concentrations Θ [4]. It was shown, in particular, that at low (close to zero) coverages of the oxidized tungsten surface by europium, the Eu ion charge is $Z_0(\text{Eu}) \approx 0.75$, whereas the charge of the oxygen ion immediately beneath it is $\tilde{Z}_0(\text{O}) \sim -1$. (In the absence of adsorbed europium, the oxygen ion charge is $Z(O) \sim 0$). At high coverages ($\Theta \geq 0.5$), the europium atom charge is close to zero because of depolarization, i.e., $Z_1(\text{Eu}) \sim 0$, and, hence, the oxygen ions located under the Eu layer have the same charge as those in the O/W system, i.e., $\tilde{Z}_1(\text{O}) \sim 0$. To interpret some of the results obtained in [1], we shall use the scenario put forward in [4].

2. WHY THE OXYGEN MECHANISM OF ESD DOES NOT OPERATE IN THE CASE OF EUROPIUM AND BARIUM

The first question that should be answered is why the so-called oxygen mechanism of ESD is not operative in the case of europium (as well as of barium [5])?

In order to explain the ESD of alkali metal neutrals from an oxidized surface of high-melting substrates at low coverages (the case where oxygen can be considered to be in the O^- state and the alkali metal, in the form of M^+), Ageev *et al.* [1–3, 5] developed the oxygen mechanism of ESD. By this mechanism one understands the following scenario: (a) the primary electron creates a vacancy at the 2*s* level of the oxygen ion O^-; (b) this vacancy is occupied by an electron from the 2*p* oxygen level, and the corresponding Auger electron neutralizes the adsorbed alkali-metal ion M^+ ($\text{O}^- \longrightarrow \text{O}^+$; $\text{M}^+ \longrightarrow \text{M}^0$); and (c) if the O^+ ion thus formed regains its negative charge (by capturing electrons from the metal substrate, i.e., $\text{O}^+ \longrightarrow \text{O}^-$) faster than the alkali metal atom becomes reionized ($\text{M}^0 \longrightarrow \text{M}^+$), the O^- ion will repel the M^0 atom, forcing it to desorb.

Consider items (a) and (b) of the above scenario in more detail. Let $\varepsilon_a^{(0)}$ be the single-particle energy of the outer *s*-electron of the metal atom reckoned from the vacuum level. For an alkali metal atom with one outer *s* electron in the ground state, $\varepsilon_a^{(0)} = -I_1$, where I_1 is the ionization energy of a single-electron atom. In accordance with the unrestricted Hartree–Fock treatment [6], for a two-electron atom (i.e., an atom with a filled outer *s* shell), the ground-state energy is $E_a^0 = 2\varepsilon_a^{(0)} + U$, where U is the intratomic Coulomb repulsion energy of electrons in the *s* shell [$E_a^0 = -I_2^{(1)}$, where $I_2^{(1)}$ is the first ionization potential of the two-electron atom]. The energy U can be calculated as the difference between the second, $I_2^{(2)}$, and the first, $I_2^{(1)}$, ionization potentials. Using the data quoted in [7], we come to $U = 5.57$ and 4.79 eV and $\varepsilon_a^0 = -2.36$ and -1.77 eV for europium and barium, respectively.

Taking into account the Coulomb level shift Δ due to the interaction of the adatom electrons with the electrons of the metal substrate, whose magnitude can be estimated from the simple expression [8]

$$\Delta = \frac{e^2}{4(2r_\text{O} + r_a)}, \qquad (1)$$

where r_O and r_a are the atomic radii of the oxygen and the adatom (the image plane is matched to the surface of the metal substrate), one obtains the following relation for the position of the single-particle adatom level relative to the substrate Fermi level:

$$\tilde{\varepsilon}_a^{(0)} = \varepsilon_a^{(0)} + \Delta + \varphi, \quad (2)$$

where φ is the work function of the oxidized metal substrate.

Following [9], we take into account the Coulomb attraction V between the hole left at the oxygen ion after the escape of the Auger electron and this electron trapped by the metal adatom ion (the exciton mechanism). In this way, we obtain the following resultant energies ε_a^1 and ε_a^2 of the s level being filled for single-electron (alkali metal) and two-electron (barium, europium) adatoms, respectively:

$$\varepsilon_a^1 = \tilde{\varepsilon}_a^0 - V, \quad \varepsilon_a^2 = \tilde{\varepsilon}_a^0 + U - V. \quad (3)$$

These relations were derived under the assumption that, following [9], the levels are infinitely narrow, the oxygen has one hole, and the adatom has an extra electron. If the ε_a^1 and ε_a^2 levels lie below the Fermi level, i.e., they are negative, this state is stable. (The last statement is valid for the outer-electron levels only. The system as a whole is in an excited state because of the core hole and, thus, has a finite lifetime.) Otherwise, an electron transition from the oxygen to the metal adatom is energetically unfavorable.

To estimate the energy V, we use the screened potential (the Yukawa potential) [10]

$$V = \frac{e^2}{r_{\mathrm{O}} + r_a}\exp[-(r_{\mathrm{O}} + r_a)/l_s], \quad (4)$$

where the surface screening length is $l_s \sim v_{\mathrm{F}}(2\pi/\omega_s)$, v_{F} is the electron velocity at the Fermi level, and ω_s is the surface plasmon frequency. Note that the metal substrate parameters used in our estimates are only the substrate work function φ_0 (the work function of an oxidized surface $\varphi = \varphi_0 + \Delta\varphi > \varphi_0$) and l_s. For a typical metal, $l_s \sim 0.7$ Å [10].

Taking the atomic radii from [11] and setting $\varphi = 5.5$ eV ($\varphi_0 \approx 4.5$ eV [11], $\Delta\varphi \approx 1$ eV [12]), we obtain $V = 0.74$ and 0.60 eV and $\Delta = 1.02$ and 0.97 eV for Eu and Ba, respectively. Thus, we find $\varepsilon_a^2 = 3.49$ and 3.40 eV (for europium and barium, respectively), i.e., essentially positive values, which means that electron transfer to the second s orbital is unfavorable. It should also be stressed that the s shell of a two-electron atom that already has one electron in it can only accept an electron of opposite spin. Thus, the Pauli principle likewise does not favor realization of the oxygen mechanism in a two-electron atom.

For comparison, the same ESD processes calculated, for instance, for adsorbed sodium, yield $\varepsilon_a^{(0)} = -5.14$, $\Delta = 1.27$, $V = 3.40$, and $\varepsilon_a^1 = -1.77$ eV, so that filling of an empty s shell by one electron is energetically favorable.

At high coverages, metal adatoms (both single- and two-electron) reside in a virtually neutral state, which is certain to preclude realization of the oxygen ESD mechanism for a two-electron atom.

3. POSSIBLE MECHANISMS FOR ESD OF EUROPIUM ATOMS

A second essential difference of the europium ESD from the well-studied ESD of alkali metals from the O/W surface [2, 3] consists in that the dependences of the europium atom yield q on the incident electron energy E_e exhibit a distinct resonant character. At low but, as shown experimentally, finite coverages (see [1, Fig. 1]), $\Theta \approx 0.07$, europium atoms are observed to desorb at $(E_e)_{\mathrm{th}} = 25$ eV (threshold energy). As the incident electron energy increases, a peak appears in the $q(E_e)$ spectrum at $E_e \approx 33$ eV, and increasing the coverage to $\Theta \approx 0.35$ brings about the formation of a peak at $E_e \approx 37$ eV. Both the ESD threshold of the Eu neutrals and the above peaks are related [1] to the ionization of the europium $5p$ levels at an energy $E(O_3) = 26$ eV (here and subsequently, the energies of the O and L shells are given for free atoms from the data of [7]). Note, however, that the oxygen term $E(L_1) = 28.5$ eV ($2s$ state) and the europium term $E(O_2) = 30$ eV ($5p$) have similar energies. The peak at 37 eV can be related to the tungsten term $E(O_3) = 41$ eV and europium term $E(O_1) = 45$ eV ($5s$). As the Eu surface concentration Θ (coverage) increases, peaks at 50 and 80 eV appear in the $q(E_e)$ spectrum; they are apparently associated with the corresponding tungsten terms $E(O_2) = 51$ eV and $E(O_1) = 80$ eV. Thus, viewed from the purely energy standpoint, there is a set of terms (particularly if one takes into account the possible chemical shifts) which can be involved in the ESD of Eu atoms.

The Eu ESD mechanism operating at low coverages can be associated with the ionization of the europium $5p$ levels, formation of the Eu^{2+} ion, and its motion (because of the Coulomb attraction) toward the surface, with its subsequent neutralization and desorption in the neutral state Eu^0 [1]. This scenario of the process is in agreement with our energy estimates [4]. Indeed, at low coverages, a Eu^{1+}–O^{1-} pair exists in an equilibrium state. An incident electron ionizes the $5p$ level of the europium ion by transferring the knocked-out electron to an oxygen ion, which produces an Eu^{2+}–O^{2-} pair (the electron transfers into the oxygen p band [4] while remaining localized beneath the europium atom as a result of Coulomb attraction). The O^{2-} state is apparently energetically unfavorable; i.e., it is unstable with a lifetime τ_1, primarily because of the Coulomb repulsion U_1 of electrons at the oxygen ion ($U_1 = 14.47$ eV [13]).

As a result of the charge doubling of the europium and oxygen ions, they should start to approach one another. Let us estimate first the Eu^0–O^0, Eu^{1+}–O^{1-}, and Eu^{2+}–O^{2-} bond lengths using the values of the atomic and ionic radii of oxygen [$r(O^0) = 0.74$ Å, $r(O^{2-}) = 1.36$ Å, $r(O^{1-}) = 1.76$ Å] and europium [$r(Eu^0) = 2.04$ Å, $r(Eu^{3+}) = 0.95$ Å] [11]; unfortunately, we do not know the ionic radii of Eu^{1+} and Eu^{2+}. This yields, for the bond lengths, $d_0 \equiv d(Eu^0\text{–}O^0) = 2.78$, $2.71 < d_1 \equiv d(Eu^{1+}\text{–}O^{1-}) < 3.80$, $2.31 < d_{12} \equiv d(Eu^{1+}\text{–}O^{2-}) < 3.40$, and $2.31 < d_2 \equiv d(Eu^{2+}\text{–}O^{2-}) < 3.40$ (all the distances are given in Å). The lower estimate of d was derived from the value of $r(Eu^{3+})$; the upper one, from $r(Eu^0)$.

If we assume that in moving toward one another the Eu^{2+} and O^{2-} ions approach a distance $d^* \sim d_0 < d_1$ and become neutralized, then in their reverse motion they will drift by inertia to a distance in excess of d_1, and, if its stored kinetic energy is large enough, the Eu^0 atom will be able to surmount the potential barrier and desorb (see, e.g., the discussion of the desorption mechanism by Antonevich in [3]). The necessary condition for the ESD of neutrals is that, first, the lifetime τ_{22} of the Eu^{2+}–O^{2-} excited state be much longer than the time $\bar{\tau}_{22}$ needed to approach the neutralization point and, second, the lifetime τ_{00} of the Eu^0–O^0 state (which is likewise unstable at low coverages) exceed the desorption time τ_{des}, i.e., the time taken by an Eu atom to overcome the potential barrier.

We now estimate the $\bar{\tau}_{22}$ time. In the initial state corresponding to the interionic separation d_1 (the Franck–Condon transition [3]) and to the Eu^{2+}–O^{2-} charge state, the energy of the pair is $-Z_1Z_2e^2/d_1$, where Z_1 and Z_2 are the absolute values of the europium and oxygen ionic charges, respectively (for the sake of simplicity, the image charges are neglected). In the final state, at a distance d_0 from one another, these ions possess the energy $-Z_1Z_2e^2/d_0 + Mv^2/2$, where M is the atomic mass of europium (the oxygen ion is considered to be fixed at the surface) and v is its velocity at the instant of neutralization. Estimates yield $v = 3.76 \times 10^{13}$ Å/s. Hence, the distance $\Delta S = d_1 - d_0 = 1.02$ Å is traversed by a Eu^{2+} ion in a time $\tau_{22} \sim 2.7 \times 10^{-14}$ s. This time coincides in order of magnitude with the lifetime of two-hole states in narrow bands [3, 14]. Based on electron–hole symmetry, one can assume that $\tau_{22} \sim 10^{-14}$ s. Because Eu atoms do desorb, we have to set $\tau_{22} > \bar{\tau}_{22}$.

The fact that europium neutrals do not desorb (at low coverages) if the tungsten inner electron levels (5*p* and 5*s*) are ionized can be explained in the following way. Ionization produces an Eu^{1+}–O^{2-} pair separated by a distance d_1. The lifetime τ_{12} of this unstable state is of the same order of magnitude as τ_{22}, because the instability is due, in our opinion, to the O^{2-} ion. On the other hand, the time $\bar{\tau}_{12}$ required for the above motion of ions (approaching d_0 with subsequent neutralization) should be longer than $\bar{\tau}_{22}$ by a factor of $\sqrt{2}$, because the electrostatic attraction between the ions in this case is only half of what it was in the beginning. Thus, it appears probable that $\tau_{12} < \bar{\tau}_{12}$ and Eu^0 will not desorb.

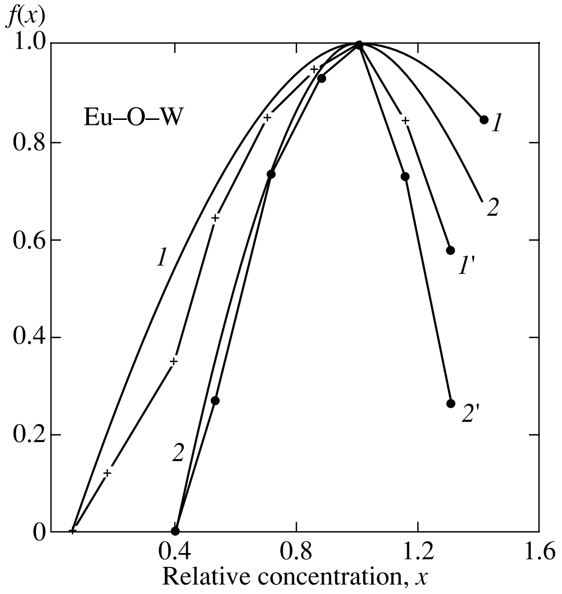

(*1*, *2*) Theoretical and (*1'*, *2'*) experimental dependences of normalized europium atom yield $f(x)$ on the relative adatom surface concentration x. E_e = (*1*, *1'*) 50 and (*2*, *2'*) 80 eV.

We now consider high coverages. One should discriminate here between the two cases of surface filling by adatoms, namely, a uniform (a distinct coherent structure or a totally disordered layer with adatoms occupying random positions) and a nonuniform one, where adatoms can form clusters, chains, or two-dimensional islands [15, 16]. In the case of nonuniform surface filling, the integrated coverage Θ_{int} (which is the ratio of the area occupied by all islands to that of the substrate) can constitute only a few tenths, whereas for the adatoms residing inside an island, the local coverage is $\Theta_{loc} = 1$. For chains which are formed, for instance, by the adatoms of La, Gd, and Dy on W(112) [15, 16], one can assume $\Theta_{loc} \approx 0.5$. We shall further assume that the peak at 33 eV disappears and the peaks at 50 and 80 eV appear when Θ_{loc} can be considered large and when the local band structure is like that shown in [4, Fig. 1b].

It is now easy to understand why europium atoms do not desorb at $E_e \approx 33$ eV at high local coverages; indeed, ionization of the europium 5*p* level gives rise to the formation of a surface ion pair Eu^{1+}–O^{1-}, which is unstable at high coverages. The formation of a charge drives the ions toward one another with a force only one forth that in the case of the Eu^{2+}–O^{2-} pair and one half that for Eu^{1+}–O^{2-}. In this case, the time taken by the motion will be $\bar{\tau}_{22} = \bar{\tau}_2/\sqrt{2} = \bar{\tau}_{11}/2$. On the other hand, it is well known [14] that the lifetime of a two-hole state in a narrow band exceeds by far that of the one-hole one, the state that is realized in the process under consideration: $\tau_{11} < \tau_{22} \sim \tau_{12}$. Hence, in this case, no Eu^0 desorption should take place.[1]

On the other hand, electron transfer from the inner electron 5*p* and 5*s* levels of tungsten into the practically empty oxygen band results in the formation of an Eu^0–O^{1-} pair. Because the oxygen radius increases in the $O^0 \longrightarrow O^{1-}$ transition, the europium atom experiences repulsion and desorbs as a neutral.

Note that the resonant features in the $q^0(E_e)$ curve at the E_e energies of 40 and 70 eV and corresponding coverages were also observed in the ESD of potassium, cesium [20], and sodium [21] from a molybdenum surface coated by an oxygen monolayer; this was assigned to the ionization of the 4*s* and 4*p* levels of Mo. The amplitude of the peaks increased with coverage, and for Na, the resonant features became observable only for $\Theta \geq 0.5$. These observations differ, however, qualitatively from the data on europium ESD [5] in that the resonant peaks reported in [20, 21] are superposed on the yield q^0 of neutrals, which increases monotonically with increasing E_e. It is believed [20] that this monotonic growth of q^0 is associated with the 2*s* ionization of adsorbed oxygen, which, as shown in Section 2, is not observed to occur in the case of europium ESD.

Unfortunately, it would be extremely difficult to make more or less rigorous numerical estimates of the lifetimes of the above-mentioned nonequilibrium states and of the ion motion processes. Moreover, considering that the kinematics of a particle immediately preceding its desorption is not observed experimentally, any model of the process we could build would be largely speculative, because one will never be able to exclude the possibility that some other model would yield the same result. The only way out of this situation lies in analyzing experiments like (i) the ESD of a number of rare-earth elements from the same substrate and (ii) the ESD of some rare-earth elements from different substrates. These experiments have thus far not been made.

4. CONCENTRATION DEPENDENCES OF THE EUROPIUM ATOM YIELD

Let us turn now to a description of the dependence of the europium atom yield q on coverage Θ for two values of the bombarding electron energy, $E_e = 50$ and 80 eV [1, Fig. 2]. The theory of the $q(\Theta)$ relation developed in [22, 23] for both ions and neutrals took into account the dependence of the charge exchange of the escaping particle on the width of the surface band formed by them, which, in turn, depends on the coverage Θ. However, the quoted publications considered the ESD of alkali metals where the particles start to desorb already from zero coverage. The universal function describing the $q(\Theta)$ relation, $f(x) \equiv q(\Theta)/q_{max}(\hat{\Theta})$, where $\hat{\Theta}$ is the coverage at which the particle yield q reaches its maximum value q_{max}, is given by the expression

$$f(x) = x\exp[(1-x^{\alpha})/\alpha], \quad x \equiv \Theta/\hat{\Theta}. \tag{5}$$

Here, $\alpha = 1$ for a disordered and $\alpha = 2$ for an ordered structure of the adsorbed layer.

Unlike the alkali metals, the yield q of europium atoms starts above a certain threshold coverage Θ_{th}, which is 0.07 and 0.35 for $E_e = 50$ and 80 eV, respectively [1]. Therefore, in order to describe the Eu yield by means of function (5), we introduce, in place of x, a new variable,

$$\zeta = \frac{x - x_{th}}{1 - x_{th}}, \text{ where } x_{th} \equiv \Theta/\Theta_{th}, \tag{6}$$

and assume $f(\zeta) \equiv 0$ for $\zeta \leq 0$. The results of calculations made for an ordered europium adatom film ($\alpha = 2$) are presented graphically in the figure.[2] The agreement with the experimental data for $x \leq 1$ is very good. The disagreement between the theory and experiment for $x > 1$ is in no way unexpected, because the maxima in the $q(\Theta)$ curves obtained for both values of the energy E_e correspond to monolayer coverage, i.e., $\hat{\Theta} = 1$ [1] or $x = 1$, whereas the theory of the concentration dependence of the ESD yield was developed only for submonolayer ($0 \leq \Theta \leq 1$) coverages [22, 23].

5. CONCLUSION

We note in conclusion that despite the crudeness of the estimates made in this work, one can make the following statement. The ESD of Eu neutrals from oxidized tungsten has a specific feature in that the electron knocked out from the inner shells of europium or tungsten will be inevitably localized in the surface band formed by the oxygen monolayer and the adsorbed europium atoms. It is this factor that is responsible for the resonant character of the Eu atom yield $q(E_e)$ on the energy of the electrons stimulating the desorption.

---

[1] In principle, one can also conceive here another process, in which, instead of the hole in the Eu 5*p* level being filled by an outer electron of the same atom, a screening charge supplied by other europium atoms spreads to fill the first unoccupied orbital of europium (see, e.g., [17–19]). The screened Eu ion becomes now, as it were, a Gd atom, which has a smaller atomic radius. Thus, there is no momentum needed to desorb the europium atom.

[2] We have limited ourselves only to this case, because the agreement with experimental data for a disordered film is worse.

ACKNOWLEDGMENTS

The author is indebted to V.N. Ageev, Yu.A. Kuznetsov, and N.D. Potekhina for useful discussions.

This study was supported by the Russian Foundation for Basic Research, project no. 99-02-17972, within the frame of the Russian State program "Surface Atomic Structures," project no. 4.5.99.

REFERENCES

1. V. N. Ageev and Yu. A. Kuznetsov, Pis'ma Zh. Tekh. Fiz. **26** (13), 86 (2000) [Tech. Phys. Lett. **26**, 579 (2000)].
2. V. N. Ageev, O. P. Burmistrova, and Yu. A. Kuznetsov, Usp. Fiz. Nauk **158** (3), 389 (1989) [Sov. Phys. Usp. **32**, 588 (1989)].
3. V. N. Ageev, Prog. Surf. Sci. **47** (1/2), 55 (1994).
4. S. Yu. Davydov, Pis'ma Zh. Tekh. Fiz. **27** (7), 68 (2001) [Tech. Phys. Lett. **27**, 295 (2001)].
5. V. N. Ageev, Yu. A. Kuznetsov, and N. D. Potekhina, Surf. Sci. **367** (1/2), 113 (1996).
6. P. W. Anderson, Phys. Rev. **124** (1), 41 (1961).
7. A. A. Radtsig and B. M. Smirnov, *Reference Data on Atoms, Molecules, and Ions* (Énergoatomizdat, Moscow, 1986; Springer-Verlag, Berlin, 1985).
8. J. W. Gadzuk, Phys. Rev. B **1** (5), 2110 (1970).
9. J. W. Gadzuk and S. Doniach, Surf. Sci. **77** (3), 427 (1978).
10. N. H. March and M. Parrinello, *Collective Effects in Solids and Liquids* (Hilger, Bristol, 1982; Mir, Moscow, 1986).
11. *Physical Quantities: Handbook*, Ed. by I. S. Grigor'ev and E. Z. Meĭlikhov (Énergoizdat, Moscow, 1991).
12. E. V. Klimenko and A. G. Naumovets, Zh. Tekh. Fiz. **49** (6), 1282 (1979) [Sov. Phys. Tech. Phys. **24**, 710 (1979)].
13. W. A. Harrison, Phys. Rev. B **31** (4), 2121 (1985).
14. P. J. Feibelman, Surf. Sci. **102** (2/3), L51 (1981).
15. O. M. Braun and V. K. Medvedev, Usp. Fiz. Nauk **157** (4), 631 (1989) [Sov. Phys. Usp. **32**, 328 (1989)].
16. L. A. Bol'shov, A. P. Napartovich, A. G. Naumovets, and A. G. Fedorus, Usp. Fiz. Nauk **122** (1), 125 (1977) [Sov. Phys. Usp. **20**, 432 (1977)].
17. O. Gunnarson and K. Schonhammer, Solid State Commun. **26** (3), 147 (1978).
18. O. Gunnarson and K. Schonhammer, Phys. Rev. B **22** (8), 3710 (1980).
19. R. Murphy, E. W. Plummer, C. T. Chen, *et al.*, Phys. Rev. B **39** (11), 7517 (1989).
20. V. N. Ageev and Yu. A. Kuznetsov, Fiz. Tverd. Tela (St. Petersburg) **39** (4), 758 (1997) [Phys. Solid State **39**, 671 (1997)].
21. V. N. Ageev and Yu. A. Kuznetsov, Fiz. Tverd. Tela (St. Petersburg) **40** (4), 768 (1998) [Phys. Solid State **40**, 707 (1998)].
22. S. Y. Davydov, Surf. Sci. **407** (1–3), L652 (1998).
23. S. Y. Davydov, Surf. Sci. **411** (1–3), L878 (1998).

Translated by G. Skrebtsov

Physics of the Solid State, Vol. 43, No. 9, 2001, pp. 1788–1793. Translated from Fizika Tverdogo Tela, Vol. 43, No. 9, 2001, pp. 1715–1720.
Original Russian Text Copyright © 2001 by Pronin, Gomoyunova, Valdaĭtsev, Faradzhev.

LOW-DIMENSIONAL SYSTEMS AND SURFACE PHYSICS

Initial Stages in the Intercalation of $1T$–TiS_2(0001) Single Crystals by Potassium

I. I. Pronin, M. V. Gomoyunova, D. A. Valdaĭtsev, and N. S. Faradzhev

Ioffe Physicotechnical Institute, Russian Academy of Sciences, ul. Politekhnicheskaya 26, St. Petersburg, 194021 Russia

e-mail: Igor.Pronin@pop.ioffe.rssi.ru

Received February 13, 2001

Abstract—A study is reported of spontaneous intercalation of $1T$–TiS_2(0001) by potassium, which takes place when an alkali metal is deposited on the surface of this layered material. The experiments were carried out in ultrahigh vacuum at room temperature within the 0–10 adsorbate monolayer range. An analysis of electron diffraction patterns visualizing the crystalline structure of the nanometer-scale surface layer of the studied samples showed that penetration of the intercalant into TiS_2 stimulates a $1T \longrightarrow 3R$(I) structural phase transition and brings about a substantial (by 2.2 Å) increase in the interlayer separation in this compound. It was found that the process passes through stages of gradual filling of the interlayer gaps and that this is accompanied by a lateral displacement of the titanium and sulfur layer sandwiches in the original crystal. *© 2001 MAIK “Nauka/Interperiodica”.*

1. INTRODUCTION

The interest in the phenomenon of intercalation, which consists essentially in the penetration of guest atoms and molecules into the interlayer gaps in layered host crystals, stems from the possibility of purposefully modifying the electrical, magnetic, mechanical, adsorptive, catalytic, and other properties of these materials [1–3]. Proper understanding of the nature of the changes this leads to requires a comprehensive investigation into the relations governing the transformation of the crystal structure of intercalated compounds. Until recently, such information was obtained only for the bulk of a crystal. We also primarily studied powder materials prepared through immersion in solutions containing ions of an intercalant, as well as through electrolysis or annealing in intercalant vapor. In the past decade, it has been found possible to achieve spontaneous intercalation of the surface layer in single crystals of transition-metal dichalcogenides (TMDs); this takes place when alkali metal atoms are deposited on them in an ultrahigh vacuum [4–10]. Major attention in these studies was focused on the intercalation-stimulated transformation of the electronic structure of the crystal surface. As for the modification of its atomic structure, it was judged from indirect indications only, and direct structural information obtained *in situ* is extremely scarce. A scanning tunneling microscopy study [11] presented revealing evidence in support of changes in the morphology of the outermost atomic layer of a VSe_2 single crystal occurring in the course of its intercalation by sodium. At the same time, that study did not contain any information on the crystal structure rearrangement initiated by penetration of the intercalant atoms into the surface region of the sample. Such changes were first found to occur in [12, 13], where the process of VSe_2(0001) intercalation by potassium was *in situ* visualized by observing the diffraction patterns produced by medium-energy electrons. It was shown that incorporation of alkali-metal atoms into a crystal gives rise not only to a substantial widening of interlayer gaps in the starting material but also to a structural phase transition from the $1T$–VSe_2 to $3R$(I)–K_xVSe_2 polytype. In [12, 13], however, the initial stages of the process were not investigated in considerable detail; in particular, its dynamics was not revealed.

The subject of the present work is another typical representative of the TMD family, namely, titanium disulfide. The purpose of the investigation was, first, to learn the extent to which the relations found earlier by us for the K/VSe_2 system are of a general nature and, second, to study the mechanism of spontaneous intercalation of TiS_2 by potassium in the very early stages of the process.

2. EXPERIMENTAL

The experimental setup used in the measurements was described in [14]. Its main unit is a special LEED optics instrument permitting one to visualize in real time the crystal structure of the surface layer of a sample under study on a nanometer scale. The method is based on an analysis of spatial distributions of inelastically scattered electrons, which distinctly reveal the maxima produced through the focusing of electrons escaping from the crystal along closely-packed atomic rows [15, 16]. The samples under study were bombarded by a 2-keV electron beam that hit them at a grazing angle of (~80°). The beam current was approximately 10^{-7} A, and its transverse size did not exceed 0.1 mm. The scattering patterns were observed within a cone whose axis was perpendicular to the sample surface, and the vertex angle was 114°. They were measured with the above-mentioned instrument based on a hemispherical, double-grid, retarding-field analyzer with a microchannel image-brightness intensifier. The analyzer transmitted scattered electrons which underwent energy losses $\Delta E < 200$ eV in reflection. The diffraction patterns produced by these electrons could be observed on a luminescent display and were recorded by a digital, computer-interfaced video camera.

The $TiS_2(0001)$ samples studied were prepared in a gas-phase reaction and were identical to those used in [8]. They were approximately $2 \times 2 \times 0.1$ mm in size. The surface cleanness of the single crystals was ensured by cleaving them in vacuum immediately before measurement. The potassium deposition was effected on a room-temperature substrate from an IKO 30-40-15 outgassed getter source. The adsorbate flux was $\sim 5 \times 10^{15}$ atoms/(cm^2 min). The experiments were performed within a metal deposition range of up to 10 monolayers (one monolayer corresponds to a potassium concentration of 10^{15} atoms/cm^2). The surface elemental composition of the samples was monitored using electron Auger spectroscopy. The measurements were made at a pressure of $\sim 5 \times 10^{-10}$ Torr.

3. RESULTS AND DISCUSSION

3.1 Atomic Structure of the Surface Layer of a $TiS_2(0001)$ Single Crystal

Because literature information on the atomic structure of surface layers of $TiS_2(0001)$ is lacking, the first stage of the work was aimed at obtaining such data. Figure 1a displays a typical diffraction pattern of a $TiS_2(0001)$ single crystal with a clean surface. This is shown in a stereographic projection as a two-dimensional intensity distribution of scattered electrons in the polar and azimuthal angles of departure. The pattern is presented in a linear gray-contrast code, in which the most intense electron reflection maxima are given in white and the minima in black. This pattern clearly reveals a diffraction pattern, which implies an ordered structure of the probed surface region. The pattern has a threefold rotation axis characteristic of the $TiS_2(0001)$ face studied and is similar to that observed earlier for $VSe_2(0001)$ [12, 17], which can be accounted for by the crystal structures of these substances having common features. We may recall that both substances crystallize in the 1*T*-CdI_2 structure, in which the atoms are grouped in sandwiches of planes. In the case of TiS_2, these are S–Ti–S sandwiches with titanium atoms located between two sulfur layers [1]. Within the sandwiches, the atoms are bonded by strong ionic covalent forces and the sandwiches themselves are coupled by substantially weaker van der Waals forces; this is what accounts for the layered character of these compounds.

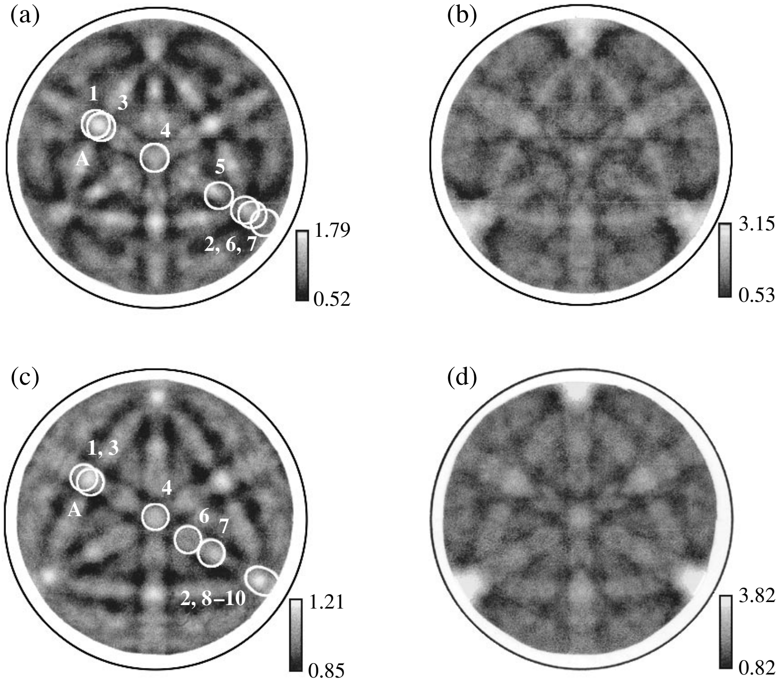

Fig. 1. Electron diffraction patterns measured on (a) a clean and (c) a potassium-saturated $TiS_2(0001)$ crystal at an electron energy of 2 keV. (b) and (d) computer simulations of the patterns (a) and (c), respectively.

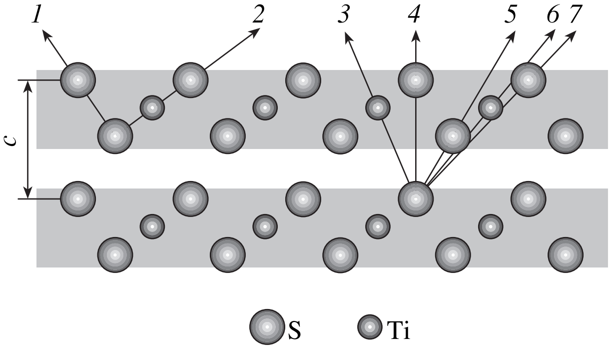

Fig. 2. Schematic representation of the $(\bar{2}110)$ plane perpendicular to the $TiS_2(0001)$ surface. Arrows *1–7* specify various interatomic directions.

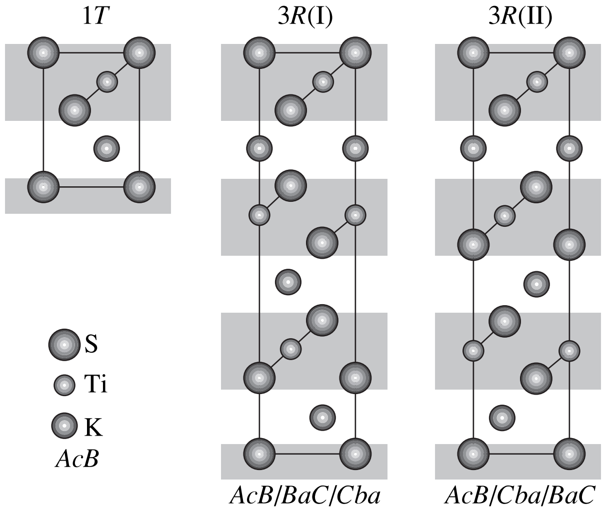

Fig. 3. Schematic representation of the unit cells of the three main polytypes of intercalated TiS_2 cut by the $(\bar{2}110)$ plane.

Figure 2 shows the structure of the most closely packed $(\bar{2}110)$ plane of the TiS_2 crystal, which is perpendicular to the sample plane. As seen from Fig. 1a, it is along this plane or physically equivalent planes that most of the strongest electron reflection maxima are oriented. These maxima form when electrons escape along the atomic chains in the crystal specified by arrows *1–7* in Fig. 2. The spatial orientation of the specified interatomic directions is identified in Fig. 1a by circles. The coincidence of the main maxima in orientation with the given directions suggests convincingly that the pattern does indeed visualize the crystal structure of the studied surface region in real space.

The spatial orientation of the atomic chains was determined using the lattice constants for bulk TiS_2 (a = 3.41 Å, c = 5.70 Å). Therefore, the above-mentioned coincidence between the angular positions of the maxima and the interatomic directions implies that the surface layer of $TiS_2(0001)$ has the same structure as the bulk crystal. This conclusion is supported convincingly by a computer simulation of the observed diffraction pattern, which was carried out in terms of a single-scattering cluster model under variation of the structural parameters of the probed layer. We were looking for the crystal lattice constants (a and c) of a layer approximated by a cluster consisting of about 5000 atoms forming four sandwiches of the planes. The technique of these calculations is described in [15, 16]. The parameters were varied independently within the intervals a = 3.0–3.8 Å and c = 7.5–7.8 Å with a step of 0.05 and 0.1 Å. The calculations were compared with experimental data in a standard way based on reliability factors [13, 18].

The numerical simulation also showed that the best fit of the theory to experimental data is reached in the case where the structural parameters of the surface layer coincide with those of the bulk crystal. The corresponding diffraction pattern is presented in Fig. 1b. We readily see that it reproduces quite well all the main maxima of the experimental pattern, as well as many of its fine structure features, which argues for the correctness of the above conclusion. It should be stressed that it also agrees well with the results of studying the atomic structure of the $VSe_2(0001)$ surface layer [17]. Summing up the data obtained for these two typical representatives of TMDs, we can maintain that the discontinuity in translational symmetry at the crystal–vacuum interface does not bring about any noticeable relaxation in the surface layer, which retains the atomic structure characteristic of the crystal bulk.

3.2. Intercalation-Stimulated Structural Rearrangement of the $TiS_2(0001)$ Surface Layer

Deposition of potassium on the crystal surface noticeably changes the electron scattering pattern. Changes are observed to occur already on deposition of the first potassium monolayer and become ever more pronounced with increasing the amount of the deposited alkali metal. The formation of the new pattern shown in Fig. 1c comes to an end after deposition of approximately five potassium monolayers. At the same time, the K *LMM* Auger line intensity for this state of the sample does not differ from that obtained for coverages of less than one monolayer. Whence it follows that the potassium atoms adsorbing on the crystal penetrate under its surface and initiate structural rearrangement of the probed layer.

Consider now the results obtained in a numerical simulation of the observed diffraction pattern. As for the clean crystal, the simulation was made in single-scattering cluster approximation. In choosing a cluster to approximate the intercalated surface layer, we considered the possibility of existence of structural phase

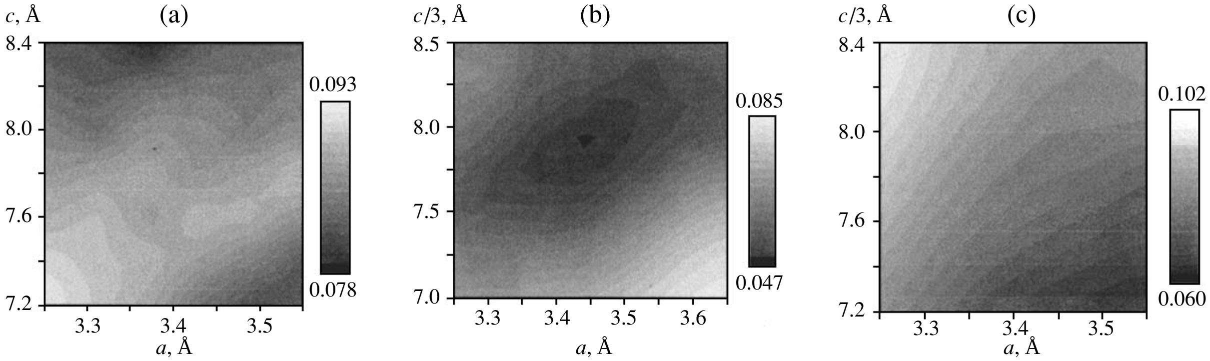

Fig. 4. Two-dimensional contour maps of the R_1 factor showing its dependence on the varied lattice parameters *a* and *c* for the three main polytypes of the intercalated crystal: (a) 1*T*, (b) 3*R*(I), and (c) 3*R*(II).

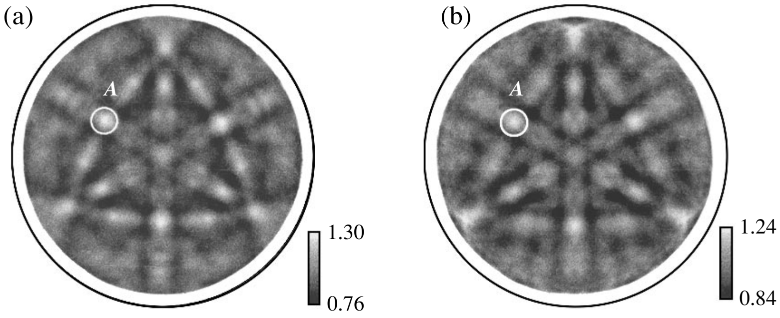

Fig. 5. Electron diffraction patterns measured after deposition of (a) one and (b) three potassium monolayers on the TiS_2 surface.

transitions revealed both in studies of powder materials [1–3] and in the recent *in situ* observation of experiments carried out on single crystals [12, 13]. Therefore, in addition to the possibility of the TiS_2 retaining its original 1*T* structure in the course of intercalation, we also studied its other two main polytypes, 3*R*(I) and 3*R*(II). They differ from the original crystal in the order of their S–Ti–S sandwich stacking. While the 1*T* structure is characterized by the *AcB*/*AcB*… sequence, where the upper-case letters refer to the layers of sulfur and the lower-case letters refer to those of titanium, the 3*R*(I) polytype forms as *AcB*/*BaC*/*CbA*/*AcB*… and the 3*R*(II) polytype forms as *AcB*/*CbA*/*BaC*/*AcB*…. Figure 3 illustrates the unit cells of the above polytypes with the incorporated potassium atoms. Significantly, the intercalant atoms in the two polytypes are seen to feature different coordination in the interlayer gaps; more specifically, in the 1*T* and 3*R*(II) structures, it is octahedral and in the 3*R*(I), it is trigonal-prismatic.

The clusters corresponding to these polytypes consisted of ~5000 atoms of sulfur, titanium, and potassium, which were used to construct four triads of planes sandwiching intercalant atoms. The lattice constants *a* and *c* (*c*/3 for the 3*R*(I) and 3*R*(II) polytypes) were varied independently within the 3.25–3.7 and 5.7–8.5 Å intervals, with steps of 0.05 and 0.1 Å, respectively. As for the Ti–S bond length in the sandwiches, it was assumed, as in [19], to be the same as in the original compound. The diffraction patterns calculated for each pair of unknown structural parameters of the polytypes were quantitatively compared using *R* factors.

The results obtained in this series of calculations are illustrated in Fig. 4, which shows the dependences of the R_1 factor on the variable parameters. They are presented in the form of two-dimensional maps constructed in a gray contrast code. The region of the minimum values of R_1, which corresponds to the best agreement of the theory with the experiment, is shown in black. One readily sees that only the 3*R*(I) model is capable of adequately describing the diffraction pattern observed. Indeed, it is this model (Fig. 4b) that exhibits the deepest minimum localized within the parameter region studied. As for the 1*T* and 3*R*(II) polytypes, the corresponding maps do not exhibit stable minima and the darkest regions (Figs. 4a, 4c) lie in the opposite corners and have typically larger values of the *R* factor. Thus, these data suggest that intercalation of the surface layer of the TiS_2(0001) crystal by potassium atoms brings about a 1*T* ⟶ 3*R*(I) structural phase transition. This occurs through the S–Ti–S layer sandwiches slid-

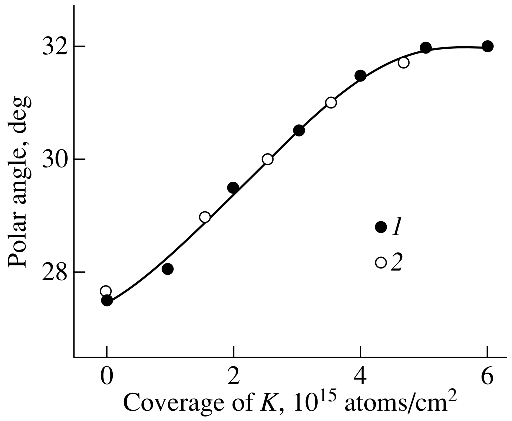

Fig. 6. Angular position of peak *A* in the electron scattering pattern (Fig. 5) versus the amount of potassium deposited on the crystal surface. *1* is the experiment and *2* is a calculation.

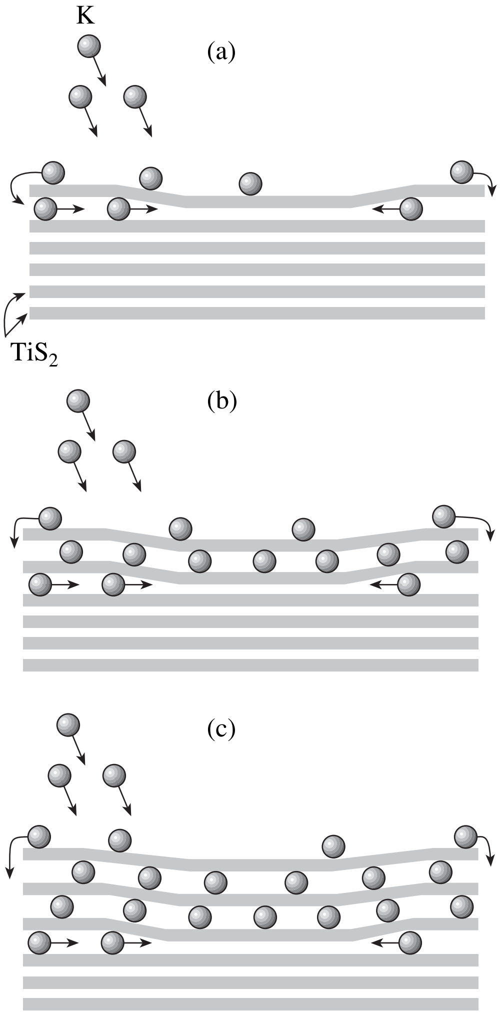

Fig. 7. Schematic illustration of the initial stages in the intercalation of TiS_2 by potassium observed *in situ*. The amount of adsorbate coverage increases in the order of the (a)–(c) figures.

ing with respect to one another and is stimulated by the trigonal-prismatic coordination of potassium atoms in the 3*R*(I) polytype of this compound being apparently energetically more favorable than the octahedral coordination characteristic of the original 1*T* polytype.

The minimum in Fig. 4b is observed at $a = 3.45$ Å and $c/3 = 7.9$ Å. It is these figures that are the lattice constants of the intercalated TiS_2 layer for which we have been looking. The corresponding calculated diffraction pattern is shown in Fig. 1d, and it is seen to be in good agreement with the measurements (Fig. 1c). As follows from a comparison of the values of a and $c/3$ found here and the corresponding values for the original crystal, intercalation very minimally changes the interatomic distance in the planes parallel to the surface. At the same time, the lattice constant in the direction perpendicular to the surface grows sharply. Its change is due in large measure to the considerable increase (by 2.2 Å) in the width of the interlayer gaps, which is initiated by the penetration of the potassium atoms. Note that this value agrees well with the estimate made from the ionic radii of potassium and sulfur. It also fits in with the similar value found by us for the $K/VSe_2(0001)$ system [13], where an intercalation-stimulated structural phase transition $1T \longrightarrow 3R(\mathrm{I})$ was likewise observed. Thus, this relation is common for these two representatives of the TMD family.

3.3. The Mechanism of Atomic Rearrangement in the $TiS_2(0001)$ Surface Layer

This stage of the work was aimed at following *in situ*, step by step, the formation of the new structure, 3*R*(I), in the earliest stages of intercalation. This was done by analyzing in detail the dynamics of the diffraction pattern variation in the course of deposition of the first potassium monolayers on the surface. Two of these patterns are shown in Fig. 5.

One of the most revealing manifestations of the structural rearrangement occurring in the surface layer, which grows in intensity with increasing potassium coverage, is the gradual shift of the main pattern maxima toward larger values of the polar angle of departure of electrons. This is seen particularly clearly when studying the pattern features making up their basic motif in the form of a distinct triangle. In particular, maximum *A*, which is circled in Fig. 5 and lies in the middle of the side of this triangle, shifts by nearly 4° for the coverage range studied (Fig. 6). In addition, as the potassium coverage increases, the spots in the patterns vary in relative intensity and exhibit new features. All these changes account for the formation of the above pattern, which corresponds to the 3*R*(I) polytype.

To reveal the mechanism responsible for these changes, we carried out a computer simulation of the whole family of measured diffraction patterns under the assumption of incomplete intercalation of the probed layer. We analyzed various versions of the surface-layer structure corresponding to different combinations of filling of the interlayer gaps by potassium atoms. In particular, cases were considered where potassium penetrates sequentially into only one, two, three, or four van der Waals gaps closest to the surface or, conversely, where it is distributed uniformly throughout the surface layer. This was done taking into account the probable widening of the interlayer gaps caused by the intercalant atoms. We also considered the cases of the presence and absence of a shift of the adjacent layer sandwiches relative to one another; this presence or absence corresponds to the trigonal-prismatic or octahedral coordination of the potassium atoms in the interlayer gaps, respectively. Indeed, although the former coordination, as follows from the above results for an intercalant-saturated surface layer, is energetically favorable, one cannot exclude the possibility that the $1T \longrightarrow 3R$(I) structural phase transition is of a threshold nature and, thus, occurs only after a certain critical filling of the crystal by potassium has been overcome. As before, the results obtained in the simulation were compared quantitatively with experimental data and optimum structural models for different stages of the process were selected through minimizing the R factors.

The calculations showed convincingly that the observed transformation of the diffraction patterns can be correctly reproduced only by the scenario that assumes sequential filling and widening of the interlayer gaps, starting from the one closest to the surface (Fig. 7). This process propagates gradually into the bulk of the crystal and is accompanied by a lateral displacement of adjacent layers, as a result of which the void geometry in interlayer gaps changes from octahedral to trigonal-prismatic. The calculations performed for this scenario of spontaneous intercalation are illustrated by several points in Fig. 6, which show the angular displacement of peak A in the simulated diffraction patterns in the course of sequential filling of one, two, etc. interlayer gaps with increasing deposition dose. The points obtained for other models of the intercalation-stimulated $TiS_2(0001)$ rearrangement do not fall on the experimental curve of Fig. 6.

4. CONCLUSION

Thus, we have demonstrated the common nature of the main processes governing the intercalation-stimulated structural rearrangement of the surface layers in $TiS_2(0001)$ and $VSe_2(0001)$ single crystals. It has also been shown that the penetration of potassium atoms into TiS_2 starts with gradual filling of the van der Waals gaps in the compound, which initiates a phase transition from the $1T$ to the $3R$(I) structure.

ACKNOWLEDGMENTS

The authors are indebted to H.I. Starnberg for his cooperation.

This study was supported by the Russian Foundation for Basic Research, project no. 99-02-18267.

REFERENCES

1. W. Y. Liang, in *Intercalation in Layered Materials*, Ed. by M. S. Dresselhaus (Plenum, New York, 1986), p. 31.
2. R. Brec and J. Rouxel, in *Intercalation in Layered Materials*, Ed. by M. S. Dresselhaus (Plenum, New York, 1986), p. 93.
3. R. H. Friend and A. D. Yoffe, Adv. Phys. **36**, 1 (1987).
4. F. S. Ohuchi, W. Jaegermann, C. Pettenkofer, and B. A. Parkinson, Langmuir **5**, 439 (1989).
5. A. Schellenberger, W. Jaegermann, C. Pettenkofer, *et al.*, Ber. Bunsenges. Phys. Chem. **96**, 1755 (1992).
6. H. I. Starnberg, H. E. Brauer, L. J. Holleboom, and H. P. Hughes, Phys. Rev. Lett. **70**, 3111 (1993).
7. W. Jaegermann, C. Pettenkofer, A. Schellenberger, *et al.*, Chem. Phys. Lett. **221**, 441 (1994).
8. H. I. Starnberg, H. E. Brauer, and H. P. Hughes, J. Phys.: Condens. Matter **8**, 1229 (1996).
9. H. E. Brauer, H. I. Starnberg, L. J. Holleboom, *et al.*, Phys. Rev. B **58**, 10031 (1998).
10. H. E. Brauer, H. I. Starnberg, L. J. Holleboom, *et al.*, J. Phys.: Condens. Matter **11**, 8957 (1999).
11. H. E. Brauer, I. Ekvall, H. Olin, *et al.*, Phys. Rev. B **55**, 10022 (1997).
12. D. A. Valdaĭtsev, M. V. Gomoyunova, I. I. Pronin, and N. S. Faradzhev, Poverkhnost, No. 5, 44 (2000).
13. I. I. Pronin, M. V. Gomoyunova, N. S. Faradzhev, *et al.*, Surf. Sci. **461**, 137 (2000).
14. I. I. Pronin, D. A. Valdaĭtsev, M. V. Gomoyunova, *et al.*, Zh. Tekh. Fiz. **68** (12), 80 (1998) [Tech. Phys. **43**, 1475 (1998)].
15. N. S. Faradzhev, M. V. Gomoyunova, and I. I. Pronin, Phys. Low-Dimens. Struct. **3/4**, 93 (1997).
16. I. I. Pronin and M. V. Gomoyunova, Prog. Surf. Sci. **59** (1–4), 53 (1998).
17. M. V. Gomoyunova, I. I. Pronin, D. A. Valdaĭtsev, and N. S. Faradzhev, Fiz. Tverd. Tela (St. Petersburg) **42** (3), 542 (2000) [Phys. Solid State **42**, 554 (2000)].
18. R. S. Saiki, A. P. Kaduwela, M. Sagurton, *et al.*, Surf. Sci. **282**, 33 (1993).
19. G. A. Weigers, Physica B & C (Amsterdam) **99**, 151 (1980).

Translated by G. Skrebtsov

Physics of the Solid State, Vol. 43, No. 9, 2001, pp. 1794–1799. Translated from Fizika Tverdogo Tela, Vol. 43, No. 9, 2001, pp. 1721–1726.
Original Russian Text Copyright © 2001 by Kuzubov, Avramov, Ovchinnikov, Varganov, Tomilin.

Electronic and Atomic Structures of the Isomers of Endohedral and Exohedral Fullerene Complexes with Two Lithium Atoms

A. A. Kuzubov*, **, P. V. Avramov*, **, S. G. Ovchinnikov*, **,
S. A. Varganov, and F. N. Tomilin**, *****

**Krasnoyarsk State Technical University, Krasnoyarsk, Russia*
***Kirenskiĭ Institute of Physics, Siberian Division, Russian Academy of Sciences,*
Akademgorodok, Krasnoyarsk, 660036 Russia
****Institute of Chemistry and Chemical Technology, Siberian Division, Russian Academy of Sciences,*
Akademgorodok, Krasnoyarsk, 660036 Russia
e-mail: felix@iph.krasn.ru

Received January 18, 2001

Abstract—The electronic structures of all the possible isomers of endohedral and exohedral C_{60} fullerene complexes with two lithium atoms are theoretically investigated. It is found that the electronic structures of these compounds are characterized by an impurity filled-level state determining the band gap. The location of the impurity state and, correspondingly, the band gap of the exohedral fullerene complexes depend on the coordination mode and the distance between the alkali metal ions. A similar dependence is observed for the total energy of the exohedral fullerene complex under investigation. *© 2001 MAIK “Nauka/Interperiodica”.*

1. INTRODUCTION

Fullerene molecules are capable of forming complexes with metals in which the metal atoms are arranged either inside the carbon cluster sphere (endohedral complex) or outside the fullerene cage (exohedral complex). Since the discovery of fullerenes, a large number of their complexes with metals have been prepared and studied experimentally [1–9].

The effects of the nature and the number of intercalated atoms on the electronic structure of fullerene complexes are widely covered in the literature [9–19]. However, the isomers of fullerene complexes with metals have not been adequately investigated. In recent works [1, 19], exohedral and endohedral fullerene complexes with different numbers of lithium atoms were prepared and studied experimentally and theoretically. Nonetheless, the influence of the lithium coordination in exohedral and endohedral metallocomplexes on their electronic structure is still not clearly understood.

2. METHODS AND OBJECTS OF INVESTIGATION

The calculations were performed by the semiempirical (MNDO) and *ab initio* Hartree–Fock (3-21G basis set) methods using the GAMESS [20] (*ab initio* calculations) and HyperChem 5.02 (semiempirical calculations) program packages.

In this work, we studied all the possible isomers of endohedral and exohedral C_{60} metallocomplexes with two lithium atoms ($Li_2@C_{60}$ and Li_2C_{60}, respectively) (Fig. 1). Among these isomers, we considered only one endohedral complex whose geometry corresponded to the state with the minimum energy. In the endohedral complex (Fig. 1b), the lithium atoms were arranged in the vicinity of the fullerene center along the C_2 axis, thus forming an Li_2 dimer (the distance between the lithium atoms was equal to ~3 Å). Moreover, we calculated 12 different isomers of the exohedral fullerene complex (Figs. 1c–1f). These isomers differed in the arrangement of the metal atoms with respect to particular faces of the carbon polyhedron. To every possible combination of polygons comprising a spherical C_{60} molecule there corresponded a certain mode of the lithium coordination. All the exohedral complexes can be divided into three groups depending on the position of lithium atoms with respect to the polygons forming the fullerene cage. In the first and second groups, alkali metal atoms were coordinated near pentagons (three isomers) and hexagons (five isomers), respectively. In complexes of the third group (four isomers), one lithium atom was placed over a pentagon and the other atom was located over a hexagon. Within each group, the isomers differed in the distance between the polygons near which the metal atoms were coordinated (Figs. 1c–1f). It should be noted that we also investigated exohedral complexes with lithium atoms located near edges and vertices of the carbon polyhedron. However, in the course of geometry optimization, the lithium atoms changed their mutual arrangement and occu-

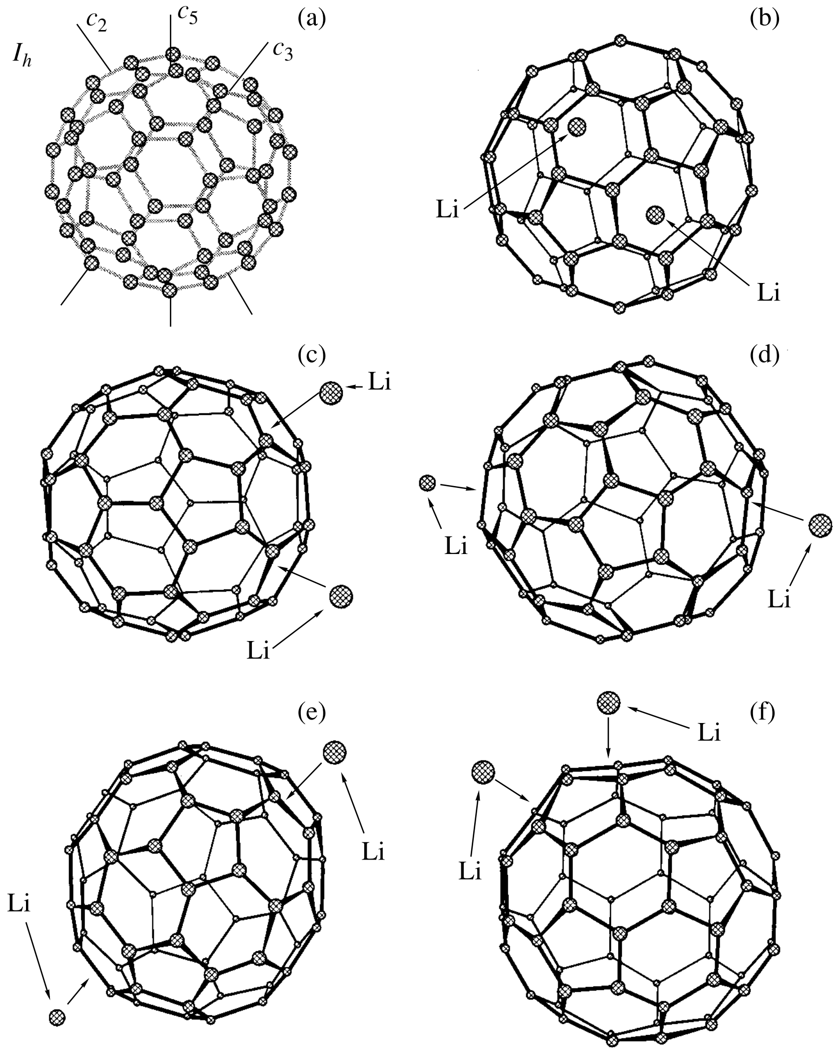

Fig. 1. Structures of a C_{60} molecule and different isomers of the fullerene complexes with two lithium atoms: (a) C_{60} molecule, (b) $Li_2@C_{60}$ endohedral complex, (c) exohedral complex with lithium atoms coordinated over the most closely spaced pentagons, (d) exohedral complex with lithium atoms coordinated over the most widely spaced hexagons, (e) exohedral complex with lithium atoms coordinated over the most widely spaced pentagons, and (f) exohedral complex with lithium atoms coordinated over the most closely spaced hexagons.

pied positions over the centers of the distorted polygons. In this case, the distance between the metal atom and the polygon plane was equal to ~2.3 Å.

Distortion of the high-symmetry carbon cage of the fullerene complex was observed in all the studied isomers. Upon attachment of lithium atoms to the fullerene molecule, the distance between carbon atoms in regular polygons typical of a C_{60} molecule increased differently.

In order to describe the electronic structure of the molecules under investigation, we constructed the total and partial densities of states. The theoretical densities of states were compared with the experimental photoelectron spectra. As follows from a comparison of the spectra of the valence band, the results of the *ab initio* and semiempirical calculations agree well with the experimental spectra. At the same time, the semiempirical methods offer an adequate description of the fullerene geometry, because the interatomic distances and bond angles determined in the semiempirical calculation are in better agreement with the experimental data as compared to the results obtained in the *ab initio* calculation with the 3-21G basis set [19].

The calculations were carried out for both the singlet and triplet states of the fullerene complexes. In all the cases under consideration, the energies of the singlet states of the fullerene complexes were less than those of the triplet states.

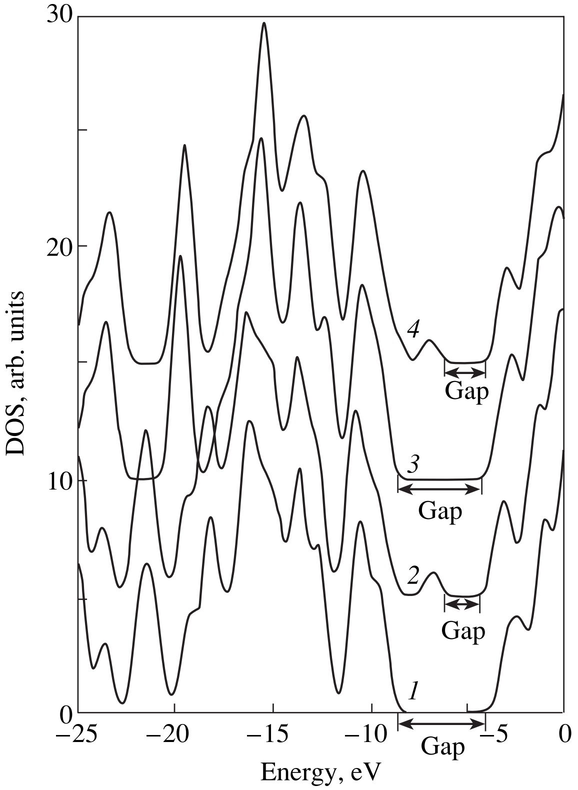

Fig. 2. Total densities of states for (*1*) C_{60}, (*2*) C_{60}^{2-}, (*3*) $Li_2@C_{60}^{2+}$, and (*4*) $Li_2@C_{60}$.

3. RESULTS AND DISCUSSION

The analysis performed in this work revealed considerable differences between the electronic structures of the studied complexes and the electronic structure of the C_{60} molecule. The attachment of lithium atoms to the fullerene molecule led to relief of the multiple degeneracy of the electronic levels, which is characteristic of undoped C_{60} fullerenes. This can be explained by a substantial lowering in the symmetry of the fullerene complexes as compared to the initial high-symmetry C_{60} molecule. Consequently, the previously degenerate energy levels of the carbon cage were grouped into packets in the fullerene complexes. The energy-level separation in each packet was equal to ~0.01–0.5 eV, depending on the symmetry of the isomer. In some cases, this resulted in a mixing of different packets of energy levels at the valence band top. In addition to the differences between the symmetries of the metallocomplexes and the C_{60} molecule, the positive charge of lithium ions also contributes to the shift of the energy levels. In the fullerene complexes with alkali metals, electrons are transferred from the metal to the carbon cage of the molecule. As a result, the carbon cage acquires a negative charge, whereas the lithium atoms become positively charged (the charge of each lithium ion is ~0.6). Therefore, the C_{60} fullerene with an extra pair of electrons in the field of positively charged lithium ions can be treated as a model of the metallocomplexes under investigation. With the aim of verifying this model, we calculated the $Li@C_{60}^{2+}$ system. A comparative analysis of the total densities of states for the ions and isomers of the metallocomplexes demonstrated that the energy levels of the ions lie below the corresponding levels of the complexes. However, being aligned on the energy scale, their electronic level patterns are virtually identical (Fig. 2).

Another difference between the electronic structures of the metallocomplexes and the C_{60} molecule is in the occurrence of an extra filled level (i.e., an impurity state), which lies ~1–3 eV above the packets of filled levels and 3.5–5 eV below the vacant energy levels (the energy of the impurity state in the studied complexes is equal to ~–7 eV). The formation of the impurity state is explained by the occurrence of two electrons of lithium atoms on the carbon cage of the fullerene complex. This is confirmed by the model calculations of the C_{60}^{2-} ion (singlet). A comparison of the total densities of states for the model ion and one of the structural isomers of the fullerene complex with two lithium atoms (Fig. 2) showed that the impurity state is observed for both structures with an extra pair of electrons.

Let us now elucidate the nature of the energy level under consideration. For this purpose, it is necessary to investigate in more detail the electronic structure of the C_{60} molecule. Of particular interest is the valence band top of this compound. It is expedient to compare the structure of the electronic levels of the C_{60} fullerene and the electronic structures of the molecules characterized by the π-electron system, for example, benzene, anthracene, pyrine, etc. (Fig. 3).

Molecular electronic levels in the benzene molecule can be classified into two groups: the σ levels, which involve mixed contributions from the p_x, p_y, and s atomic orbitals of carbon and hydrogen atoms, and the π states, which are formed only by the carbon p_z orbitals. Analysis of the partial densities of states demonstrates clear separation between the peaks associated with the π-electron system (two maxima) and the peaks of all the remaining electronic levels (Fig. 3a). An increase in the number of atoms in the molecule (anthracene or pyrine) results in an increase in the number of peaks attributed to the π-electron system, even though the location and nature of the energy levels remain virtually unchanged (Fig. 3b).

Since the spherical C_{60} molecule has a surface curvature, the atomic orbitals lying in the plane of the molecular surface ($p_\|$) overlap with atomic orbitals aligned perpendicular to this surface ($p_\perp$). As a result, the fullerene molecule contains no σ- or π-type levels inherent in planar aromatic molecules (Fig. 3c). For the systems with different charges on the carbon cage of the fullerene complex, the ratios of the contributions from the $p_\perp$ and $p_\parallel$ electrons to energy levels of the valence band top also differ (see table). For the C_{60} molecule, the ratio $p_\perp/p_\parallel$ is equal to 1.1. A change in the charge of the system leads to a decrease in the $p_\perp/p_\parallel$ ratio, except for the C_{60}^{2-} cluster with a multiplicity of 1. It is evident that the ratio of the contributions from the $p_\perp$ and $p_\parallel$ electrons to a particular energy level determines its nature.

In the C_{60} molecule, the upper filled level is the quintuply degenerate bonding state h_u and the lower vacant level is the triply degenerate antibonding state t_{1u}. For singlet states of the fullerene complexes with two lithium atoms, the electron pair of the metal occupies one of the three previously triply degenerate levels (the t_{1u} state), which is split upon attachment of the lithium atoms. The nature of the impurity filled-level state remains unchanged; i.e., this is an antibonding orbital [21, 22]. This is also confirmed by the differences between the spatial structures of the fullerene metallocomplexes and the C_{60} molecule: the interatomic distances in the isomers of the metallocomplex under investigation are longer than those in the C_{60} molecule. The C_{60} molecule is characterized by two types of bonds. Bonds of the first type have a length of ~1.44 Å and are shared by hexagons and adjacent pentagons (the 6–5 bonds). Bonds of the second type have a length of ~1.39 Å and are shared by two adjacent hexagons (the 6–6 bonds). In the studied complexes, the majority of bonds between the carbon atoms become inequivalent. The observed increase in the distance between the carbon atoms is associated with the fact that the carbon orbitals make the main contribution to the impurity state of an antibonding nature. After the formation of the metallocomplex, changes in the 6–6 bond lengths of the carbon cage are most pronounced ($\Delta R_{\max}$ ~ 0.1 Å). However, for the most part, the bonds between hexagons in all the studied isomers, as before, remain shorter than those between the hexagons and pentagons.

The electronic structures of the isomers of the metallocomplexes differ in the location of the impurity filled-level state. In the exohedral complexes with the most widely spaced lithium atoms (Fig. 1d), the impurity filled level most closely approaches the vacant levels. In the case when the lithium atoms are arranged over adjacent polygons (Fig. 1f), the shift of the impurity filled level toward the packet of vacant levels is minimum. The impurity levels for other Li_2C_{60} isomers, including the endohedral complex, are intermediate in location between the above extreme cases. The distance between the lithium atoms in the isomers of the exohedral complexes has a determining effect on the location of the impurity state and, as a consequence, on the band gap (Figs. 4, 5).

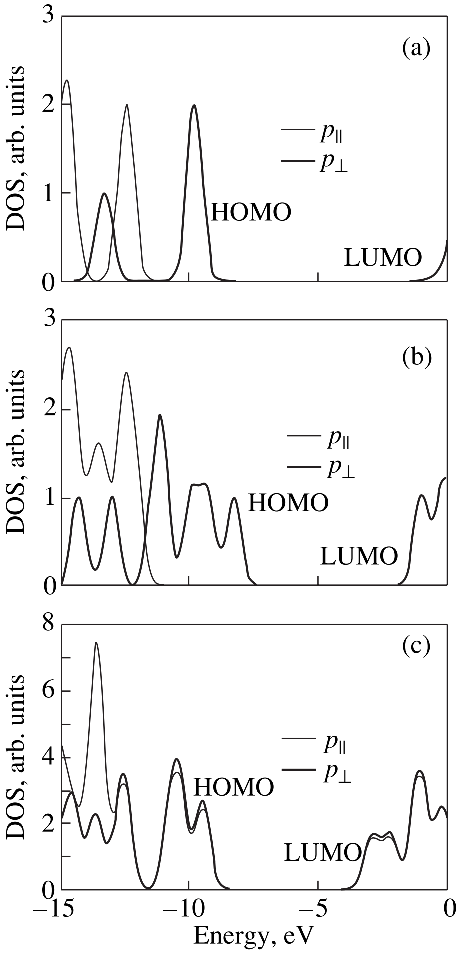

Fig. 3. Partial densities of states for (a) C_6H_6, (b) $C_{14}H_{10}$, and (c) C_{60} molecules.

As was noted above, the exohedral complexes can be divided into three groups depending on the position of the coordinated lithium ions with respect to particular faces of the fullerene polyhedron.

For each group of exohedral complexes, the band gap decreases with an increase in the distance between the lithium atoms. The dependence of the band gap on

Ratios of the contributions from the $p_\perp$ and $p_\parallel$ electrons to energy levels of the valence band top for different carbon clusters

Carbon cluster	Ratio $p_\perp/p_\parallel$ in HOMO
C_{60}	1.11
C_{60}^{1}	0.65
C_{60}^{2} MULT 1	0.98
C_{60}^{-1}	0.92
C_{60}^{-2} MULT 1	1.19
C_{60}^{-2} MULT 3	0.84

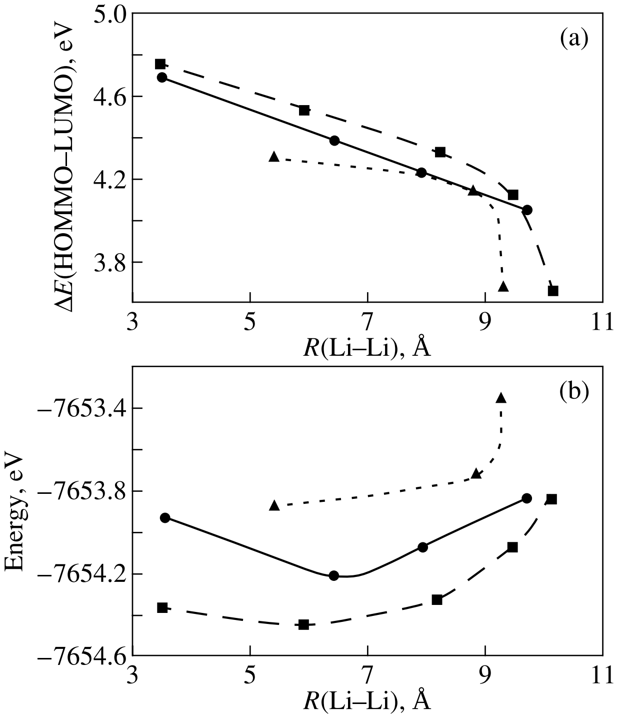

Fig. 4. Dependences of (a) the band gap and (b) the total energy of the molecule on the distance between the lithium atoms coordinated in the immediate vicinity of different polygons (pentagon–pentagon, hexagon–hexagon, and hexagon–pentagon).

the distance between lithium atoms has a linear character, except for the case of the two isomers in which the lithium atoms are located at a maximum distance from each other. In these two cases (when the lithium atoms are coordinated near either two opposite pentagons or two opposite hexagons), the band gap decreases drastically.

The situation when the metallocomplex has several isomers should be reflected in the photoelectron and optical spectra. Since the impurity levels in the electronic structure of the particular isomers of the metallocomplex differ in location, their superposition should manifest itself in the spectra. This brings about the broadening of the peak associated with the impurity state and, hence, the narrowing of the band gap.

In the exohedral complexes, the total energy, like the band gap, depends on the distance between the lithium ions and their mutual arrangement with respect to particular polygons. For each group of the studied isomers, an increase in the distance between lithium atoms leads to an increase in the total energy. The exception is provided by the isomers in which lithium atoms are arranged over adjacent polygons (either over two hexagons or over a hexagon and an adjacent pentagon). It seems likely that the increase in the total energy for these complexes is caused by the strong electrostatic repulsion between positively charged lithium ions.

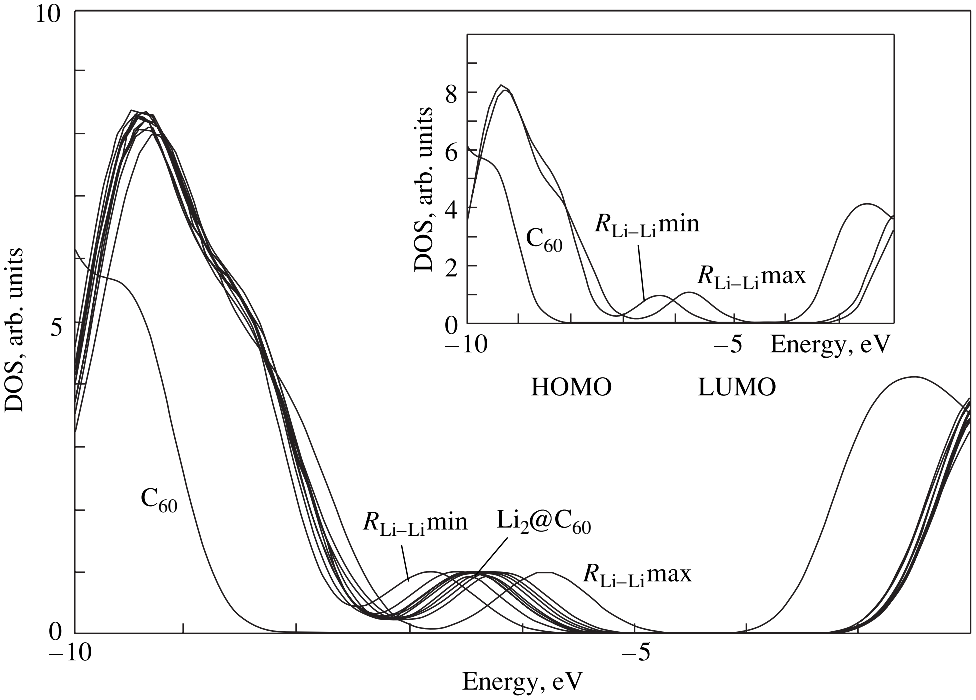

Fig. 5. Total densities of states for different Li_2C_{60} isomers.

4. CONCLUSION

Thus, the calculations demonstrated that the electronic structures of the isomers of exohedral metallocomplexes can differ in the band gap and the total energy depending on the lithium coordination. The occurrence of several isomers in the system should bring about broadening of the impurity state due to the superposition of the corresponding states of particular isomers and, as a consequence, the narrowing of the band gap, which should be reflected in the photoelectron and optical spectra of the metallocomplexes under investigation.

ACKNOWLEDGMENTS

This work was supported by the State Scientific and Technological Program "Fullerenes and Atomic Clusters" (project no. 97018), the State Program "High-Temperature Superconductivity," and the Federal Program "Integration" (project no. 69).

REFERENCES

1. N. Krawez, A. Gromov, R. Tellgmann, and E. E. B. Campbell, in *Electronic Properties of Novel Materials—Progress in Molecular Nanostructures: XII International Winterschool, Kirchberg, Tyrol, Austria, 1998*, Ed. by H. Kuzmany (American Inst. of Physics, Woodbury, 1998), p. 368.
2. Y. Yoshinari, H. Alloul, V. Brouet, *et al.*, Phys. Rev. B **54**, 6155 (1996).
3. T. Pichler, M. S. Golden, M. Knupfer, and J. Fink, in *Electronic Properties of Novel Materials—Progress in Molecular Nanostructures: XII International Winterschool, Kirchberg, Tyrol, Austria, 1998*, Ed. by H. Kuzmany (American Inst. of Physics, Woodbury, 1998), p. 271.
4. D. M. Poirier, M. Knupfer, J. H. Weaver, *et al.*, Phys. Rev. B **49**, 17403 (1994).
5. J. H. Weaver, Acc. Chem. Res. **25**, 143 (1992).
6. M. Takata, B. Umeda, E. Nishibori, *et al.*, Nature (London) **377**, 46 (1995).
7. W. Sato, K. Sueki, K. Kikuchi, *et al.*, Phys. Rev. B **58**, 10850 (1998).
8. C. Gu, F. Stepniak, D. M. Poirier, *et al.*, Phys. Rev. B **45**, 6348 (1992).
9. A. V. Eletskiĭ and B. M. Smirnov, Usp. Fiz. Nauk **165** (9), 977 (1995) [Phys. Usp. **38**, 935 (1995)].
10. H. W. Kroto, J. R. Heath, S. O. O'Brien, *et al.*, Nature (London) **318**, 162 (1985).
11. M. Takata, B. Umeda, E. Nishibori, *et al.*, Nature (London) **377**, 46 (1995).
12. S. Patchkovskii and W. Thiel, J. Chem. Phys. **106**, 1796 (1997).
13. C. G. Joslin, J. Yang, C. G. Gray, *et al.*, Chem. Phys. Lett. **211**, 587 (1993).
14. L. Pang and F. Brisse, J. Phys. Chem. **97**, 8562 (1993).
15. C. G. Joslin, J. Yang, C. G. Gray, *et al.*, Chem. Phys. Lett. **208**, 86 (1993).
16. J. Chioslovski and E. D. Fleischmann, J. Chem. Phys. **94**, 3730 (1991).
17. J. L. Ballester and B. I. Dunlop, Phys. Rev. A **45**, 7985 (1992).
18. A. B. Roĭtsin, L. V. Artamonov, and A. A. Klimov, Fiz. Nizk. Temp. **23**, 1112 (1997) [Low Temp. Phys. **23**, 835 (1997)].
19. S. A. Varganov, P. V. Avramov, and S. G. Ovchinnikov, Fiz. Tverd. Tela (St. Petersburg) **42** (2), 378 (2000) [Phys. Solid State **42**, 388 (2000)].
20. M. W. Schmidt, K. K. Baldridge, J. A. Boatz, *et al.*, J. Comput. Chem. **14**, 1347 (1993).
21. J. H. Weaver, Acc. Chem. Res. **25** (3), 143 (1992).
22. D. A. Bochvar and E. G. Gal'pern, Dokl. Akad. Nauk SSSR **209**, 610 (1973).

Translated by O. Borovik-Romanova